Extracellular vesicles as surrogated biomarkers of Prostate Cancer metabolism

A metabolomics approach to study their role in prostate cancer progression

Guillermo Bordanaba Florit

2024

Extracellular vesicles as surrogated biomarkers of Prostate Cancer metabolism

A metabolomics approach to study their role in prostate cancer progression

Guillermo Bordanaba Florit

Supervised by: Juan Manuel Falcón Pérez

Félix Royo López

2019 - 2024

eman ta zabal zazu

CIC bioGUNE
MEMBER OF BASQUE RESEARCH
& TECHNOLOGY ALLIANCE

UPV EHU

Port D'Addaia, Cala Molí
raconet meu estimat;
em sent més al teu costat
com més lluny estàs de mi
I record s'estiu passat
que semblava sense fi
i que em va fer dir en un esclat:
S'any que ve, quedaré aquí.

Acknowledgements

que de verdad te importa. La verdad has sido mi sorpresa y ya no es solo que te quiera muchísimo sino lo que confío en ti. Luego está mi Agu, mi medio olivo aquí. Uno más de la familia y así me he sentido yo también siempre contigo. Admiro lo empático y generoso que eres en todas las facetas de la vida, no te haces idea de lo mucho que me has ayudado. Todo tiene su fin, pero yo no quiero que *la casa* termine nunca.

Todo el mundo que se cruza en tu vida puede formar parte de ella de forma fugaz, temporal o quedarse para siempre. Todos ellos pueden, en un solo momento, cambiarte la vida o tu percepción de ella para siempre. Desconocidos cuando llegas y que luego parece que hayan estado siempre ahí. Muchas gracias a todos los que me habéis hecho sentir así en Bilbo, en cuatro años he compartido grandes momentos con todos y sabéis que siempre os llevaré conmigo. Y a María, sabes todo de mí y has estado siempre ahí, eres mi *Augenstern.*

Dicen los sabios que somos cada momento y cada persona que nos haya dejado un pedacito dentro. Agradezco a todas y cada uno de mis amigos que han formado y que forman parte de mí. Els dijous de Mundo, les birres a la Cívica, Festònomes, Colònies biotec, findes de matar-nos a la biblio, Sant Joans, bàsicament totes les primeres vegades de tantes coses i qualsevol plan que acabi en –tec. Also, to all *de Bongerd* drinks, liberation days, Droevendaal parties, Dutch weird events, Panda points, ICA club, library days, TT with the Greeks; basically to my Wageningen family. A Natalia, porque hiciste una mejor versión de mí y porque básicamente si no fuese por ti nunca jamás hubiese hecho un doctorado y menos en España. To the craziest lab I have ever been and I will ever be, the AG Bar-Evens. Nico, my supervisor back then, the one who made me love science again.

Por último, a mi familia. No és ni la familia més extensa del món ni tampoc la més normal del món. Però ens estimem, els estimo i m'estimen. Saber que sempre hi són, de forma incondicional és el major acte d'amor que mai he pogut sentir. Tinc sort de tenir-vos. Y volveré al castellano para mi familia aragonesa. La de sangre, que me trae recuerdos inolvidables y son mi mesa redonda donde voy a buscar opinión. La familia está creciendo y no puedo sentirme más orgulloso de poder formar parte de ello. Luego está mi otra familia aragonesa, mis primos. No haría falta ni mencionaros, siempre habéis estado en mi vida y siempre lo vais a estar. A s'àvia, s'única que tenc i sa que sempre a mirat de fer-me feliç i cuidar-me. Bé, tu i l'avi. Adrián José, qué voy a decir de ti si es que estás siendo ahora mismo para mí un gran ejemplo en todo. Sa mamà y papá, lo que soy es únicamente por vosotros.

Table of Content

Abstract

Prostate cancer is an exclusive disease suffered by men which signifies an important thread upon aging. Indeed, it causes a huge socio-economic impact due to the lack of sensitive and specific diagnostic tools to surveil early stages during disease progression. Prostate cancer is a multifocal with several molecular and histopathological arrangements. Even though many of the different underlying mechanisms of progression have been studied, the physiological drivers and consequences in the disease's evolution are not fully understood. Prostate cancer grows and further invades adjacent tissues; upon progression, it exhibits a wide variety of metabolic, proteomic and transcriptomic landscapes. This heterogeneity provides a high flexibility and adaptability to treatments and complicates its diagnosis.

The interaction between cells is imperative for a disease to progress. In 1967, Peter Wolf was the first scientist to report a new subcellular structure, mammalian-like vesicles secreted by cells. Nowadays, these secreted vesicles are considered important cell-to-cell communication players and they are known as the extracellular vesicles. Extracellular vesicles are bilayer lipid containers secreted by most cell types to extracellular space. They are multi-purpose carriers, nano- to micrometre-sized, that can carry lipids, proteins, metabolites, sugars, RNA and even DNA. They are highly heterogeneous with a diversity of biogenesis pathways that govern partly their composition. Both surface molecules and their internal cargo can trigger intracellular signalling processes that activate downstream physiological responses i.e. cell maturation, coagulation or establishment of pre-metastatic niche in recipient cells, among others.

Metabolic reprograming mediated via extracellular vesicles is present in many biological systems where cell types with various functionalities exchange metabolic assets. During oncogenesis, extracellular vesicles from cancer tissues or supporting tissues can drive metabolic changes by providing metabolic resources or triggering signals required for cancer progression. An increasing number of publications describe extracellular vesicles as relevant mediators in cancer progression processes. Until the appearance of *metabolomics* technologies, molecular biology and physiology approaches were utilised to acquire data that could describe the interaction between biological components and functions. Metabolomics enables to measure, identify and (semi-)quantify a large number of metabolites in a biological system. Then,

the metabolomics output is utilised to explain physiological processes or observed phenotypes. A targeted approach using liquid chromatography coupled to a mass spectrometer was the most well-suited for the objectives of this thesis.

The present thesis dissertation focused on the study of extracellular vesicles cargo and the manner it interacts with and transfer cargo to recipient cells. Thence, it has been organised according to specific work packages that included:

On chapter dedicated to the bibliographic identification and review of the current methodologies to characterise extracellular vesicles. The heterogeneity of their structure and composition hinders their application in medical diagnosis and therapies. This diversity makes it difficult to establish their exact physiological roles, and the functions and composition of different extracellular vesicle (sub)populations. Ensemble averaging approaches, i.e. omics, tend to obscure rather than reveal these heterogeneities. Recent developments in single-vesicle analysis revealed new insights in cell-to-cell communication and, identification and validation of biomarkers. Nonetheless, omics approaches are still relevant to study extracellular vesicle-mediated physiological processes in biological models.

Chapter 2 of the thesis focussed on the exploration of the role of extracellular vesicles cargo in early stages of prostate cancer progression and the identification of markers to understand the progression of a disease. In this context, steroid hormones play a vital role in the regulation of cellular processes, and dysregulation of these metabolites can provoke or aggravate pathological issues, such as autoimmune diseases and cancer. In prostate cancer, they are the main drivers of oncogenicity at the very early stages of the disease. Therefore, the quantification of specific mRNAs in relevant biological samples such as urine is a powerful asset to diagnose tumoral growth. In this section, 32 potential markers of prostate cancer progression were identified using CANCERTOOL. These candidates discriminate between prostate cancer and benign hyperplasia patient samples and can also consider metastatic stages. Moreover, different scientific studies have described such mRNAs in extracellular vesicle samples. A panel of these candidates was quantified in a human cohort of urines. Unfortunately, it was not possible to describe any candidate as a valid biomarker in patient samples to be tested further.

Chapter 4 is focussed in functional studies, in particular the oncogenic status of cancer cells was assessed by measuring the expression of specific genes associated to androgen dependent growth. The proliferative rate of cells is also a complementary indicator of oncogenicity. In these experiments, LNCaP was the most appropriate model to study androgen-dependency and *KLK3* expression the best reporter of androgen-depletion treatment. By treating androgen dependent LNCaP model with extracellular vesicles, one aimed to describe whether extracellular vesicles stimuli could sustain oncogenic growth in recipient cells. The oncogenic status was assessed by *KLK3* expression, since it demonstrated to report loss of oncogenicity. The proliferative status of prostate cancer cells was also considered to evaluate extracellular vesicle treatments. Upon depletion of steroids, *KLK3* expression dramatically decreased over time. This loss of oncogenic phenotype was neutralised with the presence of extracellular vesicles isolated from cell cultures with steroid hormones in growing media. Therefore, extracellular vesicles delivered physiological functionalities that are yet to be described. Furthermore, additional experiments should be performed to evaluate the capabilities of extracellular vesicles to stimulate such oncogenic growth in a cell culture.

These results support the hypothesis of a transference of functionalities between extracellular vesicles and recipient cells. In order to study the presence of steroid hormones related metabolites in transfer events, chapter 3 describes a metabolomics assay developed to explore more in detail the role of steroid metabolites in prostate cancer and EV-mediated progression. The extraction and quantification of 11 key members of the different steroid classes, including androgens, estrogens, progestogens and corticoids is described in this work. Yet, additional metabolites can be implemented to the assay. It consists of a biphasic liquid/liquid extraction step and subsequent quantification by high-resolution liquid chromatography coupled to time-of-flight mass spectrometry. The recoveries range between 74.2 to 126.9% and 54.9 to 110.7% for apolar and polar steroid related metabolites, respectively. In general, the signal intensity loss due to matrix effect is no more than 30%. In order to assess its performance in relevant biological samples, the method has been tested in many matrices as rat tissues, human urines, human cell lines and extracellular vesicles. Overall, the proposed methodology measures steroid hormone related analytes simultaneously in 6 min runtime and, cholesterol can be included by extending the chromatographic gradient and the run time to 9 min. Nonetheless, another application of the method was to validate a steroid hormone metabolic signature as a biomarker for prostate cancer.

In prostate cancer, lipids and specifically cholesterol play a pivotal role in its progression. Cholesterol serves as signal for protumorigenic metabolic pathways because it is the main precursor of steroid hormone metabolism. Remarkably, extracellular vesicles are enriched with cholesterol, being approximately a 50 to 60% of their lipid content. The effective transfer of extracellular vesicle-associated metabolites to recipient cells has not been extensively explored yet. In chapter 4 of this thesis, prostate cancer cell cultures were treated with labelled cholesterol in lipid-depleted media. Then, purified extracellular vesicles were fed to non-labelled recipient cells to trace the internalisation of cholesterol by confocal microscopy and its further metabolisation with the presented UPLC-MS assay. Cholesterol associated to extracellular vesicles was detected in unlabelled recipient cells. Moreover, by labelling prostate cancer cells with a cholesterol stable isotope, labelled extracellular vesicles were reported. In summary, it has been demonstrated that a targeted metabolomics assay combined to a molecular biology approach is useful to study extracellular vesicle-mediated internalisation and the effective transfer of relevant metabolites as cholesterol.

Finally, a broader metabolomics approach was utilised to study the interaction between different compartments of the prostate gland (Chapter 5). The prostate gland is a complex and heterogeneous organ composed of epithelium and stroma. Prostatic stroma is complex, and in concert with disease progression undergoes alterations which include the emergence of a cancer associated fibroblast phenotype. The heterogeneous cell population in tumorigenic stroma often includes cells with a myofibroblast-like phenotype that are not normally present in healthy prostate tissue. By using patient-matched normal and tumour-associated needle biopsies, the metabolic rewiring of stromal fibroblasts undergoing myofibroblast differentiation was evaluated. It was determined that cancer-associated fibroblasts are metabolically more active and, therefore, energy producing metabolic pathways are enhanced. Also, cancer-associated fibroblasts show heightened lipogenic metabolism as both reservoir species and building block compounds were quantified in higher levels. In addition, prostate cancer-derived extracellular vesicles were incubated with healthy fibroblasts. An increased basal respiration was reported, mirroring the disease-like phenotype. One can propose the change in the metabolomics profile of tumour-associated stromal fibroblasts is driven by oxygen-dependent metabolism; however, the specific mechanisms are still unclear.

Resumen

El cáncer de próstata es una enfermedad que únicamente padecen los hombres y una de las más amenazantes con la edad. Esta afección causa un grave problema socio-económico debido a la falta de sensibilidad y especificidad en el diagnóstico durante fases iniciales de su desarrollo. El cáncer de próstata es multifocal y extremadamente diverso tanto a nivel molecular como histopatológico. También posee una gran variedad de mecanismos de progresión, pero las consecuencias fisiológicas derivadas y manera de evolucionar son todavía una incógnita. El crecimiento tumoral descontrolado y metástasis a tejidos cercanos genera una gran diversidad de perfiles metabólicos, proteómicos y transcriptómicos. Esta heterogeneidad sus diferentes fases proporciona flexibilidad y adaptabilidad a los tratamientos y, por lo tanto, también complica su diagnóstico.

La comunicación celular es imprescindible para el progreso de cualquier enfermedad. Fue en 1967 cuándo Peter Wolf describió una nueva estructura subcelular: vesículas expulsadas por células. Actualmente, se ha demostrado que estas vesículas juegan un papel importante en la interacción celular. Estas vesículas extracelulares son estructuras delimitadas por bicapas lipídicas expulsadas por la gran mayoría de células. Su tamaño oscila entre nanómetros y micrómetros de diámetro y, pueden contener lípidos, proteínas, metabolitos y ácidos nucleicos, incluyendo ARN y ADN. Se trata de estructuras extremadamente heterogéneas en tamaño y composición, que está determinada en gran medida por las rutas de biogénesis que las formen. Tanto las moléculas de la membrana como las encapsuladas en el interior pueden activar cascadas de señalización que pueden producir respuestas fisiológicas como la maduración celular, eventos de coagulación o el establecimiento de nichos premetastáticos, entre otros.

La reprogramación metabólica mediada por vesículas extracelulares se ha observado en muchos sistemas biológicos donde diferentes células, que pueden tener distintas funciones y orígenes, intercambian recursos metabólicos. Durante la oncogénesis, las vesículas extracelulares de los tejidos cancerosos o los tejidos adyacentes pueden inducir cambios metabólicos al proporcionar recursos metabólicos o desencadenando señales necesarias para su progresión. De hecho, las vesículas extracelulares se describen como mediadores relevantes en

los procesos de progresión del cáncer. Hasta la aparición de las tecnologías "omicas", se utilizaron enfoques de biología molecular y fisiología para obtener datos que pudieran describir la interacción entre componentes y funciones biológicas específicas. La metabolómica tiene como objetivo medir, identificar y cuantificar un gran número de metabolitos en un sistema biológico determinado. Una estrategia de metabolómica dirigida utilizando cromatografía líquida acoplada a un espectrómetro de masas es el más adecuado para los objetivos de esta tesis.

La presente tesis se centra en el estudio del contenido de las vesículas extracelulares y la manera en que interactúa con las células receptoras. Con este propósito, se ha dividido según paquetes de trabajo específicos que incluyeron:

Un primer capítulo dedicado a la identificación bibliográfica y revisión de las metodologías actuales para caracterizar las vesículas extracelulares. La heterogeneidad de su estructura y composición dificulta su aplicación en diagnósticos médicos y terapias. Dicha diversidad también dificulta el establecimiento de roles fisiológicos, así como las funciones y composición de diferentes (sub)poblaciones de vesículas extracelulares. Los métodos que promedian el contenido de las muestras, como es el caso de las "ómicas", tienden a diluir estas heterogeneidades. Los desarrollos recientes en el análisis individual de vesículas han revelado nuevas perspectivas en la comunicación entre células, así como la identificación y validación de biomarcadores. Sin embargo, hay que tener en cuenta que los enfoques 'ómicos' siguen siendo relevantes para estudiar procesos fisiológicos asociados a vesículas extracelulares a escala más global dentro de un modelo biológico.

La investigación más detallada de la carga de vesículas extracelulares es de gran utilidad para determinar posibles mecanismos de progresión del cáncer en etapas tempranas de su desarrollo. En este sentido, las hormonas esteroides desempeñan un papel vital en la regulación de procesos celulares, y la desregulación de estos metabolitos puede provocar o agravar problemas patológicos, como enfermedades autoinmunes y cáncer. En el cáncer de próstata, son los principales impulsores de la oncogenicidad en las etapas muy tempranas de la enfermedad. Por lo tanto, la cuantificación de ARNm específicos en muestras biológicas relevantes, como la orina, es un recurso poderoso para diagnosticar la enfermedad. En el capítulo 2, se desarrollaron ensayos cuantitativos de ADN para estudiar la expresión de ARNm específicos. Primero, se identificaron 32 posibles marcadores de progresión del cáncer de

próstata utilizando CANCERTOOL. Estos candidatos discriminan entre muestras de pacientes con cáncer de próstata e hiperplasia benigna, ya sea incluyendo muestras con presencia de metástasis o ambas. Además, diferentes estudios científicos los han descrito en vesículas extracelulares. Un panel de dichos candidatos, se cuantificó en una cohorte de orinas de pacientes humanos. Lamentablemente, no fue posible describir a ningún candidato como un biomarcador válido en muestras de orina para ser probado más a fondo.

Focalizando en estudios funcionales, el estado oncogénico de las células cancerosas puede evaluarse midiendo la expresión de genes asociados al crecimiento dependiente de andrógenos (Capítulo 4.2.). La tasa proliferativa de las células también es un indicador complementario de la oncogenicidad. La línea celular LNCaP fue el modelo más apropiado para estudiar la dependencia de andrógenos y la expresión de *KLK3* el mejor indicador del tratamiento de depleción de andrógenos. Tratando el modelo dependiente de andrógenos LNCaP con vesículas extracelulares, se perseguía describir si las vesículas extracelulares podían mantener el fenotipo oncogénico en las células receptoras. El estado oncogénico se evaluó midiendo la expresión de *KLK3*, que está asociado a la cascada de señalización de andrógenos. También se consideró el estado proliferativo de las células de cáncer de próstata para evaluar los tratamientos con vesículas extracelulares pero este no proporcionó resultados significativos. Tras la depleción de esteroides, la expresión de *KLK3* disminuyó drásticamente con el tiempo. Esta pérdida de fenotipo oncogénico fue neutralizada con la presencia de vesículas extracelulares aisladas de cultivos celulares con crecimiento oncogénico. Esto indica la participación de vesículas en la transferencia de fenotipo oncogénico aunque no explica las implicaciones en la fisiología del cáncer.

Estos resultados sugieren una transferencia de funcionalidades entre las vesículas extracelulares y las células receptoras. Esta transferencia puede darse a través de proteínas que activen cascadas de señalización o con diferentes recursos metabólicos. En el capítulo 3, para estudiar la presencia de metabolitos relacionados con hormonas esteroides en estos eventos de transferencia, se desarrolló un ensayo de metabolómica. La extracción y cuantificación de 11 miembros clave en la red metabólica de hormonas esteroideas, incluyendo andrógenos, estrógenos, progestágenos y corticoides, se describe en el capítulo 3 de esta tesis. Una característica importante de este tipo de ensayos es que se pueden implementar metabolitos adicionales *a posteriori*. El ensayo consiste en una extracción bifásica líquido/líquido y la subsiguiente cuantificación mediante cromatografía líquida de alta resolución acoplada a

espectrometría de masas de tiempo de vuelo. Las eficiencias de recuperación oscilan entre el 74.2% y el 126.9%, y el 54.9% y el 110.7%, para los compuestos apolares y polares, respectivamente. En general, la pérdida de intensidad de señal debido al efecto de matriz no supera el 30%. El método se ha probado en diversas matrices, como tejidos de ratas, orinas humanas, líneas celulares humanas y vesículas extracelulares. En resumen, este ensayo puede medir simultáneamente metabolitos relacionados con hormonas esteroideas en un tiempo de ejecución de 6 minutos el cual puede incrementarse a 9 min para incluir el colesterol en el análisis. Además de su uso en estudios de transferencia, otro propósito del método era el de validar una firma metabólica de hormonas esteroides como biomarcador para el cáncer de próstata.

Los lípidos y específicamente el colesterol desempeñan un papel fundamental en la progresión del cáncer de próstata. El colesterol es importante en vías metabólicas protumorales ya que es el precursor principal del metabolismo de hormonas esteroideas. Además, las vesículas extracelulares están enriquecidas con colesterol, constituyendo aproximadamente del 50 a 60% de su contenido lipídico. La transferencia efectiva de metabolitos asociados a vesículas extracelulares todavía no se ha explorado. En el capítulo 4.1. se trataron cultivos de células de cáncer de próstata con colesterol marcado en medios desprovistos de lípidos. Luego, las vesículas extracelulares purificadas se suministraron a células receptoras no marcadas para rastrear la internalización de colesterol mediante microscopía confocal y su posterior metabolización mediante el ensayo dirigido UPLC-MS descrito anteriormente. En este trabajo, se detectó colesterol asociado a vesículas extracelulares en células receptoras no marcadas. Además, al marcar las células de cáncer de próstata con un isótopo estable de colesterol, se detectaron vesículas extracelulares marcadas. En resumen, se ha demostrado que un ensayo de metabolómica dirigida combinado con un enfoque de biología molecular es útil para estudiar la internalización mediada por vesículas extracelulares y la transferencia efectiva de metabolitos relevantes como el colesterol.

Finalmente, se utilizó una estrategia metabolómica semidirigida para estudiar la interacción entre diferentes compartimentos de la glándula prostática (Capítulo 5). La glándula prostática es un órgano complejo y heterogéneo compuesto por el epitelio y el estroma. El estroma prostático es complejo y, en conjunto con la progresión del tumor, experimenta alteraciones que incluyen la aparición de un fenotipo de fibroblasto asociado al cáncer. Esta población celular tan heterogénea a menudo incluye células con un fenotipo similar al miofibroblasto

que no están presentes en tejido prostático sano. Al utilizar biopsias de aguja de tejidos tumorales y normales asociados al mismo paciente, se pudo estudiar la reconfiguración metabólica de los fibroblastos estromales que experimentan una diferenciación hacia miofibroblastos. Se determinó que los fibroblastos asociados al cáncer son metabólicamente más activos y, por lo tanto, se ven aumentadas las vías metabólicas de producción de energía. Además, los fibroblastos asociados al cáncer muestran un metabolismo lipogénico elevado tanto por la presencia de compuestos de reserva lipídica como de vertiente estructural. Así como en estrategias anteriores, se incubaron vesículas extracelulares derivadas de líneas celulares de cáncer de próstata con fibroblastos primarios sanos. Se detectó un aumento en la respiración basal de los fibroblastos, reflejando el fenotipo similar a la enfermedad. Con estos resultados, se puede proponer que el cambio en el perfil metabolómico de los fibroblastos estromales asociados tejido tumoral está impulsado por vías metabólicas dependientes de oxígeno; sin embargo, los mecanismos específicos aún no están claros.
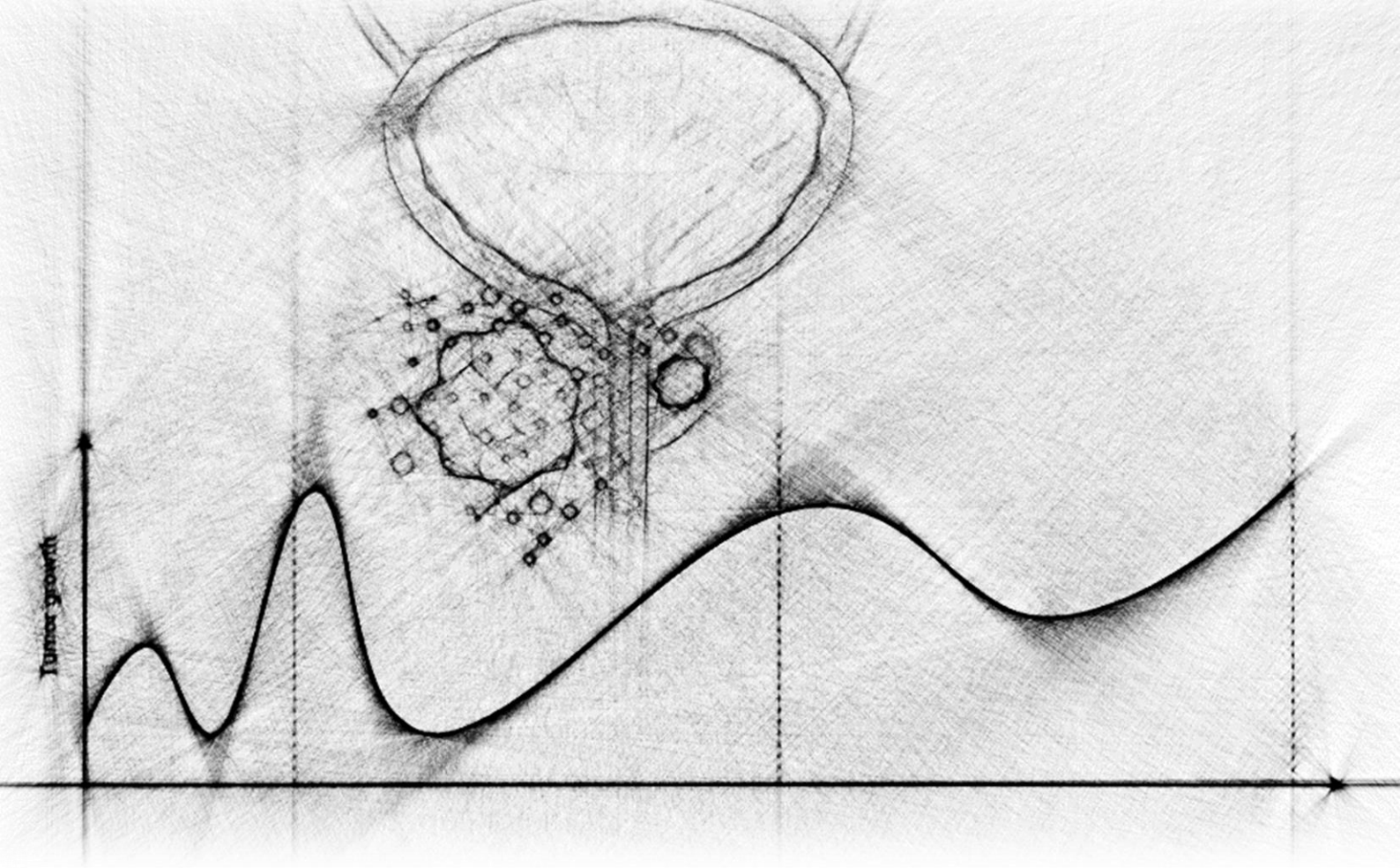
INTRODUCTION

I.   Prostate Cancer Disease

The World Health Organisation describes prostate cancer as one of the most frequently diagnosed and deadly types of carcinomas. It is a global healthcare problem with an incidence of approximately a quarter of all cancer diagnoses in Europe. Prostate cancer (PCa) is an exclusive disease of men that misses sensitive and specific diagnostic tools to surveil early stages of its progression. This causes a huge socio-economic problem for families, partners and caregivers, through loss of life or protracted palliative incapacity. In fact, many men initially attend clinic with a tumour that is already in an advanced and incurable state. Prostate cancer is often a multifocal disease and even within a single tumour, several molecular and histo-pathological arrangements are observed. Many of the underlying mechanisms of progression have been proposed as possible targets for diagnostics and therapeutics; however, the physiological drivers and consequences in its evolution are not fully understood.

Nowadays, prostate-specific antigen (PSA) blood screening tests are the cornerstone for PCa surveillance at early stages. Up to 40% of men undergo unnecessary biopsies due to its poor specificity. Upon biopsy of the patient, the serum PSA test is combined with the clinical T-stage and Gleason score as standard tests to discriminate patients with low, intermediate or high risk to suffer PCa[1]. The progression of PCa within prostatic tissue is very diverse, so it is at metastatic stages. Metastases principally occur in bone and lymph node tissues but they are also reported in liver, lung and brain tissues[2]. This diversity causes variation in therapy response and resistance mechanisms. A high proportion of men exhibit slow growing tumours that are unlikely to progress to a life-threatening stage. Often, initial treatments of androgen-ablation reliably trigger regression but this is temporary, and within 2-3 years, castrate resistant PCa may recur, becoming a particularly intractable and aggressive disease. Yet, discrimination of indolent from aggressive disease is difficult. For these men, the identification of novel targetable pathways to be considered during decision-making process for therapeutic intervention. Furthermore, a better understanding of PCa disease will also help to design improved treatment strategies.

Above all, understanding the molecular and physiological mechanisms of PCa disease hold an enormous potential to transform disease diagnosis, patient stratification and novel treatment modalities; providing superior information of wealth. Researchers need to decipher the secrets of PCa, from the spark that unleashes cancer development to the survival strategies improved by tumour cells.

Prostate gland

The prostate is the main accessory gland of the male reproductive system. The human prostate is a walnut-sized organ whose base is located at the urinary bladder neck and the apex at the urogenital diaphragm (Figure 1). As far back as the mid-sixteenth century, when Andreas Vesalius published his observations of the male accessory glands, prostate anatomy was of medical interest[3]. Interestingly, the macroscopic anatomy of this organ differs considerably between species. Rodent model organisms such as rats or mice utilised are to model human diseases; therefore, it is important to acknowledge the differences in the structure of human and rodent prostates. Unlike human, rat or mouse prostate is not merged into a unique anatomical structure with three glandular regions but it is composed of four distinct

lobular structures (Figure 1). Nonetheless, there is no existing evidence that supports a direct relation-ship between the specific mouse prostate lobes and the specific zones in the human prostate[4].
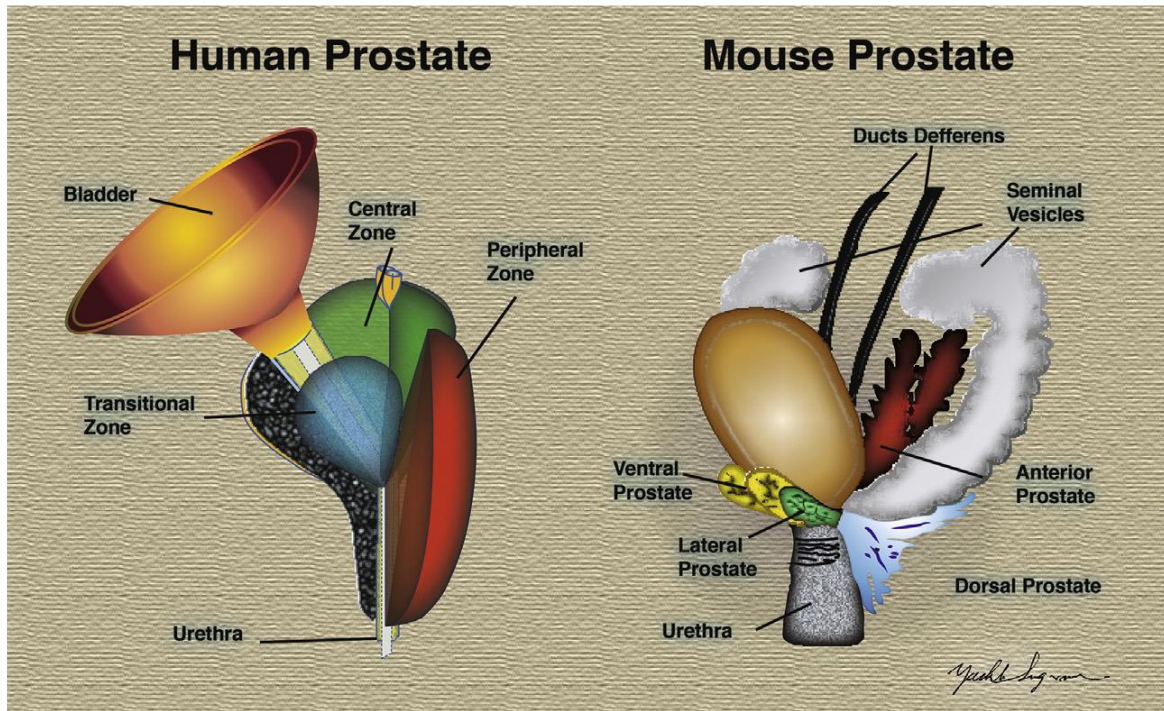
Figure 1. Representation of a human and a mouse prostate. On the left, a diagram of an adult human prostate where the urethra, the bladder and the three major regions of a prostate are indicated. On the right, a mouse prostate is depicted. It is structured in four lobes (similar to rat organization): lateral prostate, dorsal prostate, ventral prostate and anterior prostate. [5]Reprinted from Urologic Clinics of North America, 282, LaTayia Aaron, Omar E. Franco, Simon W. Hayward, *Review of Prostate Anatomy and Embryology and the Etiology of Benign Prostatic Hyperplasia*, Volume 43, Issue 3, Copyright 2016, with permission from Elsevier.

In humans, the prostate gland contains three major glandular regions, which differ both histologically and biologically: the peripheral zone, the central zone, and the transition zone. The latter is the main origin of prostate hyperplasia[6] and carcinoma is more common in the peripheral zone[7]. At a histological level, the prostate is a branched duct organ organized in glandular acinis constructed by the epithelium and sustained by the stroma[7]. The two compartments influence each other via signalling pathways to promote prostate development and correct functioning[8]. Both tissues are extremely heterogeneous with many types of cells participating in different physiological functions. The epithelium contains secretory epithelial cells around the glandular lumen, where they secrete the prostatic fluid (Figure 2A). These secretory cells, also called luminal cells, are surrounded by basal cells and sparse neuroendocrine cells, both attached to a basal lamina[9,10]. Basal cells are associated to ductal integrity and secretory cell supportive functions while neuroendocrine cells role is rather unclear. Yet, it is known they secrete specific hormones and lack the expression of androgen receptor. Fundamentally, the prostate epithelial compartment holds the man glandular function: The secretion of prostatic fluid to the lumen (Figure 2A). The prostatic fluid is the major contributor to the ejaculate volume and contains factors to control maturation and motility of sperm or the ejaculate's fluidity, among others.

Beyond the basal lamina, a prominent fibromuscular stroma offers physical support and contraction of the gland (Figure 2A). A major function of the stromal compartment is to ensure the appropriate microenvironment for the epithelial compartment, which is provided principally by surrounding fibroblasts. In addition, it participates in the vascularisation of the prostate but also evacuates prostatic fluid towards the urethra by contraction. Remarkably, the stromal compartment provides many supportive signals to retain or restore gland homeostasis in healthy conditions or during regeneration processes[6].

Prostate cancer progression

The structure and well-functioning of the prostate is often impaired with aging and, finding the molecular or physiological mechanism that triggers PCa to spark is the one-billion dollar question. In general, it is accepted that tumour initiating cells undergo specific biological modifications such as the inactivation of certain pathways or the expression of specific genes. The prostate gland frequently suffers from inflammation due to an overgrowth of stromal cells (and epithelial cells) at transition zone and periurethral areas, which is usually associated to benign prostatic hyperplasia (BPH). However, when the growth is localised in specific *loci* of the prostate and associated to the epithelium it is prone to be an initiating tumour. The identification on gross inspection of PCa by palpation of the gland is often challenging. According to experts, the foci should be at least 5 mm in diameter for reliable diagnosis as tumours tend to be multifocal[6]. Besides, much larger areas can neither be accurately identified. As mentioned, tumours are mainly found in the peripheral zone[11,12], followed by the transition zone and then central zone.
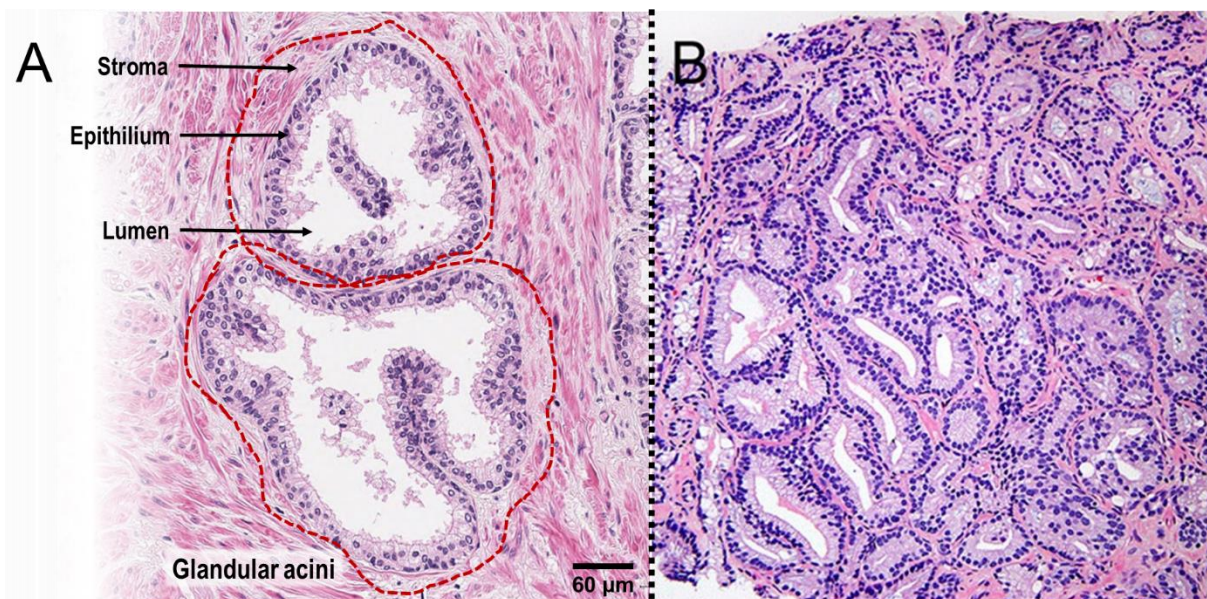
Figure 2. Histological section of a human prostate tissue slice. Hematoxylin plus eosin provides a comprehensive picture of microanatomy of tissues by precisely staining nuclear (hematoxylin) and cytoplasmic (eosin) components. A. Healthy prostate tissue with glandular acini is depicted; a dotted red line delimitates the structure. The three different compartments are indicated with black arrows. B. Prostate cancer tissue in an advanced stage, with Gleason score 7 (3+4) and minor components of cribriform glands. Images are adapted from http://commons.wikimedia.org, and reproduced with permission under Creative Commons Attribution 4.0 International License http://creativecommons.org/licenses/by/4.0/.

Table 1. Summary of the current TNM staging classification based on AJCC's classification. Adapted from [7,13,14].

Stage	Definition
Primary tumour, clinical (T)	
TX	Primary tumour cannot be assessed.
T0	No evidence of primary tumour
T1	Clinically inapparent tumour not palpable or visible by imaging. Slow growing and PSA levels are low.
	T1a: Tumour incidental histologic finding in 5 % or less of tissue resected.
	T1b: Tumour incidental histologic finding in more than 5 % of tissue resected.
	T1c: Tumour identified by needle biopsy (i.e. because of elevated PSA levels.
T2	Tumour confined within the prostate[a]. PSA levels are medium or low.
	T2a: Unilateral. Tumour involves half of one lobe or less.
	T2b: Unilateral. Tumour involves more than half of one lobe but not both. It can be large enough to be felt by DRE.
	T2c: Bilateral. Tumour involves both lobes.
T3	Tumour extends through the prostate capsule[b].Locally advanced tumour with high levels of PSA.
	T3a: Extracapsular extension (unilateral or bilateral).
	T3b: Tumour invades seminal vesicle(s).
	T3c: Tumour cells are poorly differentiated. Perhaps, invasion of bladder or rectum.
T4	Tumour is fixed or invades adjacent structures other than the seminal vesicle(s): bladder neck, external sphincter, rectum, levator muscles, pelvic wall, or all the above.
	T4a: Tumour has spread to regional lymph nodes.
	T4b: Tumour has invaded distant lymph nodes or other tissues such as bones (i.e. pelvic wall), levator muscles, external sphincter and others.
Regional lymph nodes (N)	
NX	Regional lymph nodes cannot be assessed.
N0	No regional lymph node metastasis.
N1	Metastasis in regional lymph node or nodes.
Distant metastases[d] (M)	
MX	Distant metastasis cannot be assessed.
M0	No distant metastasis.
M1	Distant metastasis.
	M1a: Non-regional lymph node(s).
	M1b: Bone(s).
	M1c: Other site(s).

[a] Tumour that is found in one or both lobes by needle biopsy, but not palpable or reliably visible by imaging, is classified as T1c.

[b] Invasion into the prostatic apex or into (but not beyond) the prostatic capsule is classified as T2, not T3.

[c] There is no pathologic T1 classification.

[d] When more than one site of metastasis is present, the most advanced category is used; pM1c is most advanced.

After palpation a patient may undergo a biopsy procedure. At this stage, in both surgical specimen and needle biopsy, the histologic grading of PCa by the Gleason system is the strongest prognostic factor[7,15,16]. The Gleason system describes the histological architecture of PCa with a scoring grading from 1 to 5. Well-differentiated PCa (Gleason grade 1 or 2) is characterized by a proliferation of micro-acinar structures lined by prostatic luminal cells without an accompanying basal cell layer while Gleason pattern 5 includes a solid pattern with central necrosis or infiltrating individual cells. Considering the high heterogeneity of PCa, Gleason decided to include a primary and a secondary grading to the system[17]; further obtaining a combined Gleason score which ranges from 2 (1+1) to 10 (5+5). Yet internationally accepted, there are several issues concerning this grading system since it is dependent on the observer's expertise and, it may vary regarding the clinical history of the patient. Moreover, intermediate scores i.e. 7 should better be redefined as 3+4 or 4+3 because their prognosis is also different. Other histological parameters as perineural invasion, lymph node status or seminal vesicle involvement also hold prognostic information and must be considered in tumour classification tables (Table 1).

In the last century, there have been several efforts to classify PCa stages of progression. It was in the early 1950s when the PCa community established the first staging system for solid tumours. It can be associated to other staging systems as Gleason score and it considers a Tumour-Lymph node-Metastasis (TNM) classification to analyse tumour's level of development and prognosis (Table 1). There are sublevels based on tumour volume or extent (T1–T4), amount and/or size of lymph node metastases (N0–N3), and distant metastases (M0–M1). Considering all the attempts, the American Joint Committee on Cancer (AJCC) decided to release (in 1992) a staging system which mirrors the TNM system and considers a particular clinico-pathological classification of each tumour[13]. This new system led to a more precise analysis of the tumour and stratification of patients into prognostically distinct groups. However, staging systems are in constant revision and improvement to evaluate each patient's prognosis. For example, 90% of prostatic adenocarcinomas exhibit a typical acinar morphology but there is a spectrum of morphologies that differ and hence, PCa subtypes not well classified nor described. Variants of the conventional PCa such as pseudohyperplastic, foamy gland, hypernephroid, atrophic, ductal carcinoma, sarcomatoid carcinoma, basal cell and adenoid cystic carcinoma, primary urothelial carcinoma of the prostate can be graded according to Gleason system, however, they do not have any know prognostic significance or it is very poor[18]. Rarer prostatic adenocarcinoma cannot be properly assessed with the current systems henceforth, continuous evaluation and development of diagnostic system is required.

PCa metabolic rewiring

Prostate cancer is a multifactorial and heterogeneous disease with wide variety of metabolic, proteomic and transcriptomic landscapes along stages of progression. During its development, the tumour grows and invades neighbour and distal tissues as summarised in the previous section. Upon progression, cancer cells become metabolically auto-sufficient by maximizing the consumption and production of energy by means of specific molecular mechanisms that trigger a set of metabolic adaptations[19]. The specialised and unique metabolism of prostate gland, characterised by the active production and secretion of citrate[20–22], is switched to fuel-efficient metabolic routes capable of producing energy in the

onset and progression of PCa. From an extremely unproductive secretion of citric acid, cancer cells can increase their glycolysis rate for a faster energy production of energy, run Krebs cycle normally, and produce fatty acids using citric acid as a reservoir or ferment pyruvate to lactate.
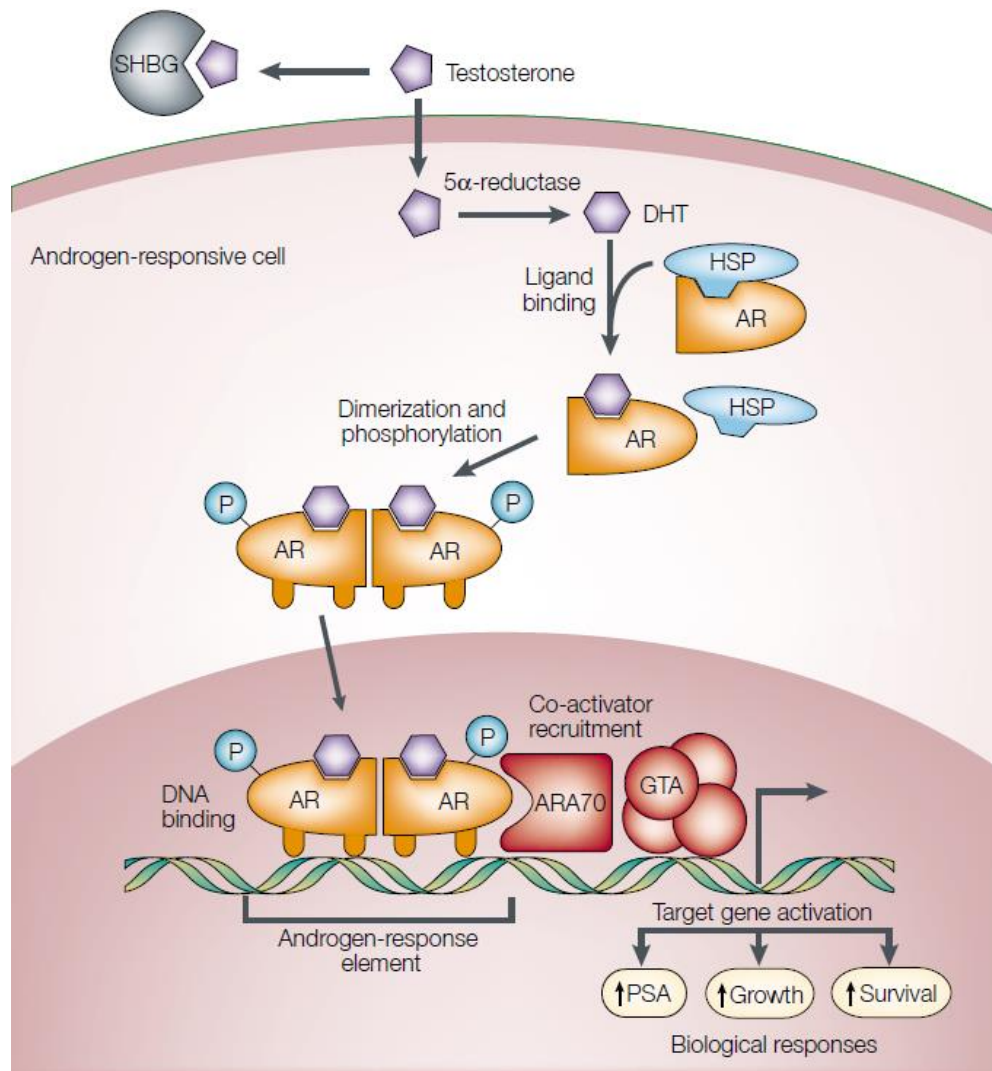
Figure 3. Summary of androgen signal transduction in androgen-responsive cells. Circulating testosterone bound to albumin and SHBG is internalised and converted to DHT. DHT binds to AR, which is now able to dimerise and penetrate the nucleus. This coupling allows AR to bind androgen response elements (AREs) in the promoter regions of target genes.
AR: Androgen receptor; ARE: androgen response element; DHT: Dihydrotestosterone; HSP: Heat shock protein; PSA: prostate-specific antigen; SHBG: sex-hormone-binding globulin.
Extracted from [23].

Cancer cells manifest an enhanced glycolytic activity that usually implies the ineffective burning of glucose via aerobic glycolysis. This metabolic adaptation, known as *Warburg effect*, satisfies the high energy demands and proliferative rates of tumorigenic cells. In such glycolytic cells, pyruvate – a glycolysis product – is fermented to lactate instead of being shuttled to mitochondria (for further oxidative phosphorylation or OXPHOS) even in high O_2 concentrations. Remarkably, PCa displays active glycolysis and OXPHOS, becoming more efficient in the use of glucose as substrate since it also provides metabolic intermediates for anabolic processes and biomass growth[19,24]. One can only observe *Warburg effect* in metastatic stages of PCa[22,25]. The non-essential aminoacid glutamine is also a key factor

in fuelling cancer cell growth[26]. Uptake of glutamine is increased in PCa cells as well as the expression of glutaminase in mitochondria, where glutamine is converted into glutamate and further transformed to α-ketoglutarate, a component of tricarboxylic acid (TCA) cycle. By feeding TCA (or Krebs) cycle, glutamine participates in fuelling OXPHOS reaction.

Other pathways such as urea cycle[27] or polyamine production[28] are also implicated in tumour progression. While PCa expands, cancer cells undergo a rewiring process to sustain their catabolic and anabolic needs. Lipids are crucial structural components of cell membranes and hence, anabolic building blocks. Also, they participate in intracellular signalling, trafficking regulation and they are an important source of energy. PCa cells increase their lipid uptake, fatty acid (FA) biosynthesis, FA oxidation and storage; denoting lipid metabolism as a relevant mechanism in invasiveness and progression[19,29–31]. Actually, there are several studies showing alterations in many types of lipids such as acylcarnitines, cholesteryl esters or triglycerides[32–34]. This metabolic plasticity contributes to tumour growth, increase of activity and hence, invasion and metastasis[35].
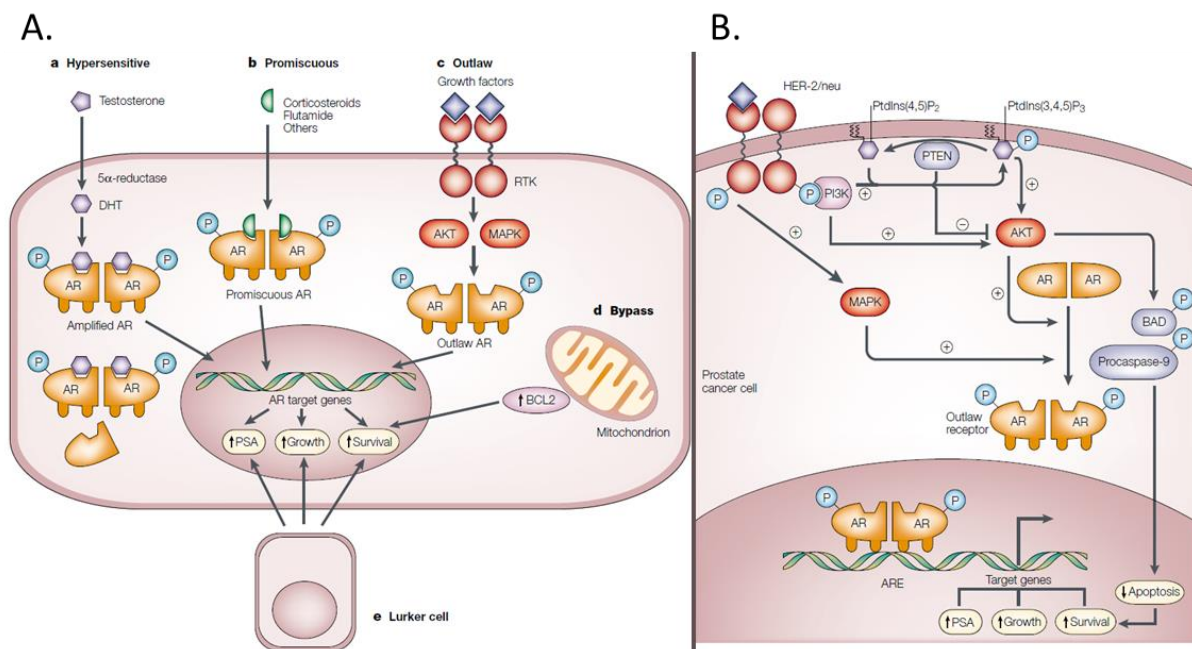
Figure 4. Summary of pathways and mechanisms of androgen-independent progression. A. Five possible pathways to androgen independence are depicted. (a.) The *hypersensitive pathway* compensates low levels of androgen with a higher production of AR or a more sensitive AR. (b.) The *promiscuous pathway* uses non-androgenic molecules to activate AR. (c.) In the *outlaw pathway*, receptor tyrosine kinases (RTKs) are activated, and the AR is activated by phosphorylation. (d.) *Bypass pathway* involves the anti-apoptotic protein BCL2 as a survival signal. (e.) Androgen-independent pathways are present all time in lurker cells inhabiting the prostate. B. Summarises the transduction of signals in the *outlaw pathway*. Nowadays, a larger number of pathways and interactions are known. In this pathway, the activation of receptor tyrosine kinases initiates a cascade that further activates or phosphorylates MAPK, PI3K or AKT. Thence, outlaw AR is phosphorylated and it can enter the nucleus, triggering the transcription of target genes.
ARE: androgen response element; DHT: Dihydrotestosterone PSA: prostate-specific antigen.
Adapted from [23].

Above all crucial metabolic routes in prostate physiology, androgens – a class of steroid hormones – are essential in prostate cell growth and differentiation. Generally, early-stage progression of PCa is tightly dependent on hormone sensing. High levels of testosterone in serum are associated with a high

risk of suffering this malignancy[36]. Actually, PCa cells are hormone-dependent beings that require a steroid triggered signal to sustain tumorigenesis in their first stages of progression (Figure 3). Testosterone and its active form, 5α-dihydrotestosterone (DHT) are the major ligands of this cascade; however, other androgens (C-19 steroids) can also participate in this process (Figure 4A). Upon ligand binding to the androgen receptor (AR), it can dimerise and trigger the transcription of targeted genes, which further enhance growth and survival.

Besides the high level of macroscopic (and histological) heterogeneity of PCa described in the previous section, its molecular heterogeneity is not lagged behind. Although the androgen-dependent or canonical is the major progression pathway (Figure 3), androgen-independent pathways (AR-dependent or independent) gradually increase their relevance upon tumour development. The latter are regulated over membrane-bound receptors such as tyrosine kinases and interleukin receptors that further phosphorylate (and activate AR), trigger anti-apoptotic proteins and activate growth or transcription factor receptors to promote i.e. actin polymerisation or Calcium release (Figure 4B). Overall, cancer cells are regulated in a very complex manner. The deprivation of steroids mitigates tumour but it can further grow androgen-independently over time, indicating a high degree of plasticity and adaptability. Consequently, each developmental stage exhibits specific metabolic profiles of PCa and cancer-associated cells in response to the demands of tumour cells[19,37].

Steroid hormones metabolism

During embrionary phases of development, the prostate gland requires DHT synthesised from fetal testosterone[7,38]. This means steroid hormones are involved, already in early developmental stages, in important physiological processes. Due to their prevalence, they are involved in hormone-dependent diseases. In prostate cancer, for instance, the aberrant activation of AR by steroid hormones causes the tumour development[19,39]. Regulation is, amongst other things, subject to circadian rhythm, stress and sex. However, their production and delivery are regulated via the hypothalamus–pituitary–adrenal gland and -gonadal axes[40]. Corticotropin-releasing hormone (CRH) stimulate the release of adrenocorticotropin (ACTH), to regulate hormone production in adrenal glands (Figure 19). Testosterone production in the testis is directly stimulated by the luteinizing hormone (LH) via pulses of gonadotropin-releasing hormone (GnRH) from hypothalamic neurons.

In mammals, there are 99 metabolites involved in the steroid hormone biosynthesis pathway and over 100 reactions catalysed by 61 different enzymes[41,42]. Cholesterol is processed in adrenal glands and gonads to produce steroid hormones. Even though almost all steroid hormones enzymes are expressed in several organs, they are specialised on particular modules that are physiologically relevant in that compartment. For instance, adrenal glands are the producers of C-21 hormones while prostate shows a SRD5A activity, which catalyses the conversion of testosterone to DHT.

In the first step of the steroid hormone biosynthesis, cholesterol is internalised into mitochondria where it is fed as substrate to produce pregnenolone (Figure 20). Pregnenolone is the main precursor for *de novo* steroid hormones and, it is transported to the endoplasmic reticulum (ER) to be further

converted to progesterone or dehydroepiandrosterone (DHEA). The enzymes 3β-Hydroxysteroid dehydrogenase (3β-HSD) or steroid 17-alpha-monooxygenase (CYP17A1) catalyse each of these reactions, respectively. At this point, DHEA is utilised to generate C-19 steroids also known as androgens, which are associated to a male physiology regulation or C-18 steroids – estrogens – which are often regulating female physiological processes. Actually, androgens and estrogens regulate cellular proliferation, development and differentiation in sexual tissues. Progesterone is the substrate of glycocorticoids and mineralocorticoids that are involved in stress and immune response and, maintaining cell homeostasis, respectively[40,43].

The layout of double bonds, hydroxyl and keto groups around a basic sterane backbone structure primarily define the physiological role of each individual steroid hormone. All steroid compounds share a sterane backbone structure provided by cholesterol molecule (Figure 6), substrate of this pathway and one of the end-products of steroid biosynthesis. Steroid biosynthesis starts with the conversion of acetyl-CoA molecules to build isoprenoid units that are further closed up into four rings, constituting the sterane nucleus. Even though cholesterol is the solely precursor of steroid hormones, there exists an anapleurotically feeding of the pathway at intermediate steps[44]. Therefore, upstream compounds different than cholesterol can be provided externally by cell environment, nearby cells or body fluids. In this line, sulphated steroids are of interest since they are, unlike their unsulphated counterparts, readily soluble in the cytoplasm and in biofluids such as blood or urine. Active transmembrane transporters participate in the influx and efflux of hydrophilic sulphated steroids[44,45], meaning that sulphontation may not only be an inactivation feature to excrete steroid hormones. Actually, sulphonation facilitates the accessibility to steroid hormones by nonsteroidogneic tissues, i.e. brain or prostate. Upon internalization, these steroids are desulphonated[44,45] to make them biologically available.

Nevertheless, the main substrate to feed this hormone metabolic network is still cholesterol and, even though it can be produced *de novo*, the major source of cholesterol is exogenous[46,47]. Lipoparticles are highly enriched in cholesterol and other lipids in normal physiological conditions; besides, they are manufactured in the liver prior their release to the bloodstream[46,47]. Once internalised, these cholesterol-containing particles are endocytosed and accommodated in early endosomes[46]. Subsequently, these endosomes undergo a maturation process towards late endosomes and lysosomes, which includes the acidification and hydrolisation activity of acid lipase (LAL) to generate accessible cholesterol. By means of protein complexes as Niemann–Pick C (NPC) or other proteins as SapA, LAMP-2, LIMP-2 or STARD3[46,48,49], cholesterol is shuttled to the lysosomal membrane. At this point, cholesterol can be distributed to other organelles as mitochondria, Golgi apparatus or endoplasmic reticulum (ER) via contact site events or active transportation[46]. In these cellular compartments, cholesterol can be accumulated in reservoirs - i.e. lipid rafts - or metabolised as steroid hormones.

Hormone steroids and related cargoes are transported by blood and other body fluids as sulphated species; however, they could also be encapsulated into vesicles secreted by specialised cell types. Lipids and specifically cholesterol, which play a pivotal role in prostate cancer progression[34,50,51], are particularly abundant in vesicle membranes[52,53]. In this line, although there is literature reporting the

transport of metabolic components within these cell secreted vesicles[54–58], the manner this cargo interacts with the metabolic network and the entire physiological implications of this transfer is yet to be fully understood. A recent lipidomics study performed in these vesicles collected from urine revealed several lipid species present in PCa-derived urinary vesicles not present in healthy ones[59]. In fact, a study evaluated 248 metabolites belonging to different chemical natures present vesicles isolated from either PCa or BPH patient urines[60]. This study found 76 metabolites altered in vesicles from PCa patient urines. Interestingly, several steroid hormone metabolites were detected and DHEAS was among the most significantly altered metabolites in PCa samples. The fact these vesicles contain androgen-related metabolites is suggestive of the relevance of this biosynthetic pathway in cancer disease and the potential participation of vesicles in transporting such valuable assets.

II. Extracellular Vesicles

Technological advances offered the opportunity to gather biological information that was not accessible decades or even centuries ago. From describing a single cell in a piece of cork[61] to identify cell structures such as the mitochondria[62] and nuclei[63], technology made humans capable of understanding biology and describing yet-unknown cellular structures and functions. In 1967, the physician Peter Wolf visualised *platelet dust* in fresh platelet-free blood plasma using an electron microscope[64]. By then, a mammalian vesicle-like structure was described for the first time.

Nowadays, these secreted vesicles are extensively reported and coined as extracellular vesicles (EVs). They are heterogeneous, nano- to micrometre-sized, bilayer lipid containers secreted by most cell types to the extracellular space. EVs are multi-purpose carriers that can contain a wide variety of cargoes (Figure 5a) including lipids, proteins, metabolites, sugars, RNA and even DNA[65]. They are classified into different groups according to their biogenesis mechanisms and biophysical properties:

- exosomes: typically 30–150 nm in diameter, derived from intracellular endosomal compartments,
- microvesicles: 100–1000 nm in diameter, produced by outward budding and pinching-off the plasma membrane, and
- apoptotic bodies: 50–5000 nm in diameter, released as blebs by cells undergoing apoptosis[65,66].

When they are taken up, EVs can trigger intracellular signalling through surface molecules or by the release of their cargo into cell compartments via different endocytic pathways (Figure 5bc). These processes can further activate downstream genetic or metabolic responses in the recipient cell[67,68]. Indeed, later discoveries showed that secreted vesicles participate actively in many physiological processes in mammals, for example coagulation, inflammatory response, cell maturation, adaptive immune response, bone calcification and neural cell communication, among others[65,68]. In addition to their critical functions in normal physiology[69,70], secreted vesicles mediate in several pathological processes[71,72], such as the establishment of a pre-metastatic niche during cancer progression[73,74].

Importantly, the International Society for Extracellular Vesicles (ISEV)[75] endorsed a categorisation of EVs into large, medium and small EVs due to limitations in isolation methodologies. Such practical

categorisation includes not only vesicles but also lipoproteins, viruses, protein aggregates, ribonucleo-protein complexes and exomeres[76–78], which provides an additional layer of diversity. This is because such structures can participate in similar (pato)physiological processes along with EVs.
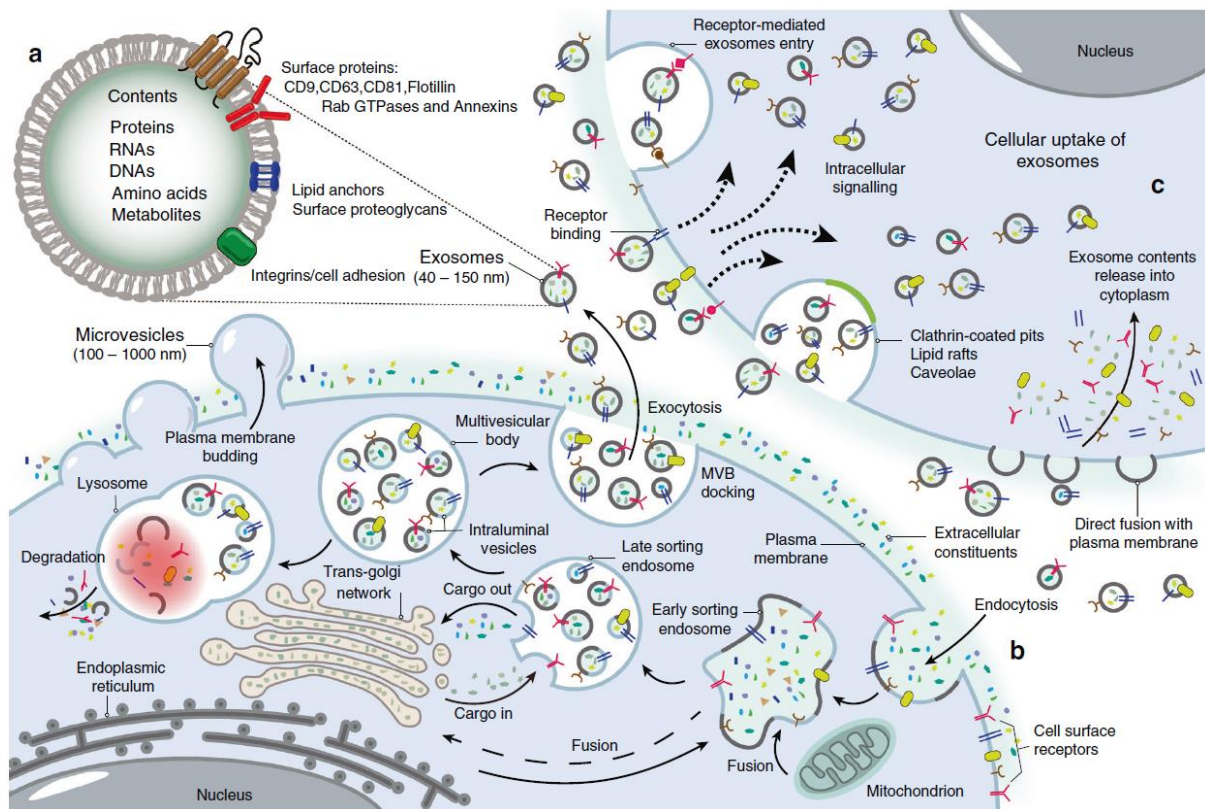
Figure 5. Summary of EV biogenesis, EV-mediated cell-to-cell interaction and intracellular trafficking. (a) Cargo of EVs includes different types of proteins nucleic acids and metabolites. (b) Plasma membrane invagination endocytose extracellular constituents and cell surface proteins. This structure can fuse with constituents of the ER, trans-Golgi network and mitochondria, which leads to the formation of early sorting endosomes (ESEs). Then, ESEs mature to late sorting endosomes (LSEs) forming intraluminal vesicles (ILVs) by a second invagination of the membrane. Finally, multivesicular bodies (MVBs) are generated and they can be sorted to lysosome, undergoing degradation; or transported to plasma membrane, docking on luminal side of cells. Exocytosis of MVBs releases ILVs as EVs to the extracellular space. (c) EVs can be internalised by cells using different pathways: fusion with cell membranes, a receptor-mediated entry, clathrin-coated invaginations or lipid rafts interactions, among others. Reproduced from [79] with permission under Creative Commons Attribution 4.0 International License http://creativecommons.org/licenses/by/4.0/.

EVs as biomarkers

In 1989, a task group on Biomarkers and Risk Assessment proposed a definition for biomarkers, which are chemicals, metabolites of chemicals, enzymes and other biochemical substances to document their interaction with biological systems. In this line, biomarkers can be defined a broader sense by including chemical, physical and biological interactions between these systems. The use of biomarkers in research has grown exponentially during the last decades seeking to establish direct measurements of disease causes and affections[80,81]. One of the most important criteria is their accessibility and biological relevance. A biomarker should be present in a minimally invasive source and it should be as much sensitive as possible. Moreover, it has to be meaningful in a biological framework and often provide a better understanding of the disease's mechanism. This will definitely lead to describe fast

response biomarkers upon disease progression or treatment and hence, provide risk stratification and prognosis. Currently, biomarkers for PCa do not guarantee an effective and reliable diagnosis due to the high heterogeneity and plasticity of the disease. On top of that, its diversity is usually assessed relying on tissue biopsies. This strategy is rather invasive and does not provide a reliable prognostic output. For this reason, and considering that current diagnostic tools present several flaws, finding other biomarker sources is fundamental in the diagnosis field.

Nearly all cell types expel EVs to the *extracellular milleu* with signalling or disposal purposes[65,82]. These physiologically relevant cell goods are exchanged safely thanks to the protection offered by the lipid membrane. As cellular components are not easily degraded, EVs represent a new source of biomarkers that could describe physiological processes or cellular stages in disease progression. Depending on the information provided, biomarkers can be used as predictors when they provide information on the biological response to therapeutic interventions, prognostic assets when they provide information on disease progression and/or recurrence or diagnostic assets if they can distinguish healthy and disease samples[83–85]. Remarkably, EVs have been identified in wide variety of human tissues or fluids, including blood, urine, saliva, synovial fluid, cerebrospinal fluid, uterine fluid, bile, breast milk or faeces, among others[65]. In this line, liquid biopsy may be highly informative as it is low-invasive and could reflect the status of a disease better than a conventional biopsy. Therefore, novel biomarkers can be described from EVs and their concomitant compounds to inform about the progression of a disease or a physiological response.

Role of Lipids in EVs

The biogenesis of EVs commences with processes of microautophagy in late endosomes or outward budding at the plasma membrane[86]. Historically, the resulting vesicles have been called exosomes and microvesicles, respectively. The biological events governing their formation are different; however, they are all somehow driven by their lipid composition. For instance, the translocation of acid sphingomyelinase generates ceramides in the outer leaflet of the plasma membrane, inducing a curvature in the plasma membrane that triggers microvesicle budding[87]. Actually, the disruption of lipid organization appears to be critical; not only ceramides affect their formation but also cholesterol/sphingomyelin ratio, and phosphatidylserine asymmetry to the outer leaflet. After microautophagy in late endosomes, multivesicular bodies (MVBs) containing intraluminal vesicles (ILVs) can reach the plasma membrane in a dynamic process regulated by cholesterol. Upon fusion with plasma membrane, ILVs are released to the extracellular space where they are called exosomes. Exosomes are enriched in disaturated molecular species of phospholipids, which accounts for their increased membrane rigidity[87]. In summary, there are many lipid-related pathways involved in the biogenesis of EVs.

The release of vesicles implies more steps previous to budding events in which the composition of membranes plays a critical role. Studies working with cells *in vitro* show a remarkable enrichment of cholesterol, sphingomyelin, glycosphingolipids and phosphatidylserine in EV membranes[88]. Moreover, the presence of lipids with small head groups as ceramide, diacylglycerol and phosphatidic acid has been associated with the formation and release of EVs[89]. Considering the role of lipids in EVs one

should consider both their structural role in membranes and the manner they modify membrane fluidity and curvature, but also their potential role as signalling molecules[89].
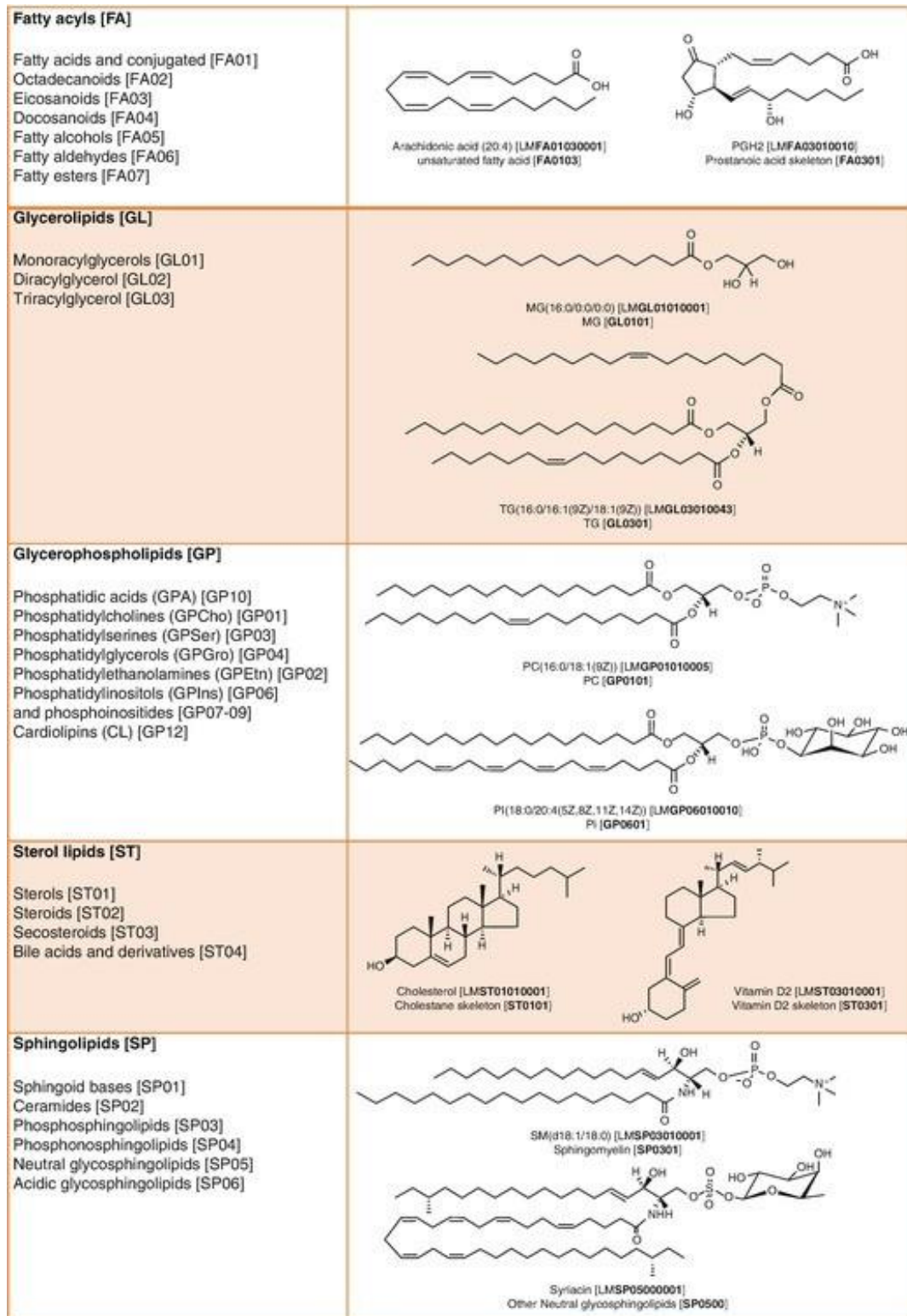
Figure 6. Classes of lipids. Different groups are displayed according to their structure and synthesis pathways.

EVs in metabolism

The membrane-enclosed entities that we baptised as EVs carry proteins, nuclear acids, lipids and metabolites. Indeed, EVs are often considered metabolic machineries since they can contain active enzymes, metabolic substrates or ligands to carry out enzymatic reactions or regulate enzyme activities. There are various mechanisms by which metabolic cargoes are loaded into EVs: identifying specific miRNA[90], proteins[91] or performing posttranslational modifications, such as acetylation, sumoylation or phosphorylation[92,93] on proteins and RNA to increase the likely hood of actively or passively loading EVs with specific compounds. In addition, EVs are entities with a high content of lipids, a wide family of metabolites (Figure 6) with a very diverse chemical structure and hence, several properties physiological function. Although EV membranes are similar to donor cells they are enriched in specific lipids as cholesterol, sphingomyelins, ceramides and glycosphingolipids[94–96]. This may explain why proteins with affinity to certain lipids are enriched in EVs, i.e. tetraspanins or flotillin. While some of the mechanisms of cargo recruitment have been described, the involvement of metabolic assets in actual physiological processes is often overlooked[97]. It is known that metabolic resources are transported by EVs yet, the manner their cargo (reaction substrate -metabolites- or activity -enzymes-) interacts with recipient cell is not understood neither comprehensibly studied.

Table 2. Glycolytic enzymes and occurrence in exosomes and PCa-derived EVs. Enzymes in the glycolytic pathway and their frequent appearance in EVs are listed. The numbers refer to their placement in the top 100 most frequently identified proteins.
H = Human; D = Dog; S = Stallion; B = Bull.
Proteomic data was retrieved on 2018-10-16 and the original table is extracted from[98].

Enzyme	EVpedia	ExoCarta	Protasomal lipid raft	Specie
Hexokinase	-	-	No	H, D, S, B
Glucose-6-phosphate isomerase	63	-	Yes	H, D, S, B
6-Phosphofructokinase	-	-	No	H, S
Frusctose-biphosphate aldolase	12	18	Yes	H, D, S, B
Triosephosphate isomerase	20	27	Yes	H, D, S, B
Glyceraldehyde-3-phosphate dehydrogenase	1	4	Yes	H, D, S, B
Phosphoglycerate kinase	16	16	Yes	H, D, S, B
Phosphoglycerate mutase	87	-	Yes	H, D, S, B
Enolase	2	9	Yes	H, D, S, B
Pyruvate kinase	3	12	Yes	H, D, S, B
Lactate dehydrogenase-A	7	13	Yes	H, D, S, B

Glycolytic enzymes frequently appear in EVs (Table 2) and prostasomes – EVs produced by prostatic cells – from living cells[98]. Several mechanisms can explain the presence of these enzymes in EVs such as the fact they are anchored to lipid rafts or tetraspanin microdomains[99]. Indeed, a majority of the glycolytic enzymes are related to lipid rafts (Table 2). Up-to-date, the full set of glycolytic enzymes has been identified in EVs[100] through the efforts of multiple initiatives as EVpedia[101], Vesiclepedia[102] or Exocarta[103]. These databases have been compiling identified proteins in EVs by means of proteomics analysis. Intriguingly, lactate dehydrogenase-A, the enzyme responsible of converting pyruvate to lactate by oxidation of NADH to NAD^+, is among the most frequently identified proteins in EVs (Table 2).

Nonetheless, EVs do not only convey components but they can transfer their activity. Extracellular ATP production was observed upon addition of fructose to purified prostasomes[104]. Other studies described arginase activity of hepatocyte-derived EVs[105] or L-asparaginase activity in EVs derived from neural stem/progenitor cell[106]. This suggests EVs may function as independent metabolic units with a potential impact to the composition of the extracellular microenvironment.

Metabolic reprograming mediated via EVs is present in many biological systems where cell types with different or the same functionality exchange metabolic assets[107]. Besides metabolites and enzymes, EVs can modify metabolic pathways by the transfer of nucleic acids, which can further regulates glycolysis[108,109] or OXPHOS[110], among others. During oncogenesis, not only cancer cells influence the environment by means of EV release but also stromal cells can drive metabolic changes in cancer cells by providing metabolic resources required for cancer progression[111]. Cancer-associated fibroblasts (CAFs) are defined by specific morphological features or expression of markers including α-smooth muscle actin (α-SMA), fibroblast-specific protein-1 (FSP1/S100A4), and fibroblast activation protein (FAP)[112]. Recent studies showed the crosstalk between cancer cells and CAFs plays a vital role in tumour growth by regulating their metabolism. Cancer cells promote an enhanced glycolysis of CAFs which, in turn, provide TCA- and OXPHOS-related metabolites[113]. This phenomenon was recognized as the "*Reverse Warburg Effect*". Interestingly, EVs derived from CAFs have been described as partially responsible for tumour cell survival in the hostile, nutrient-deprived, and hypoxic environment of PCa. These EVs contain several metabolites, including lactate, acetate, aminoacids, lipids, and TCA cycle intermediates, that further favours glycolysis, reductive glutamine metabolism, and proliferation of cancer cells[67]. Reductive carboxylation of glutamine replenishes TCA intermediates through glutamate and citrate, which are also precursors of major macromolecules related to anabolism and catabolism. In addition, lactate facilitates tumour cell survival under hypoxic and nutrient-deficient conditions[114]. These results further demonstrate that the existing metabolic symbiosis between PCa cells and CAFs.

Increasing evidence are piled up reporting EVs as relevant mediators between CAFs and cancer cells. PCa cells releasing EVs can trigger normal fibroblast differentiation towards myofibroblasts or CAFs. In 2010, Webber *et al.* described that TGF-β1 contained in EVs could activate fibroblasts as soluble TGF-β1 does[115]. However, in further studies they showed PCa-derived EVs triggered TGF-β1-dependent fibroblast differentiation that resembles cancerous stromal cells while soluble TGF-β1 did not deliver pro-angiogenic or tumour-promoting phenotype[116]. Other studies performed in neonatal fibroblast cells noted that colorectal cancer-derived EVs could drive the expression of the activated fibroblast marker α-SMA. In the same study, the authors described metabolic modifications such as aminoacid biosynthesis, enhanced glycolysis via glucose and lactate transport or upregulation of glycogen metabolism, upon EV treatment[117]. In breast cancer models, a metabolic remodelling of fibroblasts and increased glycolysis through cancer-released EVs was described[117,118]. These results contribute to the idea of an EV-mediated signalling that sustains tumour growth and the activation of fibroblast. It further suggests that in specific systems or conditions, EVs could be rather relevant contributors for cancer progression.

III. Metabolomics

Until the rise of the omics era, molecular biology and physiology approaches were utilised to acquire data that could describe biological components and functions, separately. Nowadays, the interaction between those is an essential focus in the systems biology paradigm, which aims to explore physiological processes of an organism as a whole in a holistic manner. *Omics* strategies hold the potential to identify the entire set of biomolecules (Figure 7) contained in biological samples. This generates a bast amount of data that can be correlated to describe a biological system in a complete and integrated way.

Metabolomics is defined as the comprehensive and quantitative analysis of small molecules within a biological system including cells, biofluids, tissues or entire organisms, commonly known as metabolites. In literature, the term metabolome first appeared in 1998 referring to the entire set of metabolites present in an organism of any kind. Metabolites are biologically active compounds - smaller than 1500 Da - which participate in all biological processes of a living cell as i.e. building blocks for macromolecules, energy carriers, signal effectors or inhibitors[85,119]. Distinct classes of compounds constitute the metabolome: lipids, aminoacids, inorganic species or nucleotides, among others. Metabolites are difficult to study due to their extreme variety of chemical and physical properties, such as molecular weight, polarity, solubility and volatility. Moreover, the number of metabolites considered in a metabolome is highly variable and tightly dependent on the studied organism. It ranges from 600 metabolites estimated in *Saccharomyces cerevisiae* to approximately 200,000 metabolites annotated in the plant kingdom. It is accepted human's metabolome is smaller than plant's one but more than 4,000 compounds have already been annotated[120]. There are two groups of metabolites regarding their implication in the biological system. Primary metabolites are those involved in biological processes, thus making them essential to life. This is the case of amino acids, organic acids, lipids, etc. Instead, secondary metabolites are those metabolites not essential for the cell to live. This is because they do not have a role in any essential biological process. Therefore, they are restricted to a selected set of cells, which synthetize them for specific biological functions.

Metabolomics aims to identify and quantify a large number of metabolites in a biological system to resolve specific scientific hypotheses[121]. In general, the methods of choice are Nuclear Magnetic Resonance spectroscopy (NMR) or Mass Spectrometry (MS). The most widely used mass spectrometers are Orbitrap and Time-Of-Flight (TOF) based systems because they provide the advantage of analysing a complete mass range with relatively high acquisition rates[122]. Triple quadrupole (QQQ) or Quadrupole-TOF (Q-TOF) provide a higher sensitivity and the opportunity to analyse fragmentation patterns, which is very useful to identify known analytes in certain metabolomics approaches. MS is usually coupled to a separation system such as Gas Chromatography (GC-MS), Liquid Chromatography (LC-MS) or Capillary Electrophoresis (CE-MS) to deliver the identification of nay metabolite. To increase the separation power, the combination of several separation approaches into multidimensional systems is becoming common[119]. All these analytical platforms and methodologies generate large amounts of high-dimensional and complex experimental raw data when used in a metabolomics context. The amount of

data, the need for reproducible research, and the complexities of the biological problem under investigation necessitate a high degree of automation and standardise analytical workflows. Many tools and methods have been developed to facilitate the processing and analysis of metabolomics data; most seek to perform reproducible data analysis and to work with different types of raw data.
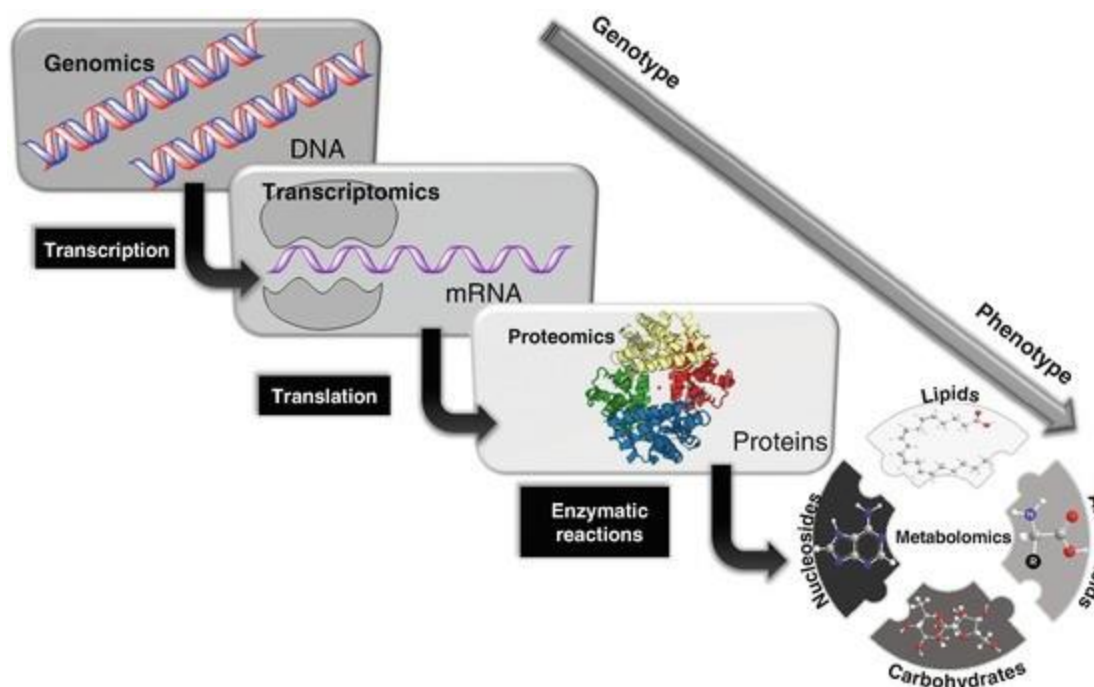
Figure 7. Scheme of the main *omics* strategies utilised in systems biology approach. The scheme represents the correlation of each *omic* approach to genotype or phenotype in any biological systems.

Currently, there is no actual consensus regarding the classification of metabolomics studies. For this reason, we prefer to use a classification based on whether the researcher knows *a priori* which metabolites will be quantified[119]. A general metabolomics workflow is represented in Figure 8 considering this classification. A targeted metabolomics approach is the quantitative analysis – concentrations in the samples are determined – or semiquantitative analysis – relative intensities are registered – of few upfront-known metabolites that are associated to common chemical classes or linked to selected metabolic pathways[119]. This approach provides a metabolic profiling of specific biochemical pathways with biological relevance to the hypothesis. The use of isotope-labelled metabolites (with ^{13}C, ^{15}N or deuterium) in experiments permits to trace metabolic reactions and pathways. It also allows assessing the utilisation of a substrate by a metabolic network. This type of analysis can also be performed in an untargeted manner. The term untargeted metabolomics was coined to define the qualitative or semiquantitative analysis of the largest possible number of metabolites from different chemical and biological classes which are contained in a biological specimen[119]. This approach enables a rapid classification of samples according to their origin or status but also the analysis of different compartments of a system, for instance, cell content (fingerprint) and secretome (footprint) under controlled conditions. In this way, an alteration of a small subset of metabolites can be pinpointed in a broader context of analytes and describe the potential interactions with other metabolites and/or pleiotropic effects considering several pathways (or modules) of the entire metabolomics network. In contrast, identification reliability is loss.

Ideally, one would start with an untargeted analysis to provide a potential answer to the hypothesis and finally, confirm it by using a targeted approach.

In this thesis, we will work with liquid chromatography coupled to mass spectrometry with a targeted metabolomics manner. In this approach, sample preparation is adapted to the chemical properties of the selected compounds and the sample matrix hence, reducing signal alteration of targeted analytes by non-desired compounds[123,124]. As mentioned, some hypotheses may require a broader set of metabolites to properly describe the impact to the biological system. As the inclusion of the whole metabolome has technical limitation and complications, different extraction and sample preparations have been combined in so-called analytical platforms. These platforms enable the extraction of chemically similar metabolites in different sets to analyse them separately. Therefore, we can analyse polar and apolar compounds separately yet maintaining a strong resolving and identification power without compromising the selectivity and sensitivity of the assay.

For targeted metabolomics, the typical metabolomics workflow (Figure 8) is organised in six general steps: establish the biological problem and experimental design (1), ideally within the input from a statistician, sample preparation (2), further data acquisition (3), data processing (4), statistical analysis (5) and pathway functional analyses (6).

Biological problem and experimental design

A clear formulation of the biological problem is crucial because it will govern further decisions during the experiment design. The integration of all subjects related to the workflow is essential to both consider all the potential confounding variables and obtain readily interpretable results. At this point, the type of metabolomics approach is defined considering the sample size and type – cells, fluids, EVs, tissues or intact organisms -, the experimental conditions, frequency of collection, storage conditions, metabolic quenching to interrupt metabolism and, the analytical platforms and preparation strategies.

Sample preparation

Once the researchers of the roundtable ruled the most appropriate experiment design, the appropriate sample preparation must be defined. Because of the wide variety of physicochemical properties of metabolites, the extraction procedure is usually optimised for a specific set of compounds or chemical classes in the analytical platforms. It usually involves clean-up steps to remove sample matrix interferents (i.e. protein precipitation with methanol), preconcentration strategies to boost detectability and the selection of appropriate extraction solvents[125]. An important consideration to make is that metabolism is a constant flux; thus, stopping any potential metabolic reaction is imperative in sample collection, preservation and manipulation to avoid any potential loss of metabolite signals.

Metabolite extraction methods from the collected samples have been developed to be effective for specific compound classes. This implies each method will lead to the loss of metabolites not specific of the assay. Considering all potential issues in extraction methods, an ideal preparation should: (i) incorporate a preservative so that the metabolite composition reflects the original one at the sampling moment; (ii) be as non-selective as possible in order to incorporate the broader range of metabolites. To

this aim, a combination of distinct extraction protocols may be considered; (iii) be simple and fast, to avoid metabolite loss; (iv) be reproducible.

Data acquisition

The chemical diversity of the metabolome, as well as its wide dynamic range, is a drawback to achieve a comprehensive identification and quantification of an entire metabolite set in a biological system. It is important to emphasize that not only distinct chemical properties, structural arrangements and functionalities differentiate metabolic compounds but also their concentration levels. For instance, sugars and concomitant intermediates range between micromolar or millimolar depending on the matrix[126,127] but steroid hormones are at the nanomolar range.

Typically, the analytical techniques employed for data acquisition are NMR and MS. Their strengths and limitations must be considered to decide the best approach. While NMR spectroscopy is considered as a universal metabolite detection technique, with a low sample manipulation and a wide variety of chemical classes detected simultaneously, MS is much more sensitive and specific, however, it usually requires a separation technique to reduce sample complexity and ion suppression[128–130]. Nowadays, MS is usually coupled to high-pressure liquid chromatography (HPLC) and ultra-high pressure liquid chromatography (UPLC). The mass spectrometer is composed of an ion source, which is the entry point for the ionized metabolites into the equipment, a mass analyser to separate the analytes by mass-to-charge ratio (m/z) and the detector. The m/z abbreviation stands from the value resulting from dividing the mass number (m) of an ion by the corresponding charge number (z) and it is characteristic of each chemical formula[131]. Analytical platforms often exhibit stability issues over time, which can be circumvent with the use of a quality control (QC). It is prepared by mixing small volumes of all running samples. QC is normally run several times upfront samples to check for instrumental stability and intercalated during samples run to ensure data reliability.

Data processing

A correct analyte quantitation or semiquantitation is imperative in targeted metabolomics. Usually, an assay is developed under specific and optimised conditions for a specific set of metabolites. Therefore, further validation of the parameters specificity/selectivity, accuracy, linearity, resolution, limits of detection and quantification and, reproducibility is required to establish a methodology[119].

Raw data collected from the mass spectrometer is colossal and unmanageable. Henceforth, the aim of this step is to generate a 2D data table of features or metabolites defined as m/z - RT pairs where data has been already corrected according to QC, normalised and, if required, transformed, centered and/or scaled. For more detailed information relate to Chapter 6 of the book [119].
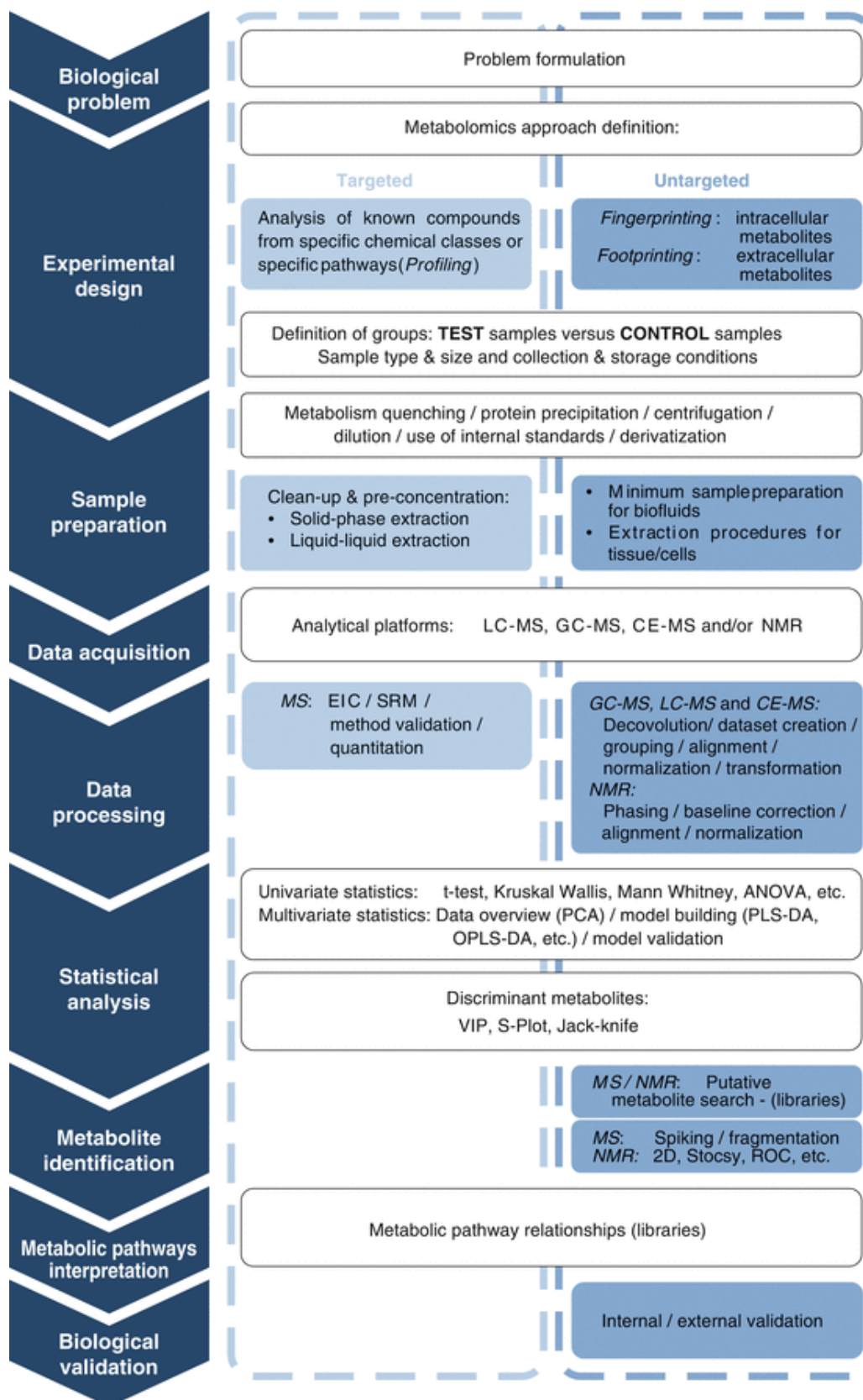
Figure 8. Analytical workflow for studies in metabolomics. This metabolomics workflow comprises the sequential steps that underline both targeted and untargeted analyses. Starting from a problem or hypothesis formulation it provides metabolic pathway relationships. Reprinted from [119].

Statistical analysis

At this point, the aim is to provide data of biological context and significance to the analysis[132]. As already discussed, metabolomics data is quite complex and require chemometric tools to reveal discriminant metabolites between groups of samples[133]. Data analysis of high-throughput data often present several issues that includes: (i) overfitting, due to a larger number of variables compared to samples; (ii) interconnection of variables and variable dependency; (iii) high background noise; (iv) discrimination between informative from non-informative data[134].

To provide a samples overview and general classification, multivariate analyses (MVA) are regularly performed[135]. All potential interactions – considering correlations and/or variances – between variables are included in these analyses in an either unsupervised (i.e. Principal Component Analysis, PCA) or supervised manner (i.e. partial least square discriminant analysis, PLS-DA). In order to corroborate and expand MVA results, individualised metabolites are assessed in a so-called univariate analysis. This approach is usually based upon significance tests such as Student's t-test, Mann-Whitney U test or ANOVA, among others. When utilised in an *omics* study, a multi-test correction should be applied to eliminate false positives of the analysis. However, one must be aware it may increase the false negatives count.

As the Economics Nobel Prize Laurate, Ronald Coase, proclaimed: "*Torture data, and it will confess to anything*". In any scientific field the statistical treatment of data has to be addressed carefully. Because every approach considers different features and uses different mathematical models, it is quite ordinary they provide distinct results. Statistical approaches are based upon assumptions or null hypothesis that may explain these differences. Indeed, this is expectable and nullifies neither multivariate nor univariate results. It actually reinforces the recommendation of using both approaches to provide a more holistic and biologically relevant explanation of the results[132].

Metabolic pathways association

A proper biological interpretation is crucial for any study and metabolomics is not an exception. It usually lays at the whim of the scientist's expertise who can elaborate a rationale of altered metabolites to provide a functional analysis. To do so, the researcher can use databases such as KEGG[41,42], HMDB[136], WikiPathways[137], MetaCyc[138] or Reactome[139] to identify related biological processes.

Primarily, the ultimate goal is to deliver a comprehensive metabolome measurement interpretable in the context of different experimental conditions. This will provide a biologically relevant explanation to the hypothesis formulated. The conventional procedure involves reading relevant literature and manually searching metabolites in database to synthesize the information into a justifiable biological tale. This approach is still necessary to validate our conclusions and it is the reason why researcher's expertise and judgement is currently a cornerstone in metabolisms studies. Yet, over the past decade, many computer-assisted data interpretation strategies known as functional analyses have been developed to aid researchers' comprehension of the output data. Three main statistical approaches for functional analysis are used in metabolomics studies[119]:

I. Over-representation analysis (ORA) evaluates whether certain metabolites or metabolite groups appear more often than expected by random chance.

II. Metabolite set enrichment analysis (MSEA) assesses the enrichment of functional groups without preselecting significant metabolites nor considering concentration data.

III. Metabolic pathway and network analysis which integrates a pathway/network topology analysis to the MSEA to enhance the accuracy while ranking relevant biological processes.

IV. Models in Research

PCa presents to the investigator a very dynamic, biologically diverse set of characteristics during its course from early disease to metastasis. Unfortunately, no single model mimics all of the features of this intricate disease[140]. The improvement of culturing techniques to model the environment and physiological conditions surrounding tumours has been applied to the study of EVs in cancer research. By choosing the appropriate biological model, one can evaluate the intricate physiological aspects of any disease. In the case of PCa, the models should aim to cover all the different stages possibly described in this disease. Metabolic alterations or protein mutations but also their ability to metastasize are key properties of the PCa models that must be considered during the experiment design. In this thesis, one only worked with simple bi-dimensional cultures instead of 3D cell cultures because the latter are not well characterised, yet. Remarkably, 3D cell cultures could qualitatively improve cancer research because they provide a closer response to *in vivo* physiology including the preservation of the topology and cell-to-matrix interactions. In Table 3 there is a comparative between 2D and 3D characteristics, a complete review of 3D culture possibilities is described in [141], which has also been part of this thesis.

Table 3. Main advantages and limitations of the different cellular models in cancer research.

Model	Advantages	Limitations
2D Monolayers	Easy and cost effective	Reduced cell-to-cell interactions
	Large amount of data available	Different sensitivity to drugs
	Reproducible cultures, easy to work for downstream applications and imaging	Loss of biological characteristics
Gel based 3D cultures	Cell–ECM interactions	Difficult to dispense cells
	Easy to incorporate different factors	Change growth media could be irregular
	Uniform spheroids/ organoids	Difficult to retrieve cells
Low- attachment plates	Simpler and cheaper when compared to gel based systems	Time consuming and low yield
	Long-term culture	Heterogeneous spheroids
Microfluidic systems	Possible chemical gradients	Expensive commercial devices or not well-characterized "in house" build devices
	Control of fluid rates	
	Convenient for multicellular cultures controlling cell locations	Fluidic problems related to bubbles and clogging

Over decades, *in vitro* models have been based on 2D monolayers of immortalized human (or non-human) cancer-derived cell lines. Researchers have immortalised cells by transfection with constructs

of different nature[142–144] that interact with p53, further losing its function. A listing of the major human prostate cell lines with important characteristics for PCa research is shown in Table 4. Most of these cell lines have been established from metastatic deposits usually xenografted in nude mice to develop the cell line in substrains with different characteristics.

For many years, LNCaP and PC-346 were the only xenografts available for progression studies related to steroid signalling[140]. LNCaP produces PSA but has a mutated androgen receptor. This mutation results in a promiscuous androgen receptor that can bind to other steroids[145]. Until recently, the LNCaP was the only human prostate cancer cell line demonstrating androgen sensitivity[146], for this reason, it is still the most widely used. There has been some variation in LNCaP response to castration because it differs slightly between laboratories, probably due to a drifting over long periods of *in vitro* maintenance[140]. In addition, a stromal myofibroblast line has been established for studies of epithelial–stromal interactions. This line, WPMY-1, expresses α-SMA and vimentin, is positive for AR and grows in serum-free medium[147]. It is an interesting model to study the interaction studies as it still maintains androgen response as well as the malignant hTERT cancer-associated fibroblast.

Table 4. Summary of the major immortalised cell lines in PCa research. Different characteristics important to decide which cell line is more suitable for a specific project or experiment are compiled.

2-D model	Source	Origin	Sensitivity	Tumoral	AR expression	PSA	Cellosaurus	Description	Ref.
RWPE-1	Human prostate	Primary Prostate Epithelium	Androgen responsive	No	Yes	Yes	CVCL_3791	Immortalized with SV40-large-T antigen gene.	[148]
WPMY-1 hNAF	Human prostate (stroma)	Primary Prostate myofibroblast	Androgen responsive	No	Yes	Yes	CVCL_3814	Immortalized with SV40-large-T antigen gene. Prostate origin as RWPE-1.	[147]
BPH-1	Human prostate	Primary Prostate Epithelium	n.d.	No	No	No	CVCL_1091	Patient with Bening Prostatic Hyperplasia. Immortalized with SV40 large T antigen.	[149]
PWR-1E	Non-neoplastic human prostate	Primary Prostate Epithelium	Androgen responsive	No	Yes	Yes	CVCL_3775	Immortalised by an adenovirus 12-Simian virus 40 (Ad12-SV40)	[150]
hTERT CAF	Prostate tumour	Primary Prostate Fibroblast	n.d.	Yes	n.d.	n.d.	CVCL_JL59	hTERT-immortalised cell. Lost chromosome Y.	[151]
LNCaP	Lymph node	Human prostate metastasis	Androgen responsive	Yes	Yes	Yes	CVCL_0395	Tumour progression mimics human prostate cancer.	[152]
LN3	Prostate tumour (xenograft in mice)	LNCaP	Androgen responsive	Yes	Yes	Yes	CVCL_L162	Highly metastatic (Liver and lymph node). High levels of PSA and less androgen sensitivity upon progression.	[153]
C4	Prostate tumour (xenograft in mice)	LNCaP	Androgen unresponsive	Yes	Yes	Yes	CVCL_4783	LNCaP inoculated with human fibroblasts (osteosarcoma)	[154]
C4-2	Prostate tumour (xenograft in mice)	C4	Androgen unresponsive	Yes	Yes	Yes	CVCL_4782	Highly tumorigenic and metastatic.	[154]
VCaP	Vertebral bone	Human prostate metastasis	Androgen responsive	Yes	Yes	Yes	CVCL_2235	Patient with hormone refractory PCa	[155]
DuCaP	Dura matter (Brain)	Human prostate metastasis	Androgen responsive	Yes	Yes	Yes	CVCL_2025	Patient with hormone refractory PCa	[156]
ARCaP	Ascitic fluid	Human prostate metastasis	Androgen repressed	Yes	Yes	Yes	CVCL_4830	Low levels of AR. Androgens supress growth.	[157]
CWR 22	Prostate tumour (xenograft in mice)	Human prostate carcinoma	Androgen responsive	Yes	Yes	Yes	CVCL_3967	Very sensitive to androgens. Prostatic resections xenografted in nude mice.	[158]

Table 1. (Continued)

2-D model	Source	Origin	Sensitivity	Tumoral	AR expression	PSA	Cellosaurus	Description	Ref.
22Rv1	Prostate tumour (xenograft in mice)	CWR 22R	Androgen unresponsive (Low sensitivity)	Yes	Yes	Yes	CVCL_1045	Mutation in AR of CWR 22 which provides cell line to behave as AI. Low levels of PSA. Low metastatic	[159]
TEN12	Prostate tumour (xenograft in mice)	Human prostate carcinoma	Androgen responsive	Yes	Yes	Yes	CVCL_4765	No metastases at any time in patient's clinical history	[160]
TEN12F	Prostate tumour (xenograft in mice)	TEN12	Androgen unresponsive	Yes	Yes	Yes	CVCL_K061		[160]
ALVA-31	Prostate tumour (xenograft in mice)	Human prostate carcinoma	Androgen unresponsive	Yes	Very low	Yes	CVCL_4737	Caution: Shown to be a PC-3 derivative [161,162]	[163]
ALVA-101	Bone	Human prostate metastasis	Androgen responsive	Yes	Low	Yes	CVCL_4735	Caution: Shown to be a PC-3 derivative [162,164]	[165]
PC-93	Prostate tumour	Human prostate carcinoma	Androgen unresponsive	Yes	n.d.	No	CVCL_4888	Caution: Recently reported as a HeLa derivative [162,164]	[166]
PC346C	Prostate tumour (xenograft in mice)	Human prostate carcinoma	Androgen responsive	Yes	Yes	Yes	CVCL_4883	Not stimulated by estradiol or flutamide. Initial regression upon androgen withdrawal is followed by tumor relapse	[167]
LAPC-3	Prostate tumour (xenograft in mice)	Human prostate carcinoma	Androgen unresponsive	Yes	Yes	Yes	CVCL_4743	Unique because androgen receptor and PSA levels are comparable to clinical material.	[168]
MDA Pca 2a	Bone	Human prostate metastasis	Androgen unresponsive (sensitive)	Yes	Yes	Yes	CVCL_4747	Its relative MDA Pca 2b reflects tumour heterogeneity in progression	[169]
PC-3	Bone (Skull)	Human prostate metastasis	Androgen unresponsive	Yes	No	No	CVCL_0035	Grade IV prostatic adenocarcinoma. Highly metastatic	[170]
DU145	Brain	Human prostate metastasis	Androgen unresponsive	Yes	No	No	CVCL_0105	Built after long reculturing. Highly metastatic	[171]

V. Hypothesis and Objectives

Back in 2006, the exosomes research group began investigations on EVs in CIC bioGUNE. Then, they were studied as carriers of compounds that could participate in several physiological processes. In 2012, the metabolomics platform provided the ability to use metabolomics approaches to pinpoint markers and metabolic pathways altered in diseases. The interest in EVs as a metabolic surrogated biomarkers rose in 2018 when metabolic alterations associated to urinary EVs were linked to PCa pathogenesis and progression. This work compared the metabolome of EVs contained in urine of PCa and BPH patients. Many metabolic alterations reported in PCa were recapitulated in associated EVs and, importantly, high levels of few steroid hormones were described. These findings suggested a role of EVs carrying important signalling metabolites for PCa progression.

The project was devised as part of a Marie-Sklowdowska Curie Action called proEVLifeCycle, a consortia of 10 early stage researchers aiming to unravel the mysteries of EV biogenesis, homing and uptake to explain how EVs operate in disease processes, their heterogeneity, their molecular complexity, the biological functions they drive, their local and systemic dissemination and how these may be manipulated. Specifically, this thesis collects a PhD project seeking to utilise "*Extracellular vesicles as surrogated biomarkers of Prostate Cancer metabolism*". The introduction summarised the theoretical background required to understand the scope of the research and the approach utilised. The work has been divided according to general and specific objectives, including the published articles related to them. General and specific objectives of this thesis were:

- To identify, review and summarise the current methodologies to characterise EV and determine their mechanisms of action in physiological processes. *Chapter 1.*
- To establish a targeted metabolomics assay to study the steroid hormones pathway in biological samples. *Chapter 3.*
    i. Test the metabolomics assays in tissues and biological samples of interest for the thesis and further projects of the lab. *Chapter 3.1.*
    ii. Test steroid hormone compounds or signature in urine samples as a biomarker for diagnosis of PCa. *Chapter 3.2.*
    iii. Describe a method to trace steroid hormone metabolites in biological samples and EVs. *Chapter 4.*
- To determine possible steroid-related mechanisms by which EVs can participate in PCa early progression. *Chapter 2 and Chapter 4.*
    i. Explore potential transcripts contained in EVs from urine important in PCa progression. *Chapter 2.*
    ii. Explore transfer of EV material as oncogenicity maintenance (*Chapter 4.2*) or to feed metabolic pathways (*Chapter 4.1*)
- To assess the metabolic rewiring capabilities of EVs in the progression of PCa. *Chapter 5.*
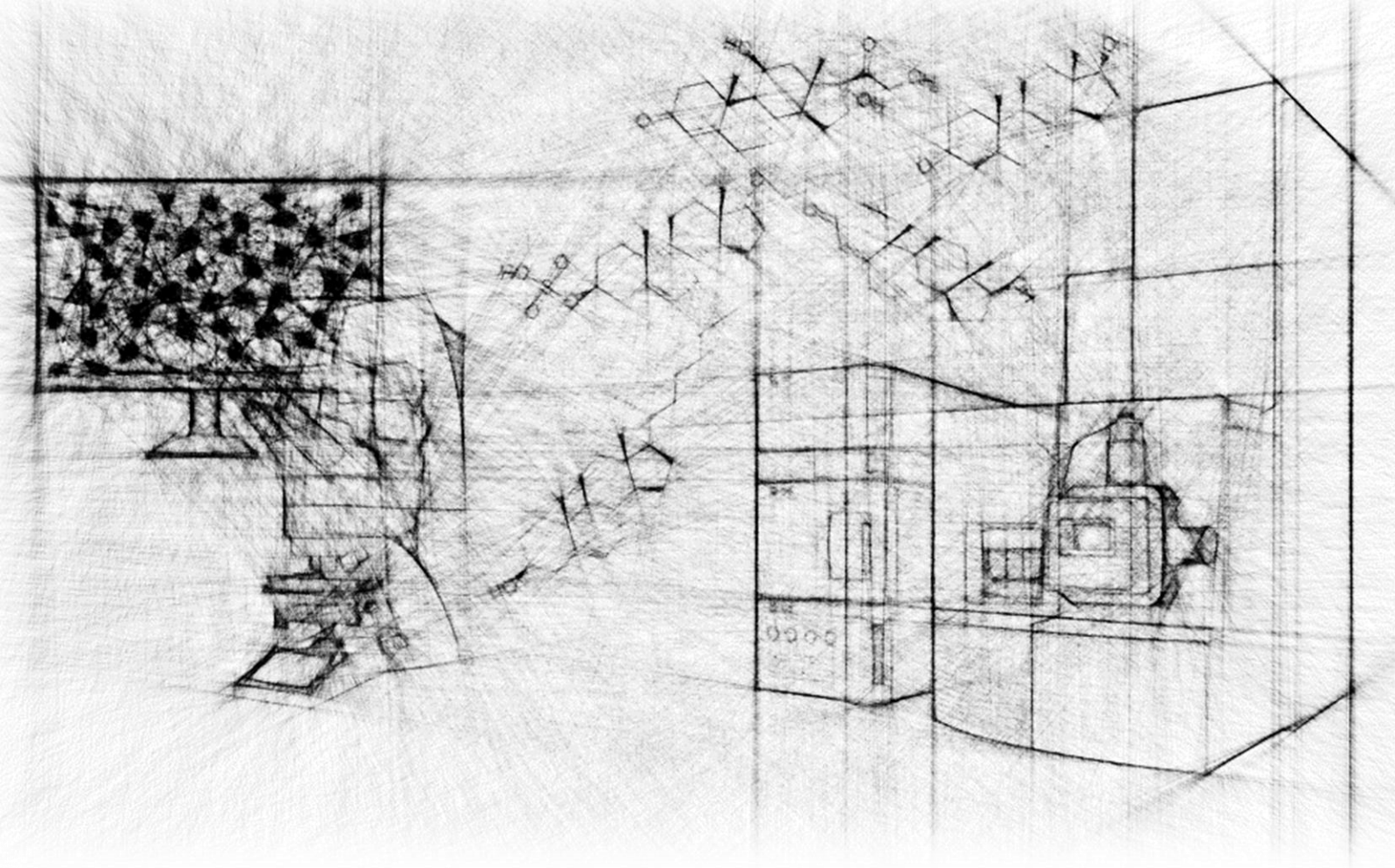
RESULTS

Chapter 1. Current Approaches to Study Extracellular Vesicles in Cell Physiology and Its Applications

This chapter focusses in assessing current approaches in the EV field including recent advances derived from the access to new technologies. Their application in cancer physiology and biomarker discovery is also discussed. It has been published as a Review Article in *Nature Protocols* journal and it is appended in the supplementary material.

Bordanaba-Florit, G. *et al.* Using single-vesicle technologies to unravel the heterogeneity of extracellular vesicles. *Nat Protoc* **16**, 3163–3185 (2021). DOI: 10.1038/s41596-021-00551-z

1.1. Introduction

Since the description of *minute bodies* found in a piece of cork by Robert Hooke in 1665[61], both our scientific knowledge and technical abilities have increased enormously. As techniques have become more accurate and intricate, so has our understanding of biological processes and structures. Technological advances in the field of imaging have resulted in the identification of cell structures, such as the mitochondria[62] and nuclei[63], and the discovery of different levels of cellular complexity. In 1967, Peter Wolf visualised *platelet dust* in fresh platelet-free blood plasma using an electron microscope[64]; thus, a mammalian vesicle-like structure was described for the first time. Gradually, these vesicles were characterised in more detail. It has been established that they are released by all kinds of cells (prokaryotic and eukaryotic) into the *extracellular milleu*[172–175]. The process of vesicle secretion is conserved throughout evolution, suggesting that such vesicles are likely to have specific roles in the cellular and organismal development and survival[176]. Indeed, later discoveries showed that secreted vesicles participate actively in many physiological processes in mammals, for example coagulation, inflammatory response, cell maturation, adaptive immune response, bone calcification and neural cell communication, among others[65,68]. In addition to their critical functions in normal physiology[69,70], secreted vesicles mediate in several pathological processes[71,72], such as the establishment of pre-metastatic niche during cancer progression[73,74].

Nowadays, these secreted vesicles are extensively reported and widely known as extracellular vesicles (EVs). EVs are heterogeneous, nano- to micrometre-sized, bilayer lipid containers secreted by most cell types. They are multi-purpose carriers that can contain a wide variety of cargos such as lipids, proteins, metabolites, sugars, RNA (mRNA, miRNA, siRNA) and even DNA[65]. When they are taken up by recipient cells, they trigger intracellular signalling through EV surface molecules or by the release of cargo into cell compartments via endocytic pathways. These processes can further activate downstream genetic or metabolic pathways in the recipient cell[67,68]. In mammals, EVs have been found in body fluids like plasma, urine, saliva, breast milk and seminal fluid, among others. They are classified into three groups according to their biogenesis mechanisms and biophysical properties:

- exosomes: typically 30–150 nm in diameter, derived from intracellular endosomal compartments,

- microvesicles: 100–1000 nm in diameter, produced by outward budding and pinching-off the plasma membrane, and

- apoptotic bodies: 50–5000 nm in diameter, released as blebs by cells undergoing apoptosis[64,65].

In a systematic review of guidelines for this field, the International Society for Extracellular Vesicles (ISEV)[75] endorsed a categorisation of EVs isolated using ultracentrifugation into large, medium and small EVs. However, it is important to note that ultracentrifugation precipitates not only vesicles but also lipoproteins, viruses, protein aggregates, ribonucleoprotein complexes and exomeres[76–78], which provides an additional layer or diversity but also a bias upon analysis of EV samples. Furthermore, there is evidence that exosomes, microvesicles and apoptotic bodies contain subpopulations with unique roles in biological processes[177,178]. These subpopulations are tightly integrated with a broad range of biological processes and exhibit a wide range of functionalities, which makes them an outstanding source of potential biomarkers for early diagnosis, drug delivery systems for therapeutics, or vaccine production systems[72,179–181].

During the last few decades, the interest in EVs and their applications has grown considerably. Many articles and reviews have focused on the functional role of EV heterogeneity. Their role in specific biological processes, such as cargo trafficking or regulation of signalling pathways, and their potential as biomarkers have also been examined[68,72,178,182,183]. Nonetheless, most of these studies examine the vesicles in bulk and use ensemble-averaging assays. Although such methods have been proven useful in specific cases, it is important to realise that the extensive heterogeneity of structure, composition and function of single vesicles are masked in such assays[177,182–184]. For example, the inability to detect the heterogeneity of molecular states of reaction pathways, individual proteins or nucleic acids may lead to a misinterpretation of ensemble measurements[185,186]. Recent developments in single-vesicle analysis (SVA) have opened new opportunities for the examination of heterogeneity within EV (sub)populations at the individual EV level and their characterisation on the nanometre scale[176,182]. This new information is paramount for understanding the biological functions of EVs and for their potential clinical use.

Different EV populations and subpopulations can be isolated according to their physicochemical properties, yet the existing isolation technologies are intricate and still need to be further developed[177,182]. There are five main groups of techniques for sorting EV populations and subpopulations, based on ultracentrifugation, size, immunoaffinity capture, polymer precipitation and microfluidics[65]. Since each technique type sorts EVs using a different principle, each method can yield different EV subpopulations from the same sample[187,188]. Moreover, the highly concentrated EV preparations may contain contaminants, such as large protein aggregates and lipoproteins, left behind by some of the isolation techniques[189,190]. Interestingly, different approaches can also affect the physicochemical surface characteristics of EVs[191].

In consequence, some techniques tend to enrich or discriminate against specific EV populations. As sorting EVs into populations is usually based on physical properties only, we have to assume that such classification is largely arbitrary with respect to the composition or function of EVs. Vesicle isolation and

enrichment techniques can help to yield more homogeneous EV subpopulations, albeit only for particular technique-specific parameters. In conclusion, although various isolation methods could help driving EV analysis towards a single-vesicle approach[176], many different compositions and functionalities are still expected to be found within such EV populations.

In this review, we describe the current methods used to study single-vesicles , and their contributions to the understanding of EV biology and biomarker discovery. Single-vesicle experiments can deliver direct information on the heterogeneous composition of EVs. They reveal multiple molecular states that govern EV functionality and transport and provide statistically valid information often lost in large ensemble experiments[66,182,192].

1.1.1.   EV heterogeneity and biomarker discovery.

There are many technological challenges to be met in the development of EV-based diagnostics. The relevant vesicles must be identified and isolated from complex biofluids, and a specific disease-related EV population or population mix has to be detected. Biomedical studies of EVs often focus on seeking suitable biomarkers for the diagnosis of various diseases[193,194]. For example, the functional role of EVs in various types of cancer has been extensively studied[71,73,74,180]. In this review, we concentrate on prostate cancer (PCa) diagnostics as an example application to which the SVA of EVs has made important contributions. According to the World Health Organization, PCa is among the most frequently diagnosed types of cancer, accounting for approximately a quarter of all cancer diagnoses in Europe[195], yet the lack of sensitive diagnostic tools and insufficient knowledge of the mechanisms of cancer emergence and progression are of major concern. PCa is a heterogeneous pathological state, both in the primary tumour in the prostate tissue and at the metastatic stage. It is unfortunately not recommendable to examine PCa diversity relying solely on tissue biopsies, since these are highly invasive procedures and do not guarantee an effective and reliable diagnosis[196–199]. The serum prostate-specific antigen (PSA) test—still the cornerstone of PCa screening—is particularly questionable. Up to 40% of men undergo unnecessary biopsies as a result of poor specificity of the assay.

Remarkably, liquid biopsy has a potential for marker identification and provides better evidence of PCa diversity than the conventional solid tissue biopsy. In particular, prostate- and PCa-derived EVs and concomitant markers are highly abundant in urine, blood and ejaculate samples[60,200]. Hence, these body fluids could be used for detecting and measuring the progression of the disease. For example, the EVs released by PCa cells carry unique prostate-specific membrane proteins (e.g. TMPRSS2, STEAP2, PSMA, PPAP2A, etc.) that enable the detection of pathogenic prostate EVs and their capture for *ex vivo* characterisation[201]. Although these data show that liquid biopsies may be highly informative and minimally invasive procedures, the methods for vesicle isolation, characterisation and identification for disease diagnostics remain challenging. Up to date, there are no standardised operating procedures for vesicle isolation and characterization for different types of samples and diseases, which complicates the employment of liquid biopsies as a clinical source for EV biomarkers.

1.1.2. Single vesicle analysis techniques for biological characterisation of EVs.

Most of the studies reviewed in this article examine the three problems that can be addressed by taking advantage of SVA techniques: (1) characterisation of EV heterogeneity including subpopulations, surface (membrane protein and lipid) composition and vesicle content, (2) structural studies of EV membrane and soluble proteins and the assays to probe the metabolic activity of these proteins in a native-like environment and (3) characterisation of the EV content and function depending on the cells of origin. The last task presents an interesting dichotomy: do the EVs reflect the properties of their cells of origin, or are they completely independent communication assets? On the one hand, it has been reported that EV surface and content depend on the parental cells[202–204]. On the other hand, some recent reports describe several EV subpopulations, with a range of different functionalities, originating from the same cell type[66,67,176,182,205,206]. Intriguingly, another recent article using SVA techniques demonstrates that the T2SS-like family of proteins is, in fact, responsible for selective cargo loading into EVs generated by the microorganism *Shewanella vesiculosa*[207].

1.2. Single-vesicle techniques

As increasing numbers of researchers have highlighted the importance of accurate EV (sub)population sorting and phenotyping, so far, more than 20 new SVA techniques have been developed[66,176,182]. Many of these use microfluidic devices designed to integrate various technologies to improve EV sorting and detection. Moreover, several of these methods have been used for characterising EVs at the single-vesicle level[208–219]. Some of these techniques can directly provide information on vesicle surface, content, size and shape while other may require an upstream physicochemical characterisation of the selected EV subpopulations to conduct surface profiling, monitor the expression of biomarkers and quantify them in body fluids. These technological advances should help to design new diagnostic devices for small sample sizes, using minimally invasive methods.

Twelve different methods are presented in Table 5 and discussed in detail in the following sections. Some of these methods utilise labelling techniques (such as fluorescence or nanoparticle coating) to visualise the EVs, and others work as label-free systems (Figure 9). It is important to note that in some cases label-free approaches may hinder the detection of EVs because they often produce weak signals, which can be enhanced using a supporting labelling technique.

1.2.1. Label-free methodologies.

Nanoparticle tracking analysis (NTA) is a technique based on the Brownian motion of microparticles in suspension and it is used to determine the size distribution in particle populations[208,220]. In this approach, microparticles are detected by scattering the light of a laser beam, which is tracked and recorded at video frame rates. However, this approach has some disadvantages and limitations. For instance, the accurate assessment of particle size distribution requires specific track lengths, a steady temperature and a large number of replicates to provide robust results. Care should be taken when comparing different samples because variations in buffer viscosity and microparticle concentration introduce statistical errors. Moreover, the close proximity of two particles can result in overlap of the

scattering signals. Accurate detection of particles with a diameter below 60 nm is challenging, regardless of the NTA machine used[221]. Furthermore, vesicles cannot be discriminated from other particles, such as protein aggregates or virus particles. The vesicles can be probed specifically, and undesired particles excluded from the analysis only by employing fluorescent markers, yet only a fraction of EVs may carry known markers that can be used for labelling a specific subpopulation. General fluorescent labels (such as lipophilic carbocyanines DiO or DiI) can be used instead. However, it is important any non-attached label is removed since this can mask the fluorescence signal emitted by labelled EVs[66].
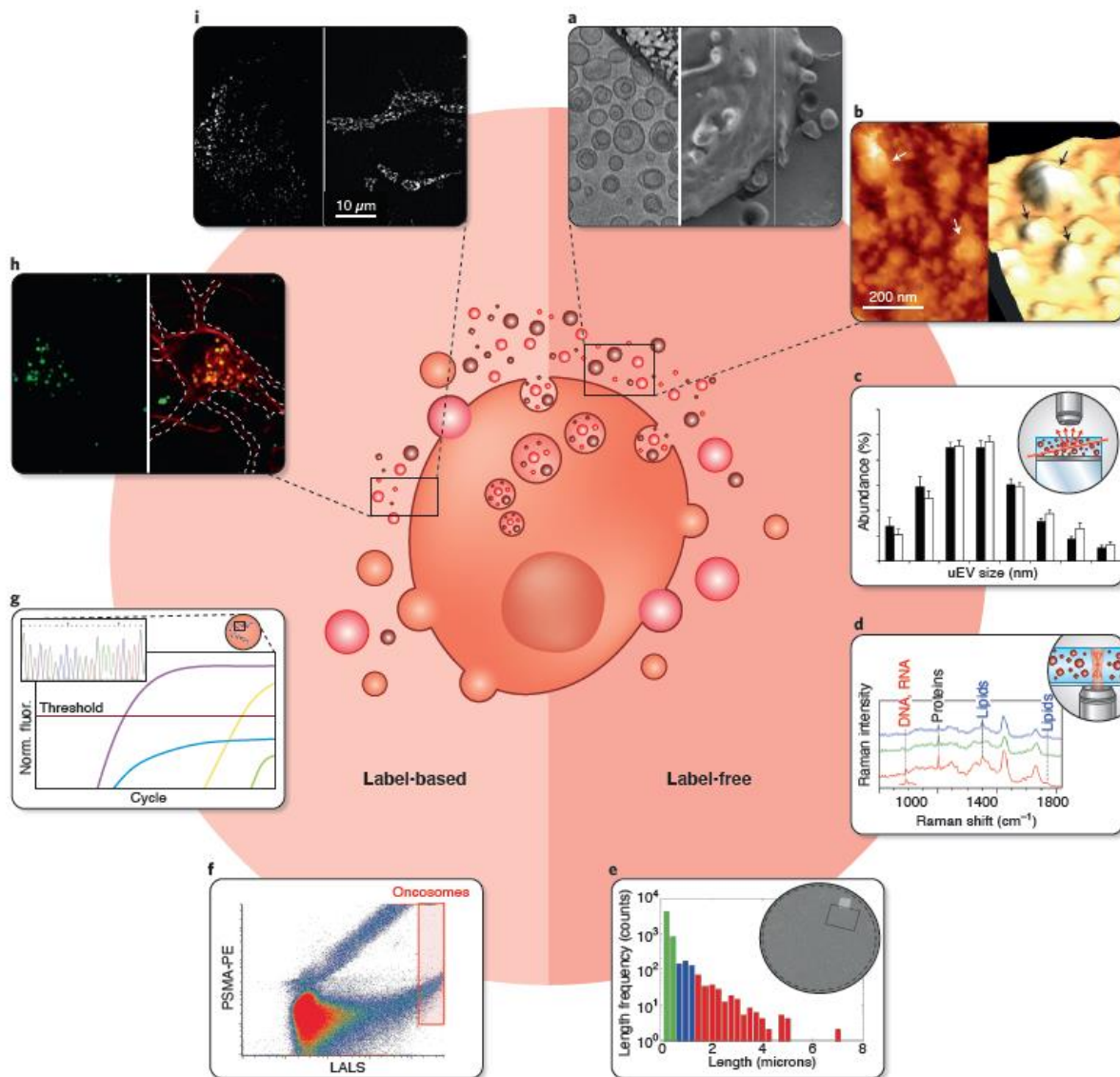
Figure 9. Schematic overview of the main SVA techniques discussed in this review. Data visualisation and single-vesicle interpretation using each SVA methodology are depicted. In the centre of the figure, a (tumorigenic) cell releasing EVs is shown. The techniques can be divided into two groups: label-free (a-e) and label-based (f-i) methodologies. The methods used here are: a) Cryo-electron microscopy[222,223], b) AFM, c) NTA[176,224], d) RTM[223], e) SP-IRIS[225], f) hrFC[226], g) ddPCR[227], h) SRM[228] and i) fluorescence microscopy (TIRF image of synaptic vesicles is depicted)[229]. References show the source of the images.

Raman tweezers microspectroscopy (RTM), also known as laser tweezers Raman spectroscopy (LTRS), can be employed to examine the chemical content of EVs. This approach can be used to

investigate both the surface and the internal volume of single EVs, revealing specific biomolecular signatures of proteins, lipids, nucleic acids and carotenoids as major contributors[204–206,216,225–231]. RTM is an inelastic scattering-based method. It employs a tightly focused laser beam for both optical trapping of single (or very few) vesicles in aqueous medium and excitation for subsequent Raman scattering, which provides a vibrational fingerprint from the trapped constituent biomolecules. The main inherent advantage of RTM lies in the signal linearity, which allows both qualitative and quantitative biochemical characterisation of single EVs. This method is also label-free and provides data with high information content[209,223,230]. The main disadvantage is that the scattering efficiency is usually very low and thus provides a rather low level of informative Raman signal. As a result, an extended data collection time is required. Therefore, RTM, with a typical processing capacity of 0.2 particles per min, is not considered a high-throughput methodology[230]. RTM can, however, be used to obtain interesting, unique information not only for EVs[209–211,223,230–236] but also for many other bioparticles like liposomes, lipid layers on synthetic nanoparticles and others[237–242].

Several methods have been developed to compensate for the low Raman signal strength in RTM. For example, the vesicle concentration can be increased by drop-coating deposition of the sample, followed by drying[243–247]. Unfortunately, this approach results in loss of information about individual EVs, as does any other analytical study of a bulk sample. Another strategy to increase the Raman signal is to use surface-enhanced Raman spectroscopy (SERS). In this method, EVs can be exposed to various signal-enhancing nanoparticles and/or substrates to obtain a strengthened biomolecular signal[212,248–254]. The main problem of label-free SERS is that the enhancement effect depends strongly on the distance between the biomolecule and the nanoparticle/substrate, and vanishes at distances longer than a few nanometers[248]. Therefore, this method is mainly suitable for characterisation of biomolecules on the outer surface of EVs. In addition, Raman modes corresponding to molecular vibrations perpendicular to the SERS surface are preferably enhanced[248]. As a result, the overall SERS vibrational spectrum is usually distorted, lacks reproducibility, and is often difficult to interpret.

In electron microscopy, a beam of electrons is emitted onto a sample in a vacuum environment. The wavelength of electrons is shorter than the visible light used in optical microscopy; thus, the method gives images of much higher resolution, typically below 1 nm[66]. Cryogenic transmission electron microscopy (cryo-TEM) is among the electron microscopy methods most commonly utilised for EV characterisation. In contrast to the lengthy sample preparation needed for other TEM methods (usually taking hours), no heavy metals or fixatives are added, and no dehydration steps are required. This also limits sample damage and artefact effects, but yields lower contrast images[255]. In cryo-TEM, the samples are prepared by rapid freezing, typically with liquid ethane[209,256]. In this process, the water vitrifies, instead of forming ordered crystals, and the native structure of EVs is preserved[257]. The first exosome visualisation was achieved using cryo-EM in 2008[258]. Since then, this technique has successfully revealed EV polymorphism by imaging the membrane bilayers, EV structures and internal features of individual EVs[209,213,255,259]. Even though cryo-TEM is an extremely useful technique for high-resolution visualisation of EVs, this approach is relatively low-throughput. Cryo-TEM images typically only contain a few EVs (although the throughput could be enhanced by using automated search). In addition, cryo-

Table 5. Summary of main SVA techniques for individual EV characterisation.

Technique	Detection principle	Information obtained	Throughput	Time per analysis [a]	Sample preparation [b]	Is sample reusable?	Loading volume	Working concentration (mL^{-1})
High-resolution flow cytometry	Elastic light scattering. Auto-fluorescence or fluorescence from external labels.	Profiling[c] of EVs in a heterogeneous fluid mixture. Functionalised fluorescent labels characterise specific populations.	High	~1 min	Immunofluorescence or fluorescent conjugate staining protocol.	No [d]	20–100 µL	10^7–10^{10} [e]
Nanoparticle tracking analysis	Imaging of Brownian motion pathways for EVs, using elastic light scattering or fluorescent labels.	Particle concentration, size distribution.	Moderate	~1 min	Dilution or concentration of EVs to the range optimal for the method.	Yes	0.3–1mL[f]	10^8–10^9
Raman tweezers microspectroscopy	Raman scattering from optically trapped single EVs.	Biomolecular[g] composition of the surface and the interior of single EVs.	Low	~1-5 min[h] per one[i] trapping event	Concentration of EVs to the range optimal for the method.	Yes	~100 µL	10^7–10^{11}[j]
Surface-enhanced Raman spectroscopy (SERS)	Raman scattering enhanced by external active surface/coating.	Partial[k] biomolecular[g] composition of the membrane of single EVs.	Moderate	~1-10 s per one[i] EV	Fixation and coating protocol.	No	50–100 µL	10^9–10^{11}
SERS with external labels	Enhanced Raman signal from SERS nanotags.	Number of EVs with specific functionalised SERS nanotags attached.	High	~10 s	Fixation and SERS-label staining.	No	10–100 µL	10–10^7[l]
Cryo-transmission electron microscopy (Cryo-TEM)	Transmission electron microscopy imaging.	Morphological EV characterisation[m]. Direct visualisation of single EVs and examination of contaminants.	Low	~1 hour [h]	Vitrification of water in EVs dispersed on carbon grid, using fast-plunge freezing.	No	2–10 µL	10^{10}–10^{12}
Atomic force microscopy (AFM)	Imaging (raster scanning) exploiting interaction force between the probing tip and immobilised EV.	Precise[q] morphological, mechanical and biochemical [o] characterisation of the EV surface.	Low	~1 min per image[s]	Immobilisation protocol.[p]	No	5–25 µL	Relative[q]

Table 5. (Continued)

Technique	Detection principle	Information obtained	Throughput	Time per analysis [a]	Sample preparation [b]	Is sample reusable?	Loading volume	Working concentration (mL^{-1})
Total internal reflection fluorescence microscopy (TIRF)	Imaging using fluorescence from external labels in an ultra-thin layer[r] of induced evanescent field[s].	Background fluorescence suppression. Visualisation of specific biomolecules[t] in vesicles of living cells. Information on EV interaction and trafficking.	Moderate	10–60 min	Fluorophore internalisation protocol. Calibration of the angle of incidence.	Yes	10–200 µL	Relative[q]
Fluorescence resonance energy transfer (FRET)	Excitation energy transfer between donor and acceptor fluorophores via non-radiative resonance interaction. Change[u] in fluorescence colour.	Structural information[v] derived from short-range[w] interactions in the donor-acceptor pair.	Moderate	10–60 min	Fluorescence staining.	Yes	10–200 µL	Relative[q]
Super-resolution microscopy	Fluorescence from external labels.	Visualisation of single vesicles in biological samples.	Low	~1 sec per image	Fluorescence staining. Fixation protocol.	No[x]	50–100 µL	Relative[q]
Droplet PCR	PCR amplification in partitions.	Absolute quantification of specific targets in individual EVs or small *identical*[y] subpopulations.	Moderate	~5 hours per loading volume	EV droplet encapsulation protocol.	No	20–150 µL	10^2–10^3
SP-IRIS	Enhanced scattering signal from particles bound to a substrate.	Multiplexed phenotyping (surface biomarkers) and sizing EV populations in a single measurement.	High	-	EV incubation on array.	Yes	20 µL (microfluidics)	$<10^9$

[a]Time required for analysis once the sample and instrument are ready for the measurement. [b]Sample preparation protocol, for all techniques, contains the first obligatory step of EV purification and separation. [c]Obtaining size distribution, number of labeled particles, counting and sorting. [d]Attempts to sort the selected vesicles are under way and are likely to be successful in the future. [e]Dilution of the sample will be required to avoid swarm effect. [f]20 µL in microfluidics devices. [g]Distribution of proteins, lipids, nucleic acids, carotenoids and other biomolecules with pronounced, strong Raman bands. [h]Time for optimal working concentration. For particle concentration lower than optimal, the measurement time can increase considerably. [i]The total number of single EVs analyzed per sample depends on the task and measurement statistics and will be different for each particular experiment. [j]Concentration range is determined using the waiting time for the event of EV optical trapping. For larger/heavier EVs, lower concentrations are used: 10^7–10^9 mL^{-1} is suitable for large ~1 µm EVs, 10^8–10^{10} mL^{-1} is optimal for smaller exosomes, and up to 10^{11} mL^{-1} is required for the smallest (~50 nm) bioparticles. [k]Within the area of sufficient Raman-signal enhancement (depending on the geometry of interaction between EVs and the signal-enhancing surface/coating). [l]Exosome concentration logarithm is linear over the range of 40 particles/µL to 4×10^7 particles/µL plotted against Raman intensity[250]. [m]Polymorphism, membrane layers, internal-structure features, etc. [n]Lateral resolution 1–3 nm, axial resolution below 0.1 nm. [o]Using an immunofunctionalized probe tip. [p]On glass, mica or graphite (HOPG-type). [q]Working concentration spreads over a rather broad range and the optimal concentration strongly depends on EVs location in the microscope field. [r]Signal collection layer is usually less than ~100 nm thick, depending on the excitation wavelength and objective numerical aperture. [s]Evanescent field is created when the angle of incidence of excitation beam is larger than the angle of total reflection, so that the excitation beam does not penetrate into the sample. [t]miRNA, surface proteins. [u]Donor fluorescence disappears, acceptor fluorescence appears. [v]Assessment of conformational fluctuations, folding pathways, macromolecular interactions, kinetics of structural changes, etc. [w]When distance between donor and acceptor fluorophores becomes <8–10 nm. [x]Some SRM approaches damage the sample to such an extent that only one measurement is possible, and others permit several SRM imaging analyses of a sample. [y]EV subpopulations with a specific surface protein in common.

TEM images provide only limited information regarding EV composition.To overcome this problem, nanoparticles functionalised with immunogold-labelled antibodies targeting markers of interest have recently been employed to characterise the biochemical composition of the EV surface[66,260].

Yet another type of microscopy method used for SVA is atomic force microscopy (AFM), which exploits the interaction between a probing tip and a sample surface. The deflection of the probing tip caused by interaction forces is detected and recorded using a laser and a sensor[215]. AFM allows an accurate morphological and mechanical characterisation of EVs; its lateral resolution is 1 to 3 nm and the vertical resolution, below 0.1 nm[215]. Typically, visualisation of a few EVs using AFM is labour-intensive and time-consuming in comparison with other microscopy methods. However, a relatively high-throughput AFM-based method has been reported which measures the size and stiffness distribution of 100 vesicles within an hour[261]. It is important to note that the tethering surface, to which the EV is bound, strongly affects the shape of the EVs. Therefore, the vesicles must be bound to a perfectly flat surface[262–264]. To characterise the biochemical properties of an EV surface, either the probing tip or the surface itself can be further (immuno)functionalised[265,266]. AFM can also be coupled with infrared spectroscopy (AFM-IR), allowing simultaneous measurements with a finer spatial resolution. AFM-IR has been extensively utilised in various applications; however, few papers report its implementation in the single-EV field[216,267]. We assume this is because the weak IR signal thwarts reliable characterisation of individual vesicles.

Single-particle interferometric reflectance imaging sensor (SP-IRIS) is employed in assays based on interferometric imaging. It is used to detect individual enhanced scattering signals from the bound vesicle. The signals are produced by the interference between the scattered field from a vesicle and the reference field reflected off the layered substrate[66,114]. The method can detect several surface biomarkers and simultaneously measure the size of individual EVs. It can be used to accurately count and distinguish individual vesicles, with a low level of false positives and negatives[268]. However, as the lateral resolution of the microscope (approximately 400nm) could accommodate several small vesicles, some detected signals could be erroneously assigned and categorised as larger vesicles instead of several smaller vesicles. This could be an issue specially in highly concentrated sample preparations[269].

1.2.2. Label-based methodologies.

Label-based methodologies are strongly dependent on the detection of a signal from a fluorescent protein, immuno- or lipophilic fluorophore or signal-enhancing nanoparticles. High-resolution flow cytometry (hrFC) is one of the first techniques extensively employed for individual EV analysis. hrFC can be used to quantify the size distribution and diversity of EV populations by detecting multiparametric scattered light and fluorescence emitted by the labelled vesicles. This fluorescence assay can be used to characterise the vesicle population by profiling the protein or nucleic acid content using antibody-fluorophore conjugates. However, any remaining free fluorescent dyes in the sample will cause high background fluorescence. This can be avoided by using density-based ultracentrifugation to purify labelled EVs, which leaves the non-reacted dye in the supernatant and sediments the vesicles into the

pellet fraction[270,271]. Furthermore, multiple EVs (or particles) arriving simultaneously at the flow cytometer detector may be identified as single particles. This phenomenon is known as the *swarm effect*. The danger of such misidentification limits the concentration range within which the EVs (or particles) can be characterised effectively and makes it necessary to examine multiple diluted samples.

Fluorescence microscopy is an imaging technique particularly useful in localising lipophilic fluorescent dyes or fluorescently labelled targets (either using fluorescent proteins or f*luorescent dye*-conjugated *antibodies*) in cells, tissues or EVs[176]. Another, rather elegant approach, now commonly used in the SVA field is total internal reflection fluorescent (TIRF) microscopy. It can be used in an aqueous environment to image selectively the fluorescent molecules located near a highly refractive solid substance[272]. TIRF exploits the reflection of an excitation light beam at a high incident angle, typically between 60º and 80º, at which the beam of light is completely reflected by the glass/water interface. This reflection phenomenon generates a very thin electromagnetic field, called an evanescent wave, which is parallel to the substrate surface. This enables limited specimen illumination and thereby eliminates out-of-focus fluorescence and enhances the signal-to-noise ratio[272]. TIRF is predominantly used for studying intracellular single-vesicle processes like endocytosis or exocytosis, cell–substrate contacts or internalisation of plasma membrane receptors[271,273]. It can also directly localise fluorescently labelled molecules in EV preparations and allows tracking EVs in tissue preparations. However, the fluorophores can be excited only within a few hundred nanometres from the solid substrate, and the calibration of the incident angle can be difficult (depending on the set-up)[271,273]. Moreover, the fluorophore instability and gradual photobleaching (although less pronounced than in other light microscopy techniques) during prolonged illumination may produce misleading results[274].

Fluorescence (or Förster) resonance energy transfer (FRET) is a phenomenon where the excitation energy from a fluorophore is transferred non-radiatively to another fluorophore. This happens via resonance energy transfer at distances shorter than 10 nm. FRET imaging offers unique opportunities for the assessment of kinetic and structural dynamics and studies of the interaction and fusion events between EVs and cells[275–280]. Notably, this imaging-based technique is capable of producing a considerable amount of single-particle and single-vesicle fluorescence data very fast[278–281]. However, fluorescent signal fluctuations due to a low signal-to-noise ratio and poor photostability of certain dyes may lead to changes in the FRET signal that are unrelated to the biological processes. Like in other fluorescence-based techniques, the presence of multiple fluorophores within the observation volume may result in ensemble averaging of the population[277,282].

Super-resolution microscopy (SRM) is one of the most advanced applications of fluorescence imaging. It can be used to visualise biological features smaller than the optical diffraction limit and, therefore, below the conventional optical microscopy resolution limits (which are typically limited to ~250 nm axial and ~500 nm lateral resolution). This attribute provides an important advantage in imaging single EVs and permits investigation of their physiological functions[217,228,283–287]. Briefly, SRM techniques can be divided into two groups: (i) methods based on spatial patterning of the excitation light and (ii) methods based on single-molecule localisation.

Excitation-patterning methods include structured illumination microscopy (SIM), in which the specimen is illuminated in a striped pattern[176,288] and stimulated emission depletion microscopy (STED), which sharpens the excitation laser focus using a second laser that temporarily bleaches the fluorophores surrounding a small observation volume in the specimen[289].

Single-molecule localisation methods detect fluorescence emitted from spatially isolated photo-switchable or blinking fluorophores to determine their position[290]. Photoactivation localisation microscopy (PALM) relies on photoactivatable fluorescent recombinant proteins[291], whereas stochastic optical reconstruction microscopy (STORM) takes advantage of fluorophores that blink in a non-controlled fashion. In both cases, only a small subset of fluorophores will be emitting simultaneously, allowing the precise localisation of the fluorophores and reconstruction of the complete image at high spatial resolution[288]. Importantly, single-molecule localisation approaches can be used in combination with TIRF, improving the signal-to-noise ratio and shortening imaging time[273]. Furthermore, all SRM techniques are based on the optics of classical diffraction-limited far-field light microscopes. This makes them compatible with existing sample preparation procedures, and also permits them access beyond the surface of a specimen. SRM techniques are also often minimally invasive[290,292]. It is important to note that most SRM approaches work only on fixed samples, thus one should always be aware of potential artefacts introduced by the fixation method[288,293]. Another relevant aspect to consider is that in general the labelling of proteins using fluorescence markers or other tags might affect their localisation, interaction partners and function[292]. In addition, although lipophilic- or genetic-labelling could both allow the visualization of single vesicles, lipid labelling in some cases might result in unspecific labeling or dye aggregates.

Digital droplet PCR (ddPCR) can be employed to distribute single EVs into individual droplets, which allows to amplifying and characterising their genetic cargo[219,294,295]. Such cargo is usually RNA-based and mainly comprises miRNA, mRNA and non-coding RNA. In ddPCR, the EVs are tagged using anchoring molecules or antibodies and further distributed into microfluidic chambers according to their surface markers[219]. This methodology enables high-throughput quantitative analysis of EV content and can be used for the identification of biomarkers[296–299]. So far ddPCR use has been limited to validation purposes, however, it can be used as a screening technique (compromising its high-throughput capabilities)[66,300]. Interestingly, ddPCR has been already adopted for multiple mutation analysis to examine specific mutations in distinct populations of EVs. Next-generation sequencing could allow for parallel analysis of multiple mutations in many genes[301].

Finally, SERS nanotags functionalised with bio-recognition molecules (such as target-specific antibodies) can be used to bind specifically to target EVs expressing the biomarker of interest. This approach is gradually becoming an important alternative to fluorescent molecular probes[253,302–306]. The major advantage of SERS labelling lies in the superior photochemical stability of Raman reporters compared to fluorescent labels, due to the vibrational nature of the generated signal. Moreover, several high-throughput Raman/SERS screening platforms for characterising cells and EVs have been recently reported[236,307–310].

1.3. Recent advances in the EV field due to single vesicle analysis

The recent breakthroughs in SVA techniques help to tackle the intrinsic limitations of ensemble EV measurements and analyses. In the following sections, we review the impact of SVA method development on recent advances and discoveries in the EV field (EV characterisation, internalisation, the role of EVs in cell–to-cell communication and biomarker discovery). In Table 6, we provide an overview of recent scientific articles describing the characterisation of EVs, including studies of their heterogeneity and phenotyping of PCa-derived EVs. Current studies of EV internalisation pathways and the role of EVs in cell–to–cell communication are summarised in Table 7. SVA techniques have been used in the successful identification and validation of a wide range of biomarkers for many different diseases. As an example, Table 8 lists recent discoveries in cancer research with a strong focus on PCa.

1.3.1. EV characterisation.

Several techniques mentioned in the previous section—NTA, cryo-TEM and flow cytometry—are established as customary characterisation procedures for EV studies[298]. Notably, the results obtained employing these methodologies usually require validation using a complementary technique. This is because none of them is considered the gold standard procedure and all of these approaches come with their own challenges and limitations[311]. For example, NTA is routinely utilised to obtain the size of EVs and quantify their abundance. However, since this technique is not vesicle-specific and can detect other particles, the reliability of the results must be cross-checked with other techniques. Therefore, EV studies that draw their conclusions solely from NTA are now uncommon, especially when compared to earlier EV characterisation studies (from 2012 to 2015) when NTA was commonly utilised. Nowadays, NTA is often used as a supplementary characterisation technique instead as it requires minimal sample preparation to introduce fluorescent markers for specific EV population studies. Likewise, labelling-based flow cytometry serves as a high-throughput sorting method for the characterisation of certain EV features; however, it needs some technological improvements in separating unbound dye and dye aggregates from EVs to be utilised as a unique characterisation approach[312]. Direct visualisation of EVs using microscopy lets researchers assess the shape and size of vesicles in their native state[313] and in various biological processes[314] while other techniques, such as RTM, can be employed to examine further the morphology of bioparticles without direct visualisation. For example, the effect of membrane lipid composition on the shape and size of giant unilamellar vesicles has been first described using Raman tweezers, demonstrating that a decrease in cholesterol concentration increases the local membrane curvature and stretches the vesicle[241].

A large diversity in the morphology of exosomes has been reported for many types of cells[302]. For example, in the early 2010s, plasma EVs were comprehensively characterised and phenotyped using cryo-TEM in combination with gold nanoparticle-based immunolabelling[315]. This study found that platelet-free plasma samples contain a mixture of EVs with different morphologies, including spheres, cylinders and membrane fragments that are neither tubular nor spherical. Moreover, it has been shown that EVs come in a wide range of sizes[315]. Despite this morphological heterogeneity, only a minority of EVs in plasma expose phosphatidylserine on the surface. This is at odds with the classical theory of EV

formation at the cell's plasma membrane, in which the loss of phospholipid asymmetry and exposure of phosphatidylserine precedes membrane blebbing and shedding[316–320]. The authors have suggested that some EV (sub)populations ought to be generated and regulated via different pathways[315]. Likewise, Emelyanov *et al.* have described a large spectrum of EV morphologies and (sub)populations after isolating EVs from cerebrospinal fluid and visualising them using cryo-TEM[321]. They have reported several different morphologies, including multi-layered, single- and double-membrane vesicles, as well as internal vesicular structures. Interestingly, a subpopulation of these EVs plays a key role in Parkinson's disease progression[321]. Another study, using NTA-based technology, has identified several EV populations released by human glioblastoma cells[322]. Moreover, fluorescence-based NTA approaches are being used to examine the concentration and particle distribution of specific EV subpopulations[323,324].

The relative chemical abundance of major biomolecules comprising EVs, namely proteins, lipids, nucleic acids and carotenoids, can be obtained from the vibrational fingerprints acquired using RTM. Tatischeff *et al.* have shown that *Dictyostelium discoideum* in two different physiological states (i.e. cell growth and starvation-induced aggregation) produce EVs with drastically different biomolecular compositions[209]. In another study, Smith *et al.* have categorised four EV populations according to specific protein, phospholipid and cholesterol vibrational signatures, which are shared among several cell types from different species[230]. The authors have found that human lung carcinoma A549, human hepatocarcinoma Huh-7 and mouse embryonic fibroblast 3T3 cells have similar EV populations. In contrast, Kruglik *et al.* have reported direct Raman evidence of pronounced biomolecular heterogeneity of single EVs in the same sample (using rat hepatocytes and human urine)[223]. In their study, the heterogeneity was determined by quantitative measurements of nucleic acid concentration within single EVs, based on the intensity of the pyrimidine ring stretching band[223].

Further heterogeneity studies performed with cryo-TEM and AFM have described the physical characteristics of EVs. One cryo-TEM analysis has reported that the shedding process and hence, the type of EV released, is strongly affected by external stimuli, such as lipopolysaccharides or starvation conditions, in a human leukaemia cell line[222]. By using the tapping mode in AFM, biomechanical properties such as elasticity, stiffness, and deformability of single EVs can be assessed[325]. It has been reported that rat hepatocyte-derived EVs are more fragile and easily warped than liver-progenitor mouse EVs[326]. Another study performed using AFM-IR has allowed, for the first time, to probe the molecular constituents and structures of individual vesicles[266]. In this study, the researchers were able to differentiate between the molecular compositions of EVs derived from two subtypes of placenta stem cells. Moreover, their approach has allowed discriminating between protein aggregates and EVs. The examination of DNA, lipids and proteins using AFM-IR, in just a few vesicles, has a remarkable potential in early disease diagnosis[266].

Table 6. Summary of EV characterisation studies using SVA techniques.

Technique	Main conclusion	Ref
AFM	The first time that plant exosomes have been visualised in their native state. They have been observed on the internal layers of the cell walls and their cargo assessed.	[313]
	Matrix vesicles initiate changes during the mineralisation of the extracellular matrix. In the course of this process, the matrix vesicles increase their size and crystallinity and change shape.	[314]
AFM-IR	The first attempt to probe the differences between the molecular constituents (proteins, lipids and DNA) and structures of individual vesicles in two subtypes of placenta stem cells. In this work, protein aggregates have been successfully differentiated from vesicle structures.	[266]
RTM	Vesicle shape and size depend on the lipid composition of the membrane. A decrease in cholesterol concentration increases the local membrane curvature and stretches the vesicle.	[241]
Cancer research		
hrFC (immuno-fluorescence)	Microenvironment acidity of the prostate tumour increases the release of prostate-specific EVs.	[331]
	EVs from PCa cells are very heterogeneous, but specific populations are not associated with different cancer stages. Mainly microvesicles and several exosome subpopulations are found, according to the surface signature.	[332]
NTA	Increase in the number of released exosomes under acid pH (6.5), independent of tumour histotype.	[330]
	Tumour cells release more EVs than non-tumorigenic cells (most likely due to the acidic environment in tumour cells).	[327]
Heterogeneity-related research		
NTA	Description of different EV populations in human glioblastoma cells.	[322]
NTA (with fluorescence)	The first attempt to use this technique to determine the concentration and particle distribution in specific EV subpopulations, according to surface markers such as CD9, CD63, vimentin and LAMP-1.	[328]
Electron microscopy (cryo-TEM)	Large diversity of exosome morphology revealed, regardless of the cell type and origin, suggesting that different exosome subpopulations from the same cell line perform different functions.	[302]
	Visualisation of a large spectrum of EVs from cerebrospinal fluid, including multilayer vesicles, single, double and double-membrane vesicles, and internal vesicular structures. These specific subpopulations are suggested to serve as potential biomarkers for Parkinson's disease.	[321]
	Two different stimuli affecting EV release. Lipopolysaccharides and starvation conditions in human leukaemia monocytic cell line (THP-1) affect the type of EVs shed and, probably, the shedding process.	[222]
AFM	EVs isolated from different species are imaged. Using the tapping mode, the mechanical properties of EVs are assessed, concluding that the rat EVs are more fragile than the mouse vesicles.	[326]
RTM	During cell growth and starvation-induced aggregation, *Dictyostelium discoideum* produces EVs that differ drastically in their biomolecular composition (nucleic acids, proteins, lipids, carotenoids).	[209]
	Detection of four EV populations with specific protein, phospholipid and cholesterol surface signatures. Their functionality determines their distribution; the populations are shared among several cell types.	[230]
	In EV preparations from rat hepatocytes and human urine, single EVs from the same sample have different biochemical properties, well beyond the "usual" variations for EVs from rat hepatocytes or human urine. A quantitative method developed to measure the concentration of nucleic acids in a single EV.	[223]
	Combined morpho-chemical profiling of individual EVs is proposed based on Raman-enabled nanoparticle trapping analysis.	[233]

SVAs have been extensively utilised in cancer research, for example, to characterise the EVs in PCa. NTA-based research has established cancer cells produce larger amounts of EVs than non-tumorigenic cells[194,217,327] and that low extracellular pH increases the release of EVs from cancer cells[328,329]. Interestingly, NTA studies also support the idea that tumorigenic cells upregulate EV production due to the acidification of the immediate microenvironment[327–330]. Logozzi *et al.* have employed a combination of hrFC and immunofluorescence to discover that acidic microenvironment of prostate tumours induces the release of PCa-specific EVs[330]. These EVs are very heterogeneous, and several populations can be identified, according to their surface composition. However, it is important to note that this heterogeneity is not related directly to different cancer stages[333].

In summary, the highlighted reports of single-EV characterisation demonstrate that EV morphology and composition are largely independent of cell origin and that certain (sub)populations are involved in various diseases. These discoveries indicate that morphologically different EV populations may be distributed according to specific functions and biogenesis pathway, rather than their original cell-type.

1.3.2.   *EV trafficking and signalling mechanisms.*

SVA approaches have advanced EV research by tracking particular molecules and examining the changes in cells under different conditions. Early in 2020, FRET studies in T cells showed that the concentration of free zinc in cells is a major regulator of the maturation process in insulin-storing vesicles[334]. SVA has also contributed to discoveries reporting an increase in intracellular Ca^{2+} and/or protein C under certain stimulating and activating conditions in red blood cells. These conditions alter cell morphology and cause an increase in the release of microvesicles[335]. Table 7 summaries more examples of recent advances in research in (a) vesicle–cell communication and trafficking and (b) vesicle fusion and endocytic pathways.

EVs are serve as information carriers for cell pathways and may trigger some diseases due to this activity. Neurodegenerative diseases like Alzheimer's are caused by the misfolding and aggregation of tau protein. Polanco *et al.* have described a prion-like spread of tau protein seeds brought about by EVs, employing cryo-TEM[336] and SRM (PALM and STORM)[228]. The contribution of EVs to trans-synaptic tau transmission has been confirmed using cryo-TEM in another study[337]. This single-vesicle methodology has also been utilised recently to study the near-native 3-D architecture of EVs secreted after infection with poliovirus. Cryo-TEM tomography has generated images of virions and viral structures contained in EVs before cell lysis[338]. Moreover, FRET microscopy has been used to track the triad protein VOR (VAP-A, ORP3, Rab7), paramount for the transfer of EV-derived components to the nucleus[339]. This type of research has therapeutic potential for diminishing the progression of neurodegenerative diseases (in the case of the VOR complex, by inhibiting EV-mediated intercellular communication).

Cancer mechanisms have also been analysed using single-molecule techniques. Mannavola *et al.* have performed a ddPCR experiment using osteotropic melanoma cells and observed that EVs could induce the upregulation of genes such as CXCR7[340]. Thus, EVs may act as chemotaxis agents and,

hence, participate in the progression of cancer; however, additional research in this field is still required to achieve better understanding of how EVs contribute to cancer[340].

Table 7. Mechanistic studies of vesicles using SVA techniques focusing on vesicle–cell communication, trafficking and vesicle fusion and endocytic pathways.

Technique	Main conclusion	Ref
	Vesicle–cell communication and trafficking research	
FRET microscopy	Tau protein misfolding and monomer aggregates spread in a prion-like manner causing neurodegenerative diseases such as Alzheimer's. Extracellular vesicles play a role in the transmission of pathological tau seeds.	336
	The triad protein VOR is essential in the regulation of the endocytic nuclear transfer of EV-derived components. Targeting VOR might have therapeutic potential by inhibiting EV-mediated intracellular communication.	339
Fluorescence microscopy (SRM)	*In vivo* visualisation of EVs in the zebrafish embryo. Uptake of EVs by endothelial cells and blood patrolling macrophages is shown. The study demonstrates tumour EVs activating macrophages and promoting metastasis.	218
Electron microscopy (cryo-TEM)	Multiple virions and unique morphological components forming a mat-like structure are transported via infectious EVs of 100–1000 nm in diameter. These vesicle-containing enterovirus are secreted from host cells prior lysis.	338
ddPCR	EVs from osteotropic melanoma cells induce chemotaxis and cancer progression via upregulation of CXCR7 of non-osteotropic melanoma cells.	340
	Vesicle fusion and endocytic pathway research	
AFM	Description of mechanical properties of erythrocyte-derived EVs according to their protein–lipid ratio. While a high ratio is associated with soft vesicles, a low ratio corresponds to stiff EVs. These mechanical differences are linked to several vesiculation and budding mechanisms.	341
Electron microscopy (cryo-TEM)	Visualisation of the SNARE-mediated membrane fusion-by-hemifusion of small vesicles with cellsshows fusion intermediates where lipid monolayers partially mix en route to complete bilayer merger.	342
FRET microscopy	Description of the molecular mechanism of SNAREs during different membrane fusion stages, (docking, hemifusion and full fusion) by tracking the lipid-mixing process at the single-vesicle level.	343
Fluorescence microscopy	The fusion pathways are heterogeneous with an arrested hemifusion state predominating. The fusion of two lipid bilayers occurs spontaneously in a single step when they are brought into close proximity.	344
Fluorescence microscopy (TIRF)	Heterogeneity of endocytic vesicle behaviours upon internalisation. Prior to scission, vesicles remain proximal to the plasma membrane for variable periods. Clathrin uncoating is also variable.	345
	Calcium activates synaptotagmin-1, resulting in SNARE-mediated fusion of synthetic vesicles used as an exocytic model for synaptic events. An optimal distance for the fusion is 5 nm.	346
	Alterations in membrane cholesterol content shift hemifusion intermediates to full fusion membrane and affect the stability of fusion pores. A large increase in cholesterol levels boosts individual SNARE-mediated fusion events.	347
	Disassembly of the clathrin lattice surrounding coated vesicles is the obligatory last stage in their life cycle. The study visualises the recruitment of auxilin and Hsc70 which essential for this well-studied endocytic process.	348
hrFC (fluorescent conjugates)	Characterisation of microvesicles from red blood cells under stimulation conditions. An increase in intracellular Ca^{2+} or protein kinase C levels leads to alterations in cell morphology and increased release of microvesicles.	335
FRET microscopy	Free zinc concentration in insulin-storing vesicles is quantified using a novel FRET-based zinc sensor. The concentration of free zinc is important for insulin-storing vesicle maturity, hence it alters insulin trafficking.	334

Vesicle budding and shedding and the mechanical properties of the vesicles are poorly understood. Remarkably, a recent comparative review suggests that biomechanical analysis of single EVs provides key insights into their biological structure, biomarker functions, and potential therapeutic functions[325]. Sorkin et al. have used AFM to study these properties in erythrocyte and EV membranes under different conditions[342]. They have established that stiffness is inversely proportional to the protein–lipid ratio and linked it to several different budding mechanisms[341]. On the one hand, budding of protein-rich soft vesicles is possibly driven by protein aggregation, and on the other, budding of stiff vesicles with low membrane-protein content is likely to be driven by cytoskeleton-induced buckling[341]. A further investigation comparing EVs originating from healthy erythrocytes and from those with hereditary spherocytosis has supported these observations. It also uncovered mechanical and vesiculation differences between these two EV populations with potential use as diagnostic parameters[349].

Vesicle endocytic pathways have been investigated primarily using microscopy-based techniques. One major EV endocytosis pathway is mediated by the formation of clathrin-coated vesicles (Figure 10b). In this process, intracellular clathrin interacts with the membrane, producing a membrane invagination that will form an endosome through which the EVs can be internalised. The disassembly of the clathrin lattice surrounding coated endosomes is a mandatory last step in their life cycle. The recruitment of auxilin and Hsc70 (fluorescently labelled) was directly visualized using an inverted fluorescence microscope equipped with TIRF hardware and described as essential for clathrin-based internalisation events[348]. The clathrin-driven uncoating is a variable process in which the endocytosing clathrin-coated vesicles remain proximal to the membrane for different periods prior to the scission of plasma membrane. The dynamics of clathrin mediated endocytosis were assayed using fluorescently tagged proteins and TIRF microscopy[345].

Fusion states, dynamics and mechanisms of vesicle internalisation during single-vesicle fusion events have been directly examined using cryo-TEM, FRET and TIRF microscopy. Characteristics and kinetics of individual fusion events can be quantified for the lipids or DNA-lipid complexes involved in the process. Different fusion pathways exist: vesicles and cell membrane merge via a direct fusion of membranes (Figure 10a) or using protein-mediated mechanisms (Figure 10c). These mechanisms are involved in both endocytosis and exocytosis events. Examining individual giant unilamellar vesicles by fluorescence microscopy, it has been shown that during a direct fusion event, the hemifusion state predominates, and the fusion of two bilipid layers occurs in a single step when they are sufficiently close[344].

During the last decade, the fusion mechanism based upon SNARE-mediated internalisation pathways (Figure 10c) has been investigated employing SVA. At the molecular level, SNARE proteins mediate vesicle fusion with the target membrane and with membrane-bound compartments. Recently, Mattie et al. have visualised SNARE single-fusion events using cryo-TEM[342]. The sequence of fusion intermediates from lipid monolayers to a complete bilayer merge has been reported in homotypic vacuoles[342]. Hu et al. have correlated the membrane fusion stages with a molecular mechanism using reconstituted vesicles[343]. At a single-vesicle level, they have traced the lipid-mixing process using FRET microscopy and correlated it with the docking, hemifusion and full fusion stages[343]. They also report

that an optimal distance for a SNARE-mediated fusion is 5 nm. Interestingly, some regulators of fusion pathways were identified in related studies. Calcium acts as an activator of synaptotagmin-1, leading to the fusion of synaptic vesicles with the presynaptic membrane[346]. Stratton *et al.* have identified cholesterol as an important regulator of fusion dynamics, shifting the process from hemifusion intermediates towards full fusion membranes[347]. Large amounts of cholesterol precluster t-SNAREs, which serve as functional docking and fusion platforms. These clusters substantially affect the stability of pores by increasing the fraction of fully open pores and accelerating fusion events. Consequently, high cholesterol content triggers fast and individual SNARE-mediated fusion events[347].
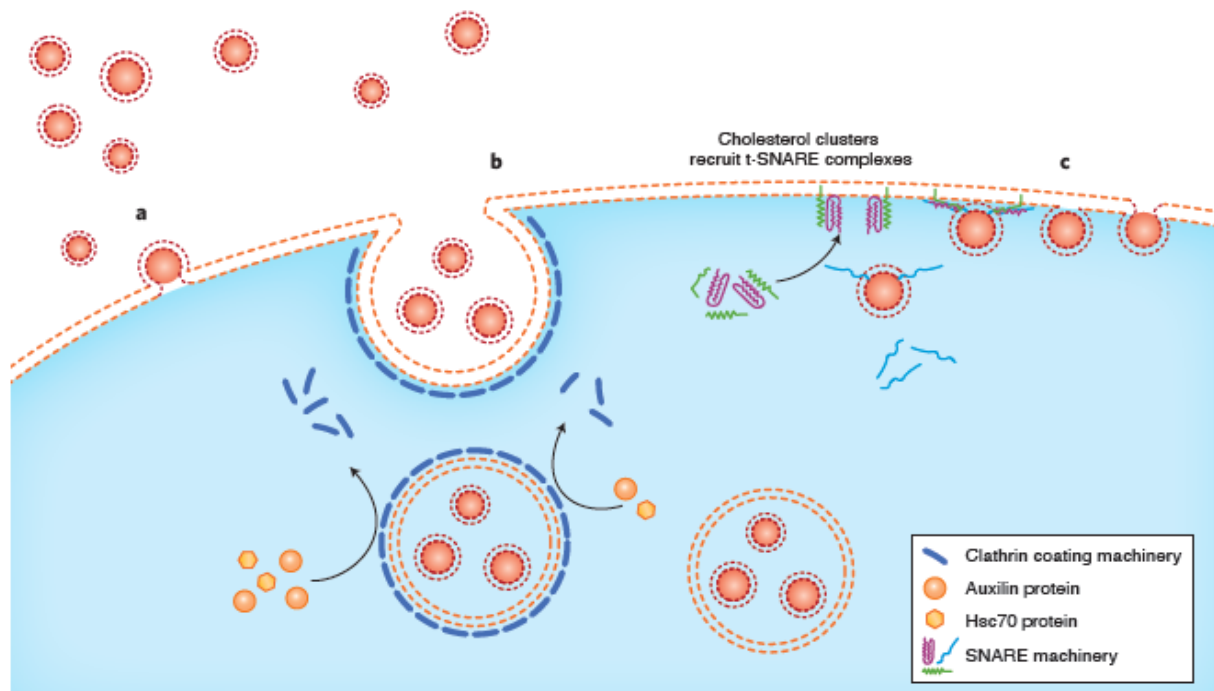
Figure 10. Schematic representation of endocytic and fusion pathways recently investigated using SVA techniques. A lipid bilayer from a recipient cell is shown in dotted orange and EVs lipid bilayer in dotted red; the intracellular content is shaded in blue and vesicle content, in red. (a) direct fusion of EVs with the plasma membrane[348]. (b) Clathrin-based internalisation[349,352]. TIRF microscopy allows the examination of the clathrin uncoating process. In (c), SNARE-mediated membrane fusion is shown[346]. FRET microscopy facilitates the analysis of the three main stages of endocytic and fusion pathways: docking, hemifusion and full fusion. Membrane composition enhances this fusion pathway through t-SNARE-machinery recruitment and enrichment[351].

During the last decade, multimodal imaging platforms have been tested *in vitro* in a number of different cellular models of disease [350–352]. These platforms have considerable potential to be used *in vivo*, for instance, in mice[353–356]. However, these systems usually fail to perform single-EV tracking and have been successful only in *ex vivo* cultures[350]. Nevertheless, there is an animal model worth mentioning due to its physiological characteristics and transparency. Zebrafish embryo has emerged recently as a prospective model for tracking EVs and assessing their dissemination and uptake *in vivo*[357,358]. In 2019, Hyenne *et al.* reported an approach for tracking individual circulating tumour EVs in the zebrafish embryo[218] using confocal microscopy and a combination of chemical and genetically encoded probes to image EVs *in vivo*. The authors described, for the first time, the hemodynamic behaviour of tumour EVs and their intravascular arrest. The study shows that the endothelial cells and blood macrophages rapidly

take up circulating tumour EVs. These EVs activate blood patrolling macrophages and promote meta-static outgrowth[218]. A back-to-back study performed by Verweij *et al.* combined the genetic labelling (using a CD63-pHluorin exosomal reporter) of specific tissues with electron microscopy to track endogenous EVs in blood and further unravel their mechanisms of biogenesis, biodistribution, and target cells throughout the zebrafish embrio[357]. Intriguingly, Sung *et al.* have recently reported a CD63-pHluorin-mScarlett fusion protein that can be used to image several stages of the exosome lifecycle *in vitro*[359]. This reporter likely can be used to visualize exosomes *in vivo* and is a prospective tool for understanding the physiological roles of exosomes.

1.3.3.   EV biomarkers.

SVA techniques hold the capacity to discover new, specific and effective biomarkers in EVs that have been missed by ensemble methods and can be used in disease diagnostics. While the resolution and sensitivity of SVA techniques still needs improving, they provide an accurate characterisation of EV subpopulations and assessment of biomarkers. Extensive research has been carried out seeking the biological biomarkers for several diseases such as prostate cancer[60,224,308], fibromyalgia[360], endometrial cancer[361], colorectal cancer[362,363] and liver-associated diseases[364], among others. Figure 3 summarises recent advances in cancer research at the single-vesicle level. Currently, fluorescent assays, which are often used in cancer screening[365], can detect miRNAs and correlate their presence with individual EVs and EV populations. Exosome-localised miRNA-21 might be used to differentiate between cancer patients and assess tumour progression and response to treatment[365]. Moreover, a specific lipid-protein signature may identify tumour-derived EVs as Raman spectra within the range of 2800 to 3100 cm^{-1} appear to be a distinguishing feature of genuine cancer EVs[234]. These findings open the way for early cancer detection. Nevertheless, the biomarkers discussed here are either generic (cannot discriminate between different cancers) or come from 2-D cancer model research and may not adequately diagnose clinical cancers.

The development of next-generation sequencing SVA methods has optimised the identification of cancer biomarkers. Specifically, targeted sequencing using cancer gene panels has allowed the study of EV-derived and circulating free DNA[300], resulting in the discovery of genetic biomarkers for several diseases. For instance, nine miRNAs have been profiled in serum EVs. Using these profiles, chronic hepatitis C patients can be distinguished from healthy individuals with accuracy above 95%[366]. Diagnostic opportunities presented by EV-specific genetic biomarkers have been widely reviewed[367–370]. It has been shown that cancer-derived EVs rewire and modify the pre-metastatic microenvironment, supporting tumour growth and metastasis during cancer progression[67,71,74,295]. This research describes a set of potential marker targets to be used as early diagnosis of PCa. The promotion and proliferation of PCa triggered by EVs produced as a result of DIAPH3 loss or growth factor stimulation have also been reported[295]. Other studies have shown that miRNA quantification in tissues can identify PCa by detecting the expression of RNU24[371] or miR-130b[372].

Recently, several studies have reported specific and sensitive biomarkers for cancer detection[227,251,296,298,373–375]. ddPCR has detected and quantified the IDH1 transcript in cerebrospinal fluid-

derived EVs of patients with glioma tumours in the brain[296]. In lung cancer, eleven cancer-specific SERS signals have been obtained, allowing to differentiate between EV populations derived from healthy and lung cancer cells with high sensitivity[251]. Additionally, the CD147 protein found in EVs has been identified as a biomarker for colorectal cancer (CRC) diagnosis[362]. Further studies have identified BRAF and KRAS somatic mutations in plasma-derived EV populations from CRC patients[227]. Intriguingly, Melo *et al.* have described an explicit biomarker, glypican 1 (GPC1), found in EV populations from pancreatic cells containing different KRAS oncogenic isomers[374]. Hence, GPC1-EV identification could facilitate early pancreatic cancer diagnosis[374]. In 2020, the EV-transported HULC lncRNA (long non-coding RNA highly upregulated in liver cancer) was suggested as a chemotaxis agent for cell invasion and migration. This encapsulated HULC is a potential biomarker for human pancreatic adenocarcinoma diagnosis[298].
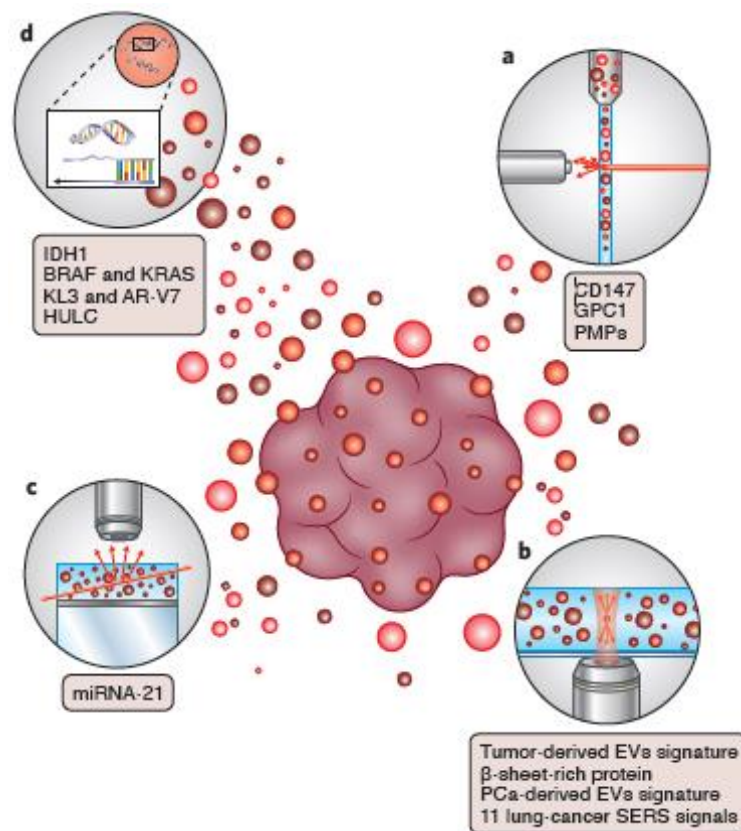
Figure 11. Schematic overview of reviewed biomarkers discovered using SVA techniques. The methods shown here are: (A) hrFC[226,362,374], (B) RTM[211,232,235,243,251], (C) TIRF[361] and (D) ddPCR[227,296,298,370]. More information for specific biomarkers discovered using each method can be found in Table 8.

The recent advances in cancer biomarker research are a proof-of-concept for non-invasive diagnostic tools based on EV fingerprinting in combination with multivariate statistical analysis[212]. The investigations in the field of non-invasive diagnostics for PCa have been stimulated by the discovery of intrinsic biomarkers detected in urinary-derived EVs. As a result of SVA research, several biomarkers have been associated with different stages of PCa. Biggs *et al.* have measured the levels of circulating prostate microparticles in plasma from PCa patients[226] and used these microparticles in a liquid biopsy platform to identify and characterise patients. This study found that subjects with an advanced and aggressive tumor (in Gleason scale, scoring 8 or higher) can be identified independently of their PSA value[226]. The

lipid and surface protein signatures of prostate-derived EVs have been described using RTM[210,232,235,243]. Several characteristics have been highlighted, indicating potential PCa biomarkers. For example, a shift in the structure of surface proteins from alpha-helix-rich in prostate EVs to beta-sheet-rich proteins in PCa-specific EVs (isolated from blood samples) has been observed[243]. Moreover, Otto *et al.* have detected chemical signatures in the Raman and Rayleigh scattering data[232] that efficiently differentiate between the EV populations from normal prostate and PCa cells[211,234]. The authors have trained a convolutional neural network to predict precisely the cellular origin of EVs for an automated diagnosis of PCa[235]. In another study, using various SVA techniques such as nanoscale flow cytometry and ddPCR, Joncas *et al.* have explored castration-resistant PCa[370], identifying KLK3 and the androgen receptor variant 7 (AR-V7) as specific biomarkers for this cancer[370].

Table 8. Summary of recent EV biomarker-related discoveries achieved using SVA techniques, focused on cancer diagnostic biomarkers.

Technique	Main conclusion	Ref
Flow cytometry (immunofluorescence)	Detection of CD147 as EV biomarker for CRC diagnosis.	362
	Detection of GPC1 as EV biomarker for pancreatic cancer diagnosis. Cancer-cell EVs contain oncogenic KrasG12D.	374
	Measures circulating prostate microparticles (PMPs) levels in plasma. This PCa "liquid biopsy" can identify patients with Gleason score ≥ 8, irrespective of their PSA.	226
Fluorescence microscopy (TIRF)	Employs a fluorescent assay to detect exosome miRNA-21 (miR-21-EX) as a cancer-screening assay. miR-21-EX can be used to distinguish between cancer patients, tumour progression stages and treatment responses.	365
Raman (dry EVs)	The surface protein signature shifts from alpha-helix-rich proteins to beta-sheet-rich proteins in prostate cancer-specific blood EVs.	243
RTM	Chemical signatures from Raman spectra can be used to differentiate between EV populations derived from healthy and prostate cancer cells. A trained convolutional neural network can identify the cellular origin of EVs.	232,235
	Raman analysis coupled with Rayleigh scattering distribution is used to detect specific lipid and protein signatures of tumour-derived EVs.	234
Label-free SERS	Report of real-time and label-free diagnosis of lung cancer by detecting 11 cancer-specific SERS signals (proteins and lipids) that distinguish EV populations from healthy and lung cancer cells with high sensitivity.	251
ddPCR	Detection and quantification of mutant and wild-type IDH1 RNA transcripts in EVs from cerebrospinal fluid of patients with glioma tumours.	296
	Identifies somatic BRAF and KRAS mutations in plasma-derived EVs from CRC patients. Probes a wide range of cancer cells and the derived EV populations.	227
	Identifies KLK3 and AR-V7 (androgen receptor variant) as biomarkers for castration-resistant prostate cancer (which progresses even under steroid deprivation therapy).	370
	Extracellular vesicle-transported HULC promotes cell invasion and migration. This encapsulated HULC is identified as a biomarker for human pancreatic ductal adenocarcinoma (PDAC).	298

1.4. Future outlook

Individually analysed EVs provide excellent prospects for future basic and practical research with a view to halt disease progression and control cell–to–cell communication processes. To exploit the full potential of SVA techniques, biological validation and reproducibility must meet the demands of clinical applications. Each technique has its specific advantages and disadvantages, and the exact choice of the method of analysis depends on the research question, the nature of the samples and EV characteristics. These techniques still need to improve their quantitative detection power, lower their cost and increase their reliability, resolution and throughput. In addition to technologies in use for SVA detection, we highlight several promising approaches that have yet to prove their potential in SVA.

Conventional methodologies have the potential to be applied in SVA, and flow cytometry is a good example. Its implementation using innovative approaches can provide new features and capabilities, as shown by vesicle impact electrochemical cytometry (VIEC). This electrochemistry-based flow cytometry technique uses single ruptured vesicles whose content is detected and quantified based on Faraday's law exploiting the produced oxidation current[376,377]. Extensive studies of the regulation of neurotransmitter trafficking by Ewing and colleagues, focusing on catecholamine exocytosis[377–384] have demonstrated the prospective application of this approach in the EV field, highlighting electrochemical flow cytometry as prospective asset in the studies of EV functions and biology in the near future. The VIEC-based experiments have examined neurotransmitter content at a single-vesicle level in a pheochromocytoma cell line. Several studies have established that the neurotransmitter catecholamine is only partially released from the vesicles during an exocytosis event[377]. Moreover, catecholamine concentration is a key factor in regulating vesicle size since vesicular transmitter content is relatively constant and independent of vesicle size[381]. Nonetheless, many different agents may regulate exocytosis events. Using VIEC, the group has later verified that the zinc and cisplatin content serve as major regulators in these processes[382,385].

Video microscopy is another common technique that is potentially useful in EV analysis. In 2010, Zupanc *et al.* developed an efficient algorithm to transform video sequences into quantitative data[383]. Their work was a crucial step towards the creation of automated computer analysis and led to the development of another, more popular, methodology, NTA. In 2008, the-then emerging fluorescent ratiometric image analysis (FRIA) method was used to determine the post-endocytic fate and transport kinetics of internalised cargo[384]. FRIA presented a breakthrough in this field at the time and its application led to colocalization of EV cargo with organelle markers. However, the technique has not been very successful in further EV research possibly due to the emergence of other microscopy approaches such as TIRF or SRM that enable the study of EV internalization and fate with a better resolution in fluorescence images and a more straightforward analysis.

The last decade has seen the development of several techniques with primary applications in analytical fields other than EV analysis. However, some, most notably radio-frequency analysis and SP-IRIS, are applicable to single-vesicle research and could play an important role in scanning and evaluation of specific EV populations or characterising several EV parameters in a single experiment.

Radio-frequency analysis, also known as electrically controlled tuneable broadband interferometric dielectric spectroscopy, has only been presented in several conference papers[386–389] after its first publication. In this method, specific sensors are used to perform a highly sensitive and tuneable broadband radio-frequency analysis. One study applying this method to EVs showed that the highly concentrated radio-frequency fields stimulates strong interactions between vesicles, which can be detected and quantified[390]. Specifically, the authors could detect and scan a type of EVs, giant unilamellar vesicles, at multiple frequency points and determine their molecular composition. In 2017, Wu *et al.* reported a separation method based on acoustofluidics and created a platform employing these acoustic trapping or tweezers phenomenon[391]. This technique isolates EVs from whole blood in a label-free and contact-free manner[391]. An acoustic wave falls upon a vesicle, and its scattering acts as a driving force to retain it. A year later, Ku *et al.* demonstrated isolation and enrichment of EVs using a similar acoustic trap technology[392]. In follow-up research, the method was used to isolate RNA and sequence miRNAs from EVs. Since then, an acoustic-based microfluidic platform has been released, coupling EV trapping technology with next-generation sequencing techniques. Together, these platforms form a robust and automated strategy for biomarker discovery in small sample volumes[393].

SP-IRIS, has so far found limited use in EV research, but has the potential to fill a unique experimental niche. SP-IRIS can characterise the size and phenotype (surface biomarkers) of EVs with no need to correlate two separate measurements[214,394]. This feature provides SP-IRIS with a high throughput and substantially reduces the amount of false negatives and positives compared to techniques that assess two characteristics in individual measurements. Due to the lateral resolution of microscopy (340–435 nm), highly concentrated samples cause signal overlap and a subsequent shift in the apparent vesicle size. Strikingly, despite the microscope resolution drawback individual *Flaviviridae* particles of approximately 40 nm have been identified and characterised using SP-IRIS[269]. Besides the examples presented in Table 9, there is a commercialised platform for EV phenotyping developed by Nanoview Biosciences using SP-IRIS, highlighting its potential application in characterising limited input EV samples. Several papers have proposed other highly-promising automated on-chip platforms using SP-IRIS for EV characterization[214,269,395–397]. These platforms have been combined with immunoblotting to sort and characterise EV populations from a sample and can detect size and phenotype at a single-particle level, visualising and quantifying either viruses or single EVs or both, in an uncharacterised sample.

One of the greatest advantages of such microfluidic platforms is that they only need very small sample volume (~20 µL) for an effective analysis[396,398]. Other techniques different from SP-IRIS have been implemented in such devices to characterise EVs from EV-regulated diseases and examine their future use as diagnostic tools. EVs derived from transfusion-related acute lung injury (TRALI) have been investigated using SP-IRIS coupled with AFM mechanics. Obeid *et al.* used this approach to determine that certain types of EVs trigger neutrophil extracellular traps (NETs) and that these NETs are likely to mediate in TRALI[399].

Fluorescence microscopy coupled with on-chip nanoflow cytometry enables automated quantitative SVA of body fluid samples[398]. According to Yokota *et al.*, the morphology and deformability of EVs from different cell lines can be investigated using nanopatterned tethering of EVs in combination with AFM[400].

Table 9. Summary of on-chip platforms utilised to characterise EVs and to detect specific biomarkers using SVA techniques.

On-chip techniques	Objective	Description	Ref
Dark-field microscopy and immunoelectrophoresis	Surface protein/marker profiling of EV populations.	On-chip immunoelectrophoresis device that separates EV populations according to the surface zeta potential (due to overexpression of certain markers) and quantifies the populations. Promising approach for minimally invasive diagnosis.	[397]
SP-IRIS and immunoplotting	Sizing and phenotyping at single EV level.	Multiplexed phenotyping and digital counting of various populations of individual exosomes (< 50nm) captured on a microarray-based solid phase chip.	[214]
	Visualising and quantifying virus particles with a single label-free imaging technique.	A silicon chip with virus-specific antibodies on printed spots can visualise and identify intact Ebola viruses and Ebola virus-like particles without labelling. The device also performs an automated quantitative analysis of the captured viruses.	[395]
	Sizing, phenotyping and quantifying EVs and virus populations.	Multiplexed detection based on protein immobilisation on a sensor chip. DNA-directed immobilised antibodies are used as protein microarrays to capture EVs or viruses. Several types of analytes in a small volume can be simultaneously characterised.	[396]
Nanoflow cytometry and fluorescence microscopy	Automated lab-on-a-chip quantitative analytical tool for single-vesicle analysis.	A nanofluidic device that can visualise and characterise individual vesicles by quantifying vesicle content and fluorescence signals from sample volumes of 20 µL. This nanofluidic-based methodology can be used for characterisation of small vesicles and their interacting molecules without ensemble averaging.	[398]
Atomic force microscopy (AFM) and nanopatterned tethering	Morphological and deformability characterisation of single EVs from different cell lines.	A nanoarray chip allows tethering of individual EVs from two cell lines (Sk-Br-3 and HEK293), employing a silane-coupling agent as a linker between PEG-lipid molecules and silicon surface. These tethered EVs are further characterised using AFM.	[400]
Raman/SERS screening	Identification and quantification of EV surface biomarkers in cancer.	A microfluidic device performs a rapid (8 min) and ultrasensitive identification, comparable to ELISA, of specific biomarkers in several samples at the same time. Protein biomarkers for prostate (PSA), colorectal (CEA), and hepatocellular prostate (AFP) cancers are detected.	[309]
Raman imaging, SEM, AFM combined with immunoplotting	Size distribution, shape and chemical fingerprint characterisation of tumour-derived EVs.	Multimodal analysis platform that captures tumour-derived EVs on an antibody-functionalised stainless-steel chip. A lipid-protein fingerprint is obtained using Raman imaging and the particle distribution and surface density are measured employing SEM and AFM. The correlation between SEM and Raman discriminates tumour derived EVs from contaminants.	[236,310]
Multicolour fluorescence digital PCR	Highly sensitive detection (compared to qPCR) of cancer-specific gene expression.	The miDER chip multiplex assay is an innovative digital PCR method capable of detecting and quantifying extremely low quantities of EV-related RNA. It can measure expression levels of two lung cancer-related genes (SLC9A3-AS1 and PCAT6) in peripheral blood samples, with a limit of detection of 10 copies per µL.	[402]
SP-IRIS and atomic force microscopy (AFM) with immunoplotting	Investigates whether plasma- or activated platelet-EVs trigger neutrophil extracellular traps (NETs).	Plasma transfusion can cause transfusion-related acute lung injury (TRALI) mediated by NETs. NanoBioAnalytical platform based on EV immunocapture biochip can detect EVs with a diameter in the 25–1000 nm range (mainly ≤ 100 nm). The study shows that EVs from both plasma and activated platelets trigger NETs formation.	[399]
Antibody barcodes (immuno-sandwich ELISA)	Quantification and phenotyping of EV secretion.	Microchip platform for multiplexed profiling of single-cell EV secretion by antibody barcodes. It addresses the heterogeneity of EVs of the same origin. For example, the study shows protein and EV secretion is performed by certain cell subgroups.	[401]

A multiplexed profiling antibody-based barcoding method enables sorting and further from different cell lines can be investigated using nanopatterned tethering of EVs in combination with AFM[400]. A multiplexed profiling antibody-based barcoding method enables sorting and further quantification of EV populations[401]. Notably, promising minimally invasive approaches for cancer detection and analysis have also been developed. For example, a multicolour fluorescence digital PCR platform has been designed to detect the expression of cancer-specific genes with high sensitivity[402]. This platform detects miRNA, lncRNA or any other genetic biomarkers of cancer. Furthermore, several devices for PCa detection have been described. For instance, EV populations from PCa can be separated according to the zeta potential of the surface and examined using dark-field microscopy[403]. Due to the overexpression of certain markers, different numbers of antibodies are bound to the EV surfaces, modifying their surface potential. This implies that EVs are differentially separated according to this potential. The biochemical composition of each EV is profiled and quantified; hence, subpopulations can be described. Moreover, two RTM approaches that can effectively identify and quantify EVs and their surface biomarkers in several cancers have been reported[308,309]. Beekman *et al*. have presented a multimodal analysis platform combining Raman imaging, scanning electron microscopy, AFM and immunoblotting as the ultimate prostate cancer diagnosis platform capable of measuring size distribution, shapes and chemical fingerprints of tumour-derived EVs[309].

The remarkable advances in single-vesicle imaging and analysis brought about by employing microfluidic devices promise to deliver rapid and effective practical applications. Moreover, such analytical systems need only very small, microliter-scale sample volumes. These innovative technologies and affiliated research pave the way towards unravelling the biological significance of EVs and using minimally invasive systems to diagnose diseases for which EVs serve as prognostic biomarkers.

1.5. Concluding remarks

EVs are key drivers of cell–to–cell communication. Understanding their biochemistry and physiological roles is paramount for unravelling biological processes such as disease progression, physiological responses or environmental regulation. EVs are also remarkably heterogeneous which often complicates their accurate analysis by bulk and ensemble studies that often misrepresent their functionalities. Indeed, EVs comprise several populations that further branch into subpopulations according to their morphology or phenotype. These (sub)populations could have specific functions or several (sub)populations might perform the same task as an amalgam. It is now becoming clear that not only the phenotype of an EV community but also its relative representation among the rest of the (sub)populations might be of important. Studies using SVA methodologies represent the most encouraging attempts towards highlighting and pinpointing specific EV phenotypes within a biological system. While SVA methods are well suited for the high-resolution phenotypical characterisation of EVs that is necessary for biomarker discovery, they might not be appropriate for carrying out further functional studies. So far, these methods have only been successful in identifying the uptake and fusion pathways but future advances in system models or single-vesicle technology may encourage its wider use. Ultimately, single-vesicle techniques will provide the foundation for describing an entirely new cell–to–cell communication paradigm built upon an EV-based network.

Chapter 2. Evaluation of Steroid Hormone Transcripts Associated to Urinary Extracellular Vesicles in Prostate Cancer Progression

This chapter collects the *in silico* analysis of potential PCa mRNA biomarkers associated to EVs and, the first steps taken towards a clinical trial to categorise and diagnose PCa patients by measuring mRNA markers in urine samples. This section was designed in collaboration with Exosome Diagnostics Inc. (Exosome Dx) who first developed a prostate PSA independent test associated to EV signatures.

First, we explored the transcriptome ever measured in EVs. As the steroid hormones pathway is the main signalling route altered at early stage in PCa, the output was filtered to this metabolic network. Then, mRNA targets were interrogated in PCa databases to evaluate their diagnostic potential. Finally, several targets were tested in patient urine samples by qPCR. This design was performed with the assistance of Mikkel Noerholm, former Director of product Development at Exosome Dx.

2.1. Background

Progression of PCa walks through many diverging molecular routes. This complicates its diagnosis and treatment excessively. Actually, the lack of sensitive diagnostic tools is one of the major challenges in PCa disease, especially at early stages. Hence, it is important to discover sensitive and specific biomarkers to improve PCa surveillance upon progression. Although it is well-known the early progression mechanism is dependent on androgens, there are no appropriate biomarkers to monitor it. PSA blood screening tests, together with clinical T-stage and Gleason score cannot accurately evaluate the disease at this stage. Due to its easy availability, handling and proximity to prostate, urine samples emerge as a very convenient source of biomarkers.

The major drawback using urines for biomarker discovery is sample dilution because underrepresented molecules might be hindered and undetected by current technologies. In this line, the analysis of EVs in urine could pave the way to identify more sensitive and specific PCa biomarkers. Protected by a lipid bilayer membrane, EVs contain a wide diversity of molecules that could serve as signature to determine cell and tissue status. Over the last decades, the interest in using EVs as biomarker source has risen enormously because they represent a novel source of information to properly categorise patient samples at both early and late stages of diseases.

2.2. Materials and methods

2.2.1. Database resources.

EV biomarker datasets

All datasets utilised in the analysis *in silico* of markers associated to EVs were mRNA or protein-based. Datasets were extracted either from literature or obtained by experimental EV *omics* data.

Vesiclepedia: This database compiles proteomics and mRNA data from over 500 publications related to EVs. To date, this database is active with regular updates. The data is collected together with metadata of samples and includes parameters such as type of sample, origin of sample, method of isolation, species studied or method of analysis.

Vesiclepedia database was limited to *Homo sapiens* studies. Then, data was filtered to studies focusing on prostate research and biomarkers research in urine to generate two specific datasets. Data was filtered considering PCa studies performed in cell lines, generating another specific dataset. Cell lines included in this subset were: LnCaP, PC-3, DU145, 22Rv1, VCaP, C4-2, RWPE-1, DUCaP and PC346C.

Exocarta: Similar database to vesiclepedia that started back in 2009[103]. However, the last update was released in 2015 and it contains exactly the same data as vesiclepedia. Therefore, it was decided to only include vesiclepedia retrieved data.

EVpedia: This integrated database for systemic analyses of EVs was released in 2013[101] and it contains studies independent to vesiclepedia. It has been included in this thesis because future studies in the lab should consider its use. However, it was not implemented because the web portal was not accessible at least until November 2021.

Finally, these datasets were interrogated against steroid hormone biosynthesis enzymes extracted from KEGG database[41,42].

PCa biomarker datasets

CANCERTOOL is a web-based software that was utilised t osearch for biomarkers relevant in PCa[404]. It refers to databases of transcript expression in prostate specimens upon removal. They include, in some cases, longitudinal data (over time) of patients in terms of survival. Databases can give information about:

- Status and progression (Healthy, PCa and metastatic patients):
  i. Grasso   n = 88
  ii. Lapointe   n = 26
  iii. Taylor   n =179
  iv. Tomlins   n = 75
  v. Varambaly   n = 19
- Recurrence and Gleason score categorisation
  i. Glinsky   (No healthy group)
  ii. Taylor   n =179
  iii. TCGA   n =496

Therefore, with a list of filtered markers, CANCERTOOL can perform a statistical analysis to assess whether they can discriminate PCa specimens and hence, hold the potential to be biomarkers. *Status in prostate cancer* informs about the expression of the gene of interest between non-tumoral (N) and prostate cancer specimens (PCa) in each dataset[404]. A Student's t-test is performed in order to compare

the mean gene expression between two groups. *Status by progression* informs about the expression of the gene of interest between non-tumoral (N), primary tumor (PT) and metastatic (M) PCa specimens in the indicated datasets)[404]. An ANOVA test is performed in order to compare the mean gene expression among two groups. *Status by Gleason grade* categorises PCa specimens in Gleason groups as GS6, GS7, GS8, GS8+9, GS9, GS10 according to the gene of interest [404]. An ANOVA test is performed in order to compare the mean among groups. *Disease free survival* performs informs about Kaplan-Meier curves representing the disease-free survival (DFS) of patient groups selected according to the quartile expression of the gene of interest [404]. A Mantel-Cox test is performed to compare the differences between curves, while a Cox proportional hazards regression model is performed to calculate de Hazard Ratio between the indicated groups.

2.2.2. *Real time quantitative PCR analyses.*

Sample preparation

Urine samples were selected from a PCa patients cohort collected at Basurto's Hospital in Bilbao. A demographic study of the biobank determined parameters such as age, PSA in blood or body mass index (BMI) in the 646 patients participating (Figure 12). The percentages of patients categorized in different groups according to their Gleason score (GS) were determined as well as the most common tumour characteristics based upon the TNM staging classification, being pT2c, pT3a and pT3b the most prevalent along samples. According to their Gleason score, there were 39.8% BPH patients, 12.5% GG1 (GS: 3+3), 32.7% GG2 (GS: 3+4), 6.0% GG3 (GS: 4+3), 3.1% GG4 (GS: 8) and 5.9% GG5 (GS: 9-10) patients. In this chapter, all mentioned demographic characteristics were considered to select urine samples representative of the whole urine cohort. Three groups of samples were selected: 5 urines with BPH outcome, 5 urines with GG2 and pT2c outcome (low aggressive PCa) and, 5 urines with GG5 outcome and pT3a (Highly aggressive PCa).
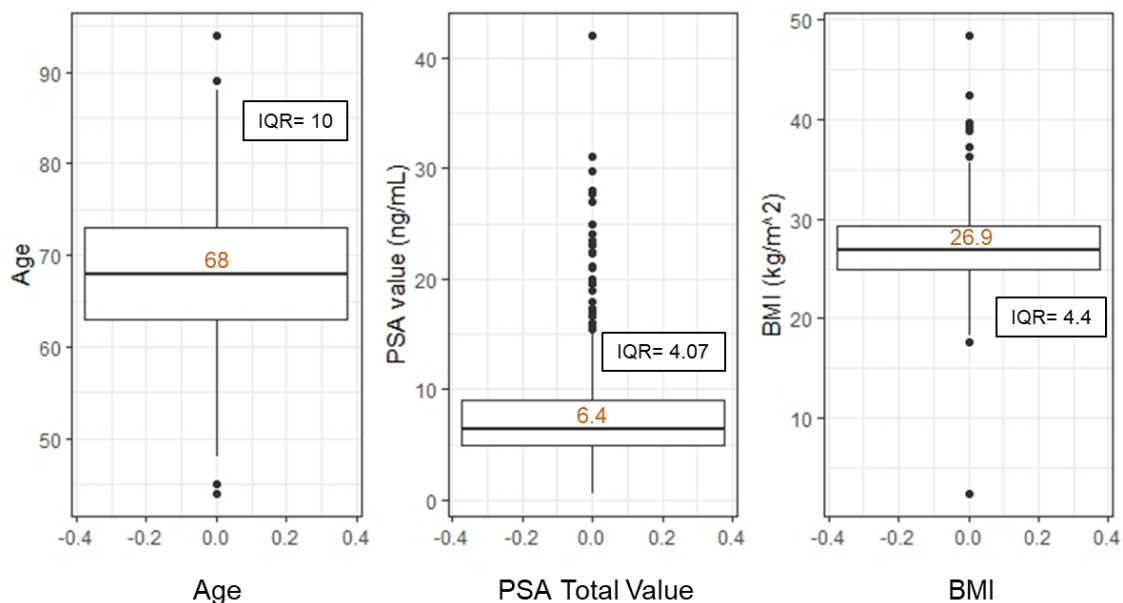
Figure 12. Summary of relevant demographic characteristics of Basurto's hospital cohort. A total of 646 patients donated their urines over time. To homogenise patient's population in our experimental cohorts according to demographic characteristics, their distribution in age, PSA titer and BMI was analysed.

Urinary EVs (uEVs) were obtained by ultracentrifuging urine samples as described elsewhere[59]. In brief, approximately 50 to 100 mL of urine were collected of which aliquots of 50 mL were centrifuged at 2,000g for 10 min, filter sterilised (0.22 µm pore size) and immediately frozen at -80 °C for further processing. When collection was higher than 50 mL, aliquots of either 1 mL or 10 mL were generated prior freezing. In these experiments, urine samples of 1 mL or 10 mL were thawed at room temperature and centrifuged for 5 min at 2,000g to remove any precipitate. Then, RNA associated to uEVs was isolated by using a Urine Exosome RNA Isolation Kit (Product #47200, Norgen Biotek Corporation, Canada). Protocol is extensively described elsewhere[188]. The isolated RNA was quantified in nucleic acid concentration using a NanoDrop™ (ND-1000 Spectrophotometer, Thermo Fisher Scientific, MA, USA) device in order to optimize the retrotranscription to cDNA by means of SuperScript™ VILO™ polymerase (#11754-050, Invitrogen™, MA, USA). An approximately 100% cDNA conversion efficiency was considered to proceed with further assays.

Real-time quantitative PCR methodology

Real-time quantitative PCR (qPCR) was utilised to quantify the expression of selected target genes in uEV-derived RNA. RNA derived from PCa cell lines (PC-3, DU145, 22Rv1, LNCaP, BPH-1) and a universal human RNA template (QS0639, ThermoFisher Scientific, MA, USA)) were utilised to optimise qPCR methodology. To perform qPCR assays, SYBR® Green Select Master Mix was purchased from Applied Biosystems (#4472897, MA, USA). Reaction mix was prepared following manufacturer's instructions and qPCR was run as specified in Table 10. Melting curves of each amplicon were determined to evaluate the efficiency and specificity of the amplification. A QuantStudio™ 5 Real-Time PCR Instrument (Thermo Fisher Scientific, MA, USA) was utilised to run the reaction and QuantStudio™ Real-Time PCR Software v1.3 for the analysis. Unless specified, all experiments were run with 1 ng of DNA per reaction.

Design of primers for SYBR Green and TaqMan qPCR

Primers for the selected target genes were designed following a protocol shared by ExosomeDx for clinical trials in urine. The specific procedure and parameters cannot be specified as it is their industrial property. Remarkably, the design was performed considering a future application in a clinical trial. This means the screening of potential biomarker targets was designed to work with two flanking primers when using SYBR Green polymerase – that requires less optimisation – with a TaqMan probe in case we could move forward to a clinical trial, which will require a higher sensitivity. The target genes tested in this chapter are: *SRD5A2, CYP1A2, CYP3A5, CYP3A7, CYP3A4, SULT1A, STS, SULT2B1, SRD5A1, SRD5A3, AKR1C2* and *CYP11B1*. As housekeeping genes (HKG) *GAPDH, ACTB, 18srRNA, SPEDF, EEA1F1, RPL6* and *KLK3* were tested.

Housekeeping genes analysis

To ensure an adequate normalisation of quantitative RNA content, appropriate HKG are required. In general, cell lines and other well-established matrices already have HKG described in literature. Due to the heterogeneity of human samples, the establishment of a steadily expressed transcript is required. To perform such analysis there are many normalisation algorithms available[405]. As in every modelling strategy, when many algorithms are available the use of several approaches provides a more robust

and trustable outcome. For this reason, several reference genes were tested in these urine samples with NormFinder[406] and BestKeeper[407] algorithms. Both with their limitations and strengths found out the most robust HKG in PCa cell lines was *GADPH* combined with *ACTB* (data not shown). *EE1AF1* is also a top candidate as a HKG but in some samples it does not amplify, therefore, should not be considered as a HKG *a priori*. They were also applied to urine samples (Figure 16).

Table 10. Real-time qPCR conditions. These qPCR conditions were optimised for housekeeping genes and target genes in uEVs.

#	Temperature	Time	Temperature gradient
Hold stage			
1	50.0 ℃	120 s	1.6 ℃ per s
2	95.0 ℃	120 s	1.6 ℃ per s
PCR stage (40 cycles)			
1	95.0 ℃	15 s	1.6 ℃ per s
2	60.0 ℃	60 s	1.6 ℃ per s
Melt Curve Stage			
1	95.0 ℃	15 s	1.6 ℃ per s
2	60.0 ℃	60 s	1.6 ℃ per s
3	95.0 ℃	15 s	0.5 ℃ per s

2.3.   Results

2.3.1.   *Selection of targets.*

Study of steroid hormones mRNA related to EVs

The luminous darkness of PCa works in mysterious ways in advanced stages, however, it is well-defined steroid hormones are crucial in early PCa progression. For this reason, gene transcripts related to this pathway associated to EVs were the objective in this section. Over the decades, mRNA encapsulated inside the EV lipid bilayer have been increasingly utilised as progression markers for several diseases. In fact, mRNA associated to EVs emerged as an outstanding source of information to characterise biological samples and hence, to describe specific signatures of their composition as biomarkers. A web-based database containing over 500 datasets related to EV studies – Vesiclepedia – was used to discover potential markers of early stage progression of PCa associated to EVs.

Vesiclepedia compiles more 18,000 different proteins associated to EVs in more than 500 different studies (Retrieval: November, 2021). Approximately 8,000 proteins have been linked to prostate research with studies using either cell lines or urine samples. Interestingly, there are unique sets of proteins related to cell lines, which are also specific to different types of cells. In this unmanageable database, there is a set of 61 enzymes participating in the biosynthesis of steroid hormones (Extracted from *KEGG*) and it concerns this chapter. Figure 13 shows a total of 43 mRNAs associated to EVs considering only datasets uploaded to Vesiclepedia; this also means 18 enzyme-related protein or mRNA have not been ever described in EVs. Remarkably, 24 of these mRNAs have been linked to EVs but none was identified in prostate related research. There are 10 mRNAs – *AKR1C3, AKR1C2, AKR1C1,*

CYP17A1, SULT2B1, SULT1E1, HSD17B8, HSD17B12, DHRS11 and *COMT*- that are associated to both cell line- and urine-related research while 9 mRNAs - *HSD17B2, HSD17B6, CYP1A1, UGT1A6, UGT1A9, UGT2B7, UGT1A8, HSD11B2* and *CYP7B1* - are unique to studies performed with uEVs.
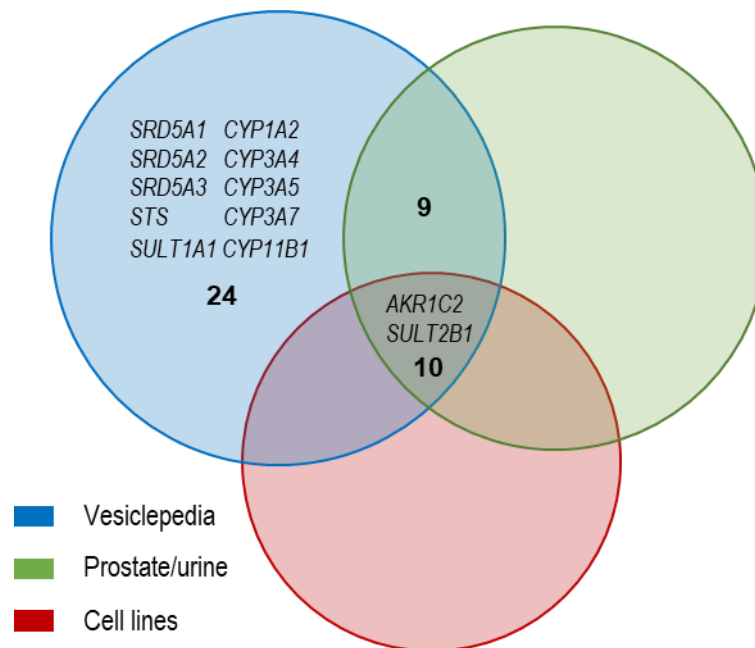
Figure 13. Venn Diagram including the enzymes of steroid hormone biosynthesis detected in EVs and in different datasets *in silico*. Datasets included were all filtered to all enzymes related to steroid hormones biosynthesis. Moreover, it reports the names of the target genes we selected to test in this chapter.

Biomarker potential of steroid hormone enzymes expression

The next step was to evaluate which of the 61 hormone steroid-related genes could be relevant in categorising patient samples. The statistical appliance CANCERTOOL was utilised to report the expression of these genes of interest along groups of samples in different study cases. In the Y-axis a Log2-normalized gene expression is represented and depending on the groups of samples compared it informs about the status of the gene:

A. In prostate cancer: comparing non-tumoral vs PCa specimens.
B. By progression: comparing non-tumoral, primary tumor and metastatic PCa specimens.
C. By Gleason Grade: it is indicated as GS6, GS7, GS8, GS8+9, GS9 and GS10 and; it informs about the presence of a transcript in a specific Gleason architecture.
D. Disease Free Survival: Kaplan-Meier curves representing the disease-free survival (DFS) of patient groups according to the expression of target genes. It indicates whether the gene prognoses PCa aggressiveness.

The tool provides a report for each single gene in every definition above. These reports were checked manually to assess whether each specific transcript expression could define cancer progression. The discrimination between normal and PCa specimens (Status in PCa) and, including metastatic stages (Status by progression) were considered the most relevant aspects to aim for early stage biomarkers.

In Table 11, a summary of this analysis is reported. Only the transcripts able to significantly discriminate patients according to definitions A and B are shown. The plus sign (+) indicates a significancy close to 0.05 and double sign (++) close or over 0.01; *unsure* means that there missing results or that they are not conclusive and a minus sign (-) indicates no significance in discrimination. The stratification by GS was not robust and in many cases expression data was spread out due to a short number of samples per group. This categorisation is of importance because including very aggressive PCa samples to compute statistical differences may hinder relevant information for early stages of progression. Finally, DFS indicates aggressiveness of the cancer followed over time and considering death by cancer as a measure. This indicator is not much relevant to consider disease recurrences at this stage.

Among the 32 candidates we have filtered using CANCERTOOL (Table 11), the first 12 most relevant entries in this classification were selected to be tested as mRNA biomarkers associated to uEVs. Figure 13 summarises the analysis and further indicates whether candidates have been already identified. According to vesiclepedia, 10 of them have not been ever detected in urine samples. There are two interesting candidates, *AKR1C2* and *SULT2B1*, reported in EVs and urine samples that are also relevant as a patient classifier. Anyway, the 12 candidates will be assessed once the cohorts are designed.

2.3.2. *Selection of cohorts.*

One of the most important hallmarks of PCa is its poor prognosis. Although the classification of PCa patients is becoming more specific, the tools or parameters utilised to categorise them are not backing up. The diagnostic tools are highly invasive, time consuming and require high expertise in examination. Nowadays, the gold standard biomarker before undergoing a biopsy is PSA concentration in blood. Its poor prognosis at early stages of development has already been discussed in this thesis (see in INTRODUCTION), demonstrating the existence of a research niche. Therefore, biomarkers with a superior capacity to stratify patient samples claim the spotlight of cancer diagnosis.

Indeed, an analysis with a binary classifier model demonstrated PSA is not a good classifier of PCa patient groups in this urinary cohort of 646 patients (Figure 14). A receiver operating characteristic (ROC) curve illustrates the true positive fraction against the false positive fraction of a sample population at different threshold values. Thus, by incrementing the value of the classifier the successfulness in classification is assessed. The area under the curve (AUC) estimates how well the classifier discriminates between two groups of samples. In Figure 14, ROC curves and AUC values for each comparison between groups of patients are presented. To note, an AUC value close to 0.5 or lower indicates random-driven classification by the analysed parameter; the higher the value, the better the classifier is. From this data, one can conclude PSA is not a good classifier of patient groups in this cohort. Only when comparing rather advanced PCa (GG4 and GG5) to very low developed PCa (GG1) the ROC curves discriminate groups reasonably. This means PSA could be appropriate to classify low developed cancer and advanced cancer patients. In this regard, the lack of an appropriate classifier at early stages of development highlights the importance on patient stratification research.
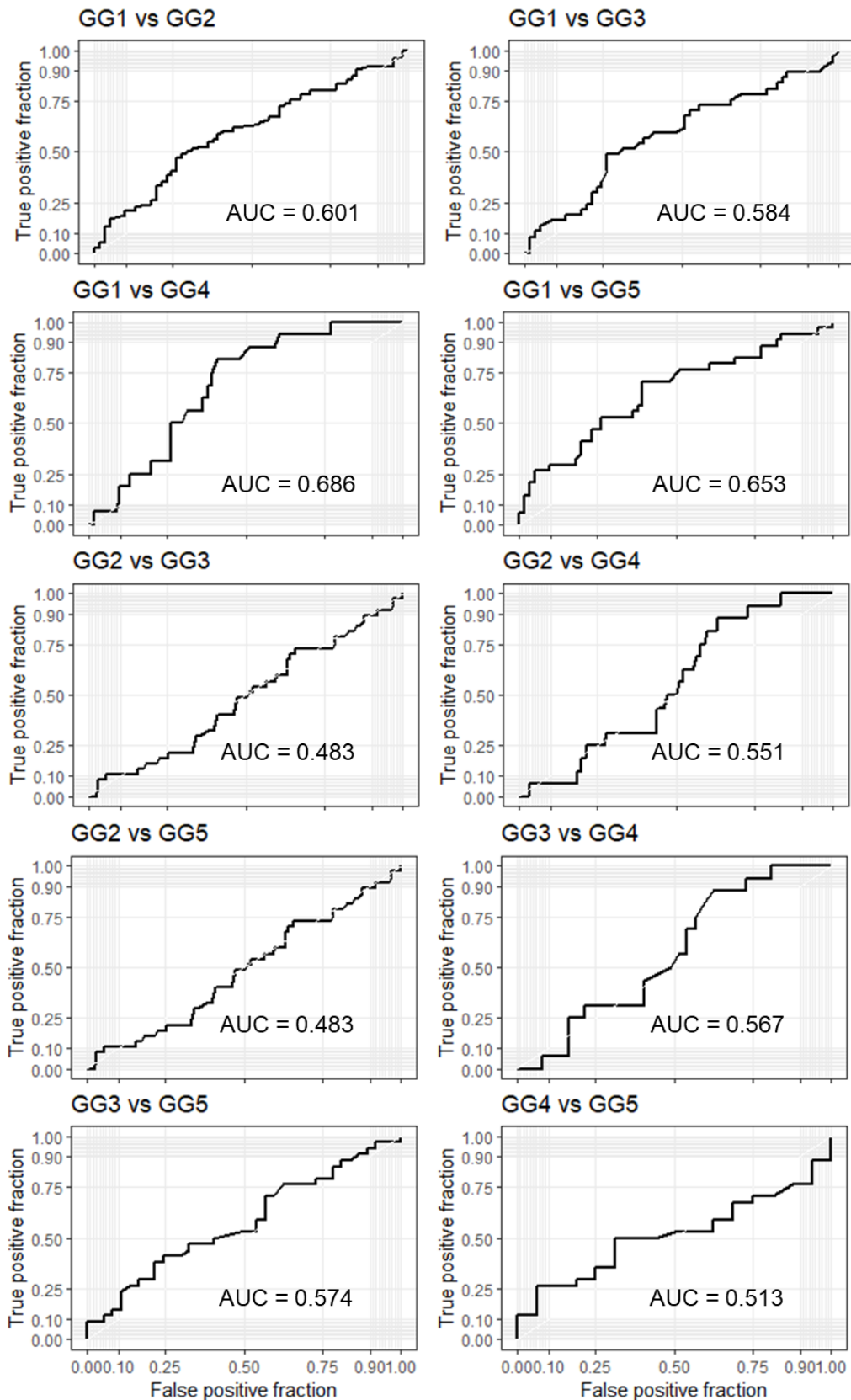
Figure 14. ROC curves comparing all groups of patients in the sample cohort (n=646). The AUC are indicated to assess PSA performance as a biomarker.

Table 11. Summary of CANCERTOOL results of significant genes of interest in discriminating PCa specimens. The columns indicate discrimination of status: A. in PCa B. by progression C. by Gleason grade D. Disease free survival. Reports of all genes are included in the Supplementary material. A plus sign (+) indicates significancy

close to 0.05 and double sign (++) close or over 0.01; *unsure* means that there are no conclusive and a minus sign (-) indicates no significance in discrimination.

Gene	Description	A	B	C	D
SRD5A2	Steroid 5 alpha-reductase 2	++	++	+	+
CYP1A2	Cytochrome P450 family 1 subfamily A member 2	++	++	+	-
CYP3A5	Cytochrome P450 family 3 subfamily A member 5	++	++	+	+
CYP3A7	Cytochrome P450 family 3 subfamily A member 7	++	+	-	-
CYP3A4	Cytochrome P450 family 3 subfamily A member 4	++	++	-	Unsure
SULT1A1	aryl sulfotransferase	++	++	-	-
STS	Steroid Sulfatase	+	+	+	-
SULT2B1	Sulfotransferase family 2B member 1	+	+	Unsure	+
SRD5A1	Steroid 5 alpha-reductase 1	+	+	-	Unsure
SRD5A3	Steroid 5 alpha-reductase 3	+	Unsure	-	Unsure
AKR1C2	Aldo-keto reductase family 1 member C2	+	+	-	Unsure
CYP11B1	Cytochrome P450 family 11 subfamily B member 1	+	+	-	-
AKR1D1	Aldo-keto reductase family 1 member D1	+	-	Unsure	-
CYP7B1	Cytochrome P450 family 7 subfamily B member 1	+	+	-	Unsure
HSD17B6	Hydroxysteroid 17-beta dehydrogenase 6	+	++	-	-
HSD17B7	Hydroxysteroid 17-beta dehydrogenase 7	+	+	-	Unsure
HSD17B8	Hydroxysteroid 17-beta dehydrogenase 8	+	+	-	+
DHRS11	Dehydrogenase/Reductase 11	+	+	-	-
CYP2E1	Cytochrome P450 family 2 subfamily E member 1	+	Unsure	-	Unsure
CYP1B1	Cytochrome P450 family 1 subfamily B member 1	+	+	-	Unsure
CYP19A1	Cytochrome P450 family 19 subfamily A member 1	+	Unsure	-	+
UGT2B11	UDP glucuronosyltransferase family 2 member B11	+	Unsure	+	Unsure
UGT2B28	UDP glucuronosyltransferase family 2 member B28	+	Unsure	Unsure	-
UGT2B10	UDP glucuronosyltransferase family 2 member B10	+	-	-	Unsure
UGT2B7	UDP glucuronosyltransferase family 2 member B7	+	+	-	-
UGT2B4	UDP glucuronosyltransferase family 2 member B4	+	Unsure	-	-
COMT	Catechol-O-methyltransferase	+	+	Unsure	-
LRTOMT	Leucine-rich transmembrane and O-methyltransferase domain containing	+	+	-	-
HSD11B1L	Hydroxysteroid 11-beta dehydrogenase 1 like	-	+	-	-
HSD11B1	Hydroxysteroid 11-beta dehydrogenase 1	Unsure	+	-	Unsure
SULT1E1	Sulfotransferase family 1E member 1	Unsure	+	+	-
CYP1A1	Cytochrome P450 family 1 subfamily A member 1	Unsure	++	Unsure	Unsure

As a consequence, small cohorts mimicking demographic parameters of the whole population were designed to test the proposed biomarkers. Two cohorts of 15 urine samples (of either 1 mL volume or

10 mL volume) with BPH, low aggressive and highly aggressive PCa samples were established. The objective was to find good HKG to be used in hypothetical clinical trials as well as assessing which specific biomarkers are associated to EVs and still hold potential to discriminate between patient groups.

2.3.3. Normalisation and Housekeeping genes.

The genes *18srRNA, ACTB, EE1AF1, GAPDH, KLK3, RPL6* and *SPDEF* were examined as HKG to normalise urine cohorts in upcoming assays. Once primers were designed, a qPCR assay was run using RNA extractions from the 1 mL volume cohort. Two control RNA extractions from water and PBS were included. None of the HKG amplified using these samples in exception to *18srRNA* that showed quite convincing amplification curves with amplification cycle (Ct) values around 34 cycles (data not shown in Figure 15). Yet, the HKG could still be used as its Ct values using sample RNA extraction range from 17 to 22 cycles, approximately. Figure 15 depicts the mean (± SD) of Ct values of each HKG in all RNA samples of the cohort. The qPCR assay determined *SPDEF* and *RPL6* are not amplifiable in all samples and they exhibit a high variability in Ct values along samples. Hence, they may introduce more uncertainty rather than normalisation capacity.
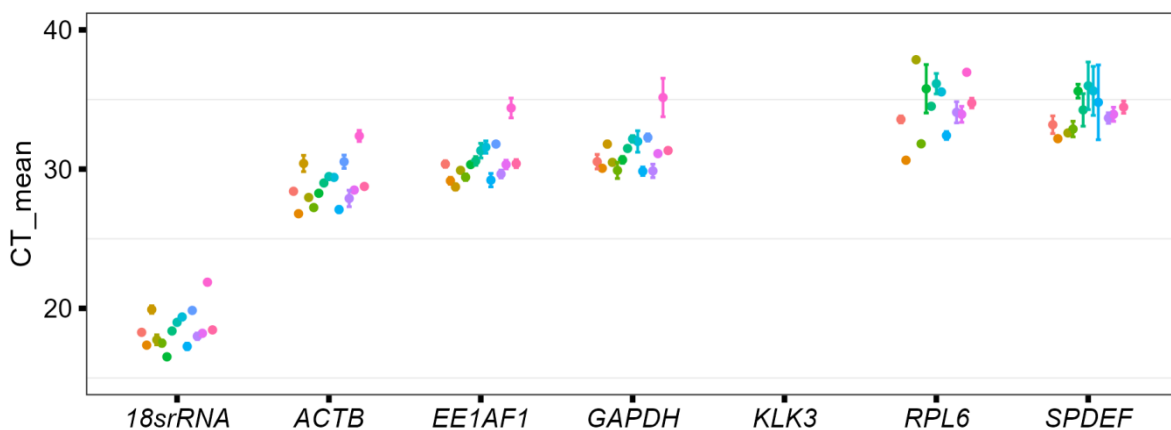
Figure 15. Representation of mean (± SD) amplification cycle (Ct) values of HKG testes in 1 mL volume cohort. It is expressed as an average of technical replicates (n=3) and the error bars correspond to standard deviation of these technical replicates. In this type of assays, Ct values are a quantification measurement. The bigger the Ct is, the lower the concentration of DNA/RNA.

In general, Ct values of these HKG candidates are somewhat high (except for *18srRNA*). To determine the best candidate, a comprehensive analysis of HKG expression along samples and between groups is required. The establishment of a gene or combination of genes whose expression is treatment- and group-independent is imperative to find a gene that only provides RNA/DNA content information. BestKeeper and NormFinder algorithms were selected to perform such evaluation.

```
> Result_NoX11X5X8$Ordered              > Result_NoX11X5X8$PairOfGenes
        GroupDif GroupSD Stability         Gene1  Gene2 Stability
ACTB        0.26    0.21      0.08     1 18srRNA   ACTB      0.17
EE1AF1      0.18    0.31      0.15     2 18srRNA EE1AF1      0.18
GADPH       0.34    0.41      0.16     3 18srRNA  GADPH      0.20
18srRNA     0.79    0.70      0.32     4   ACTB EE1AF1      0.09
SPDEF       0.73    1.01      0.41     5   ACTB  GADPH      0.10
RPL6        1.33    1.60      0.69     6 EE1AF1  GADPH      0.11
```

Figure 16. Outcome of the HKG analysis by NormFinder algorithm. Stability values determine the likeliness of each gene to be an appropriate HKG in these set of samples.

BestKeeper describes the general variability of samples for the analysed gene. This algorithm determined *EE1AF1* and *GAPDH* showed the lowest variability. In addition, it described that the best combination of genes where those including *ACTB* and *GAPDH*. NormFinder results are reported in Figure 16. This algorithm considers sample variability but it also includes the standard deviation along samples and variation between groups to report a *stability value*. The lower the stability value is the better the HKG. NormFinder pointed out *ACTB*, *EE1AF1* and *GAPDH* as the best HKG but also the combination of them. For this reason, we have selected *ACTB*, *EE1AF1* and *GAPDH* as HKG to analyse these cohorts and use them for normalisation purposes upon RNA quantification.

2.3.4. *Evaluation of mRNA in EVs as targets.*

The *in silico* approach issued 12 candidates of which only the expression of six could be reported in cell lines (Table 12). At this stage, a PCa cell line set was utilised to assess primers performance. Remarkably, *SULT2B1* has been reported in PCa cell lines while vesiclepedia only describes it in urine studies. The use of cell line based templates has its own limitations since several genes may not be expressed in all of them. The use of a universal RNA derived from tissues could overcome this limitation and primer design can be validated reliably.

Table 12. Summary of target hormone steroid genes tested in cell line-derived RNA. The table reports whether the target gene was detected in the two available templates. Universal RNA stands for a commercial template composed of a mixture of 10 different human cell lines (ThermoFisher Scientific, MA, USA). In house PCa cells are RNA extracted from PCa cell lines cultured in our lab.

Gene target	Universal RNA	In house PCa cells	Gene target	Universal RNA	In house PCa cells
SRD5A2	*Non detected*	*Non detected*	*STS*	Detected	Detected
CYP1A2	*Non detected*	*Non detected*	*SULT2B1*	Detected	Detected*
CYP3A5	Detected	Detected	*SRD5A1*	*Non detected*	*Non detected*
CYP3A7	Detected	Detected*	*SRD5A3*	*Non detected*	*Non detected*
CYP3A4	*Non detected*	*Non detected*	*AKR1C2*	Detected	*Non detected*
SULT1A1	Detected	Detected	*CYP11B1*	*Non detected*	*Non detected*

* Detection in only one type of PCa cell line

Another limitation of the study are the low yields in RNA obtained in urine samples. Upon RNA extraction, 1 mL volume cohort yielded 0.388±0.301 µg of RNA while 10 mL volume cohort yielded 0.541±1.100 µg of RNA in total. These are, in general, low yields except for few 10 mL volume samples of which high concentration of RNA was obtained after isolation. The fact that 10 mL extraction were only 2-fold the yield of the 1 mL cohort already indicates a loss efficiency upon volume increase or a poor extraction specificity of EV-associated RNA from urine.

In Figure 17, the selected HKG and target genes that showed amplification in our templates are analysed. The Ct values of each gene of interest per sample are represented. It is observed HKG behave similar to normalisation analysis. Strikingly, RNA extractions from 10 mL volume samples measured lower RNA expression of normalising genes. This already hints that either the RNA extraction or the qPCR assay might have been inefficient. To assess whether a larger volume of initial sample may carry salts or other contaminants hampering the extraction or qPCR assay, a serial dilution (1:5 and 1:10 of the extracted RNA) and a higher amount of template (4 ng instead of 1 ng) were analysed by qPCR. Values of Ct varied according to serial dilution of template in each reaction: a higher amount of template improved qPCR outcome by a decrease of approximately 2 Ct and the dilution increased Ct values as expected. This suggests that there are no compounds impairing qPCR reaction and hence, issues may be due to RNA extraction or a low initial quantity of EV-associated RNA in samples. Perhaps a higher amount of extracted RNA would increase reliability in the assay or could improve the sensitivity of quantification. In fact, quantification sensitivity could be improved in future works by screening target genes directly using TaqMan quenching approach.
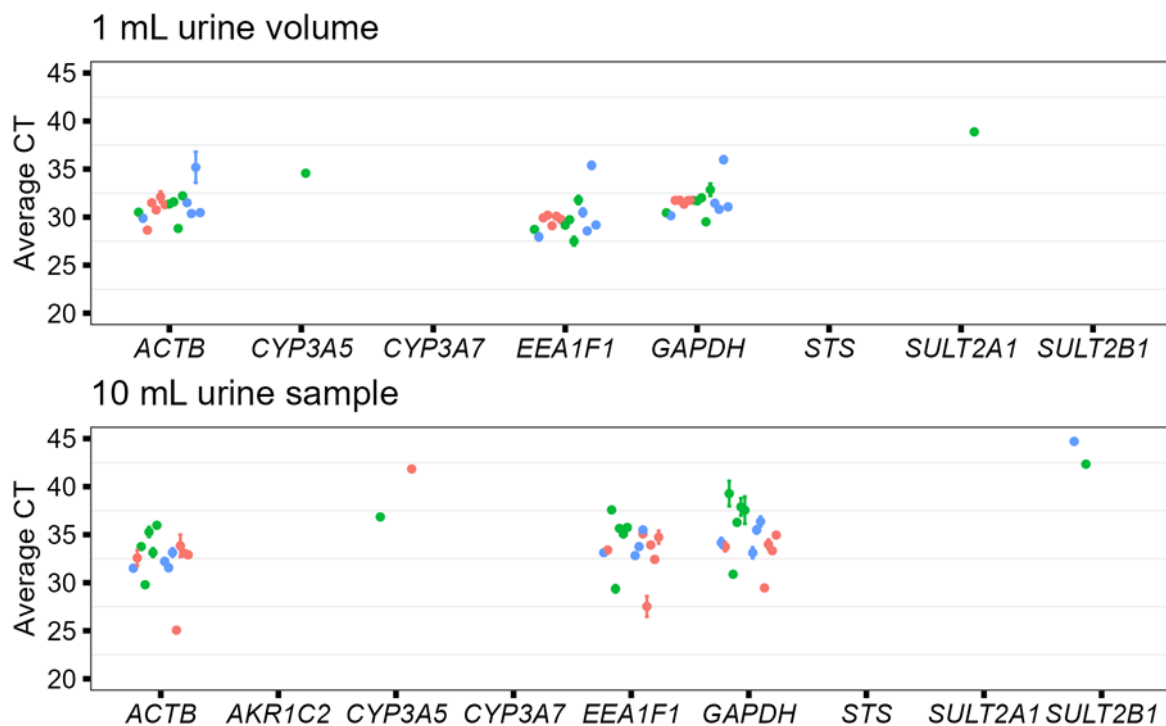
Figure 17. Average Ct values (± SD) of each RNA sample extracted from urine in analysed genes. The top graph depicts the results from 1 mL volume samples and the bottom the results from 10 mL volume sample. Each dot corresponds to a single urinary RNA preparation analysed for one single gene. They are coloured as follows: in blue, GG5 patient RNA samples; in green, GG2 patient RNA samples; in red, BPH patient RNA samples.

Focussing on the six tested genes with confirmed working primers only CYP3A5, SULT2A1 or SULT2B1 amplified in urine samples. They were measured only occasionally and in few samples. Also, Ct values were higher than 38 in general. Non-specific amplifications start occurring from this standard threshold. Indeed, a melting curve analysis confirmed that melting temperature of primers - a characteristic that indicates an adequate and specific annealing to the template – was incorrect, suggesting unspecific amplifications.

2.4. Discussion and Conclusions

The exploration of new biomarkers in cancer research rose interest due to the limitations that suppose a poor diagnosis and prognosis of cancer disease. The appearance of novel biomarkers carriers such as EVs combined with cutting-edge methodologies as single-vesicle approaches can provide alternatives to discover disease markers. In this line, the bioinformatics analysis performed in this work aimed to describe potential candidates associated to EVs to discriminate between patient groups. Web-based databases compile several proteins or mRNA related to steroid hormones and associated to EVs. These EV datasets derive from hundreds of studies which include cell lines, tissues and body samples. Besides, EV-associated candidates were further filtered using CANCERTOOL to consider their relevance in discriminating cancer groups. To note, CANCERTOOL databases compile transcriptomic analyses of prostate primary samples. One could argue that specific mRNAs found in PCa primary samples would not necessary be present in EV samples of any kind.

Up-to-date, concentration of PSA in blood is measured routinely to diagnose a patient with prostate issues. Its poor prognosis at early stages is well documented but also its poor patient stratification; this highlights the need to discover novel biomarkers. Interestingly, Exosome Dx released in 2020 a PSA-independent tool to diagnose PCa. By combining the gene expression of PCA3, ERG and SPDEF in uEVs they could predict the likelihood of high grade PCa occurrence[408]. The launch of such test demonstrates the potential using uEVs content as biomarkers. However, I also points out the challenge in establishing biomarkers for very early stages. According to SCOPUS, over 18,000 studies have been released describing biomarkers associated to PCa disease; however, only 35 consider EVs and steroid hormone enzymes. Joncas *et al.*[370] is the unique work one could find describing an EV-associated mRNA that could discriminate plasma samples at different stages of disease progression using ddPCR. Moreover, section *1.3.3. EV biomarkers.* of Chapter 1 demonstrates the potential of SVA techniques to optimise the identification of cancer biomarkers. Specifically, the use of ddPCR may enable the detection of transcripts that are present in a small subset of EVs in body fluids. This approach is able to distribute single EVs into individual droplets, which allows the identification of their genetic cargo of interest.

In this chapter, the collaborative work with Exosome Dx is summarised. A clinical trial after validation of assays was projected, however, it turned out to not happen. Still one was able to:

i. Design an *in silico* study from which markers present in EVs were determined. Moreover, one analysed which biomarkers hold a potential in early classification of patients.

ii. Demonstrate PSA was not a good classifier in a large urine cohort. PSA could only be acceptable to discriminate GG1 patients to highly aggressive PCa patients.

iii. Design a qPCR assay for the screening of EV-associated mRNA targets. This assay found out appropriate HKG and normalising genes and; could test some of the potential biomarkers. Sadly, no positive results were obtained but we included several suggestions in the chapter to optimise this approach in future work or studies of the same kind.

Chapter 3. Liquid Chromatography Coupled to Mass Spectrometry Assay to Measure Steroid Hormone Biosynthesis Pathway

This chapter focusses in the development and application of a steroid quantification methodology based on ultra-performance liquid chromatography coupled to a high resolution time-of-flight mass spectrometer (UPLC-MS). This part has been published as an Original Article in *Metabolites* journal and it is appended in the supplementary material. The application of this methodology in urinary samples of patients is not published and hence, it is included as a separated section in the chapter.

Bordanaba-Florit, G., van Liempd, S., Cabrera, D. et al. Simultaneous Quantification of Steroid Hormones Using hrLC-MS in Endocrine Tissues of Male Rats and Human Samples. *Metabolites*. 12, 714 (2022).

In this work, we have developed and optimized the extraction and quantification of 11 key members of the different steroid classes, including androgens, estrogens, progestogens and corticoids. The assay consists of a liquid/liquid extraction step and subsequent quantification by high-resolution liquid chromatography coupled time-of-flight mass spectrometry. The recoveries range between 74.2 to 126.9% and 54.9 to 110.7%, using a cell culture or urine as matrix, respectively. This is a fast and sensitive method, which has been successfully applied in animal and human relevant samples. Using rat tissues, the assay was validated and it described different hormone levels in tissues due to the compartmentalisation of the steroid hormone pathway. Also, the presence of steroid hormones in EV samples was reported. In the next subsection (unpublished work), the analysis of steroid hormones in human urinary samples is described. Significant differences between benign hyperplasia and Prostate cancer groups of samples in androsterone, cortisol and DHEAS is reported.

3.1. Development of a Targeted Metabolomics Assay in Endocrine Tissues of Male Rats and Human Samples

Steroid hormones play a vital role in the regulation of cellular processes, and dysregulation of these metabolites can provoke or aggravate pathological issues, such as autoimmune diseases and cancer. Regulation of steroid hormones involves different organs and biological compartments. Therefore, it is important to accurately determine their levels in tissues and biofluids to monitor changes after challenge or during disease. In this work, we have developed and optimized the extraction and quantification of 11 key members of the different steroid classes, including androgens, estrogens, progestogens and corticoids. The assay consists of a liquid/liquid extraction step and subsequent quantification by high-resolution liquid chromatography coupled time-of-flight mass spectrometry. The recoveries range between 74.2 to 126.9% and 54.9 to 110.7%, using a cell culture or urine as matrix, respectively. In general, the signal intensity loss due to matrix effect is no more than 30%. The method has been tested in

relevant steroidogenic tissues in rat models and it has also been tested in human urine samples. Overall, this assay measures 11 analytes simultaneously in 6 min runtime and it has been applied in adrenal gland, testis, prostate, brain and serum from rats, and urine and extracellular vesicles from humans.

Figure 18. Graphical abstract of the metabolomics assay. It depicts the pipeline followed since metabolites from samples are extracted until they are associated to a metabolic pathway.

3.1.1. Introduction

Steroid hormones are involved in a wide range of physiological processes and their production and delivery is regulated via the hypothalamus–pituitary–adrenal gland and -gonadal axes (Figure 19)[40]. Regulation is, amongst other things, subject to circadian rhythm, stress and sex. There are five classes of steroid hormones, namely glycocorticoids, mineralocorticoids, progestogens, androgens, and estrogens. These different classes have distinct biological functions. Glycocorticoids are involved in stress and immune response while mineralocorticoids are more related to maintain cell homeostasis[40,43]. Besides, androgens and estrogens highly regulate cellular proliferation, development and differentiation. Hence, dysregulation of steroid signal cascades often results in hormone-dependent pathologies. For

instance, the carcinogenesis of breast and prostate cancer (PCa) are strongly influenced by the systemic presence of active estrogens[403] and androgens[19,60], respectively. Specifically in PCa, androgen receptor triggers the tumorigenic growth at a molecular level. Active steroid hormones, such as 5-α dihydrotestosterone (DHT), are the major ligands in this molecular pathway and cause the progression of PCa at early stages[19,39].
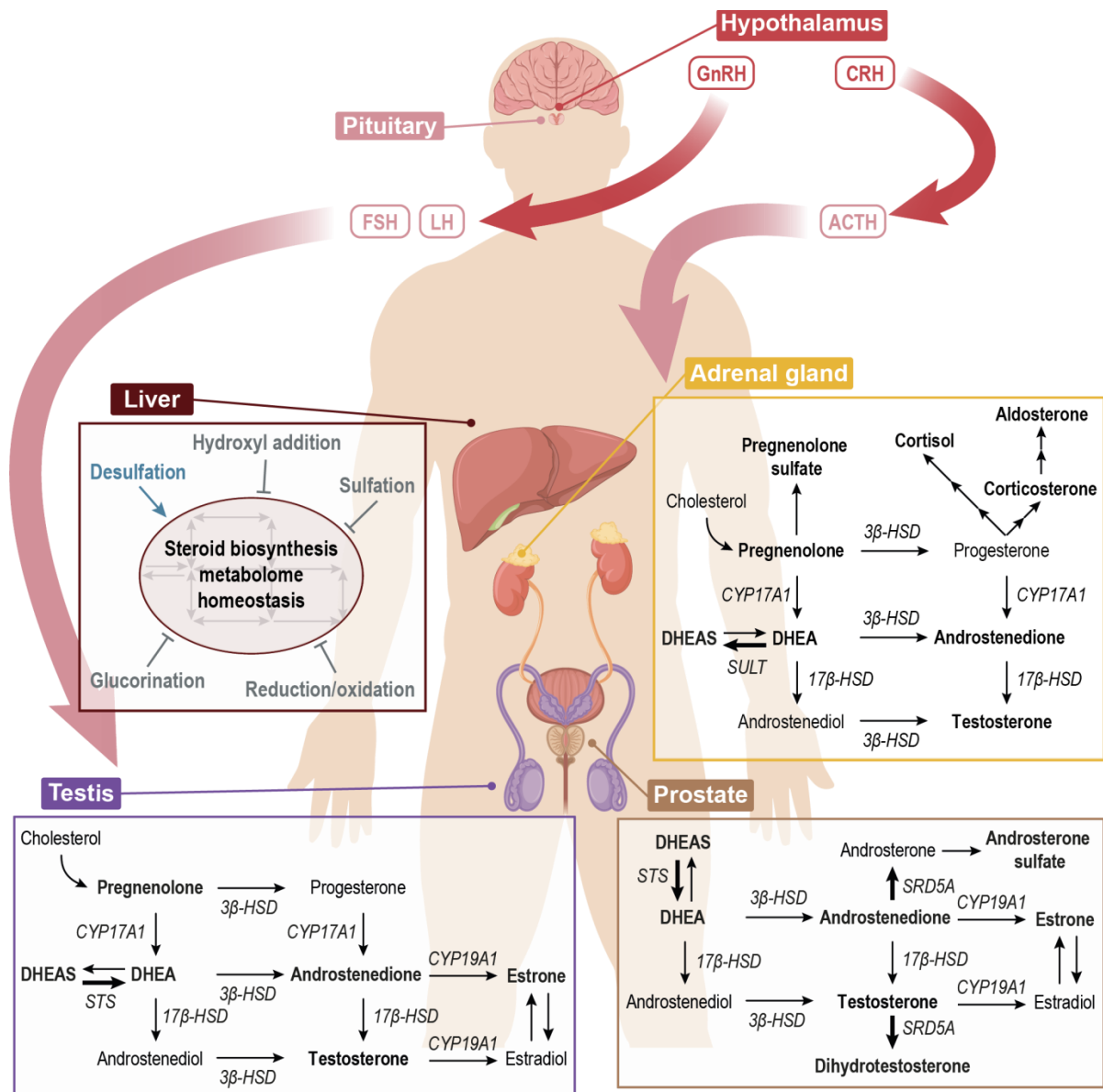
Figure 19. Schematic representation of the steroid hormone biosynthesis pathway in relevant organs and its regulation. CRH stimulates the release of ACTH from the pituitary gland. ACTH stimulates the production of cortisol (exerts negative feedback on CRH and ACTH) and DHEAS in adrenal glands. Pulses of GnRH from hypothalamic neurons stimulate pulses of LH as well as FSH. LH stimulates testosterone production in testis. Liver maintains pathway's homeostasis and several processes may happen: sulfdesulfation makes metabolites available to feed the pathway while processes indicated with a flat end arrow inactivate metabolites that are in circulation. Bold arrows indicate a higher activity of the specific reaction. In bold, the metabolites majorly produced in each specific organ are represented. ACTH: adrenocorticotropin; CRH: corticotropin-releasing hormone; FSH: follicle stimulating hormone; GnRH: gonadotropin-releasing hormone; LH: luteinizing hormone; CYP17A1: Steroid 17-alpha-monooxygenase; CYP19A1: aromatase; SULT: hydroxysteroid sulfotransferase; STS: steroid sulfatase; 3β-HSD: 3β-Hydroxysteroid dehydrogenase; 17β-HSD: 17β-Hydroxysteroid dehydrogenase; DHEA: dehydroepiandrosterone; DHEAS: DHEA sulfate.

In mammals, the precursor of sterol biosynthesis is cholesterol, which is further utilized in adrenal glands, gonads and sexual-derived tissues to produce steroid hormones. There are 99 metabolites involved in the steroid hormone biosynthesis pathway and over 100 reactions catalysed by 61 different enzymes[41,42]. All steroid compounds share a sterane backbone structure. The physiological role of each individual steroid hormone is primarily defined by the layout of double bonds, hydroxyl and keto groups around this basic sterane backbone structure[40]. The main structural difference between classes is the carbon atom arrangement i.e. androgens are C-19, estrogen are C-18, progestogens are C-20 and corticoids are C-21.
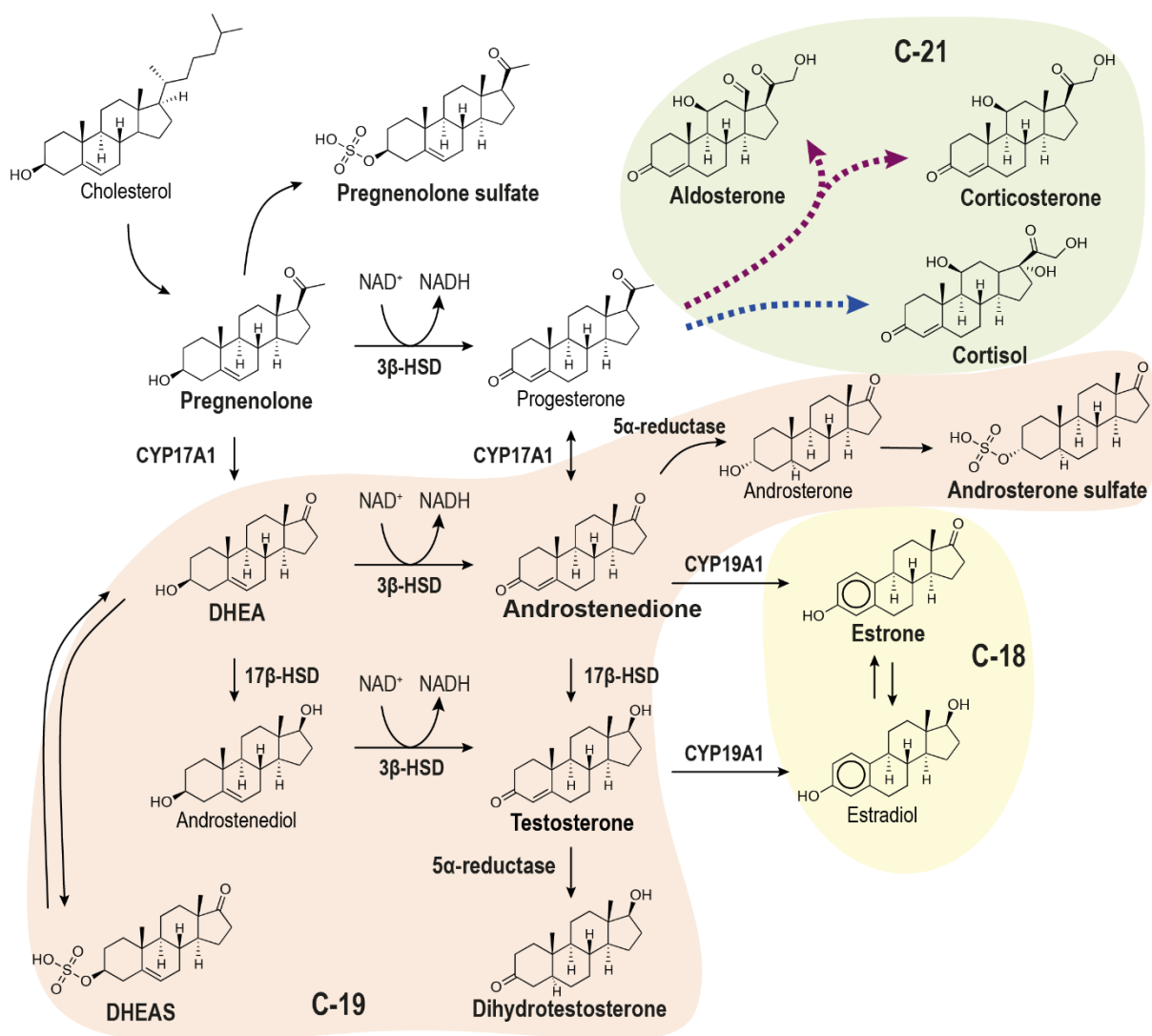
Figure 20. Schematic representation of the steroid hormones biosynthesis pathway. In bold, relevant metabolites of the metabolic network (chosen as analytical standards) are highlighted. The dotted lines indicate a pathway diversion towards C-21 steroid compounds; mineralocortoids and glycorticoids which are depicted in purple and blue, respectively. Each arrow represents a reaction driven by an enzyme or groups of enzymes while a dotted line indicates a metabolic path but no direct reactions. Modules of steroid hormones are categorised in three groups: C-18 in yellow, C-19 in orange and C-21 in green. DHEA, Dehydroepindrosterone; DHEAS, Dehydroepiandrosterone sulphate.

In the first step of the steroid hormone biosynthesis, cholesterol is internalised into mitochondria where it is fed as substrate to produce pregnenolone (Figure 20). This is the main precursor for steroid

hormones produced *de novo*[19] inside the mitochondria. Pregnenolone can be converted to progesterone or dehydroepiandrosterone (DHEA), which can be further metabolized to glycocorticoids and mineralocorticoids (C-21) or to androgens (C-19) such as testosterone, DHT or androsterone and estrogens (C-18), respectively (Figure 20). Interestingly, this metabolic network is tissue-dependent. Different organs are specialised on particular modules of the pathway that are physiologically relevant to perform their function. For instance, adrenal glands are the producers of C-21 hormones while prostate shows a high SRD5A activity, which catalyses the conversion of testosterone to DHT (Figure 19).

Indeed, this is an intricate network of metabolites. Many of these metabolites participate as ligands in a wide span of signalling cascades and biological processes and their levels vary strongly between different biological compartments. While cholesterol is the unique *de novo* precursor in steroid hormone biosynthesis, there exists an interchange between cells and tissues that anaplerotically feeds the pathway at intermediate steps[409]. This means that compounds upstream the pathway can be provided by cell environment. In this line, sulfated steroids are of interest since they are, unlike their unsulfated counterparts, readily soluble in the cytoplasm and in biofluids such as blood or urine. Notably, sulfates of steroids are considered endogenous and active neurosteroids[44,409]. Over the past few decades, it has been established sulfonation is not only a process to inactivate and excrete steroid hormones; it also acts as a systemic reservoir for peripheral or local steroidogenesis in non-steroidogenic tissues, i.e brain or prostate[45,409]. Besides, it has been reported that secreted vesicles, also known as extracellular vesicles (EVs), participate in many physiological processes[410,411] and they can contain a wide variety of cargos such as lipids, proteins, metabolites, sugars and even DNA[65,102,410]. Hormone steroids and related cargoes are transported by blood and other body fluids as sulfated species but they could also be transported by EVs to reach target tissues.

Steroid hormone metabolism and the consequences of dysregulation have gained interest within the biomedical community to understand and diagnose hormone-dependent diseases rather than the historic usage of steroid hormones in therapeutics. Indeed, a number of methods to detect and quantify steroid hormones have been reported during the last two decades. Many studies describe methodologies to detect steroids from several biological sources: cell cultures[403,412,413], urine samples[414–416], animal tissues[417–419], human serum[420–422], human hair[423–425] and waste water. In general, steroid metabolomics methodologies focus on profiling a specific set of metabolites of interest in targeted tissues (or in circulation) rather than analysing steroidogenesis status in a system of organs and related fluids. Methods are usually developed for similar non-sulfated steroids that efficiently ionize in the same mode, avoiding to explore the detection and quantification of many different steroids simultaneously[412,419,421,422]. Methodologically, these studies describe a variety of extraction, separation and detection methods. Especially solid phase extraction (SPE) and reversed phase liquid chromatographic based methods are deployed in the isolation and separation of these compounds. Detection is mostly performed with triple quadrupole instruments. In addition, also gas chromatography-coupled MS methods utilized in few studies. All these methods have their advantages and disadvantages.

We describe a method for the detection of endogenous steroid hormones and their intermediates using liquid/liquid extraction and ultra-performance liquid chromatography (UPLC) coupled to high resolution time-of-flight mass spectrometry (hrLCMS). UPLC provides fast cycling times and a high chromatographic resolution. The high mass resolution obtained with time-of-flight mass spectrometry results in high specificity while sensitivities are on par with triple quadrupole methods. This method was applied to metabolically profile several animal tissues and urinary EVs (uEVs). Different biological matrices including prostate, adrenal gland, testicle, brain and liver of Wistar male rats but also human urinary samples were tested in this assay. To our knowledge, the present work presents for the first time a reliable and optimized hrLCMS assay to analyse key endogenous steroid hormones in endocrine tissue, bioliquids and EVs.

3.1.2. Materials and Methods

3.1.2.1. Tissue and biofluid samples

Tissues and serum were obtained from three wild-type (Wistar, RjHan:WI) rats obtained from Janvier Labs, Le Genest-Saint-Isle, France. All urine samples were obtained from a healthy male on either the morning or the afternoon. uEVs were obtained by ultracentrifuging urine samples as described elsewhere[60]. Urine samples and uEVs were characterized in several physicochemical parameters and protein markers, respectively.

Tissue and serum sample preparations from rats

Tissues and serum were obtained from three wild-type (Wistar, RjHan:WI) male rats which are 17 weeks old. Rats were fed with sterile water and a standard diet *ad libitum* in a temperature- and light cycle-controlled animal facility following the Spanish Guide for the Care and Use of Laboratory Animals (RD 53/2013 - BOE-A-2013-1337). All rats underwent a liver perfusion procedure and were sacrificed by bleeding. Immediately after the perfusion, brain, prostate, testicles and adrenal gland tissues were removed and directly frozen at -80 ºC in dry ice for further use. Liver tissue was collected from animals in which liver perfusion could not be completed. Liver, prostate and testicle tissues were cut on dry ice and aliquoted into portions between 50 to 80 mg prior metabolite extraction. Adrenal glands were stored individually as each individual weighted approximately 80 mg. The exact weight of all tissue samples was calculated and utilised normalise the detected metabolites. Blood was collected during the perfusion procedure into a BD Microtainer® blood collection tube with separator gel (BD, Franklin Lakes, NJ). Then, it was centrifuged at 8,000g for 15 min and the serum fraction transferred into a clean Eppendorf® tube prior storage at -80 ºC for further processing.

Human urine samples

All urine samples were obtained from a healthy male on either the morning (first urine of the day after fasting) or the afternoon (after lunch, approximately at 4pm) to observe circadian variations intra-individual. Each sample group (morning and afternoon samples) has three replicates collected in independent days by spontaneous micturition. Approximately 80 mL of urine were collected of which 50 mL

were centrifuged at 2,000g for 10 min, filter sterilised (0.22 µm pore size) and immediately frozen at -80 ⁰C for further processing. An aliquot of the original urine was also stored at -80⁰C for further analysis. The six different urine samples were characterized regarding the following parameters: blood and ketone bodies presence in urine, glucose concentration, pH value and density (Table 19). Dip-and-read stripes were introduced into thawed urines samples and physicochemical parameters were measured with an OneStepTM Plus Stripe Urine Analyser (Henry Schein Inc., Melville, NY).

EV isolation procedure

Urine samples were thawed at room temperature and centrifuged for 5 min at 2,000g to remove any precipitate . Then, they were centrifuged at 10,000 g for 30 min to obtain a pellet (P10K fraction) containing EVs of bigger size than in the remaining supernatant. In a next step, the urine supernatant was ultracentrifuged at 100,000g for 90 min; the resulting pellet (Fraction P100K) contains EVs of smaller size than P10K. Fraction P10K and P100K were both washed in 50 mL of phosphate-saline buffer (PBS) and ultracentrifugated at 100,000g for 90 min. Afterwards, both fractions were resuspended in 50 µL of PBS and stored at -80 ⁰C together with the urine supernatant (SN100K) of P100K for further analysis.

3.1.2.2.   *Western blot Analysis*

An aliquot of 6 µL of each urinary EV (uEV) preparation was loaded and separated under non-reducing conditions in 4–12% Bis-Tris Protein gels (Invitrogen Inc., Waltham, MA). Western blotting was performed to determine the presence and relative amount of uEVs in each sample and fraction, for this reason only the approximately 10% of each uEV isolated fraction was utilized. In brief, the proteins were transferred to nitrocellulose membranes and then, they were blocked for 1 h (in 5% non-fat milk and 0.1% Tween-20 PBS solution). Then, the primary antibody was incubated overnight (approximately 16 h) at 4 ⁰C, washed and incubated for 1 h with a secondary HRP-conjugated antibody at room temperature. The primary antibodies used in this study were: MoαCD63 (clone H5C6) purchased from Developmental Studies Hybridoma Bank (Iowa, IA), MoαCD9 (clone 209306) from R&D Systems (Minneapolis, MN), RbαAQP2 (clone A7310) obtained from Sigma-Aldrich (St. Louis, MO), RbαCOX-IV (clone 3E11) from Cell Signaling Technology (Danvers, MA), MoαCD10 (clone F-4) from Santa Cruz Biotechnology Inc. (Dallas, TX), and finally, RbαAnnexin V (ab14196) and RbαLAMP2A (clone EPR4207(2)) were both purchased from Abcam (Cambridge, UK). Jackson ImmunoResearch, Inc. provided the mouse and rabbit HRP-conjugated secondary antibodies. A Clarity Western ECL kit from Bio-Rad (Hercules, CA) was utilized for the chemiluminescence detection of bands. Either by scanning Amersham™ Hyperfilm™ MP photosensible films (Cytiva, Uppsala, Sweden) or using a luminescent image analyser ImageQuant™ LAS 4000 (GE Healthcare, Chicago, IL), the proteins in the nitrocellulose membranes coming from different urine samples and fractions were identified.

3.1.2.3.   Chemicals and standards

DHEA, DHT, cortisol (in methanol solution) and the sodium salt of androsterone sulfate were obtained from Cerilliant Corporation (Round Rock, TX). Supelco (Bellefonte, PA) procured androstenedione. The sodium salts of DHEAS and pregnenolone were obtained from Avanti Polar Lipids, Inc. (Alabaster, AL). Testosterone, aldosterone, corticosterone, estrone, pregnenolone 3-sulfate (sodium salt form), leucine-enkefaline (Leu-Enk), chloroform (>99.8% pure; of chromatography grade) and ammonia solution were purchased from Sigma-Aldrich (St. Louis, MO). LC-MS grade water, acetonitrile, formic acid and methanol were purchased from Fisher chemical (Fair Lawn, NJ).

3.1.2.4.   LC-MS sample preparation

Steroid metabolites were extracted by liquid-liquid extraction using a methanol/water mixture and chloroform as extraction liquids. EV fractions were sonicated for 15 min in a total volume of 400 µL 50% *v/v* methanol/water mixture containing 1 mM ammonia to lysate EVs. The cell culture (DU145 cell line), fixed on culture well plates, was scrapped after 5 min incubation with 500 µL 50% *v/v* methanol/water mixture containing 1 mM ammonia. Tissue aliquots - approximately 50 mg - were lysed using 1.4 mm zirconium oxide beads into standard 2 mL homogenizer tubes (Precellys, Montigny, France). Each sample was homogenized in 500 µL 50% *v/v* methanol/water mixture containing 1 mM ammonia by performing two cycles of 40 s at 6,000 rpm in a FastPrep-24TM 5G bead beating grinder (MP Biomedicals, Solon, OH). After lysis, 400 µL of the homogenate – either tissue, EV fraction or DU145 cell culture - was transferred to a clean Eppendorf® tube. Subsequently, 400 µL of LC-MS grade chloroform was added on top of the 400 µL of any lysated sample and shaken for 60 min at 1,400 rpm at 4 ºC. Then, the samples were centrifuged for 30 min at 14,000 rpm at 4 ºC in order to precipitate proteins and to separate the organic from the aqueous phases.

The aqueous (top) and organic (bottom) phases were separated. The protein fraction precipitated on the meniscus between these two immiscible phases. Then, 250 µL of each fraction was transferred to clean Eppendorf® tubes and evaporated using a centrifugal vacuum concentrator. The pellets from the organic fraction were dissolved in 100 µL pure methanol and the pellets from the aqueous fractions were dissolved in 50% *v/v* methanol/water. All resuspended pellets were centrifuged for 30 min at 13,000 rpm and 4 ºC. Finally, 80 µL of the resuspended pellets were transferred to deactivated glass vials or 96-wells plates for injection into the hrLCMS system.

3.1.2.5.   Ultra-high performance liquid chromatography

The chromatographic separation of the analytes was performed with an ACQUITY UPLC I-Class PLUS System (Waters Inc.). This system was equipped with a cooled (10 ºC) Process Sample Manager with a sample loop of 10 µL and a Sample Organizer, a Binary Solvent Manager and a High Temperature Column Heater. A reversed-phased 1.0 mm x 100 mm BEH C18 column (Waters Inc.), thermostated at 40ºC, was used for separating the analytes. Samples were injected from either 2 mL deactivated glass vials or 700 µL Round 96-well polypropylene plates.

Chromatographic behaviour was optimized with respect to peak intensity and an adequate separation of the 11 analytes along the run. Gradient elution was accomplished with an aqueous mobile phase (eluent A) consisting of 99.9% water with 0.1% formic acid and an organic mobile phase (eluent B) consisting of 99.9% acetonitrile with 0.1% formic acid. The flow rate was 140 µL per min. Several gradients were tested during the optimization process (Table 13) in order to avoid break-through (elution of analyte in the injection peak) and obtain good peak separation. The optimal gradient was as follows: start at 30% B, a linear increase to 80% B in 3.8 min., a step increase from 80% to 99%, constant at 99% for 1.0 min and back to 30% B in 0.2 minutes. The total cycle time from injection to injection was 6 minutes. The injection volume for all samples was 2 µL.

Table 13. Summary of the six gradient utilised in optimization rounds to establish the best methodology with respect to peak intensity and analyte separation.

Time (min)	Gradient 1		Gradient 2		Gradient 3		Gradient 4		Gradient 5		Gradient 6	
	% A	% B	% A	% B	% A	% B	% A	% B	% A	% B	% A	% B
0	95	5	90	10	85	15	80	20	80	20	70	30
3.8	-	-	10	90	10	90	10	90	20	80	20	80
4	1	99	1	99	1	99	1	99	1	99	1	99
4.8	1	99	1	99	1	99	1	99	1	99	1	99
5	95	5	90	10	85	15	80	20	80	20	70	30

3.1.2.6. *Mass spectrometry*

A Time-Of-Flight mass spectrometer SYNAPT G2-S (Waters Inc.) was utilized for the detection of analytes. The instrument was operated in either positive (ESI+) or negative (ESI-) electrospray ionization mode and in full-scan mode with a scan range between 50 Da and 1200 Da and scan time of 0.2 seconds.

Table 14. Summary z-spray source parameters optimized for *m/z* 556.2771 in ESI+ and ESI-.

Parameter	ESI+	ESI-
Capillary voltage	1.00 kV	2.00 kV
Sampling cone voltage	25	40
Source Offset	80	80
Source temperature	120 ºC	120 ºC
Desolvation temperature	450 ºC	450 ºC
Desolvation gas flow	5.00 L/h	5.00 L/h
Cone gas flow	1,000 L/h	600 L/h
Nebuliser	6.00 bar	6.00 bar

The z-spray source parameters: temperatures, gas flows, capillary position and voltages were tuned as detailed elsewhere. Optimal source parameters for this assay in either ESI+ or ESI- are summarised in Table 14. Ion optics were fine-tuned by spraying Leu-Enk (100 ppb), at a rate of 10 µL per min, to a

resolution over 20,000 (FWHM) for *m/z* 556.2771. The same Leu-Enk solution was sprayed as a lock mass to correct for *m/z* fluctuations along the assay. The lock mass solution was introduced into the source every 90 seconds using a second ESI probe and it was recorded for 0.5 s. Mass spectrometer spectra was corrected according to fluctuations detected in the lock mass.

3.1.2.7. *Statistical Analysis*

Analyte recovery study

The extraction step efficiency was assessed by performing a recovery assay with various mixtures of organic solvents and water. Five different extraction buffers were tested in this assay: 25/75% *v/v* and 50/50% *v/v* of methanol/water mixture, 25/74.9/0.1% *v/v/v* and 50/49.9/0.1% *v/v/v* of methanol/water/formic acid mixture and 50/50% *v/v* of methanol/water mixture with 1mM ammonia. To compare and calculate the recoveries of 10 different analytes, a culture of a prostate cancer cell line - DU145 - was spiked with analyte standards. Each well containing $5 \cdot 10^5$ cells was spiked with a mix of standards at 2 µM before lysis (pre-spiked) and at the resuspension stage (post-spiked) with a standard mix at 10 µM. Thus, the pre-spikes contained 1 nmol in 500 µL and post-spikes (aqueous and organic fractions) contained the same total amount in 100 µL, which would be the theoretical maximum absolute if no loss during the extraction. In addition, for each extraction solution, non-spiked samples were prepared in order to correct for endogenous metabolites in the matrix. Samples for pre-spiked, post-spiked and non-spiked conditions and the five different extraction buffers were prepared in biological triplicates.

Only the absolute peak areas were taken into consideration to establish the recovery efficiency in the extraction step. Average peak areas were obtained by mean smoothing the raw signals of triplicates. The recovery (R) was determined by dividing the corrected pre-spike average by the corrected post-spike average and represented as a percentage (Eq. 1). Both pre-spiked and post-spiked raw signals ought to be corrected by subtracting the endogenous analytes signal in DU145 culture matrix ($S_{non-spike}$). However, as $S_{non-spike}$ of DU145 culture matrix was less than 0.05% of the signal, endogenous correction was neglected during calculation. Importantly, pre-spikes were corrected with respect to analyte loss (α) during extraction procedure. Moreover, raw signals of each sample did not have to be corrected by the amount of initial samples because every well contained the same amount of cells.

$$R\ (\%) = \frac{\alpha(S_{pre-spike} - S_{non-spike})}{S_{post-spike} - S_{non-spike}} x100 \tag{1}$$

Study of matrix effect in analyte quantification

$$ME\ (\%) = \frac{S_{post-spike} - S_{non-spike}}{S_{standards}} x100 \tag{2}$$

In order to assess the matrix effect (ME) in the quantification of the analytes, the post-spiked raw signal was compared to an equivalent raw signal of a mixture of analytes (10 µM) in solution. Post-spiked raw signals were corrected by subtracting the endogenous analytes detected in the non-spiked

DU145 culture samples. Then, the numerator was divided by the average peak areas of the standards and expressed as a percentage (Eq. 2).

Analyte semi-quantification

In this work, a calibration curve was prepared in solution with 50% v/v methanol/water for the semi-quantification of analytes. This calibration curve consisted of a serially diluted mixture containing all the analytes starting at a concentration of 10 µM. The initial concentration was diluted to half concentration twice, resulting in 5 µM and 2.5 µM concentration is the curve. Then, this set of triplets was diluted in five decades; it resulted in the following 15 different concentrations per analyte: 10, 5, 2.5, 1, 0.5, 0.25, 0.1, 0.05, 0.025, 0.01, 0.005, 0.0025, 0.001, 0.0005 and 0.00025 µM. The calibration samples were injected at the beginning and at the end of each experiment; the average of these two points was used to semi-quantify of metabolites in tissues.

The limit of detection (LOD) for each analyte was set to be the lowest concentration at which the signal-to-noise (S/N) ratio was above 3. The LOQ was defined as the lowest concentration at which S/N ratio was above 10. The highest quantifiable concentration is the highest concentration per analyte that fits the calibration curve with an acceptable accuracy and precision (CV ≤ 15%)[413].

In general, the data of a calibration curve ranges over several orders of magnitude, it is not linear and tends to be heteroscedastic[426]. For this reason, the relation between the peak area and sample concentration was determined by power-fitting[427]. Power fitting resulted in a calibration curve (Eq. 3) with α and b as the fitted parameters. Once the sample concentrations were calculated using a calibration method in solution, the amount (in nanomole) per gram of tissue weight was estimated.

$$Peak\ area = \alpha[concentration]^{b} \tag{3}$$

3.1.3. Results

3.1.3.1. Liquid chromatography and mass spectrometry method

We have compared six different chromatographic methodologies (Table 13) to separate the analytes satisfactorily. The gradient 6 (30% B to 80% B in 3.8 min; detailed steps in Table 13) showed the best peak separation along this run time compared to other tested gradients (data available in [430]). Due to the nature of the stationary phase, analytes elute in order of increasing hydrophobicity. The resulting extracted ion current (XIC) chromatograms of a standard mixture at 10 µM are depicted in Figure 21. In brief, aldosterone (*m/z* 361.2015; ESI+) elutes at 0.99 min, cortisol (*m/z* 363.2171; ESI+) at 1.20 min, DHEAS (*m/z* 367.1579; ESI-) at 1.60 min, corticosterone (*m/z* 347.2222; ESI+) at 1.68 min, androsterone sulfate (*m/z* 369.1736; ESI-) at 1.85 min, pregnenolone sulfate (*m/z* 395.1892; ESI-) at 2.23 min, estrone (*m/z* 271.1698; ESI+) at 2.39 min, androstenedione (*m/z* 287.2011; ESI+) and DHEA (*m/z* 289.2168; ESI+) coelute at 2.40 min, DHT (*m/z* 291.2324; ESI+) at 2.65 min, pregnenolone (*m/z* 317.2481; ESI+) at 3.25 min.

Table 15. Summary of the five different extraction buffers tested in the recovery efficiency experiments.

Extraction buffer	% methanol	% H$_2$O	pH modifier
Buffer 1	50	50	None
Buffer 2	50	49	1% formic acid
Buffer 3	25	75	None
Buffer 4	25	74	1% formic acid
Buffer 5	50	49.975	1 mM ammonia

The buffers differ in their methanol content and the compound utilised to tune the pH of the buffer (pH modifier).

Regarding the mass spectrometry method, Leu-Enk signal (*m/z* 556.2771) was aimed at a resolution of over 20,000 (FWHM) and provided the necessary mass accuracy to evaluate assay analytes. Isotope pattern matching and the use of chemical standards confirming elution times further ensured specificity. In general, mass accuracies for the analytes in solution were between -1 to 1 mDa. Note-worthy, several analytes were not adequately separated during chromatographic elution. Corticosterone and DHEAS elute at similar retention times - 1.60 min and 1.68 min -, however, the MS could properly distinguish them by their *m/z* difference and their fragmentation pattern. Moreover, DHEAS was not detected with a high intensity signal in ESI+ mode. For this reason, corticosterone was measured in ESI+ and DHEAS in ESI- mode. Likewise, estrone, DHEA and androstenedione eluted in approximately 2.40 min. In this case, one could only rely in MS sensitivity (estrone *m/z* 271.1698, DHEA *m/z* 289.2168, androstenedione *m/z* 287.2011) and fragmentation pattern that was sensitive enough to distinguish and quantify them separately.

3.1.3.2. *Analyte recovery optimization*

Afterwards, we evaluated the recovery of 11 analytes using a biphasic liquid-liquid method and analysing them with the optimized hrLCMS method. Extraction was performed using DU145 cell line as matrix. Five different mixtures of organic solvents and water, containing either formic acid or ammonia to modify the pH of the extraction buffer or no pH modifier were assessed (Table 15). Addition of formic acid strived for lowering the pH approximately to 3 while 1mM ammonia modified the extraction buffer to pH 8-9 in order to chemically neutralize functional groups of steroid compounds. From previous experiments in our metabolomics platform, we observed that in liquid-liquid extraction requires at least 25% organic solvent during the extraction step to precipitate the proteins. This is important to avoid clogging the chromatographic system[427]. Moreover, the effectivity of tissue homogenization using beads has been reported as high and does not differ much to the homogenization of other matrices such as urine or cell cultures[427,428]. Therefore, the calculated recoveries are ultimately dependent on the extraction buffer utilized regardless the homogenization methodology.

During the optimization process, it was determined steroid sulfate compounds are recovered completely in the aqueous fraction whilst steroids without sulfate group are found in the organic fraction. Notably, only cortisol was detected systematically in both fractions (Figure 22); however, it was majorly recovered in the organic (80% or higher) rather than in the aqueous (approximately 20%) fraction.
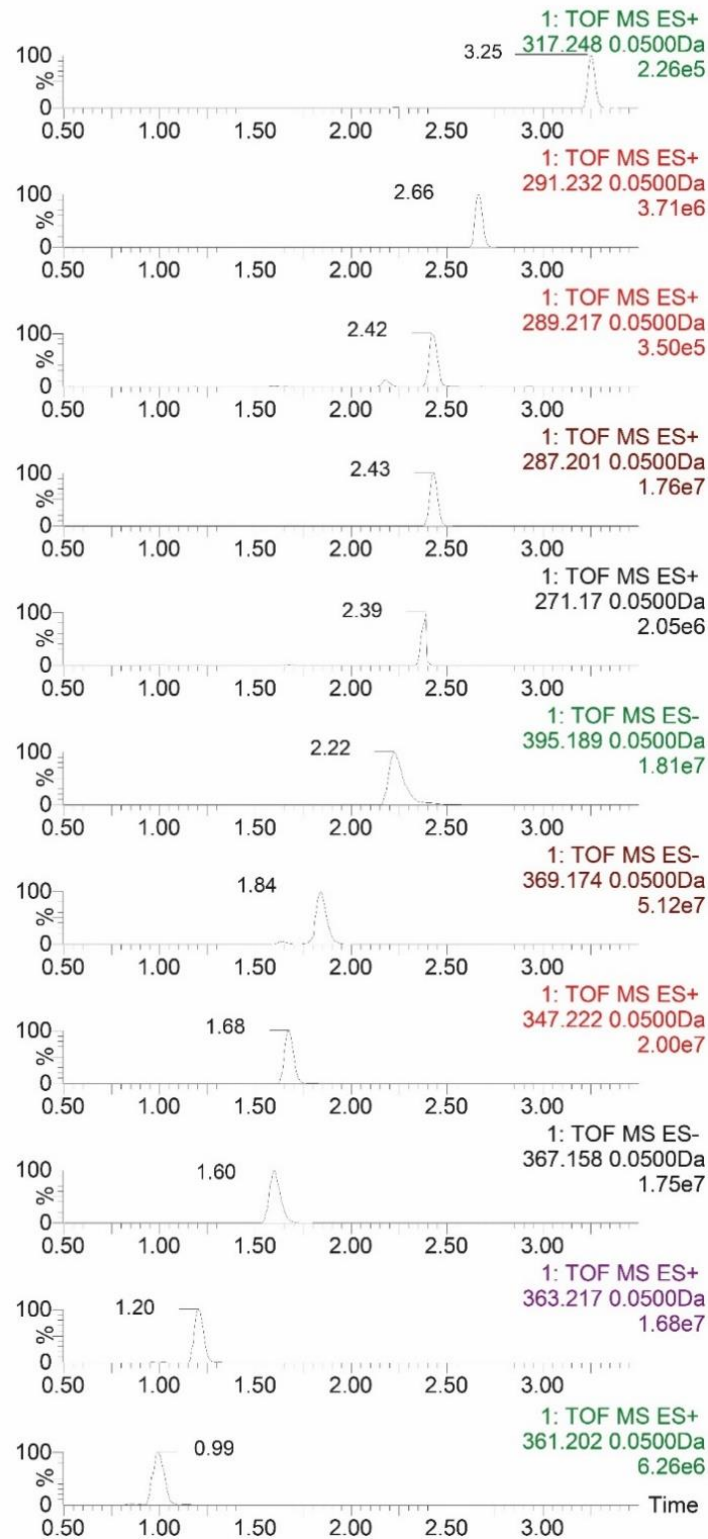
Figure 21. Extracted ion current chromatograms of the analytes from a mixture at 10 uM concentration of each standard. In each chromatogram, the optimal ES (+ or -), m/z value and signal intensity of detection are indicated. They are ordered by decreasing retention time. From top to bottom pregnenolone, dihydrotestosterone, DHEA, androstenedione, estrone, pregnenolone sulphate, androsterone sulphate corticosterone, DHEAS, cortisol

and aldosterone. In green, the parameters of the analytes detected in ES- mode; in dark orange, the parameters of the analytes detected in ES+ mode.

Moreover, the addition of formic acid to the extraction buffer led to a dramatic decay of recoveries in sulfate compounds and a slight decrease in the rest of steroid analytes (Figure 22). One can infer that the presence of protons in the buffer do not stabilize steroid charges and severely hampers the extraction of sulfate steroids in a polar environment. Supplementation of 1mM ammonia outperformed the extraction in terms of recovery and robustness com-pared to the other extraction liquids. Notably, recovery values using different percentages of methanol in the ex-traction buffer do not differ much. However, the extraction efficiency of sulfate compounds using 25% *v/v* methanol underperforms 50% *v/v* methanol with a recovery loss of 40 to 50%.
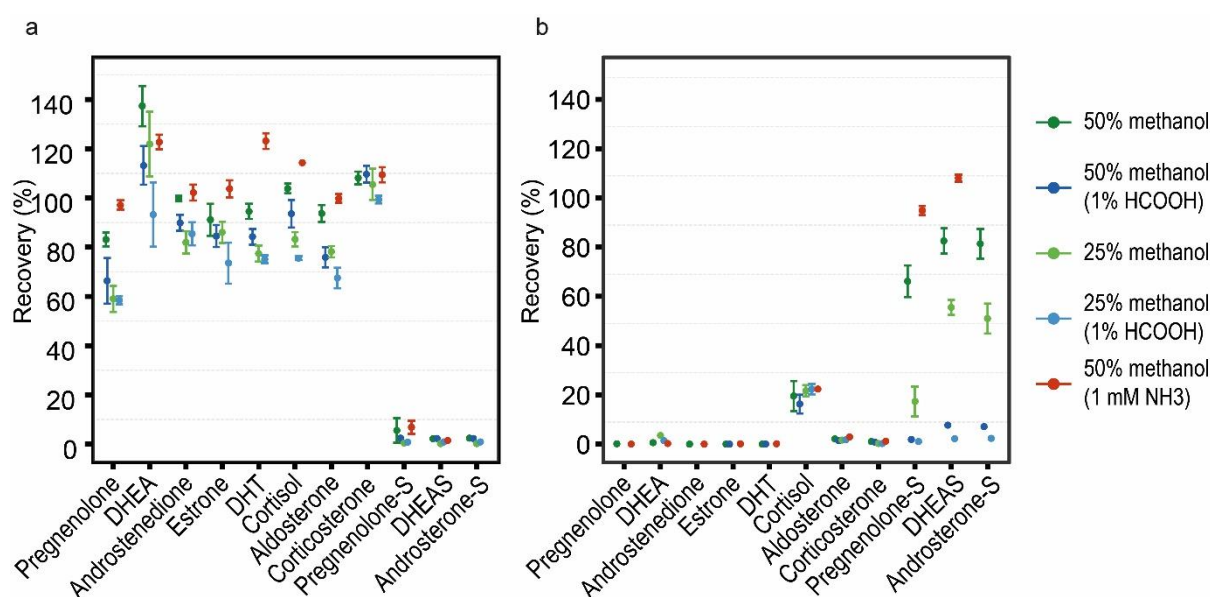
Figure 22. Recoveries (± standard deviation) of the selected panel of standard analytes are shown (n=6). For each analyte, the recoveries using different extraction buffers are depicted. In green, the results of an extraction using only a mixture with the solvent (50% methanol dark green and 25% methanol light green). In blue, the results with extraction buffers containing 1% of formic acid (50% methanol dark blue and 25% methanol light blue). Re-coveries obtained with a 50% methanol (1mM NH$_3$) extraction are depicted in red. a, analyte recoveries of the organic fraction. b, analyte recoveries of the aqueous fraction.

In Table 16, the recoveries of 11 selected analytes using a mixture of 50/50% *v/v* methanol/water with 1mM ammonia as extraction buffer are reported. In general, the present methodology is able to recover and detect over 90% of the initially spiked analyte. Only DHT was detected in a lower percent-age, approximately 80% of the initially spiked DHT was recovered. As expected in a biphasic extraction, hormone steroids were retrieved in an apolar environment and sulfated steroids in a polar solvent. Besides cortisol, pregnenolone sulfate was also reported in both fractions; it was mainly recovered in the more polar solvent and a derisory amount in the organic fraction. Using this methodology, the re-coveries for 10 µM of analyte ranged from 74.2% to 126.9%. These values are acceptable for routine muti-analyte hrLCMS analysis since all the results are reproducible[429]. Thus, extraction using 50/50% *v/v* of methanol/water mixture with 1 mM ammonia was selected for further experiments in different biological matrices.

Furthermore, the performance of the optimized methodology was tested using urine as matrix since it has a high interest for clinical applications. Six urines from a male individual were pooled and aliquoted in different two volumes to assess matrix effect to recovery efficiency. Table 17, the recoveries of 10 analytes are reported; DHEA recovery has not been retrieved because its peak was masked by testosterone's signal. In general, over 85% of the initially spiked analyte is recovered and detected in 50 µL urine matrix. Importantly, sulfated steroids are not recovered with the same efficiency; DHEAS and pregnenolone sulfate report a recovery efficiency of 75.7% and 54.9%, respectively. Recoveries of the analytes using 250 µL urine as matrix describes a slight decrease in non-sulfated steroids while the efficiency decay is dramatic in sulfated species.

Table 16. Summary of the optimized method characteristics. The recoveries (± standard deviation) and matrix effect as signal loss (± standard deviation) of the extraction procedure in two different biological matrices (n=6; biological matrix: DU145 cell) are reported. In addition, LOD and LOQ values of the analytes in the adequate fraction are compiled. LOD: Limit of detection; LOQ: Limit of quantification.

Analyte	Fraction	Recovery [%]	Matrix effect [%]	LOD [nM]	LOQ [nM]
Pregnenolone	Organic	97.2 (± 1.9)	25.2 (± 3.1)	2.5 nM	10 nM
	Aqueous	-	24.0 (± 2.8)		
DHEA	Organic	122.7 (± 2.9)	37.7 (± 5.7)	5.0 nM	50 nM
	Aqueous	-	28.0 (± 6.2)	-	-
Androstenedione	Organic	102.2 (± 3.2)	30.8 (± 4.6)	0.25 nM	0.5 nM
	Aqueous	-	23.2 (± 4.5)		
Estrone	Organic	103.7 (± 3.8)	25.5 (± 4.8)	5.0 nM	10 nM
	Aqueous	-	25.7 (± 4.0)		
DHT	Organic	74.2 (± 3.4)	23.1 (± 3.9)	0.25 nM	1.0 nM
	Aqueous	-	23.4 (± 2.9)		
Cortisol	Organic	114.3 (± 3.8)	25.9 (± 4.2)	0.5 nM	1.0 nM
	Aqueous	22.28 (± 4.5)	17.6 (± 4.7)		
Aldosterone	Organic	99.8 (± 1.77)	18.7 (± 4.3)	0.5 nM	2.5 nM
	Aqueous	-	17.7 (± 5.1)		
Corticosterone	Organic	109.4 (± 3.1)	25.1 (± 3.6)	0.25 nM	1.0 nM
	Aqueous	-	20.2 (± 3.2)		
Testosterone	Organic	126.9 (± 1.7)	14.3 (± 1.9)	0.25 nM	0.25 nM
	Aqueous	-	8.0 (± 2.1)		
Pregnenolone sulfate	Organic	6.9 (± 2.7)	25.2 (± 3.1)	0.25 nM	1.0 nM
	Aqueous	94.8 (± 1.9)	24.0 (± 2.8)		
DHEAS	Organic	-	42.6 (± 1.1)	0.25 nM	0.5 nM
	Aqueous	108.0 (± 1.4)	42.5 (± 0.1)		

3.1.3.3.   Matrix effect

It is well known that phospholipids and other lipids typically enriched in biological matrices such as tissues, body fluids or cell cultures can cause ion suppression in mass spectrometry, thereby hampering the analyte signal[129,130]. This phenomenon negatively influences the detection of analytes and may underestimate their quantification. For a specific matrix, the higher the ion suppression effect is the higher

the signal loss. Therefore, conclusions drawn by detecting and quantifying analytes under these conditions could be misleading.

The matrix effect of each analyte was defined as the signal loss measured at the resuspension step (sample spiked with 10 μM analyte mix) compared to 10 μM of each analyte in solution. The signal loss was calculated in five different extraction procedures because they can influence ion suppression. The matrix effect reported in this work was estimated for a prostate cancer cell line (DU145) culture and urine samples. To note, signal loss is specific of each matrix and each independent experiment. In further experiments, in which quantification is required, the matrix effect should be calculated in every particular assay. From our optimization experiments, one can infer that matrix effect is fraction dependent because there is a significant difference between signal loss comparing organic and aqueous fractions (Figure 23). This phenomenon is likely observed due to a differential extraction of phosphatidylcholine (or other lipid) compounds. Strikingly, this fraction dependency was not observed upon addition of ammonia to the extraction liquid[129,427]. Moreover, the presence of ammonia resulted in a signal loss of up to half-fold compared to extraction liquids with acidic modifier or no pH modifier addition. This suggests the ammonia impairs the extraction of lipidic compounds from the biological matrix hence, decreasing the ion suppression phenomenon in mass spectrometry.

Table 17. Summary of the recoveries using the optimized methodology in urine matrix. The recoveries (± standard deviation) of two different volumes (50 μL and 250 μL) of pre pooled urine are reported (n=3).

Analyte	Urine volume	Recovery [%]
Pregnenolone	50 μL	92.4 (±3.6)
	250 μL	99.3 (±4.8)
Androstenedione	50 μL	93.0 (±3.9)
	250 μL	79.3 (±3.8)
Estrone	50 μL	94.2 (±3.3)
	250 μL	84.8 (±4.8)
DHT	50 μL	76.3 (±4.1)
	250 μL	71.2 (±3.76)
Cortisol	50 μL	87.0 (±3.0)
	250 μL	72.4 (±3.6)
Aldosterone	50 μL	110.7 (±2.9)
	250 μL	103.1 (±3.2)
Corticosterone	50 μL	96.2 (±2.8)
	250 μL	84.3 (±3.6)
Testosterone	50 μL	104.1 (±2.1)
	250 μL	96.3 (±5.1)
Pregnenolone sulfate	50 μL	54.9 (±1.5)
	250 μL	25.5 (±1.2)
DHEAS	50 μL	75.7 (±2.5)
	250 μL	44.0 (±4.2)

In Table 16, the matrix effect (expressed as signal loss (%)) of a DU145 culture of 11 selected analytes using a 50/50% *v/v* of methanol/water mixture with 1mM ammonia for extraction are reported. In general, the present methodology loses approximately 15 to 40% of the signal of non-sulfated analytes but it mainly lays between 20 to 30% loss. On the other hand, sulfated steroids display a 40 to 50% loss of signal regardless the extraction fraction. The signal loss of 10 µM analytes spiked in DU145 cell line were: 25.2% for pregnenolone, 37.7% for DHEA, 30.8% for androstenedione, 25.5% for estrone, 23.1% for DHT, 25.9% and 20.2 % for cortisol in organic and aqueous fraction, respectively, 18.6% for aldosterone, 25.0% for corticosterone, 46.1% for pregnenolone sulfate, and 42.5% for DHEAS. All analytes are majorly recovered back in a particular fraction of the extraction procedure, which is the one selected to report the matrix effect. Signal loss of sulfate compounds refer to aqueous fraction measurement and the other steroids refer to signal loss in organic fraction.
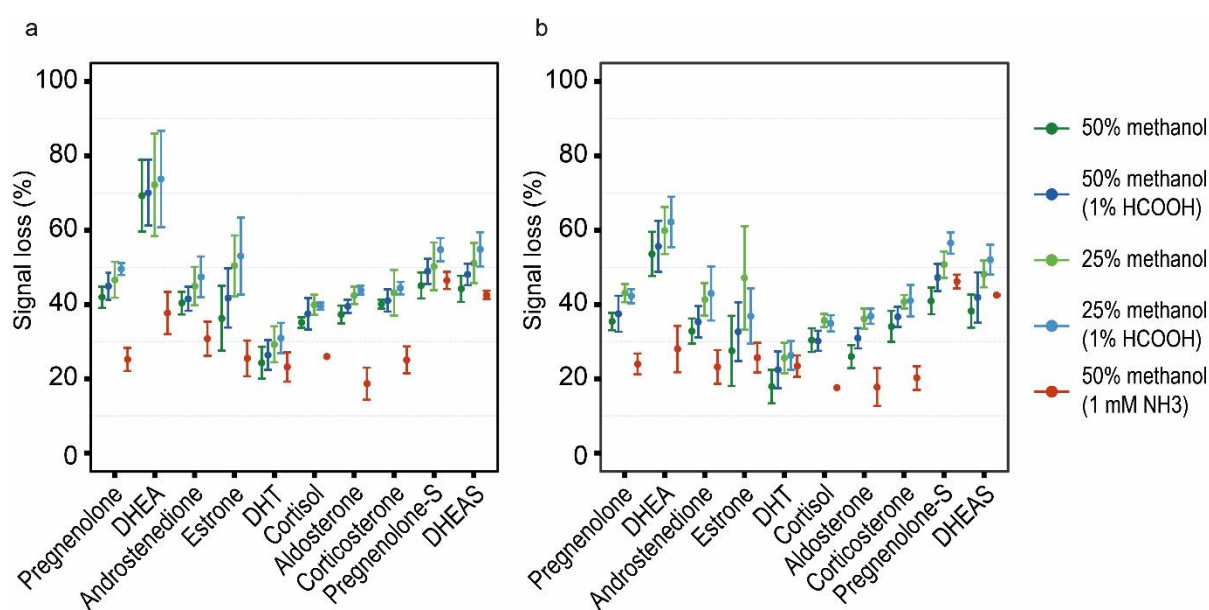
Figure 23. Matrix effect in the detection and quantification of the panel of analytes represented as signal loss (± standard deviation). The matrix effect per analyte in both organic (a) and aqueous fraction (b) is depicted (n=6). In green, the signal loss after extracting metabolites with mixture of only a solvent (50% methanol dark green and 25% methanol light green). In blue, the results with extraction buffers containing 1% of formic acid (50% methanol dark blue and 25% methanol light blue). Matrix effect after a 50% methanol (1mM NH$_3$) extraction is depicted in red.

3.1.3.4. Semi-quantitation of steroids in animal tissues

The hrLCMS method was most sensitive in detecting androstenedione, DHT, corticosterone, prenenolone sulfate and DHEAS with a LOD (S/N>3) of 250 pM in a 50/50% v/v methanol/water solution. Detection limit for cortisol and aldosterone was 0.5 nM, and a LOD of 2.5 nM was determined for pregnenolone. The least responsive ions were the ones of DHEA and estrone with a LOD of 5.0 nM. In regards to quantification limits, androstendione and DHEAS were the most sensitive compounds with a LOQ (S/N>10) of 0.5 nM in solution. Cortisol, corticosterone, pregnenolone sulfate and DHT were in the second group of most quantifiable ions showing a LOQ of 1.0 nM. The quantitation limit for aldosterone was 2.5 nM while a LOQ of 0.01 µM was estimated for pregnenolone and estrone. DHEA was the compound with the highest quantitation threshold (0.05 µM).

We found that the concentration range of steroid hormones is typically low in tissues, ranging from pico- to nanomol per gram of tissue, and cannot detected in some tissues (Table 18). Only pregnenolone, androstenedione, DHT, corticosterone, cortisol and testosterone were detected in tissues or serum of Wistar rats. Pregnenolone and cortisol are only quantified in adrenal gland tissue, however, pregnenolone is also detected in brain and testicle. Adrenal gland and testicle reported picomol amount of androstenedione per gram of tissue. Moreover, DHT was quantified in prostate, adrenal gland and testicle. In prostate, the amount of DHT was 2-fold the quantitation in the other tissues. Testosterone and corticosterone were quantified in all measured rat samples. In general, they were reported in the picomol per gram range in tissues. In serum, they were quantified in the nM range. Interestingly, adrenal gland described nanomol per gram concentrations of corticosterone. Furthermore, testosterone is found in one order of magnitude higher amount in adrenal gland and testicle compared to prostate and brain.

Table 18. Quantitation of three independent Wistar rat tissues: adrenal gland, prostate and brain. Adrenal glands of the same animal were tittered independently, also the prostate lobes of each rat. The averages in nmol per gram of tissue, standard deviations and coefficients of variation (%) of the three groups of samples are reported.

Analyte	Quantification [nmol/ g tissue]	Adrenal gland	Prostate	Brain	Testicle	Serum [nM]
Pregnenolone	Amount	7.04	-	Detected	Detected	-
	St. dev.	3.74				
	%cv	53				
Androstenedione	Amount	$5.97 \cdot 10^{-3}$	-	Detected	$1.45 \cdot 10^{-3}$	Detected
	St. dev.	$3.35 \cdot 10^{-3}$			$1.38 \cdot 10^{-3}$	
	%cv	56			95	
DHT	Amount	$3.47 \cdot 10^{-3}$	$7.57 \cdot 10^{-3}$	Detected	$2.70 \cdot 10^{-3}$	Detected
	St. dev.	$1.02 \cdot 10^{-3}$	$2.40 \cdot 10^{-3}$		$7.92 \cdot 10^{-4}$	
	%cv	29	31		29	
Corticosterone	Amount	18.89	$4.01 \cdot 10^{-3}$	$2.42 \cdot 10^{-2}$	$1.25 \cdot 10^{-3}$	28.01
	St. dev.	10.05	$5.15 \cdot 10^{-3}$	$7.04 \cdot 10^{-3}$	$7.98 \cdot 10^{-4}$	3.31
	%cv	53	128	29	63	12
Cortisol	Amount	0.45	-	-	-	-
	St. dev.	0.19				
	%cv	43				
Testosterone	Amount	$4.53 \cdot 10^{-3}$	$6.92 \cdot 10^{-4}$	$7.02 \cdot 10^{-4}$	$9.18 \cdot 10^{-3}$	0.20
	St. dev.	$1.47 \cdot 10^{-3}$	$2.36 \cdot 10^{-4}$	$4.29 \cdot 10^{-4}$	$4.53 \cdot 10^{-3}$	0.02
	%cv	32	34	60	49	

Standard deviations and coefficients of variation are rather large, indicating an important variability among samples obtained from the same strain but independent animals. One could expect this biological variation and it suggests that treatments, stress or any procedure applied to animals can potentially influence the outcome in further experiments.

3.1.3.5. *Quantitation of steroid hormones in human urinary samples*

Table 19. Summary of the six urine samples collected to test the metabolomics assay.

Parameter	U001	U002	U003	U004	U005	U006
Date (yyyymmdd)	20210521	20210514	20210423	20210524	20210428	20210505
Collection time	Afternoon	Morning	Morning	Afternoon	Morning	Afternoon
Blood	NEG	NEG	NEG	NEG	NEG	NEG
Ketone bodies	NEG	NEG	NEG	NEG	NEG	NEG
Glucose	NEG	NEG	NEG	NEG	NEG	NEG
pH	6	5	6	6	6	5
Density (g/mL)	1.025	1.025	1.020	1.015	1.025	1.025

Collection time and urine characteristics of each sample are reported.

Six different urine samples were characterised in several physicochemical parameters (Table 19) to examine whether sample collection resulted in homogenous sample groups regardless metabolomics analysis. No blood, ketone bodies or glucose were detected in urines, and pH value and density of urine were similar in all samples. Urine samples were centrifuged in two serial steps at 10,000g for 30 min to isolate the so-called P10K fraction - typically containing vesicles of 150 to 200 nm diameter and above – followed by a 100,000g centrifugation for 90 min to isolate the so-called P100K - typically containing vesicles of 100 to 150 nm diameter and below (up to 50 nm)[430]. The supernatant of the second centrifugation is also analysed and referred to as SN100K.

i. LNCaP pellet	vi. EVs (P32K) U004	xi. SN32K U003	xvi. U006
ii. BPH-1 pellet	vii. EVs (P32K) U005	xii. U001	xvii. SN32K U004
iii. EVs (P32K) U001	viii. EVs (P32K) U006	xiii. U002	xviii. SN32K U005
iv. EVs (P32K) U002	ix. SN32K U001	xiv. U004	xix. SN32K U006
v. EVs (P32K) U003	x. SN32K U002	xv. U005	* M_w Marker
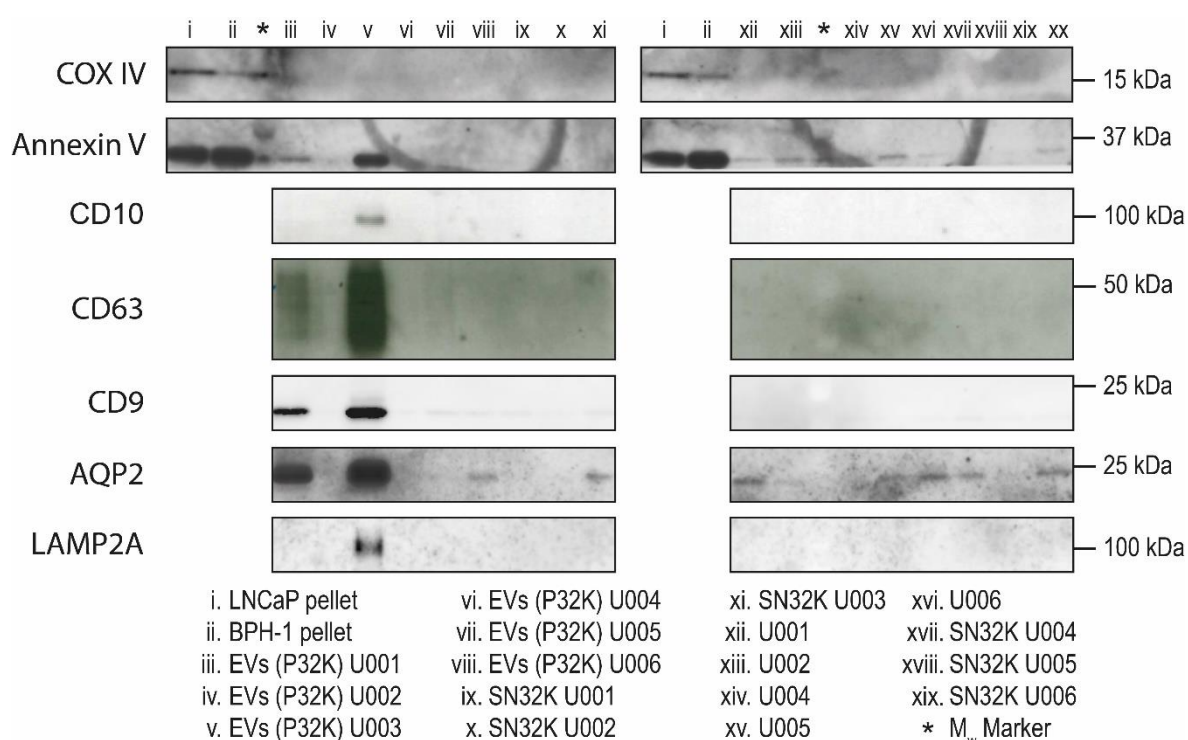
Figure 24. Western blot of the urine-derived fractions of samples detailed in Table 19. Each lane is numbered and each number is related to a specific fraction. COX IV, Annexin V, CD10, CD63, CD9, AQP2 and LAMP2 antibodies were tested for all the fractions. On the right, the molecular weight (in kDa) of each specific antibody result. Asterisc (*): protein ladder (Marker).

Table 20. Quantitation of urine human samples (n=6, U001 to U006, Table 19). The isolated EV fraction are also included in the table. In the table, the three analytes detected in the urine-derived samples.

Sample	Collection time	Androstenedione [nM]	Cortisol [nM]	DHEAS		
				Conc. [µM]	EV-associated DHEAS [µM]	EV-associated DHEAS in urine [ppm]
Urine	Morning	2.25 (±0.92)	40.1 (±33.5)	0.36 (±0.16)	-	-
Urine	Afternoon	1.95 (±0.78)	35.7 (±0.7)	1.27 (±0.87)	-	-
SN100K	Morning	2.31 (±1.53)	29.9 (±14.7)	1.33 (±0.94)	-	-
SN100K	Afternoon	1.82 (±0.64)	31.4 (±0.7)	0.87 (±0.92)	-	-
P10K	Morning	-	-	-	1.75	0.90
P10K	Afternoon	-	-	-	0.76 (±0.08)	0.79 (±0.41)
P100K	Morning	-	-	-	6.17	3.19
P100K	Afternoon	-	-	-	0.74 (±0.01)	

Concentration (± standard deviation) of the analytes in urine and supernatant fraction of both morning and afternoon collected urines is shown. Absolute amount and relative amount (± standard deviation) of DHEAS is calculated in 50 mL of initial sample of both morning and afternoon collected urines.

In this set of urine samples, the current methodology is able to detect and quantify androstenedione, cortisol and DHEAS (Table 20). The other steroids of the panel were below LOQ and, in general, also below LOD. Androstenedione and cortisol were detected only in urine and SN100K. It was not possible to detect them associated to EVs and they are majorly solubilised in urine. Androstenedione was found in lower concentrations compared to cortisol and the variability between collection days was high (40 to 60%) regardless the collection time. Concerning cortisol, the variability is extremely high between morning collection days (approximately 50 to 85%) whilst concentration of afternoon collected samples is stable (approximately 2% variation). DHEAS was the compound detected in the highest concentration (µM range) soluble in urine compared to androstenedione and cortisol (nM range). Similar to androstenedione, DHEAS showed a high variability over independent collection days in both morning and afternoon collection times. To note, DHEAS is the only metabolite detectable in EV fraction. In Table 4, the absolute amount (µmol) in 50 mL of urine is reported but also the relative amount (in ppm) of the total detected metabolite that is associated to EVs. Importantly, DHEAS was not quantifiable (S/N<10) in all samples collected at morning time but it was detectable in all cases (S/N>3). According to our analysis, a range of 0.5 to 3.0 ppm of DHEAS was associated to EVs in urine samples (Table 20; detailed calculations available in[431]).

The isolation of EVs in the pellet fractions was confirmed with the presence of typical EV markers by Western blotting (Figure 24). Typical urine exosome markers such as CD9, CD63, AQP2 were intensified in P100K fractions, confirming this fraction is enriched in EVs. However, they are sample dependent and were detected in various amounts. Also, LAMP2A and CD10 were detected only in the P100K fraction of U003-derived EVs preparation. Annexin V and AQP2 were found in both P100K and P10K but also in different amounts among urine samples.

3.1.4. Discussion

This work describes a fast and simple hrLCMS methodology able to detect and quantify 11 key metabolites of the steroid hormones biosynthesis in several biological matrices. Their importance in diseases such as PCa and other steroid-dependent diseases spotlights this assay as a powerful tool to study the role of steroid hormones in the development and progression of hormone-dependent diseases and assess the metabolic status of patients via liquid biopsy analysis. In brief, this method identifies and quantifies 11 steroids including corticoids, androgens and metabolic intermediates in a high-throughput method of 6 min. Although testosterone and androsterone sulfate were not included in the recovery experiment, the methodology is able to separate, identify and quantify them.

All steroid hormones are primarily derived from cholesterol, which provides the sterane ring structure shared by all these compounds (Figure 20). Subtle chemical differences, unique to each steroid hormone, significantly complicate the separation of such structurally similar molecules. Furthermore, the structure of steroids and position of functional groups determine their preferred ionisation mode and efficiency[415,421]. For instance, testosterone and DHEA – with the same molecular formula – display different ionization efficiencies. DHT or androstenedione are readily ionised in positive mode, in contrast to DHEA or pregnenolone, which are not strongly ionised due to the presence keto groups in the ionisable region (Figure 20). In order to increase signal intensity, the MS could be operated in enhanced duty cycle (EDC) mode; this is a more appropriate approach in targeted analyses, where the analyte empirical formulas are known. In this strategy, MS signals of a given retention time are measured in separate scan functions to enhance the *m/z* of the selected analyte. Measuring in EDC instead of full-scan mode may increase several folds the S/N ratio of a given metabolite[427,432,433]. Therefore, EDC mode is an option to consider for those samples in which analytes S/N ratio falls above the LOD but are not always quantifiable.

An LCMS method is usually evaluated in terms of efficiency, accuracy and sensitivity of the measurement. The process efficiency is a combination of recovery efficiency and matrix effect of each metabolite[434], and the sensitivity is evaluated with the LOD and LOQ of each metabolite. Different studies identifying and quantifying steroid compounds in biological matrices report a wide range of efficiency recoveries. For example, in PCa cell cultures a recovery range of 54.7% to 78.1% was reported[413] while breast cancer cell cultures report recoveries ranging 95.7 to 102.0%[413]. Our data, with recoveries ranging from approximately 75% to 125%, suggests that a cell culture as matrix does not impair the extraction of steroid metabolites. Urine matrix does not impair the extraction of non-sulfated steroids but sulfated species suffer a recovery efficiency decay. To note, studies measuring steroid in urine and tissues as biological matrices report recovery efficiencies over 100% in some cases[414–416]. An explanation for this phenomenon might be metabolites can be either free in solution or tethered to other molecules such as membrane lipids during the extraction process. For this reason, the organic and aqueous phase recoveries are not adding up 100% in this assay. In case of detecting a metabolite in two fractions, the addition of both signals is perhaps a better approach to quantify that specific metabolite. However, our

assay is very convenient as all metabolites (except cortisol) are recovered in one fraction. This permits a faster measurement of steroid hormones in diverse biological matrices.

Existing quantitation methods for steroid hormone compound have a wide span of LOQ, ranging from 0.002 to 10 ng per mL. However, it is highly dependent on the analysed matrix, i.e. a urine matrix shows a range from 0.002 to 0.2 ng per mL[415,416], whilst cell matrices display a higher LOQ up to 10 ng per mL[413]. This suggests the matrix effect also depends on the specific matrix where the metabolites are contained. Comparing these studies, cell matrices report a lower sensitivity compared to urine; this is important when applying this method in future experiments or assays. In fact, this observation spotlights the major limitation of this study: The quantitation has been performed semiquantitavely. Ion suppression in mass spectrometry affects negatively the analyte signal, and subsequently underestimates its quantitation or it simply hampers its detection. Moreover, ion suppression may be limiting the detection of certain steroid compounds in several matrices, i.e. EV preparations. In consequence, this method should be utilised in matrices that facilitate steroids detection. A matrix-spiked calibration is usually the appropriate method to quantify absolute amounts of analytes in samples[427]. In this work, a calibration curve of the analyte standards was prepared in solution with 50% *v/v* methanol/water as solvent. Such approach cannot compute absolute amounts of the analytes in tissue since the matrix effect is not considered, however, a semi-quantitative approximation of the metabolites in tissues can be calculated. In this assay, the reported LOQ range lays between 0.50 and 50 nM (equivalent to 0.14 and 14.42 ng per mL) in solution, similarly to previous studies. However, it is advised to use matrix-spiked curves in further experiments using this assay.

The time required to perform the chromatographic separation is typically long in literature; they report runtimes from over 10 min up to 45 min[59,409,416–420,425]. Only the work of Quanson *et al.*[413] and Indapurkar *et al.*[414] described a methodology with a short runtime (4 to 5 min); however, they tested and applied the method solely in cell matrices: PCa and induced pluripotent stem cell lines, respectively. Indapurkar *et al.*[414] developed a methodology specific for estradiol-related metabolites and Quanson *et al.*[413] measured androgens with ultra-performance convergence chromatography. In 2012, Maeda *et al.*[418] accomplished the separation, detection and quantification of a panel of steroids in rat organs except in the liver but using an HPLC system. For this reason, sample preparation strategy demanded high volumes of extraction buffer – 15 mL of acetonitrile per sample – and required a total run time of 11 min. In this work, the volumes and run time are lower than 1 mL and the 10 min.

In order to test the performance of our methodology, we have measured steroid hormone analytes from several rat tissues: adrenal glands, testis, prostate, liver and brain. The data shown in Table 18 is in accordance with the fact that the pathway is tissue-dependent in regular physiological conditions. Two metabolites upstream the pathway, pregnenolone and androstenedione, were quantified in adrenal glands but could not be quantified in prostate or brain. This hints that adrenal glands are in charge of metabolising cholesterol into steroid compounds in complex organisms such as rats; it is in line with previous findings in literature[435–437]. Likewise, adrenal glands are known to produce corticoid hormones. Our data confirms this since corticosterone is quantified in a higher amount – three to four orders of

magnitude – when compared to prostate, brain and testicles. Adrenal glands also seem to accumulate androgens (Table 18); however, the presence of active androgens (DHT) is 2-fold higher in prostate compared to other tissues. Importantly, the ratio DHT/testosterone, which are the active and non-active paired androgens, was approximately 11 in prostate while adrenal gland and testis were below 1. Because the presence of active androgen plays a physiological role in prostate, the ratio DHT/testosterone was also higher in this tissue.

Since the first urinary metabolomics attempts to analyse urinary samples and other biofluids, several methodologies have been developed during the last years[416–418]. Nevertheless, none of the reported methodologies was optimal to assess steroids in EV sample preparations, tissues or body fluids in a fast and simple manner. Up to date, many studies have shown metabolomics in EVs[60,417,438], but none of them has reported the detection of steroid hormones in a targeted approach. A plausible explanation is that the identification and detection of compounds similar in molecular mass – even the same one in some cases – hampers the allocation of mass signals with the corresponding chromatographic peak. For those steroids, i.e. DHEA and testosterone, which share empirical formula, the identification of each specific compound remains challenging using MS and it relies on chromatographic separation.

Importantly, we have been able to quantify steroid hormones in urine samples and derived uEV in a fast and simple manner. However, only one DHEAS was detected in uEVS and cortisol, androstenedione and DHEAS were detected in urine samples. These EVs were isolated by ultracentrifugation including a washing step to avoid any contamination from the soluble fraction. Urine samples from a healthy man were collected in different days and in time collection (morning and afternoon). Time collection was a parameter to be assessed from a metabolomics perspective but we found out that interday variability had also a high impact in the analysis. Morning samples are considered to contain a higher concentration of steroids coming from the prostate, possibly due to accumulation and leakage towards the urinary tract at night. However, this trend was not described in our morning samples. The reason may be that urine sample U003 (Table 19) was not available for metabolomics analysis since the analysis of the soluble fractions of urine (after uEV isolation), which includes U003, morning samples had a higher concentration of DHEAS. This highlights the importance of analysing a larger cohort to obtain significant results non-dependent of a unique high concentrated sample.

In the end, this is a fast and sensitive method that was successfully applied for the detection and quantification of a panel of steroid hormone compounds in biological samples in 6 min runtime per sample. The sensitivity of this method makes it ideally suited for multiple *in vivo* applications. In this manuscript, we explore the analysis of steroids in several rat tissues and also human urine and uEV samples. This has evident applications in profiling the metabolic status of patients suffering any hormone-dependent disease. To note, the assay requires a longer cleanse step to wash the column out of lipids and peptides when running a long experiment with many tissue samples. To our knowledge, this is the first hrLCMS-based method able to detect and quantify steroid hormones associated to EVs isolated from body fluids in a targeted approach.

3.2. Clinical Evaluation of Metabolic Signatures as Biomarkers of Prostate Cancer Progression in Patient Urines

3.2.1. Background

The use of body fluids as a source of biomarkers have been intensified over last years. Currently, urine samples are one of the most important sources to identify PCa biomarkers since it is near the prostate and they can provide biological information. Documented studies have shown metabolites and metabolic signatures contained in urine samples can discriminate healthy and disease patients[439–441]. Moreover, a metabolomics study in uEVs described several altered metabolites of which few steroid hormones were heightened[60]. In general, these type of approaches aim to describe metabolic biomarkers in already distinct samples. This provides a valuable diagnosis information; however, they often present a poor prognosis, as they cannot predict the likeliness of a patient to develop the disease or how it will progress.

In this section, a method for the detection and quantification of steroid hormones in biological samples has been developed and optimised as these hormones are the major drivers of progression at early stages. This approach will be used in upcoming chapter to describe the transference of metabolites via EVs. Nonetheless, another purpose of the method was to validate a steroid hormone metabolic signature as a biomarker for PCa.

3.2.2. Results and discussion

3.2.2.1. Clinical cohort characteristics

In *Chapter 2. Evaluation of Steroid Hormone Transcripts Associated to Urinary Extracellular Vesicles in Prostate Cancer Progression* a cohort of samples obtained from Basurto's Hospital has been presented. From that cohort, a clinically relevant cohort was designed to seek for specific signatures to define the status of disease in patients. In this section, it has been utilised to assess the hormone steroid metabolic signature of patients in urine. This cohort consists of 85 urine samples of 1 mL volume selected to cover the 5 groups of PCa patients (GG1, GG2, GG3, GG4 and GG5) and control BPH. Relevant information about the patients and samples is compiled in Table 21. To note, all urine samples were collected prior any biopsy hence, metabolic signatures of patients inform about their status at first visit to clinician. Diagnosis in terms of GS, pT, Pn and pN were reported after undergoing a second biopsy, a so-called surgical specimen biopsy, which was performed after 1 to 3 years. The staging mentioned in Table 21 is well explained in Prostate Cancer Disease section in the INTRODUCTION. Importantly, whether perineural invasion was observed clinically (Pn) or validated anatomopathologically (pN) is specified.

Table 21. Summary of clinical characteristics of urinary samples included in the study. Patient groups, pT and Pn stages were determined upon surgical specimen biopsy.

Parameter		Patients (%, n=85)
Median Age (IQR)		67(63,73)
BMI (IQR)		26.6 (25.3,28.1)
PSA value, ng/mL		
< 4		41 (48)
4-10		35 (41)
> 10		9 (11)
ADT treatment		not available
Prior prostatectomy		
Yes		84 (99)
Unknown		1 (1)
Family history		
PCa		6 (7)
Other cancer		39 (46)
None		33 (39)
Unknown		7 (8)
Patient group (GS)		
BPH		35 (41)
GG1	(3+3)	10 (12)
GG2	(3+4)	10 (12)
GG3	(4+3)	10 (12)
GG4	(8)	6 (7)
GG5	(9-10)	14 (16)
pT stage		
None		37 (43)
2		26 (31)
3	a	10 (12)
	b	12 (14)
Pn stage		
Not reported		38 (44)
Pn0		3 (4)
Pn1		44 (52)
pN stage		
Not reported		44 (52)
pN0		10 (12)
pNx		30 (35)
pN1		1 (1)

ADT, androgen deprivation therapy; GS, Gleason score; IQR, interquartile range; pT, PCa progression stage; Pn, Perineural invasion (Clinical); pN, positive lymph nodes (Anatomopathological)

3.2.2.2. Signature result

Metabolomics assays require an adequate performance in the specific biological matrices to be analysed. In terms of accuracy and sensitivity, the utilised matrix may influence on the outcome; however, the most important parameter to test are the efficiencies of analyte recovery. This parameter will inform whether the assay is working successfully. Similar to section *3.1. Development of a Targeted Metabolomics Assay in Endocrine Tissues of Male Rats and Human Samples*, recoveries of the analytes in different volumes of urine were calculated (Figure 25). Non-sulphated metabolites were recovered in

a range between 70 to 110%, approximately. In contrast, sulphated metabolites - DHEAS - range between 45 to 75% approximately, exhibiting a decreased recovery values compared to previous section. In general, an increase in urine volume leads to a lower recovery of analyte; in sulphated metabolites they suffer a dramatic decay. This result indicates that urine matrix negatively affects the performance of the assay. In the case of polar analytes, the loss is rather relevant and it is something to consider in the decision making process upon designing an experiment. Anyway, recoveries are still adequate so we decided to proceed quantifying the cohort.
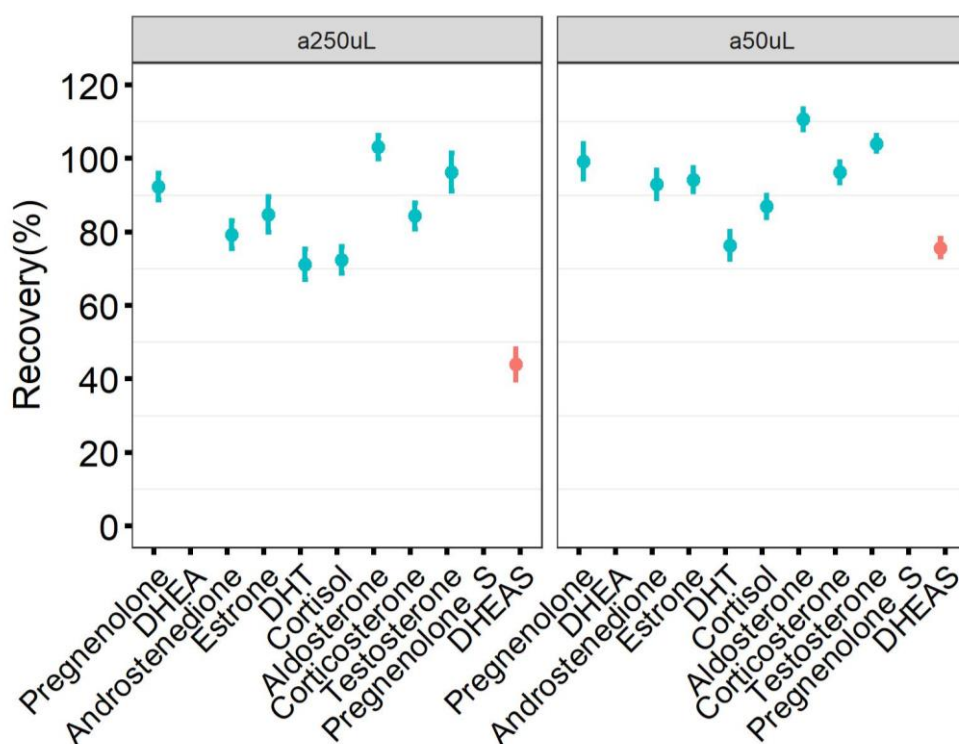

Figure 25. Recoveries (± standard deviation) of a selected panel of standard analytes with urines as matrix are shown (n=6). For each analyte, the recoveries using a different volume of urine to undergo analyte extraction are depicted. Either starting with 250 µL or 50 µL of urines was tested. In blue, the analytes recovered in the aqueous organic fraction. In red, the analytes recovered in the aqueous organic fraction. Extraction with 50% methanol (1mM NH_3) was utilised for urines.

Thence, a total of 85 urine samples were analysed and quantified in steroid hormones content. The urine volume utilised in this approach was 250 µL since apolar hormones are present in low levels and one would like to maximise detection even compromising analyte efficiency of recovery. The analytes aldosterone, androstenedione, testosterone, cortisol, cholesterol, androsterone sulphate and DHEAS were successfully detected in this cohort. Prior analysis, analyte signal was normalised using median fold change[442,443] to correct for metabolite abundance intrinsic of the urine sample. Hormone steroid levels in urines failed to discriminate between PCa and BPH patients (Figure 26). The score plot indicates a tendency to spread out but the two groups of samples are not separated. Further univariate analysis confirmed this result. Interestingly, few significant differences were measured when PCa samples were categorised according to their disease stage (Figure 27). Figure 27 depicts the four most relevant metabolites found back in urine samples. It shows that androsterone, DHEAS and cortisol levels are differentially quantified between BPH and some PCa groups but also, within PCa groups.

The major issue of these results is that no signature can determine whether a sample is diagnosed with PCa or BPH. Documented reports using EV preparations described DHEAS as a potential marker of PCa[60]; however, analysed urine samples do not support this hypothesis. The fact the metabolite DHEAS is readily soluble in biofluids and it is residual in EV samples derived from urines[444] suggested that its evaluation in urine could have been more informative of the status of the disease. Nonetheless, the new data offers a better classification of PCa sample groups and shows few significant differences between them. A limitation of this subgrouping is the sample size because it is rather small at group level. Moreover, steroid hormone levels do not describe a classification pattern nor describe all the different subgroups. Notably, the classification of samples is very relevant in proceeding with these approaches, therefore differences in classification or building up cohort may hinder significant results. This makes the data quite difficult to interpret. Hence, predictive tools or validation models might be of interest to treat this data.
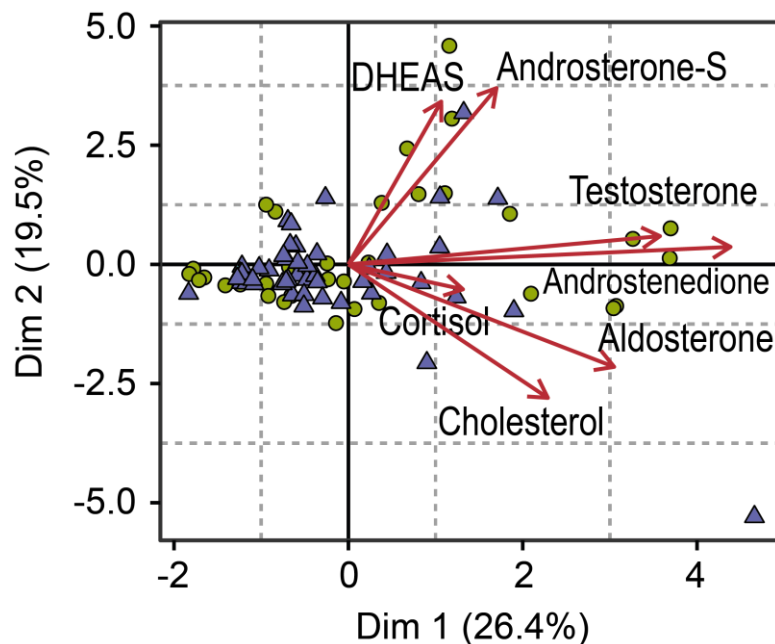
Figure 26. Score plot corresponding to PCA analysis of PCa and BPH urine samples. This PCA model was generated with all the samples in order to differentiate both groups. In the axes, top two most representative features to distinguish samples groups are plotted. In purple triangles PCa samples and in green circle, BPH samples. Red arrows indicate the variables that explain variability.
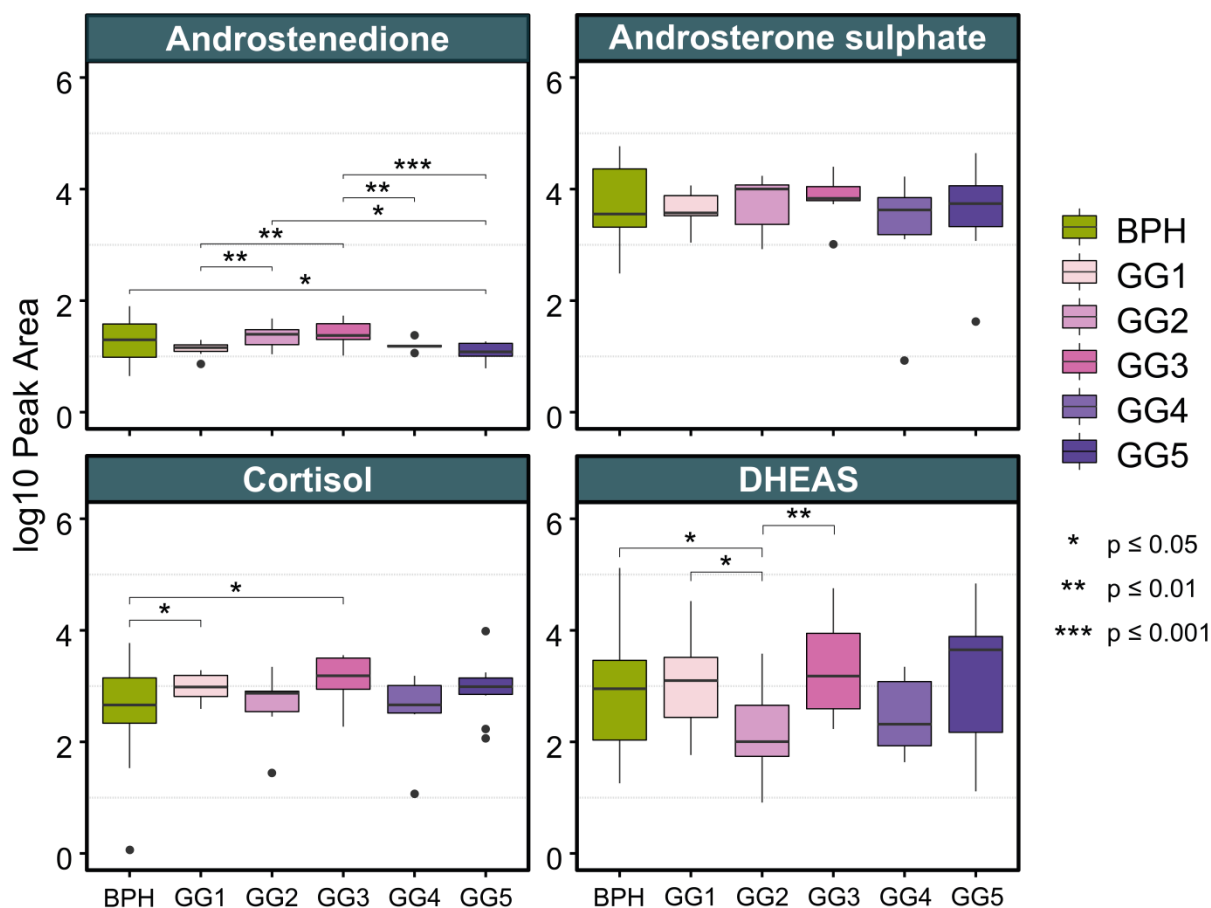
Figure 27. Normalised quantification of the relevant analytes detected majorly in the cohort of urine samples. The BPH and PCa levels of androstenedione, androsterone sulphate, cortisol and DHEAS are reported as well as the significant differences between the groups.

3.2.2.3. Approaches to give an outcome

As urine samples of this cohort were collected at first visit, metabolomics data represents the status of the patient at that time. This metabolomics data is of use if it can discriminate between patient groups. A logistic regression is a widely used binary classification model, which could provide a decision system by giving a matrix with data as an input. This means that a matrix with steroid hormones data, a multivariate logistic regression can be written to decide the output in a binary manner i.e. PCa or BPH (Eq. 4). However, the decision can also be triggered between PCa groups. In this approach, the idea was to build up a model, a logistic regression with diagnosis data. Then, challenge the model with a number of random samples to test whether it classifies the samples successfully. Because no metabolite was differentially present in PCa vs BPH, no valid model could be built. One could neither apply it successfully to classify PCa groups.

$$F(x) = \beta_0 + \beta_1 x_1 + \beta_2 x_2 + \cdots + \beta_p x_p$$

$$where\ x\ are\ metabolites\ participating\ in\ the\ signature$$

(4)

Such binary approaches are not useful in assessing the classification of several groups using a metabolic signature. For this reason, other predicting model found in literature are suggested: Gaussian

Naïve Bayes, Random Forest, XGBoost, deep neural network or support vector machines. However, the development of a proper pipeline to evaluate a metabolic signature for clinical purposes lays beyond the scope of this thesis.

Until diagnosis (via cylinder and/or surgical specimen) is completed, a couple of years could have elapsed hence, the data can also be considered longitudinal. The approaches already described do not consider longitudinal data and it could also be an interesting approach. One possibility would be the usage of a machine learning framework, which requires a longitudinal collection of data. This means the analysis of a urine sample is required in each time point to determine the variation of signature. The R package 'MetabolicSurv' identifies biomarker signatures by discovering predictive metabolites to classify the expected progress into groups. These approaches are interesting but do not quite fit the data gathered in this clinical cohort. One has to acknowledge his limitations and perhaps propose to build up a model with patient diagnosis outputs. In this manner, known metabolic signatures lead to specific trajectories of diagnosis over time. Hence, a predictive model can calculate probabilities of specific outcomes. Nevertheless, one is hypothesising and proposing here a possible follow up or an interesting research field for computing sciences.

3.2.3. Conclusions

In this section, the metabolomics assay has been further described and evaluated for urine samples. It has been further utilised with clinical purposes to test whether previous results can be reproduced. One can conclude:

i.   Steroid hormones can be measured and quantified in urines from patients. The efficiencies of their recoveries are acceptable for this type of analysis.

ii. Significant differences have been reported between PCa groups and, between BPH and PCa groups in cortisol, androstenedione and DHEAS levels. Unfortunately, no steroid hormone signature could distinguish between BPH and PCa urine samples. This suggests that a correct evaluation and classification of the sample is also required to find out biomarkers and compare studies.

iii. No model could have been successfully built up with the provided data. One has suggested follow up opportunities; however, to continue with this type of research was beyond the scope of this thesis.

Chapter 4. Transference of Biological Components and Functionalities Driven by Extracellular Vesicles

This chapter focusses in describing two approaches to assess the transfer of metabolites or functions to recipient cells by means of EVs. The assay described in Chapter 3.1 has been further developed to trace labelled metabolites in recipient cells and hence, determine whether EVs may participate in feeding metabolic pathways important in PCa early progression. This work has been compiled in a manuscript, which is under a submission procedure, and has not been accepted yet. Chapter 4.1 includes the last version of the manuscript. Furthermore, the transfer of oncogenic signalling driven by EVs has been explored. This approach consists in establishing a PCa model with a readout responsive to androgen signalling. Thence, oncogenic markers were measured upon treatment with EVs. This part has been included in Chapter 4.2.
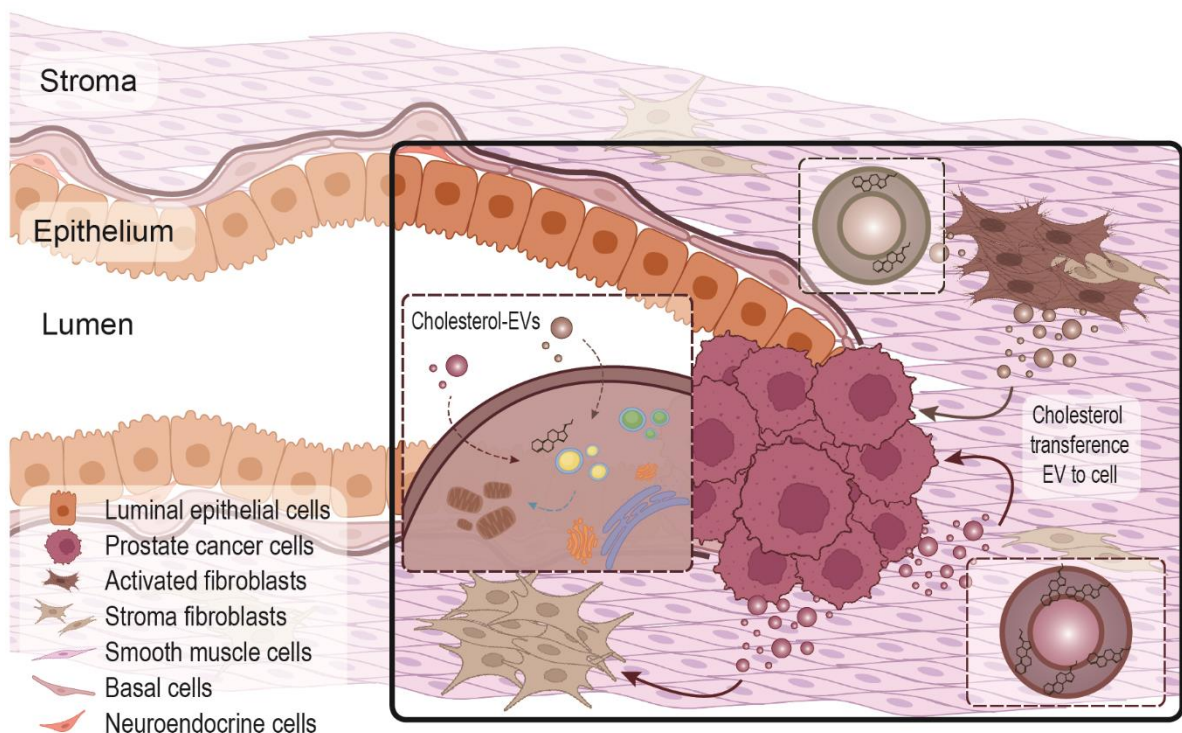
Bordanaba-Florit, G., van Liempd, S., Cabrera, D. *et al.* Labelled-cholesterol demonstrates effective EV-mediated metabolite transfer in a prostate cancer model. *Under submission.*

4.1. Labelled Cholesterol Demonstrates Effective EV-Mediated Metabolite Transfer in Prostate Cancer

Lipids and specifically cholesterol play a pivotal role in prostate cancer progression. Cholesterol serves as signal for protumorigenic metabolic pathways because it is the main precursor of steroid hormone metabolism. Typically, the source of cholesterol is extracellular (apo)lipoparticles; however, extracellular vesicles could also provide cholesterol. The effective transfer of extracellular vesicle-associated metabolites to recipient cells has not been explored yet.

In this work, prostate cancer cell cultures were treated with labelled cholesterol in lipid-depleted media. Then, purified extracellular vesicles were fed to non-labelled recipient cells to trace the internalisation of cholesterol by confocal microscopy and its further metabolization by targeted UPLC-MS assay. Cholesterol associated to extracellular vesicles was detected in unlabelled recipient cells. Upon treatment with an inhibitor of cholesterol trafficking, an accumulation of cholesterol was observed but the regular transport to mitochondrial compartment was not fully impaired. Moreover, we show stable isotope labelling in prostate cancer cells, which produce labelled extracellular vesicles. Upon treatment with these vesicles, stable isotope was detected in prostate recipient cells.

In summary, we report an optimized and rapid UPLC-MS assay for detection of steroid-related metabolites from cells and extracellular vesicles. Furthermore, we demonstrated that a targeted metabolomics assay combined to a molecular biology approach is useful to study extracellular vesicle-mediated internalisation and the effective transfer of relevant metabolites as cholesterol.

Figure 28. Graphical abstract of the section 4.1. Labelled Cholesterol Demonstrates Effective EV-Mediated Metabolite Transfer in Prostate Cancer. The structure and cellular composition of glandular acini is depicted including cancer cells and fibroblasts. Solid arrows represent the transfer of cholesterol driven by EVs while dotted arrows show intracellular transport of labelled cholesterol.

4.1.1.   Introduction

Prostate cancer is a heterogeneous disease with a wide variety of metabolomic, proteomic and transcriptomic landscapes according to its stage. Upon progression, cancer cells rewire their metabolism to sustain tumorigenesis[37,445–448]. At early stages, prostate cancer cells are hormone-dependent beings that require a steroid triggered signal to initiate and sustain tumorigenesis[23,449]. Steroid hormones play a vital role in regulating cellular processes and the dysregulation of these metabolites can provoke or aggravate pathological issues like autoimmune diseases and cancer. In prostate cancer, active steroid hormones such as dihydrotestosterone or androsterone trigger the androgen receptor molecular signalling which further drives tumour progression. The main substrate to feed this hormone metabolic network is cholesterol and, even though it can be produced *de novo*, the major source of cholesterol is exogenous[46,47]. Importantly, the first step in steroid hormone production requires the translocation of cholesterol into the mitochondria[450].

The major source of cholesterol and other lipids in normal physiological conditions are (apo)lipoparticles produced in the liver and released to the bloodstream[46,451]. Upon internalisation by cells, these cholesterol-containing particles are endocytosed and accommodated in early endosomes[46]. Subsequently, these endosomes undergo a maturation process towards late endosomes and lysosomes, which includes the acidification and hydrolisation activity of acid lipase (LAL) to generate accessible cholesterol. Then, cholesterol is shuttled to the membrane by means of protein complexes - Niemann–Pick C (NPC) 1 and NPC2 proteins - , which capture and translocate cholesterol to the inner membrane. Besides the prevalence of NPC1 and NPC2, other proteins as SapA, LAMP-2, LIMP-2 or STARD3 have

102

been reported as cholesterol reservoirs or cholesterol transporters, diversifying the cholesterol handling pathways within the cell[46,48,49].

Remarkably, extracellular vesicles (EVs) can participate locally in cell communication by exchanging metabolic assets as they can be internalised in a similar manner[86,452,453]. EVs are small lipid containers with a complex molecular cargo, which includes proteins, nucleic acids and metabolites[86,454,455]. Actually, EVs participate in (patho)physiological processes by actively triggering genetic or metabolic responses in cell-to-cell communication events. Lipids and specifically cholesterol, which play a pivotal role in prostate cancer progression[34,50,51,445], are particularly abundant in EV membranes[52,53]. The transference of such molecules mediated by EVs has being extensively studied during the last decades by identifying specific proteins carried by EVs in recipient cells[69,456–461] or designing reporter probes, often based on protein and nucleic acid detection[351,462–466]. Even though EVs are linked to transfer events, the actual transport of metabolic assets has not been comprehensively characterised yet. In this line, although there is literature reporting the transport of metabolic components using EVs[54–58], the manner this cargo interacts with the metabolic network and the entire physiological implications this transfer is yet to be fully understood.

The prostate gland is organized as glandular acinis constructed by the epithelium and sustained by the stroma. Both tissues are extremely heterogeneous with many types of cells that participate in different physiological function. The epithelium contains secretory epithelial cells around the glandular lumen and are surrounded by basal cells and sparse neuroendocrine cells, both attached to a basal lamina[9,10]. Beyond the basal lamina, a promiment fibromuscular stroma offers physical support and contraction of the gland. In PCa, the interstitial stroma is often enriched with activated fibroblasts (or cancer-associated fibroblasts, CAFs) capable of supporting tumour growth, vascularization, and metastasis [115,467,468] while epithelial (tumorigenic) cells abnormally grow and invade surrounding tissues. The interaction between these tissues (and cell types) has been extensively studied, describing how tumorigenic cells can activate stroma fibroblasts, but also, how these stroma-associated cells support the progression and survival of cancer cells[9,469,470]. This highlights the importance of establishing the manner these cells communicate among each other.

In this work, we have utilised an ultra-high-performance liquid chromatography coupled Time-of-Flight mass spectrometry (UHPLC-MS) assay to trace labelled cholesterol transfer *in vitro*. This targeted method was validated in samples relevant to steroid homeostasis, including adrenal gland, testis, prostate, brain, serum, urine[444] but also in prostate cancer cell cultures and associated extracellular vesicles. Cell cultures were incubated with labelled cholesterol in lipid-depleted media. Then, labelled media was removed and EVs were isolated after 48 hour of releasing time. With this method, we show the effective uptake of labelled cholesterol by cells from medium and subsequent transfer to EVs. Furthermore, our approach shows uptake of labelled cholesterol in prostate cancer cultures upon treatment with these cholesterol-labelled EVs, and the incorporation of this cholesterol into the metabolism of the recipient cell.

In this line, we consider that a targeted metabolomics approach is useful to measure relevant steroid hormone-related metabolites in EVs. Also, we show that cholesterol can be effectively transferred to recipient cells carried by EVs.

4.1.2.   Materials and methods

4.1.2.1.   *Cell culture, EV production and drug treatments.*

Prostate cancer LNCaP (ATCC CRL-1740™) cells were cultured in RPMI (Gibco, Life Technologies Ltd., UK) supplemented with 10% v/v Fetal Bovine Serum (Gibco, Life Technologies Ltd., UK) and Penincillin-Streptomycin (Corning, UK) at appropriate concentration. Prostate-derived fibroblasts WPMY-1 (ATCC CRL-2854™) (hNAF) and prostate cancer-associated fibroblasts hTERT PF179T (ATCC CRL-3290™) (hCAF) were cultured in DMEM (Gibco, Life Technologies Ltd., UK) supplemented with 10% v/v Fetal Bovine Serum (Gibco, Life Technologies Ltd., UK) and Penincillin-Streptomycin (Corning, UK) at appropriate concentration according to manufacturer's instructions. In this work, we refer to them as hNAF and hCAF, respectively. Where specified, FBS was substituted by Lipoprotein Deficient Serum (LPDS), obtained from Sigma-Aldrich (St. Louis, MO, USA). Cells were maintained at 37°C, 5% *v/v* CO_2, 95% *v/v* H_2O in a CO_2 incubator (ThermoFisher Scientific, MA, USA).

LNCaP and hCAF were used to produce labelled EVs for uptake experiments - producing cells - while hNAF and LNCaP were used as recipient cells in those experiments. Recipient cells were treated with 1 µM BODIPY-cholesterol, 70 µM cholesterol or 70 µM cholesterol-2,2,3,4,4,6-d6 (D_6-cholesterol) as experiment control or for optimization purposes for 20 hour. All were purchased from Sigma-Aldrich (St. Louis, MO, USA). The trafficking inhibitor treatments consisted of adding U18666A (Sigma Aldrich chimie) at a final concentration of 2 µM.

4.1.2.2.   *Isolation of EVs.*

Producing cells were grown in LPDS-supplemented media with either BODIPY-cholesterol (1 µM), cholesterol (70 µM) or D_6-cholesterol (70 µM) for 16 hours. Conditioned media was prepared by incubating producing cells in fresh LPDS-supplemented media (without cholesterol supplementation) for 48 hour on sub-confluent cells. Then, conditioned media was collected and centrifuged at 500g for 10 min at 4ºC and 2,000g for 25 min at 4ºC to remove cell debris. The supernatant was concentrated by ultra-filtration using an AMICON 10,000 MWCO filter (Merck Millipore Ltd, Darmstadt, Germany) and centrifuging at 5,000g for 25 min at 4ºC. When specified, this concentrated conditioned media was incubated with MemBright 640 (Idylle, Lipilight) for 30 min at room temperature. Then, the conditioned media (incubated or not with MemBright 640) was fractioned by size exclusion chromatography (SEC) using a qEVoriginal 35nm column (IZON Science, Lyon, France). Fractions from 1 to 4 (considering 2.5 mL of void volume) were collected, pooled and concentrated again using an AMICON 10,000 MWCO filter (Merck Millipore Ltd, Darmstadt, Germany). Purified EVs were characterized and used freshly after isolation.

4.1.2.3.   Characterisation of EVs.

Nanoparticle-tracking analysis

Nanoparticle-tracking analysis (NTA) measurements of EV size and concentration were performed using a NanoSight LM10 system equipped with a fast video capture device (Malvern Panalytical Ltd., UK). Samples were pre-diluted with 100nm-filtered PBS and the size of particles was determined by recording their Brownian motion in 3 videos of 40s each. The NanoSight NTA 3.4 Software (Malvern Panalytical Ltd., UK) was utilised to process the videos.

Western blot analysis

Aliquots of each concentrated EV sample was loaded and separated under non-reducing conditions in 4–12% Bis-Tris Protein gels (Invitrogen Inc., Waltham, MA, USA). Western blotting was performed to determine the presence of EV and (apo)lipoparticle markers in each sample and fraction. In brief, the proteins were transferred to iBlot PVDF membranes (Invitrogen Inc., Waltham, MA, USA) and then, they were blocked (in 5% non-fat milk and 0.1% Tween-20 PBS solution) for 1 hour. Then, the primary antibody was incubated overnight (approximately 16 hour) at 4 °C, washed and incubated for 1 hour with a secondary HRP-conjugated antibody at room temperature. The primary antibodies used in this study were: MoαCD63 (clone H5C6) purchased from Developmental Studies Hybridoma Bank (Iowa, IA, USA), MoαCD9 (clone 209306) from R&D Systems (Minneapolis, MN), RbαCOX-IV (clone 3E11) from Cell Signaling Technology (Danvers, MA, USA) and RbαApoB48-100 (#BP2050) from Acris Antibodies GmbH (Rockville, MD, USA). Jackson ImmunoResearch, Inc. provided the mouse and rabbit HRP-conjugated secondary antibodies. A Clarity Max Western ECL kit from Bio-Rad (Hercules, CA, USA) was utilized for the chemiluminescence detection of bands. The protein markers in PVDF membranes were identified using a luminescent image analyser ImageQuant™ LAS 4000 (GE Healthcare, Chicago, IL, USA).

Cholesterol levels measurement

An aliquot of the SEC fractions was used to titter cholesterol concentration of EV preparations for uptake experiments. Measurement of cholesterol levels were performed using the Amplex™ Red Cholesterol assay kit (Invitrogen Inc., Waltham, MA, USA) according to the manufacturer's protocol.

4.1.2.4.   EV uptake experiments.

Recipient cells were grown in LPDS-supplemented media with or without U18666A and fed or not with purified EVs from producing cells (considering a ratio of approximately 5 producing cells per 1 recipient cell) for 20 hours. Treatments with BODIPY-cholesterol underwent a fixation and imaging with confocal microscopy while cholesterol isotopes were analysed by UPLC-MS.

Immunofluorescence and microscopy

Cells treated with BODIPY-cholesterol (TopF) or with EV derived from TopF treated cells were fixed for 15 min at RT with 4% PFA/PBS in LPDS media followed by 2% PFA/PBS for 15 min at RT. Coverslips were washed and collected; then, the nuclei of cells were stained with 0.7% DAPI (Invitrogen

Inc., Waltham, MA) in Fluormount-G (Southern Biotech, AL, USA). Cells were imaged with a confocal microscope Leica SP8 with a 63x 1.4 NA objective. Z-stack images were acquired every 0.4 to 0.6 µm.

Prior fixation, cells could have been incubated with MitoTracker™ Red CM-H2Xros for mitochondrial staining purposes was purchased from Invitrogen Inc. (Waltham, MA, USA). MitoTracker was incubated at a final concentration of 100 nM for 45 min.

Image analysis and quantifications

Localisation of intracellular cholesterol using Manders' correlation coefficient and object-based: Z-stacks were acquired every 0.4 to 0.6 µm. A threshold or limit value was set up to pixel values of the images with JACoP plugin to filter out regions with unrelevant fluorescence. The threshold value was defined manually following visual inspection to eliminate most of the noise[471]. Colocalisation of cholesterol fluorescence and mitochondria fluorescence was assessed using Mander's correlation co-efficient and object-based analyses[471]. These analyses were performed by comparing and quantifying the two channels using JACoP plugin of ImageJ Fiji software.

TopFluor cholesterol or Mitotracker fluorescence intensity: TopF is represented in the green channel and MitoTracker in the red channel. The mean intracellular fluorescence intensity was measured using a macro for ImageJ Fiji software that selects the area covered by the cell and averages the signal intensity detected in each channel.

Statistical analysis: Quantifications and derived statistical data are presented as mean ± SEM. Statistics were calculated in GraphPad PRISM 9.5 software using Student's test or Mann-Whitney's test depending on sample distribution (parametric or non-parametric). Significant differences between control or treated samples are indicated as: ****, $p<0.0001$; ***, $p<0.001$; **, $p<0.01$; *, $p<0.05$. Only $p<0.05$ was considered as statistically significant.

Steroid hormone metabolomics analysis

Reagents: The DHEA, DHT and cortisol (in methanol solution were obtained from Cerilliant Corporation (Round Rock, TX, USA). Supelco (Bellefonte, PA, USA) procured androstenedione. The sodium salt of pregnenolone was obtained from Avanti Polar Lipids, Inc. (Alabaster, AL, USA). The testosterone, aldosterone, corticosterone, estrone, cholesterol, deuterated (D_6-)cholesterol (Cholesterol-2,2,3,4,4,6-d6), leucine-enkephalin (Leu-Enk), chloroform (>99.8% pure; of chromatography grade) and ammonia solution were purchased from Sigma-Aldrich (St. Louis, MO, USA). The LC-MS grade water, acetonitrile, formic acid and methanol were purchased from Fisher Chemical (Fair Lawn, NJ, USA).

Sample Preparation: Metabolites were extracted by liquid–liquid extraction using a methanol/water mixture and chloroform as extraction liquids. Organic and aqueous phases were separated; steroid-containing phase (organic) was further concentrated and resuspended in 100% methanol prior injection into the chromatography system[444].

Ultra-High Performance Liquid Chromatography (UHPLC): The chromatographic separation of the analytes was performed with an ACQUITY UPLC I-Class PLUS System (Waters Inc., Milford, MA,

USA). The gradient elution was accomplished with an aqueous mobile phase (A) consisting of 99.9% water with 0.1% formic acid and an organic mobile phase (B) consisting of 99.9% acetonitrile with 0.1% formic acid. The flow rate was 140 µL per min. An optimal gradient was applied to include the detection of cholesterol as follows: start at 30% B; a linear increase to 80% B in 3.8 min.; a step increase from 80% to 99%; constant at 99% for 4.5 min and back to 30% B.

Mass spectrometry: A time-of-flight mass spectrometer SYNAPT G2-S (Waters Inc.) was utilized for the detection of the analytes. The instrument was operated using positive electrospray ionisation (ESI+) in enhanced duty-cycle (EDC) mode to increase detection of signal intensity. The z-spray source parameters: temperatures; gas flows; capillary position and voltages were tuned, as detailed elsewhere[444].

Data pre-processing: Standards mentioned in reagents section were injected simultaneously in a quantification curve between the samples of each experiment to semi-quantify the metabolites in the samples[444]. Peaks detected in the samples were compared in retention time and in *m/z* to standards for identification and quantification. Quality control (QC) samples were injected repeatedly along the experiment to correct for any variations intrinsic to the assay. MassLynx V4.2 SCN982 (Waters Inc.) software was utilised to determine all baseline-separated peaks and specifically, TargetLynx XS tool aided in the quantification of analytes by defining their peak area. Here, raw data was processed and converted to concentration of each analyte with R studio 2022.12.0 software with R version 4.2.2 and using an in-house script to normalise and quantify data.

Metabolomics analysis: Labelling quantification in recipient cells was calculated by diving the concentration of D_6-cholesterol detected in samples by total cholesterol (the sum of cholesterol and D_6-cholesterol in each sample). If appropriate, labelled cholesterol in treated samples was corrected by subtracting the labelled cholesterol quantified in untreated samples. Statistics were calculated in GraphPad PRISM 9.5 software using Student's test or Mann-Whitney's test depending on sample distribution (parametric or non-parametric). Significant differences are indicated as: ****, $p < 0.0001$; ***, $p < 0.001$; **, $p < 0.01$; *, $p < 0.05$. Only $p < 0.05$ was considered as statistically significant.

4.1.3. Results

4.1.3.1. *Cholesterol is quantifiable in cell models and extracellular vesicles.*

BODIPY-labelled cholesterol (TopF) and deuterium isotope-labelled cholesterol (D_6-cholesterol) were supplemented to LPDS media in which recipient LNCaP and hNAF cells were incubated for 16 hours. Both recipient cells showed cholesterol uptake associated to TopF (Figure 29A.) where LNCaP cells accumulated approximately 3-fold the cholesterol uptake by hNAF cells. A similar experiment with D_6-cholesterol showed that recipient cells uptake cholesterol from media but only approximately 50% - 44.3 ($\pm$4.3)% to 50.0 ($\pm$10.9)% in LNCaP and 48.5 ($\pm$4.7)% to 53.1 ($\pm$3.9)% in hNAF - of total cholesterol is replaced by the isotope (Figure 29B). In line with previous results, total amount of cholesterol was higher in LNCaP than in hNAF (*data not shown*) although difference was not as significant as shown in

TopF uptake. Notably, labelled steroid-related hormones were not detected after 24 hour incubation with D_6-cholesterol in these prostate cancer cells.
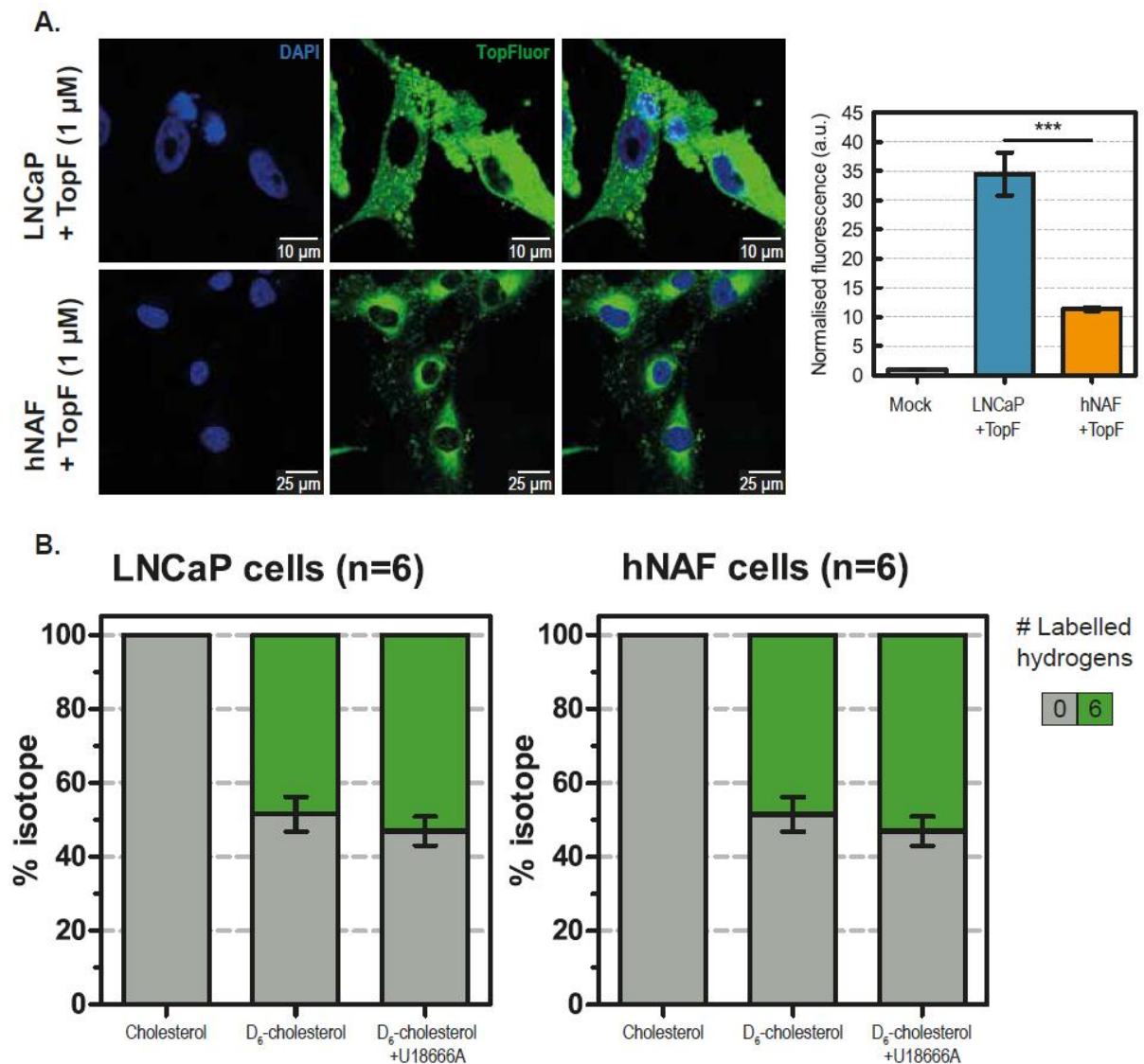
Figure 29. Cholesterol uptake by recipient LNCaP and hNAF cells when labelled cholesterol is supplemented in LPDS media. (A) Confocal images of both recipient cells upon treatment with 1 µM TopF (in the left) and the normalised fluorescence quantification of TopF signal to the basal signal detected in recipient cells not treated with TopF (in the right). In confocal panel, from left to right the columns show: DAPI staining of nuclei (in blue channel), TopF signal (in green channel) and the result of merging the two channels. (B) Relative quantification of cholesterol isotopes in LNCaP and hNAF recipient cells (n=6) upon treatment with cholesterol supplemented media, D6-cholesterol supplemented media and, D6-cholesterol and U18666A inhibitor supplemented media.

Next, EVs were isolated and purified after incubating the producing LNCaP and hCAF cells with 1 µM BODIPY-cholesterol (TopF) or 70 µM D_6-cholesterol (Scheme of production in Figure 31A). EV preparations were characterised and quantified to use them in following treatments. As an example, in Figure 30 we compiled the typical characterisation experiments done in any EV production. Figure 30B shows that EV fractions in both producing cells are the first four fractions of the SEC protocol used in this work according to typical EV markers. Also, in the first fractions it shows no presence of ApoB100, a marker of VLDL apolipoparticles. The bulk of soluble proteins are eluted in the latter fractions of the SEC purification (Figure 30A and B). Importantly, cholesterol content is more prominent in the first

fractions with an approximately 2- to 3-fold higher concentration of cholesterol in LNCaP-derived EVs compared to hCAF EVs (Figure 30A). EV fractions were further pooled together and quantified by NTA prior treating recipient cells. NTA shows that particle populations contained in EV fractions are homogeneous since they exhibit a similar distribution of particle diameter (Mode of 157 nm in LNCaP and 177 nm in hCAF) with a unique peak (Figure 30C). The quantification was used in the following section to treat recipient cells with a similar number of EVs.
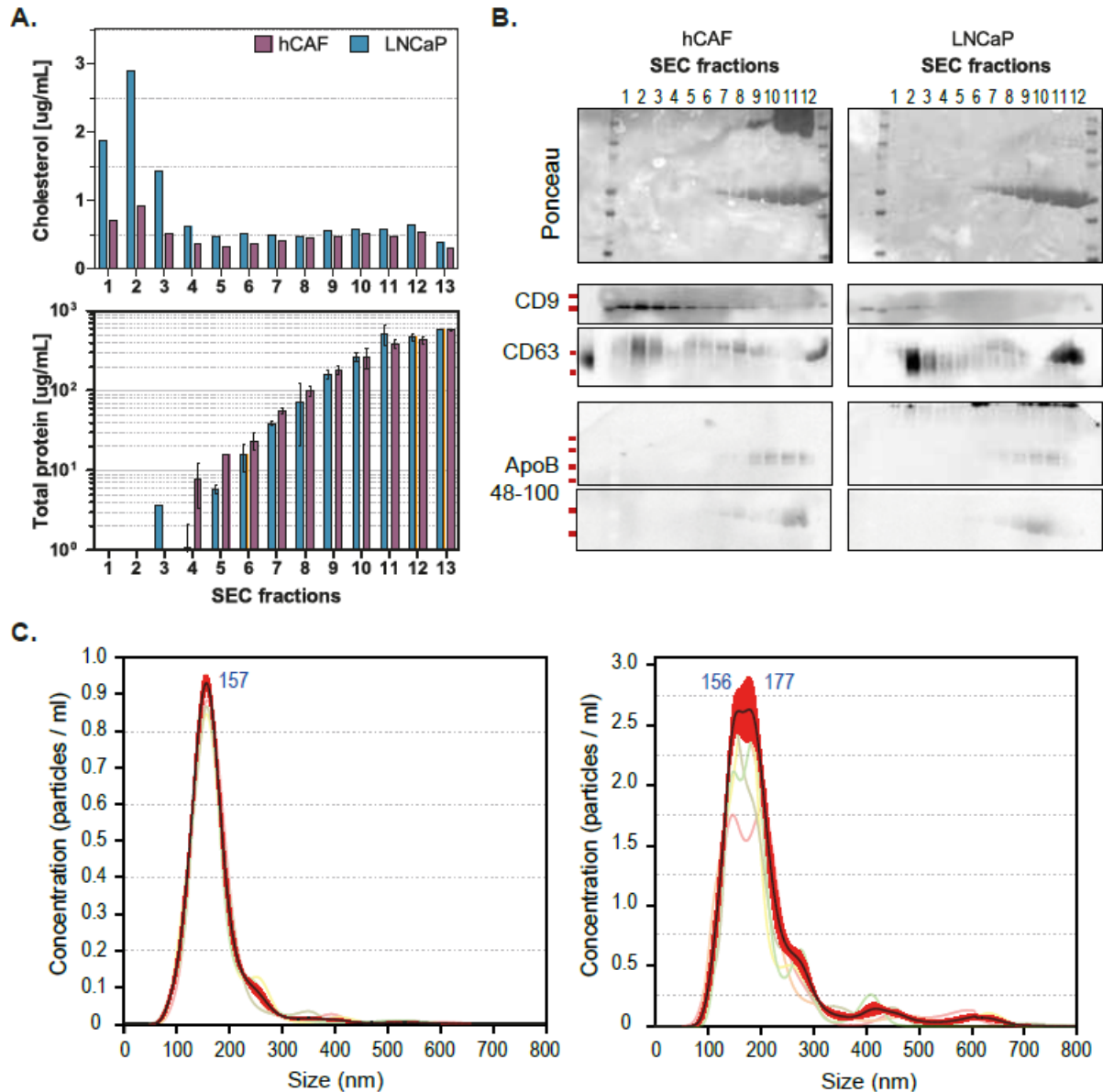
Figure 30. Characterisation of cholesterol-containing EVs (EV preparations used in Figure 32) in our production approach and experiments. (A) Cholesterol content and protein quantification of the 13 fractions obtained by SEC separation of conditioned media in producing LNCaP (in blue) and hCAF (in purple) cells. (B) Ponceau and Western blotting results for CD9, CD63 and ApoB antibodies in the first 12 fractions obtained by SEC separation of conditioned media. (C) Nanoparticle tracking profile of the pooled first four fractions obtained in SEC (EV-enriched fractions). In blue, the modes in nm of particle diameter populations are indicated.

4.1.3.2. *Extracellular vesicles can transfer cholesterol to recipient cells.*

Once producing cells were labelled and their released EVs purified, we obtained cholesterol-labelled (fluorescently or isotopically) EVs ready to treat recipient cells (Figure 31A). By UPLC-MS we were able to identify and quantify cholesterol and D_6-cholesterol upon treatment with EV preparations.
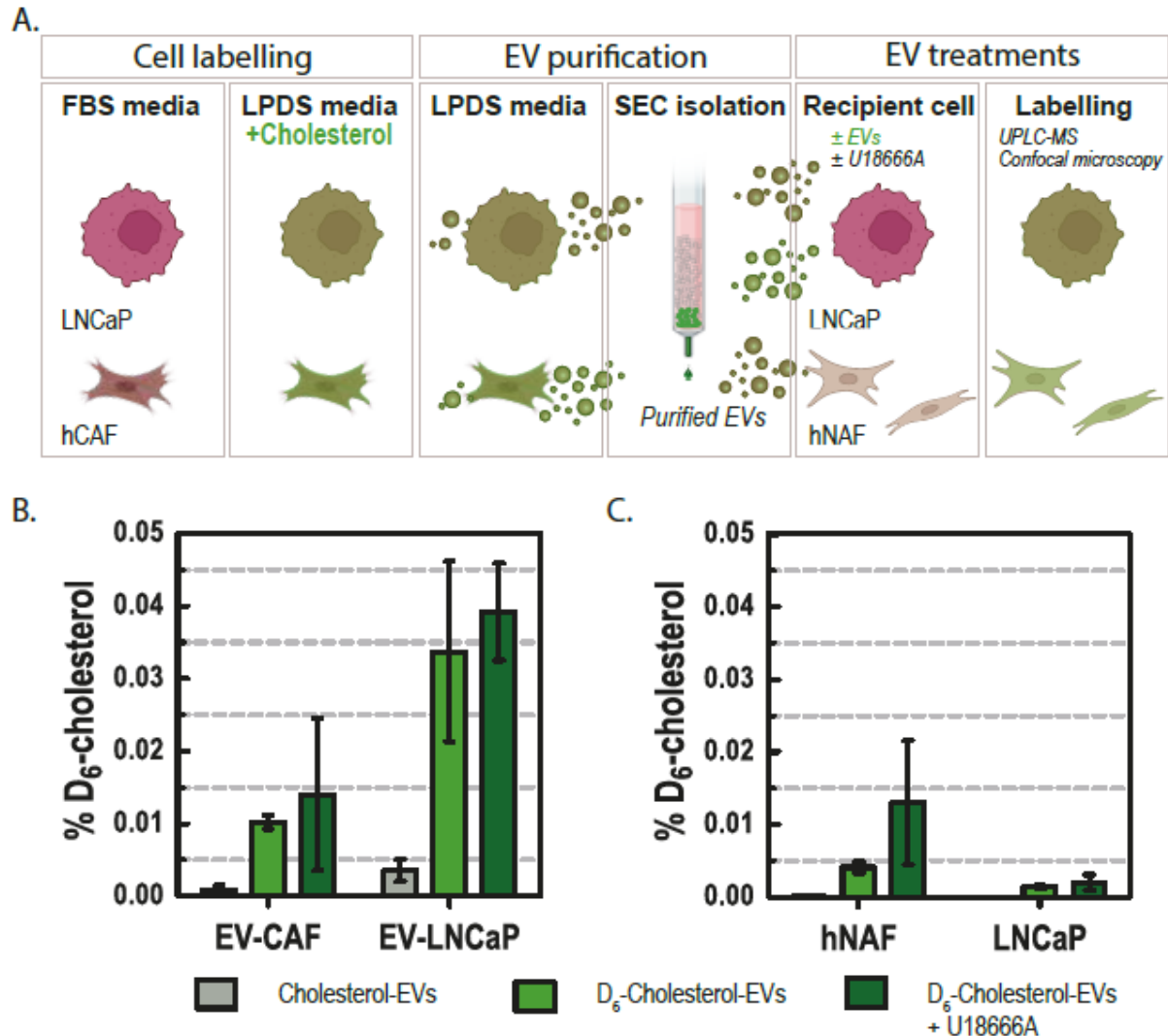
Figure 31. Transfer of isotope labelled cholesterol mediated by EVs using a UPLC-MS assay for detection.
(A) Schematic overview of the production and purification of EVs from cholesterol-labelled LNCaP and hCAF cells that are used to treat recipient LNCaP and hNAF cells. (B) D_6-cholesterol detected in recipient LNCaP cell as a percentage of total detected cholesterol upon treatment with: EVs produced in cholesterol supplemented media (grey), EVs produced in D_6-cholesterol supplemented media (light green) or EVs produced in D6-cholesterol supplemented media and U18666A supplementation (dark green). EVs from producing LNCaP and hCAF cells were used in this experiment. (C) D_6-cholesterol detected in recipient LNCaP and hNAF cells as a percentage of total detected cholesterol upon treatment with: EVs produced in cholesterol supplemented media (grey), EVs produced in D_6-cholesterol supplemented media (light green) or EVs produced in D_6-cholesterol supplemented media and U18666A supplementation(dark green). Only EVs produced by LNCaP cells were used in this experiment.

In Figure 31BC, we show the results of two independent experiments in which recipient cells were treated with EVs carrying either cholesterol or D_6-cholesterol. Recipient LNCaP cells incubated with similar number of EVs produced by cholesterol and D6-cholesterol treated hCAF or LNCaP retained D_6-cholesterol associated to EVs (Figure 31B). It is observed that D_6-cholesterol associated to EVs was

uptake by recipient hNAF and LNCaP cells in minute relative amounts, representing less than 0.1% of total cholesterol in recipient cells. Importantly, D_6-cholesterol uptake was consistent in both experiments and specific to labelled EVs because there was no trace of the isotope in recipient cells treated with cholesterol-EVs. Figure 31B describes a higher uptake of D_6-cholesterol by recipient LNCaP cells when treated with LNCaP-derived EVs rather than hCAF-derived EVs. Similarly, when treating recipient hNAF and LNCaP cells with approximately half the number of LNCaP-derived EVs (Figure 31C) compared to Figure 31B, hNAF showed a higher uptake of cholesterol. To note, the observed relative quantifications are very small so results may be highly variable from every other experiment. Ultimately, one can conclude D_6-cholesterol associated to EVs was transferred to (non-labelled) recipient cells.

4.1.3.3. *Cholesterol associated to extracellular vesicles is transported to mitochondrial compartment.*

Tracing labelled metabolites demonstrated the ability of EVs to transfer their associated cholesterol to the recipient cells LNCaP and hNAF. However, such a bulk ensemble approach cannot image the uptake of EVs to different cellular locations. To image the uptake of TopF associated to EVs by recipient LNCaP and hNAF cells, we used a dual tagging workflow to load EVs from producing cells with TopF and label them with the membrane dye MemBright [472]. Then, unlabelled recipient cells underwent different treatments while fed with these labelled EV preparations.

We first confirmed the uptake of cholesterol was associated to EVs by monitoring the cholesterol as TopF signal and EVs associated to MemBright signal (Figure 35). Recipient LNCaP treated with dual tagged EVs showed partial colocalisation of both signals (Figure 35A) while the treatment with free cholesterol followed by a MemBright staining of cells did not show a similar colocalisation phenotype (Figure 32B). Co-tracking of cholesterol and EV-associated MemBright in similar compartments suggests cholesterol signal is associated to EVs.

Then, we treated recipient cells with the NPC1 inhibitor U18666A, which hampers intracellular trafficking of cholesterol in endosomal compartment[473]. The treatment did not affect recipient LNCaP uptake of cholesterol (Figure 32B) but it induced an accumulation phenotype of cholesterol not observed in absence of the inhibitor (Figure 32A). MitoTracker staining and colocalisation analysis confirmed that the intracellular transport of cholesterol was slightly impaired (Figure 32C) suggesting cholesterol from EVs is transported by the endocytic pathway to other cellular compartments. Importantly, cholesterol shows a high degree of colocalisation in mitochondrial compartment (Figure 32C), ranging from 50% to 70% approximately and depending on the image analysis approach, denoting a high presence of cholesterol in mitochondrial membranes. The fact that a well characterised cholesterol trafficking inhibitor as U18666A did not dramatically hampered cholesterol colocalisation to mitochondria (still up to 50%) indicates that there might be other pathways in recipient LNCaP overtaking the transport of cholesterol to make it available in mitochondria.

Identical experiments in recipient hNAF - prostatic stroma fibroblast – did not show a similar accumulation phenotype by treating with U18666A inhibitor (Figure 33A). Co-tracking of TopF and Mito-Tracker confirms that the transport towards mitochondrial compartment was not significantly impaired (Figure 33C). Nonetheless, the treatment affected cholesterol uptake from EVs (Figure 33B).
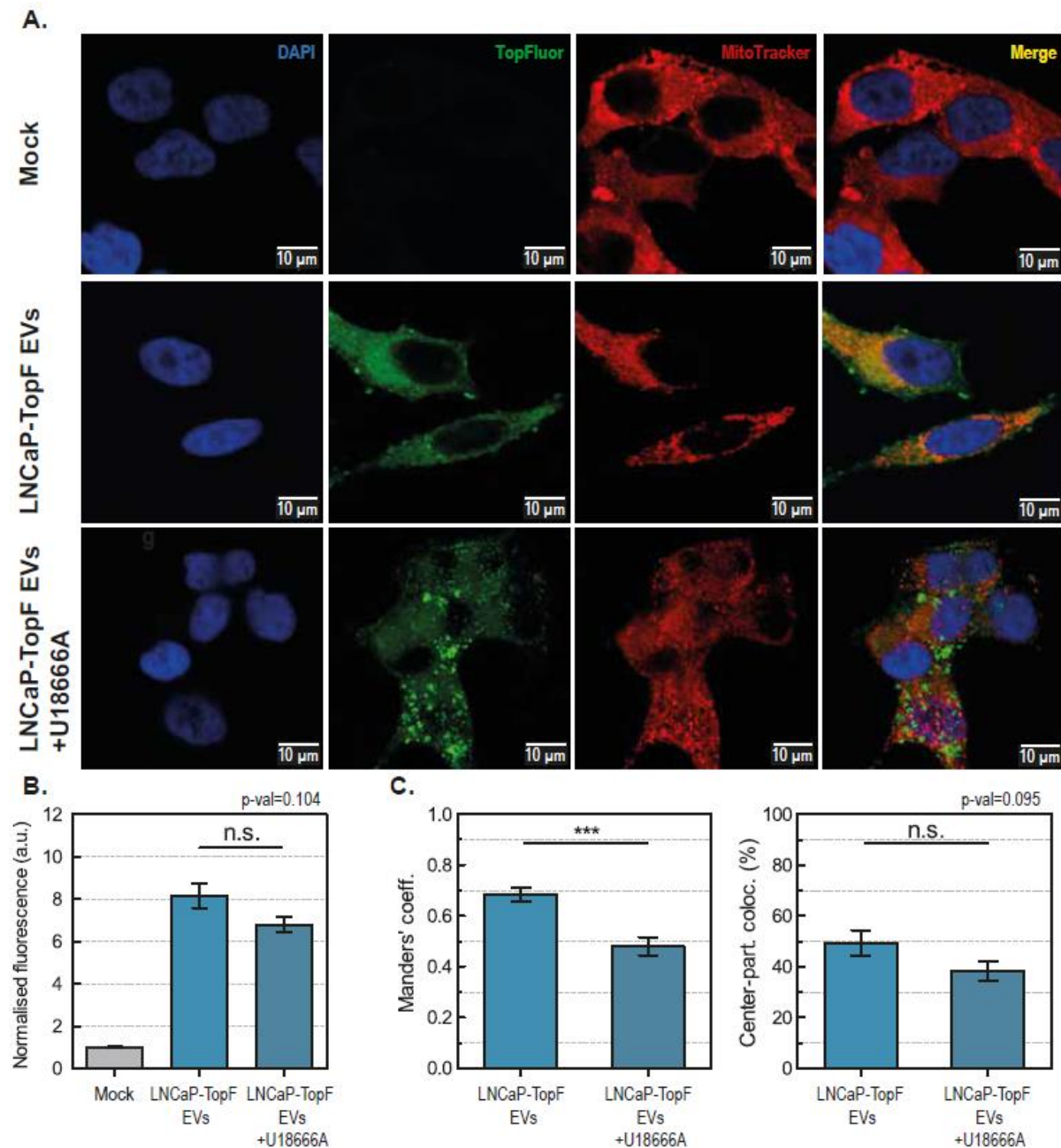
Figure 32. EV-associated cholesterol is transported to mitochondrial compartment in LNCaP recipient cells. (A) Confocal images of LNCaP recipient cells upon treatment with LNCaP EVs (Mock), LNCaP-TopF EVs (BODIPY-cholesterol loaded EVs) and LNCaP-TopF EVs and U18866A inhibitor. All treatments were incubated with MitoTracker. From left to right the columns show: DAPI staining of nuclei (in blue channel), TopF signal (in green channel), Mitotracker signal (in red channel) and the result of merging the three channels. (B) Normalised fluorescence quantification of TopF signal to the basal signal detected in Mock. (C) Co-tracking quantification of TopF signal to MitoTracker signal using a corrected Mander's coefficient and object-based colocalisation.

Figure 33. EV-associated cholesterol is transported to mitochondrial compartment in hNAF recipient cells. (A) Confocal images of hNAF recipient cells upon treatment with LNCaP EVs (Mock), LNCaP-TopF EVs (BODIPY-cholesterol loaded EVs) and LNCaP-TopF EVs and U18866A inhibitor. All treatments were incubated with Mito-Tracker. From left to right the columns show: DAPI staining of nuclei (in blue channel), TopF signal (in green channel), Mitotracker signal (in red channel) and the result of merging the three channels. (B) Normalised fluorescence quantification of TopF signal to the basal signal detected in Mock. (C) Co-tracking quantification of TopF signal to MitoTracker signal using a corrected Mander's coefficient and object-based colocalisation.

In line with describing the transfer of metabolites associated to EVs from PCa models to other PCa models, we performed experiments with a similar layout but using producing LNCaP and hCAF cells. Both EV preparations were given as a treatment – with similar number of EVs – to recipient LNCaP cells. In Figure 34A one can observe the transfer of cholesterol associated to EVs, showing a similar phenotype even with different EV preparations. Moreover, co-tracking of TopF and MitoTracker shows no significant quantitative differences in the localisation of cholesterol in the mitochondrial compartment

113

(Figure 34C). Interestingly, the treatment with different EV preparations affected significantly the uptake of cholesterol by recipient LNCaP cells. Uptake variations are similar to the differences in cholesterol content described in Figure 29B, therefore, the fact that EV-associated fractions from LNCaP carry three times more cholesterol than hCAF EVs (Figure 30A.) may explain these uptake differences. This supports the idea that the transferred cholesterol is associated to EVs since uptake quantifications are dose dependent on EV preparations.

Figure 34. EV-associated cholesterol from LNCaP and hCAF producing cells is transported to mitochondrial compartment in LNCaP recipient cells. (A) Confocal images of LNCaP recipient cells upon treatment with LPDS media (Mock), LNCaP-TopF EVs (BODIPY-cholesterol EVs) and hCAF-TopF EVs. All treatments were incubated with MitoTracker. From left to right the columns show: DAPI staining of nuclei (in blue channel), TopF signal (in green channel), Mitotracker signal (in red channel) and the result of merging the three channels. (B) Normalised fluorescence quantification of TopF signal to the basal signal detected in Mock. (C) Co-tracking quantification of TopF signal to MitoTracker signal using a corrected Mander's coefficient and object-based colocalisation.
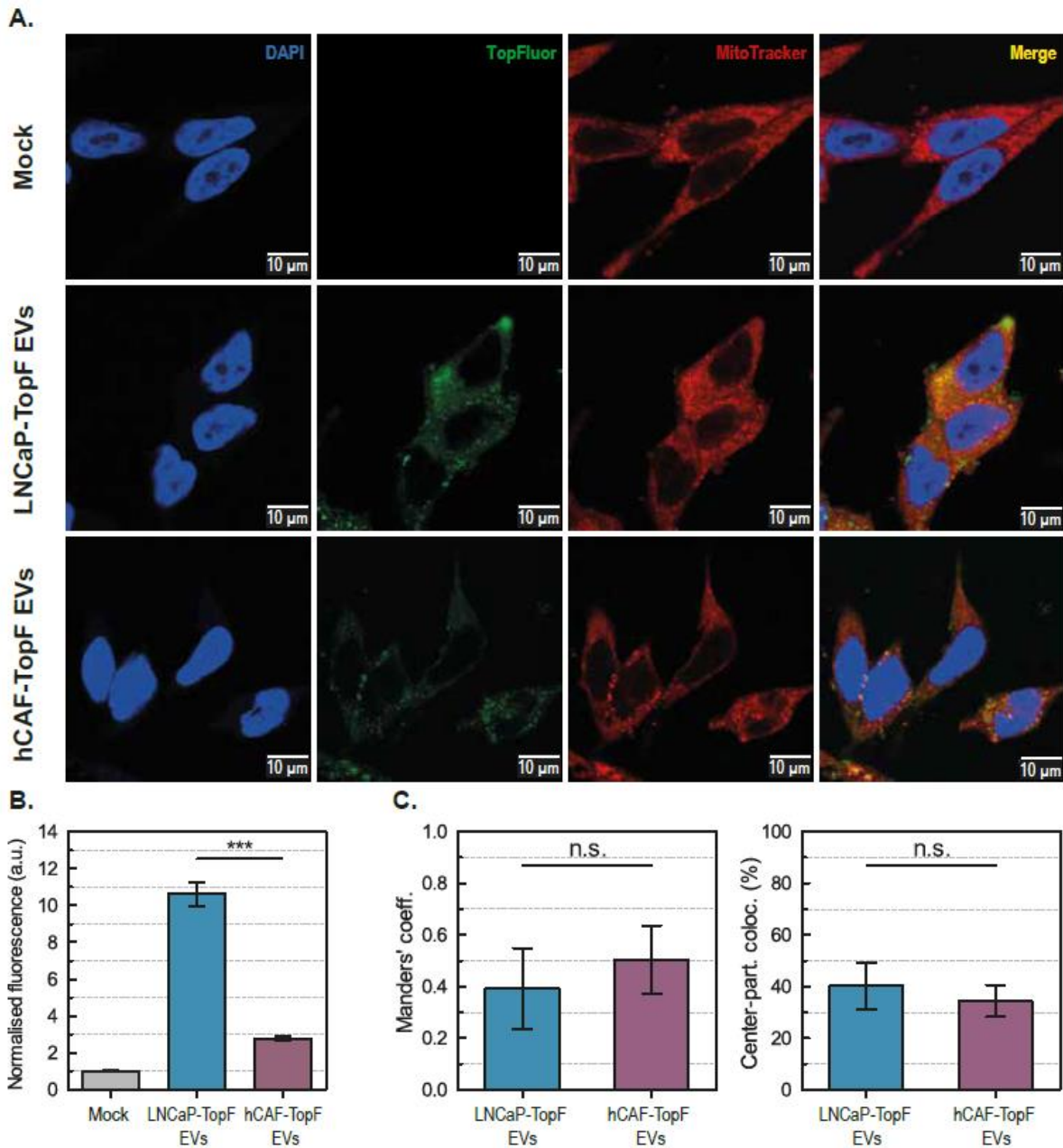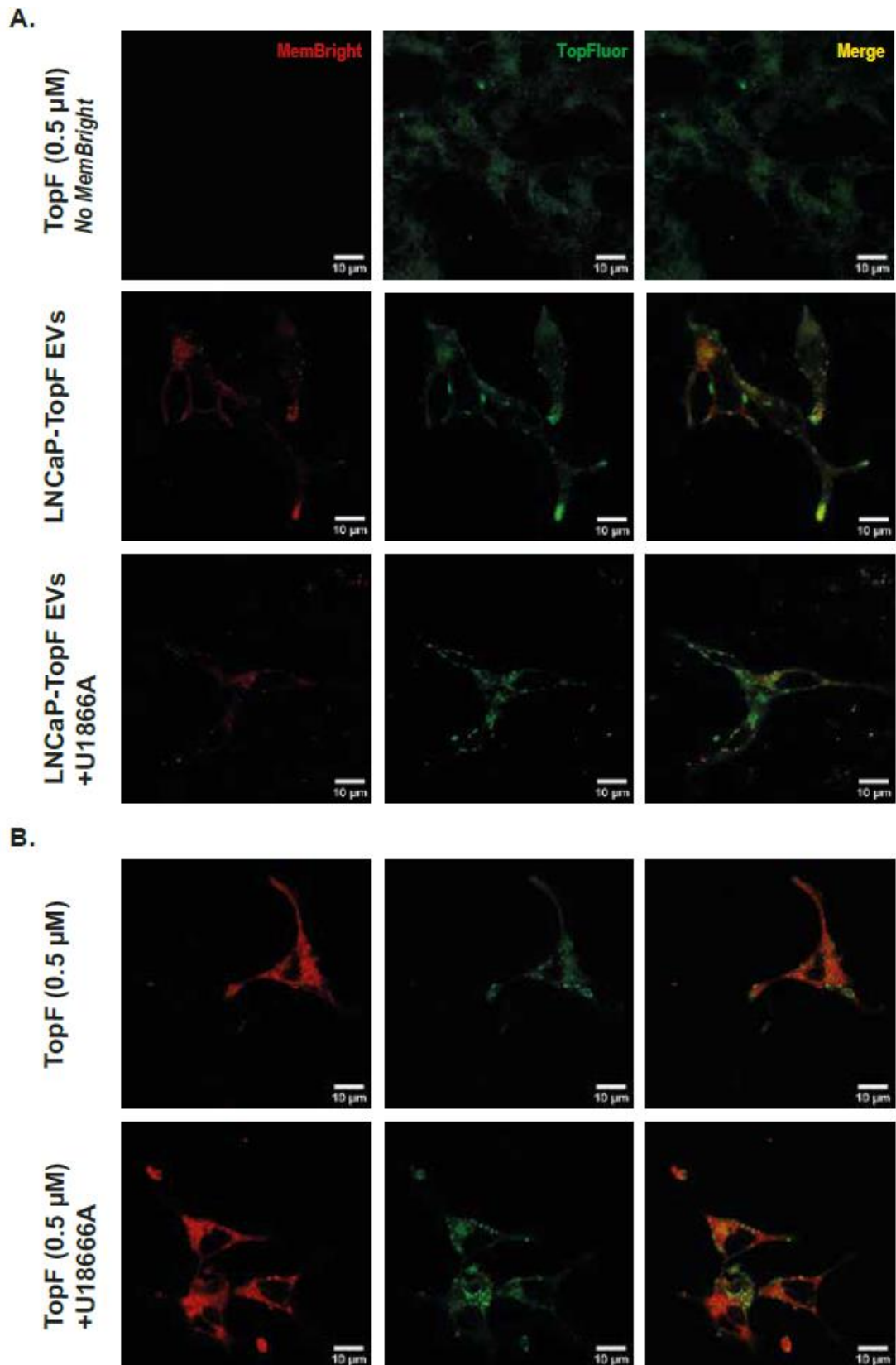
Figure 35. LNCaP recipient cells uptake TopF and MemBright signals associated to EVs. (A) Confocal images of LNCaP recipient cells upon treatment with TopF supplemented media and no MemBright, LNCaP-TopF EVs labelled with MemBright or LNCaP-TopF EVs labelled with MemBright and U18666A inhibitor. (B) Confocal images of LNCaP recipient cells treated with TopF and MemBright supplemented media and TopF, MemBright and U18666A inhibitor supplemented media. In confocal panels, from left to right the columns show: Mitotracker signal (in red channel), TopF signal (in green channel) and the result of merging the two channels.

4.1.4. Discussion

The relevance of metabolomics approaches beyond the discovery of biomarkers and the metabolic profiling of tissues in different disease stages is in the spotlight. Many efforts have been done in describing metabolic differences between the epithelium and stroma in PCa but also between those tissues in different progression stages of the disease. Further to that, this work describes a metabolomics approach to study the transfer of metabolites in cell-to-cell communication events mediated by EVs. The detection of D_6-cholesterol recipient cells treated with EV preparations containing labelled cholesterol demonstrated the transfer of cholesterol between physiologically relevant cells in prostate cancer disease.

On one hand, fluorescently-labelled cholesterol showed its transport to mitochondria where it can be further metabolised into pregnenolone, the first precursor to produce other steroid hormones. This suggests that cholesterol carried by EVs can potentially be metabolised into other steroid hormones relevant to PCa progression. On the other hand, isotope labelled cholesterol associated to EVs was uptake by recipient hNAF and LNCaP cells. The fact only a small percentage of cholesterol was labelled – less than 0.1% of total cholesterol in recipient cells – indicates the treatment with EVs was not sufficient. For metabolomics, we require ten times more cells per treatment compared to fluorescence assays due to reproducibility and, the production of labelled EVs is limiting. Even so, D_6-cholesterol was quantified consistently through experiments and its detection is specific to labelled EV preparations since it could not be detected upon treatment with unlabelled EV preparations. Besides the detection of labelled cholesterol in recipient cells, its usage to metabolise other steroid could not be demonstrated yet.

In this study we showed the transferred cholesterol is related to extracellular material derived from labelled (producing) cell cultures. The results of co-tagging EVs with TopF and MemBright and, experiments using EV preparations with different cholesterol content confirmed this hypothesis. Furthermore, experiments inhibiting the transport of cholesterol via endocytic pathway strengthened the hypothesis labelled cholesterol came from an external source and it undergoes internalization towards lysosomes prior distribution to other compartments. By using the well-known endosomal trafficking inhibitor U18666A, we would have expected an accumulation of cholesterol in the endocytic compartment and therefore, a dramatic decay of cholesterol in the mitochondrial compartment. Even though colocalisation experiments showed a decrease of cholesterol uptake or a decrease of cholesterol in mitochondrial compartment and, the characterising intracellular accumulation in confocal images, cholesterol was still transported to mitochondria. U18666A impairs NPC1 activity, in charge of translocating cholesterol captured by NPC2 to vesicular membranes. Thus, this finding indicates that recipient cells may be using other pathways different to NPC complex to overtake cholesterol trafficking towards mitochondrial compartment. Mitochondria are known to not participate in vesicular trafficking as other organelles and, it is STARD3 the protein in charge of translocating cholesterol from vesicular to mitochondrial compartment upon generation of contact sites[474,475]. Therefore, other proteins than NPC1 and NPC2 might be trans-

locating cholesterol towards endocytic compartment membranes prior transport to mitochondria. Perhaps other protein transporters such as LIMP2 and LAMP2 can make cholesterol available to be transported to mitochondria[46].

Cholesterol is essentially transported and delivered by (apo)lipoparticles via bloodstream. Lipids (and cholesterol) are processed in the liver, the organ in charge of manufacturing these lipid-containing particles for further delivering to other tissues. Therefore, one would expect that only liver-derived models exhibit lipid reservoirs and majorly expel lipid-containing particles instead of EVs. Indeed, the main limitation of this study is the possible presence of lipid-containing particles in the EV preparations because EV isolation techniques are mainly based on size or precipitation parameters and the ones based on protein markers or other parameters are not well-standardised yet. For this reason, we purified EVs with SEC because it is cleaner than other techniques such as ultracentrifugation and the main contamination we could find is of VLDL because they have a similar size compared to EVs. Nonetheless, the source of LNCaP, hCAF and hNAF are human excised prostate tissues and they have not been reported to produce any lipoparticles. Also, apolipoproteins characteristic of VLDL particles – ApoB100 and ApoE (data not shown) - were not found in EV preparations. The fact we observe a degradation pattern of ApoB100 in soluble protein fractions by Western blotting indicates the cells are not using apolipoproteins to manufacture particles and are eliminating them instead.

4.1.5.   Conclusions

In conclusion, the UHPLC-MS assay developed in this work demonstrated to be suitable for tracing isotope labelled metabolites of the hormone steroids pathway. We have been able to detect D_6-cholesterol in cell cultures and thence, to produce EVs carrying D_6-cholesterol. Furthermore, EVs were able to transfer cholesterol to recipient cells. Although this transfer was confirmed, no production of other steroid hormones could be reported using LNCaP and hNAF as reference cell lines.

In addition, treatment of recipient cells with EVs labelled with fluorescent cholesterol demonstrated the internalisation of cholesterol to cellular compartments. Also, the quantification of TopF was dose dependent upon cholesterol concentration in EV preparations and; the quantification of D_6-cholesterol in recipient cells decreased with a treatment of a minor number of EVs per cell. This suggests that EV preparations are the source of D_6-cholesterol detected in recipient cells. Finally, co-tracing cholesterol and MitoTracker showed EV-associated cholesterol is transported partially to mitochondrial compartment.

4.2. Extracellular Vesicle-Mediated Transfer of Oncogenic Signalling in Prostate Cancer

4.2.1. Background

Early stage progression of PCa is tightly dependent on steroid hormone sensing. The deprivation of such hormones mitigates tumour growth but, upon time, it can further expand and spread in an androgen independent manner. Actually, PCa cells are hormone-dependent beings that require a dysregulation in hormone signalling to sustain tumorigenesis (Figure 36A). Androgens are the main ligands of this cascade that triggers the transcription of specific genes associated to PCa progression. In fact, their expression can be used as oncogenic markers in PCa samples. Nearly all cell types expel EVs to the *extracellular milleu* with signalling or disposal purposes[65,75]. Documented studies have shown the exchange of some physiologically relevant goods and described the manner EVs could deliver pro-angiogenic or tumour-promoting phenotype[116] to recipient cells. It has also been shown that EV-associated proteins can trigger signalling pathways or cell differentiation processes.
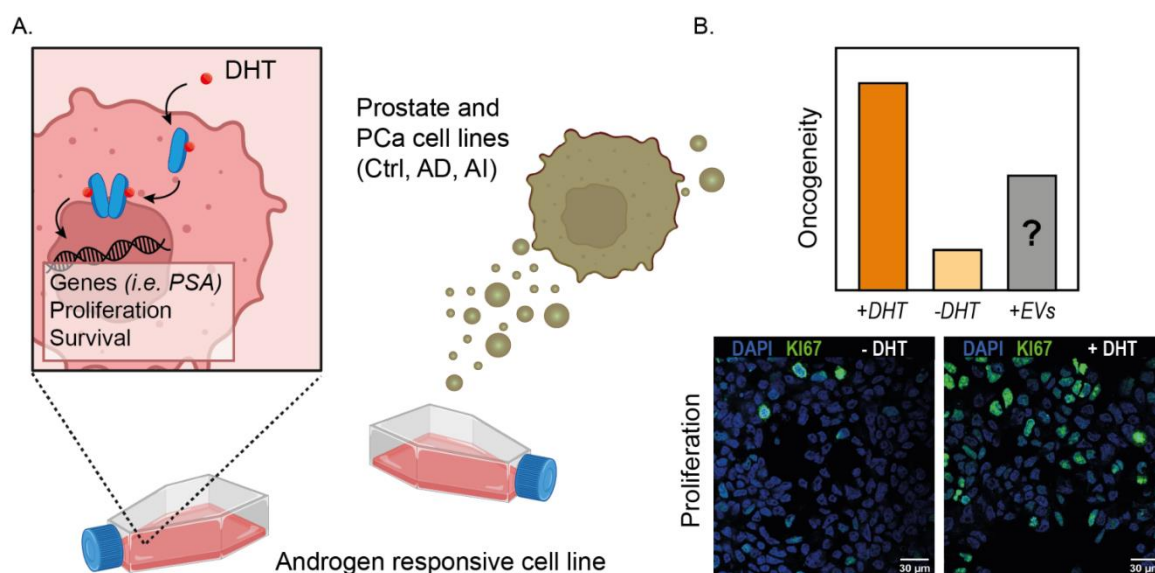
Figure 36. Graphical abstract of the section 4.2. *EV-mediated transfer of oncogenic related signalling in PCa.* **A.** EVs obtained from different PCa models are incubated with an androgen responsive cell line. A scheme of the androgen-dependent signalling is included. **B.** The assessment of oncogenic phenotype or oncogenicity of cells was performed measuring the expression of certain oncogenic targets and proliferation status of cells. The latter consisted in counting the number of cells expressing *KI-67*, a well-known marker of proliferation.

In this section, the induction of oncogenic growth mediated by EVs is evaluated. By treating androgen dependent PCa models with EVs, this approach aims to describe whether EVs can sustain oncogenic growth via the androgen signalling cascade (Figure 36A). The oncogenic status was assessed by measuring the expression of specific genes associated to androgen dependent growth. The proliferative status of PCa cells was also considered to evaluate EV treatments.

4.2.2. Materials and methods

4.2.2.1.   *Cell culture, EV production and drug treatments.*

Prostate cancer LNCaP (ATCC CRL-1740[TM]), 22Rv1 (ATCC CRL-2505[TM]) cells and the control BPH-1 (SCC256, Sigma Aldrich) were cultured in RPMI or DMEM (Gibco, Life Technologies Ltd., UK) supplemented with 10% *v/v* Fetal Bovine Serum (FBS; Gibco, Life Technologies Ltd., UK) and Penincil-lin-Streptomycin (Corning, UK) according to manufacturer's instructions. Cells were maintained at 37 ^{o}C, 5% *v/v* CO_2, 95% *v/v* H_2O in a CO_2 incubator (ThermoFisher Scientific, MA, USA).

When androgen-depleted media is specified, FBS was depleted of all kinds of steroid hormones. Dextran-coated charcoal (C6241, Sigma-Aldrich) was added to an activation buffer (0.25 M sucrose/1.5 mM $MgCl_2$/10 mM HEPES; pH 7.4) at 0.25% *m/v* and incubated overnight at 4 ^{o}C under agitation. Then, the mixture was centrifuged at 500g for 20 min and the charcoal washed twice with phosphate-saline buffer (PBS). Then, FBS volume was mixed with the activated charcoal at 0.25% *m/v* and further incu-bated 12 hours at 4 ^{o}C under agitation. Finally, steroid-depleted FBS was centrifuged at 500g for 20 min and then, it was decanted before using it in cell cultures. When EV-depleted media is specified, FBS was ultracentrifuged for 16 hour at 100,000g and then, the supernatant was decanted to remove any EV or EV-like structure from FBS formulation. These FBS were added to either RPMI or DMEM media.

EV isolation procedure

EV producing LNCaP (ATCC CRL-1740[TM]), PC-3 (ATCC CRL-1435[TM]) and BPH-1 (SCC256, Sigma Aldrich) cells were cultured according to manufacturer's recommendations. To produce EV-containing media, $3 \cdot 10^6$ cells per plate were seeded in 24 P_{150} Petri Dishes (Corning Inc., MA, USA). Cells were incubated for 48 hour in EV-depleted media. When specified, LNCaP was also cultured with 10 mM DHT to trigger an oncogenic phenotype. EV-containing media was collected and further centrifuged for 5 min at 500g to remove any cell debris. Then, it was ultracentrifuged at 10,000g for 30 min to obtain a pellet (P10K) containing EVs of bigger size than vesicles in the remaining supernatant. In a next step, the supernatant was ultracentrifuged at 100,000g for 90 min; the resulting pellet (P100K) contains EVs of smaller size than P10K. Fraction P10K and P100K were both washed in 50 mL of PBS and ultra-centrifugated at 100,000g for 90 min. Afterwards, both fractions were resuspended in 500 μL of PBS and stored in aliquots at -80 ^{o}C for further analysis.

Oncogenicity treatments

Once EV preparations were quantified in protein content, they were supplied to LNCaP cell line cultures ($3 \cdot 10^5$ cell per well in 6-well plates) in similar concentrations to reduce variability within treatments. EV preparations were a mixture of purified P10K and P100K fractions. The treatment was calculated as approximately 3 producing cells providing EVs to 1 recipient cell. The treatment lacking androgen sig-nalling (-DHT) consisted of androgen-depleted RPMI media and androgen-containing treatment con-sisted of regular RPMI media with FBS. Treatments were given at day 0 and, cell cultures were collected at days 0, 3, 6 and 9.

4.2.2.2.   *Real time quantitative PCR analyses.*

Sample preparation

Treated LNCaP adherent cells were collected by scrapping. Then, cells were washed twice with PBS. RNA was isolated from approximately 10^5 cells using the RNeasy Mini Kit (#74104, Qiagen) and following manufacturer's protocol. The isolated RNA was quantified in acid nucleic concentration using a NanoDrop^{TM} (ND-1000 Spectrophotometer, Thermo Fisher Scientific, MA, USA) device in order to optimize the retrotranscription to cDNA by means of qScript cDNA SuperMix polymerase (Quantabio). Approximately a 100% cDNA conversion efficiency was considered to proceed with further assays. The remaining cell culture was centrifuged at 500g for 5 min and then, cells were fixed by adding cold 70% ethanol dropwise while vortexing. Incubate at -20 ºC for 2 hours; after this time, fixed cells can be stored up to 60 days until proceeding with further assays.

Real-time quantitative PCR methodology

Real-time quantitative PCR (qPCR) was utilised to quantify the expression of target genes in treated cells. To perform qPCR assays, SYBR® Green Select Master Mix was purchased from Applied Biosystems (#4472897, MA, USA). Reaction mix was prepared following manufacturer's instructions and qPCR was run as specified in Table 10. A melting curve was included to evaluate its efficiency and specificity. A QuantStudio™ 5 Real-Time PCR Instrument (Thermo Fisher Scientific, MA, USA) was utilised to run the reaction and QuantStudio™ Real-Time PCR Software v1.3 for the analysis. Unless specified, all experiments were run using 1 ng of DNA per reaction.

Table 22. Summary of primers utilised for oncogenicity assessement of PCa cell lines. Names include the following indication: F stands for forward and R for reverse primer.

Name	Sequence	Name	Sequence
KLK3_F	CACGGATGCTGTGAAGGTCAT	**ACTB_F**	TGACGTGGACATCCGCAAAG
KLK3_R	GCACACAGCATGAACTTGGTC	**ACTB_R**	CTGGAAGGTGGACAGCGAGG
HOXC6_F	TTACCCCTGGATGCAGCGAATG	**GAPDH_F**	TCAAGGCTGAGAACGGGAAG
HOXC6_R	CCGCGTTAGGTAGCGATTGAAG	**GAPDH_R**	TGGACTCCACGACGTACTCA
DXL1_F	CTCTGGAGGGTAGTGCGTTG	**18srRNA_F**	CTCAACACGGGAAACCTCAC
DXL1_R	GTTTCCTCCTGAGCCCTTCC	**18srRNA_R**	CGCTCCACCAACTAAGAACG
PCA3_F	GCACATTTCCAGCCCCTTTA	**SPDEF_F**	CCACCTGGACATCTGGAAG
PCA3_R	GGCATTTCTCCCAGGGATCT	**SPDEF_R**	AATCGCCCCAGGTGAAGT

Primers for either HKG or oncogenicity target genes are compiled in Table 22. Tested HKG were *GAPDH, ACTB* and *18srRNA* and their normaliser capacity was assessed using NormFinder[406] and BestKeeper[407] algorithms; similar to the approach presented in Materials and methods of Chapter 2. Target genes analysed as potential oncogenic markers were *SPDEF*[476]*, KLK3*[476]*, HOXC6*[477]*, DXL1*[477] and *PCA3*[439]. Fold change expression was calculated following equation:

$$Fold\ change = 2^{-((Ct\ _{target}-Ct\ _{target\ (time\ 0)})-(Ct\ _{normaliser}-Ct_{normaliser\ (time\ 0)}))} \qquad (4)$$

4.2.2.3. KI-67 flow cytometry staining.

Ethanol fixed cells were thawed in ice and washed twice with staining buffer (PBS with 1% FBS and 0.05% azide). Then, centrifuged for 10 min at 200g and resuspended in 100 µL of staining buffer. Then, 20 µL of anti-KI-67 (clone B56, BD Biosciences) in an appropriate concentration was added and further incubated at room temperature for 30 min in the dark. Cells were washed twice with staining buffer and then, incubate with secondary Alexa-488 antibody (clone B56, BD Biosciences) at room temperature for 30 min in the dark. After the incubation, samples were washed twice with staining buffer and resuspended in 500 µL to proceed with flow cytometry analysis.

Samples were analysed using a CytoFLEX flow cytometer (Beckman Coulter Inc.) and the CytExpert software. The fluorescent signal was acquired using a 488 nm laser and a 525/40 nm band pass filter (FITC channel). Laser powers were adjusted with the aid of quality control beads so that fluorescence intensity was inside the detection range with the aid of quality control beads. Stained cells were measured for a maximum of 300 seconds or 10,000 positive events using the forward scatter detector. All samples were analysed at a flow rate of 60 µL/min and event rate setting high activated. In every measurement, the tubing was washed with filtered PBS to avoid carryover of fluorescently positive events.

Statistical analysis of percentage of FITC positive events was carried out with GraphPad 9.5 software using Student's test or Mann-Whitney's test depending on sample distribution (parametric or non-parametric). Significant differences between control and treated samples are indicated as: ****, $p<0.0001$; ***, $p<0.001$; **, $p<0.01$; *, $p<0.05$. Only $p<0.05$ was considered as statistically significant.

4.2.3. Results and discussion

4.2.3.1. Experiment model.

The objective of these experiments was to explore the capability of EVs to maintain or provide an oncogenic phenotype to PCa cells. In the previous section, cell models were selected according to their physiological interaction during the progression of a tumour. In here, it was required to establish a methodology to describe oncogenic growth and then, determine cell models dependent to androgen signalling that could respond to EV treatments.

Choice of cell model and normaliser behaviour

It is well known that PCa sustains its development in cells by an overexpression of oncogenic target genes. These genes support growth and survival and, prevent apoptosis. In particular, the increased expression of *KLK3*, which translates to PSA, is a hallmark of PCa. For this reason, we first utilised *KLK3* expression in LNCaP, 22Rv1 and BPH-1 cell models as a marker of their oncogenic status. By depleting androgen signalling over time, we have measured the altered expression of *KLK3* compared to a normal culture containing androgens (Figure 37). In Figure 37, the fold change of *KLK3* normalised with three different HKG is shown. It is observed that only LNCaP model responds to a depletion of androgens in a 9-day time experiment. The lack of androgens dramatically decreases the transcription of *KLK3* and, on contrary; their presence enhances the expression of this oncogenic marker. For this reason, upcoming experiments were only performed with this cell model.
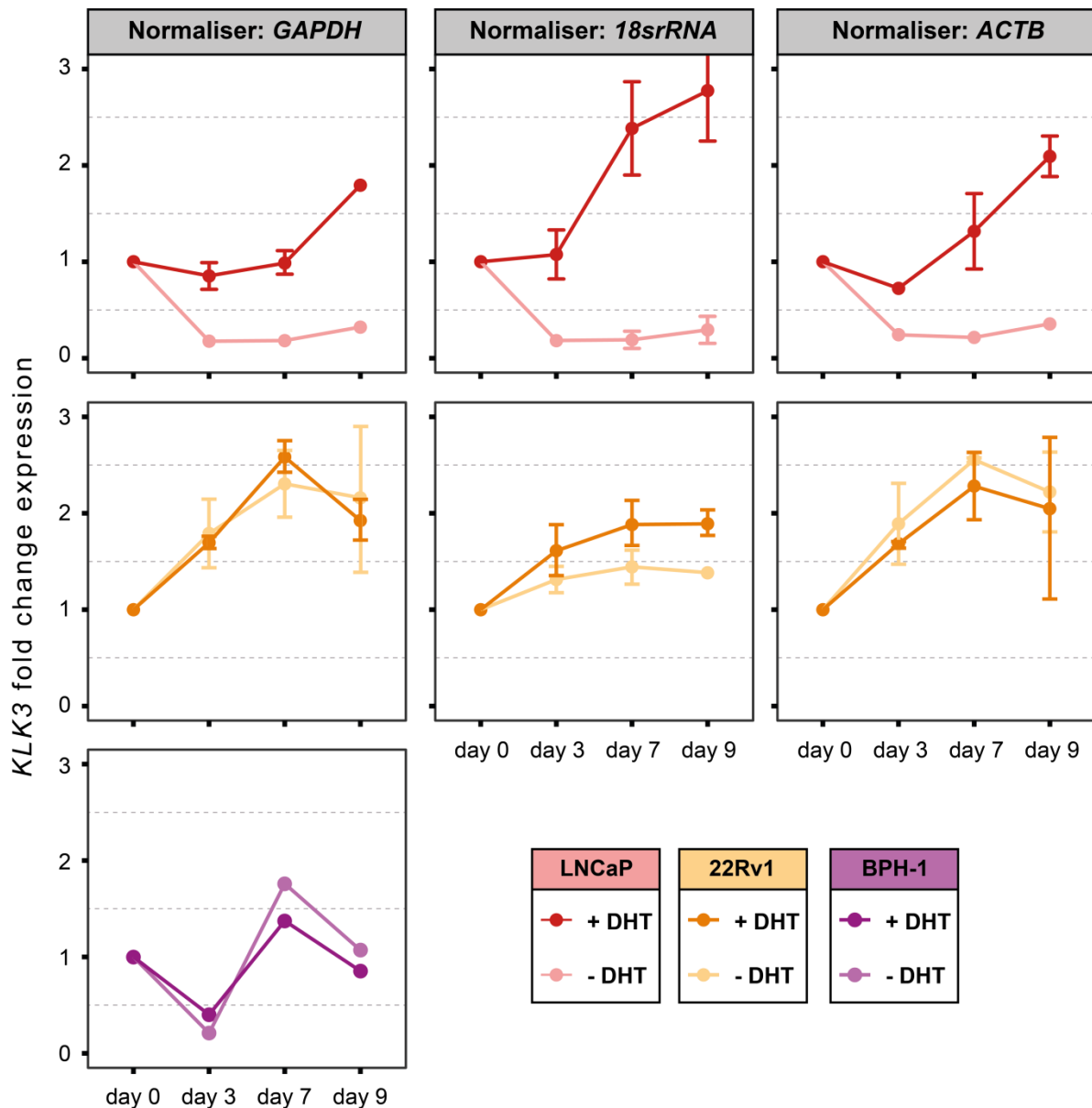
Figure 37. Fold change expression of target *KLK3* gene (mean ± SD; n=2) over time (in days) . Target gene expression is calculated as $2^{-\Delta\Delta Ct}$ compared to expression at day 0. *GAPDH*, *ACTB* and *18srRNA* expression levels were considered for normalisation but were not included in all samples due to technical limitations. In red, LNCaP recipient cell line; in orange, 22RV1 and; in purple, BPH-1. In dark colour, the treatment with androgen-containing media and, in light colour, with androgen-depleted media.

The other proposed models: 22Rv1 and BPH-1 were not appropriate to measure the effect of androgens in oncogenicity. In the case of 22Rv1, oncogenic marker *KLK3* increases its expression despite depletion of androgen signalling, indicating a potential AI oncogenic growth. According to literature, this cell line displays few phenotypes characteristic of AD, however, AI growth has been also reported [140,146]. Cell line BPH-1 does not report expression of androgen receptor at a protein level[140,146]. The analysis of its concomitant mRNA *KLK3* indicates a poor sensitivity in quantification since the quantification cycles (Ct) were rather high. High Cts indicate a low amount of the measured
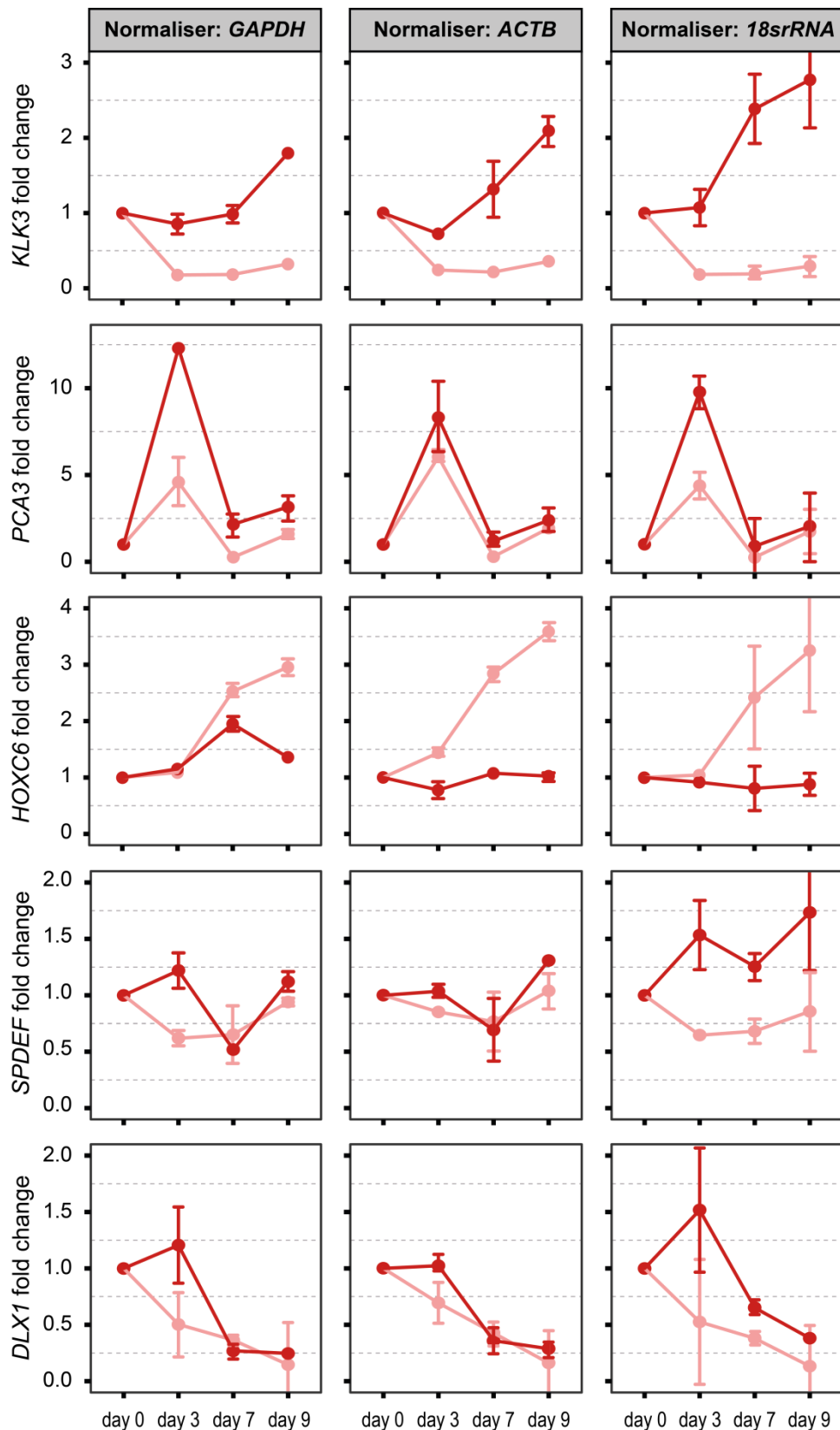
Figure 38. Fold change expression of different target genes (mean ± SD; n=2) over time (in days) in recipient LNCaP cell line. Target gene expression is calculated as $2^{-\Delta\Delta Ct}$ compared to expression at day 0. *GAPDH*, *ACTB* and *18srRNA* expression levels were considered for normalisation. In dark red, treatment with androgen-containing media and, in light red, androgen depleted media. Solid lines do not represent experimental data, they are added just as a guide for the eye.

mRNA and it usually leads to a very high variability because of the loss in sensitivity. Actually, the error bars are not included in the graph because they are large and lay beyond the graph range, which makes meaningless any analysis Therefore, the assay would not confidently provide an output for the androgen depletion treatment.

Oncogenicity markers

Although KLK3 is described in literature as the major marker of oncogenicity in androgen-dependent progression[476], other markers were also tested in LNCaP model to strengthen the evaluation of the oncogenic phenotype. The selected genes have been presented in documented reports as biomarkers in PCa diagnostic tests: *SPDEF*[478]*, HOXC6*[477]*, DLX1*[477] and *PCA3*[439]. *SPDEF* is a transactivator of PSA promoter and is expressed in men with advanced PCa. *HOXC6* is a homebox gene involved in organ development and cell proliferation. *PCA3* is long non-coding RNA highly overexpressed in PCa cells. *DLX1* may function as a transcriptional regulator of multiple TGF superfamily members.
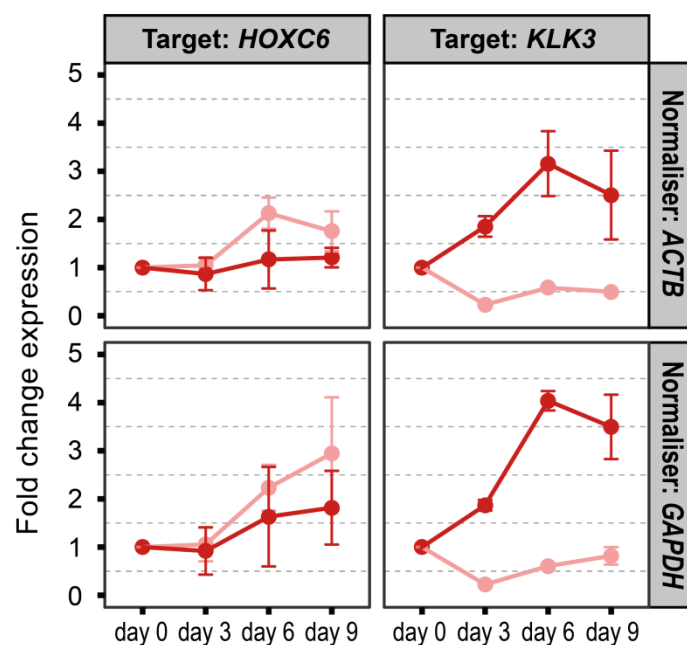

Figure 39. Fold change expression of target genes (mean ± SD; n=3) over time (in days) in recipient LNCaP cell line. Target gene expression is calculated as $2^{-\Delta\Delta Ct}$ compared to expression at day 0. *ACTB* and *GAPDH* expression levels were considered for normalisation. In dark red, treatment with androgen-containing media and, in light red, androgen depleted media. Solid lines do not represent experimental data, they are added just as a guide for the eye.

Using a similar approach, Figure 38 represents the fold change over time of 5 different potential oncogenic markers normalised with 3 HKG upon androgen signalling depletion. Target *SPDEF, DLX1* and *PCA3* gene expressions were not responsive to androgen depletion. One could expect this result because those transcripts were described in highly grade PCa, usually androgen independent. However, *HOXC6* appeared as an adequate marker of oncogenicity when normalised with *ACTB* and *18srRNA* expression. No error bars are shown until now because experiments were not yet performed in biological triplicates, only technical triplicates were included.

According to the results, LNCaP was a suitable model to follow androgen-dependent oncogenicity and, the transcripts *KLK3* and *HOXC6* the oncogenic markers responding to this hormone signalling. Thence, a fold change expression was analysed over time including appropriate biological replicates and the two best normalisers of previous experiments in terms of reproducibility and stability (Figure 39). This experiment confirmed *KLK3* expression was dependent on androgen signalling, however; *HOXC6* expression was rather variable and, although its expression over time displays a similar tendency as in Figure 38, the potential response to androgen signalling was not significant. Therefore, LNCaP was selected as the cell model to be treated with EVs and *KLK3* expression the marker to follow oncogenicity over time.

EV-mediated transfer of oncogenicity

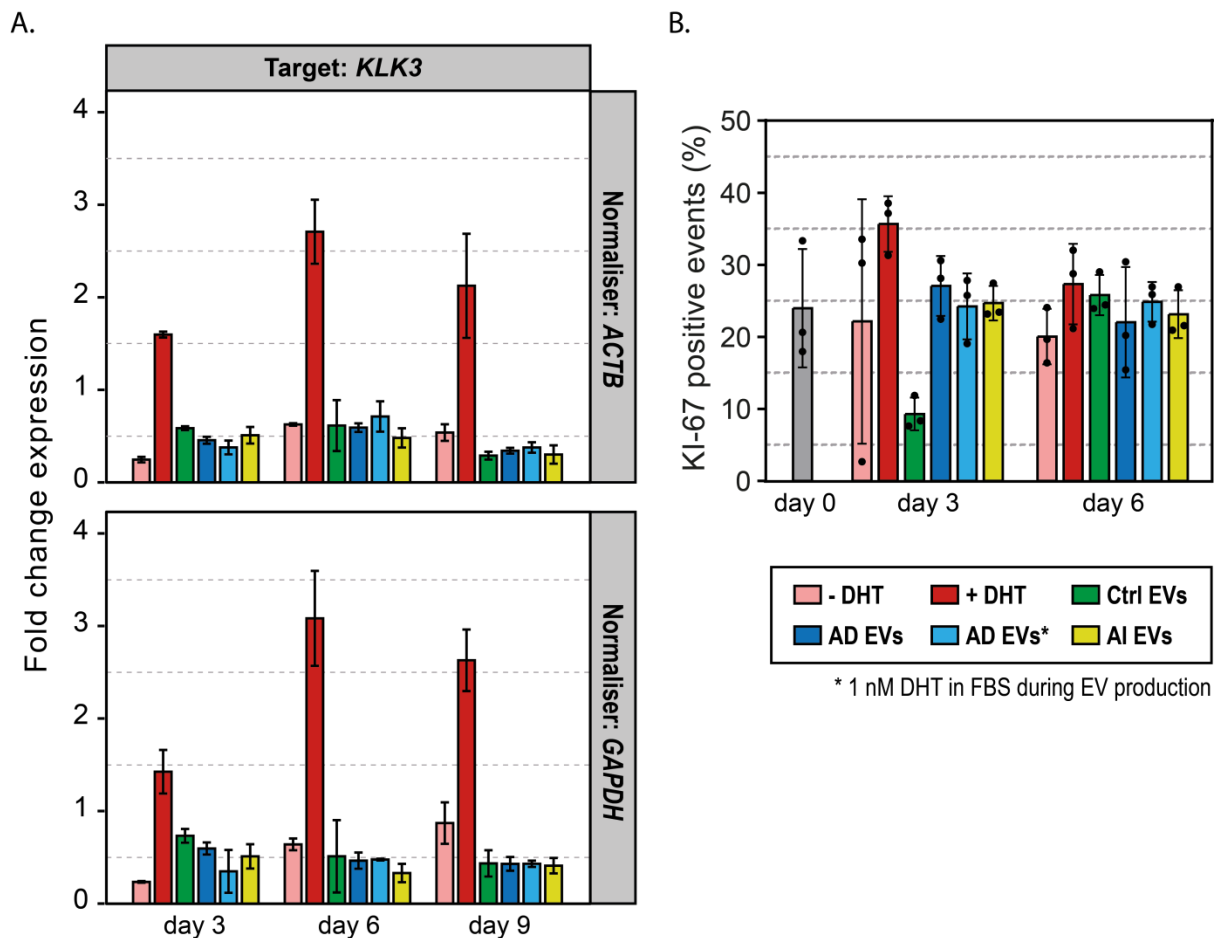**Figure 40. Summary of oncogenic markers over time (in days) under presence or absence of steroid hormones and upon treatment with EV preparations. A.** Fold change expression of target *KLK3* gene (mean ± SD; n=3) over time (in days) in recipient LNCaP cell line. Target gene expression is calculated as $2^{-\Delta\Delta Ct}$ compared to expression at day 0. *ACTB* and *GAPDH* expression levels were considered for normalisation. **B.** Positive events of nuclear KI-67 (%) over rime (in days) in recipient LNCaP cell line. Positive events were counted using a citometer. The colours correspond to different treatments as indicated in the legend. Addition or depletion of androgens are depicted in dark or light red (+/- DHT); BPH-1 derived EVs (Ctrl EVs) in green, LNCaP derived EVs (AD EVs) in dark or light blue and, in yellow, PC-3 derived EVs (AI EVs).

Once the model was evaluated, it was challenged with EV treatments in absence of androgens. EVs were isolated from three recognised PCa models that were selected according to their status and re-

sponse to androgen signalling. Control (Ctrl) stands for the non-tumoral cell line BPH-1, androgen dependent (AD) LNCaP line requires androgen signalling to sustain tumoral growth and androgen independent (AI) PC-3 uses non-androgen signalling to promote outgrowth. In order to generate EV samples, cells were cultured in complete media and LNCaP was also stimulated with 10 mM DHT. Protein titter of EV preparations was similar in all treatments and those were calculated as 3 producing cells providing EVs to 1 recipient cell.

Expression of *KLK3* (as fold change) was calculated using different normalisers over time (Figure 40). As in previous experiments, a higher fold change of *KLK3* describes oncogenic growth of the cell culture. In Figure 40, the fold change of *KLK3* using two different pairs of primers and two different normalisers at days 3, 6 and 9 is represented. Similar to previous sections, LNCaP responded with a decrease in oncogenic growth upon depletion of androgens and, when androgens were supplied, oncogenic markers increased their transcription levels. This confirms an appropriate performance of the model to further analyse EV treatments depicted in the same figure. In general, the impact of EV treatments in *KLK3* expression is rather low; and in some cases, it is negligible. Even though, the treatment with AI-derived EVs tends to show a lower *KLK3* expression compared to AD-derived EVs the differences are not quite relevant. Moreover, the expression of *KLK3* increased in LNCaP cells growing in androgen-depleted media at treatment days 6 and 9. This finding suggests that treatments with EVs have no long-term effect in sustaining oncogenic growth. Undoubtedly, the layout of this experiment does not represent a reliable picture of a physiological context. EVs are continuously released by producing cells and so they are provided to recipient cells. Perhaps, a continuous supply of EVs would result in an oncogenic phenotype sustained over time. The limitation turns into technical because EV production is highly variable, and it requires time and a high volume of conditioned media to outline such approach.

Nonetheless, Figure 40 depicted a relevant effect of EV treatments at day 3 (short-term). Although EV treatments cannot mimic results observed with androgen-supplemented media, the dramatic decrease in *KLK3* expression is slightly neutralised. While androgen depletion decreases its expression by approximately 75%, EV treatments neutralise this decay to 50%. In other words, the fold change expression of *KLK3* at day 3 is approximately 2- to 2.5-fold the expression in androgen-depleted media. As already suggested, the supply of EVs over time is relevant to assess whether they can support the oncogenic growth observed in previous experiments with androgen ligands in the media. However, EV samples and their production is highly variable and so are EV treatments; hence, one would expect a high variability in the oncogenic marker expression caused by the treatments in recipient LNCaP cells. An EV migration assay, using Transwell® migration chambers of 400 nm pore size, is of interest to solve issues in EV production and to assess this functional transfer in a more physiological approach.

4.2.4. Conclusions

In the previous section of the chapter, the transfer of metabolites contained in EVs has been evaluated. In the present section, the transfer of biologically relevant functionalities mediated by EVs is shown. The main purpose was to establish a functional interaction of EVs with recipient cells and, study the capability of EVs to sustain androgen-dependent oncogenicity. Since the actual composition of EVs driving oncogenic phenotype have not been evaluated, a mechanistic explanation is missing. However, one can conclude that:

   i.   LNCaP is an appropriate model to study androgen-dependent signalling in PCa. Moreover, it was the only cell line with oncogenic markers responding to androgen treatments; according to the oncogenic markers tested, 22Rv1 and BPH-1 did not show androgen-dependency to sustain growth.

   ii.   Not all the oncogenic reported genes were appropriate markers to inform about androgen dependent progression. Measuring the expression of the genes *SPDEF, DXL1* and *PCA3* could not inform about oncogenic growth of PCa cells. The expression of transcripts *HOXC6* and *KLK3* was altered upon androgen depletion, suggesting them as markers of oncogenicity. However, *HOXC6* was rather variable and hence, only KLK3 was utilised in this work.

   iii.   EV treatment provoked an effect regardless the type of producing cells from where they were isolated. At day 3, the fold change expression of *KLK3* was approximately 2- to 2.5-fold the expression in androgen-depleted media.

   iv.   EVs showed a neutralisation in the loss of oncogenic phenotype. However, a one shot treatment with EVs could not sustain this oncogenic phenotype over time.
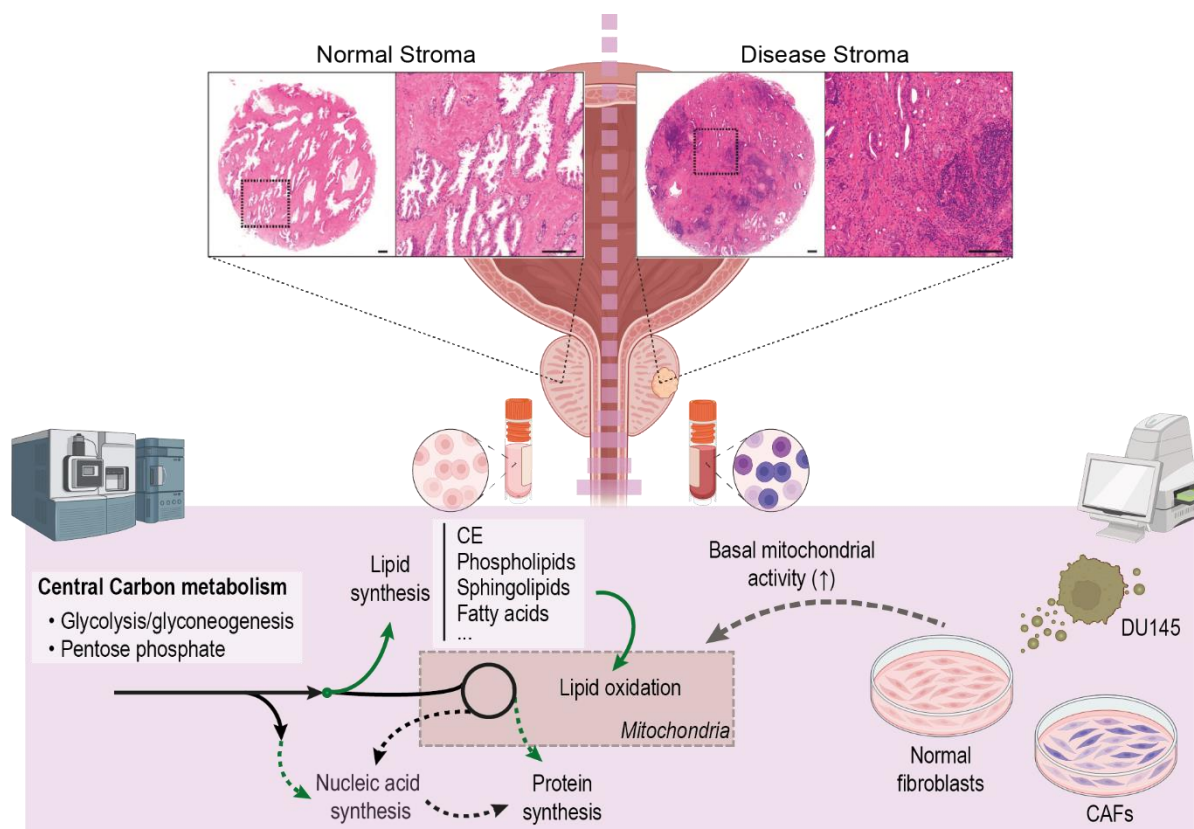
Chapter 5. Metabolic Alterations of Normal and Cancer-Associated Fibroblasts from Human Stroma Samples

This chapter focusses in studying the interaction between the two main compartments of prostate. The metabolic rewiring of stromal-derived fibroblasts from a normal region of the prostate compared to a region with the presence of a tumour was evaluated. It is well-known that epithelium interacts with stroma and viceversa. Documented reports show EVs are one of the players of this communication driving differentiation of fibroblasts to cancer-associated fibroblasts. In this chapter, we also discuss metabolic alterations in normal fibroblasts caused by PCa-derived EVs. The work has been published as an Original Article in *Biochimica et Biophysica Acta (BBA) - Molecular Basis of Disease Journal* and it is appended in the supplementary material. The original manuscript utilised in the publication is included and formatted in this section.

Bordanaba-Florit, G., Royo, F., Albóniga, O.E. *et al.* Integration of proteomics and metabolomics reveals metabolic alterations of prostate cancer fibroblasts from patient's stroma samples. *Biochim. Biophys. Acta. Mol. Basis. Dis.* Under revision

Figure 41. Graphical abstract of Chapter 5. Metabolic Alterations of Normal and Cancer- Associated Fibroblasts from Human Stroma Samples. Matched-needle biopsies from PCa patients were obtained and associated fibroblasts were obtained. Metabolomics analysis was performed to determine the distinct metabolic profile of normal and tumour fibroblasts. Seahorse analysis was utilised to determine any central metabolism changes related to TGF-β and EVs.

The prostate gland is a complex and heterogeneous organ composed of epithelium and stroma. Prostate cancer is most commonly seen emerging from luminal epithelial cells and requires the assistance of adjacent stroma. Prostatic stroma is compositionally complex, and in concert with disease progression undergoes many alterations which include the emergence of cancer associated fibroblasts (CAFs). This heterogeneous cell population often contains cells with a myofibroblast-like phenotype that are not normally present in healthy prostate tissue. In this work, we studied the metabolic rewiring of stromal fibroblasts following myofibroblast differentiation. First, the metabolic abundances of normal- and cancer-associated fibroblasts derived from needle biopsies of the same patient was analysed using UPLC-MS. It was determined CAFs were metabolically more active and, therefore, energy producing metabolic pathways were enhanced. Also, CAFs showed a heightened lipogenic metabolism as both reservoir species and building block compounds. Interestingly, lipid metabolism affects mitochondria functioning yet the mechanisms of lipid-mediated functions are unclear. The fact oxidised fatty acids and glutathione system are elevated in CAFs strengthens the hypothesis that increased metabolic activity is related to mitochondria. In further experiments measuring the metabolic flux with a Seahorse bioanalyser, we studied whether TGF-β1 and extracellular vesicles (EVs) could stimulate myofibroblast differentiation in normal fibroblasts. An increase of basal respiration in normal fibroblasts was reported, mirroring the disease-like phenotype. This indicates an altered metabolism associated to mitochondria in CAFs and treated fibroblasts. Hence, one proposes that the change in the metabolomics profile of tumour-associated stromal fibroblasts is driven by oxygen-dependent metabolism, possibly associated to mitochondria; however, the specific mechanisms are still unclear.

5.1. Introduction

The prostate gland is globally composed of epithelium and stroma, which are extremely heterogeneous tissues. The epithelium is organized as glandular acini and it contains cuboidal to columnar secretory epithelial cells with apical junction complexes, a continuous layer of basal cells[10], and sparse neuroendocrine cells, each attached to a basal lamina[9]. Beyond the basal lamina, a prominent fibromuscular stroma composed of smooth muscle, fibroblasts, blood vessels, autonomic nerve fibres, inflammatory cells, and extracellular matrix components offers physical support and contraction of the gland[479]. In prostate carcinoma (PCa), the interstitial stroma is often abnormally rich in myofibroblastic cells[467,468], capable of supporting tumour growth, vascularization, angiogenesis, and metastasis *in vivo*[115]. Transforming growth factor β1, TGF-β1, remains among the most critical factors for myofibroblastic differentiation and the generation of a tumour reactive stroma. Intriguingly, we have previously shown that cancer extracellular vesicles (EVs) can trigger fibroblast to myofibroblast differentiation in an EV-TGF-β1 dependent manner[115]. In further studies, the essential role of EVs in directing this stromal cell differentiation towards cancer-associated myofibroblast-like phenotype was described[116]. However, the mechanisms by which EV-activated stromal cells support tumour growth remain unclear.

Our previous studies with biopsy material from patients where tumoral growth was located in one half of the prostate and not the other, revealed clear differences between normal and disease regions. Histological examination showed a smooth muscle stromal architecture around glandular structures in

normal tissue while the glands were disorganised and showed an altered, fibrosis-like interstitial stroma observed in disease-associated tissue[480]. A panel of antibody markers confirmed the higher abundance of α-Smooth Muscle Actin (α-SMA)-positive myofibroblast cells in tumour-associated tissue. Strikingly, EVs isolated from prostate cancer epithelial cell lines generated a myofibroblast-like phenotype in normal fibroblasts[116]. In that work, we demonstrated the essential role of EVs in directing stromal differentiation to a pro-tumorigenic phenotype, exhibiting pro-angiogenic properties and enhancement of tumour growth in xenograft models. Further functional assays and proteomics profiling work highlighted that stroma activation mediated by EV stimulation mirrors the naturally occurring fibroblast differentiation during disease[480].

Altered metabolism is a hallmark of PCa and several metabolites and metabolic pathways are already distinctive in different prostate types of tissue[481,482]. In this line, Andersen *et al.* reported higher levels of energy-related pathway metabolites, such as ADP, ATP, and glucose as well as higher levels of the antioxidant taurine in stromal tissue compared to cancer and non-cancer epithelium[483]. Besides, increased levels of crucial metabolites for fatty acid oxidation and building blocks in lipid synthesis were described in cancer tissue. Other studies also reported metabolic rewiring of reactive stroma, showing different levels of certain metabolites between highly differentiated stroma compared to poorly differentiated stroma[484]. The stromal-epithelial interactions have a dominant role in tumour growth, invasion and metastasis. Actually, many reports over the last decades showed the interaction of reactive stroma with PCa[9,469,484–488] and EVs influencing aspects of cancer biology such as angiogenesis[116,480,489,490] and tumour progression[488,491–493]. Yet, few studies have investigated the role of tumour EVs in altering metabolic processes in stromal cell compartments.

With the rise of *omics* era, entire sets of biomolecules – genes, proteins or metabolites - contained in a biological tissue, cell, fluid, or organism can be identified. A proteomics analysis of the same matched- normal and disease stroma tissues was able to distinguish both phenotypes and describe a disease-like phenotype[480]. Similarly, a transcriptomic analysis of derived EVs from the same type of samples discriminated normal from disease stroma samples[494]. This manuscript presents a broad semitargeted metabolomics approach, which analyses the metabolome of normal and disease stroma tissues, highlighting the metabolic differences of matched normal fibroblasts and cancer-associated fibroblasts within individual PCa patients. Furthermore, we show an altered metabolism of normal fibroblasts treated with EVs from a PCa cell line.

5.2. Material and methods

5.2.1. Stromal primary cell cultures.

Six patient-matched normal and tumour-associated needle biopsies were isolated from radical prostatectomy. These were taken from sites of palpable disease and also from apparently normal tissue from the opposite side of the same prostate. Tissue collection and consenting was managed through the Wales Cancer Bank. Cores were manually dissected into 1mm^3 pieces and subjected to mechanical homogenization followed by 200 U per mL collagenase-I digestion for 15 to 20 hours at 37 °C. Cells

were cultured in Stromal Cell Basal Medium (SCBM) supplemented with human fibroblast growth factor-B, insulin, fetal bovine serum (FBS) and GA-1000 (Lonza, Wokingham, UK). for around two weeks until only stromal cells were retained. [8,23]Subsequent cultures were maintained in DMEM/F12 media (Lonza) with 10% FBS depleted of bovine EVs. Cultures were confirmed free of epithelial cells by immuno-fluorescence staining for cytokeratin prior seeding stromal cells in 96 well plates [480,494]. A sample of each patient-matched prostatic stromal cell culture was collected and frozen for metabolomics analysis using liquid chromatography coupled to mass spectrometry.

5.2.2.   Metabolite extraction.

In metabolomics, there is no single platform or method able to analyse the entire metabolome of a biological sample. Therefore, metabolites were extracted by fractionating the cell samples into pools of species with similar physicochemical properties. In brief, proteins were precipitated by adding methanol to the cell lysate. Chloroform solvent was added to the methanol extraction mixture and this biphasic mixture was incubated at -20 ºC for 30 min. Then, three different fractions were collected: (1) fatty acyls, bile acids, steroids and lysoglycerophospholipids, were obtained after centrifuging the supernatant at 16,000g for 15 min, drying and reconstituting in methanol, (2) for aminoacids, aliquots of 5 µL from the first fraction were derivatised and dried, and (3) glycerolipids, cholesteryl esters, sphingolipids and glycerophospholipids were obtained by mixing the chloroform extraction mixture with H_2O (pH 9) and incubating at -20 ºC for 60 min. After centrifuging at 16,000g for 15 min, the organic phase from this third fraction was collected then, dried and reconstituted in 50/50% *v/v* acetonitrile/isopropanol. The aqueous phase that contains polar metabolites, including central carbon metabolism, was collected, dried and reconstituted in H_2O.

Quality control (QC) sample for calibration and validation were included in this workflow to correct for response factors between and within batches; and to assess the quality of data.

5.2.3.   LC-MS analysis.

An appropriate UPLC-MS method was used for each platform. The instruments and the conditions for the chromatographic separation and mass spectrometric detection are summarized in Table 23. A test mixture of standards was analyzed before and after the entire set of randomized, duplicated sample injections to check for retention time stability, mass accuracy and sensitivity. All data were processed using the TargetLynx application manager for MassLynx 4.1 software (Waters Corp., Milford, USA). A set of predefined features, defined as retention time - mass-to-charge ratio pairs, *Rt-m/z*, corresponding to metabolites included in the analysis are fed into the program. Associated extracted ion chromatograms (mass tolerance window = 0.05 Da) are then peak-detected and noise-reduced in both the LC and MS domains such that only true metabolite related features are processed by the software. Then, a list of chromatographic peak areas is generated for each sample injection.

Table 23. UPLC-MS Analysis platforms for metabolomics analysis.

	Platform 1	Platform 2	Platform 3	Platform 4
Column type	UPLC BEH C18, 1.0 x 100 mm, 1.7 µm	UPLC BEH C18m 2.1 x 100 mm, 1.7 µm	UPLC BEH C18, 1.0 x 100 mm, 1.7 µm	UPLC HSS T3, 1.0 x 150 mm, 1.8 µm
Flow rate	0.14 mL per min	0.40 mL per min	0.14 mL per min	0.10 mL per min
Solvent A	H_2O + 0.05% Formic acid	H_2O + ACN + 10 mM Ammonium Formate	10 mM Ammonium Bi-carbonate (pH = 8.8)	10 mM Tributylamine + 15 mM Acetic Acid + 2% Methanol (pH = 5.0)
Solvent B	ACN + 0.05% Formic acid	ACN + Isopropanol + 10 mM Ammonium Formate	ACN	Methanol
(%B), time	0%, 0 min	40%, 0 min	2%, 0 min	0%, 0 min
(%B), time	50%, 2 min	100%, 10 min	8%, 6.5 min	4%, 1.5 min
(%B), time	100%, 13 min	40%, 15 min	20%, 10 min	20%, 3 min
(%B), time	0%, 18 min	40%, 17 min	30%, 11 min	25%, 8 min
(%B), time	-	-	100%, 12 min	50%, 10 min
(%B), time	-	-	2%, 14 min	45%, 15 min
(%B), time	-	-	-	100%, 16-20 min
(%B), time	-	-	-	0%, 21-25 min
Column temperature	40 ºC	60 ºC	40 ºC	40 ºC
Injection volume	2 µL	3 µL	2 µL	2 µL
Source temperature	120 ºC	120 ºC	120 ºC	120 ºC
Nebulisation N_2 flow	600 L per hour	1000 L per hour	600 L per hour	600 L per hour
Nebulisation N_2 temperature	350 ºC	500 ºC	350 ºC	300 ºC
Cone N_2 flow	30 L per hour	30 L per hour	10 L per hour	50 L per hour
Capillary voltage	2.8 kV	3.2 kV	3.2 kV	2.8 kV
Cone voltage	50 V	30 V	30 V	100

5.2.4. Data analysis.

Data normalisation and quality control

After data inspection in terms of reproducibility and peak integration, each metabolite was corrected and normalized using the intensity of an appropriate internal standard included in the analysis and following the procedure fully described by van der Kloet et al.[495]. Finally, any remaining zero values in the corrected dataset were replaced with missing values prior averaging to obtain a dataset further used for statistical analyses. A final normalization procedure was applied by dividing every sample by its protein content.

Multivariate and univariate analysis

Once data was normalized and prepare for statistical analysis, a first approach based on multivariate analysis was performed with SIMCA-P (version 13.0). Firstly, a non-supervised principal component analysis (PCA) was utilised to reduce dimensionality and to study data quality, assess reproducibility of

the analytical procedure, visualize tendencies between groups and determine the presence of outliers. Afterwards, supervised partial least squares discriminant analysis (PLS-DA) and orthogonal PLS-DA (OPLS-DA) were performed followed by a suitable validation method, a cross-validation analysis of variance (CV-ANOVA), integrated in SIMCA-P software. Supervised models that were validated were further used for variable selection. To this end, a variable importance on projection (VIP) score and absolute value of p(corr) greater than 1 and 0.8, respectively, were used as cut-off points for variable selection.

Finally, and as a complementary statistical analysis, univariate analysis was perfomed. In order to test normality, Shaphiro test was used; thence either paired student's test[496] or Wilcoxon signed-rank test was applied to assess comparisons significance. After that, the dataset was expressed as a metabolite fold-change and significance (p-value) and further depicted in a *volcano plot*.

Pathway analysis and pathway enrichment

A proper biological interpretation is crucial in any metabolomics study to deliver a comprehensive assessment of experimental conditions. To evaluate the prominence of certain metabolic pathways, a Pathway analysis was computed using MetaboAnalyst 5.0 and inputting a dataset of samples and quantified metabolites. It performs an o-representation analysis that integrates enrichment and pathway topology analysis to visualise specific altered pathways in the human metabolic network[497]. Then, proteomics data was included in a Joint-pathway analysis to evaluate metabolic alterations considering two sets of physiologically relevant molecules in fibroblast samples. This over-representation analysis module performs an integrated metabolic pathway analysis by combining metabolomics and proteomics data collected from the exact same samples and methodology[497]. The MetaboAnalyst 5.0 web-based tool includes the normalisation, transformation and scaling of data to complete data integration.

Furthermore, a lipid metabolic network analysis[498] performed with LINEX 2.4.1 webapp to observe functional associations of lipid classes. It computes specific lipid networks based on compounds and lipid classes connections using a lipidomics dataset.

5.2.5.   Extracellular vesicle isolation.

EVs were purified from conditioned media of DU145 prostate cancer cell (ATCC, Teddington, UK) grown in Integra bioreactor flasks (Integra Biosciences Corp, Hudson, NH, USA)[499]. EV samples were collected using the sucrose cushion method and resuspended in PBS. Thence, samples were quantified using the BCA-protein assay (Pierce/Thermo, Northumberland, UK), and stored at -80°C. For treatments of stromal cell cultures, EV were used at 200 µg per mL (approximately equivalent to 1.5 ng per mL of EV-associated TGF-β) for 72 hours.

5.2.6. *Seahorse assay.*

Oxygen consumption rate and glycolytic activity were assessed using a XF24 Extracellular Flux Analyser (Seahorse Biosciences) to probe O_2 and pH, respectively. Fibroblasts were equilibrated in unbuffered media (60 min at 37 ºC in a CO_2-free incubator) prior transfer to the XF24 analyser. For mitochondrial respiration, the oxygen consumption was measured over the assay. First, basal oxygen consumption (OCR) was determined, and then oligomycin (1 µg per ml), FCCP (0.3 µM), FCCP (0.6 µM), and 2 µM rotenone were sequentially injected to assess maximal oxidative capacity, ATP production, coupling efficiency (OCR percentage dedicated to produce ATP) and basal respiration. To analyse glycolytic activity, the extracellular pH was measured over the assay. First, base-line (non-glycolytic) extracellular acidification (ECAR) was determined, and then media alone followed by glucose (10 mM), oligomycin (1 µg per ml), and 2-Deoxyglucose (0.1 M) were sequentially injected to assess maximal glycolytic capacity and glycolysis rate.

Statistical analyses were performed by paired Student's t-test using GraphPad PRISM 9.5 software (Graph Pad, San Diego, CA, USA). Each experiment was analysed individually then, the mean ± SEM was represented. All p-values lower than 0.05 are considered significant as: * P>0.05, ** P>0.01, *** P>0.001.

5.3. Results

5.3.1. *CAFs exhibit a differential proteomic, transcriptomic and metabolomics landscapes.*
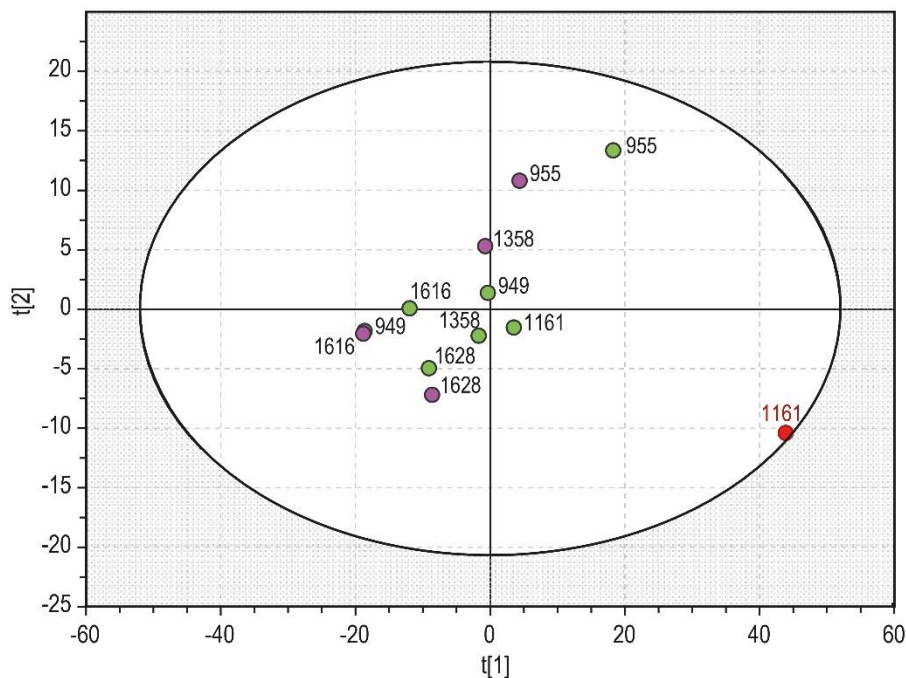
Figure 42. Score scatter plot of the PCA model of fibroblasts obtained from normal and cancer of all needle biopsies. This PCA model was generated with all the samples. Model diagnostics (A = 2; R2X = 0.814; Q2 = 0.615) with UV scaling. In green, CAF samples and, in purple, normal fibroblasts. Samples IDs are added to depict matched samples and observe outlier. In red, sample 1161-normal which is on the Hotelling's T2 confidence ellipse.

Table 24. Summary table of variables that significantly influence group separation. It compares normal fibroblasts and CAFs based on their VIP and p(corr) values in PLS-DA and OPLS-DA models. Criteria to selected significant features/metabolites: VIP > 1 and |p(corr)| > 0.8. The features common in both models are highlighted and marked (*).

PLS-DA model					
Name	**p (corr)**	**VIP**	**Name**	**p (corr)**	**VIP**
(*) Cer(d18:1/24:0)	**-0.901**	**1.295**	PC(P-16:0/22:6)	-0.848	1.188
Cer(d43:1)	-0.811	1.187	**(*) PC(O-40:5)**	**-0.867**	**1.093**
(*) Cer(d18:1/25:0)	**-0.826**	**1.546**	**(*) PC(O-22:1/20:4)**	**-0.937**	**1.492**
CMH(d18:1/22:0)	-0.833	1.198	PC(O-22:0/20:4)	-0.941	1.456
CMH(d18:1/24:0)	-0.882	1.064	PC(O-24:1/20:4)	-0.891	1.087
CMH(d18:1/23:0)	-0.878	1.170	PE(P-18:0/20:4)	-0.833	1.121
ChoE(16:0)	-0.890	1.139	PE(P-16:0/22:6)	-0.829	1.246
ChoE(18:0)	-0.846	1.276	PE(18:1e/22:6)	-0.912	1.077
ChoE(18:1)	-0.935	1.022	SM(d18:0/15:0)	-0.824	1.130
ChoE(20:3)	-0.864	1.119	SM(32:1)	-0.957	1.079
ChoE(20:4)	-0.946	1.276	SM(d18:1/16:0)	-0.829	1.166
(*) ChoE(20:5)	**-0.840**	**1.904**	SM(d18:1/18:0)	-0.839	1.194
ChoE(22:6)	-0.872	1.076	SM(36:2)	-0.817	1.278
PC(32:1)	-0.838	1.182	SM(38:1)	-0.811	1.162
PC(16:0/18:1)	-0.840	1.193	SM(39:1)	-0.894	1.147
PC(16:0/18:2)	-0.852	1.165	TG(51:1)	-0.814	1.048
PC(18:1/22:6)	-0.899	1.085	Lithocholic acid	-0.903	1.258
PC(36:3)	-0.846	1.188	PC(16:0/0:0)	-0.806	1.002
PC(30:0)	-0.821	1.209	PC(18:0/0:0)	-0.808	1.025
PE(16:0/18:2)	-0.807	1.268	PC(0:0/20:5)	-0.882	1.099
PC(16:0/17:0)	-0.873	1.033	PC(0:0/22:5)	-0.925	1.265
PC(33:1)	-0.882	1.049	PC(22:5/0:0)	-0.958	1.039
PE(18:1/18:2)	-0.822	1.252	LPC(19:1)	-0.846	1.072
PC(17:1/18:1)	-0.886	1.116	PE(0:0/22:4)	-0.913	1.085
PE(20:4/18:2)	-0.804	1.131	**(*) PE(22:5/0:0)**	**-0.874**	**1.288**
PC(15:0/22:6)	-0.910	1.008	PC(O-20:1/0:0)	-0.830	1.036
PE(18:0/18:1)	-0.865	1.065	PE(P-16:1/0:0)	-0.823	1.037
PC(O-18:1/18:1)	-0.887	1.037	NAE(18:1n-9)	-0.953	1.108
PC(P-16:0/20:4)	-0.937	1.059	Uridine	-0.818	1.071
PC(O-16:0/22:4)	-0.884	1.029	Cer(d18:0/22:0)	-0.880	1.162
(*) PC(P-18:0/20:4)	**-0.813**	**1.193**	Cer(d18:0/23:0)	-0.917	1.153
(*) PC(P-18:0/20:4)	**-0.829**	**1.567**	Cer(d18:0/24:0)	-0.846	1.322

OPLS-DA model					
Name	**p (corr)**	**VIP**	**Name**	**p (corr)**	**VIP**
(*) Cer(d18:1/24:0)	**-0.806**	**1.794**	**(*) PC(P-18:0/20:4)**	**-0.804**	**1.956**
(*) Cer(d18:1/25:0)	**-0.834**	**1.936**	PC(O-20:0/20:4)	-0.874	2.228
(*) ChoE(20:5)	**-0.861**	**2.220**	**(*) PC(O-40:5)**	**-0.807**	**1.586**
ChoE(22:4)	-0.846	2.197	**(*) PC(O-22:1/20:4)**	**-0.852**	**1.988**
ChoE(22:5)	-0.887	2.118	TG(56:5)	-0.813	1.619
(*) PC(P-18:0/20:4)	**-0.839**	**1.640**	**(*) PE(22:5/0:0)**	**-0.846**	**1.768**

In PCa, the emergence of myofibroblasts within the interstitial stroma is described as the major difference between normal and tumour reactive stroma[484,500]. This reactive stroma coevolves with prostate cancer in it is capable of supporting its growth. In previous studies, we have characterised normal fibroblasts and CAFs derived from the same patient's needle biopsies for the typical markers of reactive stroma, α-Smooth Muscle Actin (α-SMA), Cytokeratine, Desmin and Vimentin[116,480,494]. CAFs were not

a homogeneous population of myofibroblasts but a heterogenous mixture of fibroblasts at distinct differentiation stages, including a proportion of cells which are α-SMA positive[116]. The normal fibroblasts lacked α-SMA. However, they could be induced to express α-SMA when treated with either soluble or vesicle-associated TGF-β1[480].
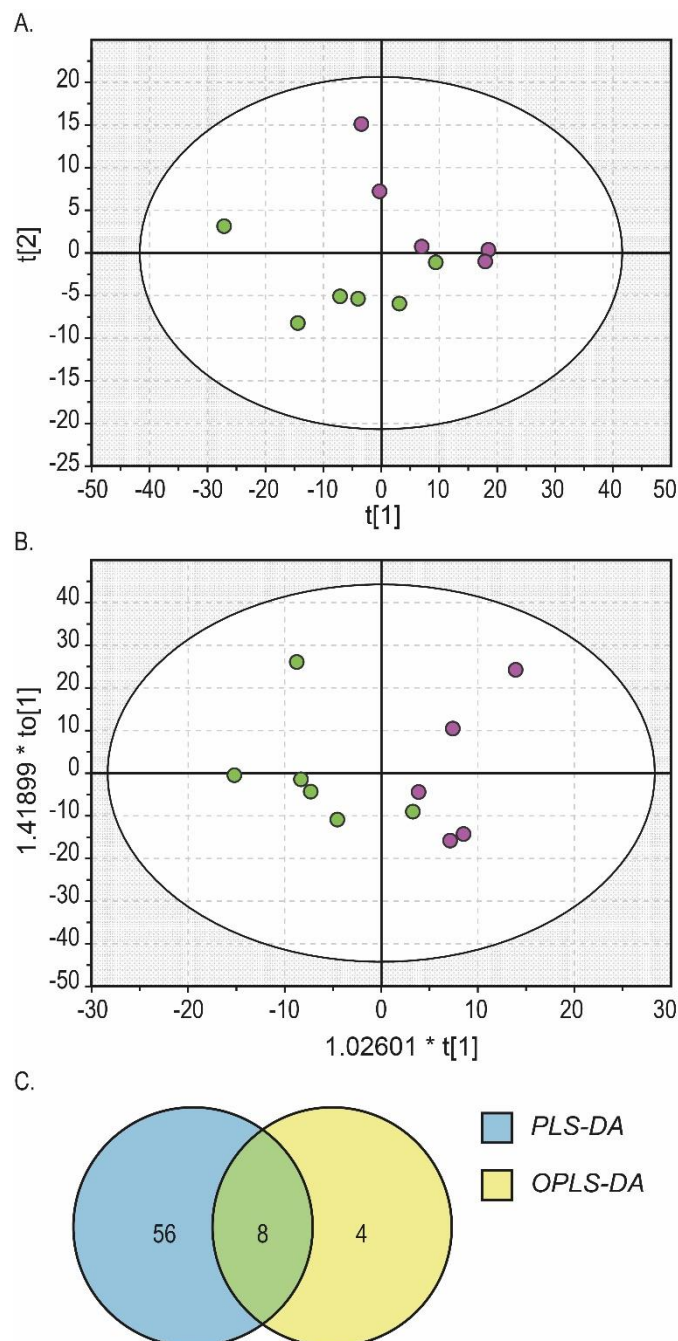
Figure 43. Summary of multivariate metabolomics analysis of normal fibroblasts and CAFs. A. Score scatter plot of the PLS-DA model of fibroblasts obtained from normal and cancer needle biopsies. Model diagnostics (A = 2; R2X = 0.682; R2Y = 0.729; Q2 = 0.337; CV-ANOVA = 0.581). In green, CAF samples and, in purple, normal fibroblasts. B. Score scatter plot of the OPLS-DA model of fibroblasts obtained from normal and cancer needle biopsies. Model diagnostics (A = 2; R2X = 0.682; R2Y = 0.721; Q2 = 0.241; CV-ANOVA = 0.799). In green, CAF samples and, in purple, normal fibroblasts. In green, CAF samples and, in purple, normal fibroblasts. C. Venn diagram of features (metabolites) that influence to the separation of CAF and normal fibroblasts groups in PLS-DA and OPLS-DA models. Results are compiled in Table 24.

In 2016, Webber et al.[480] described a set of proteins that could discriminate CAFs and normal fibro-blasts isolated from the patient—matched needle biopsies described in this study. A more recent study explored the opportunity to use EV-derived RNA from these fibroblasts as indicators of altered tumour environment[494]. In this work, Shephard *et al.* identified 19 differentially expressed transcripts that dis-criminate disease from normal stromal EVs, indicating transcriptional differences between patient sam-ples. The metabolomics study included in this work adds several findings to our published data obtained by proteomics and transcriptomics. A comprehensive evaluation of data showed a clear tendency of enhanced abundances in most of the metabolites in sample 1161-normal during data analysis and nor-malization compared to other patient-matched tissues. The behaviour of this sample was also different from the remaining samples as demonstrated by PCA (Figure 42). Moreover, it is on the line that de-scribe the confidence ellipse based on Hotelling's T^2 (significance level = 0.05). For these reasons, sample 1161-normal was excluded from further statistical analysis. Afterwards, PLS-DA and OPLS-DA models were built and the scores plots are included in Figure 43AB. A clear separation tendency was observed in both models mainly through PC1. Even with this separation tendency, none of the models was validated (CV-ANOVA p-value >0.05). However, those variables that influence on the most in group separation were selected based on their VIP and p(corr) values. In total 64 and 12 metabolites fulfil VIP greater than 1 and |p(corr)| greater than 0.8 in PLS-DA and OPLS-DA, respectively. In order to select those metabolites of relevant importance, a Venn Diagram including these metabolites was built to select only common metabolites in PLS-DA and OPLS-DA models (Figure 43C). Relevant metabolites include ceramides (Cer), phosphatidylcholines (PC) and cholesteryl esters (CE) (Table 24).

5.3.2. Disease-associated metabolism shows lipogenic and energy-producing alterations.

Reactive stroma relevance grows upon progression and invasion of tumour cells to neighbour loca-tions and tissues since it supports structural growth and nutrient availability. In this line, cell populations in normal stroma undergo a myofibroblast turnover constituting the so-called CAFs. In order to study the metabolic profile of this two tissue subtypes, four platforms based on UPLC-MS were utilised to analyse metabolites. They are fractionated in pools of species with similar physicochemical properties. The platforms include: (1) Fatty acyls, bile acids, steroids and lysoglycerophospholipids; (2) Glycer-olipids, glycerophospholipids, sterol lipids and sphingolipids; (3) Amino acids; (4) Polar metabolites pro-filing, including central carbon metabolism.

A total of 422 metabolites, of which 47 were significantly at higher levels in CAFs, were identified (Figure 44A). The volcano plot in Figure 44A reflects a general trend of raised metabolite levels in CAFs compared to normal fibroblasts. Metabolites showing a significantly different level in disease or normal fibroblasts (p-value <0.05) are compiled in Table 25. Among the significantly more prevalent metabo-lites, aminoacid tryptophan (Trp) was the only one for a p-value over 0.001. Glutathione (GSH) system was found elevated over 4-fold in cancer, indicating a high detoxification activity, transmembrane transport of organic solutes and/or response to reactive oxygen species[501]. Most of the altered metab-olites corresponded to several classes of lipids. To describe metabolic pathways altered in CAFs com-

pared to normal fibroblasts a pathway analysis was computed (Figure 44B). Indeed, this over-representation analysis pinpoints that Trp/Lys/Phe metabolism and GSH system are affected in CAF population. Among lipid pathways, the analysis highlighted steroid biosynthesis, glycerol(phospho)lipid metabolism and linoleic acid (Fatty acids) metabolism. Altogether indicates that CAFs are more active metabolically and exhibit several alterations towards a lipogenic metabolism.
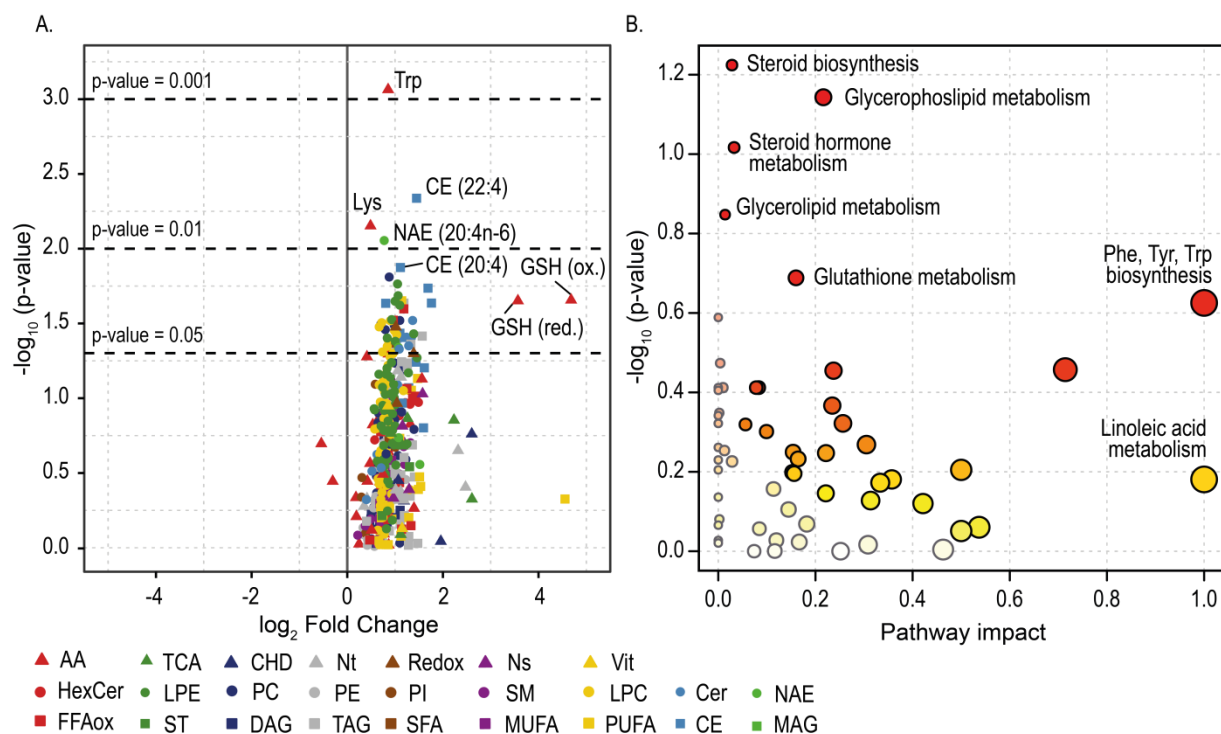
Figure 44. Summary of metabolomics study (considering individual metabolites) comparing normal and cancer-associated fibroblasts isolated from needle biopsies of radical prostatectomy specimens. A. Volcano plot comparing CAFs and normal fibroblasts as -log10(p-value) against log2(fold change). The different metabolite classes are depicted in different shapes and colours; relevant metabolites are labelled. B. Pathway overrepresentation analysis depicted as –log10 (p-value) against pathway impact. Pathway impact stands for the relative importance of each module in the analysed metabolite set. It combines pathway overrepresentation results and centrality measures. Representative pathways are labelled, size of nodes represents pathway impact and their significance ranges from high (in red) towards orange, yellow and white indicating a lower significance. Here, all individual metabolites and their fold changes were considered to rank each pathway. AA: aminoacids; TCA: tricarboxylic acid cycle related metabolites; CHD: Carbohydrates derivatives; Nt: Nucleotides; Redox: electron donor and acceptors; Ns: Nucleosides; Vit: Vitamins; HexCer: Hexosylceramides; LPE: Lysophosphatidylethanolamines; PC: Phosphatidylcholines; PE: Phosphatidylethanolamines; PI: Phosphatidylinositols; SM: Sphingomyelins; LPC: Lysophosphatidylcholines; Cer: Ceramides; NAE: N-acylethanolamines; FFAox: Oxidized fatty acids; ST: Steroids; DAG: Diacylglycerides; TAG: Triacylglycerides; SFA: Saturated fatty acids; MUFA: Monounsaturated fatty acids; PUFA: Polyunsaturated fatty acids; CE: Cholesteryl esters; MAG: Monoacylglycerides.

Considering the metabolite class, one can classify families of metabolites that participate in similar metabolic and physiological pathways. In Figure 45A, a table summarising metabolite class fold changes significant in CAFs is presented. Both analysed polypeptides of central metabolism and, nucleosides and nucleotides were elevated in the cancer group. This could explain a more active state of CAFs compared to normal fibroblasts. Besides, one could observe elevated levels of different types of lipids in cancer samples including cholesteryl esters, n-acyl ethanolamines (NAE), ceramides and glycerophospholipids. For this reason, we analysed our quantified set of lipids derived from this metabolomics study to compute lipid associations and visualise important modules of the network (Figure 45B).

Table 25. Heatmap comparison between healthy- and disease-derived cells. Each row represents a single metabolite of which Class, common name, family and HMDB (Human Metabolome DataBase) code are provided. of the comparison cancer *vs.* normal cell. Columns on the right represent the log2(fold change), and the significance of each metabolite. Fold change legend consists of dark green to light green to represent a variation from -4 towards 0 and, light red to dark red to represent a variation from 0 towards 4 or higher. In p-values column, only grey colours depict significance as: *p*-value<0.05, light grey; *p*-value<0.01, dark grey; *p*-value<0.001, black.

Class	Name	Family	HMDB	log2 FC	p-value (p)
Peptides	Glutathione (reduced)	AA	HMDB00125	3.569	**2.23E-02**
Peptides	Glutathione (oxidized)	AA	HMDB03337	4.68136	**2.20E-02**
Amino acids	Lysine	AA	HMDB00182	0.48658	**7.03E-03**
Amino acids	Tryptophan	AA	HMDB00929	0.85465	**8.63E-04**
Sphingolipids	Cer(d18:1/23:0)	Cer	HMDB00950	1.24171	**3.90E-02**
Sphingolipids	Cer(d18:1/24:1) + Cer(d18:2/24:0)	Cer	HMDB0004953	1.05385	**4.05E-02**
Sphingolipids	Cer(d18:1/25:0)	Cer	HMDB04957	1.34704	**3.91E-02**
Monosaccharides	Fructose 1,6-bisphosphate	CHD	HMDB01058	1.95681	**9.05E-01**
Disaccharides	Sedoheptulose	CHD	HMDB03219	2.60353	**1.73E-01**
Sugar Acids and Derivatives	6-Phospho-gluconate (6PG)	CHD	HMDB01316	2.23188	**1.40E-01**
Sterols	ChoE(17:0)	ChoE	HMDB0060059	1.59525	**1.58E-01**
Sterols	ChoE(18:0)	ChoE	HMDB10368	1.61198	**6.26E-02**
Sterols	ChoE(18:1)	ChoE	HMDB00918	1.15346	**3.93E-02**
Sterols	ChoE(20:3)	ChoE	HMDB10373	1.1013	**3.68E-02**
Sterols	ChoE(20:4)	ChoE	HMDB06726	1.11212	**1.34E-02**
Sterols	ChoE(20:5)	ChoE	HMDB06731	1.7609	**2.31E-02**
Sterols	ChoE(22:4)	ChoE	HMDB06729	1.44915	**4.60E-03**
Sterols	ChoE(22:5)	ChoE	HMDB10375	1.68911	**1.84E-02**
Sterols	ChoE(22:6)	ChoE	HMDB06733	0.80487	**2.32E-02**
Fatty Acid Esters	Acetyl-coenzyme A	TCA	HMDB01206	2.60724	**4.72E-01**
Non-esterified fatty acids	18:3n-3	PUFA	HMDB01388	4.55384	**4.72E-01**
Oxidized fatty acids	5-HETE	FFAox	HMDB11134	0.96419	**3.01E-02**
Oxidized fatty acids	18-HEPE	FFAox	HMDB0012611	1.18287	**2.53E-02**
Glycerophospholipids	LPC(0:0/18:0)	LPC	HMDB10384	0.85382	**4.05E-02**
Glycerophospholipids	LPC(20:2/0:0)	LPC	HMDB10392	0.83615	**4.51E-02**
Glycerophospholipids	LPC(0:0/20:5)	LPC	HMDB10397	0.90459	**3.03E-02**
Glycerophospholipids	LPC(0:0/22:4)	LPC	HMDB0010401	0.66744	**3.34E-02**
Glycerophospholipids	LPC(0:0/22:5)	LPC	HMDB0010403	0.9893	**3.53E-02**
Glycerophospholipids	LPC(22:5/0:0)	LPC	HMDB0010403	1.03379	**3.77E-02**
Glycerophospholipids	LPC(17:1/0:0)	LPC		0.74048	**4.90E-02**
Glycerophospholipids	LPE(0:0/18:0)	LPE	HMDB11129	0.92972	**2.99E-02**
Glycerophospholipids	LPE(22:4/0:0)	LPE	HMDB11523	1.00054	**2.24E-02**
Glycerophospholipids	LPE(22:5/0:0)	LPE	HMDB0011525	1.39095	**3.71E-02**
Glycerophospholipids	LPE(22:5/0:0)	LPE	HMDB0011525	1.09578	**2.38E-02**
Glycerophospholipids	LPE(22:6/0:0)	LPE	HMDB11526	1.05484	**1.72E-02**
Glycerophospholipids	LPI(16:0)	LPI	HMDB0061695	1.06009	**2.07E-02**
Fatty amides	NAE(18:1n-9)	NAE	HMDB02088	1.06931	**4.57E-02**
Fatty amides	NAE(20:4n-6)	NAE	HMDB04080	0.77401	**8.81E-03**
Pyrimidine Nucleosides	Uridine	Ns	HMDB00296	1.57504	**9.34E-02**
Purine Nucleotides	Guanosine 5'-diphosphate	Nt	HMDB01201	2.31775	**2.23E-01**
Purine Nucleotides	Inosine monophosphate	Nt	HMDB0000175	2.47342	**3.93E-01**
Glycerophospholipids	PC(16:1/20:4)	PC	HMDB0008016	0.79917	**3.48E-02**

Table continued

Table 25. (Continued)

Class	Name	Family	HMDB	log2 FC	p-value (p)
Glycerophospholipids	PC(17:0/20:4)	PC	HMDB0286107	0.70455	**3.20E-02**
Glycerophospholipids	PC(P-18:0/20:4)	PC	HMDB0011253	0.88219	**1.55E-02**
Glycerophospholipids	PC(O-20:0/20:4)	PC	HMDB13442	1.18287	**2.54E-02**
Glycerophospholipids	PC(O-22:1/20:4)	PC	HMDB0013451	1.09803	**3.02E-02**
Glycerophospholipids	PC(O-22:0/20:4)	PC	HMDB13448	0.98692	**3.25E-02**
Glycerophospholipids	PE(P-18:0/20:4)	PE	HMDB0005779	0.83646	**3.96E-02**
Glycerophospholipids	PE(P-18:1/20:4)	PE	HMDB0011386	1.00366	**4.16E-02**
Non-esterified fatty acids	14:2n-x	PUFA		1.13784	**2.23E-02**
Purine Nucleotides	NADP	Redox	HMDB00217	-1.1507	n.s.
Purine Nucleotides	NADPH	Redox	HMDB00221	-2.3943	n.s.
Purine Nucleotides	NAD	Redox	HMDB00902	1.01573	**3.34E-02**
Non-esterified fatty acids	Dodecanoic acid	SFA	HMDB00638	0.88888	**4.27E-02**
Glycerolipids	TG(16:0+20:4+16:0)	TAG	HMDB0005363	1.56709	**3.84E-02**
Glycerolipids	TG(16:0+17:0+18:1)	TAG		1.01203	**4.42E-02**
Glycerolipids	TG(18:1+20:4+16:0)	TAG	HMDB0010441	1.18483	**2.31E-02**
Glycerolipids	TG(20:4/18:1/18:0)	TAG	HMDB0044960	1.32989	**4.35E-02**

A.

| Metabolite classification	log$_2$ FC	p-val
Ceramides	1.01	0.046
Cholesteryl esters	1.53	0.013
Hydroxyeicosapentanoic acids (HEPE)	1.18	0.032
N-acyl ethanolamines	0.91	0.028
Nucleosides and nucleotides	0.95	0.025
Polipeptides of central carbon metabolism	3.50	0.019
Lysophosphatidylcholines	0.78	0.048

Figure 45. Summary of metabolomics study (considering metabolites class) comparing normal and cancer-associated fibroblasts isolated from needle biopsies of radical prostatectomy specimens. A. Comparison of metabolic variations between cancer vs normal fibroblasts. In this table, the classification of metabolites is considered - metabolites with similar chemical characteristics - instead of comparing each individual metabolite. Fold changes of these paired samples were calculated and the significances of the paired t-test are indicated. B. Representation of significant lipid metabolites found in elevated levels in matched-patient samples. Nodes (metabolites) are sized according to their fold change and they are linked according to reaction connection, blue line indicates chain elongation/reduction, green indicates head group modification and, orange indicates saturation/desaturation. Lipid classes are also represented in different colours. Cer: Ceramides; CE: Cholesteryl esters; FA: Fatty acids; LPC: Lysophosphatidylcholines; LPE: Lysophosphatidylethanolamines; LPI: Lysophosphatidylinositols; PC: Phosphatidylcholines; TG: Triacylglicerides; PCP: Ether LPC; PCO: Ether PC; PEP: Ether LPE.

The nodes are metabolites and they are connected when they can be readily metabolised between them. In general, there are few clusters of interconnected lipids, which means there are several groups of lipids relevant in CAFs with reasonably different biological function. Considering only significant lipids in the network (Figure 45A), one can observe that hydroxyeicosapentanoic acids (HEPE) and CE are the most relevant in terms of Fold change in the metabolic network. The accumulation of CE agrees with studies that show an abnormal cholesterol metabolism in cancer[502]. Notably, most elevated CE were those esterified to both polyunsaturated 20 and 22 carbon atom of acyl chains (Figure 45B). Interestingly, HEPE metabolites are oxidised fatty acids (FFAox), associated to fatty acid (FA) mobilisation for energy production in mitochondria. Most of the altered lipids corresponded to glycerophospholipids specifically, lysophosphatidylcholines (LPC) and ether-linked glycerophosphocholines (LPE), which are related to mitochondria well-functioning[503,504]. Anandamine and other NAEs have important anti-inflammatory and anti-cancer properties and, have been associated to inhibition of growth in PCa.
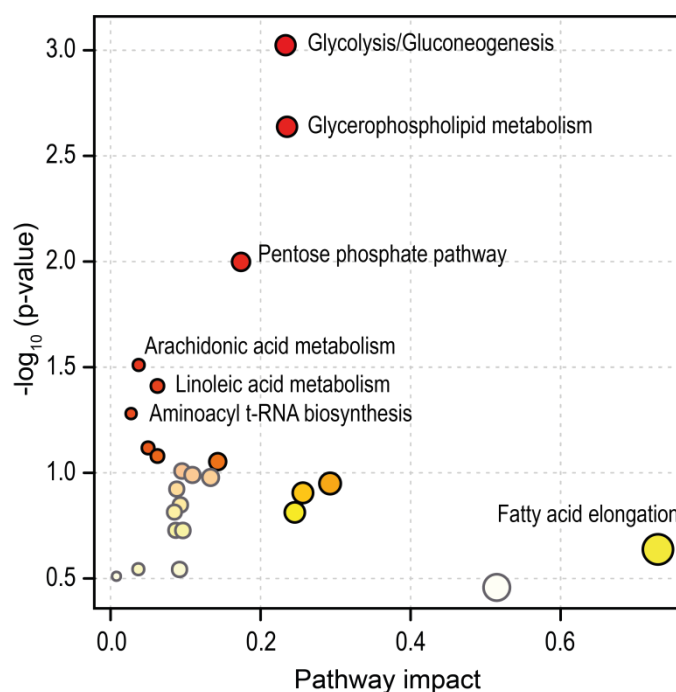
Figure 46. Joint-pathway analysis of significant proteins and metabolites differentially measured in patient-matched normal and cancer-associated stromal fibroblasts. Pathway overrepresentation analysis is depicted as –log10 (p-value) against pathway impact Pathway impact stands for the relative importance of the specific module in the analysed metabolite set. It combines pathway overrepresentation results and centrality measures. Representative pathways were labelled, size of nodes represents pathway impact and their significance ranges from high (in red) towards orange, yellow and white indicating a lower significance.

The integration of omic approaches often provides a better understanding of physiological outputs. A proteomic study performed by Webber et al.[480] processed the exact same set of patient-matched needle biopsies utilised in this study. As samples underwent the same experimental procedures, the integration of proteomics and metabolomics data may reveal relevant metabolic flux distributions. In Figure 46 one can observe a joint-pathway analysis that combines significant variations of the proteome

and metabolome comparing CAFs against normal fibroblasts. This analysis computed by Metaboanalyst provides the most relevant (p-value) and affected (Pathway impact) metabolic pathways. This integrated metabolic pathway analysis confirms the rewire of CAFs towards lipogenic metabolism since glycerophospholipid, arachidonic acid, linoleic acid and fatty acid metabolism were highlighted in CAFs (Figure 46). Moreover, the fact aminoacyl t-RNA biosynthesis was over-represented proposes the elevated levels of aminoacids, nucleosides and nucleotides are related to a higher transcriptomic activity of CAFs. This phenotype is characteristic of cancer-associated tissues[505,506]. Interestingly, it is suggested that glycolysis/gluconeogenesis and pentose phosphate pathways are also over-represented. This feature is also characteristic of highly proliferative cells or tissues, however, there were no significant differences detected in metabolites of those pathways. Hence, it suggests the main central metabolism modifications are described by proteomics data.

### 5.3.3. Treatment with EVs modifies basal respiration of normal fibroblasts to a CAF-like phenotype.

In previous studies with the same treatments and sample preparations, we have shown TGF-β1 associated to EVs was required to induce myofibroblast differentiation of normal fibroblasts, resulting in angiogenic and tumour-promoting characteristics[116]. Also, a proteomics study comparing EV-generated myofibroblasts and those naturally arising *in situ* confirmed their similarity[480]. The activation of myofibroblast-rich stroma is considered by some as a rate-limiting step, essential for cancer progression[116]. Thus, one could expect that the metabolism of normal fibroblast show alterations upon their treatment with EVs.

For this reason, we have performed glycolytic and mitochondrial stress assays on normal- and disease-derived stromal fibroblasts and also, to normal fibroblasts incubated with soluble TGF-β1 (sTGF-β1) or DU145-derived EVs. Extracellular acidification rate (ECAR) in response to glucose, oligomycin (ATP synthesis inhibitor) and 2-DG (glycolysis inhibitor) was plotted over time to study the glycolytic rate of fibroblasts (Figure 49). Glucose is taken up by the cells and converted to lactate, generating ATP and protons (Figure 47A). Glycolysis rate do not show a distinctive phenotype when comparing normal fibroblasts to CAFs. Oligomycin was used to inhibit mitochondrial ATP production, shifting energy production to glycolysis, thus revealing the maximal glycolytic capacity of fibroblasts (Figure 47B). The difference between glycolytic capacity and basal glycolysis rate was defined as the glycolytic reserve (Figure 47C). The fact glycolytic reserve is neither distinctive comparing normal fibroblasts to CAFs but its value is over 100% suggests that fibroblasts do not uniquely rely on glycolysis to obtain energy. In summary, no significant differences were measured between normal and disease fibroblasts nor upon TGF-β1 or EV treatment regarding their use of glucose to produce energy. The fact no significant differences were described in metabolomics study suggests that the typical glycolytic phenotype of PCa is not readily described in stromal cells.
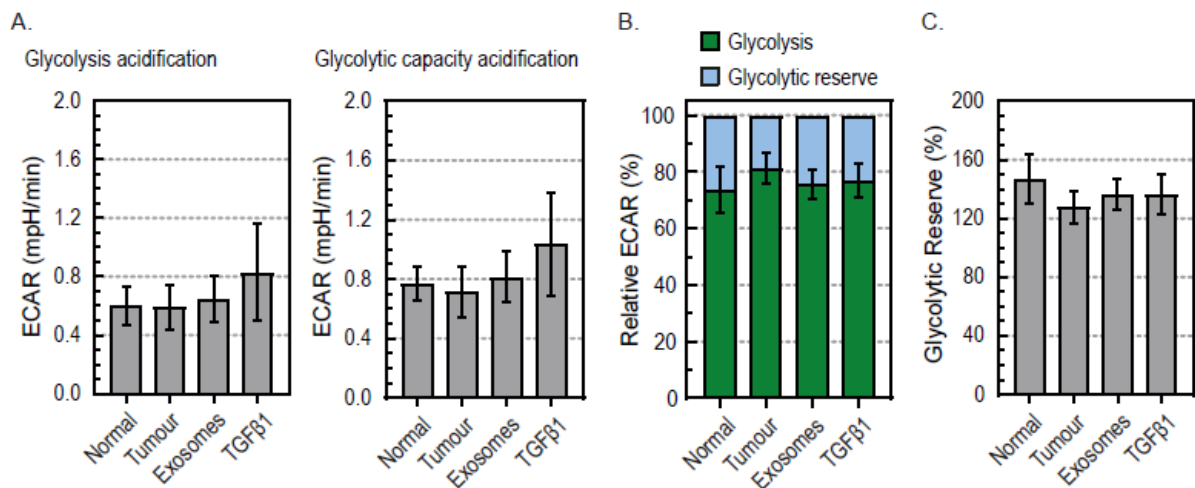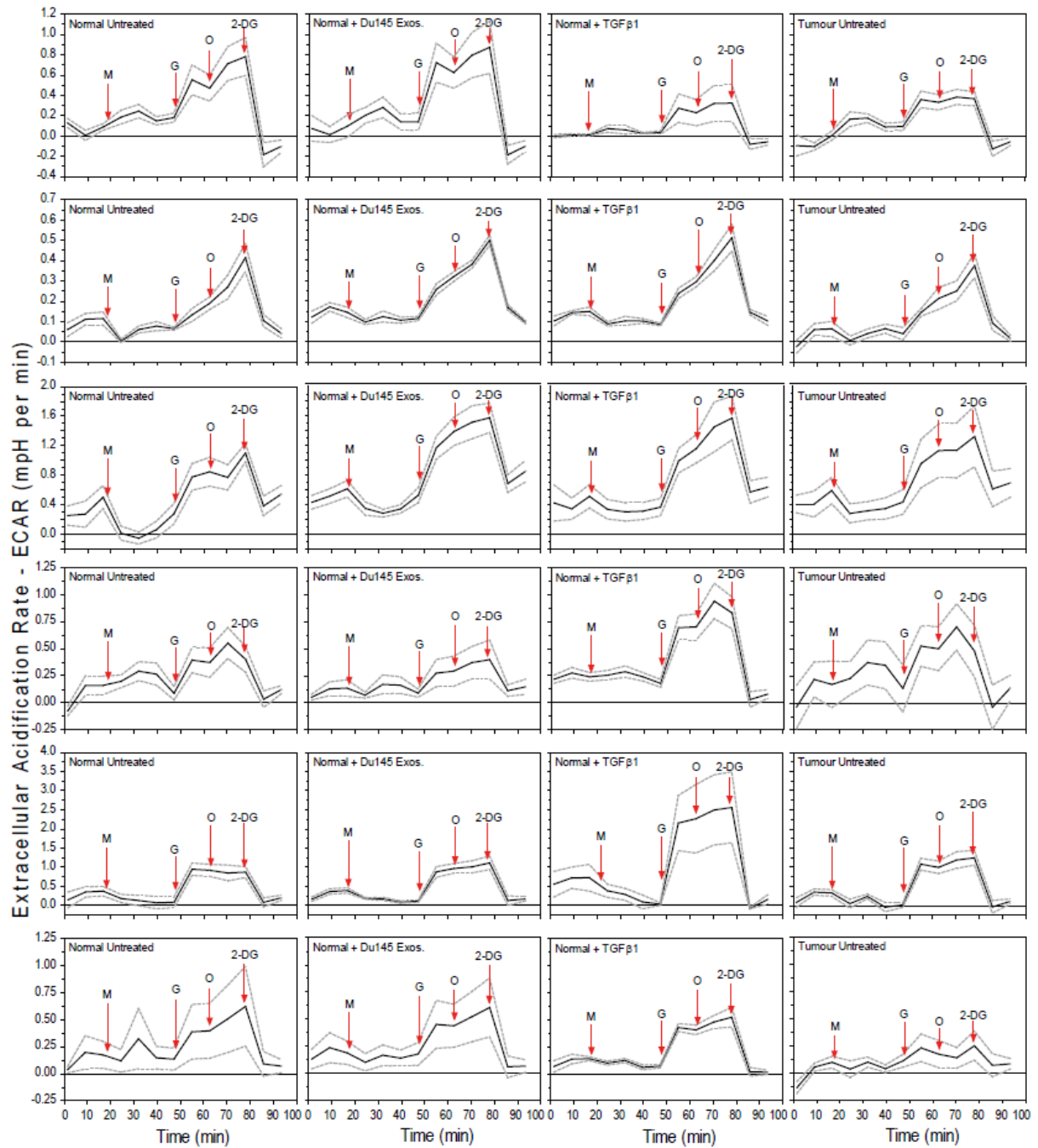
Figure 47. Analysis of glycolytic stress assay comparing healthy- and disease-associated stromal cells, untreated or pre-treated with either exosomes or TGF-β1 (data in Figure 49). A. ECAR relating to glycolysis and to glycolytic reserve (mean ± SEM; n=6) was calculated. B. Maximal glycolytic capacity ECAR was established as 100% and ECAR apportioned between glycolysis and glycolytic reserve represented C. Reserve capacity expressed as percentage of basal glycolysis was calculated.

To study mitochondrial metabolism, oxygen consumption rate (OCR) in response to oligomycin (ATP coupler), FCCP (an electron transport chain accelerator), and rotenone (mitochondrial inhibitor) was plotted over time (Figure 50). Oligomycin inhibits ATP synthesis, so it is utilised to describe the oxygen consumption devoted to ATP synthesis (Figure 48A) so the coupling efficiency, percentage of mitochondrial respiration for ATP production, could be calculated (Figure 48C). In Figure 48B the contribution of basal respiration and reserve capacity (%) is depicted. In general, both basal respiration and ATP production associated to mitochondria tend to increase in CAFs. Moreover, treatment with soluble TGF-β1 or PCa-derived EVs significantly increased basal respiration after 72 hour incubation. This result suggests normal fibroblasts inceased their mitochondrial activity upon treatment.
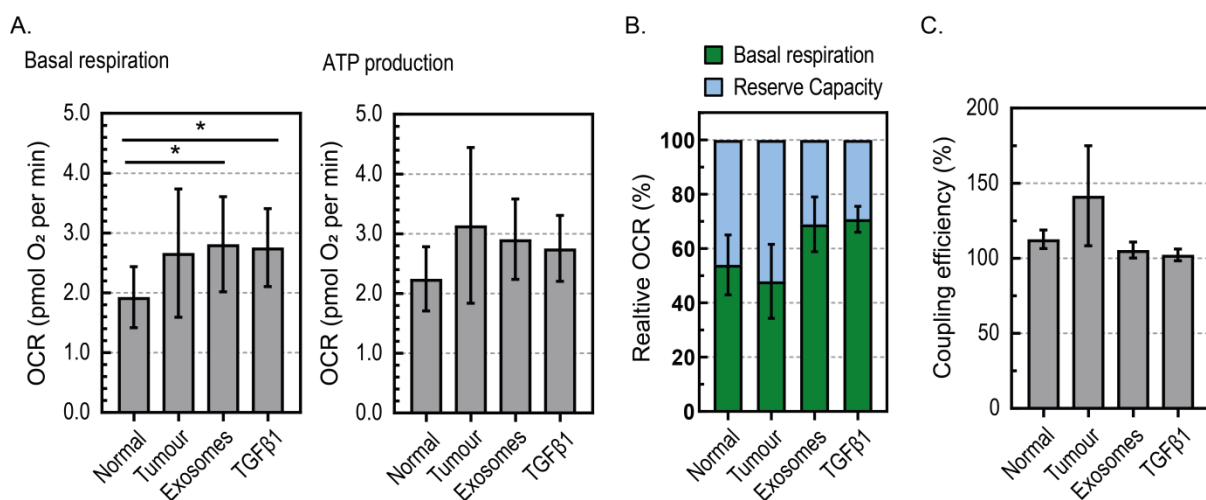

Figure 48. Analysis of mitochondrial stress assay comparing normal- and disease-associated stromal cells, untreated or pre-treated with either exosomes or TGF-β1 (data in Figure 50). A. OCR relating to basal respiration and specifically to ATP production (mean ± SEM; n=6) was calculated. B. Maximal OCR was established as 100% and OCR apportioned between basal respiration and reserve capacity represented C. Reserve capacity expressed as percentage of basal respiration was calculated (mean ± SEM; n=6) and the efficiency of basal respiration towards ATP production was represented (mean ± SEM; n=6), as coupling efficiency.

Figure 49. Glycolytic stress assay represented as Extracellular Acidification Rate (ECAR) over time in all samples and treatments are depicted (mean ± SE; n≥4). Normal- and cancer-associated fibroblasts, untreated or pre-treated with either exosomes or TGF-β1, were subjected to a mitochondrial stress test assay. ECAR was normalised to cellular protein. M: Media; G: Glucose, 10 µM; O: Oligomycin, 1 µg per mL; 2-DG: 2-Deoxy-D-glucose, 0.1 M.
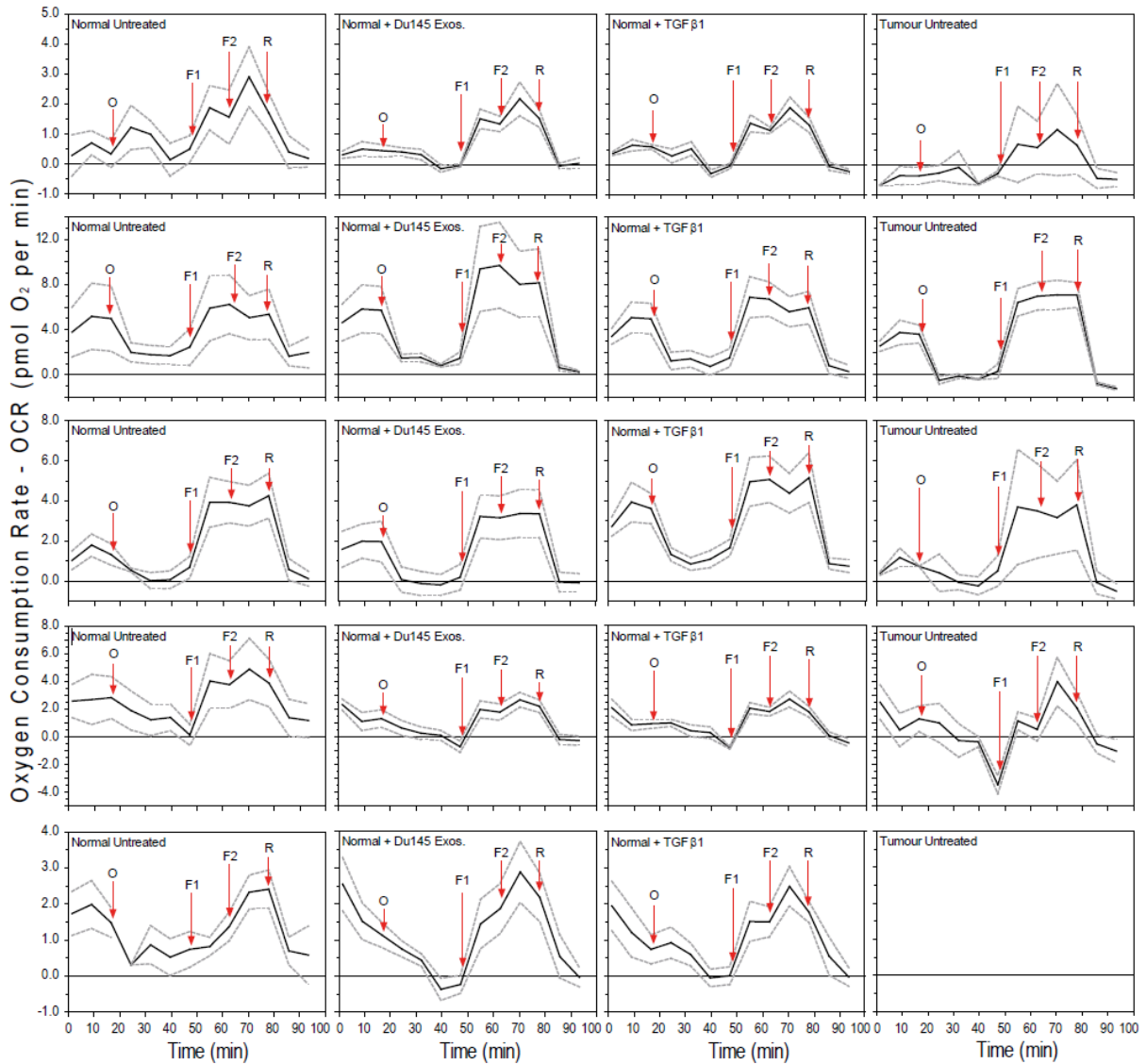
Figure 50. Mitochondrial stress assay represented as oxygen consumption rate (OCR) over time in all samples and treatments are depicted (mean ± SE; n≥4). Healthy- and disease-associated stromal, untreated or pretreated with either exosomes or TGF-β1, were subjected to a mitochondrial stress test assay. OCR was normalised to cellular protein. O: Oligomycin, 1 µg per mL; F1: FCCP, 0.3 µM; F2: FCCP, 0.6 µM; R: Rotenone, 2 µM.

5.4.   Discussion

The onset of a reactive stroma and the emergence of CAF phenotypes is a feature comprehensively studied in epithelial cancers including PCa [115,116,480,494,507]. Other PCa studies often compare metabolic alterations between different types of tissues or between low and high grade of disease. In this line, a report using mass spectrometry imaging (MSI) distinguished prostate compartments as well as disease stages in prostate slices from patients. This MSI approach described a distinctive metabolism of prostate stroma and epithelium regions as well as between non-cancerous and cancerous epithelium[483]. Many studies evaluated the interaction of PCa with reactive stroma[9,469,484–488], however, very few describe metabolite levels across different types of stroma[484].

Previous reports using the exact same set of matched-patient stroma biopsies confirmed the existence of myofibroblast-like cells within cancer regions of the tissue, by positive staining of both α-SMA, and vimentin, and lack of expression of desmin or the cytokeratins[116,480,494]. Upon stimulation with soluble or EV-associated TGF-β1, differentiation of normal tissue-derived fibroblasts into myofibroblasts was verified by the onset of α-SMA expression[480]. Nonetheless, the cancer-associated stroma was a mixture of varying proportions of fibroblasts and myofibroblasts-like cells[500,508]. One can expect that although such heterogeneity is an important factor in promoting tumour growth it may well hinder our capacity to fully appreciate metabolic alterations arising in CAFs. This metabolomics study has identified some altered metabolites and metabolic pathways, however, it could not definitively distinguish stromal CAFs from normal fibroblasts using a non-supervised PCA approach. Remarkably, adding information about class, a clear tendency was observed in both PLS-DA and OPLS-DA models. Even no significant model was generated; important metabolites were obtained from multivariate analysis that matches with univariate analysis. This highlighted the importance of these metabolites – CE (20:5), Cer (d18:1/25:0), PC (O-22:1/20:4) and PC (P-18:0/20:4) - involved in lipid biosynthesis pathways and pointed them out for further studies with more samples and individuals. In fact, the lack of clear significant results could be due to CAF heterogeneity. Moreover, one should be aware that prior frozen samples can influence metabolomics analyses if they are not well prepared because protein content could affect metabolite recoveries. Since all samples underwent the same procedures, the output in this analysis will not change. In this manuscript, we present metabolomics data comparing normal and cancer-associated fibroblasts from the same patient which is, to our knowledge, the first such exploration. Our multiplatform analysis established elevated levels of several metabolic classes in CAFs. The increment of cholesteryl esters has been already observed in other studies concerning tumour cell lines and samples[33,502], which is on agreement with the upregulated tendency observed (see Figure 45). Actually, cells make reservoirs of cholesteryl ester that can be transferred to nearby or even distal cells[509]. This might well be the reason myofibroblasts accumulate lipids. Seeking for energy sources, epithelial cancer cells undergo a characteristic rewiring of their metabolism from an extremely unproductive secretion of citric acid to a closed TCA cycle with an elevated mitochondrial respiration. Besides, this rewiring is accompanied with the uptake of circulating lipids[510,511] as well as translocation of lipids from adipocytes[512]. As they consume lipids and specifically, cholesteryl esters[33], supportive CAFs could be fuelling either themselves with these compounds, nearby cancer cells or both. Interestingly, CAFs seem to mobilise *de novo* free fatty acids as energy source; oxidised fatty acid species as HEPE were elevated in cancer-associated fibroblasts. Altogether indicates a consumption of newly built lipids to fuel themselves while building up cholesteryl esters reservoirs, which are easily transported and readily available to transfer it between cells. The fact acyclglycerols were not accumulated in CAFs, although few triacyclglycerols were increased and, acetyl-CoA shows a quite high fold change (Table 25) hints that myofibroblasts preferentially store energy as cholesteryl ester compounds while the oxidation of free fatty acids satisfy their energy needs.

The higher metabolic activity suggested by an over-representation of mostly all metabolites measured in this study is further confirmed with elevated levels of nucleosides and nucleotides. When proteomics data is considered the biosynthesis of tRNA aminoacyls is highlighted, which indicates a higher

transcriptional and translational activities. Specifically, the increment of NAD suggests a mobilisation of fibroblast reducing power to generate energy in mitochondria or fuel anabolic reactions. Besides, accumulation of ceramides has been comprehensively related to cell differentiation, arrest of cell cycle and apoptosis[513–515]. This class, and concretely Cer(d18:1/25:0), followed the described tendency (see Figure 45, Table 24 and Table 25). Newly differentiated fibroblasts exhibit higher levels of ceramidesand possibly, apoptotic mechanisms are counteracted by other compounds as anandamide. Anandamide is an endocannabinoid - detected in higher levels in CAFs - with important anti-inflammatory and anti-cancer properties[516] that demonstrated inhibition of growth in transformed cell lines from human prostate[517,518].

A limitation of this study has been the arguably low number of samples available for metabolomics. In contrast, the strength is the collection of donor matched-paired biopsy samples that reflect healthy and disease tissue regions of stroma from the same patient. This type of data draws relevant conclusions of processes and alterations occurring in each patient. Even so, the outcome of this study described metabolic differences with sparse impact in the entire metabolome. Once combined with proteomics data from the exact same set of samples, the outcome acquired a higher relevance in determining important metabolic processes driving myofibroblast differentiation. The integration of significant proteins and metabolites differentially measured in normal and cancer fibroblasts confirmed a major alteration in lipid metabolism. A variation of glycerophospolipids - i.e. PC(O-22:1/20:4) and PC(P-18:0/20:4) - indicates an enrichment of the major membrane type of lipids. Interestingly, this class of lipids have been associated to mitochondria dynamics and well-functioning[503,504]. Although lipids can participate in signalling processes or be used as building blocks, in this study most metabolic alterations point out fuelling or energy storage processes. Major free fatty acid pathways – linoleic and arachidonic - are altered together with an accumulation of cholesteryl esters and few oxidised fatty acids. This indicates a mobilisation of lipids to produce energy but also the production of lipid reservoirs readily available for transport. Moreover, central metabolism pathways – glycolysis/gluconeogenesis and pentose phosphate - are positively altered in CAFs only including the proteome to the analysis. This suggests that as protein queries were the most prominent and overlapped a higher number of pathways compared to metabolites, the output of this integrative analysis could be determined majorly by differences in the proteome.

Back in 2016, this proteomics study described many proteins altered in normal and cancer fibroblasts. However, several of those were unique to specific treatments with either sTGF-β1 or EV-associated TGF-β1. For instance, they described a higher presence of Annexin-I, which has a role in regulating VEGF function, in CAFs as well as altered mitochondrial proteins, linking CAFs to mitochondrial rearrangement. In this manuscript, we approached the assessment of metabolic alterations upon sTGF-β1 or EV-associated TGF-β1 treatments by Seahorse stress assays. Even considering the limitation of such assays, where O_2 consumption and pH acidification are recorded over time, the glycolytic rate and oxidative mitochondrial activity of cells was assessed. ECAR informs that glycolytic activity associated to CAFs was not increased. This, together with the fact that the integration of proteomics and metabolomics indicates an alteration in central metabolism, suggests that these pathways were not
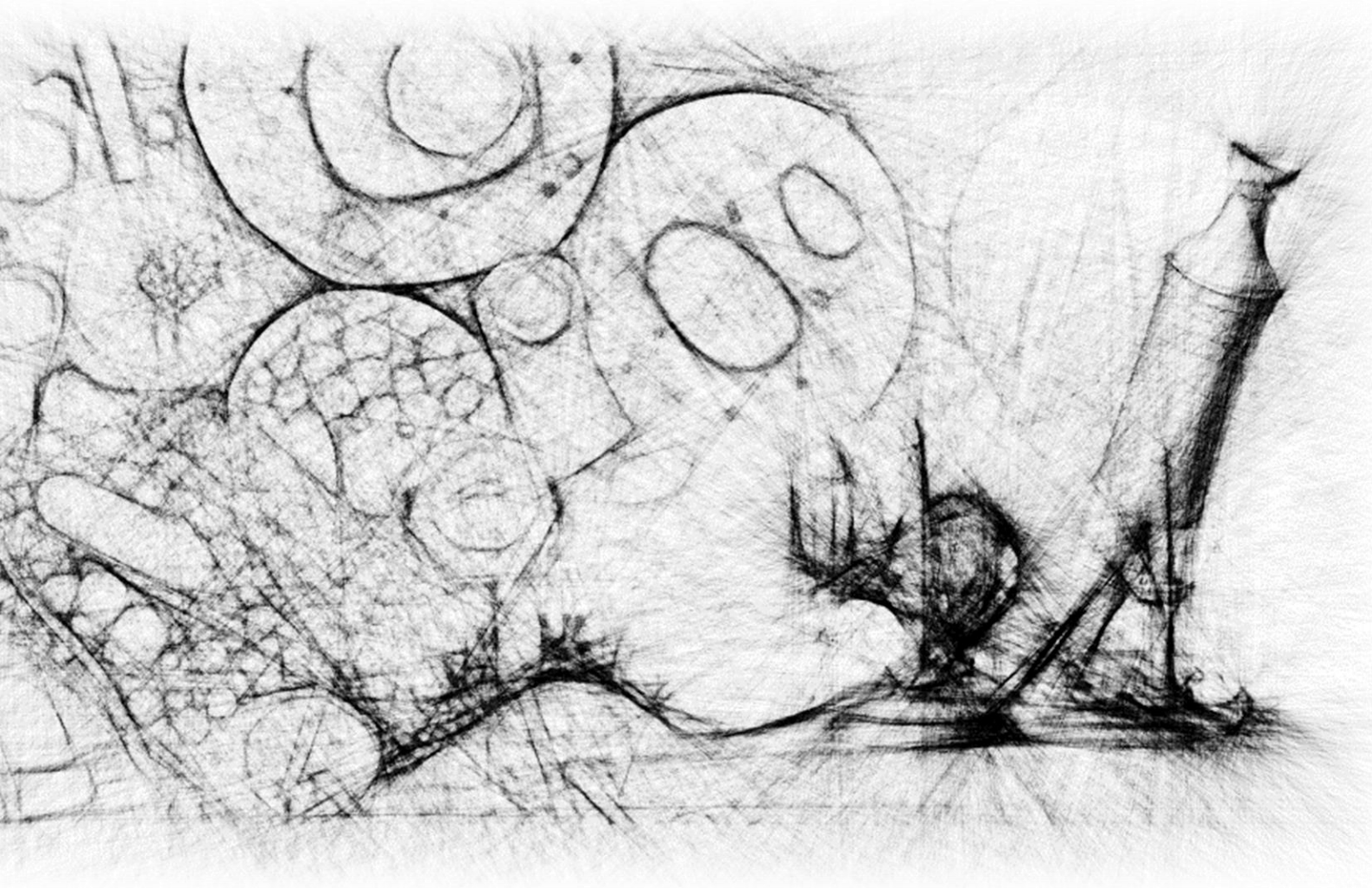
used in the catabolic but in the anabolic direction. Only basal respiration, in the mitochondrial stress assay, was distinctive when comparing CAFs and normal fibroblasts. Moreover, the treatment with sTGF-β1 and EVs containing TGF-β1 showed a similar outcome. This result links the distinctive metabolic abundances to mitochondrial metabolism. Our metabolomics data offers a plausible explanation because elevated levels of GSH are usually correlated to the presence of ROS due to mitochondrial activity while altered levels of FFAox may indicate the burning of lipids in mitochondria seeking for energy and counteracting ROS. Perhaps a longer stimulation or a higher dose of sTGF-β1 or EVs is required to observe further metabolic alterations associated to cancer in normal fibroblasts. Nonetheless, this data demonstrates that metabolic alterations are related to a higher activity of mitochondria, yet the specific role of cancer-associated EVs and the metabolic mechanisms in stromal differentiation and shift towards its reactive state remain unclear.

5.5.   Conclusions

The phenotype of cancer-associated stroma is characteristic and diverge from healthy stroma at both transcriptional and proteomic level. In this manuscript, we discussed metabolic differences measured in patient-matched normal and tumour fibroblasts from prostate adjacent regions. This approach has no precedents in literature. A multiplatform metabolomics analysis of these fibroblasts determined an increased metabolic activity of CAFs. Also, many lipid classes were altered, indicating an enhanced lipogenic metabolism. Lipid reservoir species as cholesteryl ester were measured in CAFs together with building block compounds as lysophosphatidylcholines. Furthermore, alterations in GSH system and oxidised fatty acids suggests the involvement of mitochondria in CAF distinct metabolism. Herewith, this integrated study points out several pathways that may be relevant during fibroblast differentiation.

Previous studies demonstrated the treatment with TGF-β1 or TGF-β1-EVs provoke a response in normal fibroblasts towards myofibroblasts. Thence, we assessed whether EVs containing TGF-β1 or soluble TGF-β1 could trigger a metabolic response in normal fibroblasts. Often, in such differentiation processes, cells desperately look for new energy sources and building blocks in order to sustain growth. According to our metabolomics and Seahorse data, the alternative pathway to obtain energy is not glycolysis. Moreover, Seahorse data shows that basal respiration associated to mitochondria was increased in CAFs so as normal fibroblasts upon TGF-β1 or EV stimulation. In conclusion, one can propose the alteration in metabolic abundances of tumour-associated fibroblasts is driven by an oxygen-dependent metabolism associated to mitochondria. The metabolic status of normal fibroblasts is altered upon EV (and TGF-β1) stimulation and it is associated to mitochondria metabolism. However, the specific mechanisms utilised to trigger different metabolic responses remains undefined.

DISCUSSION

EVs participate in many physiological communication events. The understanding of their biochemistry and physiological roles is paramount for unravelling biological processes such as disease progression, physiological responses or environmental regulation. EVs are also remarkably heterogeneous which often complicates their accurate analysis by bulk ensemble studies that often misrepresent their functionalities. In this line, individually analysed EVs provide excellent prospects for future basic and practical research with a view to halt disease progression and understand interaction processes.

In order to exploit the full potential of SVA techniques, biological validation and reproducibility must meet the demands of clinical applications. Each technique has its specific advantages and disadvantages, and the exact choice of the method of analysis depends on the research question, the nature of the samples and EV characteristics. These techniques still need to improve their quantitative detection power, lower their cost and increase their reliability, resolution and throughput. Nonetheless, Some of these techniques can directly provide information on vesicle surface, content, size and shape while other may require an upstream physicochemical characterisation of the selected EV subpopulations to conduct surface profiling, monitor the expression of biomarkers and quantify them in body fluids. Twelve different methods have been discussed in detail in this thesis (Table 5 in Chapter 1). Some utilise labelling techniques to visualise the EVs, and others work as label-free systems. Importantly, EV preparations often produce weak signals, which in SVA approaches is overcome by supportive labelling techniques.

The recent breakthroughs in SVA techniques help to tackle the intrinsic limitations of ensemble EV measurements and analyses. Documented reports demonstrated advances in characterization of EVs (Table 6), including EV heterogeneity and phenotyping of PCa-derived EVs, visualising internalization pathways and understanding the role of EVs in the interaction between cells (Table 7). Also, a wide range of biomarkers have been successfully identified and validated (Table 8), demonstrating their capacity to discover new, specific and effective biomarkers in EVs that could have been missed by ensemble methods. The remarkable advances in single-vesicle imaging and analysis promise to deliver rapid and effective practical applications (Table 9), since microfluidic systems need only very small, microliter-scale sample volumes. These innovative technologies and affiliated research pave the way towards unravelling the biological significance of EVs and using minimally invasive systems to diagnose diseases for which EVs serve as prognostic biomarkers[60,73,200].

Up-to-date, there is an overreliance on the concentration of PSA in blood to diagnose PCa, notoriously problematic for its poor specificity[197]. Often, patients undergoing biopsies do not verify the presence of the disease and, hence, do not require treatment. This lack of diagnostic power has been confirmed in a large urinary cohort presented in this thesis (Figure 14). An increase in PSA may indicate physiopathological changes in the prostate; however, it is not a good classifier of PCa patient groups according to a binary classification - ROC - system. Actually, the poor prognosis of PCa is one of the major challenges to design appropriate treatments and extend patient's lifetime and life quality. The appearance of novel biomarkers sources such as EVs combined with cutting-edge analytical methodologies can provide alternatives to discover disease biomarkers. A good example is the PSA-

independent tool released by Exosome Dx, which combines PCA3, ERG and SPDEF gene expression in uEVs to predict the likelihood of high grade PCa occurrence[408]. In this line, the bioinformatics analysis performed aimed to describe potential candidates associated to EVs to discriminate between patient groups. EV dataset derived from hundreds of studies were utilised to determine which biomarker candidates could be associated to EVs. Besides, EV-associated candidates were further filtered using CANCERTOOL, which compiles several transcriptomic analyses of prostate primary samples. In this way, several markers holding a potential to classify PCa patients and that could be present in EVs were identified (Table 11). In order to test the diagnostic power in patient urinary samples, qPCR probes were designed to screen these EV-associated mRNA targets. Unfortunately, no validation of candidates could be provided. One could argue that specific mRNAs found in PCa primary samples would not necessary be present in EV samples. Possibly, this is the reason no EV-associated biomarkers could be measured in urine samples. Perhaps an increment in reliability and sensibility of quantification could lead to the detection of these mRNAs so they can be further tested as biomarkers. The use of ddPCR or TaqMan quenching approach may enable the detection of transcripts in urinary EVs.

Indeed, a population of EVs as a population is very heterogeneous and they have many origins once present in a biofluid. These subpopulations could have specific functions or several subpopulations might perform the same task as an amalgam. In order to study the effect of a heterogeneous EV population in a biological model, ensemble averaging approaches such as *omics*, are still relevant to study physiological processes in biological models triggered by EVs. To note, these strategies are pertinent when the source of EVs is not a limitation. Metabolome and metabolism usually represent the first set of physiological responses upon an external stimulus. Biological systems often react with metabolic changes without any apparent changes in their genome, transcriptome or proteome. In order to study a relevant metabolic pathway in PCa, a fast and simple hrLCMS methodology able to detect and quantify key metabolites of the steroid hormones biosynthesis in several biological matrices has been optimised. The importance of steroid hormones in diseases such as PCa and other steroid-dependent diseases spotlights this assay as a powerful tool to study their role in the development and progression of such diseases. In brief, this method identifies and quantifies several steroid classes including corticoids, androgens and metabolic intermediates in a high-throughput method of 6 min.

Steroid hormones are pivotal in early stages of PCa progression since they are the main signal transmitters to overexpress specific oncogenes. All steroid hormones are primarily derived from cholesterol, which provides the sterane ring structure shared by all these compounds (Figure 20). Subtle chemical differences, unique to each steroid hormone, significantly complicate the separation of such structurally similar molecules. Furthermore, the structure of steroids and position of functional groups determine their preferred ionisation mode and efficiency[415,421]. In order to increase signal intensity, the MS could be operated in enhanced duty cycle (EDC) mode; this is a more appropriate approach in targeted analyses, where the analyte empirical formulas are known. In this strategy, MS signals of a given retention time are measured in separate scan functions to enhance the *m/z* of the selected analyte. Therefore, EDC mode is an option to consider for those samples in which analytes S/N ratio do

not permit their identification or quantification. Basically, this approach was the one utilised in Chapter 4 so labelled steroid hormones could be easily detected.

An hrLCMS method is usually evaluated in terms of efficiency, accuracy and sensitivity of the measurement. The process efficiency is a combination of recovery efficiencies and matrix effect of each metabolite[434], and the sensitivity is evaluated with the LOD and LOQ of each metabolite. Different studies identifying and quantifying steroid compounds in biological matrices report a wide range of efficiency recoveries. For example, in PCa cell cultures a recovery range of 54.7% to 78.1% was reported[413]. In this assay, with recoveries ranging from approximately 75% to 125%, a cell culture as matrix does not impair the extraction of steroid metabolites. To note, it is not strange to recovery efficiencies over 100% in some cases[414–416]. An explanation for this phenomenon might be metabolites can be either free in solution or tethered to other molecules such as membrane lipids during the extraction process. Moreover, their ionisation efficiencies in the mass spectrometer may vary. For this reason, the organic and aqueous phase recoveries are not adding up 100% in this assay. Existing quantitation methods for steroid hormone compound have a wide span of LOQ, ranging from 0.002 to 10 ng per mL. However, it is highly dependent on the analysed matrix, i.e. a urine matrix shows a range from 0.002 to 0.2 ng per mL[415,416], whilst cell matrices display a higher LOQ up to 10 ng per mL[413]. This suggests the matrix effect also depends on the specific matrix where the metabolites are contained. In this assay, the reported LOQ range lays between 0.50 and 50nM (equivalent to 0.14 and 14.42 ng per mL) in solution, similar to other documented studies. In summary, the assay is very convenient since all metabolites (except cortisol) are recovered specifically in one fraction. Also, in terms of sensitivity and accuracy of the measurement is in the range of methodologies found in literature.

Since the first urinary metabolomics attempts to analyse urinary samples and other biofluids, several methodologies have been developed during the last years[416–418]. Nevertheless, none of the reported methodologies was optimal to assess steroids in EV sample preparations, tissues or body fluids in a fast and simple manner. Up to date, many studies have shown metabolomics in EVs[60,417,438], but none of them has reported the detection of steroid hormones in a targeted approach. Importantly, we have been able to quantify steroid hormones in urine samples and derived uEV in a fast and simple manner. In urine samples, the assay was able to quantify several steroid hormone-related metabolites including cortisol, androstenedione, DHEAS, aldosterone, androsterone sulphate and cholesterol. Those metabolites were analysed in a specific cohort of urines to evaluate whether their metabolic signature could define PCa status. Steroid hormone levels were not able to discriminate between PCa and BPH urines. However, when considering PCa groups there are some significant differences, which could describe a possible signature. Yet, sample groups become rather small in such analysis. This highlights the importance of analysing a larger cohort to obtain significant results non-dependent of a unique high concentrated sample. Furthermore, this study was performed with urine samples collected prior PCa diagnosis. The fact urines were collected at first visit makes the outcome highly valuable to predict the classification of an *a priori* unknown sample. However, it is also a limitation since the analysed samples might not be fully representative of the PCa groups.

The relevance of metabolomics approaches beyond the discovery of biomarkers and the metabolic profiling of tissues in PCa is in the spotlight. Many efforts have been done in describing metabolic differences between the epithelium and stroma but also between those tissues in different progression stages of the disease. By using either fluorophore- or isotope-labelled cholesterol, the transfer of metabolites in cell-to-cell communication events mediated by EVs was evaluated. On one hand, fluorescently-labelled cholesterol showed its presence in mitochondria where it can be further metabolised into pregnenolone (Figure 32, Figure 33 and Figure 34). This suggests that cholesterol carried by EVs can potentially be metabolised into other steroid hormones relevant to PCa progression. On the other hand, isotope labelled cholesterol associated to EVs was uptake by cancer and prostatic stroma cells. The fact only a small percentage of cholesterol was labelled – less than 0.1% of total cholesterol in recipient cells – indicates that either D_6-cholesterol has been already metabolised, the treatment was not sufficient or cholesterol could not be replaced in the recipient cell. Besides the detection of labelled cholesterol in recipient cells, its usage to metabolise other steroid could not be demonstrated.

Cholesterol is essentially transported and delivered by (apo)lipoparticles via bloodstream. Lipids (and cholesterol) are processed in the liver, the organ in charge of manufacturing these lipid-containing particles for further delivering to other tissues. Therefore, one would expect that only liver-derived models exhibit lipid reservoirs and majorly expel lipid-containing particles instead of EVs. Indeed, the main limitation of these transfer assays are the possible presence of lipid-containing particles in EV preparations because EV isolation techniques are mainly based on size or precipitation parameters and, others based on protein markers or other parameters are not well-standardised yet. For this reason, we purified EVs with SEC. EV preparations are cleaner than using other techniques such as ultracentrifugation, the main contamination we expect to find is of VLDLs as they are similar to EVs. Nonetheless, the cell lines utilised to produce EVs are human excised prostate tissues and they have not been reported to produce any lipoparticles. Also, apolipoproteins characteristic of VLDL particles were not reported in western blots of EV preparations.

In further transference assays, one attempted to demonstrate whether EVs could be transferring biologically relevant functionalities. The main purpose was to establish a functional interaction of EVs with recipient cells by studying the capability of EVs to sustain androgen-dependent oncogenicity. One would like to discuss the fact EVs could sustain oncogenic growth of PCa cell lines. Hence, a recipient cell line was incubated with and without androgens to confirm its oncogenic dependency before testing the effect of EVs. Androgen-dependent LNCaP cell line was established as an appropriate model of study. Several oncogenic genes were proposed as markers of androgen-associated oncogenicity, but only *HOXC6* and *KLK3* seemed to respond to androgen treatments. PSA is expressed by *KLK3* and it is tightly associated to androgen signalling hence, *KLK3* expression was the most relevant to track in these assays. Treatment with EVs could not sustain an oncogenic phenotype over time; however, it slightly neutralised the loss of oncogenicity (Figure 39). This transfer of functionalities has been evaluated in literature[115,116,519–521] but there are no reports showing actual transference of oncogenic signalling. Since the actual composition of EVs driving oncogenic phenotype have not been assessed, a mechanistic explanation is missing.

The onset of a reactive stroma and the emergence of CAF phenotypes, is a feature comprehensively discussed and, their interaction with epithelium during PCa progression is rising scientific interest [115,116,480,494,507]. Previous reports using a set of matched-patient stroma samples confirmed the existence of myofibroblast-like cells within diseased regions of the tissue, by positive staining of both α-SMA, and vimentin, and lack of expression of desmin or the cytokeratins[116,480,494]. In Chapter 5, metabolomics data comparing healthy and disease-associated stromal cells from the same samples is presented. Elevated levels of several metabolic classes in cancer-associated stromal fibroblasts were detected, including cholesteryl esters and other lipids. This has been already suggested in other reports[33,502]. Interestingly, uptake from circulating lipids has been reported[510,511] as well as lipid translocation from adipocytes[512]. As they oxidise lipids and accumulate cholesteryl esters[33], one can suggest supportive cancer fibroblasts might be either fuelling themselves with these compounds, or fuel nearby cancer cells or, both. Interestingly, myofibroblastic stroma seem to mobilise *de novo* free fatty acids as energy source; oxidised fatty acid species (as HEPE) were elevated in cancer-associated fibroblasts. Altogether indicates a consumption of newly built lipids to fuel themselves while building up cholesteryl esters reservoirs, which are easily transported and readily available to transfer it between cells.

A limitation of this study has been the arguably low number of samples available for metabolomics. In contrast, the collection of donor matched-paired samples reflecting healthy and disease tissue-regions of stroma are relevant and not present in literature. This type of data draws relevant conclusions of processes and alterations occurring in each patient. Even so, the outcome of this study described metabolic differences with sparse impact in the entire metabolome. Once combined with proteomics data from the exact same set of samples, the outcome acquired a higher relevance in determining important metabolic processes driving myofibroblast differentiation. The integration of significant proteins and metabolites differentially measured in healthy and cancer fibroblasts confirmed a major alteration in lipid metabolism. Although lipids can participate in signalling processes or be used as building blocks, in this study metabolic alterations point out fuelling or energy storage processes.

Finally, the assessment of metabolic alterations upon sTGF-β or EV-associated TGF-β treatments by Seahorse stress assays was approached. Even considering the limitation of such assays, where O_2 consumption and pH acidification are recorded over time, the glycolysis rate and oxidative mitochondrial activity of cells can be assessed. Only basal respiration, in the mitochondrial stress assay, was distinctive comparing between cancer and healthy fibroblasts. Moreover, the treatment with sTGF-β and EVs containing TGF-β showed a similar outcome. Perhaps a longer stimulation or a higher dose of sTGF-β or EVs is required in order to observe further alterations associated to cancer development in stromal fibroblasts. In consequence, the specific role of cancer-associated EVs and the metabolic mechanisms in stromal differentiation and shift towards its reactive state remain unclear.
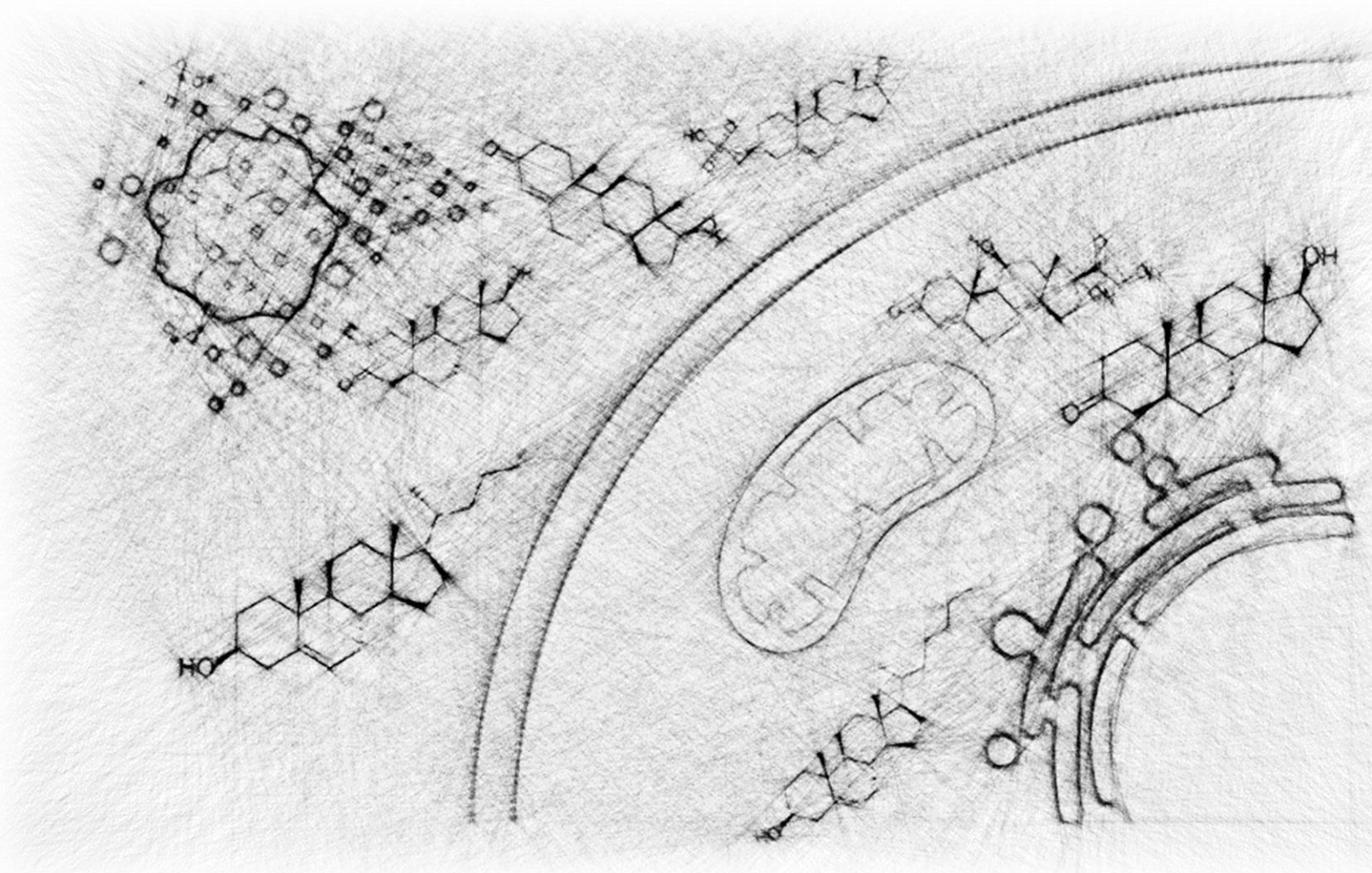
CONCLUSIONS

Extracellular vesicles are lipid bilayer vessels that contain a very heterogeneous cargo anchored either to the membrane or in the luminar space. In this thesis, the manner they participate in cell-to-cell communication events has been extensively discussed. The complete understanding of their biochemistry and physiological roles is yet a challenge in the field due to technical limitations. The work present provides an overview of the state-of-the-art of extracellular vesicle research as well as several attempts to describe their contribution to cell metabolism and prostate cancer progression. The general conclusions are:

I.   Current single vesicle approaches and methodological advances provide high-resolution phenotypical characterisation of EVs. However, they might not be appropriate for carrying out further functional studies.

II.   Actual biomarkers - PSA - of prostate cancer do not classify neither diagnose patients appropriately. Extracellular vesicles contain specific mRNAs which hold the potential to be used as biomarker of prostate cancer disease. According to scientific databases, there are 32 mRNA candidates for prostate cancer early stage progression. However, the attempts to quantify and use them as biomarkers of prostate cancer in a urinary cohort were frustrated.

III.   A fast and sensitive hrLCMS-based assay can quantify a panel of steroid hormone compounds to perform functional studies in several prostate cancer -related matrices. The assay is capable of measuring EV-associated metabolites in body fluids, tissues and biological recipient models.

IV.   Extracellular vesicle s demonstrated the transfer of cholesterol to recipient cells in a dual tagging approach. Moreover, extracellular vesicle-associated cholesterol is transported partially to mitochondria where can be used for further metabolisation.

V.   Extracellular vesicle s provoked an effect in the androgen-dependent LNCaP cell line by neutralising the loss of oncogenic phenotype. Although a mechanistic explanation is yet to be described, it suggests a functional role of extracellular vesicles in cancer progression.

VI.   Metabolomics approaches can also define tissue or cell status in prostatic stroma. Cancer-associated fibroblasts are more active metabolically than normal primary fibroblasts. The accumulation of lipid reservoir species and building block compounds suggests that lipogenic metabolism plays a central role.

VII.   The integration of metabolomics with other *omic* approaches generates a stronger and better understanding of mechanisms underlying cell rewiring.

VIII.   Extracellular vesicles induce cancer-associated phenotype to normal fibroblasts. The alteration in the metabolomics profile of tumour-associated stromal fibroblasts is driven by oxygen-dependent metabolism.
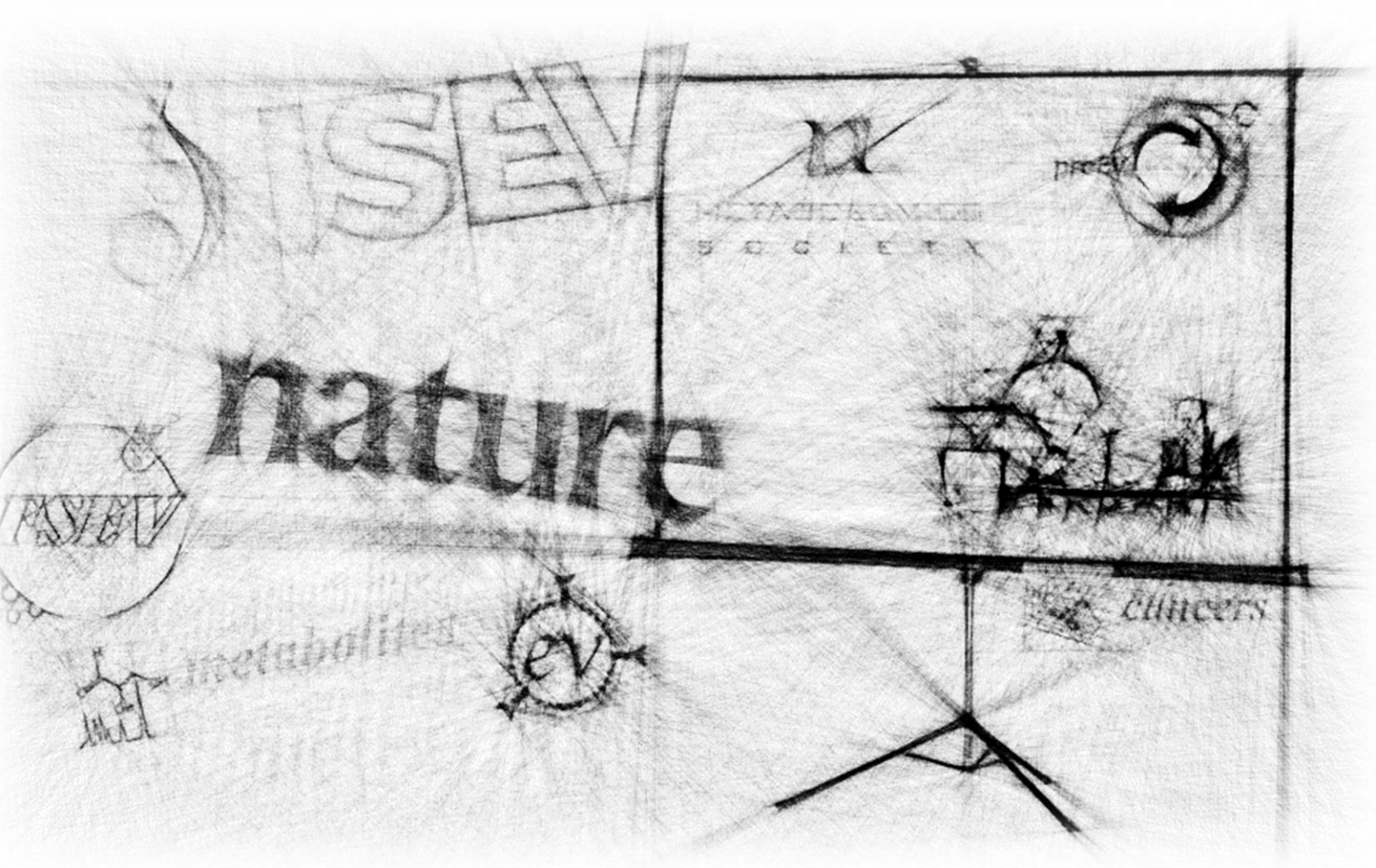
PUBLICATIONS AND CONGRESSES

Publications

Bordanaba-Florit, G., Royo, F., Kruglik, S.G. *et al.* Using single-vesicle technologies to unravel the heterogeneity of extracellular vesicles. *Nat. Protoc.* **16**, 3163–3185 (2021). https://doi.org/10.1038/s41596-021-00551-z

Bordanaba-Florit, G.; Liempd, S.v.; Cabrera, D.; Royo, F.; Falcón-Pérez, J.M. Simultaneous Quantification of Steroid Hormones Using hrLC-MS in Endocrine Tissues of Male Rats and Human Samples. *Metabolites* **2022**, *12*, 714. https://doi.org/10.3390/metabo12080714

Bordanaba-Florit, G.; Madarieta, I.; Olalde, B.; Falcón-Pérez, J.M.; Royo, F. 3D Cell Cultures as Prospective Models to Study Extracellular Vesicles in Cancer. *Cancers* **2021**, *13*, 307. https://doi.org/10.3390/cancers13020307

Bordanaba-Florit, G., Royo, F.,Albóniga, O. E. *et al.* Integration of proteomics and metabolomics reveals metabolic alterations of prostate cancer fibroblasts from patient's stroma samples. *Biochim. Biophys. Acta, Mol. Basis Dis.* **XXX**, XXXX–XXXX (XXXX). *Under revision*

Congresses and Symposiums

proEVLifeCycle Webinar 'Model for PCa research' (28 August, 2020), Virtual.

Bordanaba-Florit, G. *2D model selection: Role of EVs in metabolic signalling during prostate cancer progression.* **Oral talk invitation.**

ISEV 2021 Annual Meeting (18-21 May, 2021), Virtual.

Bordanaba-Florit, G., van Liempd, S., Cabrera, D., Royo, F. and Falcón-Pérez, J. M. *Identification and quantification of key metabolites of the steroid hormone biosynthesis pathway in extracellular vesicles.* **Poster**.

EV Club Online (13 October, 2021), Virtual Symposium.

Bordanaba-Florit, G. and Falcón-Pérez, J. M. *Using single-vesicle technologies to unravel the heterogeneity of extracellular vesicles.* **Oral talk invitation.**

uEV 2022 (15-16 February, 2022), Virtual Symposium.

Bordanaba-Florit, G., van Liempd, S., Cabrera, D., Royo, F. and Falcón-Pérez, J. M. *Simultaneous quantification of core members of the steroid synthesis pathway in endocrine tissues and biofluids of male rats and uEVs.* **Poster**.

ISEV 2022 Annual Meeting (25-29 May, 2022), Lyon, France.

Assistance and presentation of another poster.

METABOLOMICS 2022 (19-23 June, 2022), Valencia, Spain.

Bordanaba-Florit, G., van Liempd, S., Cabrera, D., Royo, F. and Falcón-Pérez, J. M. *Simultaneous quantification of core members of the steroid synthesis pathway in endocrine tissues and biofluids of male rats and human*. **Poster.**

5ème Congrès FSEV 2022 (19-21 October, 2022), París, France.

Bordanaba-Florit, G., van Liempd, S., Cabrera, D., Royo, F. and Falcón-Pérez, J. M. *A hrLC-MS based assay to study the metabolic role of extracellular vesicles in prostate cancer progression*. **Oral talk.**

ISEV 2023 Annual Meeting (25-29 May, 2023), Seattle, USA

Bordanaba-Florit, G., van Liempd, S., Cabrera, D., Couty, M., Albóniga, O. E., Royo, F., van Niel, G. and Falcón-Pérez, J. M. *The use of labelled-cholesterol demonstrates effective EV-mediated metabolite transfer in a prostate cancer model*. **Oral talk.**

Farmaforum 2023: Innovaforum (20-21 September, 2023), Madrid, SpainBordanaba-Florit, G., van Liempd, S., Cabrera, D., Royo, F. and Falcón-Pérez, J. M. *Simultaneous quantification of core members of the steroid synthesis pathway in endocrine tissues and biofluids of male rats and human*. **Poster.**

Awards

EMBO Scientific Exchange Grant (number 9685) *Fellowship programme* "Extracellular vesicles as surrogated biomarkers of prostate cancer metabolism", laboratory of Dr. Guillaume Van Niel (Endosomal Dynamics in Neuropathies, INSERM, 75014 Paris, France). **International stay (September-November, 2022).**
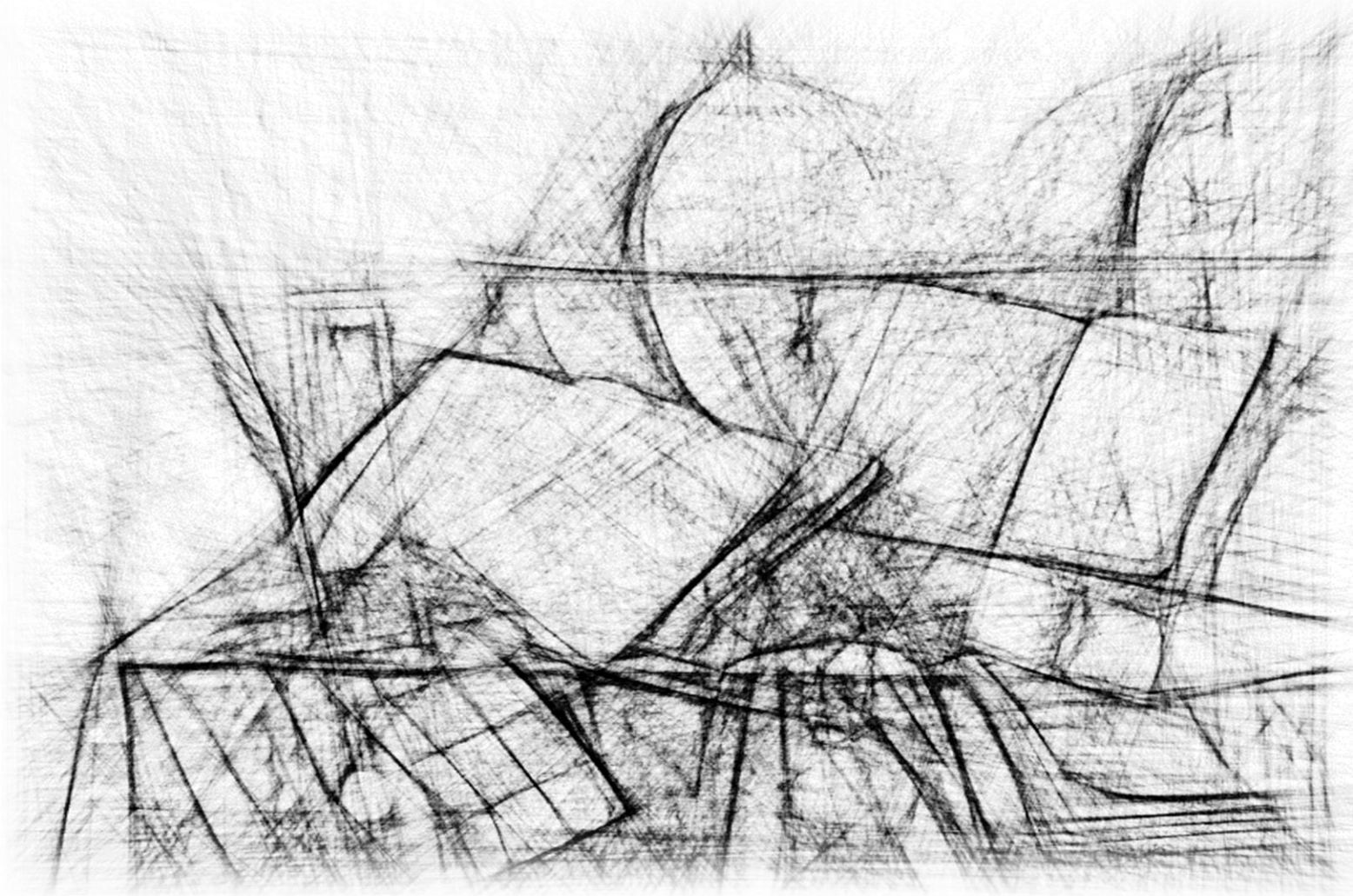
RESOURCES

List of Bibliography

1. Freedland, S. J. Screening, risk assessment, and the approach to therapy in patients with prostate cancer. *Cancer* vol. 117 1123–1135 Preprint at https://doi.org/10.1002/cncr.25477 (2011).
2. Gandaglia, G. *et al.* Distribution of metastatic sites in patients with prostate cancer: A population-based analysis. *Prostate* **74**, 210–216 (2014).
3. Saunders, J. B. de C. M. & O'Malley, C. D. *The Illustrations from the Works of Andreas Vesalius of Brussels with Annotations and Translations, a Discussion of the Plates and Their Background, Authorship and Influence, and a Biographical Sketch of Vesalius.* vol. 56 (The World Publishing Company, Cleveland, 1973).
4. Shappell, S. B. *et al.* Prostate Pathology of Genetically Engineered Mice: Definitions and Classification. The Consensus Report from the Bar Harbor Meeting of the Mouse Models of Human Cancer Consortium Prostate Pathology Committee. *Cancer Res* **64**, 2270–2305 (2004).
5. Aaron, L. T., Franco, O. E. & Hayward, S. W. Review of Prostate Anatomy and Embryology and the Etiology of Benign Prostatic Hyperplasia. *Urologic Clinics of North America* vol. 43 279–288 Preprint at https://doi.org/10.1016/j.ucl.2016.04.012 (2016).
6. Verze, P., Cai, T. & Lorenzetti, S. The role of the prostate in male fertility, health and disease. *Nature Reviews Urology* vol. 13 379–386 Preprint at https://doi.org/10.1038/nrurol.2016.89 (2016).
7. Hammerich, K. H., Ayala, G. E. & Wheeler, T. M. Anatomy of the prostate gland and surgical pathology of prostate cancer. in *Prostate Cancer* 1–14 (Cambridge University Press, 2008). doi:10.1017/CBO9780511551994.003.
8. Nieto, C. M., Rider, L. C. & Cramer, S. D. Influence of stromal-epithelial interactions on androgen action. *Endocrine-Related Cancer* vol. 21 Preprint at https://doi.org/10.1530/ERC-14-0138 (2014).
9. Barron, D. A. & Rowley, D. R. The reactive stroma microenvironment and prostate cancer progression. *Endocr Relat Cancer* **19**, 187–204 (2012).
10. El-Alfy, M., Pelletier, G., Hermo, L. S. & Labrie, F. Unique features of the basal cells of human prostate epithelium. *Microsc Res Tech* **51**, 436–446 (2000).
11. McNeal, J. E., Redwine, E. A., Freiha, F. S. & Stamey, T. A. Zonal Distribution of Prostatic Adenocarcinoma. *Am J Surg Pathol* **12**, 897–906 (1988).
12. Villers, A., McNeal, J. E., Freiha, F. S. & Stamey, T. A. Multiple cancers in the prostate. Morphologic features of clinically recognized versus incidental tumors. *Cancer* **70**, 2313–2318 (1992).
13. Burke, H. B. & Henson, D. E. Criteria for prognostic factors and for an enhanced prognostic system. *Cancer* **72**, 3131–3135 (1993).
14. Greene, F. L. *et al. AJCC Cancer Staging Manual.* (Springer, Chicago, 2002).
15. Oesterling, J. E., Brendler, C. B., Epstein, J. I., Kimball, A. W. & Walsh, P. C. Correlation of Clinical Stage, Serum Prostatic Acid Phosphatase and Preoperative Gleason Grade with Final Pathological Stage in 275 Patients with Clinically Localized Adenocarcinoma of the Prostate. *Journal of Urology* **138**, 92–98 (1987).
16. Gleason, D. Atypical hyperplasia, benign hyperplasia, and well-differentiated adenocarcinoma of the prostate. *Am J Surg Pathol* **9**, 53–67 (1985).
17. Arora, R. *et al.* Heterogeneity of Gleason grade in multifocal adenocarcinoma of the prostate. *Cancer* **100**, 2362–2366 (2004).
18. Mikuz, G. Histologic Classification of Prostate Cancer. *Analytical and Quantitative Cytopathology and Histopatholog* **37**, 39–47 (2015).
19. Cardoso, H. J. *et al.* Revisiting prostate cancer metabolism: From metabolites to disease and therapy. *Medicinal Research Reviews* vol. 41 1499–1538 Preprint at https://doi.org/10.1002/med.21766 (2021).
20. Costello, L. C. & Franklin, R. B. Concepts of citrate production and secretion by prostate 1. Metabolic relationships. *Prostate* **18**, 25–46 (1991).
21. Cooper, J. F. & Farid, I. The Role of Citric Acid in the Physiology of the Prostate: 3. Lactate/Citrate Ratios in Benign and Malignant Prostatic Homogenates as an Index of Prostatic Malignancy. *Journal of Urology* **92**, 533–536 (1964).
22. Cutruzzolà, F. *et al.* Glucose metabolism in the progression of prostate cancer. *Front Physiol* **8**, (2017).
23. Feldman, B. J. & Feldman, D. The development of androgen-independent prostate cancer. *Nat Rev Cancer* **1**, 34–45 (2001).
24. J Akhenblit, P. & D Pagel, M. Recent Advances in Targeting Tumor Energy Metabolism with Tumor Acidosis as a Biomarker of Drug Efficacy. *J Cancer Sci Ther* **08**, (2016).
25. Twum-Ampofo, J., Fu, D.-X., Passaniti, A., Hussain, A. & Siddiqui, M. M. Metabolic targets for potential prostate cancer therapeutics. *Curr Opin Oncol* **28**, 241–247 (2016).

26. Daye, D. & Wellen, K. E. Metabolic reprogramming in cancer: Unraveling the role of glutamine in tumorigenesis. *Semin Cell Dev Biol* **23**, 362–369 (2012).

27. Keshet, R., Szlosarek, P., Carracedo, A. & Erez, A. Rewiring urea cycle metabolism in cancer to support anabolism. *Nat Rev Cancer* **18**, 634–645 (2018).

28. Zabala-Letona, A. *et al.* MTORC1-dependent AMD1 regulation sustains polyamine metabolism in prostate cancer. *Nature* **547**, 109–113 (2017).

29. Tousignant, K. D. *et al.* Lipid uptake is an androgen-enhanced lipid supply pathway associated with prostate cancer disease progression and bone metastasis. *Molecular Cancer Research* **17**, 1166–1179 (2019).

30. Balaban, S. *et al.* Extracellular fatty acids are the major contributor to lipid synthesis in prostate cancer. *Molecular Cancer Research* **17**, 949–962 (2019).

31. Liu, Y. Fatty acid oxidation is a dominant bioenergetic pathway in prostate cancer. *Prostate Cancer Prostatic Dis* **9**, 230–234 (2006).

32. Giskeødegård, G. F. *et al.* Metabolic markers in blood can separate prostate cancer from benign prostatic hyperplasia. *Br J Cancer* **113**, 1712–1719 (2015).

33. Yue, S. *et al.* Cholesteryl Ester Accumulation Induced by PTEN Loss and PI3K/AKT Activation Underlies Human Prostate Cancer Aggressiveness. *Cell Metab* **19**, 393–406 (2014).

34. Pandey, M., Cuddihy, G., Gordon, J. A., Cox, M. E. & Wasan, K. M. Inhibition of scavenger receptor class b type 1 (Sr-b1) expression and activity as a potential novel target to disrupt cholesterol availability in castration-resistant prostate cancer. *Pharmaceutics* **13**, (2021).

35. Carvalho, T. MA., Cardoso, H. J., Figueira, M. I., Vaz, C. V. & Socorro, S. The peculiarities of cancer cell metabolism: A route to metastasization and a target for therapy. *Eur J Med Chem* **171**, 343–363 (2019).

36. Romero Otero, J., Garcia Gomez, B., Campos Juanatey, F. & Touijer, K. A. Prostate cancer biomarkers: An update. *Urologic Oncology: Seminars and Original Investigations* **32**, 252–260 (2014).

37. De Berardinis, R. J. & Chandel, N. S. Fundamentals of cancer metabolism. *Science Advances* vol. 2 Preprint at https://doi.org/10.1126/sciadv.1600200 (2016).

38. Wilson, J. D., Griffin, J. E., Leshin, M. & George, F. W. *Role of Gonadal Hormones in Development of the Sexual Phenotypes. Hum Genet* vol. 58 (1981).

39. Lonergan, P. & Tindall, D. Androgen receptor signaling in prostate cancer development and progression. *J Carcinog* **10**, (2011).

40. Miller, W. L. & Auchus, R. J. The molecular biology, biochemistry, and physiology of human steroidogenesis and its disorders. *Endocr Rev* **32**, 81–151 (2011).

41. Kanehisa, M. & Goto, S. KEGG: Kyoto Encyclopedia of Genes and Genomes. *Nucleic Acids Res* **28**, 27–30 (2000).

42. Kanehisa, M., Furumichi, M., Sato, Y., Ishiguro-Watanabe, M. & Tanabe, M. KEGG: Integrating viruses and cellular organisms. *Nucleic Acids Res* **49**, D545–D551 (2021).

43. Bereshchenko, O., Bruscoli, S. & Riccardi, C. Glucocorticoids, sex hormones, and immunity. *Front Immunol* **9**, 1–10 (2018).

44. Foster, P. A. & Mueller, J. W. Insights into steroid sulfation and desulfation pathways. *J Mol Endocrinol* **61**, T271–T283 (2018).

45. Langford, R., Hurrion, E. & Dawson, P. A. Genetics and pathophysiology of mammalian sulfate biology. *Journal of Genetics and Genomics* **44**, 7–20 (2017).

46. Meng, Y., Heybrock, S., Neculai, D. & Saftig, P. Cholesterol Handling in Lysosomes and Beyond. *Trends in Cell Biology* vol. 30 452–466 Preprint at https://doi.org/10.1016/j.tcb.2020.02.007 (2020).

47. Brown, M. S. & Goldstein, J. L. *A Receptor-Mediated Pathway for Cholesterol Homeostasis. Source: Science, New Series* vol. 232 (1986).

48. Eden, E. R. *et al.* Annexin A1 Tethers Membrane Contact Sites that Mediate ER to Endosome Cholesterol Transport. *Dev Cell* **37**, 473–483 (2016).

49. Horenkamp, F. A., Valverde, D. P., Nunnari, J. & Reinisch, K. M. Molecular basis for sterol transport by St ART -like lipid transfer domains . *EMBO J* **37**, (2018).

50. Patel, R. *et al.* Sprouty2 loss-induced IL 6 drives castration-resistant prostate cancer through scavenger receptor B1 . *EMBO Mol Med* **10**, (2018).

51. Cai, C. & Balk, S. P. Intratumoral androgen biosynthesis in prostate cancer pathogenesis and response to therapy. *Endocrine-Related Cancer* vol. 18 Preprint at https://doi.org/10.1530/ERC-10-0339 (2011).

52. Pfrieger, F. & Vitale, N. Cholesterol and the journey of extracellular vesicles. *J Lipid Res* **59**, (2018).

53. Zaborowski, M. P., Balaj, L., Breakefield, X. O. & Lai, C. P. Extracellular Vesicles: Composition, Biological Relevance, and Methods of Study. *BioScience* vol. 65 783–797 Preprint at https://doi.org/10.1093/biosci/biv084 (2015).

54. Marzan, A. L., Nedeva, C. & Mathivanan, S. Chapter 15 Extracellular Vesicles in Metabolism and Metabolic Diseases. in *Subcellular Biochemistry* vol. 97 393–410 (2021).

55. Mleczko, J. E. *et al.* Extracellular vesicles released by steatotic hepatocytes alter adipocyte metabolism. *Journal of Extracellular Biology* **1**, (2022).

56. Lopes-Rodrigues, V. *et al.* Identification of the metabolic alterations associated with the multidrug resistant phenotype in cancer and their intercellular transfer mediated by extracellular vesicles. *Sci Rep* **7**, (2017).

57. Clement, E. *et al.* Adipocyte extracellular vesicles carry enzymes and fatty acids that stimulate mitochondrial metabolism and remodeling in tumor cells. *EMBO J* **39**, (2020).

58. Harmati, M., Bukva, M., Böröczky, T., Buzás, K. & Gyukity-Sebestyén, E. The role of the metabolite cargo of extracellular vesicles in tumor progression. *Cancer and Metastasis Reviews* vol. 40 1203–1221 Preprint at https://doi.org/10.1007/s10555-021-10014-2 (2021).

59. Skotland, T. *et al.* Molecular lipid species in urinary exosomes as potential prostate cancer biomarkers. *Eur J Cancer* **70**, 122–132 (2017).

60. Clos-Garcia, M. *et al.* Metabolic alterations in urine extracellular vesicles are associated to prostate cancer pathogenesis and progression. *J Extracell Vesicles* **7**, (2018).

61. Hooke, R. *Micrographia: Or, Some Physiological Descriptions of Minute Bodies Made by Magnifying Glasses. With Observations and Inquiries Thereupon*. (London, 1665).

62. Altmann, R. *Die Elementarorganismen Und Ihre Beziehungen Zu DenZellen*. (Verlag von Veit and Co., Leipzig, 1890).

63. Leeuwenhoek, A. van. *Opera Omnia, Seu Arcana Naturae Ope Exactissimorum Microscopiorum Detecta, Experimentis Variis Comprobata, Epistolis Ad Varios Illustres Viros*.

64. Wolf, P. The nature and significance of platelet products in human plasma. *Br J Haematol* **13**, 269–288 (1967).

65. Yáñez-Mó, M. *et al.* Biological properties of extracellular vesicles and their physiological functions. *J Extracell Vesicles* **4**, (2015).

66. Chiang, C. Y. & Chen, C. Toward characterizing extracellular vesicles at a single-particle level. *J Biomed Sci* **26**, 1–10 (2019).

67. Zhao, H. *et al.* Tumor microenvironment derived exosomes pleiotropically modulate cancer cell metabolism. *Elife* **5**, 1–27 (2016).

68. Van Niel, G., D'Angelo, G. & Raposo, G. Shedding light on the cell biology of extracellular vesicles. *Nat Rev Mol Cell Biol* **19**, 213–228 (2018).

69. Valadi, H. *et al.* Exosome-mediated transfer of mRNAs and microRNAs is a novel mechanism of genetic exchange between cells. *Nat Cell Biol* **9**, 654–659 (2007).

70. Nieuwland, R. & Sturk, A. Why do cells release vesicles? *Thromb Res* **125**, S49–S51 (2010).

71. Anderson, H. C., Mulhall, D. & Garimella, R. Role of extracellular membrane vesicles in the pathogenesis of various diseases, including cancer, renal diseases, atherosclerosis, and arthritis. *Laboratory investigation* **90**, 1549–1557 (2010).

72. Wiklander, O. P. B., Brennan, M., Lötvall, J., Breakefield, X. O. & Andaloussi, S. E. L. Advances in therapeutic applications of extracellular vesicles. *Sci Transl Med* **11**, 1–16 (2019).

73. An, T. *et al.* Exosomes serve as tumour markers for personalized diagnostics owing to their important role in cancer metastasis. *J Extracell Vesicles* **4**, (2015).

74. Becker, A. *et al.* Extracellular Vesicles in Cancer: Cell-to-Cell Mediators of Metastasis. *Cancer Cell* **30**, 836–848 (2016).

75. Théry, C. *et al.* Minimal information for studies of extracellular vesicles 2018 (MISEV2018): a position statement of the International Society for Extracellular Vesicles and update of the MISEV2014 guidelines. *J Extracell Vesicles* **7**, (2018).

76. Zhang, H. *et al.* Identification of distinct nanoparticles and subsets of extracellular vesicles by asymmetric-flow field-flow fractionation. *Nat Cell Biol* **20**, 332–343 (2018).

77. Mathieu, M., Martin-Jaular, L., Lavieu, G. & Théry, C. Specificities of secretion and uptake of exosomes and other extracellular vesicles for cell-to-cell communication. *Nat Cell Biol* **21**, 9–17 (2019).

78. Tai, Y. L., Chen, K. C., Hsieh, J. T. & Shen, T. L. Exosomes in cancer development and clinical applications. *Cancer Sci* **109**, 2364–2374 (2018).

79. Ni, Z. *et al.* Exosomes: roles and therapeutic potential in osteoarthritis. *Bone Res* **8**, (2020).

80. Foroutan, B. Personalized Medicine: A Review with Regard to Biomarkers. *J Bioequivalence Bioavailab* **07**, (2015).

81. Mayeux, R. Biomarkers: Potential Uses and Limitations. *The Journal of the American Society for Experimental NeuroTherapeutics* **1**, 182–188 (2004).

82. Théry, C., Zitvogel, L. & Amigorena, S. Exosomes: composition, biogenesis and function. *Nat Rev Immunol* **2**, 569–579 (2002).

83. Strimbu, K. & Tavel, J. A. What are biomarkers? *Curr Opin HIV AIDS* **5**, 463–466 (2010).

84. Eskra, J. N., Rabizadeh, D., Pavlovich, C. P., Catalona, W. J. & Luo, J. Approaches to urinary detection of prostate cancer. *Prostate Cancer and Prostatic Diseases* vol. 22 362–381 Preprint at https://doi.org/10.1038/s41391-019-0127-4 (2019).

85. Kdadra, M., Höckner, S., Leung, H., Kremer, W. & Schiffer, E. Metabolomics biomarkers of prostate cancer: A systematic review. *Diagnostics* **9**, (2019).

86. Ni, Z. *et al.* Exosomes: roles and therapeutic potential in osteoarthritis. *Bone Research* vol. 8 Preprint at https://doi.org/10.1038/s41413-020-0100-9 (2020).

87. Record, M., Silvente-Poirot, S., Poirot, M. & Wakelam, MichaelJ. O. Extracellular vesicles: lipids as key components of their biogenesis and functions. *J Lipid Res* **59**, 1316–1324 (2018).

88. Skotland, T., Hessvik, N. P., Sandvig, K. & Llorente, A. Exosomal lipid composition and the role of ether lipids and phosphoinositides in exosome biology. *J Lipid Res* **60**, 9–18 (2019).

89. Skotland, T., Sagini, K., Sandvig, K. & Llorente, A. An emerging focus on lipids in extracellular vesicles. *Adv Drug Deliv Rev* **159**, 308–321 (2020).

90. Villarroya-Beltri, C. *et al.* Sumoylated hnRNPA2B1 controls the sorting of miRNAs into exosomes through binding to specific motifs. *Nat Commun* **4**, 2980 (2013).

91. Dores, M. R. *et al.* ALIX binds a YPX3L motif of the GPCR PAR1 and mediates ubiquitin-independent ESCRT-III/MVB sorting. *Journal of Cell Biology* **197**, 407–419 (2012).

92. Anand, S. *et al.* Arrestin-Domain Containing Protein 1 (Arrdc1) Regulates the Protein Cargo and Release of Extracellular Vesicles. *Proteomics* **18**, (2018).

93. Moreno-Gonzalo, O., Fernandez-Delgado, I. & Sanchez-Madrid, F. Post-translational add-ons mark the path in exosomal protein sorting. *Cellular and Molecular Life Sciences* **75**, 1–19 (2018).

94. Trajkovic, K. *et al.* Ceramide Triggers Budding of Exosome Vesicles into Multivesicular Endosomes. *Science (1979)* **319**, 1244–1247 (2008).

95. Skotland, T., Sandvig, K. & Llorente, A. Lipids in exosomes: Current knowledge and the way forward. *Prog Lipid Res* **66**, 30–41 (2017).

96. Hannafon, B. & Ding, W.-Q. Intercellular Communication by Exosome-Derived microRNAs in Cancer. *Int J Mol Sci* **14**, 14240–14269 (2013).

97. Popa, S. J. & Stewart, S. E. Socially Distanced Intercellular Communication: Mechanisms for Extracellular Vesicle Cargo Delivery. in 179–209 (2021). doi:10.1007/978-3-030-67171-6_8.

98. Göran Ronquist, K. Extracellular vesicles and energy metabolism. *Clinica Chimica Acta* vol. 488 116–121 Preprint at https://doi.org/10.1016/j.cca.2018.10.044 (2019).

99. Dubois, L., Ronquist, K. (K). G., Ek, B., Ronquist, G. & Larsson, A. Proteomic Profiling of Detergent Resistant Membranes (Lipid Rafts) of Prostasomes. *Molecular & Cellular Proteomics* **14**, 3015–3022 (2015).

100. Ronquist, K. G. *et al.* Prostasomes from four different species are able to produce extracellular adenosine triphosphate (ATP). *Biochimica et Biophysica Acta (BBA) - General Subjects* **1830**, 4604–4610 (2013).

101. Kim, D. *et al.* EVpedia: an integrated database of high-throughput data for systemic analyses of extracellular vesicles. *J Extracell Vesicles* **2**, (2013).

102. Kalra, H. *et al.* Vesiclepedia: A Compendium for Extracellular Vesicles with Continuous Community Annotation. *PLoS Biol* **10**, 8–12 (2012).

103. Keerthikumar, S. *et al.* ExoCarta: A Web-Based Compendium of Exosomal Cargo. *J Mol Biol* **428**, 688–692 (2016).

104. Ronquist, K. G., Ek, B., Stavreus-Evers, A., Larsson, A. & Ronquist, G. Human prostasomes express glycolytic enzymes with capacity for ATP production. *American Journal of Physiology-Endocrinology and Metabolism* **304**, E576–E582 (2013).

105. Royo, F. *et al.* Hepatocyte-secreted extracellular vesicles modify blood metabolome and endothelial function by an arginase-dependent mechanism. *Sci Rep* **7**, 1–15 (2017).

106. Iraci, N. *et al.* Extracellular vesicles are independent metabolic units with asparaginase activity. *Nat Chem Biol* **13**, 951–955 (2017).

107. Fridman, E. S., Ginini, L. & Gil, Z. The Role of Extracellular Vesicles in Metabolic Reprogramming of the Tumor Microenvironment. *Cells* vol. 11 Preprint at https://doi.org/10.3390/cells11091433 (2022).

108. Lv, B., Zhu, W. & Feng, C. Coptisine Blocks Secretion of Exosomal circCCT3 from Cancer-Associated Fibroblasts to Reprogram Glucose Metabolism in Hepatocellular Carcinoma. *DNA Cell Biol* **39**, 2281–2288 (2020).

109. Li, Y., Zhao, Z., Liu, W. & Li, X. SNHG3 Functions as miRNA Sponge to Promote Breast Cancer Cells Growth Through the Metabolic Reprogramming. *Appl Biochem Biotechnol* **191**, 1084–1099 (2020).

110. Sansone, P. *et al.* Packaging and transfer of mitochondrial DNA via exosomes regulate escape from dormancy in hormonal therapy-resistant breast cancer. *Proceedings of the National Academy of Sciences* **114**, (2017).

111. Tan, S. *et al.* Exosomal miRNAs in tumor microenvironment. *Journal of Experimental & Clinical Cancer Research* **39**, 67 (2020).

112. Östman, A. & Augsten, M. Cancer-associated fibroblasts and tumor growth – bystanders turning into key players. *Curr Opin Genet Dev* **19**, 67–73 (2009).

113. Martinez-Outschoorn, U. E. *et al.* Stromal–epithelial metabolic coupling in cancer: Integrating autophagy and metabolism in the tumor microenvironment. *Int J Biochem Cell Biol* **43**, 1045–1051 (2011).

114. Vallabhaneni, K. C. *et al.* Extracellular vesicles from bone marrow mesenchymal stem/stromal cells transport tumor regulatory microRNA, proteins, and metabolites. *Oncotarget* **6**, 4953–4967 (2015).

115. Webber, J., Steadman, R., Mason, M. D., Tabi, Z. & Clayton, A. Cancer exosomes trigger fibroblast to myofibroblast differentiation. *Cancer Res* **70**, 9621–9630 (2010).

116. Webber, J. P. *et al.* Differentiation of tumour-promoting stromal myofibroblasts by cancer exosomes. *Oncogene* **34**, 319–333 (2014).

117. Rai, A. *et al.* Exosomes Derived from Human Primary and Metastatic Colorectal Cancer Cells Contribute to Functional Heterogeneity of Activated Fibroblasts by Reprogramming Their Proteome. *Proteomics* **19**, (2019).

118. Yan, W. *et al.* Cancer-cell-secreted exosomal miR-105 promotes tumour growth through the MYC-dependent metabolic reprogramming of stromal cells. *Nat Cell Biol* **20**, 597–609 (2018).

119. Sussulini, A. *Metabolomics: From Fundamentals to Clinical Applications*. vol. 965 (Springer International Publishing AG, Campinas).

120. Psychogios, N. *et al.* The Human Serum Metabolome. *PLoS One* **6**, e16957 (2011).

121. Fernie, A. R., Trethewey, R. N., Krotzky, A. J. & Willmitzer I N N Ovat I O N, L. *Metabolite Profiling: From Diagnostics to Systems Biology*. www.nature.com/reviews/molcellbio (2004).

122. Perez de Souza, L., Alseekh, S., Scossa, F. & Fernie, A. R. Ultra-high-performance liquid chromatography high-resolution mass spectrometry variants for metabolomics research. *Nat Methods* **18**, 733–746 (2021).

123. Redestig, H., Kobayashi, M., Saito, K. & Kusano, M. Exploring Matrix Effects and Quantification Performance in Metabolomics Experiments Using Artificial Biological Gradients. *Anal Chem* **83**, 5645–5651 (2011).

124. Kapoore, R. V. & Vaidyanathan, S. Towards quantitative mass spectrometry-based metabolomics in microbial and mammalian systems. *Philosophical Transactions of the Royal Society A: Mathematical, Physical and Engineering Sciences* **374**, 20150363 (2016).

125. Álvarez-Sánchez, B., Priego-Capote, F. & Castro, M. D. L. de. Metabolomics analysis II. Preparation of biological samples prior to detection. *TrAC Trends in Analytical Chemistry* **29**, 120–127 (2010).

126. Wamelink, M. M. C. *et al.* Quantification of sugar phosphate intermediates of the pentose phosphate pathway by LC–MS/MS: application to two new inherited defects of metabolism. *Journal of Chromatography B* **823**, 18–25 (2005).

127. Chandel, N. S. Glycolysis. *Cold Spring Harb Perspect Biol* **13**, a040535 (2021).

128. Kuehnbaum, N. L. & Britz-McKibbin, P. New Advances in Separation Science for Metabolomics: Resolving Chemical Diversity in a Post-Genomic Era. *Chem Rev* **113**, 2437–2468 (2013).

129. Ghosh, C., Shinde, C. P. & Chakraborty, B. S. Influence of ionization source design on matrix effects during LC-ESI-MS/MS analysis. *J Chromatogr B Analyt Technol Biomed Life Sci* **893–894**, 193–200 (2012).

130. Zhou, W., Yang, S. & Wang, P. G. Matrix effects and application of matrix effect factor. *Bioanalysis* **9**, 1839–1844 (2017).

131. Todd, J. F. J. Recommendations for nomenclature and symbolism for mass spectroscopy (including an appendix of terms used in vacuum technology). (Recommendations 1991). *Pure and Applied Chemistry* **63**, 1541–1566 (1991).

132. Burgess, K., Rankin, N. & Weidt, S. Metabolomics. in *Handbook of Pharmacogenomics and Stratified Medicine* 181–205 (Elsevier, 2014). doi:10.1016/B978-0-12-386882-4.00010-4.

133. Madsen, R., Lundstedt, T. & Trygg, J. Chemometrics in metabolomics-A review in human disease diagnosis. *Anal Chim Acta* **659**, 23–33 (2010).

134. Hendriks, M. M. W. B. *et al.* Data-processing strategies for metabolomics studies. *TrAC Trends in Analytical Chemistry* **30**, 1685–1698 (2011).

135. Saccenti, E., Hoefsloot, H. C. J., Smilde, A. K., Westerhuis, J. A. & Hendriks, M. M. W. B. Reflections on univariate and multivariate analysis of metabolomics data. *Metabolomics* **10**, 361–374 (2014).

136. Wishart, D. S. *et al.* HMDB 5.0: the Human Metabolome Database for 2022. *Nucleic Acids Res* **50**, D622–D631 (2022).

137. Slenter, D. N. *et al.* WikiPathways: a multifaceted pathway database bridging metabolomics to other omics research. *Nucleic Acids Res* **46**, D661–D667 (2018).

138. Caspi, R. *et al.* The MetaCyc database of metabolic pathways and enzymes and the BioCyc collection of pathway/genome databases. *Nucleic Acids Res* **44**, D471–D480 (2016).

139. Haw, R. & Stein, L. Using the Reactome Database. *Curr Protoc Bioinformatics* **38**, (2012).

140. Corey, E. & Vessella, R. L. Xenograft Models of Human Prostate Cancer. in *Contemporary Cancer Research: Prostate Cancer: Biology, Genetics, and the New Therapeutics,* (eds. Chung, L. W. K., Isaacs, W. B. & Simons, J. W.) 2–30 (Humana Press Inc., 2007). doi:10.1007/978-1-59745-224-3_1.

141. Bordanaba-Florit, G., Madarieta, I., Olalde, B., Falcón-Pérez, J. M. & Royo, F. 3D Cell Cultures as Prospective Models to Study Extracellular Vesicles in Cancer. *Cancers (Basel)* **13**, 307 (2021).

142. Tan, J. *et al.* Dehydroepiandrosterone Activates Mutant Androgen Receptors Expressed in the Androgen-Dependent Human Prostate Cancer Xenograft CWR22 and LNCaP Cells. *Molecular Endocrinology* **11**, 450–459 (1997).

143. Nickerson, T. *et al.* In vivo progression of LAPC-9 and LNCaP prostate cancer models to androgen independence is associated with increased expression of insulin-like growth factor I (IGF-I) and IGF-I receptor (IGF-IR). *Cancer Res* **61**, 6276–80 (2001).

144. Corey, E., Quinn, J. E. & Vessella, R. L. A novel method of generating prostate cancer metastases from orthotopic implants. *Prostate* **56**, 110–114 (2003).

145. Veldscholte, J. *et al.* A mutation in the ligand binding domain of the androgen receptor of human lNCaP cells affects steroid binding characteristics and response to anti-androgens. *Biochem Biophys Res Commun* **173**, 534–540 (1990).

146. Russell, P. J. & Kingsley, E. A. Human Prostate Cancer Cell Lines. *Methods Mol Med* **81**, 21–39 (2003).

147. Webber, M. M. A human prostatic stromal myofibroblast cell line WPMY-1: a model for stromalepithelial interactions in prostatic neoplasia. *Carcinogenesis* **20**, 1185–1192 (1999).

148. Bello, D., Webber, M. M., Kleinman, H. K., Wartinger, D. D. & Rhim, J. S. Androgen responsive adult human prostatic epithelial cell lines immortalized by human papillomavirus 18. *Carcinogenesis* **18**, 1215–1223 (1997).

149. Hayward, S. W. *et al.* Establishment and characterization of an immortalized but non-transformed human prostate epithelial cell line: BPH-1. *In Vitro Cellular & Developmental Biology* **31A**, 14–24 (1995).

150. Webber, M. M. *et al.* Prostate specific antigen and androgen receptor induction and characterization of an immortalized adult human prostatic epithelial cell line. *Carcinogenesis* **17**, 1641–1646 (1996).

151. Madar, S. *et al.* Modulated expression of WFDC1 during carcinogenesis and cellular senescence. *Carcinogenesis* **30**, 20–27 (2009).

152. Horoszewicz, J. S. *et al.* LNCaP Model of Human Prostatic Carcinoma. *Cancer Res* **43**, 1809–1818 (1983).

153. Balbay, M. D. *et al.* Highly metastatic human prostate cancer growing within the prostate of athymic mice overexpresses vascular endothelial growth factor. *Clin Cancer Res* **5**, 783–789 (1999).

154. Wu, H. *et al.* Derivation of androgen-independent human LNCaP prostatic cancer cell sublines: Role of bone stromal cells. *Int J Cancer* **57**, 406–412 (1994).

155. Cunningham, D. & You, Z. In vitro and in vivo model systems used in prostate cancer research. *J Biol Methods* **2**, e17 (2015).

156. Lee, Y. G. *et al.* Establishment and characterization of a new human prostatic cancer cell line: DuCaP. *In Vivo (Brooklyn)* **15**, 157–162 (2001).

157. Zhau, H. Y. E. *et al.* Androgen-repressed phenotype in human prostate cancer. *Proc Natl Acad Sci U S A* **93**, 15152–15157 (1996).

158. Wainstein, M. A. *et al.* CWR22: Androgen-dependent Xenograft Model Derived from a Primary Human Prostatic Carcinoma. *Cancer Res* **54**, 6049–6052 (1994).

159. Sramkoski, R. M. *et al.* A new human prostate carcinoma cell line, 22Rv1. *In Vitro Cell Dev Biol Anim* **35**, 403–409 (1999).

160. Harper, M. E., Goddard, L., Smith, C. & Nicholson, R. I. Characterization of a Transplantable Hormone-Responsive Human Prostatic Cancer Xenograft TEN12 and its Androgen-Resistant Sublines. *Prostate* **58**, 13–22 (2004).

161. van Bokhoven, A., Varella-Garcia, M., Korch, C., Hessels, D. & Miller, G. J. Widely used prostate carcinoma cell lines share common origins. *Prostate* **47**, 36–51 (2001).

162.   Capes-Davis, A. *et al.* Check your cultures! A list of cross-contaminated or misidentified cell lines. *Int J Cancer* **127**, 1–8 (2010).

163.   Loop, S. M., Rozanski, T. A. & Ostenson, R. C. Human primary prostate tumor cell line, ALVA-31: A new model for studying the hormonal regulation of prostate tumor cell growth. *Prostate* **22**, 93–108 (1993).

164.   van Bokhoven, A. *et al.* Molecular characterization of human prostate carcinoma cell lines. *Prostate* **57**, 205–225 (2003).

165.   Plymate, S. R. *et al.* Effects of sex hormone binding globulin (SHBG) on human prostatic carcinoma. *Journal of Steroid Biochemistry and Molecular Biology* **40**, 833–839 (1991).

166.   Claas, F. H. J. & Steenbrugge, G. van. Expression of HLA-like structures on a permanent human tumor line PC-93. *Tissue Antigens* **21**, 227–232 (1983).

167.   Marques, R. B. *et al.* The Human PC346 Xenograft and Cell Line Panel: A Model System for Prostate Cancer Progression. *Eur Urol* **49**, 245–257 (2006).

168.   Klein, K. A. *et al.* Progression of metastatic human prostate cancer to androgen independence in immuno-deficient SCID mice. *Nat Med* **3**, 402–408 (1997).

169.   Navone, N. M. *et al.* Establishment from a Single of Two Prostate Cancer Cell Derived from a Single Bone Metastasis. *Clinical Cancer Research* **3**, 2493–2500 (1997).

170.   Kaighn, M. E., Narayan, K. S., Ohnuki, Y., Lechner, J. F. & Jones, L. W. Establishment and characterization of a human prostatic carcinoma cell line (PC-3). *Invest Urol* **17**, 16–23 (1979).

171.   Stone, K. R., Mickey, D. D., Wunderli, H., Mickey, G. H. & Paulson, D. F. Isolation of a human prostate carcinoma cell line (DU 145). *Int J Cancer* **281**, 274–281 (1978).

172.   Herr, D. R. *et al.* Ultrastructural Characteristics of DHA-Induced Pyroptosis. *Neuromolecular Med* (2020) doi:10.1007/s12017-019-08586-y.

173.   Patras, L. & Banciu, M. Intercellular Crosstalk via Extracellular Vesicles in Tumor Milieu as Emerging Therapies for Cancer Progression. *Curr Pharm Des* **25**, 1980–2006 (2019).

174.   Andaloussi, S. EL, Mäger, I., Breakefield, X. O. & Wood, M. J. A. Extracellular vesicles: biology and emerging therapeutic opportunities. *Nat Rev Drug Discov* **12**, 347–357 (2013).

175.   Buzas, E. I., György, B., Nagy, G., Falus, A. & Gay, S. Emerging role of extracellular vesicles in inflammatory diseases. *Nature Reviews Rheumatology volume* **10**, 356–364 (2014).

176.   Panagopoulou, M. S., Wark, A. W., Birch, D. J. S. & Gregory, C. D. Phenotypic analysis of extracellular vesicles: a review on the applications of fluorescence. *J Extracell Vesicles* **9**, (2020).

177.   Willms, E., Cabañas, C., Mäger, I., Wood, M. J. A. & Vader, P. Extracellular vesicle heterogeneity: Sub-populations, isolation techniques, and diverse functions in cancer progression. *Front Immunol* **9**, (2018).

178.   Kalluri, R. & LeBleu, V. S. The biology, function, and biomedical applications of exosomes. *Science (1979)* **367**, (2020).

179.   Van Der Pol, E. *et al.* Optical and non-optical methods for detection and characterization of microparticles and exosomes. *Journal of Thrombosis and Haemostasis* **8**, 2596–2607 (2010).

180.   Soung, Y. H., Ford, S., Zhang, V. & Chung, J. Exosomes in cancer diagnostics. *Cancers (Basel)* **9**, (2017).

181.   Puente-Massaguer, E., Lecina, M. & Gòdia, F. Application of advanced quantification techniques in nano-particle-based vaccine development with the Sf9 cell baculovirus expression system. *Vaccine* **38**, 1849–1859 (2020).

182.   Pick, H., Alves, A. C. & Vogel, H. Single-Vesicle Assays Using Liposomes and Cell-Derived Vesicles: From Modeling Complex Membrane Processes to Synthetic Biology and Biomedical Applications. *Chem Rev* **118**, 8598–8654 (2018).

183.   Tkach, M., Kowal, J. & Théry, C. Why the need and how to approach the functional diversity of extracellular vesicles. *Philosophical Transactions of the Royal Society B: Biological Sciences* **373**, (2018).

184.   Goñi, F. M. The basic structure and dynamics of cell membranes: An update of the Singer-Nicolson model. *Biochim Biophys Acta Biomembr* **1838**, 1467–1476 (2014).

185.   Bhatia, V. K. *et al.* Amphipathic motifs in BAR domains are essential for membrane curvature sensing. *EMBO Journal* **28**, 3303–3314 (2009).

186.   Mathiasen, S. *et al.* Nanoscale high-content analysis using compositional heterogeneities of single proteoliposomes. *Nat Methods* **11**, 931–934 (2015).

187.   Brett, S. I. *et al.* Immunoaffinity based methods are superior to kits for purification of prostate derived extracellular vesicles from plasma samples. *Prostate* **77**, 1335–1343 (2017).

188.   Royo, F. *et al.* Different EV enrichment methods suitable for clinical settings yield different subpopulations of urinary extracellular vesicles from human samples. *J Extracell Vesicles* **5**, (2016).

189.   Ramirez, M. I. *et al.* Technical challenges of working with extracellular vesicles. *Nanoscale* **10**, 881–906 (2018).

190. Sódar, B. W. *et al.* Low-density lipoprotein mimics blood plasma-derived exosomes and microvesicles during isolation and detection. *Sci Rep* **6**, 1–12 (2016).

191. Woo, J. R., Sharma, S. & Gimzewski, J. The Role of Isolation Methods on a Nanoscale Surface Structure and its Effect on the Size of Exosomes. *J Circ Biomark* **5**, 1–9 (2016).

192. Takahashi, K., Yan, I. K., Kim, C., Kim, J. & Patel, T. Analysis of extracellular RNA by digital PCR. *Front Oncol* **4**, (2014).

193. Liu, Y. & Lu, Q. Extracellular vesicle microRNAs: Biomarker discovery in various diseases based on RT-qPCR. *Biomark Med* **9**, 791–805 (2015).

194. Giannopoulou, L., Zavridou, M., Kasimir-Bauer, S. & Lianidou, E. S. Liquid biopsy in ovarian cancer: the potential of circulating miRNAs and exosomes. *Translational Research* **205**, 77–91 (2019).

195. Crocetti, E. Epidemiology of prostate cancer in Europe. *Centre for Parliamentary Studies* https://ec.europa.eu/jrc/en/publication/epidemiology-prostate-cancer-europe (2015).

196. Torrano, V. *et al.* Vesicle-MaNiA: Extracellular vesicles in liquid biopsy and cancer. *Curr Opin Pharmacol* **29**, 47–53 (2016).

197. Heidenreich, A. *et al.* EAU guidelines on prostate cancer. Part 1: Screening, diagnosis, and local treatment with curative intent - Update 2013. *Eur Urol* **65**, 124–137 (2014).

198. Humphrey, P. A. Diagnosis of adenocarcinoma in prostate needle biopsy tissue. *J Clin Pathol* **60**, 35–42 (2007).

199. Shariat, S. F. & Roehrborn, C. G. Using biopsy to detect prostate cancer. *Rev Urol* **10**, 262–80 (2008).

200. Höög, J. L. & Lötvall, J. Diversity of extracellular vesicles in human ejaculates revealed by cryo-electron microscopy. *J Extracell Vesicles* **4**, 28680 (2015).

201. Duijvesz, D. *et al.* Immuno-based detection of extracellular vesicles in urine as diagnostic marker for prostate cancer. *Int J Cancer* **137**, 2869–2878 (2015).

202. Raposo, G. & Stoorvogel, W. Extracellular vesicles: Exosomes, microvesicles, and friends. *Journal of Cell Biology* **200**, 373–383 (2013).

203. Raposo, G. & Stahl, P. D. Extracellular vesicles: a new communication paradigm? *Nat Rev Mol Cell Biol* **20**, 509–510 (2019).

204. Théry, C., Clayton, A., Amigorena, S. & Raposo, G. Isolation and Characterization of Exosomes from Cell Culture Supernatants. in *Current Protocols in Cell Biology* (2006).

205. Giulietti, M. *et al.* Exploring small extracellular vesicles for precision medicine in prostate cancer. *Front Oncol* **8**, (2018).

206. Russell, A. E. *et al.* Biological membranes in EV biogenesis , stability , uptake , and cargo transfer : an ISEV position paper arising from the ISEV membranes and EVs workshop. *J Extracell Vesicles* **8**, (2019).

207. Chen, C. *et al.* Isolation of a Novel Bacterial Strain Capable of Producing Abundant Extracellular Membrane Vesicles Carrying a Single Major Cargo Protein and Analysis of Its Transport Mechanism. *Front Microbiol* **10**, 1–16 (2020).

208. Szatanek, R. *et al.* The methods of choice for extracellular vesicles (EVs) characterization. *Int J Mol Sci* **18**, (2017).

209. Tatischeff, I., Larquet, E., Falcon-Perez, J. M., Turpin, P.-Y. & Kruglik, S. G. Fast characterisation of cell-derived extracellular vesicles by nanoparticles tracking analysis, cryo-electron microscopy, and raman tweezers micro- spectroscopy. *J Extracell Vesicles* **1**, 19179 (2012).

210. Carney, R. P. *et al.* Multispectral Optical Tweezers for Biochemical Fingerprinting of CD9-Positive Exosome Subpopulations. *Anal Chem* **89**, 5357–5363 (2017).

211. Enciso-Martinez, A. *et al.* Synchronized Rayleigh and Raman scattering for the characterization of single optically trapped extracellular vesicles. *Nanomedicine* **24**, (2020).

212. Stremersch, S. *et al.* Identification of individual exosome-like vesicles by surface enhanced raman spectroscopy. *Small* **12**, 3292–3301 (2016).

213. Yuana, Y. *et al.* Cryo-electron microscopy of extracellular vesicles in fresh plasma. *J Extracell Vesicles* **2**, 21494 (2013).

214. Daaboul, G. G. *et al.* Digital Detection of Exosomes by Interferometric Imaging. *Sci Rep* **6**, 1–10 (2016).

215. Ridolfi, A. *et al.* AFM-Based High-Throughput Nanomechanical Screening of Single Extracellular Vesicles. *Anal Chem* **92**, 10274–10282 (2020).

216. Kim, S. Y., Khanal, D., Kalionis, B. & Chrzanowski, W. High-fidelity probing of the structure and heterogeneity of extracellular vesicles by resonance-enhanced atomic force microscopy infrared spectroscopy. *Nat Protoc* **14**, 576–593 (2019).

217. Zong, S. *et al.* Single molecule localization imaging of exosomes using blinking silicon quantum dots. *Nanotechnology* **29**, (2017).

218. Hyenne, V. *et al.* Studying the Fate of Tumor Extracellular Vesicles at High Spatiotemporal Resolution Using the Zebrafish Embryo. *Dev Cell* **48**, 554-572.e7 (2019).

219. Tian, Q. *et al.* Nanoparticle Counting by Microscopic Digital Detection: Selective Quantitative Analysis of Exosomes via Surface-Anchored Nucleic Acid Amplification. *Anal Chem* **90**, 6556–6562 (2018).

220. Filipe, V., Hawe, A. & Jiskoot, W. Critical evaluation of nanoparticle tracking analysis (NTA) by NanoSight for the measurement of nanoparticles and protein aggregates. *Pharm Res* **27**, 796–810 (2010).

221. Bachurski, D. *et al.* Extracellular vesicle measurements with nanoparticle tracking analysis–An accuracy and repeatability comparison between NanoSight NS300 and ZetaView. *J Extracell Vesicles* **8**, (2019).

222. Koifman, N., Biran, I., Aharon, A., Brenner, B. & Talmon, Y. A direct-imaging cryo-EM study of shedding extracellular vesicles from leukemic monocytes. *J Struct Biol* **198**, 177–185 (2017).

223. Kruglik, S. G. *et al.* Raman tweezers microspectroscopy of circa 100 nm extracellular vesicles. *Nanoscale* **11**, 1661–1679 (2019).

224. Royo, F. *et al.* Transcriptomic profiling of urine extracellular vesicles reveals alterations of CDH3 in prostate cancer. *Oncotarget* **7**, 6835–6846 (2016).

225. Daaboul, G. G. *et al.* Enhanced light microscopy visualization of virus particles from Zika virus to filamentous ebolaviruses. *PLoS One* **12**, 1–15 (2017).

226. Biggs, C. N. *et al.* Prostate extracellular vesicles in patient plasma as a liquid biopsy platform for prostate cancer using nanoscale flow cytometry. *Oncotarget* **7**, 8839–8849 (2016).

227. Notarangelo, M. *et al.* Ultrasensitive detection of cancer biomarkers by nickel-based isolation of polydisperse extracellular vesicles from blood. *EBioMedicine* **43**, 114–126 (2019).

228. Polanco, J. C., Li, C., Durisic, N., Sullivan, R. & Götz, J. Exosomes taken up by neurons hijack the endosomal pathway to spread to interconnected neurons. *Acta Neuropathol Commun* **6**, 10 (2018).

229. Marku, A. *et al.* The LRRK2 N-terminal domain influences vesicle trafficking: impact of the E193K variant. *Sci Rep* **10**, 1–10 (2020).

230. Smith, Z. J. *et al.* Single exosome study reveals subpopulations distributed among cell lines with variability related to membrane content. *J Extracell Vesicles* **4**, (2015).

231. Carney, R. P. *et al.* Targeting Tumor-Associated Exosomes with Integrin-Binding Peptides. Advanced Biosystems. *Physiol Behav* **1**, (2017).

232. Lee, W. *et al.* Label-Free Prostate Cancer Detection by Characterization of Extracellular Vesicles Using Raman Spectroscopy. *Anal Chem* **90**, 11290–11296 (2018).

233. Dai, Y. *et al.* Combined Morpho-Chemical Profiling of Individual Extracellular Vesicles and Functional Nanoparticles without Labels. *Anal Chem* **92**, 5585–5594 (2020).

234. Enciso-Martinez, A. *et al.* Label-free identification and chemical characterisation of single extracellular vesicles and lipoproteins by synchronous Rayleigh and Raman scattering. *J Extracell Vesicles* **9**, (2020).

235. Lee, W., Lenferink, A. T. M., Otto, C. & Offerhaus, H. L. Classifying Raman spectra of extracellular vesicles based on convolutional neural networks for prostate cancer detection. *Journal of Raman Spectroscopy* **51**, 293–300 (2020).

236. Rikkert, L. G. *et al.* Cancer-ID: Toward Identification of Cancer by Tumor-Derived Extracellular Vesicles in Blood. *Front Oncol* **10**, 1–19 (2020).

237. Bryce, D. A., Kitt, J. P. & Harris, J. M. Confocal-Raman Microscopy Characterization of Supported Phospholipid Bilayers Deposited on the Interior Surfaces of Chromatographic Silica. *J Am Chem Soc* **140**, 4071–4078 (2018).

238. Kitt, J. P., Bryce, D. A., Minteer, S. D. & Harris, J. M. Confocal Raman Microscopy for in Situ Measurement of Phospholipid-Water Partitioning into Model Phospholipid Bilayers within Individual Chromatographic Particles. *Anal Chem* **90**, 7048–7055 (2018).

239. Penders, J. *et al.* Single Particle Automated Raman Trapping Analysis. *Nat Commun* **9**, 1–11 (2018).

240. Bour, A. *et al.* Lipid Unsaturation Properties Govern the Sensitivity of Membranes to Photoinduced Oxidative Stress. *Biophys J* **116**, 910–920 (2019).

241. Collard, L., Sinjab, F. & Notingher, I. Raman Spectroscopy Study of Curvature-Mediated Lipid Packing and Sorting in Single Lipid Vesicles. *Biophys J* **117**, 1589–1598 (2019).

242. Bryce, D. A., Kitt, J. P., Myres, G. J. & Harris, J. M. Confocal Raman Microscopy Investigation of Phospholipid Monolayers Deposited on Nitrile-Modified Surfaces in Porous Silica Particles. *Langmuir* **36**, 4071–4079 (2020).

243. Krafft, C. *et al.* A specific spectral signature of serum and plasma-derived extracellular vesicles for cancer screening. *Nanomedicine* **13**, 835–841 (2017).

244. Gualerzi, A. *et al.* Raman spectroscopy uncovers biochemical tissue-related features of extracellular vesicles from mesenchymal stromal cells. *Sci Rep* **7**, 1–11 (2017).

245. Gualerzi, A. *et al.* Raman spectroscopy as a quick tool to assess purity of extracellular vesicle preparations and predict their functionality. *J Extracell Vesicles* **8**, (2019).

246. Zhang, H., Silva, A. C., Zhang, W., Rutigliano, H. & Zhou, A. Raman Spectroscopy characterization extracellular vesicles from bovine placenta and peripheral blood mononuclear cells. *PLoS One* **15**, (2020).

247. Morasso, C. F. *et al.* Raman spectroscopy reveals biochemical differences in plasma derived extracellular vesicles from sporadic Amyotrophic Lateral Sclerosis patients. *Nanomedicine* **29**, (2020).

248. Cialla, D., Pollok, S., Steinbrücker, C., Weber, K. & Popp, J. SERS-based detection of biomolecules. *Nanophotonics* **3**, 383–411 (2014).

249. Lee, C. *et al.* 3D plasmonic nanobowl platform for the study of exosomes in solution. *Nanoscale* **7**, 9290–9297 (2015).

250. Fazio, B. *et al.* SERS detection of Biomolecules at Physiological pH via aggregation of Gold Nanorods mediated by Optical Forces and Plasmonic Heating. *Sci Rep* **6**, 26952 (2016).

251. Park, J. *et al.* Exosome Classification by Pattern Analysis of Surface-Enhanced Raman Spectroscopy Data for Lung Cancer Diagnosis. *Anal Chem* **89**, 6695–6701 (2017).

252. Rojalin, T., Phong, B., Koster, H. & Carney, R. P. Nanoplasmonic approaches for sensitive detection and molecular characterization of extracellular vesicles. *Front Chem* **7**, (2019).

253. Wang, J., Koo, K. M., Wang, Y. & Trau, M. Engineering State-of-the-Art Plasmonic Nanomaterials for SERS-Based Clinical Liquid Biopsy Applications. *Advanced Science* **6**, (2019).

254. Pramanik, A. *et al.* Mixed-Dimensional Heterostructure Material-Based SERS for Trace Level Identi fi cation of Breast Cancer-Derived Exosomes. *ACS Omega* **3**, 16602–16611 (2020).

255. Orlov, I. *et al.* The integrative role of cryo electron microscopy in molecular and cellular structural biology. *Biol Cell* **109**, 81–93 (2017).

256. Dubochet, J. *et al.* Cryo-electron microscopy of vitrified specimens. *Q Rev Biophys* **21**, 129–228 (1988).

257. Conde-Vancells, J. *et al.* Characterization and comprehensive proteome profiling of exosomes secreted by hepatocytes. *J Proteome Res* **7**, 5157–5166 (2008).

258. Zonneveld, M. I. *et al.* Recovery of extracellular vesicles from human breast milk is influenced by sample collection and vesicle isolation procedures. *J Extracell Vesicles* **3**, 1–12 (2014).

259. Cizmar, P. & Yuana, Y. Detection and Characterization of Extracellular Vesicles by Transmission and Cryo-Transmission Electron Microscopy. in *Extracellular Vesicles: Methods and Protocols, Methods in Molecular Biology* (eds. Kuo, W. P. & Jia, S.) vol. 1660 221–232 (2017).

260. Binnig, G., Quate, F. & Gerber, Ch. Atomic Force Microscope. *Phys Rev Lett* **56**, 930–933 (1986).

261. Sharma, S. *et al.* Structural-Mechanical Characterization of Nanoparticle Exosomes in Human Saliva, Using Correlative AFM, FESEM, and Force Spectroscopy. *ACS Nano* **4**, 1921–1926 (2010).

262. Parisse, P. *et al.* Atomic force microscopy analysis of extracellular vesicles. *European Biophysics Journal* **46**, 813–820 (2017).

263. Creasey, R. *et al.* Atomic force microscopy-based antibody recognition imaging of proteins in the pathological deposits in Pseudoexfoliation Syndrome. *Ultramicroscopy* **111**, 1055–1061 (2011).

264. Sebaihi, N., De Boeck, B., Yuana, Y., Nieuwland, R. & Pétry, J. Dimensional characterization of extracellular vesicles using atomic force microscopy. *Meas Sci Technol* **28**, (2017).

265. Skliar, M. & Chernyshev, V. S. Imaging of Extracellular Vesicles by Atomic Force Microscopy. *Journal of Visualized Experiments* 1–13 (2019).

266. Kim, S. Y., Khanal, D., Tharkar, P., Kalionis, B. & Chrzanowski, W. None of us is the same as all of us: Resolving the heterogeneity of extracellular vesicles using single-vesicle, nanoscale characterization with resonance enhanced atomic force microscope infrared spectroscopy (AFM-IR). *Nanoscale Horiz* **3**, 430–438 (2018).

267. Avci, O., Ünlü, N. L., Özkumur, A. Y. & Ünlü, M. S. Interferometric Reflectance Imaging Sensor (IRIS)—A Platform Technology for Multiplexed Diagnostics and Digital Detection. *Sensors* **15**, 17649–17665 (2015).

268. van der Vlist, E. J., Nolte-'t Hoen, E. N. M., Stoorvogel, W., Arkesteijn, G. J. A. & Wauben, M. H. M. Fluorescent labeling of nano-sized vesicles released by cells and subsequent quantitative and qualitative analysis by high-resolution flow cytometry. *Nat Protoc* **7**, 1311–1326 (2012).

269. Daaboul, G. G. *et al.* Enhanced light microscopy visualization of virus particles from Zika virus to filamentous ebolaviruses. *PLoS One* **12**, 1–15 (2017).

270. Gomes, J. *et al.* Analytical Considerations in Nanoscale Flow Cytometry of Extracellular Vesicles to Achieve Data Linearity. *Thromb Haemost* **118**, 1612–1624 (2018).

271. Fish, K. N. Total Internal Reflection Fluorescence (TIRF) Microscopy. *Curr Protoc Cytom* **50**, (2009).

272. Kudalkar, E. M., Davis, T. N. & Asbury, C. L. Single-Molecule Total Internal Reflection Fluorescence Microscopy. *Cold Spring Harb Protoc* **5**, (2016).

273. Axelrod, D. Chapter 7: Total internal reflection fluorescence microscopy. *Methods Cell Biol.* **89**, 169–221 (2008).

274. Ha, T. Single-molecule fluorescence resonance energy transfer. *Methods* **25**, 78–86 (2001).

275. Arluison, V. & Wien, F. *RNA Spectroscopy Methods and Protocols*. (Springer Protocols, 2020).

276. Cerdán, L. *et al.* FRET-assisted laser emission in colloidal suspensions of dye-doped latex nanoparticles. *Nat Photonics* **6**, 621–626 (2012).

277. Rectenwald, J. *et al.* A General TR-FRET Assay Platform for High-Throughput Screening and Characterizing Inhibitors of Methyl-Lysine Reader Proteins. *SLAS Discov.* **24**, 693–700 (2019).

278. Maurel, D. *et al.* Cell-surface protein-protein interaction analysis with time-resolved FRET and snap-tag technologies: application to GPCR oligomerization. *Nat Methods* **5**, 561–567 (2008).

279. Johnson, J. L. *et al.* Munc13-4 Is a Rab11-binding Protein That Regulates Rab11-positive Vesicle Trafficking and Docking at the Plasma Membrane. *The Journal of Biolocigal Chemistry* **291**, 3423–3438 (2016).

280. Gayrard, C. & Borghi, N. FRET-based Molecular Tension Microscopy. *Methods* **94**, 33–42 (2016).

281. Dao, T. P. T. *et al.* Mixing Block Copolymers with Phospholipids at the Nanoscale: From Hybrid Polymer/Lipid Wormlike Micelles to Vesicles Presenting Lipid Nanodomains. *Langmuir* **33**, 1705–1715 (2017).

282. Chen, C. *et al.* Visualization and intracellular dynamic tracking of exosomes and exosomal miRNAs using single molecule localization microscopy. *Nanoscale* **10**, 5154–5162 (2018).

283. Oleksiuk, O. *et al.* Single-molecule localization microscopy allows for the analysis of cancer metastasis-specific mirna distribution on the nanoscale. *Oncotarget* **6**, 44745–44757 (2015).

284. Dabrowska, S. *et al.* Imaging of extracellular vesicles derived from human bone marrow mesenchymal stem cells using fluorescent and magnetic labels. *Int J Nanomedicine* **13**, 1653–1664 (2018).

285. Willig, K. I., Rizzoli, S. O., Westphal, V., Jahn, R. & Hell, S. W. STED microscopy reveals that synaptotagmin remains clustered after synaptic vesicle exocytosis. *Nature* **440**, 935–939 (2006).

286. Chen, C. *et al.* Imaging and Intracellular Tracking of Cancer-Derived Exosomes Using Single-Molecule Localization-Based Super-Resolution Microscope. *ACS Appl Mater Interfaces* **8**, 25825–25833 (2016).

287. Gustafsson, M. G. L. Surpassing the lateral resolution limit by a factor of two using structured illumination microscopy. *J Microsc* **198**, 82–87 (2000).

288. Hell, S. W. Toward fluorescence nanoscopy. *Nat Biotechnol* **21**, 1347–1355 (2003).

289. Huang, B. Super-resolution optical microscopy: multiple choices. *Curr Opin Chem Biol* **14**, 10–14 (2010).

290. Hess, S. T., Girirajan, T. P. K. & Mason, M. D. Ultra-high resolution imaging by fluorescence photoactivation localization microscopy. *Biophys J* **91**, 4258–4272 (2006).

291. Nienhaus, K. & Nienhaus, G. U. Where Do We Stand with Super-Resolution Optical Microscopy? *J Mol Biol* **428**, 308–322 (2016).

292. Bachmann, M., Fiederling, F. & Bastmeyer, M. Practical limitations of superresolution imaging due to conventional sample preparation revealed by a direct comparison of CLSM, SIM and dSTORM. *J Microsc* **262**, 306–315 (2016).

293. Witters, D., Knez, K., Ceyssens, F., Puers, R. & Lammertyn, J. Digital microfluidics-enabled single-molecule detection by printing and sealing single magnetic beads in femtoliter droplets. *Lab Chip* **13**, 2047–2054 (2013).

294. Gao, W., Li, X., Zeng, L. & Peng, T. Rapid isothermal detection assay: a probe amplification method for the detection of nucleic acids. *Diagn Microbiol Infect Dis* **60**, 133–141 (2008).

295. Jia, S. *et al.* Emerging technologies in extracellular vesicle-based molecular diagnostics. *Expert Rev Mol Diagn* **14**, 307–321 (2014).

296. Chen, W. W. *et al.* BEAMing and Droplet Digital PCR Analysis of Mutant IDH1 mRNA in Glioma Patient Serum and Cerebrospinal Fluid Extracellular Vesicles. *Mol Ther Nucleic Acids* **2**, e109 (2013).

297. Worst, T. S. *et al.* miR-10a-5p and miR-29b-3p as Extracellular Vesicle-Associated Prostate Cancer Detection Markers. *Cancers (Basel)* **12**, (2020).

298. Takahashi, K. *et al.* Circulating extracellular vesicle-encapsulated HULC is a potential biomarker for human pancreatic cancer. *Cancer Sci* **111**, 98–111 (2020).

299. Liu, C. *et al.* Single-Exosome-Counting Immunoassays for Cancer Diagnostics. *Nano Lett* **18**, 4226–4232 (2018).

300. Diefenbach, R. J., Lee, J. H. & Rizos, H. Monitoring Melanoma Using Circulating Free DNA. *Am J Clin Dermatol* **20**, (2019).

301. Kong, L., Lee, C., Earhart, C. M., Cordovez, B. & Chan, J. W. A nanotweezer system for evanescent wave excited surface enhanced Raman spectroscopy (SERS) of single nanoparticles. *Opt Express* **23**, 6793 (2015).

302. Zabeo, D. *et al.* Exosomes purified from a single cell type have diverse morphology. *J Extracell Vesicles* **6**, (2017).

303. Zong, S. *et al.* Facile detection of tumor-derived exosomes using magnetic nanobeads and SERS nano-probes. *Analytical Methods* **8**, 5001–5008 (2016).

304. Lee, C., Carney, R., Lam, K. & Chan, J. W. SERS analysis of selectively captured exosomes using an integrin-specific peptide ligand. *Journal of Raman Spectroscopy* **48**, 1771–1776 (2017).

305. Tian, Y. F., Ning, C. F., He, F., Yin, B. C. & Ye, B. C. Highly sensitive detection of exosomes by SERS using gold nanostar@Raman reporter@nanoshell structures modified with a bivalent cholesterol-labeled DNA anchor. *Analyst* **143**, 4915–4922 (2018).

306. Zhang, W. *et al.* Enabling Sensitive Phenotypic Profiling of Cancer-Derived Small Extracellular Vesicles Using Surface-Enhanced Raman Spectroscopy Nanotags. *ACS Sens* **5**, 764–771 (2020).

307. Schie, I. W. *et al.* High-Throughput Screening Raman Spectroscopy Platform for Label-Free Cellomics. *Anal Chem* **90**, 2023–2030 (2018).

308. Xiong, Q. *et al.* Magnetic nanochain integrated microfluidic biochips. *Nat Commun* **9**, 1–11 (2018).

309. Beekman, P. *et al.* Immuno-capture of extracellular vesicles for individual multi-modal characterization using AFM, SEM and Raman spectroscopy. *Lab Chip* **19**, 2526–2536 (2019).

310. Rüger, J., Mondol, A. S., Schie, I. W., Popp, J. & Krafft, C. High-throughput screening Raman microspectroscopy for assessment of drug-induced changes in diatom cells. *Analyst* **144**, 4488–4492 (2019).

311. Noble, J. M. *et al.* Direct comparison of optical and electron microscopy methods for structural characterization of extracellular vesicles. *J Struct Biol* (2020) doi:10.1016/j.jsb.2020.107474.

312. Lian, H., He, S., Chen, C. & Yan, X. Flow Cytometric Analysis of Nanoscale Biological Particles and Organelles. *Annual Review of Analytical Chemistry* **12**, 389–409 (2019).

313. Chukhchin, D. G., Bolotova, K., Sinelnikov, I., Churilov, D. & Novozhilov, E. Exosomes in the phloem and xylem of woody plants. *Planta* **251**, 1–14 (2020).

314. Plaut, J. S. *et al.* Quantitative atomic force microscopy provides new insight into matrix vesicle mineralization. *Arch Biochem Biophys* **667**, 14–21 (2019).

315. Arraud, N. *et al.* Extracellular vesicles from blood plasma: Determination of their morphology, size, phenotype and concentration. *Journal of Thrombosis and Haemostasis* **12**, 614–627 (2014).

316. Bevers, E. M., Comfurius, P. & Zwaal, R. F. A. Changes in membrane phospholipid distribution during platelet activation. *BBA - Biomembranes* **736**, 57–66 (1983).

317. Fadok, V. A. *et al.* Exposure of phosphatidylserine on the surface of apoptotic lymphocytes triggers specific recognition and removal by macrophages. *Journal of Immunology* **148**, 2207–16 (1992).

318. Zwaal, R. F. A. & Schroit, A. J. Pathophysiologic Implications of Membrane Phospholipid Asymmetry in Blood Cells. *The Journal of The American Society of Hematology* **89**, 333–340 (1997).

319. Biró, É. *et al.* Human cell-derived microparticles promote thrombus formation in vivo in a tissue factor-dependent manner. *Journal of Thrombosis and Haemostasis* **1**, 2561–2568 (2003).

320. Morel, O., Jesel, L., Freyssinet, J. M. & Toti, F. Cellular mechanisms underlying the formation of circulating microparticles. *Arterioscler Thromb Vasc Biol* **31**, 15–26 (2011).

321. Emelyanov, A. *et al.* Cryo-electron microscopy of extracellular vesicles from cerebrospinal fluid. *PLoS One* **15**, 1–11 (2020).

322. Yekula, A. *et al.* Large and small extracellular vesicles released by glioma cells in vitro and in vivo. *J Extracell Vesicles* **9**, (2020).

323. Thane, K. E., Davis, A. M. & Hoffman, A. M. Improved methods for fluorescent labeling and detection of single extracellular vesicles using nanoparticle tracking analysis. *Sci Rep* **9**, 1–13 (2019).

324. Dragovic, R. A. *et al.* Isolation of syncytiotrophoblast microvesicles and exosomes and their characterisation by multicolour flow cytometry and fluorescence Nanoparticle Tracking Analysis. *Methods* **87**, 64–74 (2015).

325. LeClaire, M., Gimzewski, J. & Sharma, S. A review of the biomechanical properties of single extracellular vesicles. *Nano Select* (2020) doi:10.1002/nano.202000129.

326. Royo, F. *et al.* Differences in the metabolite composition and mechanical properties of extracellular vesicles secreted by hepatic cellular models. *J Extracell Vesicles* **8**, (2019).

327. Oosthuyzen, W. *et al.* Quantification of human urinary exosomes by nanoparticle tracking analysis. *Journal of Physiology* **591**, 5833–5842 (2013).

328. Weber, A., Wehmeyer, J. C., Schmidt, V., Lichtenberg, A. & Akhyari, P. Rapid fluorescence-based characterization of single extracellular vesicles in human blood with nanoparticle-tracking analysis. *Journal of Visualized Experiments* **2019**, 1–8 (2019).

329. Federici, C. *et al.* Exosome release and low pH belong to a framework of resistance of human melanoma cells to cisplatin. *PLoS One* **9**, (2014).

330. Logozzi, M. *et al.* Microenvironmental pH and exosome levels interplay in human cancer cell lines of different histotypes. *Cancers (Basel)* **10**, (2018).

331. Logozzi, M. *et al.* Increased PSA expression on prostate cancer exosomes in in vitro condition and in cancer patients. *Cancer Lett* **403**, 318–329 (2017).

332. Padda, R. S. *et al.* Nanoscale flow cytometry to distinguish subpopulations of prostate extracellular vesicles in patient plasma. *Prostate* **79**, 592–603 (2019).

333. Logozzi, M., Spugnini, E., Mizzoni, D., Di Raimo, R. & Fais, S. Extracellular acidity and increased exosome release as key phenotypes of malignant tumors. *Cancer and Metastasis Reviews* **38**, 93–101 (2019).

334. Xian, Y., Zhou, M., Han, S., Yang, R. & Wang, Y. A FRET biosensor reveals free zinc deficiency in diabetic beta-cell vesicles. *Chinese Chemical Letters* **31**, 468–472 (2020).

335. Nguyen, D. B. *et al.* Characterization of microvesicles released from human red blood cells. *Cellular Physiology and Biochemistry* **38**, 1085–1099 (2016).

336. Polanco, J. C., Scicluna, B. J., Hill, A. F. & Götz, J. Extracellular vesicles isolated from the brains of rTg4510 mice seed tau protein aggregation in a threshold-dependent manner. *Journal of Biological Chemistry* **291**, 12445–12466 (2016).

337. Wang, Y. *et al.* The release and trans-synaptic transmission of Tau via exosomes. *Mol Neurodegener* **12**, 1–25 (2017).

338. Yang, J. E. *et al.* Complexity and ultrastructure of infectious extracellular vesicles from cells infected by non-enveloped virus. *Sci Rep* **10**, 1–18 (2020).

339. Santos, M. F. *et al.* VAMP-associated protein-A and oxysterol-binding protein–related protein 3 promote the entry of late endosomes into the nucleoplasmic reticulum. *Journal of Biological Chemistry* **293**, 13834–13848 (2018).

340. Mannavola, F. *et al.* Tumor-derived exosomes promote the in vitro osteotropism of melanoma cells by activating the SDF-1/CXCR4/CXCR7 axis. *J Transl Med* **17**, 1–15 (2019).

341. Sorkin, R. *et al.* Nanomechanics of Extracellular Vesicles Reveals Vesiculation Pathways. *Small* **14**, 1–8 (2018).

342. Mattie, S., Kazmirchuk, T., Mui, J., Vali, H. & Brett, C. L. Visualization of SNARE-mediated organelle membrane hemifusion by electron microscopy. *Methods in Molecular Biology* **1860**, 361–377 (2019).

343. Hu, Y., Tian, Z. & Diao, J. Single-Molecule Fluorescence Measurement of SNARE-Mediated Vesicle Fusion. in *SNAREs: Methods and Protocols, Methods in Molecular Biology* (ed. Fratti, R.) vol. 1860 335–344 (2019).

344. Van Lengerich, B., Rawle, R. J., Bendix, P. M. & Boxer, S. G. Individual vesicle fusion events mediated by lipid-anchored DNA. *Biophys J* **105**, 409–419 (2013).

345. Mattheyses, A. L., Atkinson, C. E. & Simon, S. M. Imaging single endocytic events reveals diversity in clathrin, dynamin, and vesicle dynamics. *Traffic* **12**, 1394–1406 (2011).

346. Lin, C. C. *et al.* Control of membrane gaps by synaptotagmin-Ca2+ measured with a novel membrane distance ruler. *Nat Commun* **5**, 1–7 (2014).

347. Stratton, B. S. *et al.* Cholesterol Increases the Openness of SNARE-Mediated Flickering Fusion Pores. *Biophys J* **110**, 1538–1550 (2016).

348. Böcking, T., Upadhyayula, S., Rapoport, I., Capraro, B. R. ; & Kirchhausen, T. Reconstitution of Clathrin Coat Disassembly for Fluorescence Microscopy and Single-Molecule Analysis. *Methods in Molecular Biology* **1847**, 121–146 (2018).

349. Vorselen, D. *et al.* The fluid membrane determines mechanics of erythrocyte extracellular vesicles and is softened in hereditary spherocytosis. *Nat Commun* **9**, (2018).

350. Cao, H. *et al.* In Vivo Real-Time Imaging of Extracellular Vesicles in Liver Regeneration via Aggregation-Induced Emission Luminogens. *ACS Nano* **13**, 3522–3533 (2019).

351. Lai, C. P. *et al.* Dynamic biodistribution of extracellular vesicles in vivo using a multimodal imaging reporter. *ACS Nano* **8**, 483–494 (2014).

352. Gangadaran, P., Hong, C. M. & Ahn, B. C. Current Perspectives on in Vivo Noninvasive Tracking of Extracellular Vesicles with Molecular Imaging. *Biomed Res Int* **2017**, (2017).

353. Lai, C. P., Tannous, B. A. & Breakefield, X. O. Noninvasive In Vivo Monitoring of Extracellular Vesicles. in *Methods in Molecular Biology* vol. 1098 249–258 (2014).

354. van der Vos, K. E. *et al.* Directly visualized glioblastoma-derived extracellular vesicles transfer RNA to microglia/macrophages in the brain. *Neuro Oncol* **18**, 58–69 (2016).

355. Ricklefs, F. L. *et al.* Imaging flow cytometry facilitates multiparametric characterization of extracellular vesicles in malignant brain tumours. *J Extracell Vesicles* **8**, (2019).

356. Lai, C. P. *et al.* Visualization and tracking of tumour extracellular vesicle delivery and RNA translation using multiplexed reporters. *Nat Commun* **6**, (2015).

357. Verweij, F. J., Hyenne, V., Van Niel, G. & Goetz, J. G. Extracellular Vesicles: Catching the Light in Zebrafish. *Trends Cell Biol* **29**, 770–776 (2019).

358. Kobayashi-Sun, J. *et al.* Uptake of osteoblast-derived extracellular vesicles promotes the differentiation of osteoclasts in the zebrafish scale. *Commun Biol* **3**, 1–12 (2020).

359. Sung, B. H. *et al.* A live cell reporter of exosome secretion and uptake reveals pathfinding behavior of migrating cells. *Nat Commun* **11**, 1–15 (2020).

360. Clos-Garcia, M. *et al.* Gut microbiome and serum metabolome analyses identify molecular biomarkers and altered glutamate metabolism in fibromyalgia. *EBioMedicine* **46**, 499–511 (2019).

361. Roman-Canal, B. *et al.* EV-Associated miRNAs from Peritoneal Lavage are a Source of Biomarkers in Endometrial Cancer. *Cancers (Basel)* **11**, (2019).

362. Tian, Y. *et al.* Protein Profiling and Sizing of Extracellular Vesicles from Colorectal Cancer Patients via Flow Cytometry. *ACS Nano* **12**, 671–680 (2018).

363. Clos-Garcia, M. *et al.* Integrative Analysis of Fecal Metagenomics and Metabolomics in Colorectal Cancer. *Cancers (Basel)* **12**, 1142 (2020).

364. Royo, F. & Falcon-Perez, J. M. Liver extracellular vesicles in health and disease. *J Extracell Vesicles* **1**, (2012).

365. He, D. *et al.* Total internal reflection-based single-vesicle in situ quantitative and stoichiometric analysis of tumor-derived exosomal microRNAs for diagnosis and treatment monitoring. *Theranostics* **9**, 4494–4507 (2019).

366. Murakami, Y. *et al.* Comprehensive miRNA Expression Analysis in Peripheral Blood Can Diagnose Liver Disease. *PLoS One* **7**, (2012).

367. Pang, B. *et al.* Extracellular vesicles: The next generation of biomarkers for liquid biopsy-based prostate cancer diagnosis. *Theranostics* **10**, 2309–2326 (2020).

368. Vlaeminck-Guillem, V. Extracellular vesicles in prostate cancer carcinogenesis, diagnosis, and management. *Front Oncol* **8**, (2018).

369. Mateo, L., Guitart-Pla, O., Duran-Frigola, M. & Aloy, P. Exploring the OncoGenomic Landscape of cancer. *Genome Med* **10**, 1–8 (2018).

370. Joncas, F. H. *et al.* Plasma extracellular vesicles as phenotypic biomarkers in prostate cancer patients. *Prostate* **79**, 1767–1776 (2019).

371. Carlsson, J. *et al.* Validation of suitable endogenous control genes for expression studies of miRNA in prostate cancer tissues. *Cancer Genet Cytogenet* **202**, 71–75 (2010).

372. Schaefer, A. *et al.* Suitable reference genes for relative quantification of miRNA expression in prostate cancer. *Exp Mol Med* **42**, 749–758 (2010).

373. Haka, A. S. *et al.* Diagnosing breast cancer using Raman spectroscopy: prospective analysis. *J Biomed Opt* **14**, 054023 (2009).

374. Melo, S. A. *et al.* Glypican1 identifies cancer exosomes and facilitates early detection of cancer. *Nature* **523**, 177–182 (2015).

375. Haka, A. S. *et al.* Diagnosing breast cancer by using Raman spectroscopy. *Proc Natl Acad Sci U S A* **102**, 12371–12376 (2005).

376. Cannon, D. M., Winograd, Jr. N. & Ewing, A. G. Quantitative Chemical Analysis of Single Cells. *Annu. Rev. Biophys. Biomol. Struct.* **29**, 239–263 (2000).

377. Li, X., Dunevall, J. & Ewing, A. G. Quantitative Chemical Measurements of Vesicular Transmitters with Electrochemical Cytometry. *Acc Chem Res* **49**, 2347–2354 (2016).

378. Li, X., Dunevall, J., Ren, L. & Ewing, A. G. Mechanistic Aspects of Vesicle Opening during Analysis with Vesicle Impact Electrochemical Cytometry. *Anal Chem* **89**, 9416–9423 (2017).

379. Ranjbari, E. *et al.* Direct Measurement of Total Vesicular Catecholamine Content with Electrochemical Microwell Arrays. *Anal Chem* **92**, 11325–11331 (2020).

380. Dunevall, J., Majdi, S., Larsson, A. & Ewing, A. Vesicle impact electrochemical cytometry compared to amperometric exocytosis measurements. *Curr Opin Electrochem* **5**, 85–91 (2017).

381. Li, X., Dunevall, J. & Ewing, A. G. Electrochemical quantification of transmitter concentration in single nanoscale vesicles isolated from PC12 cells. *Faraday Discuss* **210**, 353–364 (2018).

382. Ren, L. *et al.* Zinc Regulates Chemical-Transmitter Storage in Nanometer Vesicles and Exocytosis Dynamics as Measured by Amperometry. *Angewandte Chemie - International Edition* **56**, 4970–4975 (2017).

383. Zupanc, J., Bas, E. & Erdogmus, D. Analysis of lipid vesicle populations from microscopy video sequences. *2010 Annual International Conference of the IEEE Engineering in Medicine and Biology Society, EMBC'10* 5050–5053 (2010) doi:10.1109/IEMBS.2010.5626223.

384. Barriere, H. & Lukacs, G. L. Analysis of endocytic trafficking by single-cell fluorescence ratio imaging. *Curr Protoc Cell Biol* 1–21 (2008) doi:10.1002/0471143030.cb1513s40.

385. Li, X., Dunevall, J. & Ewing, A. G. Using Single-Cell Amperometry To Reveal How Cisplatin Treatment Modulates the Release of Catecholamine Transmitters during Exocytosis. *Angewandte Chemie* **128**, 9187–9190 (2016).

386. Chen, T. *et al.* Microwave biosensor dedicated to the dielectric spectroscopy of a single alive biological cell in its culture medium. in *Microwave Symposium Digest (IMS), 2013 IEEE MTT-S International* (2013).

387. Chen, W., Dubuc, D. & Grenier, K. Parametric study of a microwave sensor dedicated to the dielectric spectroscopy of single particles and biological cells. in *2015 European Microwave Conference (EuMC 2015)* 829–832 (2015).

388. Chen, W., Dubuc, D. & Grenier, K. Impact of sensor metal thickness on microwave spectroscopy sensitivity for individual particles and biological cells analysis. in *2016 IEEE Topical Conference on Biomedical Wireless Technologies, Networks, and Sensing Systems (BioWireleSS)* 81–83 (2016).

389. Zhang, M. *et al.* Electrically Controlled Tunable Broadband Interferometric Dielectric Spectroscopy: Groundwork for Single Cell Analysis. in *2019 49th European Microwave Conference (EuMC)* 650–653 (2019).

390. Cui, Y. *et al.* Analyzing Single Giant Unilamellar Vesicles with a Slotline-Based RF Nanometer Sensor. *IEEE Trans Microw Theory Tech* **64**, 1339–1347 (2016).

391. Wu, M. *et al.* Isolation of exosomes from whole blood by integrating acoustics and microfluidics. *Proc Natl Acad Sci U S A* **114**, 10584–10589 (2017).

392. Ku, A. *et al.* Acoustic Enrichment of Extracellular Vesicles from Biological Fluids. *Anal Chem* **90**, 8011–8019 (2018).

393. Ku, A. *et al.* A urinary extracellular vesicle microRNA biomarker discovery pipeline; from automated extracellular vesicle enrichment by acoustic trapping to microRNA sequencing (PLoS ONE (2019) 14: 5 (e0217507) DOI: 10.1371/journal.pone.0217507). *PLoS One* **14**, 1–13 (2019).

394. Trueb, J. T., Avci, O., Sevenler, D., Connor, J. H. & Ünlü, M. S. Robust Visualization and Discrimination of Nanoparticles by Interferometric Imaging. *IEEE Journal of Selected Topics in Quantum Electronics* **23**, 1–11 (2017).

395. Carter, E. P. *et al.* Visualizing Ebolavirus Particles Using Single-Particle Interferometric Reflectance Imaging Sensor (SP-IRIS). in *Ebolaviruses: Methods and Protocols, Methods in Molecular Biology* (eds. Groseth, A. & Hoenen, T.) vol. 1628 373–393 (2017).

396. Ünlü, N. L., Kanik, F. E., Seymour, E., Connor, J. H. & Ünlü, M. S. DNA-Directed Antibody Immobilization for Robust Protein Microarrays: Application to Single Particle Detection 'DNA-Directed Antibody Immobilization. in *Biosensors and Biodetection: Methods and Protocols* (eds. Rasooly, A. & Prickril, B.) vol. 1571 187–206 (2017).

397. Akagi, T. *et al.* On-chip immunoelectrophoresis of extracellular vesicles released from human breast cancer cells. *PLoS One* **10**, 1–13 (2015).

398. Friedrich, R. *et al.* A nano flow cytometer for single lipid vesicle analysis. *Lab Chip* **17**, 830–841 (2017).

399. Obeid, S. *et al.* NanoBioAnalytical characterization of extracellular vesicles in 75-nm nanofiltered human plasma for transfusion: A tool to improve transfusion safety. *Nanomedicine* **20**, (2019).

400. Yokota, S. *et al.* Extracellular vesicles nanoarray technology: Immobilization of individual extracellular vesicles on nanopatterned polyethylene glycol-lipid conjugate brushes. *PLoS One* **14**, 1–13 (2019).

401. Ji, Y. *et al.* Multiplexed profiling of single-cell extracellular vesicles secretion. *Proc Natl Acad Sci U S A* **116**, 5979–5984 (2019).

402. Bai, Y. *et al.* Absolute quantification and analysis of extracellular vesicle lncRNAs from the peripheral blood of patients with lung cancer based on multi-colour fluorescence chip-based digital PCR. *Biosens Bioelectron* **142**, 1–8 (2019).

403. Akagi, T., Kato, K., Hanamura, N., Kobayashi, M. & Ichiki, T. Evaluation of desialylation effect on zeta potential of extracellular vesicles secreted from human prostate cancer cells by on-chip microcapillary electrophoresis. *Jpn J Appl Phys* **53**, (2014).

404. Cortazar, A. R. *et al.* CANCERTOOL: A Visualization and Representation Interface to Exploit Cancer Datasets. *Cancer Res* **78**, 6320–6328 (2018).

405. De Spiegelaere, W. *et al.* Reference Gene Validation for RT-qPCR, a Note on Different Available Software Packages. *PLoS One* **10**, e0122515 (2015).

406. Andersen, C. L., Jensen, J. L. & Ørntoft, T. F. Normalization of Real-Time Quantitative Reverse Transcription-PCR Data: A Model-Based Variance Estimation Approach to Identify Genes Suited for Normalization, Applied to Bladder and Colon Cancer Data Sets. *Cancer Res* **64**, 5245–5250 (2004).

407. Pfaffl, M. W., Tichopad, A., Prgomet, C. & Neuvians, T. P. *Determination of Stable Housekeeping Genes, Differentially Regulated Target Genes and Sample Integrity: BestKeeper-Excel-Based Tool Using Pair-Wise Correlations. Biotechnology Letters* vol. 26 http://www.wzw.tum.de/gene-quantification/bestkeeper.html (2004).

408. McKiernan, J. *et al.* A urine-based Exosomal gene expression test stratifies risk of high-grade prostate Cancer in men with prior negative prostate biopsy undergoing repeat biopsy. *BMC Urol* **20**, 138 (2020).

409. Poschner, S., Zehl, M., Maier-Salamon, A. & Jäger, W. Simultaneous quantification of estrogens, their precursors and conjugated metabolites in human breast cancer cells by LC–HRMS without derivatization. *J Pharm Biomed Anal* **138**, 344–350 (2017).

410. Mueller, J. W., Gilligan, L. C., Idkowiak, J., Arlt, W. & Foster, P. A. The regulation of steroid action by sulfation and desulfation. *Endocr Rev* **36**, 526–563 (2015).

411. Bordanaba-Florit, G., Royo, F., Kruglik, S. G. & Falcón-Pérez, J. M. Using single-vesicle technologies to unravel the heterogeneity of extracellular vesicles. *Nat Protoc* (2021) doi:10.1038/s41596-021-00551-z.

412. Pathan, M. *et al.* Vesiclepedia 2019: A compendium of RNA, proteins, lipids and metabolites in extracellular vesicles. *Nucleic Acids Res* **47**, D516–D519 (2019).

413. Quanson, J. L. *et al.* High-throughput analysis of 19 endogenous androgenic steroids by ultra-performance convergence chromatography tandem mass spectrometry. *J Chromatogr B Analyt Technol Biomed Life Sci* **1031**, 131–138 (2016).

414. Indapurkar, A., Hartman, N., Patel, V. & Matta, M. K. Simultaneous UHPLC-MS/MS method of estradiol metabolites to support the evaluation of Phase-2 metabolic activity of induced pluripotent stem cell derived hepatocytes. *J Chromatogr B Analyt Technol Biomed Life Sci* **1126–1127**, 121765 (2019).

415. Im, E. *et al.* Simultaneous determination of androgens and prostaglandins in human urine using ultra-high-performance liquid chromatography–tandem mass spectrometry. *J Chromatogr B Analyt Technol Biomed Life Sci* **1109**, 45–53 (2019).

416. Qin, F., Zhao, Y. Y., Sawyer, M. B. & Li, X. F. Hydrophilic interaction liquid chromatography-tandem mass spectrometry determination of estrogen conjugates in human urine. *Anal Chem* **80**, 3404–3411 (2008).

417. Lee, Y. R. *et al.* Untargeted metabolomics and steroid signatures in urine of male pattern baldness patients after finasteride treatment for a year. *Metabolites* **10**, (2020).

418. Maeda, N. *et al.* Accurate determination of tissue steroid hormones, precursors and conjugates in adult male rat. *J Biochem* **153**, 63–71 (2013).

419. Fernandes, D., Navarro, J. C., Riva, C., Bordonali, S. & Porte, C. Does exposure to testosterone significantly alter endogenous metabolism in the marine mussel Mytilus galloprovincialis? *Aquatic Toxicology* **100**, 313–320 (2010).

420. Li, Y., Yan, Z., Li, X., Yin, X. & Li, K. UPLC–TOF–MS method for simultaneous quantification of steroid hormones in tissue homogenates of zebrafish with solid-phase extraction. *Molecules* **26**, (2021).

421. Ceglarek, U. *et al.* Rapid quantification of steroid patterns in human serum by on-line solid phase extraction combined with liquid chromatography-triple quadrupole linear ion trap mass spectrometry. *Clinica Chimica Acta* **401**, 114–118 (2009).

422. Koal, T., Schmiederer, D., Pham-Tuan, H., Röhring, C. & Rauh, M. Standardized LC-MS/MS based steroid hormone profile-analysis. *Journal of Steroid Biochemistry and Molecular Biology* **129**, 129–138 (2012).

423. Yuan, T. F., Le, J., Wang, S. T. & Li, Y. An LC/MS/MS method for analyzing the steroid metabolome with high accuracy and from small serum samples. *J Lipid Res* **61**, 580–586 (2020).

424. Dong, Z., Wang, C., Zhang, J. & Wang, Z. A UHPLC-MS/MS method for profiling multifunctional steroids in human hair. *Anal Bioanal Chem* **409**, 4751–4769 (2017).

425. Isobe, T. *et al.* Determination of estrogens and their conjugates in water using solid-phase extraction followed by liquid chromatography-tandem mass spectrometry. *J Chromatogr A* **984**, 195–202 (2003).

426. Schepers, U., Ermer, J., Preu, L. & Wätzig, H. Wide concentration range investigation of recovery, precision and error structure in liquid chromatography. *Journal of Chromatography B* **810**, 111–118 (2004).

427. Van Liempd, S., Cabrera, D., Mato, J. M. & Falcon-Perez, J. M. A fast method for the quantitation of key metabolites of the methionine pathway in liver tissue by high-resolution mass spectrometry and hydrophilic interaction ultra-performance liquid chromatography. *Anal Bioanal Chem* **405**, 5301–5310 (2013).

428. Liang, X. *et al.* Evaluation of homogenization techniques for the preparation of mouse tissue samples to support drug discovery. *Bioanalysis* **3**, 1923–1933 (2011).

429. Doc. No. SANCO/12495/2011. *Method Validation & Quality Control Procedures for Pesticide REsidue Analysis in Food and Feed* 41 Preprint at (2012).

430. Bobrie, A., Colombo, M., Krumeich, S., Raposo, G. & Thery, C. Diverse subpopulations of vesicles secreted by different intracellular mechanisms are present in exosome preparations obtained by differential ultra-centrifugation. *J Ayurveda Integr Med* **1**, 18397 (2012).

431. Bordanaba-Florit, G. metabolites-185209. Preprint at https://figshare.com/articles/dataset/_/20231493 (2022).

432. Giles, K. *et al.* Applications of a travelling wave-based radio-frequency-only stacked ring ion guide. *Rapid Communications in Mass Spectrometry* **18**, 2401–2414 (2004).

433. Kenny, D. J., Worthington, K. R. & Hoyes, J. B. Scanwave: A new approach to enhancing spectral data on a tandem quadrupole mass spectrometer. *J Am Soc Mass Spectrom* **21**, 1061–1069 (2010).

434. Taylor, P. J. Matrix effects: The Achilles heel of quantitative high-performance liquid chromatography-electrospray-tandem mass spectrometry. *Clin Biochem* **38**, 328–334 (2005).

435. Campbell, I. Adrenocortical hormones. *Anaesthesia and Intensive Care Medicine* **9**, 420–423 (2008).

436. Rosol, T. J., Yarrington, J. T., Latendresse, J. & Capen, C. C. Adrenal Gland : Structure, Function, and Mechanisms of Toxicity. *Toxicol Pathol* **29**, 41–48 (2016).

437. Rainey, W. E. & Nakamura, Y. Regulation of the Adrenal Androgen Biosynthesis. *Journal of Steroid Biochemistry and Molecular Biology* **108**, 281–286 (2008).

438. Puhka, M. *et al.* Metabolomic profiling of extracellular vesicles and alternative normalization methods reveal enriched metabolites and strategies to study prostate cancer-related changes. *Theranostics* **7**, 3824–3841 (2017).

439. Yang, B. *et al.* Novel Metabolic Signatures of Prostate Cancer Revealed by 1H-NMR Metabolomics of Urine. *Diagnostics* **11**, 149 (2021).

440. Dinges, S. S. *et al.* Cancer metabolomic markers in urine: evidence, techniques and recommendations. *Nat Rev Urol* **16**, 339–362 (2019).

441. Yu, C. *et al.* Identification of the metabolic signatures of prostate cancer by mass spectrometry-based plasma and urine metabolomics analysis. *Prostate* **81**, 1320–1328 (2021).

442. Warrack, B. M. *et al.* Normalization strategies for metabonomic analysis of urine samples. *J Chromatogr B Analyt Technol Biomed Life Sci* **877**, 547–552 (2009).

443. Veselkov, K. A. *et al.* Optimized preprocessing of ultra-performance liquid chromatography/mass spectrometry urinary metabolic profiles for improved information recovery. *Anal Chem* **83**, 5864–5872 (2011).

444. Bordanaba-Florit, G., Liempd, S. van, Cabrera, D., Royo, F. & Falcón-Pérez, J. M. Simultaneous Quantification of Steroid Hormones Using hrLC-MS in Endocrine Tissues of Male Rats and Human Samples. *Metabolites* **12**, (2022).

445. Cardoso, H. J. *et al.* Revisiting prostate cancer metabolism: From metabolites to disease and therapy. *Med Res Rev* **41**, 1499–1538 (2021).

446. Cutruzzolà, F. *et al.* Glucose metabolism in the progression of prostate cancer. *Frontiers in Physiology* vol. 8 Preprint at https://doi.org/10.3389/fphys.2017.00097 (2017).

447. Keshet, R., Szlosarek, P., Carracedo, A. & Erez, A. Rewiring urea cycle metabolism in cancer to support anabolism. *Nature Reviews Cancer* vol. 18 634–645 Preprint at https://doi.org/10.1038/s41568-018-0054-z (2018).

448. Dillard, P. R., Lin, M. F. & Khan, S. A. Androgen-independent prostate cancer cells acquire the complete steroidogenic potential of synthesizing testosterone from cholesterol. *Mol Cell Endocrinol* **295**, 115–120 (2008).

449. Auchus, R. J. & Sharifi, N. Annual Review of Medicine Sex Hormones and Prostate Cancer. (2020) doi:10.1146/annurev-med-051418.

450. Miller, W. L. Steroid hormone synthesis in mitochondria. *Mol Cell Endocrinol* **379**, 62–73 (2013).

451. Simonsl, K. & Lkonenz, E. *How Cells Handle Cholesterol. 20. Y. Karnada et dl., 1. Cell Biol* vol. 349 www.sciencernag.org (1994).

452. Van Niel, G., D'Angelo, G. & Raposo, G. Shedding light on the cell biology of extracellular vesicles. *Nature Reviews Molecular Cell Biology* vol. 19 213–228 Preprint at https://doi.org/10.1038/nrm.2017.125 (2018).

453. Colombo, M., Raposo, G. & Théry, C. Biogenesis, secretion, and intercellular interactions of exosomes and other extracellular vesicles. *Annual review of cell and developmental biology* vol. 30 255–289 Preprint at https://doi.org/10.1146/annurev-cellbio-101512-122326 (2014).

454. Yáñez-Mó, M. *et al.* Biological properties of extracellular vesicles and their physiological functions. *Journal of Extracellular Vesicles* vol. 4 1–60 Preprint at https://doi.org/10.3402/jev.v4.27066 (2015).

455. Mathivanan, S., Ji, H. & Simpson, R. J. Exosomes: Extracellular organelles important in intercellular communication. *Journal of Proteomics* vol. 73 1907–1920 Preprint at https://doi.org/10.1016/j.jprot.2010.06.006 (2010).

456. Wang, M., Altinoglu, S., Takeda, Y. S. & Xu, Q. Integrating protein engineering and bioorthogonal click conjugation for extracellular vesicle modulation and intracellular delivery. *PLoS One* **10**, (2015).

457. Gupta, D. *et al.* Quantification of extracellular vesicles in vitro and in vivo using sensitive bioluminescence imaging. *J Extracell Vesicles* **9**, (2020).

458. Han, C. & Qin, G. Reporter Systems for Assessments of Extracellular Vesicle Transfer. *Frontiers in Cardiovascular Medicine* vol. 9 Preprint at https://doi.org/10.3389/fcvm.2022.922420 (2022).

459. Takahashi, Y., Nishikawa, M. & Takakura, Y. In Vivo Tracking of Extracellular Vesicles in Mice Using Fusion Protein Comprising Lactadherin and Gaussia Luciferase. *Methods Mol Biol* **1660**, 245–254 (2017).

460. Verweij, F. J. *et al.* The power of imaging to understand extracellular vesicle biology in vivo. *Nat Methods* **18**, 1013–1026 (2021).

461. Morishita, M. *et al.* Quantitative analysis of tissue distribution of the B16BL6-derived exosomes using a streptavidin-lactadherin fusion protein and Iodine-125-Labeled biotin derivative after intravenous injection in mice. *J Pharm Sci* **104**, 705–713 (2015).

462. Zomer, A. *et al.* In vivo imaging reveals extracellular vesicle-mediated phenocopying of metastatic behavior. *Cell* **161**, 1046–1057 (2015).

463. Verweij, F. J. *et al.* Live Tracking of Inter-organ Communication by Endogenous Exosomes In Vivo. *Dev Cell* **48**, 573-589.e4 (2019).

464. O'Brien, K., Breyne, K., Ughetto, S., Laurent, L. C. & Breakefield, X. O. RNA delivery by extracellular vesicles in mammalian cells and its applications. *Nature Reviews Molecular Cell Biology* vol. 21 585–606 Preprint at https://doi.org/10.1038/s41580-020-0251-y (2020).

465. Men, Y. *et al.* Exosome reporter mice reveal the involvement of exosomes in mediating neuron to astroglia communication in the CNS. *Nat Commun* **10**, (2019).

466. de Jong, O. G. *et al.* A CRISPR-Cas9-based reporter system for single-cell detection of extracellular vesicle-mediated functional transfer of RNA. *Nat Commun* **11**, (2020).

467. Yanagisawa, N. *et al.* Stromogenic prostatic carcinoma pattern (carcinomas with reactive stromal grade 3) in needle biopsies predicts biochemical recurrence-free survival in patients after radical prostatectomy. *Hum Pathol* **38**, 1611–1620 (2007).

468. Kojima, Y. *et al.* Autocrine TGF-β and stromal cell-derived factor-1 (SDF-1) signaling drives the evolution of tumor-promoting mammary stromal myofibroblasts. *Proc Natl Acad Sci U S A* **107**, 20009–20014 (2010).

469. Carstens, J. L. *et al.* FGFR1-WNT-TGF-β signaling in prostate cancer mouse models recapitulates human reactive stroma. *Cancer Res* **74**, 609–620 (2014).

470. Andersen, M. K. *et al.* Integrative metabolic and transcriptomic profiling of prostate cancer tissue containing reactive stroma. *Sci Rep* **8**, 1–11 (2018).

471. Bolte, S. & Cordelières, F. P. A guided tour into subcellular colocalization analysis in light microscopy. *J Microsc* **224**, 213–232 (2006).

472. Palmulli, R. *et al.* CD63 regulates cholesterol storage within endosomes and its distribution via exosomes. *Res Sq* **PREPRINT**, (2022).

473. Cenedella, R. J. Cholesterol synthesis inhibitor U18666A and the role of sterol metabolism and trafficking in numerous pathophysiological processes. *Lipids* vol. 44 477–487 Preprint at https://doi.org/10.1007/s11745-009-3305-7 (2009).

474. Lim, C. Y. *et al.* ER–lysosome contacts enable cholesterol sensing by mTORC1 and drive aberrant growth signalling in Niemann–Pick type C. *Nat Cell Biol* **21**, 1206–1218 (2019).

475. Castellano, B. M. *et al.* Lysosomal cholesterol activates mTORC1 via an SLC38A9-Niemann-Pick C1 signaling complex. *Science (1979)* **355**, 1306–1311 (2017).

476. Boerrigter, E. *et al.* Liquid biopsy reveals KLK3 mRNA as a prognostic marker for progression free survival in patients with metastatic castration-resistant prostate cancer undergoing first-line abiraterone acetate and prednisone treatment. *Mol Oncol* **15**, 2453–2465 (2021).

477. Visser, W. C. H. *et al.* Clinical use of the mRNA urinary biomarker SelectMDx test for prostate cancer. *Prostate Cancer Prostatic Dis* **25**, 583–589 (2022).

478. Tonry, C., Finn, S., Armstrong, J. & Pennington, S. R. Clinical proteomics for prostate cancer: understanding prostate cancer pathology and protein biomarkers for improved disease management. *Clin Proteomics* **17**, 41 (2020).

479. Tessem, M. B. *et al.* A balanced tissue composition reveals new metabolic and gene expression markers in prostate cancer. *PLoS One* **11**, 1–15 (2016).

480. Webber, J. P. *et al.* Prostate stromal cell proteomics analysis discriminates normal from tumour reactive stromal phenotypes. *Oncotarget* **7**, 20124–20139 (2016).

481. Andersen, M. K., Giskeødegård, G. F. & Tessem, M. B. Metabolic alterations in tissues and biofluids of patients with prostate cancer. *Curr Opin Endocr Metab Res* **10**, 23–28 (2020).

482. Hanahan, D. & Weinberg, R. A. Hallmarks of cancer: The next generation. *Cell* **144**, 646–674 (2011).

483. Andersen, M. K. *et al.* Spatial differentiation of metabolism in prostate cancer tissue by MALDI-TOF MSI. *Cancer Metab* **9**, 1–13 (2021).

484. Andersen, M. K. *et al.* Integrative metabolic and transcriptomic profiling of prostate cancer tissue containing reactive stroma. *Sci Rep* **8**, 1–11 (2018).

485. Giatromanolaki, A., Koukourakis, M. I., Koutsopoulos, A., Mendrinos, S. & Sivridis, E. The metabolic interactions between tumor cells and tumor-associated stroma (TAS) in prostatic cancer. *Cancer Biol Ther* **13**, 1284–1289 (2012).

486. Tyekucheva, S. *et al.* Stromal and epithelial transcriptional map of initiation progression and metastatic potential of human prostate cancer. *Nat Commun* **8**, 1–10 (2017).

487. Frankenstein, Z. *et al.* Stromal reactivity differentially drives tumour cell evolution and prostate cancer progression. *Nat Ecol Evol* **4**, 870–884 (2020).

488. Richards, Z. *et al.* Prostate Stroma Increases the Viability and Maintains the Branching Phenotype of Human Prostate Organoids. *iScience* **12**, 304–317 (2019).

489. Nazarenko, I. *et al.* Cell surface tetraspanin Tspan8 contributes to molecular pathways of exosome-induced endothelial cell activation. *Cancer Res* **70**, 1668–1678 (2010).

490. Hood, J. L., Pan, H., Lanza, G. M. & Wickline, S. A. Paracrine induction of endothelium by tumor exosomes. *Laboratory Investigation* **89**, 1317–1328 (2009).

491. Ramteke, A. *et al.* Exosomes secreted under hypoxia enhance invasiveness and stemness of prostate cancer cells by targeting adherens junction molecules. *Mol Carcinog* **54**, 554–565 (2015).

492. Josson, S. *et al.* Stromal fibroblast-derived miR-409 promotes epithelial-to-mesenchymal transition and prostate tumorigenesis. *Oncogene* **34**, 2690–2699 (2015).

493. Minciacchi, V. R. *et al.* MYC mediates large oncosome-induced fibroblast reprogramming in prostate cancer. *Cancer Res* **77**, 2306–2317 (2017).

494. Shephard, A. P. *et al.* Stroma-derived extracellular vesicle mRNA signatures inform histological nature of prostate cancer. *J Extracell Vesicles* **10**, (2021).

495. van der Kloet, F. M., Bobeldijk, I., Verheij, E. R. & Jellema, R. H. Analytical error reduction using single point calibration for accurate and precise metabolomic phenotyping. *J Proteome Res* **8**, 5132–5141 (2009).

496. Moses, L. E. Matched Pairs *t* -Tests. in *Encyclopedia of Statistical Sciences* (John Wiley & Sons, Inc., Hoboken, NJ, USA, 2006). doi:10.1002/0471667196.ess1551.pub2.

497. Pang, Z. *et al.* MetaboAnalyst 5.0: narrowing the gap between raw spectra and functional insights. *Nucleic Acids Res* **49**, W388–W396 (2021).

498. Köhler, N., Rose, T. D., Falk, L. & Pauling, J. K. Investigating Global Lipidome Alterations with the Lipid Network Explorer. *Metabolites* **11**, 488 (2021).

499. Mitchell, J. P., Court, J., Mason, M. D., Tabi, S. & Clayton, A. Increased exosome production from tumour cell cultures using the Integra CELLine Culture System. *J Immunol Methods* **335**, 98–105 (2008).

500. Tuxhorn, J. A., Ayala, G. E. & Rowley, D. R. Reactive stroma in prostate cancer progression. *Journal of Urology* **166**, 2472–2483 (2001).

501. Jefferies, H. *et al.* Glutathione. *ANZ J Surg* **73**, 517–522 (2003).

502. Tosi, M. R. & Tugnoli, V. Cholesteryl esters in malignancy. *Clinica Chimica Acta* **359**, 27–45 (2005).

503. Horvath, S. E. & Daum, G. Lipids of mitochondria. *Prog Lipid Res* **52**, 590–614 (2013).

504. Funai, K., Summers, S. A. & Rutter, J. Reign in the membrane: How common lipids govern mitochondrial function. *Curr Opin Cell Biol* **63**, 162–173 (2020).

505. Owen, J. S., Clayton, A. & Pearson, H. B. Cancer-Associated Fibroblast Heterogeneity, Activation and Function: Implications for Prostate Cancer. *Biomolecules* **13**, 67 (2022).

506. Melchionna, R., Trono, P., Di Carlo, A., Di Modugno, F. & Nisticò, P. Transcription factors in fibroblast plasticity and CAF heterogeneity. *Journal of Experimental & Clinical Cancer Research* **42**, 347 (2023).

507. Webber, J., Yeung, V. & Clayton, A. Extracellular vesicles as modulators of the cancer microenvironment. *Semin Cell Dev Biol* **40**, 27–34 (2015).

508. Franco, O. E. *et al.* Altered TGF-β Signaling in a Subpopulation of Human Stromal Cells Promotes Prostatic Carcinogenesis. *Cancer Res* **71**, 1272–1281 (2011).

509. Galbraith, L., Leung, H. Y. & Ahmad, I. Lipid pathway deregulation in advanced prostate cancer. *Pharmacol Res* **131**, 177–184 (2018).

510. Wu, X., Daniels, G., Lee, P. & Monaco, M. E. Lipid metabolism in prostate cancer. *Am J Clin Exp Urol* **2**, 111–20 (2014).

511. Kuemmerle, N. B. *et al.* Lipoprotein Lipase Links Dietary Fat to Solid Tumor Cell Proliferation. *Mol Cancer Ther* **10**, 427–436 (2011).

512. Gazi, E. *et al.* Direct evidence of lipid translocation between adipocytes and prostate cancer cells with imaging FTIR microspectroscopy. *J Lipid Res* **48**, 1846–1856 (2007).

513. Condorelli, F., Canonico, P. L. & Sortino, M. A. Distinct effects of ceramide-generating pathways in prostate adenocarcinoma cells. *Br J Pharmacol* **127**, 75–84 (1999).

514. Fiorani, F. *et al.* Ceramide releases exosomes with a specific miRNA signature for cell differentiation. *Sci Rep* **13**, 10993 (2023).

515. Kimura, K., Markowski, M., Edsall, L. C., Spiegel, S. & Gelmann, E. P. Role of ceramide in mediating apoptosis of irradiated LNCaP prostate cancer cells. *Cell Death Differ* **10**, 240–248 (2003).

516. De Petrocellis, L. *et al.* The endogenous cannabinoid anandamide inhibits human breast cancer cell proliferation. *Proceedings of the National Academy of Sciences* **95**, 8375–8380 (1998).

517. Schmid, P. C., Wold, L. E., Krebsbach, R. J., Berdyshev, E. V. & Schmid, H. H. O. Anandamide and other *N*-acylethanolamines in human tumors. *Lipids* **37**, 907–912 (2002).

518. Mimeault, M., Pommery, N., Wattez, N., Bailly, C. & Hénichart, J.-P. Anti-proliferative and apoptotic effects of anandamide in human prostatic cancer cell lines: Implication of epidermal growth factor receptor down-regulation and ceramide production. *Prostate* **56**, 1–12 (2003).

519. Read, J. *et al.* Nuclear transportation of exogenous epidermal growth factor receptor and androgen receptor via extracellular vesicles. *Eur J Cancer* **70**, 62–74 (2017).

520. Schubert, A. & Boutros, M. Extracellular vesicles and oncogenic signaling. *Mol Oncol* **15**, 3–26 (2021).

521. Soekmadji, C., Rockstroh, A., Ramm, G. A., Nelson, C. C. & Russell, P. J. Extracellular Vesicles in the Adaptive Process of Prostate Cancer during Inhibition of Androgen Receptor Signaling by Enzalutamide. *Proteomics* **17**, (2017).

List of Figures

List of Tables

Abbreviations

18srRNA	18S ribosomal RNA	**DMEM**	Dulbecco's modified eagle medium
α-SMA	α smooth muscle actin	**DNA**	Deoxyribonucleic acid
AA	Aminoacids	**DRE**	Digital rectal examination
ACTB	Actin beta	**ECAR**	Extracellular acidification rate
ACTH	Adrenocorticotropin	**EDC**	Enhance duty-cycle
AD	Androgen-dependent	**ER**	Endoplasmic reticulum
ADT	Androgen deprivation therapy	**ESE**	Early sorting endosome
AFM	Atomics force microscopy	**ESI**	Electrospray ionisation
AFM-IR	AFM coupled to infrared spectroscopy	**EV**	Extracellular vesicle
AI	Androgen independent	**FA**	Fatty acid
AJCC	American Joint Committee on Cancer	**FAP**	Fibroblast activation protein
AKR	Aldo-keto reductase	**FBS**	Fetal Bovine Serum
AKT	Serine/threonine kinase	**FCCP**	Carbonyl cyanide-p-trifluoromethoxy-phenylhydrazone
ARE	Androgen response elements	**FFAox**	Oxidised fatty acids
ATP	Adenosyl triphosphate	**FITC**	Fluoresce in isothiocyanate
AUC	Area under the curve	**FRIA**	Fluorescent ratiometric image analysis
BMI	Body mass index	**FRET**	Fluorescence resonance energy transfer
BPH	Bening prostatic hyperplasia	**FSH**	Follicle stimulating hormone
CAF	Cancer associated fibroblast	**FWHM**	Full width at half maximum
cDNA	Complementary DNA	**GAPDH**	Glyceraldehyde 3-phosphate dehydrogenase
CE	Cholesteryl esters	**GPC1**	Glypican 1
Cer	Ceramides	**GnRH**	Gonadotropin-releasing hormone
CHD	Carbohydrate derivatives	**GS**	Gleason score
CRC	Colorectal cancer	**hCAF**	Prostatic CAF, hTERT
cryo-TEM	Cryogenic transmission electron microscopy	**HEPE**	Hydroxyeicosapentaenoic acid
CRH	Corticotropin-releasing hormone	**HexCer**	Hexosylceramides
COMT	Catechol-O-methyltransferase	**HKG**	Housekeeping gene
Ctrl	Control	**HMDB**	Human metabolome database
CYP	Cytochrome P450	**hNAF**	Prostatic stroma fibroblast, WPMY-1
CYP17A1	Steroid 17-alpha-monooxygenase	**HOXC6**	Homeobox C6 protein
CYP19A1	Aromatase	**hrFC**	High resolution Flow Cytometry
DAG	Diacylglicerides	**hrLCMS**	High resolution liquid chromatography coupled to mass spectrometry
DAPI	4',6-diamidino-2-phenylindole	**HSD**	Hydroxysteroid dehydrogenase
DHT	Dihydrotestosterone	**HSP**	Heat-shock protein
DHEA	Dehydroepiandrosterone	**ILV**	Intraluminal vesicles
DHEAS	DHEA sulfate	**IQR**	Interquartile range
DHRS11	Dehydrogenase/Reductase 11	**ISEV**	International Society for Extracellular Vesicles
ddPCR	Digital droplet PCR	**KEGG**	Kyoto encyclopedia of genes and genomes
DFS	Disease-free survival	**KLK3**	Kallikrein Related Peptidase 3
DLX1	Distal-Less Homeobox 1	**LAL**	Acid lipase

LAMP-2	Lysosome-associated membrane protein 2		**PVDF**	Polyvinylidene difluoride
LH	Lutenizing hormone		**QC**	Quality control
LIMP-2	Lysosomal integral membrane protein-2		**qPCR**	Real-time quantitative PCR
LOD	Limit of detection		**RNA**	Ribonucleic acid
LOQ	Limit of quantification		**ROC**	Receiver operating curve
LPC	Lysophosphatidylethanolamines		**RPMI**	Roswell Park Memorial Institute
LPDS	Lipoprotein deficient serum		**RTK**	Receptor tyrosine kinase
LPE	Lysophosphatidylcholines		**RTM**	Raman tweezers microspectroscopy
LSE	Late sorting endosome		**SEC**	Size exclusion chromatography
LRTOMT	Leucine-rich transmembrane and O-methyltransferase domain containing		**SERS**	Surface enhanced Raman spectroscopy
MAG	Monoacylglicerides		**SFA**	Saturated fatty acids
MAPK	Mitogen-activated protein kinase		**SHBG**	Sex hormone binding globulin
mRNA	Messenger RNA		**SM**	Sphingomyelins
MS	Mass spectrometer		**S/N**	Signal-to-noise ratio
MSEA	Metabolite set enrichment analysis		**SNARE**	N-ethylmaleimide sensitive factor receptor protein
MSI	Mass spectrometry imaging		**SPDEF**	SAM pointed domain-containing Ets transcription factor
MUFA	Monounsaturated fatty acids		**SPE**	Solid phase extraction
m/z	Mass-to-charge ratio		**SP-IRIS**	Single-particle interferometric reflectance imaging sensor
MVA	Multivariate analysis		**SRD**	Steroid reductase
MVB	Multivesicular body		**SRM**	Super Resolution Microscopy
NAE	N-acylethanolamines		**STARD3**	Steroidogenic Acute Regulatory protein domain 3
NAD	Nicotinamide adenine dinucleotide		**STORM**	Stochastic optical reconstruction microscopy
NMR	Nuclear magnetic ressonance		**ST**	Steroids
NPC	Niemann–Pick complex		**STS**	Steroid sulfatase
Ns	Nucleosides		**SULT**	Hydroxysteroid sulfotransferase
Nt	Nucleotides		**SVA**	Single vesicle analysis
NTA	Nanoparticle Tracking Analysis		**TAG**	Triacylglicerides
OCR	Oxygen consumption rate		**TCA**	Tricarboxylic acid cycle
ORA	Over-representation analysis		**TGF-β**	Transforming growth factor β
OXPHOS	Oxidative phosphorylation		**TIRF**	Total internal reflection fluorescence
PALM	Photoactivation localisation microscopy		**TNM**	Tumour, Node, Metastasis
PBS	Phosphate-saline buffer		**TopF**	BODIPY-cholesterol
PC	Phosphatidylcholines		**t-SNARE**	Target membrane SNARE
PCa	Prostate cancer		**U-Drug**	U18666A inhibitor
PCA-3	Prostate cancer antigen 3		**uEV**	Urinary extracellular vesicle
PCR	Polymerase chain reaction		**UGT**	UDP glucuronosyltransferase
PE	Phosphatidylethanolamines		**UPLC**	Ultra-performance liquid chromatography
PI	Phosphatidylinositols		**XIC**	Extracted ion current
PI3K	Phosphoinositide 3-kinase		**VIEC**	Vesicle impact electrochemical cytometry
PSA	Prostate specific antigen		**Vit**	Vitamins
PUFA	Polyunsaturated fatty acids		**VLDL**	Very low density lipoparticle

Supplementary material

1	*REVIEW*	3D Cell Cultures as Prospective Models to Study Extracellular Vesicles in Cancer	*Used in Introduction*
		https://doi.org/10.3390/cancers13020307	
2	*REVIEW*	Using single-vesicle technologies to unravel the heterogeneity of extracellular vesicles	*Used in Chapter 1*
		https://doi.org/10.1038/s41596-021-00551-z	
3	*ORIGINAL ARTICLE*	Simultaneous Quantification of Steroid Hormones Using hrLC-MS in Endocrine Tissues of Male Rats and Human Samples.	*Used in Chapter 3*
		https://doi.org/10.3390/metabo12080714	
4	*ORIGINAL ARTICLE*	Integration of proteomics and metabolomics reveals metabolic alterations of prostate cancer fibroblasts from patient's stroma samples.	*Used in Chapter 5*
		Under revision	

3D Cell Cultures as Prospective Models to Study Extracellular Vesicles in Cancer

Guillermo Bordanaba-Florit [1], **Iratxe Madarieta** [2], **Beatriz Olalde** [2], **Juan M. Falcón-Pérez** [1,3,4] and **Félix Royo** [1,3,*]

1. Center for Cooperative Research in Biosciences (CIC bioGUNE), Exosomes Laboratory, Basque Research and Technology Alliance (BRTA), E48160 Derio, Spain; gbordanaba@cicbiogune.es (G.B.-F.); jfalcon@cicbiogune.es (J.M.F.-P.)
2. TECNALIA Basque Research and Technology Alliance (BRTA), E20009 Donostia San Sebastian, Spain; iratxe.madarieta@tecnalia.com (I.M.); beatriz.olalde@tecnalia.com (B.O.)
3. Centro de Investigación Biomédica en Red de Enfermedades Hepáticas y Digestivas (Ciberehd), E28029 Madrid, Spain
4. Ikerbasque, Basque Foundation for Science, E48009 Bilbao, Spain
* Correspondence: froyo.ciberehd@cicbiogune.es

Simple Summary: 3D cell cultures are a qualitative improvement in cancer research because these models preserve cancer physiological characteristics better than traditional bi-dimensional cultures. Moreover, they facilitate the study of complex 3D interactions using extracellular matrices and the co-culture of different cell types. In this manner, the cells can contact themselves in a fully physiological but also controlled arrangement. In the context of tumor interactions, extracellular vesicles are essential in number of key aspects in oncology: as major interactors with extracellular matrix, as cell-to-cell messengers, as carriers of diagnostic-valuable biomarkers, and as target-specific treatment-deliver agents. The present article aims to discuss the findings achieved using 3D culture models in oncology. We further review the involvement of extracellular vesicles in the pathogenesis of cancer as well as their potential use in diagnostics and therapeutics.

Abstract: The improvement of culturing techniques to model the environment and physiological conditions surrounding tumors has also been applied to the study of extracellular vesicles (EVs) in cancer research. EVs role is not only limited to cell-to-cell communication in tumor physiology, they are also a promising source of biomarkers, and a tool to deliver drugs and induce antitumoral activity. In the present review, we have addressed the improvements achieved by using 3D culture models to evaluate the role of EVs in tumor progression and the potential applications of EVs in diagnostics and therapeutics. The most employed assays are gel-based spheroids, often utilized to examine the cell invasion rate and angiogenesis markers upon EVs treatment. To study EVs as drug carriers, a more complex multicellular cultures and organoids from cancer stem cell populations have been developed. Such strategies provide a closer response to in vivo physiology observed responses. They are also the best models to understand the complex interactions between different populations of cells and the extracellular matrix, in which tumor-derived EVs modify epithelial or mesenchymal cells to become protumor agents. Finally, the growth of cells in 3D bioreactor-like systems is appointed as the best approach to industrial EVs production, a necessary step toward clinical translation of EVs-based therapy.

Keywords: 3D culture; extracellular vesicles; tumoral cells; cancer; therapy

1. Introduction

In recent years, the number of scientific groups dedicated to the study of extracellular vesicles has grown notably, and with it the amount of published information describing extracellular vesicles (EVs) physiology. Released by all types of cells, they are an important

tool to study cell's biology, and to look for biomarkers. Cancer research is one of the main fields that can benefit of the study of EVs associated to tumors. In fact, the vesicle-mediated cell-to-cell crosstalk seems to be important in every step of cancer progression [1]. In parallel, the study of cancer biology had evolved itself along the last years towards culture models that reflect the biological complexity of tumoral cells and their interactions with the extracellular matrix. The reason is that the traditional bidimensional (2D) cultures differ from tridimensional (3D) cultures in their morphological characteristics, proliferation rate and degree of differentiation, the level of cell-to-cell interaction and cell-to-matrix, as well as their resistance to drugs [2,3]. However, the application of complex culture models to unravel the role of EVs in cancer research has not been yet popularized among EVs research, given the difficulties that this type of cultures presents, both technically and in terms of cost. Nevertheless, several studies have highlighted the importance of 3D cultures in the study of EVs in cancer research [4–6]. In this article, we aim to emphasize the contribution of those studies as a fundamental path to understand the involvement of EVs in cancer physiology and to pinpoint possible applications to the clinical oncology. To help to understand the background of this review, we are providing a short introduction to the different roles that EVs play in cancer and cancer therapy, and a brief description of the different 3D cultures employed to study tumoral cells. Afterwards, the review summarizes different studies that employ 3D culture systems to elucidate the role of EVs in cancer biology, diagnosis and therapy.

2. The 3D Cultures as a Physiological Model of Tumoral Cells

For many years, in vitro models were based on 2D monolayers of immortalized human cancer-derived cell lines. The popularization of 3D culturing has come with the observation that this type of cell cultures often retain heterogeneity. This feature allows the study of tumor evolution. Moreover, 3D cultures offer advantages over conventional monolayered cell cultures including preservation of the topology and cell-to-matrix interactions [7,8]. On the other hand, the application of 3D cultures is also challenging, given the difficulties to stabilize the cultures, and the requirement of specific material to perform the culture. In Table 1, we present a comparative between 2D and 3D cultures characteristics. In spite of the difficulties, 3D cultures become a great model to study the interplay between cancer and non-cancer cells in order to unveil biological mechanisms involved in cancers initiation and progression [9]. Spheroids are probably the type of 3D culture most commonly used. Spheroid formation methodologies can be divided into two categories: scaffold-based models, either incorporating materials which are components of the matrix (collagen, fibronectin, agarose, laminin, and gelatin) [10], or synthetic materials that provide cell support [11], and scaffold-free models that comprise non-adherent and in suspension cells, which are forced to aggregate and form spheroids [12].

Table 1. Main advantages and limitations of the different cellular models in cancer research [13,14].

Model	Advantages	Limitations
2D Monolayers	Easy and cost effective Large amount of data available Reproducible cultures, easy to work for downstream applications and imaging	Reduced cell-to-cell interactions Different sensitivity to drugs Loss of biological characteristics over time
Gel based 3D Cultures	Cell–ECM interactions Possible to incorporate different factors in the gel, extending release over time Uniform spheroids/organoids	Difficult to dispense cells Change of growth media could be irregular Difficult to retrieve cells and downstream analysis
Low-attachment plates	Simpler and cheaper when compared to gel based systems Long-term culture	Time consuming and low yield achieved Heterogenous spheroids
Microfluidic systems	Possible chemical gradients Control of fluid rates Convenient for multicellular cultures controlling cell locations	Expensive commercial devices or not well-characterized "in house" build devices Fluidic problems related to bubbles and clogging

One of the first applications of 3D cultures was the study of tumorigenesis. Typically, the cells are cultured in a mouse sarcoma-derived gel (i.e., Matrigel®). Other alternatives exist, such human leiomyoma discs and their matrix (Myogel). This has been commercialized for in vitro assays such IncuCyte®, spheroid and sandwich assays [15].

3D culture models grown in vitro from cancer stem directly or from primary tissues are a more evolved form of organoids [16]. The latter option has an attractive potential for personalized medicine. For instance, when comparing organoids derived from primary colorectal tumors and metastatic lesions isolated from the same patients, it has been observed that they share common mutations. This implies that the driver alterations preceded metastatic dissemination [17]. Organoids display greater number of features and functions of their original organs, such architecture and gene expression, reason why they have a prospective potential for the cancer research. The combination of organoids with the co-culture of multiple cells can mimic the tumor immune microenvironment, including key features like immune check point [18]. Organoids derived from different mouse or human tumors have now been widely adopted to investigate different types of cancer, for example. colorectal cancer [19]. Moreover, by culturing organoids in the proper media conditions, they could serve as a model of the three most common subtypes of liver cancer: hepatocellular carcinoma, cholangiocarcinoma, and combined hepatocellular cholangiocarcinoma [20]. Several other models such as prostate, brain or kidney organoids have been stablished and largely reviewed in [21].

In addition to organoids, other kinds of 3D cultures have been developed. 3D bioprinting can be defined as a layer-by-layer deposition of biomaterial, such as tissue spheroids, cell pellets, microcarriers, decellularized extracellular matrix, and cell-laden hydrogels, in a well-defined structure to generate viable 3D cultures. In the last decade, the bioprinting technologies have undergone remarkable advancements [22]. Current trends utilizing scaffold technologies aim at capturing more of the micro-environmental cues than other model systems [23,24]. The scaffolds may act as a surrogate for the missing ECM, representing the available space of tumor tissue, providing the physical support for cell growth, adhesion, and proliferation, and causing the cells to form an appropriate spatial distribution and cell-cell or cell-ECM interaction [2].

A wide range of techniques are used in generating different scaffolds, including solvent casting/particulate leaching, freeze-drying, phase inversion, electrospinning, stereolithography, selective laser sintering, shape deposition manufacturing, 3D printing, robotic microassembly, and fused deposition modeling [25]. Among these techniques, freeze drying, phase inversion, and fiber electrospinning are used most of the times. Commonly materials used for tumor cells 3D culture are a laminin-rich basement membrane extract gelatin (for instance Matrigel, Myogel or Cultrex BME) [26], silk fibroin proteins [27], hyaluronic acid [28], collagen [29], or decellularized material [30,31]. Greater understandings of tumor microenvironment have identified ECM to play critical roles in orchestrating drug resistance, disease progression and tumor metastasis [32]. Two independent articles have revealed that lack of ECM during 3D culture could not elicit pathological phenotypes observed in vivo, such as maintaining cancer-associated fibroblasts behaviors [33] or stromal barriers [34]. Scaffold based 3D cell culture, using a biological basement membrane, captures many aspects of the spatial cues (cell-to-cell communication, cell-to-matrix adhesion, and physical characteristics) and provides a unique compromise between complexity and practicality [35]. The choice of a biological scaffold is not simply to deliver an anchorage site for cells but also to provide a complex structure enabling communication linked to cell behavior and function [36]. The formation of 3D structures within the culture also reproduces aspects of the nutrient and oxygen gradients found across in vivo tumors. It should be considered that those 3D scaffolds can be used not only to simulate the microenvironment but alto to assess drug research. Recently publications have showed the ability of decellularized ECM materials to encapsulate and controlled delivery of different drugs such as dexamethasone [37] or doxorubicin [38]. So, 3D scaffold

can have drug-carrier functions in therapeutic applications related to testing drugs and in predicting treatment efficacies.

In this review, we will find examples of the different 3D strategies employed to study the different roles of extracellular vesicles in cancer, and which models are the most employed to solve each question regarding the role of EVs in tumorigenicity processes (Figure 1).
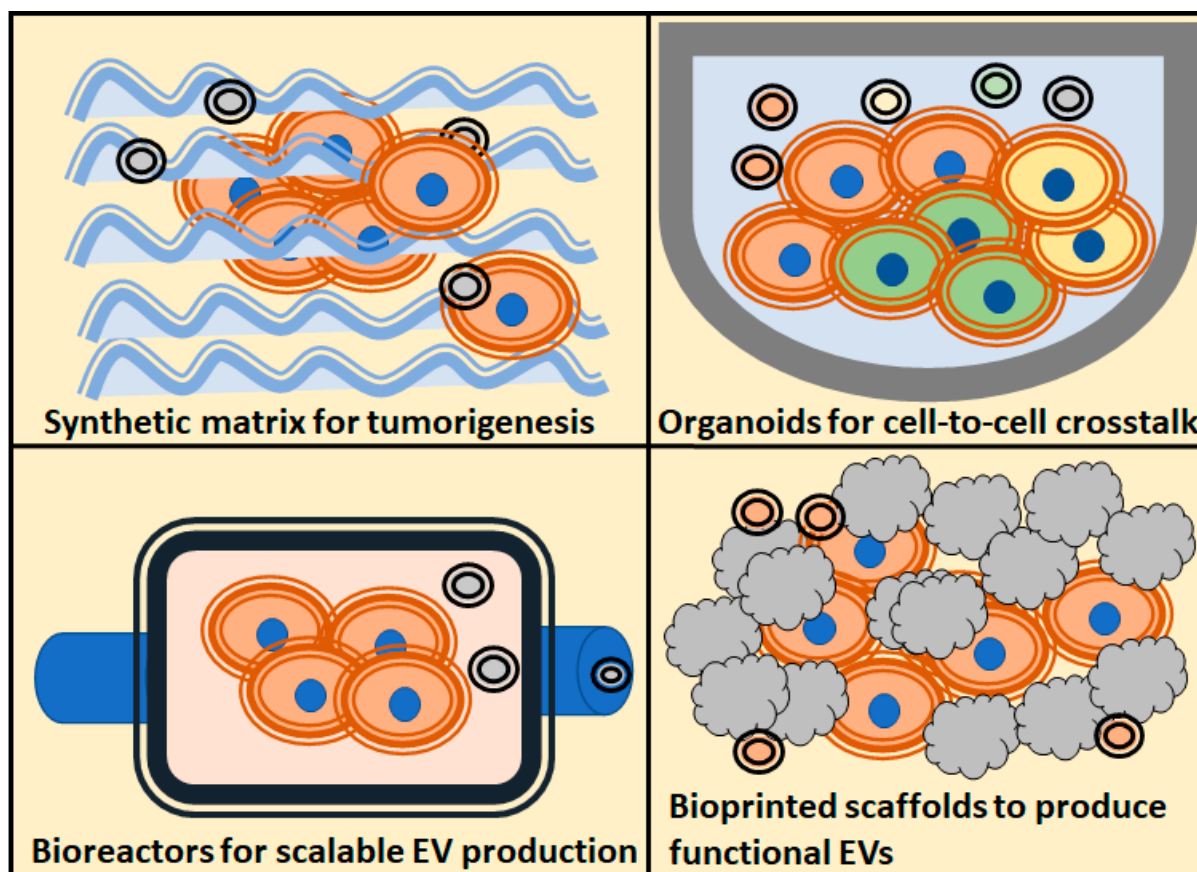
Figure 1. Schematic overview of the most popularized 3D culture techniques, and the main assays regarding extracellular vesicles (EVs) applications to the study of tumors biology, use of EVs as therapeutic agents, study of tumorigenesis and cell-to-cell crosstalk.

3. Extracellular Vesicles in Cancer Research

Since the first descriptions of EVs and their different types, it has been reported that tumoral cells secrete vesicles. These vesicles participate in the cellular cross-talk with the cellular matrix [39] and cancer cells are rather effective in vesicular-mediated intercellular transfer [40]. Actually, this transfer is a requirement of tumoral cells to stablish a connection with the surrounding matrix and to actively regulate processes involved in cancer progression and autocrine/paracrine oncogenesis. Indeed, EVs play an important role in reprogramming stromal cells, modulating the immune system, and promoting angiogenesis (reviewed in [41]). Moreover, the dependency of tumors on vesicular communication also concerns the preparation of an extracellular niche for metastasis [42–44]. For more detailed reviews about the implications of EVs in tumor biology and progression there are very interesting reviews published along the last years [5,45,46], and there are also specific publications related to prostate cancer EVs [6,8].

Tumor communication with targeted cells has a tight reliance on EVs. For this reason, many opportunities for diagnostic and treatment appeared with the analysis and the manipulation of EVs. It is well-known that most malignancies are associated with an increase of circulating EVs. Moreover, it has been described that in different tumor models

exist a correlation between tumor volumes and the concentration of circulating EVs in blood [47]. These EVs carry a cargo with precious information about the tumor, and they have become the substrate for biomarker digging in all types of malignancies [48–50] including prostate cancer [51–53].

In parallel, many studies have focused on how circulating EVs are being captured by tumoral cells, and how to increase the specificity of the capture of EVs by tumoral cells using different strategies. An interesting line of research studies EV membrane decoration with proteins. For example, LAMP2b protein has been successfully fused to ligands specific for brain, angiogenic endothelium, or IL3 receptors on myeloid leukemia cells to direct EVs specifically toward the selected tissue [54–56]. Other considerations, such as biodistribution, permeability of tumoral cells, and ability to deliver the cargo shall be taken in account and have been largely reviewed in [57].

All these examples unveil the need to deep into the understanding of the three key aspects of cancer research: pathogenesis, diagnosis, and therapy. Below, we will be described how 3D models have contributed to gain knowledge in those topics, and what are the most interesting results obtained so far. For clarity, we talk about EVs even if the original work refers to as exosomes; in most of those articles, the isolation methods employed actually enriched the preparation in small vesicles, but not necessary in vesicles originated from the endocytic pathway.

4. Production of EVs in 3D Cultures

As we mentioned previously, 3D culturing allows cells to grow in a physiological topology, and organoids and spheroids still release EVs. More importantly, the EVs produced are functional; EVs released by pancreatic cancer organoids can activate p38 MAPK and induce the expression of F-box protein 32 and UBR2 in myotubes [58]. When compared to 2D conformations, 3D cultures show an increase in EVs release in the case of colorectal cancer stem cells [59]. For colon cancer organoids, the presence of APC mutations that activate WNT pathway enhanced the EVs release in Matrigel-based cultures. This release was probably also favored by the presence of collagen (a component of the extracellular matrix), since it is part of this type of gel [60]. Moreover, another plausible explanation is that the release of EVs in 3D cultures may be partially driven by the higher expression of transporters. The expression of the ATP-binding cassette transporter G1, a cholesterol lipid efflux pump, was reported to be highly expressed in tumoroids of colon adenocarcinoma cells with enhanced stemness. Likewise, the silencing of this transporter blocks the release of EVs and increases the accumulation of intracellular vesicles [61].

Interestingly, cell architecture can be manipulated by applying different collagen concentrations and adding components that are found naturally in the dermis such as fibronectin. Breast cancer cells cultured in 3D following this approach experienced morphological alterations [62]. Moreover, these changes are translated into differences in the cargo of secreted EVs population [62]. Remarkably, there is evidence that 3D culturing presents different gene expression signatures due to the more physiological nanoenvironment of this arrangement. For instance, prostate-derived adenocarcinoma cells (PC-3 and DU145) form large and slowly growing organoids that express multiple stem cell markers, neuroendocrine markers and intercellular adhesion molecules likely to occur in vivo as well. Importantly, 3D cultures promoted the secretion of HSP90 and EpCAM loaded EVs, which are markers of cancer stem cells phenotype [63]. Another example of the physiological environment effect has been observed in cervical cancer 3D cultures. In this case, the EVs were loaded with a small RNA profile comparable (~96% similarity) to in vivo circulating plasma-derived EVs from cervical cancer patients [64].

Moreover, tridimensional architecture allows a better cell orientation and asymmetry. It implies that different populations of EVs loaded with different markers and cargo proteins are released from apical and basal sides of the cells. As an example, organoids derived from colon carcinoma cell line LIM1863 release two types of EVs. Apical EVs are characterized by the presence of EpCAM, and the exclusive identification of the trafficking

molecules CD63, mucin 13, and the apical intestinal enzyme sucrase isomaltase, but also an increase in the expression of dipeptidyl peptidase IV and the apically-restricted pentaspan membrane glycoprotein prominin 1 [65]. In contrast, EVs containing the colon epithelial cell-specific A33 marker were enriched with basolateral trafficking molecules such as early endosome antigen 1, the golgi membrane protein ADP-ribosylation factor, and clathrin. These observations are consistent with EpCAM- and A33-EVs being released from the apical and basolateral surfaces of colon carcinoma cells respectively [65].

One of the most important outcomes of the different alterations described here is that cancer cells have a wide range of responses to their environment. In cancer cells response to drugs, a higher release of EVs after chemotherapy treatments has been reported [66]. Interestingly, this observation has been useful to stablish a discovery pipeline of secreted biomarkers in the media of organoid cultures and to identify new protein markers as a response to chemotherapy [66].

Due to the lack of an established biomanufacturing platform for EVs, which is a limitation for clinical translation, one of the most interesting applications of 3D cultures is the large scale and standardizable production of EVs. A simple approach is the use of bioreactor flasks since they increase the production of EVs released by tumoral cells [67]. A more interesting application is to use cell cultures in microfluidic platforms. These automated devices can produce therapeutic exosomes, which could also be engineered, and harvest them in real-time from the on-chip cultures. For instance, this type of tool has been used in leukocytes isolated from human blood [68]. Alternatively, a 3D-printed scaffold-perfusion bioreactor system has been employed to assess the effect of dynamic cultures on the production of EVs from endothelial cells. With this approach the cells were able to maintain their functionality (i.e., pro-vascularization bioactivity or pro-angiogenic gene expression) [69].

5. Modelling the Antitumoral Effect of EVs in 3D Cultures

As we mentioned in the previous section, the arrangement of cells in tridimensional conformations often suppose a better physiological model of drug therapy. This is also an advantage to study the application of EVs as potential therapeutical assets against tumoral cells. Up to date, multiple strategies have been designed to increase the antitumoral effect of EVs (Figure 2). According to the literature, most of the 3D culture systems employed to reveal the antitumoral effect of EVs are spheroids or organoids formed with tumor-derived cell lines. Indeed, tumor spheroids are the most common models for testing drug effectivity [70]. Notably, 3D cultures with a single type of cells are likely to exhibit different drug responses than those composed of heterogenous populations of cells [70].

The spontaneous effect of normal cell-derived EVs has been investigated to use them as natural antitumoral agents. For example, glia-derived EVs have shown an antitumoral effect in spheroids of glioma cells by reducing the invasion capacity of the tumor over time [71]. Another example are EVs derived from mesenchymal stroma cells (MSCs) that can inhibit angiogenesis and maintain vascular homeostasis in activated endothelial cells [72]. However, most of the publications focus on the possibility of loading EVs with antitumoral drugs and biomolecules such amino acids, lipoproteins, or nucleic acids. The antitumoral effect of EVs loaded with a specific miRNA (miR-497) has been assayed in a microfluidic device containing a mixture of cells. These types of devices are useful in combination with an extracellular matrix since it allows the study of migration in response to a factor controlled by microfluidic channels [73]. In this case, the cells employed were the non-small cell lung cancer cell line A549 cultured together with human umbilical vein endothelial cells (HUVEC). In these conditions, the tube formation of endothelial cells was inhibited and the migration of the tumor decreased dramatically compared to the control [74]. To avoid limitation of the cocultures associated to cell separation after analysis, both types of cells were separated in the microfluidic devices by Matrigel component. This is a very interesting example of using 3D culturing to mimic the physiological complexity of tumors.
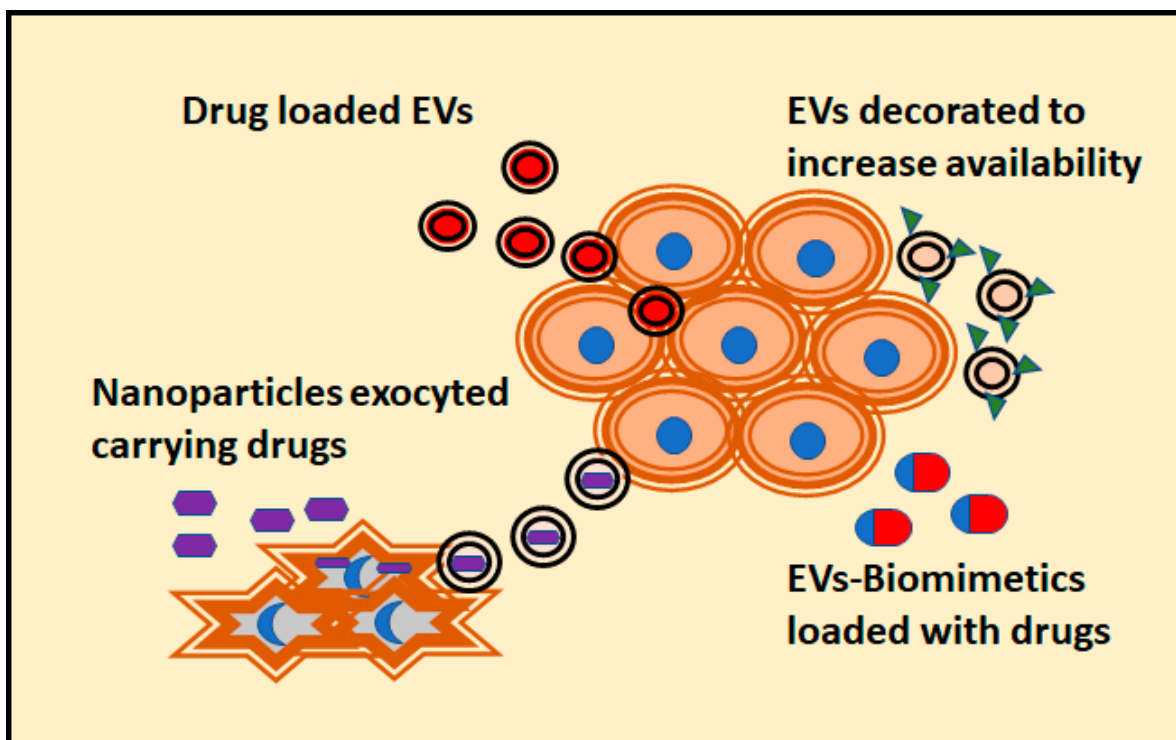
Figure 2. Different strategies attempted to confer antitumoral activity to EVs are depicted. The preferred 3D culture assay for these tests are organoids, with a closer physiological response to in vivo cells. In addition, the penetrance of the drug carried by EVs compared to its free forms can be evaluated. This measurement is not possible to obtain using 2D cultures.

The efforts for loading EVs with antitumoral drugs are well documented in the literature. The importance of EVs as antitumoral agents lays upon the tumor avidity for vesicles. Many approaches consist in loading the EVs with a chemotherapeutic agent. Although still very inefficient, there are different strategies; the simplest methods consist in incubating the drugs with purified EVs [75], and an alternative is to treat parental cells with the drug that would be released by EVs. In a more sophisticated way, a modification on the surface of the EVs allow a targeted loading of the drug (reviewed in [76]). For instance, EVs obtained from endometrial cells have been loaded with atorvastatin and can induce significant apoptotic effects and inhibit the growth of glioblastoma spheroids [77]. Moreover, endothelial cell-derived EVs loaded with meta-tetra(hydroxyphenyl)chlorine can penetrate up to 100 μm in multicellular tumor organoids. Consequently, these EVs increased photodynamic activity, which translates into higher rates of cell mortality [78]. This is a promising result that shows an improvement in the penetration capability compared to liposomes, and hence in the vectorization molecules capabilities. Furthermore, the production of EVs from patient-derived cells is an interesting strategy to overcome many of the problems associated with bioreagent-based therapy. The treatment of melanoma spheroids with macrophage-derived EVs loaded with acridine orange has maintained the delivery of this drug for longer time in comparison to the treatment with free acridine orange [79].

A more sophisticated approach to design antitumoral EVs is their decoration with molecules that promote the interaction between cells and vesicles. This strategy has described an increase of the avidity and specificity of cells to uptake the decorated EVs. For instance, HepG2 cells and human primary liver cancer-derived organoids accumulate more efficiently EVs that have been decorated with tetrahedral DNA nanostructures conjugated with DNA aptamer [80]. These EVs can effectively deliver an engineered cargo, which consists of CRISPR-Cas9 RNA-guided endonucleases, aiming to silence the expression of the protein Wnt-10b. In fact, these EVs inhibited the growth of tumoral cells in vitro [80]. Another strategy was to decorate methotrexate-loaded EVs with Lys-Leu-Ala bound to

low-density lipoprotein peptides. The functionalization of the methotrexate-loaded EVs increased the uptake by human primary glioma cell line U87 growing into 3D glioma spheroids and increased the cell mortality rate [81]. Although the use of EVs as carrier of antitumoral molecules is very promising, there are still several limitations. For example, this type of EVs-based drug delivery approach needs accurate isolation methods for those EVs subpopulation that display favorable tropism and the understanding of EVs transport properties is still scarce. In addition, scalable manufacturing remains a major hurdle for clinical translation [82]. A very detailed revision of ongoing clinical trials regarding the use of EVs can be found in [83].

An attempt to overcome some of these problems is the use of EVs mimetics. One of the first solutions to generate "on demand" EVs was to obtain them by shearing cells through a sequential filtering. When loaded with doxorubicin, these EVs mimetics were more effective in targeting ovarian cancer cells in 3D cultures than free doxorubicin. In addition, they showed a higher encapsulation efficiency and drug release over time in comparison to naturally released EVs [84]. Spheroids derived from cancer stem cell have been targeted with tumor-cell-exocytosed nanoparticles made of porous silicon. These synthetic particles loaded with doxorubicin are fed to tumoral cells, which release the nanoparticles with the doxorubicin inside of EVs. This approach greatly improves drug performance over hepatocarcinoma spheroids in comparison to free doxorubicin or the direct use of synthetic particles (Figure 2) [85].

## 6. EVs-Mediated Crosstalk between the Tumor and Cellular Matrix

6.1. Tumoral Cells Modify Surroundings Cells through EVs

EVs are released by malignant cells and can further influence the cellular components of the matrix. There are different models employed to study that effect, which vary from low to high complexity. Synthetic gel cultures are the most employed models to study the invasion or tubule formation in cultures with a single type of cell models. A classic example of these type of models is represented by the treatment of HUVEC cells cultured on Matrigel with EVs derived from chronic myelogenous leukemia. It causes the reorganization of HUVEC cells into tubes [86] but also, the movement of EVs within and between nanotubular structures further connecting the remodeled endothelial cells [87]. In addition, the effect of renal cancer cell-derived EVs, which induce VEGF expression in HUVEC cells has also been described [88].

Regarding the tumor-matrix crosstalk, MSCs probably are the most interesting players due to their response to EVs treatment in bioengineered 3D microenvironments. EVs derived from MDA-MB-231 (metastatic breast cancer cell line) have shown to convert MSCs into tumor-activated MSCs. This results in an immunomodulatory phenotype that was particularly prominent in response to bone-tropic cancer cells. In contrast, MCF7 (considered a non-metastatic breast cancer cell line) -derived EVs failed to generate this phenotype in the MSCs culture [89]. It has also been reported that colorectal EVs induce alterations in colonic MSCs morphology and increase MSCs proliferation, migration, and invasion. Colorectal EVs also provoke a higher ability to form spheroids, and an impact on the metabolic respiration by the acidification of the extracellular environment associated with a plasma membrane redistribution of vacuolar H^+-ATPase. They also increase the expression of the carcinoembryonic antigen. These modifications suggest that colorectal cell-derived EVs are able to activate MSCs to favor tumor growth and malignant progression [90]. Likewise, the treatment of ovarian cancer spheroids with cisplatin showed a release of EVs that can alter MSC cells. These MSCs displayed an increase in the migration pattern and secreted more amount of interleukin-6 (IL-6), interleukin-8 (IL-8), and VEGFA. Moreover, bone marrow MSCs induce angiogenesis in endothelial cells and the migration of low-invasive ovarian cancer cells upon contact with EVs [91].

The effect of prostate cancer EVs dominates a new program of MSC differentiation that impairs both the classical adipogenic differentiation and the skewing differentiation towards alpha-smooth muscle actin (αSMA) positive myofibroblastic cells (Figure 3). The differentiated MSC performed pro-angiogenic functions and enhanced the tumor proliferation and invasivity in a 3D co-culture model. In this case, the differentiation was dependent on TGFβ containing EVs. Remarkably, a comparable dose of soluble TGFβ could not generate the same phenotype [92]. Tumor-derived EVs can target fibroblasts directly. Moreover, early-stage primary colorectal adenocarcinoma cells have shown to be unable to invade Matrigel matrix themselves. Alternatively, they secrete EVs to reprogram normal fibroblasts and acquire a de novo capacity to invade first the matrix and thence, the adenocarcinoma cells. It is worth to mention that EVs upregulate fibroblast proteins implicated in focal adhesion, regulators of actin cytoskeleton and signaling pathways important in pro-invasive remodeling of extracellular matrix [93]. In addition, epithelial cells can be transformed by tumoral EVs; a recent study described how human peritoneal mesothelial cells treated with epithelial ovary cancer-derived EVs accumulate miR-99a-5p. The presence of miR-99a-5p drives the invasion in a 3D Matrigel culture model due to a higher expression levels of fibronectin and vitronectin [94].

Multiple cellular models are more complex than single cell cultures and are interesting structures to mimic tumor complexity. The development of multicellular lung organoids mimicking the lung microenvironment with air sac-like structures and lung surfactant proteins has shown that pretreating the cells with tumor exosomes triggered cancer cell colonization. Notably, the sensitivity to drug therapy described in this multicellular model is closer to in vivo observations rather than the sensitivity obtained with 2D or single cell 3D cultures [70]. The other major advantage of multicellular cultures is that they allow the study of different interactions simultaneously. However, it is worth to remark that these desirable characteristics can only be achieved through an extensive experimental testing, and such characterization is challenging, since synthetic multi-population systems are among the most complex systems described to date [95]. A successful example is the design of a microfluidic device with multiple cells that mimics the tumor microenvironment in situ, including extracellular matrix (ECM), interstitial flow and environmental EVs. Such device has been employed to study the endothelial-mesenchymal transition (EMT). The number of cancer-associated fibroblasts (CAFs) differentiated from HUVECs increased upon treatment with melanoma-derived EVs, hence promoting EMT. The negative pro-tumorogenic effect of cancer-derived EVs over HUVEC cells could be intensified by the enrichment of miR-221-3p containing EVs [96]. In cervical squamous carcinoma cells derived EVs, vesicular miR-221-3p promoted angiogenesis in Matrigel tube formation assay, but also an increase in spheroid sprouting and migration, and induced a faster wound healing. Moreover, cancer stem carcinoma cell-derived EVs transport miR-221-3p from cancer cells to vessel endothelial cells and promote angiogenesis by downregulating the protein THBS2 [96]. On another hand, the transformation from fibroblast to myofibroblast can be impaired by depleting RAB35. The phenotype of the remaining EVs population is insufficient to drive the fibroblast to myofibroblast differentiation, showing attenuated motile behaviors in 3D in vitro models [97]. In contrast, MSCs derived EVs suppress EMT, maintain vascular homeostasis, and ultimately lead to the recovery of CAFs back to endothelial cells [72].
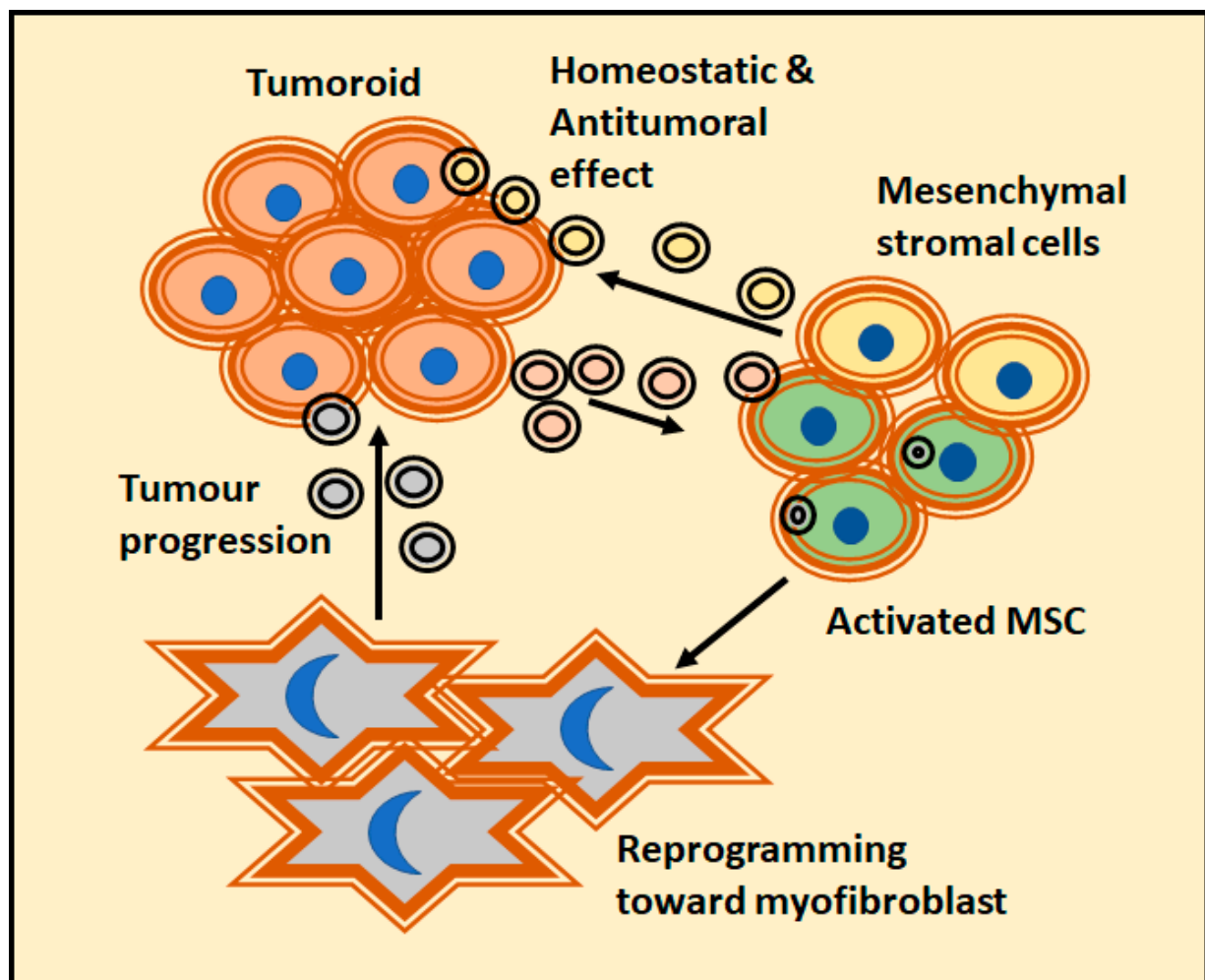
Figure 3. A clear example of tumor-matrix interaction was provided by the prostate cancer models and their action over mesenchymal stroma cells (MSCs). It is a complex relationship were EVs released by tumors could change the fate of MSC. While MSC-derived EVs have a homeostatic effect, activated MSCs usually reprogram themselves into myofibroblast and actively favor tumor progression.

6.2. Tumoral EVs Modify the Tumoral Cells

Thanks to the efficient way of capturing EVs, tumor cells have the ability to acquire or recover phenotypes from other cancer cells by recycling the cargo contained in their EVs. In this respect, MMP3 is an interesting molecule. MMP3 is a matrix metalloproteinase that enhances proliferation and tumorigenesis. Lung metastatic tumoroid cells with MMP3 knocked out (MMP3-KO) showed a significant reduction in tumoroid size and they developed a necrotic area within tumoroids. However, when MMP3-KO cells were treated with EVs from the original lung metastatic line, they recovered expression of MMP3, but also CD9 (a vesicular marker) and Ki-67 (proliferation marker) [98]. In another study, hypoxia have shown to enhance the release of EVs from colorectal cancer cells in an Hypoxia Induced Factor (HIF1)-dependent manner, and these EVs further stimulated motility, invasiveness and stemness of primary tumor cells SW480 [99]. A study with pancreatic ductal adenocarcinoma cells (PDAC) have demonstrated that the presence of asparaginyl endopeptidase-containing EVs derived from adenocarcinoma enhanced the invasive ability of PDAC cells, whereas EVs lacking that molecule decreased their invasive ability [100]. In the case of gastric cancer cells, the release of EVs with either high or low CD97 has been described. These two types of EVs had differences on their promotion of tumor invasion in Matrigel cultures in a dose-dependent manner. This supports the protumoral effect of CD97 in this model [101].

Some melanoma diseases overexpress RAB27A, a well-known protein in the mechanism of the formation of exosomes through the endocytic pathway. The silencing of RAB27A in melanoma cell lines caused an inhibition of 3D spheroid invasion and cell motility in vitro, as well as the spontaneous metastases in vivo. Interestingly, the effect can be reverted by using RAB27A-replete EVs. However, the effect cannot be reverted if EVs from melanoma RAB27A knockdown cells are used instead, suggesting that this gene is the responsible of promoting a population of pro-invasive EVs [102]. A similar interplay phenomenon can be observed using claudin-loaded EVs in claudin knockdown cells [103]. Remarkably, there is more evidence that tumoral cells are influenced by tumor-derived EVs. A 3D co-culture performed with original colorectal adenocarcinoma cell line and cellular subclones resistant to 5-fluorouracil demonstrated naïve spheroids release EVs loaded with miR-200 family members. This miRNA family is well-known to repress EMT and consequently, attenuate plasticity and migration. Horizontal miR-200 signaling prevented resistant adenocarcinoma tumor spheroids to disrupt the continuous lymphendothelial cell layer. In addition, they lost the ability to generate a circular chemorepellent-induced defect [104]. On contrary, EVs from 5-fluorouracil resistant colorectal carcinoma, which are devoid of miR200, accelerated circular chemorepellent-induced defects [105].

6.3. Effect of EVs Released by the Cellular Component of the Matrix over Tumor Cells

A common strategy to study the effect of EVs released by the cellular component of the matrix is to generate organoids or spheroids using tumor cells. This could be also translated into clinical approaches; for instance, the generation of organoids with patient-derived colorectal cancer cells organoids. Fibroblast-derived EVs induce colony formation of colorectal carcinoma organoids under hypoxia. In contrast, there is no major effect of tumor-derived EVs on the activation of fibroblasts [60]. Fibroblast-derived EVs induce cell proliferation (in an epidermal growth factor-dependent manner) to colorectal cancer patient-derived organoids, and the data pointed to vesicular amphiregulin as a major factor in inducing cell proliferation [106]. The EVs derived from macrophages had also an effect over tumoral cells, and the effect increases when the release of EVs is induced by deoxycholic acid treatment. EVs released in such condition increases the expression of spasmolytic polypeptide-expressing metaplasia markers (TFF2 and GSII lectin) in gastric organoids compared to EVs derived from macrophages without deoxycholic acid stimulation [107].

It has been also described that EVs secreted by MSCs obtained from patients with oral leukoplakia and dysplasia, or oral carcinoma, exhibited induction of proliferation, migration and invasion of oral carcinoma cells in 3D coculture. This effect is significantly higher than the one obtained co-culturing carcinoma cells and normal oral mucosa MSCs [108]. The homeostatic and antitumoral role of healthy MSC-derived EVs has been documented in complex 3D cultures ultimately reverting CAFs back to endothelial cells [72]. However, it has been also described that MSCs were capable to stimulate human glioblastoma cell proliferation through a paracrine effect mediated by TGFB1. Moreover, MSCs in direct cell-cell contact with glioblastoma cells provoked an increased proliferative and invasive tumor cell behavior under 3D culture conditions [109].

7. Conclusions

In this review, we have described examples in which different 3D culture strategies are employed to assess the effect of EVs over cells. The most common strategies are gel-based cultures; both spheroid and organoids are used depending on the cell complexity. However, there are also examples of microfluidic systems and bioreactors. These experiments showed that cells in a 3D culture system behave differently than in 2D cultures, often in a more similar manner to in vivo conditions. This should be taken in account when performing studies relative to drug sensitivity or EVs release. The possibility of implementing co-cultures in 3D models allows complex interactions and obtaining results relative to the cellular crosstalk, but we should also remark that such models require extensive characterization. By using co-cultures, it can be described how tumoral EVs can modify cells from the

matrix to display antitumoral activity, but also induce the release of EVs that feeds back the activation of tumoral cells itself. In addition to the description of tumor biology, other important application of 3D models focusses on the study of EVs as chemotherapy carriers. The use of organoids and spheroids as models allows the measure of drug penetrance, and the observed cell sensitivity to those drugs seems to be closer to in vivo results, when compared to studies using cell monolayers. Another point where 3D cultures can help is to solve the problems inherent to scale the production. Notably, bioreactors are of increasing interest as a source of standardized and scalable production platforms of EVs. Although there is still a long way to solve all the technical challenges, the adoption of 3D culture models will bring a qualitative improvement on the discovery of potential applications of EVs in cancer research.

Author Contributions: Conceptualization and original draft preparation F.R., writing—review and editing, G.B.-F., I.M., B.O., J.M.F.-P. All authors have read and agreed to the published version of the manuscript.

Institutional Review Board Statement: Not applicable.

Informed Consent Statement: Not applicable.

Data Availability Statement: Not applicable.

Conflicts of Interest: The authors declare no conflict of interest.

References

1. Meehan, K.; Vella, L.J. The contribution of tumour-derived exosomes to the hallmarks of cancer. *Crit. Rev. Clin. Lab. Sci.* **2016**, *53*, 121–131. [CrossRef]
2. Lv, D.; Hu, Z.; Lu, L.; Lu, H.; Xu, X. Three-dimensional cell culture: A powerful tool in tumor research and drug discovery. *Oncol. Lett.* **2017**, *14*, 6999–7010. [CrossRef]
3. Weigelt, B.; Ghajar, C.M.; Bissell, M.J. The need for complex 3d culture models to unravel novel pathways and identify accurate biomarkers in breast cancer. *Adv. Drug Deliv. Rev.* **2014**, *69–70*, 42–51. [CrossRef] [PubMed]
4. Katsuda, T.; Kosaka, N.; Ochiya, T. The roles of extracellular vesicles in cancer biology: Toward the development of novel cancer biomarkers. *Proteomics* **2014**, *14*, 412–425. [CrossRef] [PubMed]
5. Ruivo, C.F.; Adem, B.; Silva, M.; Melo, S.A. The biology of cancer exosomes: Insights and new perspectives. *Cancer Res.* **2017**, *77*, 6480–6488. [CrossRef] [PubMed]
6. Tai, Y.L.; Lin, C.J.; Li, T.K.; Shen, T.L.; Hsieh, J.T.; Chen, B.P.C. The role of extracellular vesicles in prostate cancer with clinical applications. *Endocr. Relat. Cancer* **2020**, *27*, R133–R144. [CrossRef]
7. Birgersdotter, A.; Sandberg, R.; Ernberg, I. Gene expression perturbation in vitro–a growing case for three-dimensional (3d) culture systems. *Semin. Cancer Biol.* **2005**, *15*, 405–412. [CrossRef]
8. Kapalczynska, M.; Kolenda, T.; Przybyla, W.; Zajaczkowska, M.; Teresiak, A.; Filas, V.; Ibbs, M.; Blizniak, R.; Luczewski, L.; Lamperska, K. 2d and 3d cell cultures—A comparison of different types of cancer cell cultures. *Arch. Med. Sci.* **2018**, *14*, 910–919. [CrossRef]
9. Fiorini, E.; Veghini, L.; Corbo, V. Modeling cell communication in cancer with organoids: Making the complex simple. *Front. Cell Dev. Biol.* **2020**, *8*, 166. [CrossRef]
10. Ravi, M.; Paramesh, V.; Kaviya, S.R.; Anuradha, E.; Solomon, F.D. 3D cell culture systems: Advantages and applications. *J. Cell Physiol.* **2015**, *230*, 16–26. [CrossRef]
11. Place, E.S.; George, J.H.; Williams, C.K.; Stevens, M.M. Synthetic polymer scaffolds for tissue engineering. *Chem. Soc. Rev.* **2009**, *38*, 1139–1151. [CrossRef] [PubMed]
12. Mehta, G.; Hsiao, A.Y.; Ingram, M.; Luker, G.D.; Takayama, S. Opportunities and challenges for use of tumor spheroids as models to test drug delivery and efficacy. *J. Control Release* **2012**, *164*, 192–204. [CrossRef] [PubMed]
13. Ryan, S.L.; Baird, A.M.; Vaz, G.; Urquhart, A.J.; Senge, M.; Richard, D.J.; O'Byrne, K.J.; Davies, A.M. Drug discovery approaches utilizing three-dimensional cell culture. *Assay Drug Dev. Technol.* **2016**, *14*, 19–28. [CrossRef] [PubMed]
14. Joshi, P.; Lee, M.Y. High content imaging (hci) on miniaturized three-dimensional (3d) cell cultures. *Biosensors (Basel)* **2015**, *5*, 768–790. [CrossRef]

15. Salo, T.; Dourado, M.R.; Sundquist, E.; Apu, E.H.; Alahuhta, I.; Tuomainen, K.; Vasara, J.; Al-Samadi, A. Organotypic three-dimensional assays based on human leiomyoma-derived matrices. *Philos. Trans. R. Soc. Lond. B Biol. Sci.* **2018**, *373*. [CrossRef]

16. Eiraku, M.; Sasai, Y. Self-formation of layered neural structures in three-dimensional culture of es cells. *Curr. Opin. Neurobiol.* **2012**, *22*, 768–777. [CrossRef]

17. Fujii, M.; Shimokawa, M.; Date, S.; Takano, A.; Matano, M.; Nanki, K.; Ohta, Y.; Toshimitsu, K.; Nakazato, Y.; Kawasaki, K.; et al. A colorectal tumor organoid library demonstrates progressive loss of niche factor requirements during tumorigenesis. *Cell Stem Cell* **2016**, *18*, 827–838. [CrossRef]

18. Neal, J.T.; Li, X.; Zhu, J.; Giangarra, V.; Grzeskowiak, C.L.; Ju, J.; Liu, I.H.; Chiou, S.H.; Salahudeen, A.A.; Smith, A.R.; et al. Organoid modeling of the tumor immune microenvironment. *Cell* **2018**, *175*, 1972–1988.e1916. [CrossRef]

19. Sato, T.; Stange, D.E.; Ferrante, M.; Vries, R.G.; Van Es, J.H.; Van den Brink, S.; Van Houdt, W.J.; Pronk, A.; Van Gorp, J.; Siersema, P.D.; et al. Long-term expansion of epithelial organoids from human colon, adenoma, adenocarcinoma, and barrett's epithelium. *Gastroenterology* **2011**, *141*, 1762–1772. [CrossRef]

20. Broutier, L.; Mastrogiovanni, G.; Verstegen, M.M.; Francies, H.E.; Gavarro, L.M.; Bradshaw, C.R.; Allen, G.E.; Arnes-Benito, R.; Sidorova, O.; Gaspersz, M.P.; et al. Human primary liver cancer-derived organoid cultures for disease modeling and drug screening. *Nat. Med.* **2017**, *23*, 1424–1435. [CrossRef]

21. Corro, C.; Novellasdemunt, L.; Li, V.S.W. A brief history of organoids. *Am. J. Physiol. Cell Physiol.* **2020**, *319*, C151–C165. [CrossRef] [PubMed]

22. Datta, P.; Dey, M.; Ataie, Z.; Unutmaz, D.; Ozbolat, I.T. 3d bioprinting for reconstituting the cancer microenvironment. *NPJ Precis Oncol.* **2020**, *4*, 18. [CrossRef] [PubMed]

23. Burdett, E.; Kasper, F.K.; Mikos, A.G.; Ludwig, J.A. Engineering tumors: A tissue engineering perspective in cancer biology. *Tissue Eng. Part B Rev.* **2010**, *16*, 351–359. [CrossRef] [PubMed]

24. Haycock, J.W. 3d cell culture: A review of current approaches and techniques. *Methods Mol. Biol.* **2011**, *695*, 1–15. [CrossRef]

25. Carletti, E.; Motta, A.; Migliaresi, C. Scaffolds for tissue engineering and 3d cell culture. *Methods Mol. Biol.* **2011**, *695*, 17–39. [CrossRef]

26. Yan, X.; Zhou, L.; Wu, Z.; Wang, X.; Chen, X.; Yang, F.; Guo, Y.; Wu, M.; Chen, Y.; Li, W.; et al. High throughput scaffold-based 3d micro-tumor array for efficient drug screening and chemosensitivity testing. *Biomaterials* **2019**, *198*, 167–179. [CrossRef]

27. Patra, C.; Talukdar, S.; Novoyatleva, T.; Velagala, S.R.; Muhlfeld, C.; Kundu, B.; Kundu, S.C.; Engel, F.B. Silk protein fibroin from antheraea mylitta for cardiac tissue engineering. *Biomaterials* **2012**, *33*, 2673–2680. [CrossRef]

28. Pedron, S.; Becka, E.; Harley, B.A. Regulation of glioma cell phenotype in 3d matrices by hyaluronic acid. *Biomaterials* **2013**, *34*, 7408–7417. [CrossRef]

29. Lv, D.; Yu, S.C.; Ping, Y.F.; Wu, H.; Zhao, X.; Zhang, H.; Cui, Y.; Chen, B.; Zhang, X.; Dai, J.; et al. A three-dimensional collagen scaffold cell culture system for screening anti-glioma therapeutics. *Oncotarget* **2016**, *7*, 56904–56914. [CrossRef]

30. Dunne, L.W.; Huang, Z.; Meng, W.; Fan, X.; Zhang, N.; Zhang, Q.; An, Z. Human decellularized adipose tissue scaffold as a model for breast cancer cell growth and drug treatments. *Biomaterials* **2014**, *35*, 4940–4949. [CrossRef]

31. Stratmann, A.T.; Fecher, D.; Wangorsch, G.; Gottlich, C.; Walles, T.; Walles, H.; Dandekar, T.; Dandekar, G.; Nietzer, S.L. Establishment of a human 3d lung cancer model based on a biological tissue matrix combined with a boolean in silico model. *Mol. Oncol.* **2014**, *8*, 351–365. [CrossRef] [PubMed]

32. Gilkes, D.M.; Semenza, G.L.; Wirtz, D. Hypoxia and the extracellular matrix: Drivers of tumour metastasis. *Nat. Rev. Cancer* **2014**, *14*, 430–439. [CrossRef] [PubMed]

33. Brancato, V.; Garziano, A.; Gioiella, F.; Urciuolo, F.; Imparato, G.; Panzetta, V.; Fusco, S.; Netti, P.A. 3d is not enough: Building up a cell instructive microenvironment for tumoral stroma microtissues. *Acta Biomater.* **2017**, *47*, 1–13. [CrossRef] [PubMed]

34. Zhu, L.; Fan, X.; Wang, B.; Liu, L.; Yan, X.; Zhou, L.; Zeng, Y.; Poznansky, M.C.; Wang, L.; Chen, H.; et al. Biomechanically primed liver microtumor array as a high-throughput mechanopharmacological screening platform for stroma-reprogrammed combinatorial therapy. *Biomaterials* **2017**, *124*, 12–24. [CrossRef] [PubMed]

35. Kleinman, H.K.; Martin, G.R. Matrigel: Basement membrane matrix with biological activity. *Semin. Cancer Biol.* **2005**, *15*, 378–386. [CrossRef] [PubMed]

36. Cukierman, E.; Pankov, R.; Yamada, K.M. Cell interactions with three-dimensional matrices. *Curr. Opin. Cell Biol.* **2002**, *14*, 633–639. [CrossRef]

37. Xu, X.; Sabanayagam, C.R.; Harrington, D.A.; Farach-Carson, M.C.; Jia, X. A hydrogel-based tumor model for the evaluation of nanoparticle-based cancer therapeutics. *Biomaterials* **2014**, *35*, 3319–3330. [CrossRef]

38. Mahoney, C.M.; Kelmindi-Doko, A.; Snowden, M.J.; Peter Rubin, J.; Marra, K.G. Adipose derived delivery vehicle for encapsulated adipogenic factors. *Acta Biomater.* **2017**, *58*, 26–33. [CrossRef]

39. Poupot, M.; Fournie, J.J. Spontaneous membrane transfer through homotypic synapses between lymphoma cells. *J. Immunol.* **2003**, *171*, 2517–2523. [CrossRef]

40. Savina, A.; Vidal, M.; Colombo, M.I. The exosome pathway in k562 cells is regulated by rab11. *J. Cell Sci.* **2002**, *115*, 2505–2515.

41. Maia, J.; Caja, S.; Strano Moraes, M.C.; Couto, N.; Costa-Silva, B. Exosome-based cell-cell communication in the tumor microenvironment. *Front. Cell Dev. Biol.* **2018**, *6*, 18. [CrossRef] [PubMed]

42. Shao, Y.; Chen, T.; Zheng, X.; Yang, S.; Xu, K.; Chen, X.; Xu, F.; Wang, L.; Shen, Y.; Wang, T.; et al. Colorectal cancer-derived small extracellular vesicles establish an inflammatory premetastatic niche in liver metastasis. *Carcinogenesis* **2018**, *39*, 1368–1379. [CrossRef] [PubMed]

43. Fong, M.Y.; Zhou, W.; Liu, L.; Alontaga, A.Y.; Chandra, M.; Ashby, J.; Chow, A.; O'Connor, S.T.; Li, S.; Chin, A.R.; et al. Breast-cancer-secreted mir-122 reprograms glucose metabolism in premetastatic niche to promote metastasis. *Nat. Cell Biol.* **2015**, *17*, 183–194. [CrossRef] [PubMed]

44. Robado de Lope, L.; Alcibar, O.L.; Amor Lopez, A.; Hergueta-Redondo, M.; Peinado, H. Tumour-adipose tissue crosstalk: Fuelling tumour metastasis by extracellular vesicles. *Philos. Trans. R. Soc. Lond. B Biol. Sci.* **2018**, *373*. [CrossRef] [PubMed]

45. Kosaka, N.; Yoshioka, Y.; Fujita, Y.; Ochiya, T. Versatile roles of extracellular vesicles in cancer. *J. Clin. Invest.* **2016**, *126*, 1163–1172. [CrossRef]

46. Tai, Y.L.; Chen, K.C.; Hsieh, J.T.; Shen, T.L. Exosomes in cancer development and clinical applications. *Cancer Sci.* **2018**, *109*, 2364–2374. [CrossRef]

47. Ferguson, S.; Weissleder, R. Modeling ev kinetics for use in early cancer detection. *Adv. Biosyst.* **2020**, *4*, e1900305. [CrossRef]

48. Takahashi, K.; Ota, Y.; Kogure, T.; Suzuki, Y.; Iwamoto, H.; Yamakita, K.; Kitano, Y.; Fujii, S.; Haneda, M.; Patel, T.; et al. Circulating extracellular vesicle-encapsulated hulc is a potential biomarker for human pancreatic cancer. *Cancer Sci.* **2020**, *111*, 98–111. [CrossRef]

49. Ma, C.; Jiang, F.; Ma, Y.; Wang, J.; Li, H.; Zhang, J. Isolation and detection technologies of extracellular vesicles and application on cancer diagnostic. *Dose Response* **2019**, *17*, 1559325819891004. [CrossRef]

50. Herrero, C.; de la Fuente, A.; Casas-Arozamena, C.; Sebastian, V.; Prieto, M.; Arruebo, M.; Abalo, A.; Colas, E.; Moreno-Bueno, G.; Gil-Moreno, A.; et al. Extracellular vesicles-based biomarkers represent a promising liquid biopsy in endometrial cancer. *Cancers (Basel)* **2019**, *11*, 2000. [CrossRef]

51. Pang, B.; Zhu, Y.; Ni, J.; Thompson, J.; Malouf, D.; Bucci, J.; Graham, P.; Li, Y. Extracellular vesicles: The next generation of biomarkers for liquid biopsy-based prostate cancer diagnosis. *Theranostics* **2020**, *10*, 2309–2326. [CrossRef] [PubMed]

52. Joncas, F.H.; Lucien, F.; Rouleau, M.; Morin, F.; Leong, H.S.; Pouliot, F.; Fradet, Y.; Gilbert, C.; Toren, P. Plasma extracellular vesicles as phenotypic biomarkers in prostate cancer patients. *Prostate* **2019**, *79*, 1767–1776. [CrossRef] [PubMed]

53. Yekula, A.; Muralidharan, K.; Kang, K.M.; Wang, L.; Balaj, L.; Carter, B.S. From laboratory to clinic: Translation of extracellular vesicle based cancer biomarkers. *Methods* **2020**, *177*, 58–66. [CrossRef] [PubMed]

54. Alvarez-Erviti, L.; Seow, Y.; Yin, H.; Betts, C.; Lakhal, S.; Wood, M.J. Delivery of sirna to the mouse brain by systemic injection of targeted exosomes. *Nat. Biotechnol.* **2011**, *29*, 341–345. [CrossRef]

55. Tian, Y.; Li, S.; Song, J.; Ji, T.; Zhu, M.; Anderson, G.J.; Wei, J.; Nie, G. A doxorubicin delivery platform using engineered natural membrane vesicle exosomes for targeted tumor therapy. *Biomaterials* **2014**, *35*, 2383–2390. [CrossRef]

56. Bellavia, D.; Raimondo, S.; Calabrese, G.; Forte, S.; Cristaldi, M.; Patinella, A.; Memeo, L.; Manno, M.; Raccosta, S.; Diana, P.; et al. Interleukin 3- receptor targeted exosomes inhibit in vitro and in vivo chronic myelogenous leukemia cell growth. *Theranostics* **2017**, *7*, 1333–1345. [CrossRef]

57. Shao, J.; Zaro, J.; Shen, Y. Advances in exosome-based drug delivery and tumor targeting: From tissue distribution to intracellular fate. *Int. J. Nanomed.* **2020**, *15*, 9355–9371. [CrossRef]

58. Yang, J.; Zhang, Z.; Zhang, Y.; Ni, X.; Zhang, G.; Cui, X.; Liu, M.; Xu, C.; Zhang, Q.; Zhu, H.; et al. Zip4 promotes muscle wasting and cachexia in mice with orthotopic pancreatic tumors by stimulating rab27b-regulated release of extracellular vesicles from cancer cells. *Gastroenterology* **2019**, *156*, 722–734.e726. [CrossRef]

59. Hwang, W.L.; Lan, H.Y.; Cheng, W.C.; Huang, S.C.; Yang, M.H. Tumor stem-like cell-derived exosomal rnas prime neutrophils for facilitating tumorigenesis of colon cancer. *J. Hematol. Oncol.* **2019**, *12*, 10. [CrossRef]

60. Szvicsek, Z.; Oszvald, A.; Szabo, L.; Sandor, G.O.; Kelemen, A.; Soos, A.A.; Paloczi, K.; Harsanyi, L.; Tolgyes, T.; Dede, K.; et al. Extracellular vesicle release from intestinal organoids is modulated by apc mutation and other colorectal cancer progression factors. *Cell Mol. Life Sci.* **2019**, *76*, 2463–2476. [CrossRef]

61. Namba, Y.; Sogawa, C.; Okusha, Y.; Kawai, H.; Itagaki, M.; Ono, K.; Murakami, J.; Aoyama, E.; Ohyama, K.; Asaumi, J.I.; et al. Depletion of lipid efflux pump abcg1 triggers the intracellular accumulation of extracellular vesicles and reduces aggregation and tumorigenesis of metastatic cancer cells. *Front. Oncol.* **2018**, *8*, 376. [CrossRef] [PubMed]

62. Franchi, M.; Piperigkou, Z.; Karamanos, K.A.; Franchi, L.; Masola, V. Extracellular matrix-mediated breast cancer cells morpho-logical alterations, invasiveness, and microvesicles/exosomes release. *Cells* **2020**, *9*, 2031. [CrossRef] [PubMed]

63. Eguchi, T.; Sogawa, C.; Okusha, Y.; Uchibe, K.; Iinuma, R.; Ono, K.; Nakano, K.; Murakami, J.; Itoh, M.; Arai, K.; et al. Organoids with cancer stem cell-like properties secrete exosomes and hsp90 in a 3d nanoenvironment. *PLoS ONE* **2018**, *13*, e0191109. [CrossRef]

64. Thippabhotla, S.; Zhong, C.; He, M. 3d cell culture stimulates the secretion of in vivo like extracellular vesicles. *Sci. Rep.* **2019**, *9*, 13012. [CrossRef] [PubMed]

65. Tauro, B.J.; Greening, D.W.; Mathias, R.A.; Mathivanan, S.; Ji, H.; Simpson, R.J. Two distinct populations of exosomes are released from lim1863 colon carcinoma cell-derived organoids. *Mol. Cell Proteom.* **2013**, *12*, 587–598. [CrossRef]

66. Huang, L.; Bockorny, B.; Paul, I.; Akshinthala, D.; Frappart, P.O.; Gandarilla, O.; Bose, A.; Sanchez-Gonzalez, V.; Rouse, E.E.; Lehoux, S.D.; et al. Pdx-derived organoids model in vivo drug response and secrete biomarkers. *JCI Insight* **2020**, *5*. [CrossRef]

67. Guerreiro, E.M.; Vestad, B.; Steffensen, L.A.; Aass, H.C.D.; Saeed, M.; Ovstebo, R.; Costea, D.E.; Galtung, H.K.; Soland, T.M. Efficient extracellular vesicle isolation by combining cell media modifications, ultrafiltration, and size-exclusion chromatography. *PLoS ONE* **2018**, *13*, e0204276. [CrossRef]

68. Zhao, Z.; McGill, J.; Gamero-Kubota, P.; He, M. Microfluidic on-demand engineering of exosomes towards cancer immunotherapy. *Lab. Chip* **2019**, *19*, 1877–1886. [CrossRef]

69. Patel, D.B.; Luthers, C.R.; Lerman, M.J.; Fisher, J.P.; Jay, S.M. Enhanced extracellular vesicle production and ethanol-mediated vascularization bioactivity via a 3d-printed scaffold-perfusion bioreactor system. *Acta Biomater.* **2019**, *95*, 236–244. [CrossRef]

70. Ramamoorthy, P.; Thomas, S.M.; Kaushik, G.; Subramaniam, D.; Chastain, K.M.; Dhar, A.; Tawfik, O.; Kasi, A.; Sun, W.; Ramalingam, S.; et al. Metastatic tumor-in-a-dish, a novel multicellular organoid to study lung colonization and predict therapeutic response. *Cancer Res.* **2019**, *79*, 1681–1695. [CrossRef]

71. Murgoci, A.N.; Cizkova, D.; Majerova, P.; Petrovova, E.; Medvecky, L.; Fournier, I.; Salzet, M. Brain-cortex microglia-derived exosomes: Nanoparticles for glioma therapy. *Chemphyschem* **2018**, *19*, 1205–1214. [CrossRef] [PubMed]

72. Yeon, J.H.; Jeong, H.E.; Seo, H.; Cho, S.; Kim, K.; Na, D.; Chung, S.; Park, J.; Choi, N.; Kang, J.Y. Cancer-derived exosomes trigger endothelial to mesenchymal transition followed by the induction of cancer-associated fibroblasts. *Acta Biomater.* **2018**, *76*, 146–153. [CrossRef]

73. Jeong, G.S.; Han, S.; Shin, Y.; Kwon, G.H.; Kamm, R.D.; Lee, S.H.; Chung, S. Sprouting angiogenesis under a chemical gradient regulated by interactions with an endothelial monolayer in a microfluidic platform. *Anal. Chem.* **2011**, *83*, 8454–8459. [CrossRef]

74. Jeong, K.; Yu, Y.J.; You, J.Y.; Rhee, W.J.; Kim, J.A. Exosome-mediated microrna-497 delivery for anti-cancer therapy in a microfluidic 3d lung cancer model. *Lab. Chip* **2020**, *20*, 548–557. [CrossRef] [PubMed]

75. Sancho-Albero, M.; Medel-Martínez, A.; Martín-Duque, P. Use of exosomes as vectors to carry advanced therapies. *RSC Advances* **2020**, *10*, 23975–23987. [CrossRef]

76. Villa, F.; Quarto, R.; Tasso, R. Extracellular vesicles as natural, safe and efficient drug delivery systems. *Pharmaceutics* **2019**, *11*, 557. [CrossRef] [PubMed]

77. Nooshabadi, V.T.; Khanmohammadi, M.; Shafei, S.; Banafshe, H.R.; Malekshahi, Z.V.; Ebrahimi-Barough, S.; Ai, J. Impact of atorvastatin loaded exosome as an anti-glioblastoma carrier to induce apoptosis of u87 cancer cells in 3d culture model. *Biochem. Biophys. Rep.* **2020**, *23*, 100792. [CrossRef] [PubMed]

78. Millard, M.; Yakavets, I.; Piffoux, M.; Brun, A.; Gazeau, F.; Guigner, J.M.; Jasniewski, J.; Lassalle, H.P.; Wilhelm, C.; Bezdetnaya, L. Mthpc-loaded extracellular vesicles outperform liposomal and free mthpc formulations by an increased stability, drug delivery efficiency and cytotoxic effect in tridimensional model of tumors. *Drug Deliv.* **2018**, *25*, 1790–1801. [CrossRef]

79. Iessi, E.; Logozzi, M.; Lugini, L.; Azzarito, T.; Federici, C.; Spugnini, E.P.; Mizzoni, D.; Di Raimo, R.; Angelini, D.F.; Battistini, L.; et al. Acridine orange/exosomes increase the delivery and the effectiveness of acridine orange in human melanoma cells: A new prototype for theranostics of tumors. *J. Enzyme Inhib. Med. Chem.* **2017**, *32*, 648–657. [CrossRef]

80. Zhuang, J.; Tan, J.; Wu, C.; Zhang, J.; Liu, T.; Fan, C.; Li, J.; Zhang, Y. Extracellular vesicles engineered with valency-controlled DNA nanostructures deliver crispr/cas9 system for gene therapy. *Nucleic Acids Res.* **2020**, *48*, 8870–8882. [CrossRef]

81. Ye, Z.; Zhang, T.; He, W.; Jin, H.; Liu, C.; Yang, Z.; Ren, J. Methotrexate-loaded extracellular vesicles functionalized with therapeutic and targeted peptides for the treatment of glioblastoma multiforme. *ACS Appl. Mater. Interfaces* **2018**, *10*, 12341–12350. [CrossRef]

82. Walker, S.; Busatto, S.; Pham, A.; Tian, M.; Suh, A.; Carson, K.; Quintero, A.; Lafrence, M.; Malik, H.; Santana, M.X.; et al. Extracellular vesicle-based drug delivery systems for cancer treatment. *Theranostics* **2019**, *9*, 8001–8017. [CrossRef] [PubMed]

83. Abdollahi, S. Extracellular vesicles from organoids and 3d culture systems. *Biotechnol. Bioeng.* **2020**. [CrossRef] [PubMed]

84. Pisano, S.; Pierini, I.; Gu, J.; Gazze, A.; Francis, L.W.; Gonzalez, D.; Conlan, R.S.; Corradetti, B. Immune (cell) derived exosome mimetics (idem) as a treatment for ovarian cancer. *Front. Cell Dev. Biol.* **2020**, *8*, 553576. [CrossRef] [PubMed]

85. Yong, T.; Zhang, X.; Bie, N.; Zhang, H.; Zhang, X.; Li, F.; Hakeem, A.; Hu, J.; Gan, L.; Santos, H.A.; et al. Tumor exosome-based nanoparticles are efficient drug carriers for chemotherapy. *Nat. Commun.* **2019**, *10*, 3838. [CrossRef]

86. Taverna, S.; Flugy, A.; Saieva, L.; Kohn, E.C.; Santoro, A.; Meraviglia, S.; De Leo, G.; Alessandro, R. Role of exosomes released by chronic myelogenous leukemia cells in angiogenesis. *Int. J. Cancer* **2012**, *130*, 2033–2043. [CrossRef]

87. Mineo, M.; Garfield, S.H.; Taverna, S.; Flugy, A.; De Leo, G.; Alessandro, R.; Kohn, E.C. Exosomes released by k562 chronic myeloid leukemia cells promote angiogenesis in a src-dependent fashion. *Angiogenesis* **2012**, *15*, 33–45. [CrossRef]

88. Zhang, L.; Wu, X.; Luo, C.; Chen, X.; Yang, L.; Tao, J.; Shi, J. The 786-0 renal cancer cell-derived exosomes promote angiogenesis by downregulating the expression of hepatocyte cell adhesion molecule. *Mol. Med. Rep.* **2013**, *8*, 272–276. [CrossRef]

89. Blache, U.; Horton, E.R.; Xia, T.; Schoof, E.M.; Blicher, L.H.; Schonenberger, A.; Snedeker, J.G.; Martin, I.; Erler, J.T.; Ehrbar, M. Mesenchymal stromal cell activation by breast cancer secretomes in bioengineered 3d microenvironments. *Life Sci. Alliance* **2019**, *2*. [CrossRef]

90. Lugini, L.; Valtieri, M.; Federici, C.; Cecchetti, S.; Meschini, S.; Condello, M.; Signore, M.; Fais, S. Exosomes from human colorectal cancer induce a tumor-like behavior in colonic mesenchymal stromal cells. *Oncotarget* **2016**, *7*, 50086–50098. [CrossRef]

91. Vera, N.; Acuna-Gallardo, S.; Grunenwald, F.; Caceres-Verschae, A.; Realini, O.; Acuna, R.; Lladser, A.; Illanes, S.E.; Varas-Godoy, M. Small extracellular vesicles released from ovarian cancer spheroids in response to cisplatin promote the pro-tumorigenic activity of mesenchymal stem cells. *Int. J. Mol. Sci.* **2019**, *20*, 4972. [CrossRef] [PubMed]

92. Chowdhury, R.; Webber, J.P.; Gurney, M.; Mason, M.D.; Tabi, Z.; Clayton, A. Cancer exosomes trigger mesenchymal stem cell differentiation into pro-angiogenic and pro-invasive myofibroblasts. *Oncotarget* **2015**, *6*, 715–731. [CrossRef]

93. Rai, A.; Greening, D.W.; Xu, R.; Suwakulsiri, W.; Simpson, R.J. Exosomes derived from the human primary colorectal cancer cell line sw480 orchestrate fibroblast-led cancer invasion. *Proteomics* **2020**, *20*, e2000016. [CrossRef] [PubMed]

94. Yoshimura, A.; Sawada, K.; Nakamura, K.; Kinose, Y.; Nakatsuka, E.; Kobayashi, M.; Miyamoto, M.; Ishida, K.; Matsumoto, Y.; Kodama, M.; et al. Exosomal mir-99a-5p is elevated in sera of ovarian cancer patients and promotes cancer cell invasion by increasing fibronectin and vitronectin expression in neighboring peritoneal mesothelial cells. *BMC Cancer* **2018**, *18*, 1065. [CrossRef]

95. Dalchau, N.; Smith, M.J.; Martin, S.; Brown, J.R.; Emmott, S.; Phillips, A. Towards the rational design of synthetic cells with prescribed population dynamics. *J. R. Soc. Interface* **2012**, *9*, 2883–2898. [CrossRef]

96. Cheng, W.C.; Liao, T.T.; Lin, C.C.; Yuan, L.E.; Lan, H.Y.; Lin, H.H.; Teng, H.W.; Chang, H.C.; Lin, C.H.; Yang, C.Y.; et al. Rab27b-activated secretion of stem-like tumor exosomes delivers the biomarker microrna-146a-5p, which promotes tumorigenesis and associates with an immunosuppressive tumor microenvironment in colorectal cancer. *Int. J. Cancer* **2019**, *145*, 2209–2224. [CrossRef]

97. Yeung, V.; Webber, J.P.; Dunlop, E.A.; Morgan, H.; Hutton, J.; Gurney, M.; Jones, E.; Falcon-Perez, J.; Tabi, Z.; Errington, R.; et al. Rab35-dependent extracellular nanovesicles are required for induction of tumour supporting stroma. *Nanoscale* **2018**, *10*, 8547–8559. [CrossRef]

98. Taha, E.A.; Sogawa, C.; Okusha, Y.; Kawai, H.; Oo, M.W.; Elseoudi, A.; Lu, Y.; Nagatsuka, H.; Kubota, S.; Satoh, A.; et al. Knockout of mmp3 weakens solid tumor organoids and cancer extracellular vesicles. *Cancers (Basel)* **2020**, *12*, 1260. [CrossRef]

99. Endzelins, E.; Abols, A.; Buss, A.; Zandberga, E.; Palviainen, M.; Siljander, P.; Line, A. Extracellular vesicles derived from hypoxic colorectal cancer cells confer metastatic phenotype to non-metastatic cancer cells. *Anticancer Res.* **2018**, *38*, 5139–5147. [CrossRef]

100. Yan, Q.; Yuan, W.B.; Sun, X.; Zhang, M.J.; Cen, F.; Zhou, S.Y.; Wu, W.B.; Xu, Y.C.; Tong, L.H.; Ma, Z.H. Asparaginyl endopeptidase enhances pancreatic ductal adenocarcinoma cell invasion in an exosome-dependent manner and correlates with poor prognosis. *Int. J. Oncol.* **2018**, *52*, 1651–1660. [CrossRef]

101. Li, C.; Liu, D.R.; Li, G.G.; Wang, H.H.; Li, X.W.; Zhang, W.; Wu, Y.L.; Chen, L. Cd97 promotes gastric cancer cell proliferation and invasion through exosome-mediated mapk signaling pathway. *World J. Gastroenterol.* **2015**, *21*, 6215–6228. [CrossRef] [PubMed]

102. Guo, D.; Lui, G.Y.L.; Lai, S.L.; Wilmott, J.S.; Tikoo, S.; Jackett, L.A.; Quek, C.; Brown, D.L.; Sharp, D.M.; Kwan, R.Y.Q.; et al. Rab27a promotes melanoma cell invasion and metastasis via regulation of pro-invasive exosomes. *Int. J. Cancer* **2019**, *144*, 3070–3085. [CrossRef]

103. Philip, R.; Heiler, S.; Mu, W.; Buchler, M.W.; Zoller, M.; Thuma, F. Claudin-7 promotes the epithelial-mesenchymal transition in human colorectal cancer. *Oncotarget* **2015**, *6*, 2046–2063. [CrossRef] [PubMed]

104. Senfter, D.; Holzner, S.; Kalipciyan, M.; Staribacher, A.; Walzl, A.; Huttary, N.; Krieger, S.; Brenner, S.; Jager, W.; Krupitza, G.; et al. Loss of mir-200 family in 5-fluorouracil resistant colon cancer drives lymphendothelial invasiveness in vitro. *Hum. Mol. Genet.* **2015**, *24*, 3689–3698. [CrossRef] [PubMed]

105. Holzner, S.; Senfter, D.; Stadler, S.; Staribacher, A.; Nguyen, C.H.; Gaggl, A.; Geleff, S.; Huttary, N.; Krieger, S.; Jager, W.; et al. Colorectal cancer cell-derived microrna200 modulates the resistance of adjacent blood endothelial barriers in vitro. *Oncol. Rep.* **2016**, *36*, 3065–3071. [CrossRef]

106. Oszvald, A.; Szvicsek, Z.; Papai, M.; Kelemen, A.; Varga, Z.; Tolgyes, T.; Dede, K.; Bursics, A.; Buzas, E.I.; Wiener, Z. Fibroblast-derived extracellular vesicles induce colorectal cancer progression by transmitting amphiregulin. *Front. Cell Dev. Biol.* **2020**, *8*, 558. [CrossRef]

107. Xu, X.; Cheng, J.; Luo, S.; Gong, X.; Huang, D.; Xu, J.; Qian, Y.; Wan, X.; Zhou, H. Deoxycholic acid-stimulated macrophage-derived exosomes promote spasmolytic polypeptide-expressing metaplasia in the stomach. *Biochem. Biophys. Res. Commun.* **2020**, *524*, 649–655. [CrossRef]

108. Li, W.; Han, Y.; Zhao, Z.; Ji, X.; Wang, X.; Jin, J.; Wang, Q.; Guo, X.; Cheng, Z.; Lu, M.; et al. Oral mucosal mesenchymal stem cellderived exosomes: A potential therapeutic target in oral premalignant lesions. *Int. J. Oncol.* **2019**, *54*, 1567–1578. [CrossRef]

109. Rodini, C.O.; Goncalves da Silva, P.B.; Assoni, A.F.; Carvalho, V.M.; Okamoto, O.K. Mesenchymal stem cells enhance tumorigenic properties of human glioblastoma through independent cell-cell communication mechanisms. *Oncotarget* **2018**, *9*, 24766–24777. [CrossRef]

Using single-vesicle technologies to unravel the heterogeneity of extracellular vesicles

Guillermo Bordanaba-Florit [1✉], Félix Royo [1,2], Sergei G. Kruglik [3] and Juan M. Falcón-Pérez [1,2,4✉]

Extracellular vesicles (EVs) are heterogeneous lipid containers with a complex molecular cargo comprising several populations with unique roles in biological processes. These vesicles are closely associated with specific physiological features, which makes them invaluable in the detection and monitoring of various diseases. EVs play a key role in pathophysiological processes by actively triggering genetic or metabolic responses. However, the heterogeneity of their structure and composition hinders their application in medical diagnosis and therapies. This diversity makes it difficult to establish their exact physiological roles, and the functions and composition of different EV (sub)populations. Ensemble averaging approaches currently employed for EV characterization, such as western blotting or 'omics' technologies, tend to obscure rather than reveal these heterogeneities. Recent developments in single-vesicle analysis have made it possible to overcome these limitations and have facilitated the development of practical clinical applications. In this review, we discuss the benefits and challenges inherent to the current methods for the analysis of single vesicles and review the contribution of these approaches to the understanding of EV biology. We describe the contributions of these recent technological advances to the characterization and phenotyping of EVs, examination of the role of EVs in cell-to-cell communication pathways and the identification and validation of EVs as disease biomarkers. Finally, we discuss the potential of innovative single-vesicle imaging and analysis methodologies using microfluidic devices, which promise to deliver rapid and effective basic and practical applications for minimally invasive prognosis systems.

Since the description of 'minute bodies' found in a piece of cork by Robert Hooke in 1665[1], both our scientific knowledge and technical abilities have increased enormously. As techniques have become more accurate and intricate, so has our understanding of biological processes and structures. Technological advances in the field of imaging have resulted in the identification of cell structures, such as the mitochondria[2] and nuclei[3], and the discovery of different levels of cellular complexity. In 1967, Peter Wolf visualized 'platelet dust' in fresh platelet-free blood plasma using an electron microscope[4]; thus, a mammalian vesicle-like structure was described for the first time. Gradually, these vesicles were characterized in more detail. It has been established that they are released by all kinds of cells (prokaryotic and eukaryotic) into the extracellular milleu[5–8]. The process of vesicle secretion is conserved throughout evolution, suggesting that such vesicles are likely to have specific roles in cellular and organismal development and survival[9]. Indeed, later discoveries showed that secreted vesicles participate actively in many physiological processes in mammals, for example coagulation, inflammatory response, cell maturation, adaptive immune response, bone calcification and neural cell communication, among others[10,11].

In addition to their critical functions in normal physiology[12,13], secreted vesicles mediate in several pathological processes[14,15], such as the establishment of premetastatic niche during cancer progression[16,17].

Nowadays, these secreted vesicles are extensively reported and widely known as extracellular vesicles (EVs). EVs are heterogeneous, nano- to micrometer-sized, bilayer lipid containers secreted by most cell types. They are multipurpose carriers that can contain a wide variety of cargos such as lipids, proteins, metabolites, sugars, RNA (mRNA, miRNA, siRNA) and even DNA[10]. When they are taken up by recipient cells, they trigger intracellular signaling through EV surface molecules or by the release of cargo into cell compartments via endocytic pathways. These processes can further activate downstream genetic or metabolic pathways in the recipient cell[11,18]. In mammals, EVs have been found in body fluids such as plasma, urine, saliva, breast milk and seminal fluid, among others[10]. They are classified into three different categories according to their biogenesis mechanisms and biophysical properties:

• Exosomes: typically 30–150 nm in diameter, derived from intracellular endosomal compartments

[1]Exosomes Laboratory, Center for Cooperative Research in Biosciences (CIC bioGUNE), Basque Research and Technology Alliance (BRTA), Derio, Spain. [2]Centro de Investigación Biomédica en Red de Enfermedades Hepáticas y Digestivas (Ciberehd), Madrid, Spain. [3]Sorbonne Université, CNRS, Institut de Biologie Paris-Seine, Laboratoire Jean Perrin, Paris, France. [4]Ikerbasque, Basque Foundation for Science, Bilbao, Spain. ✉e-mail: gbordanaba@cicbiogune.es; jfalcon@cicbiogune.es

- Microvesicles: 100–1,000 nm in diameter, produced by outward budding and pinching-off the plasma membrane
- Apoptotic bodies: 50–5,000 nm in diameter, released as blebs by cells undergoing apoptosis[10,19]

In a systematic review of guidelines for this field, the International Society for Extracellular Vesicles (ISEV)[20] endorsed a categorization of EVs isolated using ultracentrifugation into large, medium and small EVs. However, it is important to note that ultracentrifugation precipitates not only vesicles but also lipoproteins, viruses, protein aggregates, ribonucleoprotein complexes and exomeres[21–23], which provides an additional layer or diversity but also a bias upon analysis of EV samples. Furthermore, there is evidence that exosomes, microvesicles and apoptotic bodies contain subpopulations with unique roles in biological processes[24,25]. These subpopulations are tightly integrated with a broad range of biological processes and exhibit a wide range of functionalities, which makes them an outstanding source of potential biomarkers for early diagnosis, drug delivery systems for therapeutics, or vaccine production systems[15,26–28].

During the last few decades, the interest in EVs and their applications has grown considerably. Many articles and reviews have focused on the functional role of EV heterogeneity. Their role in specific biological processes, such as cargo trafficking or regulation of signaling pathways, and their potential as biomarkers have also been examined[11,15,25,29,30]. Nonetheless, most of these studies examine the vesicles in bulk and use ensemble-averaging assays. Although such methods have been proven useful in specific cases, it is important to realize that the extensive heterogeneity of structure, composition and function of single vesicles is masked in such assays[24,29–31]. For example, the inability to detect the heterogeneity of molecular states of reaction pathways, individual proteins or nucleic acids may lead to a misinterpretation of ensemble measurements[32,33]. Recent developments in single-vesicle analysis (SVA) have opened new opportunities for the examination of heterogeneity within EV (sub)populations at the individual EV level and their characterization on the nanometer scale[9,29]. This new information is paramount for understanding the biological functions of EVs and for their potential clinical use.

Different EV populations and subpopulations can be isolated according to their physicochemical properties, yet the existing isolation technologies are intricate and still need to be further developed[24,29]. There are five main groups of techniques for sorting EV populations and subpopulations, based on ultracentrifugation, size, immunoaffinity capture, polymer precipitation and microfluidics[19]. Since each technique type sorts EVs using a different principle, each method can yield different EV subpopulations from the same sample[34,35]. Moreover, the highly concentrated EV preparations might contain contaminants, such as large protein aggregates and lipoproteins, left behind by some of the isolation techniques[36,37]. Interestingly, different approaches can also affect the physicochemical surface characteristics of EVs[38].

In consequence, some techniques tend to enrich or discriminate against specific EV populations. As sorting EVs into populations is usually based on physical properties only, we have to assume that such classification is largely arbitrary with respect to the composition or function of EVs. Vesicle isolation and enrichment techniques can help to yield more homogeneous EV subpopulations, albeit only for particular technique-specific parameters. In conclusion, although various isolation methods could help drive EV analysis toward a single-vesicle approach[9], many different compositions and functionalities are still expected to be found within such EV populations.

In this review, we describe the current methods used to study single-vesicles, and their contributions to the understanding of EV biology and biomarker discovery. Single-vesicle experiments can deliver direct information on the heterogeneous composition of EVs. They reveal multiple molecular states that govern EV functionality and transport and provide statistically valid information often lost in large ensemble experiments[19,29,39].

EV heterogeneity and biomarker discovery

There are many technological challenges to be met in the development of EV-based diagnostics. The relevant vesicles must be identified and isolated from complex biofluids, and a specific disease-related EV population or population mix has to be detected. Biomedical studies of EVs often focus on seeking suitable biomarkers for the diagnosis of various diseases[40,41]. For example, the functional role of EVs in various types of cancer has been extensively studied[14,16,17,27]. In this review, we concentrate on prostate cancer (PCa) diagnostics as an example application to which the SVA of EVs has made important contributions. According to the World Health Organization, PCa is among the most frequently diagnosed types of cancer, accounting for approximately a quarter of all cancer diagnoses in Europe[42], yet the lack of sensitive diagnostic tools and insufficient knowledge of the mechanisms of cancer emergence and progression are of major concern. PCa is a heterogeneous pathological state, both in the primary tumor in the prostate tissue and at the metastatic stage. It is unfortunately not advisable to examine PCa diversity relying solely on tissue biopsies, since these are highly invasive procedures and do not guarantee an effective and reliable diagnosis[43–46]. The serum prostate-specific antigen (PSA) test—still the cornerstone of PCa screening—is particularly questionable. Up to 40% of men undergo unnecessary biopsies as a result of poor specificity of the assay.

Remarkably, liquid biopsy has a potential for marker identification and provides better evidence of PCa diversity than the conventional solid tissue biopsy. In particular, prostate- and PCa-derived EVs and concomitant markers are highly abundant in urine, blood and ejaculate samples[47,48]. Hence, these body fluids could be used for detecting and measuring the progression of the disease. For example, the EVs released by PCa cells carry unique prostate-specific membrane proteins (e.g., TMPRSS2, STEAP2, PSMA, PPAP2A) that enable the detection of pathogenic prostate EVs and their capture for ex vivo characterization[49]. Although these data show that liquid biopsies may be highly informative and minimally invasive procedures, the methods for vesicle isolation, characterization and identification for disease diagnostics remain challenging. Up to date, there are no standardized

operating procedures for vesicle isolation and characterization for different types of samples and diseases, which complicates the employment of liquid biopsies as a clinical source for EV biomarkers.

SVA techniques for biological characterization of EVs

Most of the studies reviewed in this article examine the three problems that can be addressed by taking advantage of SVA techniques: (1) characterization of EV heterogeneity including subpopulations, surface (membrane protein and lipid) composition and vesicle content, (2) structural studies of EV membrane and soluble proteins and the assays to probe the metabolic activity of these proteins in a native-like environment and (3) characterization of the EV content and function depending on the cells of origin. The last task presents an interesting dichotomy: do the EVs reflect the properties of their cells of origin, or are they completely independent communication assets? On the one hand, it has been reported that EV surface and content depend on the parental cells[50–52]. On the other hand, some recent reports describe several EV subpopulations, with a range of different functionalities, originating from the same cell type[9,18,19,29,53,54]. Intriguingly, another recent article using SVA techniques demonstrates that the T2SS-like family of proteins is, in fact, responsible for selective cargo loading into EVs generated by the microorganism *Shewanella vesiculosa*[55].

Single-vesicle techniques

As increasing numbers of researchers have highlighted the importance of accurate EV (sub)population sorting and phenotyping, so far, more than 20 new single-vesicle techniques have been developed[9,19,29]. Many of these use microfluidic devices designed to integrate various technologies to improve EV sorting and detection. Moreover, several of these methods have been used for characterizing EVs at the single-vesicle level[56–67]. Some of these techniques can directly provide information on vesicle surface, content, size and shape, while others may require an upstream physicochemical characterization of the selected EV subpopulations to conduct surface profiling, monitor the expression of biomarkers and quantify them in body fluids. These technological advances should help to design new diagnostic devices for small sample sizes, using noninvasive or minimally invasive methods.

Twelve different methods are presented in Table 1 and discussed in detail in the following sections. Some of these methods utilize labeling techniques (such as fluorescence or nanoparticle coating) to visualize the EVs, and others work as label-free systems (Fig. 1). It is important to note that, in some cases, label-free approaches might hinder the detection of EVs because they often produce weak signals, which can be enhanced using a supporting labeling technique.

Label-free methodologies

Nanoparticle tracking analysis (NTA) is a technique based on the Brownian motion of microparticles in suspension, and it is used to determine the size distribution in particle populations[56,68]. In this approach, microparticles are detected by scattering the light of a laser beam, which is tracked and recorded at video frame rates. However, this approach has some disadvantages and limitations. For instance, the accurate assessment of particle size distribution requires specific track lengths, a steady temperature and a large number of replicates to provide robust results. Care should be taken when comparing different samples because variations in buffer viscosity and microparticle concentration introduce statistical errors. Moreover, the close proximity of two particles can result in overlap of the scattering signals. Accurate detection of particles with a diameter <60 nm is challenging, regardless of the NTA machine used[69]. Furthermore, vesicles cannot be discriminated from other particles, such as protein aggregates or virus particles. The vesicles can be probed specifically, and undesired particles excluded from the analysis only by employing fluorescent markers, yet only a fraction of EVs may carry known markers that can be used for labeling a specific subpopulation. General fluorescent labels (such as lipophilic carbocyanines DiO or DiI) can be used instead. However, it is important that any nonattached label be removed since this can mask the fluorescence signal emitted by labeled EVs[19].

Raman tweezers microspectroscopy (RTM), also known as laser tweezers Raman spectroscopy (LTRS), can be employed to examine the chemical content of EVs. This approach can be used to investigate both the surface and the internal volume of single EVs, revealing specific biomolecular signatures of proteins, lipids, nucleic acids and carotenoids as major contributors[57,60,61,70–77]. RTM is an inelastic scattering-based method. It employs a tightly focused laser beam for both optical trapping of single (or very few) vesicles in aqueous medium and excitation for subsequent Raman scattering, which provides a vibrational fingerprint from the trapped constituent biomolecules. The main inherent advantage of RTM lies in the signal linearity, which allows both qualitative and quantitative biochemical characterization of single EVs. This method is also label-free and provides data with high information content[57,71,74]. The main disadvantage is that the scattering efficiency is usually very low and thus provides a rather low level of informative Raman signal. As a result, an extended data collection time is required. Therefore, RTM, with a typical processing capacity of 0.2 particles per min, is not considered a high-throughput methodology[71]. RTM can, however, be used to obtain interesting, unique information not only for EVs[57,60,61,70–77] but also for many other bioparticles such as liposomes, lipid layers on synthetic nanoparticles and others[78–83].

Several methods have been developed to compensate for the low Raman signal strength in RTM. For example, the vesicle concentration can be increased by drop-coating deposition of the sample, followed by drying[84–88]. Unfortunately, this approach results in loss of information about individual EVs, as does any other analytical study of a bulk sample. Another strategy to increase the Raman signal is to use surface-enhanced Raman spectroscopy (SERS). In this method, EVs can be exposed to various signal-enhancing nanoparticles and/or substrates to obtain a strengthened biomolecular signal[62,89–95]. The main problem of label-free SERS is that the enhancement effect depends strongly on the distance between the biomolecule and the nanoparticle/substrate, and vanishes

Table 1 | Summary of main SVA techniques for individual EV characterization

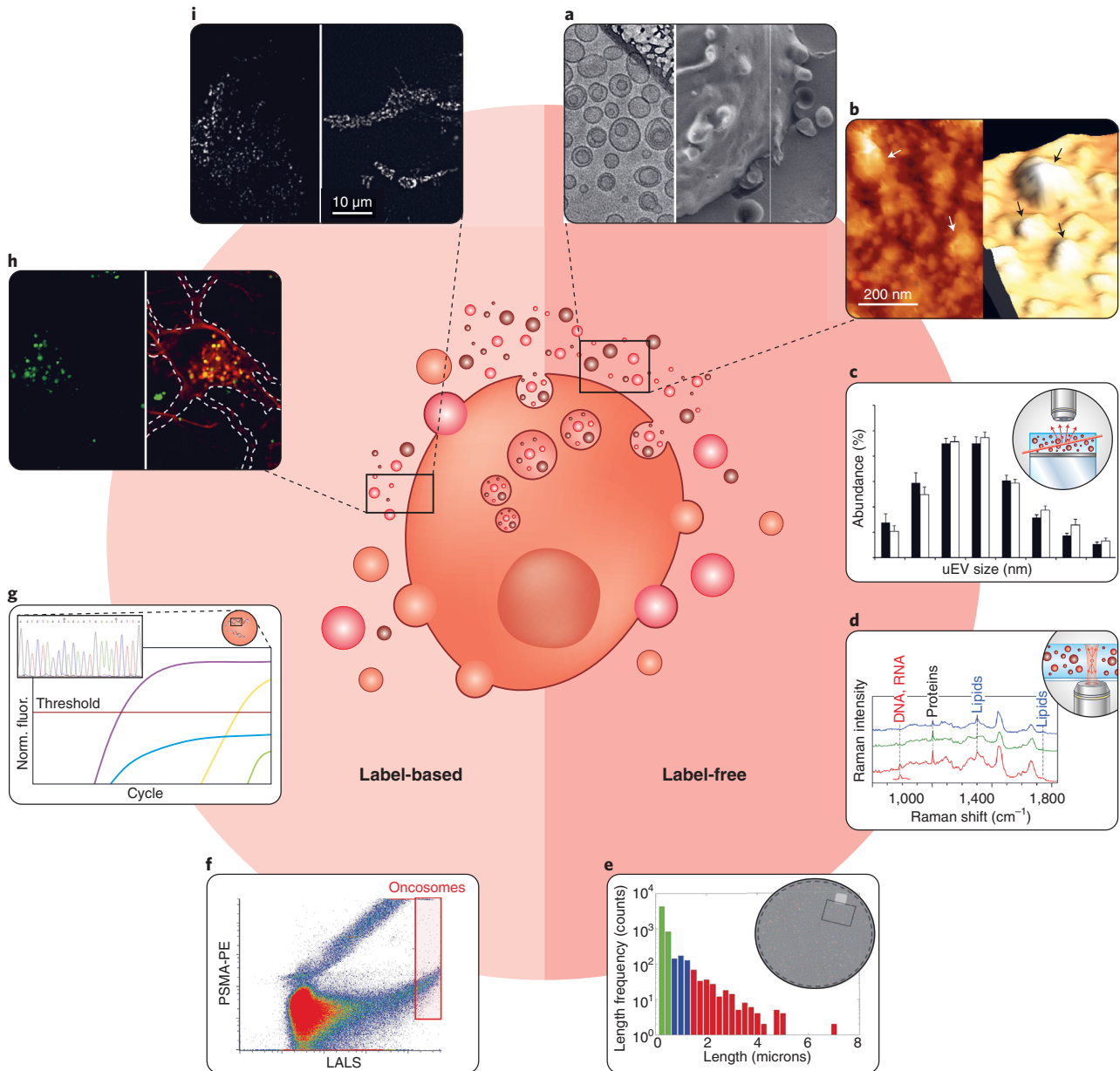| Technique	Detection principle	Information obtained	Throughput	Time per analysis[a]	Sample preparation[b]	Is sample reusable?	Loading volume	Working concentration (mL^{-1})
High-resolution flow cytometry	Elastic light scattering; autofluorescence or fluorescence from external labels	Profiling[c] of EVs in a heterogeneous fluid mixture; functionalized fluorescent labels characterize specific populations	High	~1 min	Immunofluorescence or fluorescent conjugate staining protocol	No[d]	20–100 µL	10^7–$10^{10,e}$
Nanoparticle tracking analysis	Imaging of Brownian motion pathways for EVs, using elastic light scattering or fluorescent labels	Particle concentration, size distribution	Moderate	~1 min	Dilution or concentration of Evs to the range optimal for the method	Yes	0.3–1.0 mL[f]	10^8–10^9
Raman tweezers microspectroscopy	Raman scattering from optically trapped single EVs	Biomolecular[g] composition of the surface and the interior of single EVs	Low	~1–5 min[h] per one[i] trapping event	Concentration of EVs to the range optimal for the method	Yes	~100 µL	10^7–10^{11} [j]
Surface-enhanced Raman spectroscopy (SERS)	Raman scattering enhanced by external active surface/coating	Partial[k] biomolecular[(g)] composition of the membrane of single EVs	Moderate	~1–10 s per one[(i)] EV	Fixation and coating protocol	No	50–100 µL	10^9–10^{11}
SERS with external labels	Enhanced Raman signal from SERS nanotags	Number of EVs with specific functionalized SERS nanotags attached	High	~10 s	Fixation and SERS-label staining	No	10–100 µL	10–10^7 [l]
Cryo-transmission electron microscopy (Cryo-TEM)	Transmission electron microscopy imaging	Morphological EV characterization[m]. Direct visualization of single EVs and examination of contaminants	Low	~1 h [(h)]	Vitrification of water in EVs dispersed on carbon grid, using fast-plunge freezing	No	2–10 µL	10^{10}–10^{12}
Atomic force microscopy (AFM)	Imaging (raster scanning) exploiting interaction force between the probing tip and immobilized EV	Precise[n] morphological, mechanical and biochemical[o] characterization of the EV surface	Low	~1 min per image[(i)]	Immobilization protocol.[p]	No	5–25 µL	Relative[q]

Table continued

Table 1 (continued)

Technique	Detection principle	Information obtained	Throughput	Time per analysis [a]	Sample preparation[b]	Is sample reusable?	Loading volume	Working concentration (mL^{-1})
Total internal reflection fluorescence microscopy (TIRF)	Imaging using fluorescence from external labels in an ultra-thin layer[r] of induced evanescent field[s]	Background fluorescence suppression; visualization of specific biomolecules[t] in vesicles of living cells; information on EV interaction and trafficking	Moderate	10–60 min	Fluorophore internalization protocol; calibration of the angle of incidence	Yes	10–200 µL	Relative[q]
Fluorescence resonance energy transfer (FRET)	Excitation energy transfer between donor and acceptor fluorophores via non-radiative resonance interaction; change[u] in fluorescence color	Structural information[v] derived from short-range[w] interactions in the donor–acceptor pair	Moderate	10–60 min	Fluorescence staining	Yes	10–200 µL	Relative[q]
Super-resolution microscopy	Fluorescence from external labels	Visualization of single vesicles in biological samples	Low	~1 s per image	Fluorescence staining; fixation protocol	No[x]	50–100 µL	Relative[q]
Droplet PCR	PCR amplification in partitions	Absolute quantification of specific targets in individual EVs or small *identical*[y] subpopulations	Moderate	~5 h per loading volume	EV droplet encapsulation protocol	No	20–150 µL	10^2–10^3
SP-IRIS	Enhanced scattering signal from particles bound to a substrate	Multiplexed phenotyping (surface biomarkers) and sizing of EVs populations in a single measurement	High	–	EV incubation on array	Yes	20 µL (microfluidics)	<10^9

[a]Time required for analysis once the sample and instrument are ready for the measurement. [b]Sample preparation protocol, for all techniques, contains the first obligatory step of EV purification and separation. [c]Obtaining size distribution, number of labeled particles, counting and sorting. [d]Attempts to sort the selected vesicles are under way and are likely to be successful in the future. [e]Dilution of the sample will be required to avoid swarm effect. [f]20 µL in microfluidics devices. [g]Distribution of proteins, lipids, nucleic acids, carotenoids and other biomolecules with pronounced, strong Raman bands. [h]Time for optimal working concentration. For particle concentration lower than optimal, the measurement time can increase considerably. [i]The total number of single EVs analyzed per sample depends on the task and measurement statistics and will be different for each particular experiment. [j]Concentration range is determined using the waiting time for the event of EV optical trapping. For larger/heavier EVs, lower concentrations are used: 10^7–10^9 mL^{-1} is suitable for large ~1 µm EVs, 10^8–10^{10} mL^{-1} is optimal for smaller exosomes, and up to 10^{11} mL^{-1} is required for the smallest (~50 nm) bioparticles. [k]Within the area of sufficient Raman-signal enhancement (depending on the geometry of interaction between EVs and the signal-enhancing surface/coating). [l]Exosome concentration logarithm is linear over the range of 40 particles/µL to 4×10^7 particles/µL plotted against Raman intensity[148]. [m]Polymorphism, membrane layers, internal-structure features, etc. [n]Lateral resolution 1–3 nm, axial resolution below 0.1 nm. [o]Using an immunofunctionalized probe tip. [p]On glass, mica or graphite (HOPG-type). [q]Working concentration spreads over a rather broad range and the optimal concentration strongly depends on EVs location in the microscope field. [r]Signal collection layer is usually less than ~100 nm thick, depending on the excitation wavelength and objective numerical aperture. [s]Evanescent field is created when the angle of incidence of excitation beam is larger than the angle of total reflection, so that the excitation beam does not penetrate into the sample. [t]miRNA, surface proteins. [u]Donor fluorescence disappears, acceptor fluorescence appears. [v]Assessment of conformational fluctuations, folding pathways, macromolecular interactions, kinetics of structural changes, etc. [w]When distance between donor and acceptor fluorophores becomes <8–10 nm. [x]Some SRM approaches damage the sample to such an extent that only one measurement is possible, and others permit several SRM-imaging analyses of a sample. [y]EV subpopulations with a specific surface protein in common.

Fig. 1 | Schematic overview of the main SVA techniques discussed in this review. Data visualization and single-vesicle interpretation using each SVA methodology are depicted. In the center of the figure, a (tumorigenic) cell releasing EVs is shown. **a–i**, The techniques can be divided into two groups: label-free (**a–e**) and label-based (**f–i**) methodologies. The methods used here are cryo-electron microscopy[74,168] (**a**), AFM (**b**), NTA[9,172] (**c**), RTM[74] (**d**), SP-IRIS[111] (**e**), hrFC[223] (**f**), ddPCR[221] (**g**), SRM[130] (**h**) and fluorescence microscopy (**i**; TIRF image of synaptic vesicles is depicted)[253]. References show the source of the images. Panel **a** reprinted with permission from ref. [168]. Copyright 2017 Elsevier. Panel **d** reproduced from ref. [74]. Published by The Royal Society of Chemistry. Panels **c–i** reproduced with permission under Creative Commons Attribution 4.0 International License http://creativecommons.org/licenses/by/4.0/.

at distances longer than a few nanometers[89]. Therefore, this method is mainly suitable for characterization of biomolecules on the outer surface of EVs. In addition, Raman modes corresponding to molecular vibrations perpendicular to the SERS surface are preferably enhanced[89]. As a result, the overall SERS vibrational spectrum is usually somewhat distorted, lacks reproducibility and is often difficult to interpret.

In electron microscopy, a beam of electrons is emitted onto a sample in a vacuum environment. The wavelength of electrons is shorter than the visible light used in optical

microscopy; thus, the method gives images of much higher resolution, typically below 1 nm[19]. Cryogenic transmission electron microscopy (cryo-TEM) is among the electron microscopy methods most commonly utilized for EV characterization. In contrast to the lengthy sample preparation needed for other TEM methods (usually taking hours), no heavy metals or fixatives are added, and no dehydration steps are required. This also limits sample damage and artifact effects, but yields lower-contrast images[96]. In cryo-TEM, the samples are prepared by rapid freezing, typically with liquid

ethane[57,97]. In this process, the water vitrifies, instead of forming ordered crystals, and the native structure of EVs is preserved[98]. The first exosome visualization was achieved using cryo-EM in 2008[99]. Since then, this technique has successfully revealed EV polymorphism by imaging the membrane bilayers, EV structures and internal features of individual EVs[57,63,96,100]. Even though cryo-TEM is an extremely useful technique for high-resolution visualization of EVs, this approach is relatively low-throughput. Cryo-TEM images typically only contain a few EVs (although the throughput could be enhanced by using automated search). In addition, cryo-TEM images provide only limited information regarding EV composition. To overcome this problem, nanoparticles functionalized with immunogold-labeled antibodies targeting markers of interest have recently been employed to characterize the biochemical composition of the EV surface[19,101].

Yet another type of microscopy method used for SVA is atomic force microscopy (AFM), which exploits the interaction between a probing tip and a sample surface. The deflection of the probing tip caused by interaction forces is detected and recorded using a laser and a sensor[102]. AFM allows an accurate morphological and mechanical characterization of EVs; its lateral resolution is 1–3 nm, and the vertical resolution <0.1 nm[102]. Typically, visualization of a few EVs using AFM is labor-intensive and time-consuming in comparison with other microscopy methods. However, a relatively high-throughput AFM-based method has been reported that measures the size and stiffness distribution of 100 vesicles within 1 h[65]. It is important to note that the tethering surface, to which the EV is bound, strongly affects the shape of the EVs. Therefore, the vesicles must be bound to a perfectly flat surface[103–105]. To characterize the biochemical properties of an EV surface, either the probing tip or the surface itself can be further (immuno)functionalized[106,107]. AFM can also be coupled with infrared spectroscopy (AFM-IR), allowing simultaneous measurements with a finer spatial resolution. AFM-IR has been extensively utilized in various applications; however, few papers report its implementation in the single-EV field[66,108]. We assume this is because the weak IR signal thwarts reliable characterization of individual vesicles.

Single-particle interferometric reflectance imaging sensor (SP-IRIS) is employed in assays based on interferometric imaging. It is used to detect individual enhanced scattering signals from the bound vesicle. The signals are produced by the interference between the scattered field from a vesicle and the reference field reflected off the layered substrate[109,110]. The method can detect several surface biomarkers and simultaneously measure the size of individual EVs. It can be used to accurately count and distinguish individual vesicles, with a low level of false positives and negatives[110]. However, as the lateral resolution of the microscope (~400 nm) could accommodate several small vesicles, some detected signals could be erroneously assigned and categorized as larger vesicles instead of several smaller vesicles. This could be an issue especially in highly concentrated sample preparations[111].

Label-based methodologies

Label-based methodologies are strongly dependent on the detection of a signal from a fluorescent protein, immuno- or lipophilic fluorophore or signal-enhancing nanoparticles. High-resolution flow cytometry (hrFC) is one of the first techniques extensively employed for individual EV analysis. hrFC can be used to quantify the size distribution and diversity of EV populations by detecting multiparametric scattered light and fluorescence emitted by the labeled vesicles. This fluorescence assay can be used to characterize the vesicle population by profiling the protein or nucleic acid content using antibody–fluorophore conjugates. However, any remaining free fluorescent dyes in the sample will cause high background fluorescence. This can be avoided by using density-based ultracentrifugation to purify labeled EVs, which leaves the nonreacted dye in the supernatant and sediments the vesicles into the pellet fraction[112,113]. Furthermore, multiple EVs (or particles) arriving simultaneously at the flow cytometer detector may be identified as single particles. This phenomenon is known as the swarm effect. The danger of such misidentification limits the concentration range within which the EVs (or particles) can be characterized effectively and makes it necessary to examine multiple diluted samples.

Fluorescence microscopy is an imaging technique particularly useful in localizing lipophilic fluorescent dyes or fluorescently labeled targets (either using fluorescent proteins or fluorescent dye-conjugated antibodies) in cells, tissues or EVs[9]. Another, rather elegant approach, now commonly used in the SVA field, is total internal reflection fluorescent (TIRF) microscopy. It can be used in an aqueous environment to image selectively the fluorescent molecules located near a highly refractive solid substance[114]. TIRF exploits the reflection of an excitation light beam at a high incident angle, typically between 60° and 80°, at which the beam of light is completely reflected by the glass–water interface. This reflection phenomenon generates a very thin electromagnetic field, called an evanescent wave, which is parallel to the substrate surface. This enables limited specimen illumination and thereby eliminates out-of-focus fluorescence and enhances the signal-to-noise ratio[115]. TIRF is predominantly used for studying intracellular single-vesicle processes such as endocytosis or exocytosis, cell–substrate contacts or internalization of plasma membrane receptors[114,115]. It can also directly localize fluorescently labeled molecules in EV preparations and allows tracking EVs in tissue preparations. However, the fluorophores can be excited only within a few hundred nanometers from the solid substrate, and the calibration of the incident angle can be difficult (depending on the setup)[114,115]. Moreover, the fluorophore instability and gradual photobleaching (although less pronounced than in other light microscopy techniques) during prolonged illumination might produce misleading results[9,116].

Fluorescence (or Förster) resonance energy transfer (FRET) is a phenomenon where the excitation energy from a fluorophore is transferred nonradiatively to another fluorophore. This happens via resonance energy transfer at distances <10 nm. FRET imaging offers unique opportunities for the assessment of kinetic and structural dynamics and studies of the interaction and fusion events between EVs and cells[117–119]. Notably, this imaging-based technique is capable of producing a considerable amount of single-particle and single-vesicle fluorescence data very fast[120–123]. However, fluorescent signal

fluctuations due to a low signal-to-noise ratio and poor photostability of certain dyes might lead to changes in the FRET signal that are unrelated to the biological processes. Like in other fluorescence-based techniques, the presence of multiple fluorophores within the observation volume may result in ensemble averaging of the population[119,124].

Super-resolution microscopy (SRM) is one of the most advanced applications of fluorescence imaging. It can be used to visualize biological features smaller than the optical diffraction limit and, therefore, below the conventional optical microscopy resolution limits (which are typically limited to ~250 nm axial and ~500 nm lateral resolution). This attribute provides an important advantage in imaging single EVs and permits investigation of their physiological functions[67,125–130]. Briefly, SRM techniques can be divided into two groups: (i) methods based on spatial patterning of the excitation light and (ii) methods based on single-molecule localization.

Excitation-patterning methods include structured illumination microscopy, in which the specimen is illuminated in a striped pattern[9,131] and stimulated emission depletion microscopy, which sharpens the excitation laser focus using a second laser that temporarily bleaches the fluorophores surrounding a small observation volume in the specimen[132,133].

Single-molecule localization methods detect fluorescence emitted from spatially isolated photo-switchable or blinking fluorophores to determine their position[133]. Photoactivation localization microscopy (PALM) relies on photoactivatable fluorescent recombinant proteins[134], whereas stochastic optical reconstruction microscopy (STORM) takes advantage of fluorophores that blink in a noncontrolled fashion. In both cases, only a small subset of fluorophores will be emitting simultaneously, allowing the precise localization of the fluorophores and reconstruction of the complete image at high spatial resolution[9]. Importantly, single-molecule localization approaches can be used in combination with TIRF, improving the signal-to-noise ratio and shortening imaging time[116]. Furthermore, all SRM techniques are based on the optics of classical diffraction-limited far-field light microscopes. This makes them compatible with existing sample preparation procedures, and also permits them access beyond the surface of a specimen. SRM techniques are also often minimally invasive[133,135]. It is important to note that most SRM approaches work only on fixed samples; thus, one should always be aware of potential artifacts introduced by the fixation method[9,136]. Another relevant aspect to consider is that, in general, the labeling of proteins using fluorescence markers or other tags might affect their localization, interaction partners and function[135]. In addition, although lipophilic or genetic labeling could allow visualization of single vesicles, lipid labeling in some cases might result in unspecific labeling or dye aggregates.

Digital droplet PCR (ddPCR) can be employed to distribute single EVs into individual droplets, which allows amplification and characterization of their genetic cargo[59,137,138]. Such cargo is usually RNA-based and mainly comprises miRNA, mRNA and noncoding RNA. In ddPCR, the EVs are tagged using anchoring molecules or antibodies and further distributed into microfluidic chambers according to their surface markers[59]. This methodology enables high-throughput quantitative analysis of EV content and can be used for the identification of biomarkers[139–142]. So far ddPCR use has been limited to validation purposes; however, it can be used as a screening technique (compromising its high-throughput capabilities)[19,143]. Interestingly, ddPCR has been already adopted for multiple mutation analysis to examine specific mutations in distinct populations of EVs. Next-generation sequencing could allow for parallel analysis of multiple mutations in many genes[144].

Finally, SERS nanotags functionalized with biorecognition molecules (such as target-specific antibodies) can be used to bind specifically to target EVs expressing the biomarker of interest. This approach is gradually becoming an important alternative to fluorescent molecular probes[94,145–149]. The major advantage of SERS labeling lies in the superior photochemical stability of Raman reporters compared with fluorescent labels, due to the vibrational nature of the generated signal. Moreover, several high-throughput Raman/SERS screening platforms for characterizing cells and EVs have been recently reported[70,150–153].

Recent advances in the EV field due to SVA

The recent breakthroughs in SVA techniques help to tackle the intrinsic limitations of ensemble EV measurements and analyses. In the following sections, we review the impact of SVA method development on recent advances and discoveries in the EV field (EV characterization, internalization, the role of EVs in cell-to-cell communication and biomarker discovery). In Table 2, we provide an overview of recent scientific articles describing the characterization of EVs, including studies of their heterogeneity and phenotyping of PCa-derived EVs. Current studies of EV internalization pathways and the role of EVs in cell-to-cell communication are summarized in Table 3. SVA techniques have been used in the successful identification and validation of a wide range of biomarkers for many different diseases. As an example, Table 4 lists recent discoveries in cancer research with a strong focus on PCa.

EV characterization

Several techniques mentioned in the previous section—NTA, cryo-TEM and flow cytometry—are established as customary characterization procedures for EV studies[141]. Notably, the results obtained employing these methodologies usually require validation using a complementary technique. This is because none of them is considered the gold standard procedure, and all of these approaches come with their own challenges and limitations[154]. For example, NTA is routinely utilized to obtain the size of EVs and quantify their abundance. However, since this technique is not vesicle-specific and can detect other particles, the reliability of the results must be cross-checked with other techniques. Therefore, EV studies that draw their conclusions solely from NTA are now uncommon, especially when compared with earlier EV characterization studies (from 2012 to 2015) when NTA was commonly utilized. Currently, NTA is often used as a supplementary characterization technique instead, as it requires minimal sample preparation to introduce fluorescent markers

Table 2 | Summary of EV characterization studies using SVA techniques

Technique	Main conclusion	Ref
AFM	The first time that plant exosomes have been visualized in their native state. They have been observed on the internal layers of the cell walls and their cargo assessed	156
	Matrix vesicles initiate changes during the mineralization of the extracellular matrix. In the course of this process, the matrix vesicles increase their size and crystallinity and change shape	157
AFM-IR	The first attempt to probe the differences between the molecular constituents (proteins, lipids and DNA) and structures of individual vesicles in two subtypes of placenta stem cells. In this work, protein aggregates have been successfully differentiated from vesicle structures	108
RTM	Vesicle shape and size depend on the lipid composition of the membrane. A decrease in cholesterol concentration increases the local membrane curvature and stretches the vesicle	82
Cancer research		
hrFC (immunofluorescence)	Microenvironment acidity of the prostate tumor increases the release of prostate-specific EVs	175
	EVs from PCa cells are very heterogeneous, but specific populations are not associated with different cancer stages. Mainly microvesicles and several exosome subpopulations are found, according to the surface signature	179
NTA	Increase in the number of released exosomes under acid pH (6.5), independent of tumor histotype	171
	Tumor cells release more EVs than do nontumorigenic cells (most likely due to the acidic environment in tumor cells)	174
Heterogeneity-related research		
NTA	Description of different EV populations in human glioblastoma cells	165
NTA (with fluorescence)	The first attempt to use this technique to determine the concentration and particle distribution in specific EV subpopulations, according to surface markers such as CD9, CD63, vimentin and LAMP-1	252
Electron microscopy (cryo-TEM)	Large diversity of exosome morphology revealed, regardless of the cell type and origin, suggesting that different exosome subpopulations from the same cell line perform different functions	96
	Visualization of a large spectrum of EVs from cerebrospinal fluid, including multilayer vesicles, single, double and double-membrane vesicles, and internal vesicular structures. These specific subpopulations are suggested to serve as potential biomarkers for Parkinson's disease	164
	Two different stimuli affecting EV release. Lipopolysaccharides and starvation conditions in human leukemia monocytic cell line (THP-1) affect the type of EVs shed and, probably, the shedding process	168
AFM	EVs isolated from different species are imaged. Using the tapping mode, the mechanical properties of EVs are assessed, concluding that the rat EVs are more fragile than the mouse vesicles	170
RTM	During cell growth and starvation-induced aggregation, *Dictyostelium discoideum* produces EVs that differ drastically in their biomolecular composition (nucleic acids, proteins, lipids, carotenoids)	57
	Detection of four EV populations with specific protein, phospholipid and cholesterol surface signatures. Their functionality determines their distribution; the populations are shared among several cell types	71
	In EV preparations from rat hepatocytes and human urine, single EVs from the same sample have different biochemical properties, well beyond the 'usual' variations for EVs from rat hepatocytes or human urine. A quantitative method developed to measure the concentration of nucleic acids in a single EV	74
	Combined morphochemical profiling of individual EVs is proposed based on Raman-enabled nanoparticle trapping analysis	75

for specific EV population studies. Likewise, labeling-based flow cytometry serves as a high-throughput sorting method for the characterization of certain EV features; however, it needs some technological improvements in separating unbound dye and dye aggregates from EVs to be utilized as a unique characterization approach[155]. Direct visualization of EVs using microscopy lets researchers assess the shape and size of vesicles in their native state[156] and in various biological processes[157], while other techniques, such as RTM, can be employed to examine further the morphology of bioparticles without direct

visualization. For example, the effect of membrane lipid composition on the shape and size of giant unilamellar vesicles was first described using Raman tweezers, demonstrating that a decrease in cholesterol concentration increases the local membrane curvature and stretches the vesicle[82].

A large diversity in the morphology of exosomes has been reported for many types of cells[96]. For example, in the early 2010s, plasma EVs were comprehensively characterized and phenotyped using cryo-TEM in combination with gold nanoparticle-based immunolabeling[158]. This study found that

Table 3 | Mechanistic studies of vesicles using SVA techniques focusing on vesicle–cell communication, trafficking and vesicle fusion and endocytic pathways

Technique	Main conclusion	Ref
Vesicle–cell communication and trafficking research		
FRET microscopy	Tau protein misfolding and monomer aggregates spread in a prion-like manner causing neurodegenerative diseases such as Alzheimer's. Extracellular vesicles play a role in the transmission of pathological tau seeds	182
	The triad protein VOR is essential in the regulation of the endocytic nuclear transfer of EV-derived components. Targeting VOR might have therapeutic potential by inhibiting EV-mediated intracellular communication	185
Fluorescence microscopy (SRM)	In vivo visualization of EVs in the zebrafish embryo. Uptake of EVs by endothelial cells and blood patrolling macrophages is shown. The study demonstrates that tumor EVs activate macrophages and promote metastatic outgrowth	58
Electron microscopy (cryo-TEM)	Multiple virions and unique morphological components forming a mat-like structure are transported via infectious EVs of 100–1,000 nm in diameter. These infectious vesicles containing enterovirus material are secreted from host cells before lysis	184
ddPCR	EVs from osteotropic melanoma cells induce chemotaxis and cancer progression via upregulation of CXCR7 of nonosteotropic melanoma cells	186
Vesicle fusion and endocytic pathway research		
AFM	Description of mechanical properties of erythrocyte-derived EVs according to their protein–lipid ratio. While a high ratio is associated with soft vesicles, a low ratio corresponds to stiff EVs. These mechanical differences are linked to several vesiculation and budding mechanisms	187
Electron microscopy (cryo-TEM)	Visualization of the SNARE-mediated membrane fusion-by-hemifusion of small vesicles with cells shows fusion intermediates where lipid monolayers partially mix en route to complete bilayer merger	192
FRET microscopy	Description of the molecular mechanism of SNAREs during different membrane fusion stages, (docking, hemifusion and full fusion) by tracking the lipid-mixing process at the single-vesicle level	193
Fluorescence microscopy	The fusion pathways are heterogeneous, with an arrested hemifusion state predominating. The fusion of two lipid bilayers occurs spontaneously in a single step when they are brought into close proximity	191
Fluorescence microscopy (TIRF)	Heterogeneity of endocytic vesicle behaviors upon internalization. Prior to scission, vesicles remain proximal to the plasma membrane for variable periods. Clathrin uncoating is also variable	190
	Calcium activates synaptotagmin-1, resulting in SNARE-mediated fusion of synthetic vesicles used as an exocytic model for synaptic events. An optimal distance for the fusion is 5 nm	194
	Alterations in membrane cholesterol content shift hemifusion intermediates to full-fusion membrane and affect the stability of fusion pores. A large increase in cholesterol levels boosts individual SNARE-mediated fusion events	195
	Disassembly of the clathrin lattice surrounding coated vesicles is the obligatory last stage in their life cycle. The study visualizes the recruitment of auxilin and Hsc70, which is essential for this well-studied endocytic process	189
hrFC (fluorescent conjugates)	Characterization of microvesicles from red blood cells under stimulation and activation conditions. An increase in intracellular Ca^{2+} or protein kinase C levels leads to alterations in cell morphology and increased release of microvesicles	181
FRET microscopy	Free zinc concentration in insulin-storing vesicles is quantified using a novel FRET-based zinc sensor. The concentration of free zinc is important for insulin-storing vesicle maturity; hence, it alters insulin trafficking	180

platelet-free plasma samples contain a mixture of EVs with different morphologies, including spheres, cylinders and membrane fragments that are neither tubular nor spherical. Moreover, it has been shown that EVs come in a wide range of sizes[158]. Despite this morphological heterogeneity, only a minority of EVs in plasma expose phosphatidylserine on the surface. This is at odds with the classical theory of EV formation at the cell's plasma membrane, in which the loss of phospholipid asymmetry and exposure of phosphatidylserine

precedes membrane blebbing and shedding[159–163]. The authors have suggested that some EV (sub)populations ought to be generated and regulated via different pathways[158]. Likewise, Emelyanov et al. have described a large spectrum of EV morphologies and (sub)populations after isolating EVs from cerebrospinal fluid and visualizing them using cryo-TEM[164]. They have reported several different morphologies, including multilayered, single- and double-membrane vesicles, as well as internal vesicular structures. Interestingly, a subpopulation

Table 4 | Summary of recent EV biomarker-related discoveries achieved using SVA techniques, focused on cancer diagnostic biomarkers

Technique	Main conclusion	Ref
Flow cytometry (immunofluorescence)	Detection of CD147 as EV biomarker for CRC diagnosis	208
	Detection of GPC1 as EV biomarker for pancreatic cancer diagnosis. Cancer-cell EVs contain oncogenic KrasG12D	222
	Measures circulating PMP levels in plasma. This PCa 'liquid biopsy' can identify patients with Gleason score $\geq$ 8, irrespective of their PSA	223
Fluorescence microscopy (TIRF)	Employs a fluorescent assay to detect exosome miRNA-21 (miR-21-EX) as a cancer-screening assay. miR-21-EX can be used to distinguish between cancer patients, tumor progression stages and treatment responses	211
Raman (dry EVs)	The surface protein signature shifts from alpha-helix-rich proteins to beta-sheet-rich proteins in PCa-specific blood EVs	84
RTM	Chemical signatures from Raman spectra can be used to differentiate between EV populations derived from healthy and PCa cells. A trained convolutional neural network can identify the cellular origin of EVs	73,77
RTM	Raman analysis coupled with Rayleigh scattering distribution is used to detect specific lipid and protein signatures of tumor-derived EVs	76
Label-free SERS	Report of real-time and label-free diagnosis of lung cancer by detecting 11 cancer-specific SERS signals (proteins and lipids) that distinguish EV populations from healthy and lung cancer cells with high sensitivity	92
ddPCR	Detection and quantification of mutant and wild-type IDH1 RNA transcripts in EVs from cerebrospinal fluid of patients with glioma tumors	140
	Identifies somatic BRAF and KRAS mutations in plasma-derived EVs from CRC patients. Probes a wide range of cancer cells and the derived EV populations	221
	Identifies KLK3 and AR-V7 (androgen receptor variant) as biomarkers for castration-resistant PCa (which progresses even under steroid deprivation therapy)	216
	Extracellular vesicle-transported HULC promotes cell invasion and migration. This encapsulated HULC is identified as a biomarker for human pancreatic ductal adenocarcinoma	142

of these EVs plays a key role in Parkinson's disease progression[164]. Another study, using NTA-based technology, has identified several EV populations released by human glioblastoma cells[165]. Moreover, fluorescence-based NTA approaches are being used to examine the concentration and particle distribution of specific EV subpopulations[166,167].

The relative chemical abundance of major biomolecules comprising EVs, namely proteins, lipids, nucleic acids and carotenoids, can be obtained from the vibrational fingerprints acquired using RTM. Tatischeff et al. have shown that *Dictyostelium discoideum* in two different physiological states (i.e., cell growth and starvation-induced aggregation) produce EVs with drastically different biomolecular compositions[57]. In another study, Smith et al. have categorized four EV populations according to specific protein, phospholipid and cholesterol vibrational signatures, which are shared among several cell types from different species[71]. The authors have found that human lung carcinoma A549, human hepatocarcinoma Huh-7 and mouse embryonic fibroblast 3T3 cells have similar EV populations. In contrast, Kruglik et al. have reported direct Raman evidence of pronounced biomolecular heterogeneity of single EVs in the same sample (using rat hepatocytes and human urine)[74]. In their study, the heterogeneity was determined by quantitative measurements of nucleic acid concentration within single EVs, based on the intensity of the pyrimidine ring stretching band[74].

Further heterogeneity studies performed with cryo-TEM and AFM have described the physical characteristics of EVs. One cryo-TEM analysis has reported that the shedding process and, hence, the type of EV released is strongly affected by external stimuli, such as lipopolysaccharides or starvation conditions, in a human leukemia cell line[168]. By using the tapping mode in AFM, biomechanical properties such as elasticity, stiffness and deformability of single EVs can be assessed[169]. It has been reported that rat hepatocyte-derived EVs are more fragile and easily warped than liver-progenitor mouse EVs[170]. Another study performed using AFM-IR has allowed, for the first time, probing of molecular constituents and structures of individual vesicles[108]. In this study, the researchers were able to differentiate between the molecular compositions of EVs derived from two subtypes of placenta stem cells. Moreover, their approach has allowed discrimination between protein aggregates and EVs. The examination of DNA, lipids and proteins using AFM-IR, in just a few vesicles, has remarkable potential in early disease diagnosis[108].

SVAs have been extensively utilized in cancer research, for example, to characterize the EVs in PCa. NTA-based research has established that cancer cells produce larger amounts of EVs than do nontumorigenic cells[47,171,172] and that low extracellular pH increases the release of EVs from cancer cells[173,174]. Interestingly, NTA studies also support the idea

that tumorigenic cells upregulate EV production owing to the acidification of the immediate microenvironment[175–178]. Logozzi et al. have employed a combination of hrFC and immunofluorescence to discover that acidic microenvironment of prostate tumors induces the release of PCa-specific EVs[175]. These EVs are very heterogeneous, and several populations can be identified, according to their surface composition. However, it is important to note that this heterogeneity is not related directly to different cancer stages[179].

In summary, the highlighted reports of single-EV characterization demonstrate that EV morphology and composition are largely independent of cell origin and that certain EV (sub) populations are involved in various diseases. These discoveries indicate that morphologically different EV populations may be distributed according to their specific function and biogenesis pathway, rather than the cell type of their origin.

EV trafficking and signaling mechanisms

SVA approaches have advanced EV research by tracking particular molecules and examining the changes in cells under different conditions. Early in 2020, FRET studies in T cells showed that the concentration of free zinc in cells is a major regulator of the maturation process in insulin-storing vesicles[180]. SVA has also contributed to discoveries reporting an increase in intracellular Ca^{2+} and/or protein C under certain stimulating and activating conditions in red blood cells. These conditions alter cell morphology and cause an increase in the release of microvesicles[181]. Table 3 summarizes more examples of recent advances in research in (a) vesicle–cell communication and trafficking and (b) vesicle fusion and endocytic pathways.

EVs serve as information carriers for cell pathways and may trigger some diseases due to this activity. Neurodegenerative diseases such as Alzheimer's are caused by the misfolding and aggregation of tau protein. Polanco et al. have described a prion-like spread of tau protein seeds brought about by EVs, employing cryo-TEM[182] and SRM (PALM and STORM)[130]. The contribution of EVs to trans-synaptic tau transmission has been confirmed using cryo-TEM in another study[183]. This single-vesicle methodology has also been utilized recently to study the near-native 3D architecture of EVs secreted after infection with poliovirus. Cryo-TEM tomography has generated images of virions and viral structures contained in EVs before cell lysis[184]. Moreover, FRET microscopy has been used to track the triad protein VOR (paramount for the transfer of EV-derived components to the nucleus)[185]. This type of research has therapeutic potential for diminishing the progression of neurodegenerative diseases (in the case of the VOR complex, by inhibiting EV-mediated intercellular communication).

Cancer mechanisms have also been analyzed using single-molecule techniques. Mannavola et al. performed a ddPCR experiment using osteotropic melanoma cells and observed that EVs could induce the upregulation of genes such as CXCR7[186]. Thus, EVs may act as chemotaxis agents and, hence, participate in the progression of cancer; however, additional research in this field is still required to achieve better understanding of how EVs contribute to cancer[186].

Vesicle budding and shedding and the mechanical properties of the vesicles are poorly understood. Remarkably, a recent comparative review suggests that biomechanical analysis of single EVs provides key insights into their biological structure, biomarker functions and potential therapeutic functions[169]. Sorkin et al. used AFM to study these properties in erythrocyte and EV membranes under different conditions[187]. They established that stiffness is inversely proportional to the protein–lipid ratio and linked it to several different budding mechanisms[187]. On the one hand, budding of protein-rich soft vesicles is possibly driven by protein aggregation, and on the other, budding of stiff vesicles with low membrane-protein content is likely to be driven by cytoskeleton-induced buckling[187]. A further investigation comparing EVs originating from healthy erythrocytes and from those with hereditary spherocytosis has supported these observations. It also uncovered mechanical and vesiculation differences between these two EV populations with potential use as diagnostic parameters[188].

Vesicle endocytic pathways have been investigated primarily using microscopy-based techniques. One major EV endocytosis pathway is mediated by the formation of clathrin-coated vesicles (Fig. 2b). In this process, intracellular clathrin interacts with the membrane, producing a membrane invagination that will form an endosome through which the EVs can be internalized. The disassembly of the clathrin lattice surrounding coated endosomes is a mandatory last step in their life cycle. The recruitment of auxilin and Hsc70 (fluorescently labeled) was directly visualized using an inverted fluorescence microscope equipped with TIRF hardware and described as essential for clathrin-based internalization events[189]. The clathrin-driven uncoating is a variable process in which the endocytosing clathrin-coated vesicles remain proximal to the membrane for different periods prior to the scission of plasma membrane. The dynamics of clathrin-mediated endocytosis were assayed using fluorescently tagged proteins and TIRF microscopy[190].

Fusion states, dynamics and mechanisms of vesicle internalization during single-vesicle fusion events have been directly examined using cryo-TEM, FRET and TIRF microscopy. Characteristics and kinetics of individual fusion events can be quantified for the lipids or DNA–lipid complexes involved in the process. Different fusion pathways exist: vesicles and cell membrane merge via a direct fusion of membranes (Fig. 2a) or using protein-mediated mechanisms (Fig. 2c). These mechanisms are involved in both endocytosis and exocytosis events. Examining individual giant unilamellar vesicles by fluorescence microscopy, it has been shown that, during a direct fusion event, the hemifusion state predominates, and the fusion of two bilipid layers occurs in a single step when they are sufficiently close[191].

During the last decade, the fusion mechanism based upon SNARE-mediated internalization pathways (Fig. 2c) has been investigated employing SVA. At the molecular level, SNARE proteins mediate vesicle fusion with the target membrane and with membrane-bound compartments. Recently, Mattie et al. visualized SNARE single-fusion events using cryo-TEM[192]. The sequence of fusion intermediates from lipid monolayers to a
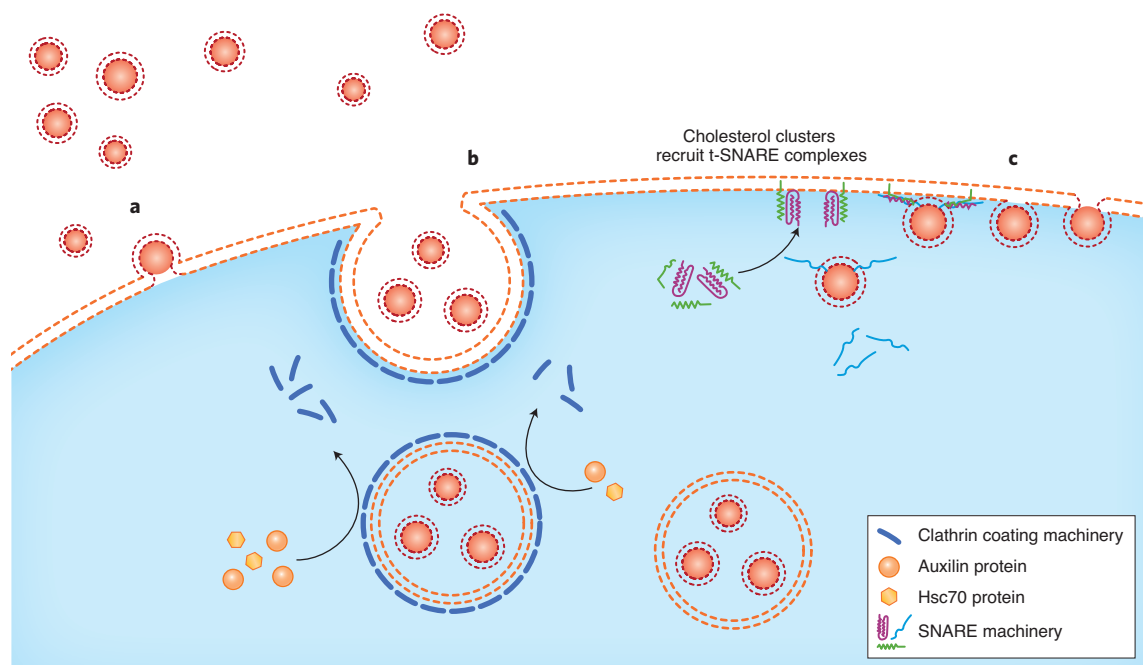
Fig. 2 | Schematic representation of endocytic and fusion pathways recently investigated using SVA techniques. A lipid bilayer from a recipient cell is shown in dotted orange, and EV lipid bilayer in dotted red; the intracellular content is shaded in blue, and vesicle content in red. **a**, direct fusion of EVs with the plasma membrane[191]. **b**, Clathrin-based internalization[189,190]. TIRF microscopy allows the examination of the clathrin uncoating process. **c**, SNARE-mediated membrane fusion[192]. FRET microscopy facilitates the analysis of the three main stages of endocytic and fusion pathways: docking, hemifusion and full fusion. Membrane composition enhances this fusion pathway through t-SNARE-machinery recruitment and enrichment[195].

complete bilayer merge has been reported in homotypic vacuoles[192]. Hu et al. correlated the membrane fusion stages with a molecular mechanism using reconstituted vesicles[193]. At a single-vesicle level, they traced the lipid-mixing process using FRET microscopy and correlated it with the docking, hemifusion and full-fusion stages[193]. They also report that an optimal distance for a SNARE-mediated fusion is 5 nm. Interestingly, some regulators of fusion pathways were identified in related studies. Calcium acts as an activator of synaptotagmin-1, leading to the fusion of synaptic vesicles with the presynaptic membrane[194]. Stratton et al. identified cholesterol as an important regulator of fusion dynamics, shifting the process from hemifusion intermediates toward full-fusion membranes[195]. Large amounts of cholesterol precluster t-SNAREs, which serve as functional docking and fusion platforms. These clusters substantially affect the stability of pores by increasing the fraction of fully open pores and accelerating fusion events. Consequently, high cholesterol content triggers fast and individual SNARE-mediated fusion events[195].

During the last decade, multimodal imaging platforms have been tested in vitro in a number of different cellular models of disease[196–198]. These platforms have considerable potential to be used in vivo, for instance, in mice[199–202]. However, these systems usually fail to perform single-EV tracking and have been successful only in ex vivo cultures[196]. Nevertheless, there is an animal model worth mentioning owing to its physiological characteristics and transparency. Zebrafish embryo has emerged recently as a prospective model for tracking EVs and assessing their dissemination and uptake in vivo[203,204]. In 2019,

Hyenne et al. reported an approach for tracking individual circulating tumor EVs in the zebrafish embryo[58] using confocal microscopy and a combination of chemical and genetically encoded probes to image EVs in vivo. The authors described, for the first time, the hemodynamic behavior of tumor EVs and their intravascular arrest. The study shows that the endothelial cells and blood macrophages rapidly take up circulating tumor EVs. These EVs activate blood patrolling macrophages and promote metastatic outgrowth[58]. A back-to-back study performed by Verweij et al. combined the genetic labeling (using a CD63-pHluorin exosomal reporter) of specific tissues with electron microscopy to track endogenous EVs in blood and further unravel their mechanisms of biogenesis, biodistribution and target cells throughout the zebrafish embryo[203]. Intriguingly, Sung et al. recently reported a CD63-pHluorin-mScarlett fusion protein that can be used to image several stages of the exosome lifecycle in vitro[205]. This reporter likely can be used to visualize exosomes in vivo and is a prospective tool for underFstanding the physiological roles of exosomes.

EV biomarkers
SVA techniques hold the capacity to discover new, specific and effective biomarkers in EVs that have been missed by ensemble methods and can be used in disease diagnostics. While the resolution and sensitivity of SVA techniques still needs improving, they provide an accurate characterization of EV subpopulations and assessment of biomarkers. Extensive research has been carried out seeking the biological biomarkers for several diseases such as PCa[47,151,172], fibromyalgia[206],
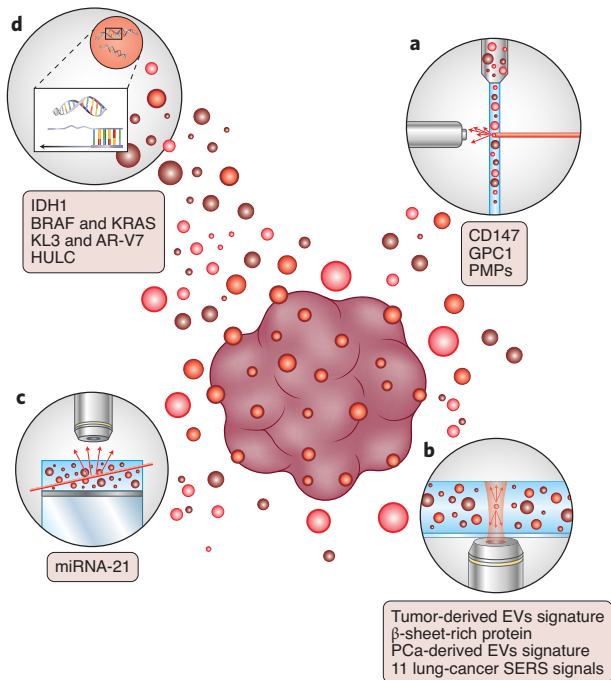
Fig. 3 | Schematic overview of reviewed biomarkers discovered using SVA techniques. a–d, The methods shown here are hrFC[208,222,223] (**a**), RTM[61,73,77,84,92] (**b**), TIRF[207] (**c**) and ddPCR (**d**) [140,142,216,221]. More information for specific biomarkers discovered using each method can be found in Table 4.

endometrial cancer[207], colorectal cancer (CRC)[208,209] and liver-associated diseases[210], among others. Figure 3 summarizes recent advances in cancer research at the single-vesicle level. Currently, fluorescent assays, which are often used in cancer screening[211], can detect miRNAs and correlate their presence with individual EVs and EV populations. Exosome-localized miRNA-21 might be used to differentiate between cancer patients and assess tumor progression and response to treatment[211]. Moreover, a specific lipid–protein signature may identify tumor-derived EVs as Raman spectra within the range of 2,800–3,100 cm^{-1} appear to be a distinguishing feature of genuine cancer EVs.[76] These findings open the way for early cancer detection. Nevertheless, the biomarkers discussed here are either generic (cannot discriminate between different cancers) or come from 2D cancer model research and might not adequately diagnose clinical cancers.

The development of next-generation sequencing SVA methods has optimized the identification of cancer biomarkers. Specifically, targeted sequencing using cancer gene panels has allowed the study of EV-derived and circulating free DNA[144], resulting in the discovery of genetic biomarkers for several diseases. For instance, nine miRNAs have been profiled in serum EVs. Using these profiles, chronic hepatitis C patients can be distinguished from healthy individuals with accuracy >95%[212]. Diagnostic opportunities presented by EV-specific genetic biomarkers have been widely reviewed[213–216]. It has been shown that cancer-derived EVs rewire and modify the premetastatic microenvironment, supporting tumor growth and metastasis during cancer progression[14,17,18,139]. This

research describes a set of potential marker targets to be used as early diagnosis of PCa. The promotion and proliferation of PCa triggered by EVs produced as a result of DIAPH3 loss or growth factor stimulation have also been reported[139]. Other studies have shown that miRNA quantification in tissues can identify PCa by detecting the expression of RNU24[217] or miR-130b[218].

Recently, several studies have reported specific and sensitive biomarkers for cancer detection[92,140,142,219–222]. ddPCR has detected and quantified the IDH1 transcript in cerebrospinal fluid-derived EVs of patients with glioma tumors in the brain[140]. In lung cancer, 11 cancer-specific SERS signals have been obtained, allowing differentiation between EV populations derived from healthy and lung cancer cells with high sensitivity[92]. Additionally, the CD147 protein found in EVs has been identified as a biomarker for CRC diagnosis[208]. Further studies have identified BRAF and KRAS somatic mutations in plasma-derived EV populations from CRC patients[221]. Intriguingly, Melo et al. have described an explicit biomarker, glypican 1 (GPC1), found in EV populations from pancreatic cells containing different KRAS oncogenic isomers[222]. Hence, GPC1-EV identification could facilitate early pancreatic cancer diagnosis[222]. In 2020, the EV-transported HULC lncRNA (long noncoding RNA highly upregulated in liver cancer) was suggested as a chemotaxis agent for cell invasion and migration. This encapsulated HULC is a potential biomarker for human pancreatic adenocarcinoma diagnosis[142].

The recent advances in cancer biomarker research are a proof-of-concept for noninvasive diagnostic tools based on EV fingerprinting in combination with multivariate statistical analysis[62]. The investigations in the field of noninvasive diagnostics for PCa have been stimulated by the discovery of intrinsic biomarkers detected in urinary-derived EVs. As a result of SVA research, several biomarkers have been associated with different stages of PCa. Biggs et al. have measured the levels of circulating prostate microparticles (PMPs) in plasma from PCa patients[223] and used these microparticles in a liquid biopsy platform to identify and characterize patients. This study found that subjects with an advanced and aggressive tumor (in Gleason scale, scoring 8 or higher) can be identified independently of their PSA value[223]. The lipid and surface protein signatures of prostate-derived EVs have been described using Raman and RTM[60,73,77,84]. Several characteristics have been highlighted indicating potential PCa biomarkers. For example, a shift in the structure of surface proteins from alpha-helix-rich in prostate EVs to beta-sheet-rich proteins in PCa-specific EVs (isolated from blood samples) has been observed[84]. Moreover, Otto et al. have detected chemical signatures in Raman and Rayleigh scattering data[73] that efficiently differentiate between the EV populations from normal prostate and PCa cells[61,76]. The authors have trained a convolutional neural network to predict precisely the cellular origin of EVs for an automated diagnosis of PCa[77]. In another study, using various SVA techniques such as nanoscale flow cytometry and ddPCR, Joncas et al. have explored castration-resistant PCa[216], identifying KLK3 and the androgen receptor variant 7 (AR-V7) as specific biomarkers for this type of cancer[216].

Future outlook

Individually analyzed EVs provide excellent prospects for future basic and practical research with a view to halt disease progression and control cell-to-cell communication processes. To exploit the full potential of SVA techniques, biological validation and reproducibility must meet the demands of clinical applications. Each technique has its specific advantages and disadvantages, and the exact choice of the method of analysis depends on the research question, the nature of the samples and EV characteristics. These techniques still need to improve their quantitative detection power, lower their cost and increase the reliability, resolution and throughput. In addition to technologies already in use for SVA detection, we highlight several promising approaches that have yet to prove their potential in SVA.

Conventional methodologies have the potential to be applied in SVA, and flow cytometry is a good example. Its implementation using innovative approaches can provide new features and capabilities, as shown by vesicle impact electrochemical cytometry (VIEC). This electrochemistry-based flow cytometry technique uses single ruptured vesicles whose content is detected and quantified based on Faraday's law exploiting the produced oxidation current[224,225]. Extensive studies of the regulation of neurotransmitter trafficking by Ewing and colleagues, focusing on catecholamine exocytosis[226–234], have demonstrated the prospective application of this approach in the EV field, highlighting electrochemical flow cytometry as a prospective asset in studies of EV functions and biology in the near future. The VIEC-based experiments have examined neurotransmitter content at a single-vesicle level in a pheochromocytoma cell line. Several studies have established that the neurotransmitter catecholamine is only partially released from the vesicles during an exocytosis event[229]. Moreover, catecholamine concentration is a key factor in regulating vesicle size since vesicular transmitter content is relatively constant and independent of vesicle size[230]. Nonetheless, many different agents may regulate exocytosis events. Using VIEC, the group later verified that the zinc and cisplatin content serve as major regulators in these processes[231,232].

Video microscopy is another common technique that is potentially useful in EV analysis. In 2010, Zupanc et al. developed an efficient algorithm to transform video sequences into quantitative data[233]. Their work was a crucial step toward the creation of automated computer analysis and led to the development of another, more popular, methodology, NTA. In 2008, the then-emerging fluorescent ratiometric image analysis (FRIA) method was used to determine the postendocytic fate and transport kinetics of internalized cargo[234]. FRIA presented a breakthrough in this field at the time, and its application led to colocalization of EV cargo with organelle markers. However, the technique has not been very successful in further EV research, possibly owing to the emergence of other microscopy approaches such as TIRF or SRM that enable the study of EV internalization and fate with a better resolution in fluorescence images and a more straightforward analysis.

The last decade has seen the development of several techniques with primary applications in analytical fields other than EV analysis. However, some—most notably radiofrequency

analysis and SP-IRIS—are applicable to single-vesicle research and could play an important role in scanning and evaluation of specific EV populations or characterizing several EV parameters in a single experiment.

Radiofrequency analysis, also known as electrically controlled tuneable broadband interferometric dielectric spectroscopy, has only been presented in several conference papers[235–238] after its first publication. In this method, specific sensors are used to perform a highly sensitive and tuneable broadband radiofrequency analysis. One study applying this method to EVs showed that the highly concentrated radiofrequency fields stimulate strong interactions between vesicles, which can be detected and quantified[239]. Specifically, the authors could detect and scan a type of EV, giant unilamellar vesicles, at multiple frequency points and determine their molecular composition. In 2017, Wu et al. reported a separation method based on acoustofluidics and created a platform employing the so-called acoustic trapping or tweezers phenomenon[240]. This technique isolates EVs from whole blood in a label-free and contact-free manner[240]. An acoustic wave falls upon a vesicle, and its scattering acts as a driving force to retain the EVs. A year later, Ku et al. demonstrated isolation and enrichment of EVs using a similar acoustic trap technology[241]. In follow-up research, the method was used to isolate RNA and sequence miRNAs from EVs. Since then, an acoustic-based microfluidic platform has been released, coupling EV trapping technology with next-generation sequencing techniques. Together, these platforms form a robust and automated strategy for biomarker discovery in small sample volumes[242].

SP-IRIS has so far found limited use in EV research, but has the potential to fill a unique experimental niche. SP-IRIS can characterize the size and phenotype (surface biomarkers) of EVs with no need to correlate two separate measurements[64,110]. This feature provides SP-IRIS with a high throughput and substantially reduces the amount of false negatives and positives compared with techniques that assess two characteristics in individual measurements. Due to the lateral resolution of microscopy (340–435 nm), highly concentrated samples cause signal overlap and a subsequent shift in the apparent vesicle size. Strikingly, despite the microscope resolution drawback, individual *Flaviviridae* particles of ~40 nm have been identified and characterized using SP-IRIS[111]. Besides the examples presented in Table 5, there is a commercialized platform for EV phenotyping developed by Nanoview Biosciences using SP-IRIS, highlighting its potential application in characterizing limited input EV samples. Several papers have proposed other highly promising automated on-chip platforms using SP-IRIS for EV characterization[64,111,243–245]. These platforms have been combined with immunoblotting to sort and characterize EV populations from a sample and can detect size and phenotype at a single-particle level, visualizing and quantifying either viruses or single EVs, or both, in an uncharacterized sample.

One of the greatest advantages of such microfluidic platforms is that they need only very small sample volume (~20 μL) for an effective analysis[244,246]. Other techniques different from SP-IRIS have been implemented in such devices to characterize EVs from EV-regulated diseases and examine their future use as diagnostic tools. EVs derived from

Table 5 | Summary of on-chip platforms utilized to characterize EVs and to detect specific biomarkers using SVA techniques

On-chip technique	Objective	Description	Ref
Dark-field microscopy and immunoelectrophoresis	Surface protein/marker profiling of EV populations	On-chip immunoelectrophoresis device that separates EV populations according to the zeta potential of their surfaces (due to overexpression of certain markers) and quantifies the populations. This is a promising approach for minimally invasive diagnosis of cancer	245
SP-IRIS and immunoplotting	Sizing and phenotyping at single exosome level	Multiplexed phenotyping and digital counting of various populations of individual exosomes (<50 nm) captured on a microarray-based solid phase chip	64
SP-IRIS and immunoplotting	Visualizing and quantifying virus particles with a single label-free imaging technique	A silicon chip with virus-specific antibodies on printed spots can visualize and identify intact Ebola viruses and Ebola virus-like particles without labeling. The device also performs an automated quantitative analysis of the captured viruses	243
SP-IRIS and immunoplotting	Sizing, phenotyping and quantifying EVs and virus populations	Multiplexed detection technology based on protein immobilization on a sensor chip. DNA-directed immobilized antibodies are used to design protein microarrays to capture EVs or viruses. Several types of analytes in a small volume can be simultaneously characterized using SP-IRIS	244
Nanoflow cytometry and fluorescence microscopy	Automated lab-on-a-chip quantitative analytical tool for SVA	A nanofluidic device that can visualize and characterize individual vesicles by quantifying vesicle content and fluorescence signals from sample volumes of 20 μL. This nanofluidic-based methodology can be used for characterization of small vesicles and their interacting molecules without ensemble averaging	246
Atomic force microscopy (AFM) and nanopatterned tethering	Morphological and deformability characterization of single EVs from different cell lines	A nanoarray chip allows tethering of individual EVs from two cell lines (Sk-Br-3 and HEK293), employing a silane-coupling agent as a linker between PEG-lipid molecules and silicon surface. These tethered EVs are further characterized using AFM	248
Raman/SERS screening	Identification and quantification of EV surface biomarkers in cancer	A microfluidic device performs a rapid (8 min) and ultrasensitive identification, comparable to ELISA, of specific biomarkers in several samples at the same time. Protein biomarkers for prostate (PSA), colorectal (CEA), and hepatocellular prostate (AFP) cancers are detected	151
Raman imaging, SEM, AFM combined with immunoplotting	Size distribution, shape and chemical fingerprint characterization of tumor-derived EVs	Multimodal analysis platform that captures specifically tumor-derived EVs on an antibody-functionalized stainless-steel chip. A lipid–protein fingerprint is obtained using Raman imaging, and the particle distribution and surface density are measured employing SEM and AFM. The correlation between SEM and Raman discriminates tumor derived EVs from contaminants. This device is tested using PCa cell lines	70,152
Multicolor fluorescence digital PCR	Highly sensitive detection (compared with qPCR) of cancer-specific gene expression	The miDER chip multiplex assay is an innovative digital PCR method capable of detecting and quantifying extremely low quantities of EV-related RNA. It can measure expression levels of two lung cancer-related genes (SLC9A3-AS1 and PCAT6) in peripheral blood samples, with a limit of detection of 10 copies per μL	250
SP-IRIS and atomic force microscopy (AFM) with immunoplotting	Investigates whether plasma- or activated platelet-EVs trigger NETs	Plasma transfusion can cause TRALI mediated by NETs. NanoBioAnalytical platform based on EV immunocapture biochip can detect EVs with a diameter in the 25–1,000 nm range (mainly ≤100 nm). The study shows that EVs from both plasma and activated platelets trigger NET formation	247
Antibody barcodes (immuno-sandwich ELISA)	Quantification and phenotyping of EV secretion	Microchip platform for multiplexed profiling of single-cell EV secretion, using antibody barcodes. This technology addresses the heterogeneity of EVs of the same origin. For example, the study shows that protein and EV secretion is performed mostly by certain cell subgroups	249

transfusion-related acute lung injury (TRALI) have been investigated using SP-IRIS coupled with AFM mechanics. Obeid et al. used this approach to determine that certain types of EVs trigger neutrophil extracellular traps (NETs) and that these NETs are likely to mediate in TRALI[247].

Fluorescence microscopy coupled with on-chip nanoflow cytometry enables automated quantitative SVA of body fluid samples[246]. According to Yokota et al., the morphology and deformability of EVs from different cell lines can be investigated using nanopatterned tethering of EVs in combination

with AFM[248]. A multiplexed profiling antibody-based barcoding method enables sorting and further quantification of EV populations[249]. Notably, promising minimally invasive approaches for cancer detection and analysis have also been developed. For example, a multicolor fluorescence digital PCR platform has been designed to detect the expression of cancer-specific genes with high sensitivity[250]. This platform detects miRNA, lncRNA or any other genetic biomarkers of cancer. Furthermore, several devices for PCa detection have been described. For instance, EV populations from PCa can be separated according to the zeta potential of the surface and examined using dark-field microscopy[251]. Due to the over-expression of certain markers, different numbers of antibodies are bound to the EV surfaces, modifying their surface potential. This implies that EVs are differentially separated according to this potential. The biochemical composition of each EV is profiled and quantified; hence, subpopulations can be described. Moreover, two RTM approaches that can effectively identify and quantify EVs and their surface biomarkers in several cancers have been reported[151,152]. Beekman et al. have presented a multimodal analysis platform combining Raman imaging, scanning electron microscopy, AFM and immunoblotting as the ultimate PCa diagnosis platform capable of measuring size distribution, shapes and chemical fingerprints of tumor-derived EVs[152].

The remarkable advances in single-vesicle imaging and analysis brought about by employing microfluidic devices promise to deliver rapid and effective practical applications. Moreover, such analytical systems need only very small, microliter-scale sample volumes. These innovative technologies and affiliated research pave the way toward unraveling the biological significance of EVs and using minimally invasive systems to diagnose diseases for which EVs serve as prognostic biomarkers.

Concluding remarks

EVs are key drivers of cell-to-cell communication. Understanding their biochemistry and physiological roles is paramount for unraveling biological processes such as disease progression, physiological responses or environmental regulation. EVs are also remarkably heterogeneous, which often complicates their accurate analysis by bulk and ensemble studies that often misrepresent their functionalities. Indeed, EVs comprise several populations that further branch into subpopulations according to their morphology or phenotype. These (sub)populations could have specific functions, or several (sub)populations might perform the same task as an amalgam. It is now becoming clear that not only the phenotype of an EV community but also its relative representation among the rest of the (sub)populations might be of importance. Studies using SVA methodologies represent the most encouraging attempts toward highlighting and pinpointing specific EV phenotypes within a biological system. While SVA methods are well suited for the high-resolution phenotypical characterization of EVs that is necessary for biomarker discovery, they might not be appropriate for carrying out further functional studies. So far, these methods have only been successful in identifying the uptake and fusion pathways, but future

advances in system models or single-vesicle technology may encourage their wider use. Ultimately, single-vesicle techniques will provide the foundation for describing an entirely new cell-to-cell communication paradigm built upon an EV-based network.

References

1. Hooke, R. *Micrographia: or Some Physiological Descriptions of Minute Bodies Made by Magnifying Glasses. With Observations and Inquiries Thereupon* (1665).
2. Die Altmann, R. *Elementarorganismen und ihre Beziehungen zu den Zellen* (von Veit, 1890).
3. van Leeuwenhoek, A. *Opera Omnia, seu Arcana Naturae ope exactissimorum Microscopiorum detecta, experimentis variis comprobata, Epistolis ad varios illustres viros*.
4. Wolf, P. The nature and significance of platelet products in human plasma. *Br. J. Haematol.* **13**, 269–288 (1967).
5. Herr, D. R. et al. Ultrastructural characteristics of DHA-induced pyroptosis. *Neuromolecular Med.* https://doi.org/10.1007/s12017-019-08586-y (2020).
6. Patras, L. & Banciu, M. Intercellular crosstalk via extracellular vesicles in tumor milieu as emerging therapies for cancer progression. *Curr. Pharm. Des.* **25**, 1980–2006 (2019).
7. Andaloussi, S. E. L., Mäger, I., Breakefield, X. O. & Wood, M. J. A. Extracellular vesicles: biology and emerging therapeutic opportunities. *Nat. Rev. Drug Discov.* **12**, 347–357 (2013).
8. Buzas, E. I., György, B., Nagy, G., Falus, A. & Gay, S. Emerging role of extracellular vesicles in inflammatory diseases. *Nat. Rev. Rheumatol.* **10**, 356–364 (2014).
9. Panagopoulou, M. S., Wark, A. W., Birch, D. J. S. & Gregory, C. D. Phenotypic analysis of extracellular vesicles: a review on the applications of fluorescence. *J. Extracell. Vesicles* **9**, 1710020 (2020).
10. Yáñez-Mó, M. et al. Biological properties of extracellular vesicles and their physiological functions. *J. Extracell. Vesicles* **4**, 27066 (2015).
11. Van Niel, G., D'Angelo, G. & Raposo, G. Shedding light on the cell biology of extracellular vesicles. *Nat. Rev. Mol. Cell Biol.* **19**, 213–228 (2018).
12. Nieuwland, R. & Sturk, A. Why do cells release vesicles? *Thromb. Res.* **125**, S49–S51 (2010).
13. Valadi, H. et al. Exosome-mediated transfer of mRNAs and microRNAs is a novel mechanism of genetic exchange between cells. *Nat. Cell Biol.* **9**, 654–659 (2007).
14. Anderson, H. C., Mulhall, D. & Garimella, R. Role of extra-cellular membrane vesicles in the pathogenesis of various diseases, including cancer, renal diseases, atherosclerosis, and arthritis. *Lab. Investig.* **90**, 1549–1557 (2010).
15. Wiklander, O. P. B., Brennan, M., Lötvall, J., Breakefield, X. O. & Andaloussi, S. E. L. Advances in therapeutic applications of extracellular vesicles. *Sci. Transl. Med.* **11**, 1–16 (2019).
16. An, T. et al. Exosomes serve as tumour markers for personalized diagnostics owing to their important role in cancer metastasis. *J. Extracell. Vesicles* **4**, 27522 (2015).
17. Becker, A. et al. Extracellular vesicles in cancer: cell-to-cell mediators of metastasis. *Cancer Cell* **30**, 836–848 (2016).
18. Zhao, H. et al. Tumor microenvironment derived exosomes pleiotropically modulate cancer cell metabolism. *eLife* **5**, e10250 (2016).
19. Chiang, C. Y. & Chen, C. Toward characterizing extracellular vesicles at a single-particle level. *J. Biomed. Sci.* **26**, 9 (2019).
20. Théry, C. et al. Minimal information for studies of extracellular vesicles 2018 (MISEV2018): a position statement of the International Society for Extracellular Vesicles and update of the MISEV2014 guidelines. *J. Extracell. Vesicles* **7**, 1535750 (2018).

21. Zhang, H. et al. Identification of distinct nanoparticles and subsets of extracellular vesicles by asymmetric-flow field-flow fractionation. *Nat. Cell Biol.* **20**, 332–343 (2018).

22. Mathieu, M., Martin-Jaular, L., Lavieu, G. & Théry, C. Specificities of secretion and uptake of exosomes and other extracellular vesicles for cell-to-cell communication. *Nat. Cell Biol.* **21**, 9–17 (2019).

23. Tai, Y. L., Chen, K. C., Hsieh, J. T. & Shen, T. L. Exosomes in cancer development and clinical applications. *Cancer Sci.* **109**, 2364–2374 (2018).

24. Willms, E., Cabañas, C., Mäger, I., Wood, M. J. A. & Vader, P. Extracellular vesicle heterogeneity: subpopulations, isolation techniques, and diverse functions in cancer progression. *Front. Immunol.* **9**, 738 (2018).

25. Kalluri, R. & LeBleu, V. S. The biology, function, and biomedical applications of exosomes. *Science* **367**, eaau6977 (2020).

26. Van Der Pol, E. et al. Optical and non-optical methods for detection and characterization of microparticles and exosomes. *J. Thromb. Haemost.* **8**, 2596–2607 (2010).

27. Soung, Y. H., Ford, S., Zhang, V. & Chung, J. Exosomes in cancer diagnostics. *Cancers (Basel)* **9**, 8 (2017).

28. Puente-Massaguer, E., Lecina, M. & Gòdia, F. Application of advanced quantification techniques in nanoparticle-based vaccine development with the Sf9 cell baculovirus expression system. *Vaccine* **38**, 1849–1859 (2020).

29. Pick, H., Alves, A. C. & Vogel, H. Single-vesicle assays using liposomes and cell-derived vesicles: from modeling complex membrane processes to synthetic biology and biomedical applications. *Chem. Rev.* **118**, 8598–8654 (2018).

30. Tkach, M., Kowal, J. & Théry, C. Why the need and how to approach the functional diversity of extracellular vesicles. *Philos. Trans. R. Soc. B Biol. Sci.* **373**, 20160479 (2018).

31. Goñi, F. M. The basic structure and dynamics of cell membranes: an update of the Singer-Nicolson model. *Biochim. Biophys. Acta* **1838**, 1467–1476 (2014).

32. Bhatia, V. K. et al. Amphipathic motifs in BAR domains are essential for membrane curvature sensing. *EMBO J.* **28**, 3303–3314 (2009).

33. Mathiasen, S. et al. Nanoscale high-content analysis using compositional heterogeneities of single proteoliposomes. *Nat. Methods* **11**, 931–934 (2015).

34. Brett, S. I. et al. Immunoaffinity based methods are superior to kits for purification of prostate derived extracellular vesicles from plasma samples. *Prostate* **77**, 1335–1343 (2017).

35. Royo, F. et al. Different EV enrichment methods suitable for clinical settings yield different subpopulations of urinary extracellular vesicles from human samples. *J. Extracell. Vesicles* **5**, 29497 (2016).

36. Ramirez, M. I. et al. Technical challenges of working with extracellular vesicles. *Nanoscale* **10**, 881–906 (2018).

37. Sódar, B. W. et al. Low-density lipoprotein mimics blood plasma-derived exosomes and microvesicles during isolation and detection. *Sci. Rep.* **6**, 24316 (2016).

38. Woo, J. R., Sharma, S. & Gimzewski, J. The role of isolation methods on a nanoscale surface structure and its effect on the size of exosomes. *J. Circ. Biomark.* **5**, 11 (2016).

39. Takahashi, K., Yan, I. K., Kim, C., Kim, J. & Patel, T. Analysis of extracellular RNA by digital PCR. *Front. Oncol.* **4**, 129 (2014).

40. Liu, Y. & Lu, Q. Extracellular vesicle microRNAs: biomarker discovery in various diseases based on RT-qPCR. *Biomark. Med.* **9**, 791–805 (2015).

41. Giannopoulou, L., Zavridou, M., Kasimir-Bauer, S. & Lianidou, E. S. Liquid biopsy in ovarian cancer: the potential of circulating miRNAs and exosomes. *Transl. Res.* **205**, 77–91 (2019).

42. Crocetti, E. *Epidemiology of prostate cancer in Europe*. Centre for Parliamentary Studies https://ec.europa.eu/jrc/en/publication/epidemiology-prostate-cancer-europe (2015).

43. Torrano, V. et al. Vesicle-MaNiA: extracellular vesicles in liquid biopsy and cancer. *Curr. Opin. Pharmacol.* **29**, 47–53 (2016).

44. Heidenreich, A. et al. EAU guidelines on prostate cancer. Part 1: screening, diagnosis, and local treatment with curative intent—update 2013. *Eur. Urol.* **65**, 124–137 (2014).

45. Humphrey, P. A. Diagnosis of adenocarcinoma in prostate needle biopsy tissue. *J. Clin. Pathol.* **60**, 35–42 (2007).

46. Shariat, S. F. & Roehrborn, C. G. Using biopsy to detect prostate cancer. *Rev. Urol.* **10**, 262–280 (2008).

47. Clos-Garcia, M. et al. Metabolic alterations in urine extracellular vesicles are associated to prostate cancer pathogenesis and progression. *J. Extracell. Vesicles* **7**, 1470442 (2018).

48. Höög, J. L. & Lötvall, J. Diversity of extracellular vesicles in human ejaculates revealed by cryo-electron microscopy. *J. Extracell. Vesicles* **4**, 28680 (2015).

49. Duijvesz, D. et al. Immuno-based detection of extracellular vesicles in urine as diagnostic marker for prostate cancer. *Int. J. Cancer* **137**, 2869–2878 (2015).

50. Raposo, G. & Stoorvogel, W. Extracellular vesicles: exosomes, microvesicles, and friends. *J. Cell Biol.* **200**, 373–383 (2013).

51. Raposo, G. & Stahl, P. D. Extracellular vesicles: a new communication paradigm? *Nat. Rev. Mol. Cell Biol.* **20**, 509–510 (2019).

52. Théry, C., Clayton, A., Amigorena, S. & Raposo, G. Isolation and characterization of exosomes from cell culture supernatants. in *Current Protocols in Cell Biology* https://doi.org/10.1002/0471143030.cb0322s30 (2006).

53. Giulietti, M. et al. Exploring small extracellular vesicles for precision medicine in prostate cancer. *Front. Oncol.* **8**, 221 (2018).

54. Russell, A. E. et al. Biological membranes in EV biogenesis, stability, uptake, and cargo transfer: an ISEV position paper arising from the ISEV membranes and EVs workshop. *J. Extracell. Vesicles* **8**, 1684862 (2019).

55. Chen, C. et al. Isolation of a novel bacterial strain capable of producing abundant extracellular membrane vesicles carrying a single major cargo protein and analysis of its transport mechanism. *Front. Microbiol.* **10**, 3001 (2020).

56. Szatanek, R. et al. The methods of choice for extracellular vesicles (EVs) characterization. *Int. J. Mol. Sci.* **18**, 1153 (2017).

57. Tatischeff, I., Larquet, E., Falcon-Perez, J. M., Turpin, P.-Y. & Kruglik, S. G. Fast characterisation of cell-derived extracellular vesicles by nanoparticles tracking analysis, cryo-electron microscopy, and raman tweezers microspectroscopy. *J. Extracell. Vesicles* **1**, 19179 (2012).

58. Hyenne, V. et al. Studying the fate of tumor extracellular vesicles at high spatiotemporal resolution using the zebrafish embryo. *Dev. Cell* **48**, 554–572.e7 (2019).

59. Tian, Q. et al. Nanoparticle counting by microscopic digital detection: selective quantitative analysis of exosomes via surface-anchored nucleic acid amplification. *Anal. Chem.* **90**, 6556–6562 (2018).

60. Carney, R. P. et al. Multispectral optical tweezers for biochemical fingerprinting of CD9-positive exosome subpopulations. *Anal. Chem.* **89**, 5357–5363 (2017).

61. Enciso-Martinez, A. et al. Synchronized Rayleigh and Raman scattering for the characterization of single optically trapped extracellular vesicles. *Nanomedicine* **24**, 102109 (2020).

62. Stremersch, S. et al. Identification of individual exosome-like vesicles by surface enhanced raman spectroscopy. *Small* **12**, 3292–3301 (2016).

63. Yuana, Y. et al. Cryo-electron microscopy of extracellular vesicles in fresh plasma. *J. Extracell. Vesicles* **2**, 21494 (2013).

64. Daaboul, G. G. et al. Digital detection of exosomes by interferometric imaging. *Sci. Rep.* **6**, 37246 (2016).

65. Ridolfi, A. et al. AFM-based high-throughput nanomechanical screening of single extracellular vesicles. *Anal. Chem.* **92**, 10274–10282 (2020).

66. Kim, S. Y., Khanal, D., Kalionis, B. & Chrzanowski, W. High-fidelity probing of the structure and heterogeneity of extracellular vesicles by resonance-enhanced atomic force microscopy infrared spectroscopy. *Nat. Protoc.* **14**, 576–593 (2019).

67. Zong, S. et al. Single molecule localization imaging of exosomes using blinking silicon quantum dots. *Nanotechnology* **29**, 065705 (2017).

68. Filipe, V., Hawe, A. & Jiskoot, W. Critical evaluation of nanoparticle tracking analysis (NTA) by NanoSight for the measurement of nanoparticles and protein aggregates. *Pharm. Res.* **27**, 796–810 (2010).

69. Bachurski, D. et al. Extracellular vesicle measurements with nanoparticle tracking analysis—an accuracy and repeatability comparison between NanoSight NS300 and ZetaView. *J. Extracell. Vesicles* **8**, 1596016 (2019).

70. Rikkert, L. G. et al. Cancer-ID: toward identification of cancer by tumor-derived extracellular vesicles in blood. *Front. Oncol.* **10**, 608 (2020).

71. Smith, Z. J. et al. Single exosome study reveals subpopulations distributed among cell lines with variability related to membrane content. *J. Extracell. Vesicles* **4**, 28533 (2015).

72. Carney, R. P. et al. Targeting tumor-associated exosomes with integrin-binding peptides. advanced biosystems. *Physiol. Behav.* **1**, 1600038 (2017).

73. Lee, W. et al. Label-free prostate cancer detection by characterization of extracellular vesicles using Raman spectroscopy. *Anal. Chem.* **90**, 11290–11296 (2018).

74. Kruglik, S. G. et al. Raman tweezers microspectroscopy of circa 100 nm extracellular vesicles. *Nanoscale* **11**, 1661–1679 (2019).

75. Dai, Y. et al. Combined morpho-chemical profiling of individual extracellular vesicles and functional nanoparticles without labels. *Anal. Chem.* **92**, 5585–5594 (2020).

76. Enciso-Martinez, A. et al. Label-free identification and chemical characterisation of single extracellular vesicles and lipoproteins by synchronous Rayleigh and Raman scattering. *J. Extracell. Vesicles* **9**, 1730134 (2020).

77. Lee, W., Lenferink, A. T. M., Otto, C. & Offerhaus, H. L. Classifying Raman spectra of extracellular vesicles based on convolutional neural networks for prostate cancer detection. *J. Raman Spectrosc.* **51**, 293–300 (2020).

78. Bryce, D. A., Kitt, J. P. & Harris, J. M. Confocal-Raman microscopy characterization of supported phospholipid bilayers deposited on the interior surfaces of chromatographic silica. *J. Am. Chem. Soc.* **140**, 4071–4078 (2018).

79. Kitt, J. P., Bryce, D. A., Minteer, S. D. & Harris, J. M. Confocal Raman microscopy for in situ measurement of phospholipid-water partitioning into model phospholipid bilayers within individual chromatographic particles. *Anal. Chem.* **90**, 7048–7055 (2018).

80. Penders, J. et al. Single particle automated Raman trapping analysis. *Nat. Commun.* **9**, 4256 (2018).

81. Bour, A. et al. Lipid unsaturation properties govern the sensitivity of membranes to photoinduced oxidative stress. *Biophys. J.* **116**, 910–920 (2019).

82. Collard, L., Sinjab, F. & Notingher, I. Raman spectroscopy study of curvature-mediated lipid packing and sorting in single lipid vesicles. *Biophys. J.* **117**, 1589–1598 (2019).

83. Bryce, D. A., Kitt, J. P., Myres, G. J. & Harris, J. M. Confocal Raman microscopy investigation of phospholipid monolayers deposited on nitrile-modified surfaces in porous silica particles. *Langmuir* **36**, 4071–4079 (2020).

84. Krafft, C. et al. A specific spectral signature of serum and plasma-derived extracellular vesicles for cancer screening. *Nanomed. Nanotechnol., Biol. Med.* **13**, 835–841 (2017).

85. Gualerzi, A. et al. Raman spectroscopy uncovers biochemical tissue-related features of extracellular vesicles from mesenchymal stromal cells. *Sci. Rep.* **7**, 9820 (2017).

86. Gualerzi, A. et al. Raman spectroscopy as a quick tool to assess purity of extracellular vesicle preparations and predict their functionality. *J. Extracell. Vesicles* **8**, 1568780 (2019).

87. Zhang, H., Silva, A. C., Zhang, W., Rutigliano, H. & Zhou, A. Raman spectroscopy characterization extracellular vesicles from bovine placenta and peripheral blood mononuclear cells. *PLoS ONE* **15**, e0235214 (2020).

88. Morasso, C. F. et al. Raman spectroscopy reveals biochemical differences in plasma derived extracellular vesicles from sporadic amyotrophic lateral sclerosis patients. *Nanomedicine* **29**, 102249 (2020).

89. Cialla, D., Pollok, S., Steinbrücker, C., Weber, K. & Popp, J. SERS-based detection of biomolecules. *Nanophotonics* **3**, 383–411 (2014).

90. Lee, C. et al. 3D plasmonic nanobowl platform for the study of exosomes in solution. *Nanoscale* **7**, 9290–9297 (2015).

91. Fazio, B. et al. SERS detection of biomolecules at physiological pH via aggregation of gold nanorods mediated by optical forces and plasmonic heating. *Sci. Rep.* **6**, 26952 (2016).

92. Park, J. et al. Exosome classification by pattern analysis of surface-enhanced Raman spectroscopy data for lung cancer diagnosis. *Anal. Chem.* **89**, 6695–6701 (2017).

93. Rojalin, T., Phong, B., Koster, H. & Carney, R. P. Nanoplasmonic approaches for sensitive detection and molecular characterization of extracellular vesicles. *Front. Chem.* **7**, 729 (2019).

94. Wang, J., Koo, K. M., Wang, Y. & Trau, M. Engineering state-of-the-art plasmonic nanomaterials for SERS-based clinical liquid biopsy applications. *Adv. Sci.* **6**, 1900730 (2019).

95. Pramanik, A. et al. Mixed-dimensional heterostructure material-based SERS for trace level identification of breast cancer-derived exosomes. *ACS Omega* **3**, 16602–16611 (2020).

96. Zabeo, D. et al. Exosomes purified from a single cell type have diverse morphology. *J. Extracell. Vesicles* **6**, 1329476 (2017).

97. Orlov, I. et al. The integrative role of cryo electron microscopy in molecular and cellular structural biology. *Biol. Cell* **109**, 81–93 (2017).

98. Dubochet, J. et al. Cryo-electron microscopy of vitrified specimens. *Q. Rev. Biophys.* **21**, 129–228 (1988).

99. Conde-Vancells, J. et al. Characterization and comprehensive proteome profiling of exosomes secreted by hepatocytes. *J. Proteome Res.* **7**, 5157–5166 (2008).

100. Zonneveld, M. I. et al. Recovery of extracellular vesicles from human breast milk is influenced by sample collection and vesicle isolation procedures. *J. Extracell. Vesicles* https://doi.org/10.3402/jev.v3.24215 (2014).

101. Cizmar, P. & Yuana, Y. Detection and characterization of extracellular vesicles by transmission and cryo-transmission electron microscopy. in *Extracellular Vesicles: Methods and Protocols* (eds. Kuo, W. P. & Shidong, J.) 221–232 (Springer, 2017).

102. Binnig, G., Quate, F. & Gerber, C. Atomic force microscope. *Phys. Rev. Lett.* **56**, 930–933 (1986).

103. Sharma, S. et al. Structural-mechanical characterization of nanoparticle exosomes in human saliva, using correlative AFM, FESEM, and force spectroscopy. *ACS Nano* **4**, 1921–1926 (2010).

104. Parisse, P. et al. Atomic force microscopy analysis of extracellular vesicles. *Eur. Biophys. J.* **46**, 813–820 (2017).

105. Creasey, R. et al. Atomic force microscopy-based antibody recognition imaging of proteins in the pathological deposits in pseudoexfoliation syndrome. *Ultramicroscopy* **111**, 1055–1061 (2011).

106. Sebaihi, N., De Boeck, B., Yuana, Y., Nieuwland, R. & Pétry, J. Dimensional characterization of extracellular vesicles using atomic force microscopy. *Meas. Sci. Technol.* **28**, 034006 (2017).

107. Skliar, M. & Chernyshev, V. S. Imaging of extracellular vesicles by atomic force microscopy. *J. Vis. Exp.* https://doi.org/10.3791/59254 (2019).

108. Kim, S. Y., Khanal, D., Tharkar, P., Kalionis, B. & Chrzanowski, W. None of us is the same as all of us: Resolving the heterogeneity of extracellular vesicles using single-vesicle, nanoscale characterization with resonance enhanced atomic force microscope infrared spectroscopy (AFM-IR). *Nanoscale Horiz.* **3**, 430–438 (2018).

109. Avci, O., Ünlü, N. L., Özkumur, A. Y. & Ünlü, M. S. Interferometric reflectance imaging sensor (IRIS)—a platform technology for multiplexed diagnostics and digital detection. *Sensors* **15**, 17649–17665 (2015).

110. Trueb, J. T., Avci, O., Sevenler, D., Connor, J. H. & Ünlü, M. S. Robust visualization and discrimination of nanoparticles by interferometric imaging. *IEEE J. Sel. Top. Quantum Electron.* https://ieeexplore.ieee.org/document/7782781 (2017).

111. Daaboul, G. G. et al. Enhanced light microscopy visualization of virus particles from Zika virus to filamentous ebolaviruses. *PLoS ONE* **12**, e0179728 (2017).

112. van der Vlist, E. J., Nolte-'t Hoen, E. N. M., Stoorvogel, W., Arkesteijn, G. J. A. & Wauben, M. H. M. Fluorescent labeling of nano-sized vesicles released by cells and subsequent quantitative and qualitative analysis by high-resolution flow cytometry. *Nat. Protoc.* **7**, 1311–1326 (2012).

113. Gomes, J. et al. Analytical considerations in nanoscale flow cytometry of extracellular vesicles to achieve data linearity. *Thromb. Haemost.* **118**, 1612–1624 (2018).

114. Fish, K. N. Total internal reflection fluorescence (TIRF) microscopy. *Curr. Protoc. Cytom.* https://doi.org/10.1002/0471142956.cy1218s50 (2009).

115. Kudalkar, E. M., Davis, T. N. & Asbury, C. L. Single-molecule total internal reflection fluorescence microscopy. *Cold Spring Harb. Protoc.* **2016**, pdb.top077800 (2016).

116. Axelrod, D. Chapter 7: total internal reflection fluorescence microscopy. *Methods Cell Biol.* **89**, 169–221 (2008).

117. Ha, T. Single-molecule fluorescence resonance energy transfer. *Methods* **25**, 78–86 (2001).

118. Arluison, V. & Wien, F. *RNA Spectroscopy: Methods and Protocols* (Springer, 2020).

119. Cerdán, L. et al. FRET-assisted laser emission in colloidal suspensions of dye-doped latex nanoparticles. *Nat. Photonics* **6**, 621–626 (2012).

120. Rectenwald, J. et al. A general TR-FRET assay platform for high-throughput screening and characterizing inhibitors of methyl-lysine reader proteins. *SLAS Discov.* **24**, 693–700 (2019).

121. Maurel, D. et al. Cell-surface protein-protein interaction analysis with time-resolved FRET and snap-tag technologies: application to GPCR oligomerization. *Nat. Methods* **5**, 561–567 (2008).

122. Dao, T. P. T. et al. Mixing block copolymers with phospholipids at the nanoscale: from hybrid polymer/lipid wormlike micelles to vesicles presenting lipid nanodomains. *Langmuir* **33**, 1705–1715 (2017).

123. Johnson, J. L. et al. Munc13-4 Is a Rab11-binding protein that regulates Rab11-positive vesicle trafficking and docking at the plasma membrane. *J. Biol. Chem.* **291**, 3423–3438 (2016).

124. Gayrard, C. & Borghi, N. FRET-based molecular tension microscopy. *Methods* **94**, 33–42 (2016).

125. Chen, C. et al. Visualization and intracellular dynamic tracking of exosomes and exosomal miRNAs using single molecule localization microscopy. *Nanoscale* **10**, 5154–5162 (2018).

126. Oleksiuk, O. et al. Single-molecule localization microscopy allows for the analysis of cancer metastasis-specific mirna distribution on the nanoscale. *Oncotarget* **6**, 44745–44757 (2015).

127. Dabrowska, S. et al. Imaging of extracellular vesicles derived from human bone marrow mesenchymal stem cells using fluorescent and magnetic labels. *Int. J. Nanomed.* **13**, 1653–1664 (2018).

128. Willig, K. I., Rizzoli, S. O., Westphal, V., Jahn, R. & Hell, S. W. STED microscopy reveals that synaptotagmin remains clustered after synaptic vesicle exocytosis. *Nature* **440**, 935–939 (2006).

129. Chen, C. et al. Imaging and intracellular tracking of cancer-derived exosomes using single-molecule localization-based super-resolution microscope. *ACS Appl. Mater. Interfaces* **8**, 25825–25833 (2016).

130. Polanco, J. C., Li, C., Durisic, N., Sullivan, R. & Götz, J. Exosomes taken up by neurons hijack the endosomal pathway to spread to interconnected neurons. *Acta Neuropathol. Commun.* **6**, 10 (2018).

131. Gustafsson, M. G. L. Surpassing the lateral resolution limit by a factor of two using structured illumination microscopy. *J. Microsc.* **198**, 82–87 (2000).

132. Hell, S. W. Toward fluorescence nanoscopy. *Nat. Biotechnol.* **21**, 1347–1355 (2003).

133. Huang, B. Super-resolution optical microscopy: multiple choices. *Curr. Opin. Chem. Biol.* **14**, 10–14 (2010).

134. Hess, S. T., Girirajan, T. P. K. & Mason, M. D. Ultra-high resolution imaging by fluorescence photoactivation localization microscopy. *Biophys. J.* **91**, 4258–4272 (2006).

135. Nienhaus, K. & Nienhaus, G. U. Where do we stand with super-resolution optical microscopy? *J. Mol. Biol.* **428**, 308–322 (2016).

136. Bachmann, M., Fiederling, F. & Bastmeyer, M. Practical limitations of superresolution imaging due to conventional sample preparation revealed by a direct comparison of CLSM, SIM and dSTORM. *J. Microsc.* **262**, 306–315 (2016).

137. Witters, D., Knez, K., Ceyssens, F., Puers, R. & Lammertyn, J. Digital microfluidics-enabled single-molecule detection by printing and sealing single magnetic beads in femtoliter droplets. *Lab Chip* **13**, 2047–2054 (2013).

138. Gao, W., Li, X., Zeng, L. & Peng, T. Rapid isothermal detection assay: a probe amplification method for the detection of nucleic acids. *Diagn. Microbiol. Infect. Dis.* **60**, 133–141 (2008).

139. Jia, S. et al. Emerging technologies in extracellular vesicle-based molecular diagnostics. *Expert Rev. Mol. Diagn.* **14**, 307–321 (2014).

140. Chen, W. W. et al. BEAMing and droplet digital PCR analysis of mutant IDH1 mRNA in glioma patient serum and cerebrospinal fluid extracellular vesicles. *Mol. Ther. Nucleic Acids* **2**, e109 (2013).

141. Worst, T. S. et al. miR-10a-5p and miR-29b-3p as extracellular vesicle-associated prostate cancer detection markers. *Cancers (Basel)* **12**, 43 (2020).

142. Takahashi, K. et al. Circulating extracellular vesicle-encapsulated HULC is a potential biomarker for human pancreatic cancer. *Cancer Sci.* **111**, 98–111 (2020).

143. Liu, C. et al. Single-exosome-counting immunoassays for cancer diagnostics. *Nano Lett.* **18**, 4226–4232 (2018).

144. Diefenbach, R. J., Lee, J. H. & Rizos, H. Monitoring melanoma using circulating free DNA. *Am. J. Clin. Dermatol.* **20**, 1–12 (2019).

145. Kong, L., Lee, C., Earhart, C. M., Cordovez, B. & Chan, J. W. A nanotweezer system for evanescent wave excited surface enhanced Raman spectroscopy (SERS) of single nanoparticles. *Opt. Express* **23**, 6793 (2015).

146. Zong, S. et al. Facile detection of tumor-derived exosomes using magnetic nanobeads and SERS nanoprobes. *Anal. Methods* **8**, 5001–5008 (2016).

147. Lee, C., Carney, R., Lam, K. & Chan, J. W. SERS analysis of selectively captured exosomes using an integrin-specific peptide ligand. *J. Raman Spectrosc.* **48**, 1771–1776 (2017).

148. Tian, Y. F., Ning, C. F., He, F., Yin, B. C. & Ye, B. C. Highly sensitive detection of exosomes by SERS using gold nanostar@Raman reporter@nanoshell structures modified with a bivalent cholesterol-labeled DNA anchor. *Analyst* **143**, 4915–4922 (2018).

149. Zhang, W. et al. Enabling sensitive phenotypic profiling of cancer-derived small extracellular vesicles using surface-enhanced raman spectroscopy nanotags. *ACS Sens.* **5**, 764–771 (2020).

150. Schie, I. W. et al. High-throughput screening raman spectroscopy platform for label-free cellomics. *Anal. Chem.* **90**, 2023–2030 (2018).

151. Xiong, Q. et al. Magnetic nanochain integrated microfluidic biochips. *Nat. Commun.* **9**, 1743 (2018).

152. Beekman, P. et al. Immuno-capture of extracellular vesicles for individual multi-modal characterization using AFM, SEM and Raman spectroscopy. *Lab Chip* **19**, 2526–2536 (2019).

153. Rüger, J., Mondol, A. S., Schie, I. W., Popp, J. & Krafft, C. High-throughput screening Raman microspectroscopy for assessment of drug-induced changes in diatom cells. *Analyst* **144**, 4488–4492 (2019).

154. Noble, J. M. et al. Direct comparison of optical and electron microscopy methods for structural characterization of extracellular vesicles. *J. Struct. Biol.* https://doi.org/10.1016/j.jsb.2020.107474 (2020).

155. Lian, H., He, S., Chen, C. & Yan, X. Flow cytometric analysis of nanoscale biological particles and organelles. *Annu. Rev. Anal. Chem.* **12**, 389–409 (2019).

156. Chukhchin, D. G., Bolotova, K., Sinelnikov, I., Churilov, D. & Novozhilov, E. Exosomes in the phloem and xylem of woody plants. *Planta* **251**, 12 (2020).

157. Plaut, J. S. et al. Quantitative atomic force microscopy provides new insight into matrix vesicle mineralization. *Arch. Biochem. Biophys.* **667**, 14–21 (2019).

158. Arraud, N. et al. Extracellular vesicles from blood plasma: determination of their morphology, size, phenotype and concentration. *J. Thromb. Haemost.* **12**, 614–627 (2014).

159. Bevers, E. M., Comfurius, P. & Zwaal, R. F. A. Changes in membrane phospholipid distribution during platelet activation. *Biochim. Biophys. Acta* **736**, 57–66 (1983).

160. Fadok, V. A. et al. Exposure of phosphatidylserine on the surface of apoptotic lymphocytes triggers specific recognition and removal by macrophages. *J. Immunol.* **148**, 2207–2216 (1992).

161. Zwaal, R. F. A. & Schroit, A. J. Pathophysiologic implications of membrane phospholipid asymmetry in blood cells. *J. Am. Soc. Hematol.* **89**, 333–340 (1997).

162. Biró, É. et al. Human cell-derived microparticles promote thrombus formation in vivo in a tissue factor-dependent manner. *J. Thromb. Haemost.* **1**, 2561–2568 (2003).

163. Morel, O., Jesel, L., Freyssinet, J. M. & Toti, F. Cellular mechanisms underlying the formation of circulating microparticles. *Arterioscler. Thromb. Vasc. Biol.* **31**, 15–26 (2011).

164. Emelyanov, A. et al. Cryo-electron microscopy of extracellular vesicles from cerebrospinal fluid. *PLoS ONE* **15**, e0227949 (2020).

165. Yekula, A. et al. Large and small extracellular vesicles released by glioma cells in vitro and in vivo. *J. Extracell. Vesicles* **9**, 1689784 (2020).

166. Thane, K. E., Davis, A. M. & Hoffman, A. M. Improved methods for fluorescent labeling and detection of single extracellular vesicles using nanoparticle tracking analysis. *Sci. Rep.* **9**, 12295 (2019).

167. Dragovic, R. A. et al. Isolation of syncytiotrophoblast microvesicles and exosomes and their characterisation by multicolour flow cytometry and fluorescence nanoparticle tracking analysis. *Methods* **87**, 64–74 (2015).

168. Koifman, N., Biran, I., Aharon, A., Brenner, B. & Talmon, Y. A direct-imaging cryo-EM study of shedding extracellular vesicles from leukemic monocytes. *J. Struct. Biol.* **198**, 177–185 (2017).

169. LeClaire, M., Gimzewski, J. & Sharma, S. A review of the biomechanical properties of single extracellular vesicles. *Nano Sel.* https://doi.org/10.1002/nano.202000129 (2020).

170. Royo, F. et al. Differences in the metabolite composition and mechanical properties of extracellular vesicles secreted by hepatic cellular models. *J. Extracell. Vesicles* **8**, 1575678 (2019).

171. Logozzi, M. et al. Microenvironmental pH and exosome levels interplay in human cancer cell lines of different histotypes. *Cancers (Basel)* **10**, 370 (2018).

172. Royo, F. et al. Transcriptomic profiling of urine extracellular vesicles reveals alterations of CDH3 in prostate cancer. *Oncotarget* **7**, 6835–6846 (2016).

173. Federici, C. et al. Exosome release and low pH belong to a framework of resistance of human melanoma cells to cisplatin. *PLoS ONE* **9**, e88193 (2014).

174. Oosthuyzen, W. et al. Quantification of human urinary exosomes by nanoparticle tracking analysis. *J. Physiol.* **591**, 5833–5842 (2013).

175. Logozzi, M. et al. Increased PSA expression on prostate cancer exosomes in in vitro condition and in cancer patients. *Cancer Lett.* **403**, 318–329 (2017).

176. Logozzi, M., Spugnini, E., Mizzoni, D., Di Raimo, R. & Fais, S. Extracellular acidity and increased exosome release as key phenotypes of malignant tumors. *Cancer Metastasis Rev.* **38**, 93–101 (2019).

177. Calorini, L., Peppicelli, S. & Bianchini, F. Extracellular acidity as favouring factor of tumor progression and metastatic dissemination. *Exp. Oncol.* **34**, 79–84 (2012).

178. Huber, V. et al. Cancer acidity: an ultimate frontier of tumor immune escape and a novel target of immunomodulation. *Semin. Cancer Biol.* **43**, 74–89 (2017).

179. Padda, R. S. et al. Nanoscale flow cytometry to distinguish subpopulations of prostate extracellular vesicles in patient plasma. *Prostate* **79**, 592–603 (2019).

180. Xian, Y., Zhou, M., Han, S., Yang, R. & Wang, Y. A FRET biosensor reveals free zinc deficiency in diabetic beta-cell vesicles. *Chin. Chem. Lett.* **31**, 468–472 (2020).

181. Nguyen, D. B. et al. Characterization of microvesicles released from human red blood cells. *Cell. Physiol. Biochem.* **38**, 1085–1099 (2016).

182. Polanco, J. C., Scicluna, B. J., Hill, A. F. & Götz, J. Extracellular vesicles isolated from the brains of rTg4510 mice seed tau protein aggregation in a threshold-dependent manner. *J. Biol. Chem.* **291**, 12445–12466 (2016).

183. Wang, Y. et al. The release and trans-synaptic transmission of Tau via exosomes. *Mol. Neurodegener.* **12**, 5 (2017).

184. Yang, J. E. et al. Complexity and ultrastructure of infectious extracellular vesicles from cells infected by non-enveloped virus. *Sci. Rep.* **10**, 7939 (2020).

185. Santos, M. F. et al. VAMP-associated protein-A and oxysterol-binding protein–related protein 3 promote the entry of late endosomes into the nucleoplasmic reticulum. *J. Biol. Chem.* **293**, 13834–13848 (2018).

186. Mannavola, F. et al. Tumor-derived exosomes promote the in vitro osteotropism of melanoma cells by activating the SDF-1/CXCR4/CXCR7 axis. *J. Transl. Med.* **17**, 230 (2019).

187. Sorkin, R. et al. Nanomechanics of extracellular vesicles reveals vesiculation pathways. *Small* **14**, e1801650 (2018).

188. Vorselen, D. et al. The fluid membrane determines mechanics of erythrocyte extracellular vesicles and is softened in hereditary spherocytosis. *Nat. Commun.* **9**, 4960 (2018).

189. Böcking, T., Upadhyayula, S., Rapoport, I., Capraro, B. R. & Kirchhausen, T. Reconstitution of clathrin coat disassembly for fluorescence microscopy and single-molecule analysis. *Methods Mol. Biol.* **1847**, 121–146 (2018).

190. Mattheyses, A. L., Atkinson, C. E. & Simon, S. M. Imaging single endocytic events reveals diversity in clathrin, dynamin, and vesicle dynamics. *Traffic* **12**, 1394–1406 (2011).

191. Van Lengerich, B., Rawle, R. J., Bendix, P. M. & Boxer, S. G. Individual vesicle fusion events mediated by lipid-anchored DNA. *Biophys. J.* **105**, 409–419 (2013).

192. Mattie, S., Kazmirchuk, T., Mui, J., Vali, H. & Brett, C. L. Visualization of SNARE-mediated organelle membrane hemifusion by electron microscopy. *Methods Mol. Biol.* **1860**, 361–377 (2019).

193. Hu, Y., Tian, Z. & Diao, J. Single-molecule fluorescence measurement of SNARE-mediated vesicle fusion. in *SNAREs: Methods and Protocols* (ed. Fratti, R.) 335–344 (2019).

194. Lin, C. C. et al. Control of membrane gaps by synaptotagmin-Ca 2+ measured with a novel membrane distance ruler. *Nat. Commun.* **5**, 5859 (2014).

195. Stratton, B. S. et al. Cholesterol increases the openness of SNARE-mediated flickering fusion pores. *Biophys. J.* **110**, 1538–1550 (2016).

196. Cao, H. et al. In vivo real-time imaging of extracellular vesicles in liver regeneration via aggregation-induced emission luminogens. *ACS Nano* **13**, 3522–3533 (2019).

197. Lai, C. P. et al. Dynamic biodistribution of extracellular vesicles in vivo using a multimodal imaging reporter. *ACS Nano* **8**, 483–494 (2014).

198. Gangadaran, P., Hong, C. M. & Ahn, B. C. Current perspectives on in vivo noninvasive tracking of extracellular vesicles with molecular imaging. *Biomed Res. Int.* **2017**, (2017).

199. Lai, C. P., Tannous, B. A. & Breakefield, X. O. Noninvasive in vivo monitoring of extracellular vesicles. in. *Methods Mol. Biol.* **1098**, 249–258 (2014).

200. Van Der Vos, K. E. et al. Directly visualized glioblastoma-derived extracellular vesicles transfer RNA to microglia/macrophages in the brain. *Neuro. Oncol.* **18**, 58–69 (2016).

201. Ricklefs, F. L. et al. Imaging flow cytometry facilitates multiparametric characterization of extracellular vesicles in malignant brain tumours. *J. Extracell. Vesicles* **8**, 1588555 (2019).

202. Lai, C. P. et al. Visualization and tracking of tumour extracellular vesicle delivery and RNA translation using multiplexed reporters. *Nat. Commun.* **6**, 7029 (2015).

203. Verweij, F. J., Hyenne, V., Van Niel, G. & Goetz, J. G. Extracellular vesicles: catching the light in zebrafish. *Trends Cell Biol.* **29**, 770–776 (2019).

204. Kobayashi-Sun, J. et al. Uptake of osteoblast-derived extracellular vesicles promotes the differentiation of osteoclasts in the zebrafish scale. *Commun. Biol.* **3**, 190 (2020).

205. Sung, B. H. et al. A live cell reporter of exosome secretion and uptake reveals pathfinding behavior of migrating cells. *Nat. Commun.* **11**, 2092 (2020).

206. Clos-Garcia, M. et al. Gut microbiome and serum metabolome analyses identify molecular biomarkers and altered glutamate metabolism in fibromyalgia. *EBioMedicine* **46**, 499–511 (2019).

207. Roman-Canal, B. et al. EV-associated miRNAs from peritoneal lavage are a source of biomarkers in endometrial cancer. *Cancers (Basel).* **11**, 839 (2019).

208. Tian, Y. et al. Protein profiling and sizing of extracellular vesicles from colorectal cancer patients via flow cytometry. *ACS Nano* **12**, 671–680 (2018).

209. Clos-Garcia, M. et al. Integrative analysis of fecal metagenomics and metabolomics in colorectal cancer. *Cancers (Basel)* **12**, 1142 (2020).

210. Royo, F. & Falcon-Perez, J. M. Liver extracellular vesicles in health and disease. *J. Extracell. Vesicles* https://doi.org/10.3402/jev.v1i0.18825 (2012).

211. He, D. et al. Total internal reflection-based single-vesicle in situ quantitative and stoichiometric analysis of tumor-derived exosomal microRNAs for diagnosis and treatment monitoring. *Theranostics* **9**, 4494–4507 (2019).

212. Murakami, Y. et al. Comprehensive miRNA expression analysis in peripheral blood can diagnose liver disease. *PLoS ONE* **7**, e48366 (2012).

213. Pang, B. et al. Extracellular vesicles: the next generation of biomarkers for liquid biopsy-based prostate cancer diagnosis. *Theranostics* **10**, 2309–2326 (2020).

214. Vlaeminck-Guillem, V. Extracellular vesicles in prostate cancer carcinogenesis, diagnosis, and management. *Front. Oncol.* **8**, 222 (2018).

215. Mateo, L., Guitart-Pla, O., Duran-Frigola, M. & Aloy, P. Exploring the OncoGenomic Landscape of cancer. *Genome Med.* **10**, 61 (2018).

216. Joncas, F. H. et al. Plasma extracellular vesicles as phenotypic biomarkers in prostate cancer patients. *Prostate* **79**, 1767–1776 (2019).

217. Carlsson, J. et al. Validation of suitable endogenous control genes for expression studies of miRNA in prostate cancer tissues. *Cancer Genet. Cytogenet.* **202**, 71–75 (2010).

218. Schaefer, A. et al. Suitable reference genes for relative quantification of miRNA expression in prostate cancer. *Exp. Mol. Med.* **42**, 749–758 (2010).

219. Haka, A. S. et al. Diagnosing breast cancer by using Raman spectroscopy. *Proc. Natl Acad. Sci. USA* **102**, 12371–12376 (2005).

220. Haka, A. S. et al. Diagnosing breast cancer using Raman spectroscopy: prospective analysis. *J. Biomed. Opt.* **14**, 054023 (2009).

221. Notarangelo, M. et al. Ultrasensitive detection of cancer biomarkers by nickel-based isolation of polydisperse extracellular vesicles from blood. *EBioMedicine* **43**, 114–126 (2019).

222. Melo, S. A. et al. Glypican1 identifies cancer exosomes and facilitates early detection of cancer. *Nature* **523**, 177–182 (2015).

223. Biggs, C. N. et al. Prostate extracellular vesicles in patient plasma as a liquid biopsy platform for prostate cancer using nanoscale flow cytometry. *Oncotarget* **7**, 8839–8849 (2016).

224. Cannon, D. M., Winograd, J. N. & Ewing, A. G. Quantitative chemical analysis of single cells. *Annu. Rev. Biophys. Biomol. Struct.* **29**, 239–263 (2000).

225. Li, X., Dunevall, J. & Ewing, A. G. Quantitative chemical measurements of vesicular transmitters with electrochemical cytometry. *Acc. Chem. Res.* **49**, 2347–2354 (2016).

226. Li, X., Dunevall, J., Ren, L. & Ewing, A. G. Mechanistic aspects of vesicle opening during analysis with vesicle impact electrochemical cytometry. *Anal. Chem.* **89**, 9416–9423 (2017).

227. Ranjbari, E. et al. Direct measurement of total vesicular catecholamine content with electrochemical microwell arrays. *Anal. Chem.* **92**, 11325–11331 (2020).

228. Dunevall, J., Majdi, S., Larsson, A. & Ewing, A. Vesicle impact electrochemical cytometry compared to amperometric exocytosis measurements. *Curr. Opin. Electrochem* **5**, 85–91 (2017).

229. Li, X., Majdi, S., Dunevall, J., Fathali, H. & Ewing, A. G. Quantitative measurements of transmitters in vesicles one at a time in single cell cytoplasm with nano-tip electrodes. *Angew. Chem. Int. Ed. Engl.* **54**, 11978–11982 (2015).

230. Li, X., Dunevall, J. & Ewing, A. G. Electrochemical quantification of transmitter concentration in single nanoscale vesicles isolated from PC12 cells. *Faraday Discuss* **210**, 353–364 (2018).

231. Ren, L. et al. Zinc regulates chemical-transmitter storage in nanometer vesicles and exocytosis dynamics as measured by amperometry. *Angew. Chem. Int. Ed. Engl.* **56**, 4970–4975 (2017).

232. Li, X., Dunevall, J. & Ewing, A. G. Using single-cell amperometry to reveal how cisplatin treatment modulates the release of catecholamine transmitters during exocytosis. *Angew. Chem.* **128**, 9187–9190 (2016).

233. Zupanc, J., Bas, E. & Erdogmus, D. Analysis of lipid vesicle populations from microscopy video sequences. *2010 Annu. Int. Conf. IEEE Eng. Med. Biol. Soc. EMBC'10* 5050–5053 https://doi.org/10.1109/IEMBS.2010.5626223 (2010)

234. Barriere, H. & Lukacs, G. L. Analysis of endocytic trafficking by single-cell fluorescence ratio imaging. *Curr. Protoc. Cell Biol.* https://doi.org/10.1002/0471143030.cb1513s40 (2008)

235. Chen, T. et al. Microwave biosensor dedicated to the dielectric spectroscopy of a single alive biological cell in its culture medium. in *Microwave Symposium Digest (IMS), 2013 IEEE MTT-S International* (2013).

236. Chen, W., Dubuc, D. & Grenier, K. Parametric study of a microwave sensor dedicated to the dielectric spectroscopy of single particles and biological cells. in *2015 European Microwave Conference (EuMC 2015)* 829–832 (2015).

237. Chen, W., Dubuc, D. & Grenier, K. Impact of sensor metal thickness on microwave spectroscopy sensitivity for individual particles and biological cells analysis. in *2016 IEEE Topical Conference on Biomedical Wireless Technologies, Networks, and Sensing Systems (BioWireleSS)* 81–83 (2016).

238. Zhang, M. *et al.* Electrically controlled tunable broadband interferometric dielectric spectroscopy: groundwork for single cell analysis. in *2019 49th European Microwave Conference (EuMC)* 650–653 (2019).

239. Cui, Y. et al. Analyzing single giant unilamellar vesicles with a slotline-based RF nanometer sensor. *IEEE Trans. Microw. Theory Tech.* **64**, 1339–1347 (2016).

240. Wu, M. et al. Isolation of exosomes from whole blood by integrating acoustics and microfluidics. *Proc. Natl Acad. Sci. USA* **114**, 10584–10589 (2017).

241. Ku, A. et al. Acoustic enrichment of extracellular vesicles from biological fluids. *Anal. Chem.* **90**, 8011–8019 (2018).

242. Ku, A. et al. A urinary extracellular vesicle microRNA biomarker discovery pipeline; from automated extracellular vesicle enrichment by acoustic trapping to microRNA sequencing. *PLoS ONE* **14**, e0217507 (2019).

243. Carter, E. P. et al. Visualizing Ebolavirus particles using single-particle interferometric reflectance imaging sensor (SP-IRIS). in *Ebolaviruses: Methods and Protocols* (eds. Groseth, A. & Hoenen, T.) 373–393 (Springer, 2017).

244. Ünlü, N. L., Kanik, F. E., Seymour, E., Connor, J. H. & Ünlü, M. S. DNA-directed antibody immobilization for robust protein microarrays: application to single particle detection DNA-directed antibody immobilization. in *Biosensors and Biodetection: Methods and Protocols* (eds. Rasooly, A. & Prickril, B.) 187–206 (Springer, 2017).

245. Akagi, T. et al. On-chip immunoelectrophoresis of extracellular vesicles released from human breast cancer cells. *PLoS ONE* **10**, e0123603 (2015).

246. Friedrich, R. et al. A nano flow cytometer for single lipid vesicle analysis. *Lab Chip* **17**, 830–841 (2017).

247. Obeid, S. et al. NanoBioAnalytical characterization of extracellular vesicles in 75-nm nanofiltered human plasma for transfusion: a tool to improve transfusion safety. *Nanomedicine* **20**, 10197 (2019).

248. Yokota, S. et al. Extracellular vesicles nanoarray technology: immobilization of individual extracellular vesicles on nano-patterned polyethylene glycol-lipid conjugate brushes. *PLoS ONE* **14**, e0224091 (2019).

249. Ji, Y. et al. Multiplexed profiling of single-cell extracellular vesicles secretion. *Proc. Natl Acad. Sci. USA* **116**, 5979–5984 (2019).

250. Bai, Y. et al. Absolute quantification and analysis of extracellular vesicle lncRNAs from the peripheral blood of patients with lung cancer based on multi-colour fluorescence chip-based digital PCR. *Biosens. Bioelectron.* **142**, 111523 (2019).

251. Akagi, T., Kato, K., Hanamura, N., Kobayashi, M. & Ichiki, T. Evaluation of desialylation effect on zeta potential of extracellular vesicles secreted from human prostate cancer cells by on-chip microcapillary electrophoresis. *Jpn. J. Appl. Phys.* **53**, 06JL01 (2014).

252. Weber, A., Wehmeyer, J. C., Schmidt, V., Lichtenberg, A. & Akhyari, P. Rapid fluorescence-based characterization of single extracellular vesicles in human blood with nanoparticle-tracking analysis. *J. Vis. Exp.* https://doi.org/10.3791/58731 (2019).

253. Marku, A. et al. The LRRK2 N-terminal domain influences vesicle trafficking: impact of the E193K variant. *Sci. Rep.* **10**, 3799 (2020).

Author contributions

All of the authors wrote, edited and discussed this review.

Competing interests

The authors declare no competing interests.

Additional information

Correspondence and requests for materials should be addressed to G.B.-F. or J.M.F.-P.

Peer review information *Nature Protocols* thanks Paolo Bergese, Cees Otto and Frederik Johannes Verweij for their contribution to the peer review of this work.

Reprints and permissions information is available at www.nature.com/reprints.

Publisher's note Springer Nature remains neutral with regard to jurisdictional claims in published maps and institutional affiliations.

Article

Simultaneous Quantification of Steroid Hormones Using hrLC-MS in Endocrine Tissues of Male Rats and Human Samples

Guillermo Bordanaba-Florit [1],* **, Sebastiaan van Liempd** [2]**, Diana Cabrera** [2]**, Félix Royo** [1,3] **and Juan Manuel Falcón-Pérez** [1,2,3,4],*

1   Exosomes Laboratory, Center for Cooperative Research in Biosciences (CIC bioGUNE), Basque Research and Technology Alliance (BRTA), 48160 Derio, Spain; froyo@cicbiogune.es
2   Metabolomics Platform, Center for Cooperative Research in Biosciences (CIC bioGUNE), Basque Research and Technology Alliance (BRTA), 48160 Derio, Spain; smvanliempd@cicbiogune.es (S.v.L.); dcabrera@cicbiogune.es (D.C.)
3   Centro de Investigación Biomédica en Red de Enfermedades Hepáticas y Digestivas (Ciberehd), 28029 Madrid, Spain
4   Ikerbasque, Basque Foundation for Science, 48011 Bilbao, Spain
*   Correspondence: gbordanaba@cicbiogune.es (G.B.-F.); jfalcon@cicbiogune.es (J.M.F.-P.)

Abstract: Steroid hormones play a vital role in the regulation of cellular processes, and dysregulation of these metabolites can provoke or aggravate pathological issues, such as autoimmune diseases and cancer. Regulation of steroid hormones involves different organs and biological compartments. Therefore, it is important to accurately determine their levels in tissues and biofluids to monitor changes after challenge or during disease. In this work, we have developed and optimized the extraction and quantification of 11 key members of the different steroid classes, including androgens, estrogens, progestogens and corticoids. The assay consists of a liquid/liquid extraction step and subsequent quantification by high-resolution liquid chromatography coupled time-of-flight mass spectrometry. The recoveries range between 74.2 to 126.9% and 54.9 to 110.7%, using a cell culture or urine as matrix, respectively. In general, the signal intensity loss due to matrix effect is no more than 30%. The method has been tested in relevant steroidogenic tissues in rat models and it has also been tested in human urine samples. Overall, this assay measures 11 analytes simultaneously in 6 min runtime and it has been applied in adrenal gland, testis, prostate, brain and serum from rats, and urine and extracellular vesicles from humans.

Keywords: liquid chromatography–mass spectrometry; time-of-flight; steroid hormones; androgens; urinary extracellular vesicles; hormone-dependent disease; metabolomics

1. Introduction

Steroid hormones are involved in a wide range of physiological processes and their production and delivery is regulated via the hypothalamus–pituitary–adrenal gland and –gonadal axes (Figure 1) [1]. Regulation is, amongst other things, subject to circadian rhythm, stress and sex. There are five classes of steroid hormones, namely glucocorticoids, mineralocorticoids, progestogens, androgens and estrogens. These different classes have distinct biological functions. The glucocorticoids are involved in the stress and immune response, while the mineralocorticoids are more related the maintenance of cell homeostasis [1,2]. In addition, the androgens and estrogens highly regulate cellular proliferation, development and differentiation. Hence, dysregulation of the steroid signal cascades often results in hormone-dependent pathologies. For instance, the carcinogenesis of breast and prostate cancer (PCa) are strongly influenced by the systemic presence of active estrogens [3] and androgens [4,5], respectively. Specifically, in PCa, the androgen receptor triggers the tumorigenic growth at a molecular level. The active steroid hormones, such as

5-α dihydrotestosterone (DHT), are the major ligands in this molecular pathway and cause the progression of PCa at early stages [4,6].
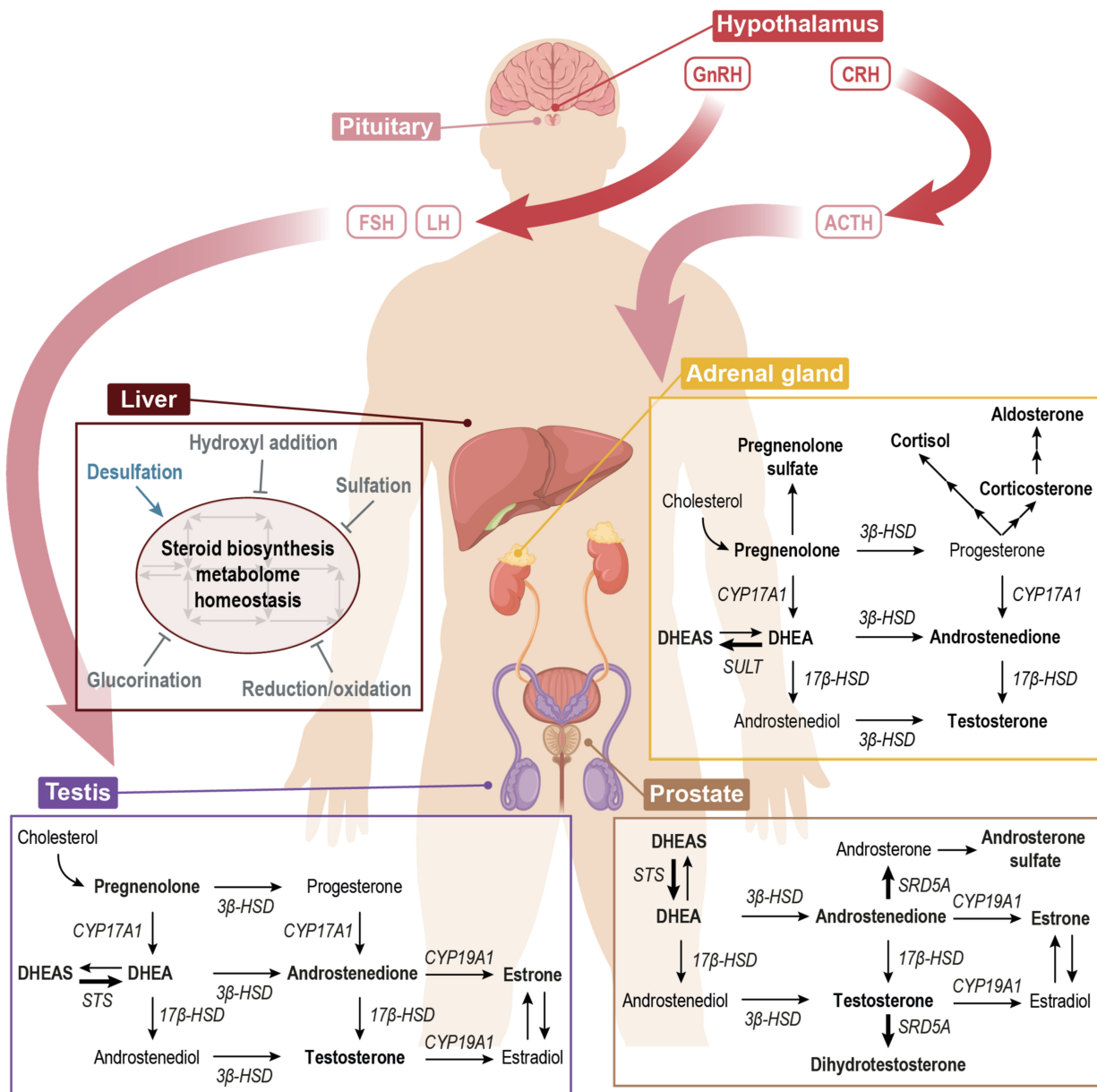
Figure 1. Schematic representation of the steroid hormone biosynthesis pathway in relevant organs and its regulation. CRH stimulates the release of ACTH from the pituitary gland. ACTH stimulates the production of cortisol (exerts negative feedback on CRH and ACTH) and DHEAS in adrenal glands. Pulses of GnRH from hypothalamic neurons stimulate pulses of LH as well as FSH. LH stimulates testosterone production in testis. Liver maintains pathway's homeostasis and several processes may happen: sulf desulfation makes metabolites available to feed the pathway while processes indicated with a flat end arrow inactivate metabolites that are in circulation. Bold arrows indicate a higher activity of the specific reaction. In bold, the metabolites that are majorly produced in each specific organ are represented. ACTH: adrenocorticotropin; CRH: corticotropin-releasing hormone; FSH: follicle stimulating hormone; GnRH: gonadotropin-releasing hormone; LH: luteinizing hormone; CYP17A1: Steroid 17-alpha-monooxygenase; CYP19A1: aromatase; SULT: hydroxysteroid sulfotransferase; STS: steroid sulfatase; 3β-HSD: 3β-Hydroxysteroid dehydrogenase; 17β-HSD: 17β-Hydroxysteroid dehydrogenase; DHEA: dehydroepiandrosterone; DHEAS: DHEA sulfate.

In mammals, the precursor of sterol biosynthesis is cholesterol, which is further utilized in the adrenal glands, gonads and sexual-derived tissues to produce steroid hormones. There are 99 metabolites involved in the steroid hormone biosynthesis pathway and over 100 reactions are catalyzed by 61 different enzymes [7,8]. All of the steroid compounds share a sterane backbone structure. The physiological role of each individual steroid hormone is primarily defined by the layout of double bonds, hydroxyl and keto groups around this basic sterane backbone structure [1]. The main structural difference between the classes is the carbon atom arrangement i.e., the androgens are C-19, the estrogens are C-18, the progestogens are C-20 and the corticoids are C-21.

In the first step of the steroid hormone biosynthesis, cholesterol is internalized into the mitochondria where it is fed as a substrate to produce pregnenolone (Figure S1, Supplementary Materials). This is the main precursor for steroid hormones produced de novo [4] inside the mitochondria. Pregnenolone can be converted to progesterone or dehydroepiandrosterone (DHEA), which can be further metabolized to glucocorticoids and mineralocorticoids (C-21) or to androgens (C-19), such as testosterone, DHT or androsterone and estrogens (C-18), respectively (Figure S1, Supplementary Materials). Interestingly, this metabolic network is tissue-dependent. Different organs are specialized on particular modules of the pathway that are physiologically relevant to perform their function. For instance, the adrenal glands are the producers of C-21 hormones, while prostate shows a high SRD5A activity, which catalyzes the conversion of testosterone to DHT (Figure 1).

Indeed, this is an intricate network of metabolites. Many of these metabolites participate as ligands in a wide span of signaling cascades and biological processes, and their levels vary strongly between different biological compartments. While cholesterol is the unique de novo precursor in steroid hormone biosynthesis, there exists an interchange between cells and tissues that anaplerotically feeds the pathway at the intermediate steps [9]. This means that the compounds upstream of the pathway can be provided by the cell environment. In this line, sulfated steroids are of interest since they are, unlike their unsulfated counterparts, readily soluble in the cytoplasm and in biofluids, such as blood or urine. Notably, the sulfates of steroids are considered endogenous and active neurosteroids [9,10]. Over the past few decades, it has been established that sulfonation is not only a process to inactivate and excrete steroid hormones; it also acts as a systemic reservoir for peripheral or local steroidogenesis in non-steroidogenic tissues, i.e., the brain or prostate [9,11]. In addition, it has been reported that the secreted vesicles, also known as extracellular vesicles (EVs), participate in many of the physiological processes [12,13] and they can contain a wide variety of cargos, such as lipids, proteins, metabolites, sugars and even DNA [12–15]. The hormone steroids and related cargos are transported by the blood and other body fluids as sulfated species, but they could also be transported by EVs to reach the target tissues.

The steroid hormone metabolism and the consequences of dysregulation have gained interest within the biomedical community to understand and diagnose hormone-dependent diseases, rather than the historic usage of steroid hormones in therapeutics. Indeed, a number of methods to detect and quantify steroid hormones have been reported during the last two decades. Many of the studies describe methodologies to detect steroids from several biological sources: cell cultures [3,16,17]; urine samples [18–20]; animal tissues [21–23]; human serum [24–26]; human hair [27] and waste water [28,29]. In general, steroid metabolomics methodologies focus on profiling a specific set of metabolites of interest in targeted tissues (or in circulation) rather than analyzing steroidogenesis status in a system of organs and related fluids. The methods are usually developed for similar non-sulfated steroids that efficiently ionize in the same mode, avoiding the exploration of the detection and quantification of many different steroids simultaneously [16,23,25,26]. Methodologically, these studies describe a variety of extraction, separation and detection methods. In particular, the solid phase extraction (SPE) and reversed phase liquid chromatographic-based methods are deployed in the isolation and separation of these compounds. The detection is mostly performed with triple quadrupole instruments. In addition, gas chromatography-coupled

MS methods was also utilized in a few of the studies. All of these methods have their advantages and disadvantages.

We describe a method for the detection of endogenous steroid hormones and their intermediates, using liquid/liquid extraction and ultra-performance liquid chromatography (UPLC), coupled with high resolution time-of-flight mass spectrometry (hrLCMS). UPLC provides fast cycling times and a high chromatographic resolution. The high mass resolution obtained with time-of-flight mass spectrometry results in high specificity, while the sensitivities are on par with triple quadrupole methods. This method was applied to metabolically profile several animal tissues and urinary EVs (uEVs). Different biological matrices, including prostate, adrenal gland, testicles, brain and liver of Wistar male rats but also human urinary samples, were tested in this assay. To our knowledge, the present work presents for the first time a reliable and optimized hrLCMS assay to analyze the key endogenous steroid hormones in endocrine tissue, bioliquids and EVs.

2. Materials and Methods

2.1. Tissue and Biofluid Samples

The tissues and serum were obtained from three wild-type (Wistar, RjHan:WI) rats obtained from Janvier Labs, Le Genest-Saint-Isle, France. All of the urine samples were obtained from a healthy male on either the morning or the afternoon. uEVs were obtained by ultracentrifuging urine samples as described elsewhere [5]. Urine samples and uEVs were characterized in several physicochemical parameters and protein markers, respectively. For a more detailed information on sample collection, preparation and characterization refer to Figure S1 (Supplementary Materials).

2.2. Chemicals and Standards

The DHEA, DHT, cortisol (in methanol solution) and the sodium salt of androsterone sulfate were obtained from Cerilliant Corporation (Round Rock, TX, USA). Supelco (Bellefonte, PA, USA) procured androstenedione. The sodium salts of DHEAS and pregnenolone were obtained from Avanti Polar Lipids, Inc. (Alabaster, AL, USA). The testosterone, aldosterone, corticosterone, estrone, pregnenolone 3-sulfate (sodium salt form), leucine-enkephalin (Leu-Enk), chloroform (>99.8% pure; of chromatography grade) and ammonia solution were purchased from Sigma-Aldrich (St. Louis, MO, USA). The LC-MS grade water, acetonitrile, formic acid and methanol were purchased from Fisher Chemical (Fair Lawn, NJ, USA).

2.3. LCMS Sample Preparation

The steroid metabolites were extracted by liquid–liquid extraction using a methanol/water mixture and chloroform as extraction liquids. The EV fractions were sonicated for 15 min in a total volume of 400 μL 50% *v/v* methanol/water mixture containing 1 mM ammonia to lysate EVs. The cell culture (DU145 cell line), fixed on culture well plates, was scrapped after 5 min incubation with 500 μL 50% *v/v* methanol/water mixture containing 1 mM ammonia. Tissue aliquots—approximately 50 mg—were lysed, using 1.4 mm zirconium oxide beads into standard 2 mL homogenizer tubes (Precellys, Montigny, France). Each sample was homogenized in 500 μL 50% *v/v* methanol/water mixture containing 1 mM ammonia by performing two cycles of 40 s at 6000 rpm in a FastPrep-24TM 5G bead beating grinder (MP Biomedicals, Solon, OH, USA). After lysis, 400 μL of the homogenate—either tissue, EV fraction or DU145 cell culture—was transferred to a clean Eppendorf® tube. Subsequently, 400 μL of LCMS grade chloroform was added on top of the 400 μL of any lysated sample and shaken for 60 min at 1400 rpm at 4 °C. Then, the samples were centrifuged for 30 min at 14,000 rpm at 4 °C in order to precipitate the proteins and to separate the organic from the aqueous phases.

The aqueous (top) and organic (bottom) phases were separated. The protein fraction was precipitated on the meniscus between these two immiscible phases. Then, 250 μL of each fraction was transferred to the clean Eppendorf® tubes and evaporated using a

centrifugal vacuum concentrator. The pellets from the organic fraction were dissolved in 100 μL pure methanol and the pellets from the aqueous fractions were dissolved in 50% v/v methanol/water. All of the resuspended pellets were centrifuged for 30 min at 13,000 rpm and 4 °C. Finally, 80 μL of the resuspended pellets were transferred to deactivated glass vials or 96-well plates for injection into the hrLCMS system.

2.4. Ultra-High Performance Liquid Chromatography (UPLC)

The chromatographic separation of the analytes was performed with an ACQUITY UPLC I-Class PLUS System (Waters Inc., Milford, MA, USA). This system was equipped with a cooled (10 °C) Process Sample Manager with a sample loop of 10 μL and a Sample Organizer, a Binary Solvent Manager and a High Temperature Column Heater. A reversed-phased 1.0 mm × 100 mm BEH C18 column (Waters Inc., Milford, MA, USA), thermostated at 40 °C, was used for separating the analytes. The samples were injected from either 2 mL deactivated glass vials or 700 μL round 96-well polypropylene plates.

The chromatographic behavior was optimized with respect to the peak intensity and an adequate separation of the 11 analytes along the run. The gradient elution was accomplished with an aqueous mobile phase (eluent A) consisting of 99.9% water with 0.1% formic acid and an organic mobile phase (eluent B) consisting of 99.9% acetonitrile with 0.1% formic acid. The flow rate was 140 μL per min. Several gradients were tested during the optimization process (Table S1, Supplementary Materials) in order to avoid break-through (elution of analyte in the injection peak) and to obtain a good peak separation. The optimal gradient was as follows: start at 30% B; a linear increase to 80% B in 3.8 min.; a step increase from 80% to 99%; constant at 99% for 1.0 min and back to 30% B in 0.2 min. The total cycle time from injection to injection was 6 min. The injection volume for all of the samples was 2 μL.

2.5. Mass Spectrometry

A time-of-flight mass spectrometer SYNAPT G2-S (Waters Inc.) was utilized for the detection of the analytes. The instrument was operated in either positive (ESI+) or negative (ESI-) electrospray ionization mode and in full-scan mode with a scan range between 50 Da and 1200 Da and scan time of 0.2 s.

The z-spray source parameters: temperatures; gas flows; capillary position and voltages were tuned, as detailed elsewhere [30]. The optimal source parameters for this assay in either ESI+ or ESI− are summarized in Table S2 (Supplementary Materials). The ion optics were fine-tuned by spraying Leu-Enk (100 ppb), at a rate of 10 μL per min, to a resolution over 20,000 (FWHM) for m/z 556.2771. The same Leu-Enk solution was sprayed as a lock mass to correct for m/z fluctuations along the assay. The lock mass solution was introduced into the source every 90 s using a second ESI probe and it was recorded for 0.5 s. Mass spectrometer spectra was corrected according to fluctuations detected in the lock mass.

2.6. Statistical Analysis
2.6.1. Analyte Recovery Study

The extraction step efficiency was assessed by performing a recovery assay with various mixtures of organic solvents and water. Five different extraction buffers were tested in this assay: 25/75% v/v and 50/50% v/v of methanol/water mixture; 25/74.9/0.1% $v/v/v$ and 50/49.9/0.1% $v/v/v$ of methanol/water/formic acid mixture and 50/50% v/v of methanol/water mixture with 1mM ammonia. To compare and calculate the recoveries of 10 different analytes, a culture of a prostate cancer cell line-DU145-was spiked with the analyte standards. Each well containing $5 \cdot \times 10^5$ cells was spiked with a mix of standards at 2 μM before lysis (pre-spiked) and at the resuspension stage (post-spiked) with a standard mix at 10 μM. Thus, the pre-spikes contained 1 nmol in 500 μL and post-spikes (aqueous and organic fractions) contained the same total amount in 100 μL, which would be the theoretical maximum absolute if there was no loss during the extraction. In ad-

dition, for each extraction solution, the non-spiked samples were prepared in order to correct for endogenous metabolites in the matrix. The samples for the pre-spiked, post-spiked and non-spiked conditions and the five different extraction buffers were prepared in biological triplicates.

Only the absolute peak areas were taken into consideration to establish the recovery efficiency in the extraction step. The average peak areas were obtained by mean smoothing the raw signals of triplicates. The recovery (R) was determined by dividing the corrected pre-spike average by the corrected post-spike average and represented as a percentage (Equation (1)). Both the pre-spiked and post-spiked raw signals ought to be corrected by subtracting the endogenous analytes signal in the DU145 culture matrix ($S_{non\text{-}spike}$). However, as the $S_{non\text{-}spike}$ of DU145 culture matrix was less than 0.05% of the signal, endogenous correction was neglected during the calculation. Importantly, the pre-spikes were corrected with respect to analyte loss (α) during the extraction procedure. Moreover, the raw signals of each sample did not have to be corrected by the amount of initial samples, because every well contained the same amount of cells.

$$R\ (\%) = \frac{\alpha\left(S_{pre\text{-}spike} - S_{non\text{-}spike}\right)}{S_{post\text{-}spike} - S_{non\text{-}spike}} \times 100 \tag{1}$$

2.6.2. Study of Matrix Effect in Analyte Quantification

In order to assess the matrix effect (ME) in the quantification of the analytes, the post-spiked raw signal was compared to an equivalent raw signal of a mixture of analytes (10 µM) in solution. The post-spiked raw signals were corrected by subtracting the endogenous analytes detected in the non-spiked DU145 culture samples. Then, the numerator was divided by the average peak areas of the standards and expressed as a percentage (Equation (2)):

$$ME\ (\%) = \frac{S_{post\text{-}spike} - S_{non\text{-}spike}}{S_{standards}} \times 100 \tag{2}$$

2.6.3. Analyte Semi-Quantification

In this work, a calibration curve was prepared in solution with 50% *v/v* methanol/water for the semi-quantification of the analytes. This calibration curve consisted of a serially diluted mixture containing all of the analytes, starting at a concentration of 10 µM. The initial concentration was diluted to half concentration twice, resulting in 5 µM and 2.5 µM concentration in the curve. Then, this set of triplets was diluted in five decades; it resulted in the following 15 different concentrations per analyte: 10; 5; 2.5; 1; 0.5; 0.25; 0.1; 0.05; 0.025; 0.01; 0.005; 0.0025; 0.001; 0.0005 and 0.00025 µM. The calibration samples were injected at the beginning and at the end of each experiment; the average of these two points was used to semi-quantify the metabolites in the tissues.

The limit of detection (LOD) for each analyte was set to be the lowest concentration at which the signal-to-noise (S/N) ratio was above three. The LOQ was defined as the lowest concentration at which the S/N ratio was above 10. The highest quantifiable concentration was the highest concentration per analyte that fits the calibration curve with an acceptable accuracy and precision (CV $\leq$ 15%) [16].

In general, the data of a calibration curve range over several orders of magnitude, the data are not linear and tend to be heteroscedastic [31]. For this reason, the relation between the peak area and the sample concentration was determined by power-fitting [30]. The power fitting resulted in a calibration curve (Equation (3)) with α and b as the fitted parameters. Once the sample concentrations were calculated using a calibration method in solution, the amount (in nanomole) per gram of tissue weight was estimated:

$$Peak\ area = \alpha[concentration]^{b} \tag{3}$$

3. Results

3.1. Liquid Chromatography and Mass Spectrometry Method

We compared six different chromatographic methodologies (Table S1, Supplementary Materials) to satisfactorily separate the analytes. The gradient 6 (30% B to 80% B in 3.8 min; detailed steps in Table S2, Supplementary Materials) showed the best peak separation along this run time compared to other tested gradients (data available in [32]). Due to the nature of the stationary phase, analytes elute in order of increasing hydrophobicity. The resulting extracted ion current (XIC) chromatograms of a standard mixture at 10 μM are depicted in Figure S2 (Supplementary Materials). In brief, aldosterone (*m/z* 361.2015; ESI+) elutes at 0.99 min, cortisol (*m/z* 363.2171; ESI+) at 1.20 min, DHEAS (*m/z* 367.1579; ESI−) at 1.60 min, corticosterone (*m/z* 347.2222; ESI+) at 1.68 min, androsterone sulfate (*m/z* 369.1736; ESI−) at 1.85 min, pregnenolone sulfate (*m/z* 395.1892; ESI−) at 2.23 min, estrone (*m/z* 271.1698; ESI+) at 2.39 min, androstenedione (*m/z* 287.2011; ESI+) and DHEA (*m/z* 289.2168; ESI+) co-elute at 2.40 min, DHT (*m/z* 291.2324; ESI+) at 2.65 min, pregnenolone (*m/z* 317.2481; ESI+) at 3.25 min.

Regarding the mass spectrometry method, the Leu-Enk signal (*m/z* 556.2771) was aimed at a resolution of over 20,000 (FWHM) and provided the necessary mass accuracy to evaluate assay analytes. Isotope pattern matching and the use of chemical standards confirming elution times further ensured the specificity. In general, the mass accuracies for the analytes in solution were between −1 to 1 mDa. It is noteworthy that several analytes were not adequately separated during the chromatographic elution. The corticosterone and DHEAS elute at similar retention times—1.60 min and 1.68 min-, however, the MS could properly distinguish them by their *m/z* difference and their fragmentation pattern. Moreover, the DHEAS was not detected with a high intensity signal in ESI+ mode. For this reason, the corticosterone was measured in ESI+ and the DHEAS in ESI− mode. Likewise, estrone, DHEA and androstenedione eluted in approximately 2.40 min. In this case, one could only rely on the MS sensitivity (estrone *m/z* 271.1698, DHEA *m/z* 289.2168, androstenedione *m/z* 287.2011) and on a fragmentation pattern that was sensitive enough to distinguish and quantify them separately.

3.2. Analyte Recovery Optimization

Afterwards, we evaluated the recovery of 11 analytes using a biphasic liquid–liquid method and analyzed them with the optimized hrLCMS method. The extraction was performed, using the DU145 cell line as a matrix. Five different mixtures of organic solvents and water, containing either formic acid or ammonia to modify the pH of the extraction buffer or no pH modifier, were assessed (Table S3, Supplementary Materials). The addition of formic acid strived for lowering the pH approximately to three, while 1mM ammonia modified the extraction buffer to pH 8–9 in order to chemically neutralize the functional groups of the steroid compounds. From the previous experiments in our metabolomics platform, we observed that in liquid–liquid extraction requires at least 25% organic solvent during the extraction step to precipitate the proteins. This is important to avoid clogging the chromatographic system [30]. Moreover, the effectivity of tissue homogenization using beads has been reported as high and does not differ much from the homogenization of other matrices, such as urine or cell cultures [30,33]. Therefore, the calculated recoveries are ultimately dependent on the extraction buffer utilized, regardless of the homogenization methodology.

During the optimization process, it was determined that the steroid sulfate compounds were recovered completely in the aqueous fraction, whilst steroids without sulfate group were found in the organic fraction. Notably, only cortisol was detected systematically in both of the fractions (Figure S3, Supplementary Materials); however, it was majorly recovered in the organic (80% or higher) rather than in the aqueous (approximately 20%) fraction. Moreover, the addition of formic acid to the extraction buffer led to a dramatic decrease in the recoveries of the sulfate compounds and a slight decrease in the rest of the steroid analytes (Figure S3, Supplementary Materials). One can infer that the

presence of protons in the buffer do not stabilize steroid charges and severely hampers the extraction of sulfate steroids in a polar environment. The supplementation of 1mM ammonia outperformed the extraction in terms of recovery and robustness, compared to the other extraction liquids. Notably, the recovery values using different percentages of methanol in the extraction buffer do not differ much. However, the extraction efficiency of the sulfate compounds using 25% *v/v* methanol underperforms 50% *v/v* methanol, with a recovery loss of 40 to 50%.

In Table 1, the recoveries of the 11 selected analytes, using a mixture of 50/50% *v/v* methanol/water with 1mM ammonia as the extraction buffer, are reported. In general, the present methodology is able to recover and detect over 90% of the initially spiked analyte. Only DHT was detected in a lower percentage; approximately 80% of the initially spiked DHT was recovered. As expected in a biphasic extraction, the hormone steroids were retrieved in an apolar environment and the sulfated steroids in a polar solvent. Besides cortisol, pregnenolone sulfate was also reported in both of the fractions; it was mainly recovered in the more polar solvent and a derisory amount in the organic fraction. Using this methodology, the recoveries for 10 µM of analyte ranged from 74.2% to 126.9%. These values are acceptable for routine muti-analyte hrLCMS analysis since all of the results are reproducible [34]. Thus, extraction using 50/50% *v/v* of methanol/water mixture with 1 mM ammonia was selected for further experiments in different biological matrices.

Table 1. Summary of the optimized method characteristics. The recoveries (±standard deviation) and matrix effect as signal loss (±standard deviation) of the extraction procedure in two different biological matrices (*n* = 6; biological matrix: DU145 cell) are reported. In addition, LOD and LOQ values of the analytes in the adequate fraction are compiled. LOD: Limit of detection; LOQ: Limit of quantification.

Analyte	Fraction	Recovery (%)	Matrix Effect (%)	LOD (nM)	LOQ (nM)
Pregnenolone	Organic	97.2 (±1.9)	25.2 (±3.1)	2.5 nM	10 nM
	Aqueous	-	24.0 (±2.8)		
DHEA	Organic	122.7 (±2.9)	37.7 (±5.7)	5.0 nM	50 nM
	Aqueous	-	28.0 (±6.2)	-	-
Androstenedione	Organic	102.2 (±3.2)	30.8 (±4.6)	0.25 nM	0.5 nM
	Aqueous	-	23.2 (±4.5)		
Estrone	Organic	103.7 (±3.8)	25.5 (±4.8)	5.0 nM	10 nM
	Aqueous	-	25.7 (±4.0)		
DHT	Organic	74.2 (±3.4)	23.1 (±3.9)	0.25 nM	1.0 nM
	Aqueous	-	23.4 (±2.9)		
Cortisol	Organic	114.3 (±3.8)	25.9 (±4.2)	0.5 nM	1.0 nM
	Aqueous	22.28 (±4.5)	17.6 (±4.7)		
Aldosterone	Organic	99.8 (±1.77)	18.7 (±4.3)	0.5 nM	2.5 nM
	Aqueous	-	17.7 (±5.1)		
Corticosterone	Organic	109.4 (±3.1)	25.1 (±3.6)	0.25 nM	1.0 nM
	Aqueous	-	20.2 (±3.2)		
Testosterone	Organic	126.9 (±1.7)	14.3 (±1.9)	0.25 nM	0.25 nM
	Aqueous	-	8.0 (±2.1)		
Pregnenolone sulfate	Organic	6.9 (±2.7)	25.2 (±3.1)	0.25 nM	1.0 nM
	Aqueous	94.8 (±1.9)	24.0 (±2.8)		
DHEAS	Organic	-	42.6 (±1.1)	0.25 nM	0.5 nM
	Aqueous	108.0 (±1.4)	42.5 (±0.1)		

Furthermore, the performance of the optimized methodology was tested, using urine as the matrix since it has a high interest for clinical applications. Six samples of urine from a male individual were pooled and aliquoted in different two volumes to assess the matrix

effect on the recovery efficiency. In Table 2, the recoveries of the 10 analytes are reported; DHEA recovery has not been retrieved, because its peak was masked by testosterone's signal. In general, over 85% of the initially spiked analyte is recovered and detected in 50 μL urine matrix. Importantly, the sulfated steroids are not recovered with the same efficiency; DHEAS and pregnenolone sulfate report a recovery efficiency of 75.7% and 54.9%, respectively. The recoveries of the analytes using 250 μL urine as matrix describes a slight decrease in the non-sulfated steroids while the efficiency decay is dramatic in the sulfated species.

Table 2. Summary of the recoveries using the optimized methodology in urine matrix. The recoveries (±standard deviation) of two different volumes (50 μL and 250 μL) of pre-pooled urine are reported (*n* = 3).

Analyte	Urine Volume	Recovery (%)
Pregnenolone	50 μL	92.4 (±3.6)
	250 μL	99.3 (±4.8)
Androstenedione	50 μL	93.0 (±3.9)
	250 μL	79.3 (±3.8)
Estrone	50 μL	94.2 (±3.3)
	250 μL	84.8 (±4.8)
DHT	50 μL	76.3 (±4.1)
	250 μL	71.2 (±3.76)
Cortisol	50 μL	87.0 (±3.0)
	250 μL	72.4 (±3.6)
Aldosterone	50 μL	110.7 (±2.9)
	250 μL	103.1 (±3.2)
Corticosterone	50 μL	96.2 (±2.8)
	250 μL	84.3 (±3.6)
Testosterone	50 μL	104.1 (±2.1)
	250 μL	96.3 (±5.1)
Pregnenolone sulfate	50 μL	54.9 (±1.5)
	250 μL	25.5 (±1.2)
DHEAS	50 μL	75.7 (±2.5)
	250 μL	44.0 (±4.2)

3.3. Matrix Effect

It is well known that the phospholipids and other lipids, typically enriched in biological matrices, such as tissues, body fluids or cell cultures, can cause ion suppression in mass spectrometry, thereby hampering the analyte signal [35,36]. This phenomenon negatively influences the detection of the analytes and may underestimate their quantification. For a specific matrix, the higher the ion suppression effect is, the higher the signal loss. Therefore, the conclusions drawn by detecting and quantifying the analytes under these conditions could be misleading.

The matrix effect of each analyte was defined as the signal loss measured at the resuspension step (sample spiked with 10 μM analyte mix) compared to 10 μM of each analyte in solution. The signal loss was calculated in five different extraction procedures, because they can influence ion suppression. The matrix effect reported in this work was estimated for a prostate cancer cell line (DU145) culture and urine samples. To note, signal loss is specific for each matrix and each independent experiment. In further experiments, in which quantification is required, the matrix effect should be calculated in every particular assay. From our optimization experiments, one can infer that the matrix effect is fraction-dependent, because there is a significant difference between signal loss comparing organic and aqueous fractions (Figure S4, Supplementary Materials). This phenomenon is likely observed due

to a differential extraction of the phosphatidylcholine (or other lipid) compounds [30,35]. Strikingly, this fraction dependency was not observed upon the addition of ammonia to the extraction liquid. Moreover, the presence of ammonia resulted in a signal loss of up to half-fold compared to extraction liquids with acidic modifier or no pH modifier addition. This suggests that the ammonia impairs the extraction of the lipidic compounds from the biological matrix, hence, decreasing the ion suppression phenomenon in mass spectrometry.

In Table 1, the matrix effect (expressed as signal loss (%)) of a DU145 culture of 11 selected analytes, using a 50/50% *v/v* of methanol/water mixture with 1mM ammonia for extraction, is reported. In general, the present methodology loses approximately 15 to 40% of the signal of non-sulfated analytes but it mainly lays between 20 to 30% loss. On the other hand, the sulfated steroids display a 40 to 50% loss of signal, regardless of the extraction fraction. The signal loss of the 10 μM analytes spiked in DU145 cell line were: 25.2% for pregnenolone, 37.7% for DHEA, 30.8% for androstenedione, 25.5% for estrone, 23.1% for DHT, 25.9% and 20.2 % for cortisol in the organic and aqueous fraction, respectively, 18.6% for aldosterone, 25.0% for corticosterone, 46.1% for pregnenolone sulfate and 42.5% for DHEAS. All of the analytes are majorly recovered back in a particular fraction of the extraction procedure, which is the one selected to report the matrix effect. Signal loss of sulfate compounds refer to aqueous fraction measurement and the other steroids refer to signal loss in organic fraction.

3.4. Semi-Quantitation of Steroids in Animal Tissues

The hrLCMS method was most sensitive in detecting androstenedione, DHT, corticosterone, pregnenolone sulfate and DHEAS with a LOD (S/N > 3) of 250 pM in a 50/50% *v/v* methanol/water solution. The detection limit for cortisol and aldosterone was 0.5 nM, and a LOD of 2.5 nM was determined for pregnenolone. The least responsive ions were those for DHEA and estrone with a LOD of 5.0 nM. With regards to the quantification limits, androstenedione and DHEAS were the most sensitive compounds, with a LOQ (S/N > 10) of 0.5 nM in solution. The cortisol, corticosterone, pregnenolone sulfate and DHT were in the second group of the most quantifiable ions showing a LOQ of 1.0 nM. The quantitation limit for aldosterone was 2.5 nM, while a LOQ of 0.01 μM was estimated for pregnenolone and estrone. The DHEA was the compound with the highest quantitation threshold (0.05 μM).

We found that the concentration range of the steroid hormones is typically low in tissues, ranging from pico- to nanomole per gram of tissue, and cannot be detected in some tissues (Table 3). Only pregnenolone, androstenedione, DHT, corticosterone, cortisol and testosterone were detected in the tissues or serum of Wistar rats. Pregnenolone and cortisol are only quantified in the adrenal gland tissue, however, pregnenolone is also detected in the brain and testicles. Adrenal gland and testicles reported picomole amounts of androstenedione per gram of tissue. Moreover, DHT was quantified in the prostate, adrenal gland and testicles. In prostate, the amount of DHT was two-fold the quantitation in the other tissues. The testosterone and corticosterone were quantified in all of the measured rat samples. In general, they were reported in the picomole per gram range in tissues. In serum, they were quantified in the nM range. Interestingly, the adrenal gland described nanomole per gram concentrations of corticosterone. Furthermore, testosterone was found in a one order of magnitude higher amount in the adrenal gland and testicles compared to prostate and brain.

Table 3. Quantitation of three independent Wistar rat tissues: adrenal gland, prostate and brain. Adrenal glands of the same animal were titered independently, also, the prostate lobes of each rat. The averages in nmol per gram of tissue, standard deviations and coefficients of variation (%) of the three groups of samples are reported.

Analyte	Quantification (nmol/g Tissue)	Adrenal Gland	Prostate	Brain	Testicle	Serum (nM)
Pregnenolone	Amount	7.04	-	Detected	Detected	-
	St. dev.	3.74				
	%cv	53				
Androstenedione	Amount	5.97×10^{-3}	-	Detected	1.45×10^{-3}	Detected
	St. dev.	3.35×10^{-3}			1.38×10^{-3}	
	%cv	56			95	
DHT	Amount	3.47×10^{-3}	7.57×10^{-3}	Detected	2.70×10^{-3}	Detected
	St. dev.	1.02×10^{-3}	2.40×10^{-3}		7.92×10^{-4}	
	%cv	29	31		29	
Corticosterone	Amount	18.89	4.01×10^{-3}	2.42×10^{-2}	1.25×10^{-3}	28.01
	St. dev.	10.05	5.15×10^{-3}	7.04×10^{-3}	7.98×10^{-4}	3.31
	%cv	53	128	29	63	12
Cortisol	Amount	0.45	-	-	-	-
	St. dev.	0.19				
	%cv	43				
Testosterone	Amount	4.53×10^{-3}	6.92×10^{-4}	7.02×10^{-4}	9.18×10^{-3}	0.20
	St. dev.	1.47×10^{-3}	2.36×10^{-4}	4.29×10^{-4}	4.53×10^{-3}	0.02
	%cv	32	34	60	49	

The standard deviations and coefficients of the variation are rather large, indicating an important variability among the samples obtained from the same strain but independent animals. One could expect this biological variation and it suggests that treatments, stress or any procedure applied to animals can potentially influence the outcome in further experiments.

3.5. Quantitation of Steroid Hormones in Human Urinary Samples

Six different urine samples were characterized in several physicochemical parameters (Table S4, Supplementary Materials) to examine whether the sample collection resulted in homogenous sample groups, regardless of the metabolomics' analysis. No blood, ketone bodies or glucose were detected in the urine sample, and the pH value and density of the urine were similar in all of the samples. The urine samples were centrifuged in two serial steps at $10,000 \times g$ for 30 min to isolate the so-called P10K fraction—typically containing vesicles of 150 to 200 nm diameter and above—followed by a $100,000 \times g$ centrifugation for 90 min to isolate the so-called P100K—typically containing vesicles of 100 to 150 nm diameter and below (up to 50 nm) [37]. The supernatant of the second centrifugation was also analyzed and referred to as SN100K.

In this set of urine samples, the current methodology is able to detect and quantify androstenedione, cortisol and DHEAS (Table 4). The other steroids of the panel were below the LOQ and, in general, also below the LOD. The androstenedione and cortisol were detected only in the urine and SN100K. It was not possible to detect them associated with the EVs, and they are majorly solubilized in the urine. The androstenedione was found in lower concentrations compared to cortisol and the variability between the collection days was high (40 to 60%) regardless of the collection time. Concerning cortisol, the variability was extremely high between the morning collection days (approximately 50 to 85%) whilst the concentration of the afternoon collected samples was stable (approximately 2% variation). DHEAS was the compound detected in the highest concentration (μM range) soluble in urine, compared to androstenedione and cortisol (nM range). Similar to androstenedione, the DHEAS showed a high variability over independent collection

days at both the morning and afternoon collection times. To note, DHEAS was the only metabolite detectable in the EV fraction. In Table 4, the absolute amount (μmol) in 50 mL of urine is reported but also the relative amount (in ppm) of the total detected metabolite that is associated with the EVs. Importantly, DHEAS was not quantifiable (S/N < 10) in all of the samples collected at morning time, but it was detectable in all of the cases (S/N > 3). According to our analysis, a range of 0.5 to 3.0 ppm of DHEAS was associated with the EVs in the urine samples (Table 4; detailed calculations available in [32]).

Table 4. Quantitation of urine human samples (*n* = 6, U001 to U006, Table S4, Supplementary Materials). The isolated EV fraction are also included in the table. In the table, the three analytes detected in the urine-derived samples.

Sample	Collection Time	Androstenedione (nM)	Cortisol (nM)	Conc. (μM)	DHEAS EV-Associated DHEAS (μM)	EV-Associated DHEAS in Urine (ppm)
Urine	Morning	2.25 (±0.92)	40.1 (±33.5)	0.36 (±0.16)	-	-
Urine	Afternoon	1.95 (±0.78)	35.7 (±0.7)	1.27 (±0.87)	-	-
SN100K	Morning	2.31 (±1.53)	29.9 (±14.7)	1.33 (±0.94)	-	-
SN100K	Afternoon	1.82 (±0.64)	31.4 (±0.7)	0.87 (±0.92)	-	-
P10K	Morning	-	-	-	1.75	0.90
P10K	Afternoon	-	-	-	0.76 (±0.08)	0.79 (±0.41)
P100K	Morning	-	-	-	6.17	3.19
P100K	Afternoon	-	-	-	0.74 (±0.01)	

Concentration (±standard deviation) of the analytes in urine and supernatant fraction of both morning and afternoon collected urine is shown. Absolute amount and relative amount (±standard deviation) of DHEAS is calculated in 50 mL of initial sample of both morning and afternoon collected urine.

The isolation of the EVs in the pellet fractions was confirmed with the presence of typical EV markers by Western blotting (Figure S5, Supplementary Materials). Typical urine exosome markers, such as CD9, CD63 and AQP2, were intensified in P100K fractions, confirming that this fraction is enriched in EVs. However, they are sample-dependent and were detected in various amounts. In addition, LAMP2A and CD10 were detected only in the P100K fraction of U003-derived EVs preparation. Annexin V and AQP2 were found in both P100K and P10K, but also in different amounts among urine samples.

4. Discussion

This work describes a fast and simple hrLCMS methodology, able to detect and quantify 11 key metabolites of the steroid hormones biosynthesis in several biological matrices. Their importance in diseases, such as PCa and other steroid-dependent diseases, spotlights this assay as a powerful tool to study the role of steroid hormones in the development and progression of hormone-dependent diseases and to assess the metabolic status of patients via liquid biopsy analysis. In brief, this method identifies and quantifies 11 steroids, including corticoids, androgens and metabolic intermediates, in a high-throughput method of 6 min. Although testosterone and androsterone sulfate were not included in the recovery experiment, the methodology is able to separate, identify and quantify them.

All of the steroid hormones are primarily derived from cholesterol, which provides the sterane ring structure shared by all of these compounds (Figure S1, Supplementary Materials). Subtle chemical differences, unique to each steroid hormone, significantly complicate the separation of such structurally similar molecules. Furthermore, the structure of the steroids and position of the functional groups determine their preferred ionization mode and efficiency [18,24]. For instance, testosterone and DHEA—with the same molecular formula—display different ionization efficiencies. DHT or androstenedione are readily ionized in positive mode, in contrast to DHEA or pregnenolone, which are not strongly ionized due to the presence of keto groups in the ionizable region (Figure S1, Supplementary Materials). In order to increase the signal intensity, the MS could be oper-

ated in enhanced duty-cycle (EDC) mode; this is a more appropriate approach in targeted analyses, where the analyte empirical formulas are known. In this strategy, the MS signals of a given retention time are measured in separate scan functions to enhance the *m/z* of the selected analyte. Measuring in EDC instead of full-scan mode may increase by several fold the S/N ratio of a given metabolite [30,38,39]. Therefore, the EDC mode is an option to consider for those samples in which the analytes S/N ratio falls above the LOD, but are not always quantifiable.

An LCMS method is usually evaluated in terms of efficiency, accuracy and sensitivity of the measurement. The process efficiency is a combination of recovery efficiency and matrix effect of each metabolite [40], and the sensitivity is evaluated with the LOD and LOQ of each metabolite. Different studies identifying and quantifying steroid compounds in biological matrices report a wide range of efficiency recoveries. For example, in PCa cell cultures, a recovery range of 54.7% to 78.1% was reported [16] while in breast cancer cell cultures, recoveries ranging 95.7 to 102.0% were reported [16]. Our data, with recoveries ranging from approximately 75% to 125%, suggest that a cell culture as matrix does not impair the extraction of the steroid metabolites. The urine matrix does not impair the extraction of the non-sulfated steroids but the sulfated species suffer a recovery efficiency decay. To note, the studies measuring steroids in urine and tissues, as biological matrices report recovery efficiencies of over 100% in some of the cases [17–19]. An explanation for this phenomenon might be that the metabolites can be either free in solution or tethered to other molecules, such as membranal lipids during the extraction process. For this reason, the organic and aqueous phase recoveries are not adding up to 100% in this assay. In case of detecting a metabolite in two fractions, the addition of both of the signals is perhaps a better approach to quantify that specific metabolite. However, our assay is very convenient, since all of the metabolites (except cortisol) are recovered in only one fraction. This permits a faster measurement of the steroid hormones in different biological matrices.

The existing quantitation methods for steroid hormone compounds have a wide span of LOQ, ranging from 0.002 to 10 ng per mL. However, it is highly dependent on the analyzed matrix, i.e., a urine matrix shows a range from 0.002 to 0.2 ng per mL [18,19], whilst the cell matrices display a higher LOQ up to 10 ng per mL [16]. This suggests that the matrix effect also depends on the specific matrix where the metabolites are contained. Comparing these studies, the cell matrices report a lower sensitivity compared to urine; this is important when applying this method in future experiments or assays. In fact, this observation spotlights the major limitation of this study: the quantitation has been performed semi-quantitively. Ion suppression in mass spectrometry negatively affects the analyte signal, and subsequently underestimates its quantitation, or it simply hampers its detection. Moreover, ion suppression may be limiting the detection of certain steroid compounds in several matrices, i.e., EV preparations. In consequence, this method should be utilized in matrices that facilitate the detection of the steroids. A matrix-spiked calibration is usually the appropriate method to quantify the absolute amounts of analytes in samples [30]. In this work, a calibration curve of the analyte standards was prepared in solution with 50% *v/v* methanol/water as a solvent. Such an approach cannot compute the absolute amounts of the analytes in tissue, since the matrix effect is not considered, however, a semi-quantitative approximation of the metabolites in tissues can be calculated. In this assay, the reported LOQ range lies between 0.50 and 50 nM (equivalent to 0.14 and 14.42 ng per mL) in solution, similar to previous studies. However, it is advised to use matrix-spiked curves in further experiments using this assay.

The time required to perform the chromatographic separation is typically long in the literature; they report runtimes from over 10 min up to 45 min [3,5,18–22,27]. Only the work of Quanson et al. [16] and Indapurkar et al. [17] described a methodology with a short runtime (4 to 5 min); however, they tested and applied the method solely in cell matrices: PCa and induced pluripotent stem cell lines, respectively. Indapurkar et al. [17] developed a methodology specific for estradiol-related metabolites and Quanson et al. [16] measured androgenic steroids using an ultra-performance convergence chromatography.

In 2012, Maeda et al. accomplished the separation, detection and quantification of a panel of steroids in rat organs except in the liver, but using an HPLC system. For this reason, their sample preparation strategy demanded high volumes of extraction buffer—15 mL of acetonitrile per sample—and required a total run time of 11 min. In this work, the volumes are lower than 1 mL and the run time for different types of samples is lower than 10 min.

In order to test the performance of our methodology, we have measured steroid hormone analytes from several rat tissues: adrenal glands; testis; prostate; liver and brain. The data shown in Table 3 are in accordance with the fact that the pathway is tissue-dependent in regular physiological conditions. Two metabolites upstream of the pathway, pregnenolone and androstenedione, were quantified in the adrenal glands, but could not be quantified in prostate or brain. This hints that the adrenal glands are in charge of the conversion of cholesterol into the steroid compounds in complex organisms, such as rats; this is in line with previous findings in the literature [41–43]. Likewise, the adrenal glands are known to produce corticoid hormones. Our data confirms this, since corticosterone is quantified in a higher amount—three to four orders of magnitude—when compared to the prostate, brain and testicles. The adrenal glands also seem to accumulate androgens (Table 3); however, the presence of active androgens (DHT) is two-fold higher in the prostate compared to other tissues. Importantly, the ratio DHT/testosterone, which are the active and non-active paired androgens, was approximately 11 in prostate, while the adrenal gland and testis were below 1. Because the presence of the active androgen plays a physiological role in prostate, the ratio of DHT/testosterone was also higher in this tissue.

Since the first urinary metabolomics attempts to analyze urinary samples and other biofluids, several methodologies have been developed during the last few years [18–20]. Nevertheless, none of the reported methodologies was optimal to assess the steroids in the EV sample preparations, tissues or body fluids in a fast and simple manner. Up to date, many of the studies have shown metabolomics in EVs [5,20,44], but none of them has reported the detection of steroid hormones in a targeted approach. A plausible explanation is that the identification and detection of compounds similar in molecular mass—even the same one in some cases—hampers the allocation of mass signals with the corresponding chromatographic peak. For those steroids, i.e., DHEA and testosterone, which share an empirical formula, the identification of each specific compound remains challenging using MS and the identification relies on chromatographic separation.

Importantly, we have been able to quantify the steroid hormones in urine samples and derived uEV in a fast and simple manner. However, only one DHEAS was detected in the uEVS and cortisol, androstenedione and DHEAS were detected in the urine samples. These EVs were isolated by ultracentrifugation, including a washing step to avoid any contamination from the soluble fraction. The urine samples from a healthy man were collected on different days and different time of collection (morning and afternoon). The time collection was a parameter to be assessed from a metabolomics perspective, but we found out that inter-day variability also had a high impact on the analysis. Morning samples are considered to contain a higher concentration of steroid analytes coming from the prostate, possibly due to accumulation and leakage towards the urinary tract during the night. However, this trend was not described in our morning samples. The reason may be that urine sample U003 (Table S4, Supplementary Materials) was not available for metabolomics analysis; the analysis of the soluble fractions of urine (after uEV isolation), which includes U003, in the morning samples had a higher concentration of DHEAS. This highlights the importance of analyzing a larger cohort to obtain significant results non-dependent on a unique highly concentrated sample.

In the end, this is a fast and sensitive method that was successfully applied for the detection and quantification of a panel of steroid hormone compounds in biological samples in 6 min runtime per sample. The sensitivity of this method makes it ideally suited for multiple in vivo applications. In this manuscript, we explored the analysis of steroids in several rat tissues and also in human urine and uEV samples. This has evident applications in profiling the metabolic status of patients suffering any hormone-dependent disease. It

should be noted that the assay requires a longer cleanse step to wash the column out of the lipids and peptides when running a long experiment with many tissue samples. To our knowledge, this is the first hrLCMS-based method able to detect and quantify steroid hormones associated with EVs isolated from body fluids in a targeted approach.

References

1. Miller, W.L.; Auchus, R.J. The Molecular Biology, Biochemistry, and Physiology of Human Steroidogenesis and Its Disorders. *Endocr. Rev.* **2011**, *32*, 81–151. [CrossRef] [PubMed]
2. Bereshchenko, O.; Bruscoli, S.; Riccardi, C. Glucocorticoids, Sex Hormones, and Immunity. *Front. Immunol.* **2018**, *9*, 1332. [CrossRef] [PubMed]
3. Poschner, S.; Zehl, M.; Maier-Salamon, A.; Jäger, W. Simultaneous Quantification of Estrogens, Their Precursors and Conjugated Metabolites in Human Breast Cancer Cells by LC–HRMS without Derivatization. *J. Pharm. Biomed. Anal.* **2017**, *138*, 344–350. [CrossRef]
4. Cardoso, H.J.; Carvalho, T.M.A.; Fonseca, L.R.S.; Figueira, M.I.; Vaz, C.V.; Socorro, S. Revisiting Prostate Cancer Metabolism: From Metabolites to Disease and Therapy. *Med. Res. Rev.* **2021**, *41*, 1499–1538. [CrossRef] [PubMed]
5. Clos-Garcia, M.; Loizaga-Iriarte, A.; Zuñiga-Garcia, P.; Sánchez-Mosquera, P.; Rosa Cortazar, A.; González, E.; Torrano, V.; Alonso, C.; Pérez-Cormenzana, M.; Ugalde-Olano, A.; et al. Metabolic Alterations in Urine Extracellular Vesicles Are Associated to Prostate Cancer Pathogenesis and Progression. *J. Extracell. Vesicles* **2018**, *7*, 1470442. [CrossRef] [PubMed]
6. Lonergan, P.; Tindall, D. Androgen Receptor Signaling in Prostate Cancer Development and Progression. *J. Carcinog.* **2011**, *10*, 20. [CrossRef] [PubMed]
7. Kanehisa, M.; Goto, S. KEGG: Kyoto Encyclopedia of Genes and Genomes. *Nucleic Acids Res.* **2000**, *28*, 27–30. [CrossRef]
8. Kanehisa, M.; Furumichi, M.; Sato, Y.; Ishiguro-Watanabe, M.; Tanabe, M. KEGG: Integrating Viruses and Cellular Organisms. *Nucleic Acids Res.* **2021**, *49*, D545–D551. [CrossRef]
9. Mueller, J.W.; Gilligan, L.C.; Idkowiak, J.; Arlt, W.; Foster, P.A. The Regulation of Steroid Action by Sulfation and Desulfation. *Endocr. Rev.* **2015**, *36*, 526–563. [CrossRef]

10. Foster, P.A.; Mueller, J.W. Insights into Steroid Sulfation and Desulfation Pathways. *J. Mol. Endocrinol.* **2018**, *61*, T271–T283. [CrossRef]

11. Langford, R.; Hurrion, E.; Dawson, P.A. Genetics and Pathophysiology of Mammalian Sulfate Biology. *J. Genet. Genom.* **2017**, *44*, 7–20. [CrossRef] [PubMed]

12. Bordanaba-Florit, G.; Royo, F.; Kruglik, S.G.; Falcón-Pérez, J.M. Using Single-Vesicle Technologies to Unravel the Heterogeneity of Extracellular Vesicles. *Nat. Protoc.* **2021**, *16*, 3163–3185. [CrossRef] [PubMed]

13. Yáñez-Mó, M.; Siljander, P.R.-M.; Andreu, Z.; Zavec, A.B.; Borràs, F.E.; Buzas, E.I.; Buzas, K.; Casal, E.; Cappello, F.; Carvalho, J.; et al. Biological Properties of Extracellular Vesicles and Their Physiological Functions. *J. Extracell. Vesicles* **2015**, *4*, 27066. [CrossRef] [PubMed]

14. Kalra, H.; Simpson, R.J.; Ji, H.; Aikawa, E.; Altevogt, P.; Askenase, P.; Bond, V.C.; Borràs, F.E.; Breakefield, X.; Budnik, V.; et al. Vesiclepedia: A Compendium for Extracellular Vesicles with Continuous Community Annotation. *PLoS Biol.* **2012**, *10*, 8–12. [CrossRef]

15. Pathan, M.; Fonseka, P.; Chitti, S.V.; Kang, T.; Sanwlani, R.; Van Deun, J.; Hendrix, A.; Mathivanan, S. Vesiclepedia 2019: A Compendium of RNA, Proteins, Lipids and Metabolites in Extracellular Vesicles. *Nucleic Acids Res.* **2019**, *47*, D516–D519. [CrossRef]

16. Quanson, J.L.; Stander, M.A.; Pretorius, E.; Jenkinson, C.; Taylor, A.E.; Storbeck, K.H. High-Throughput Analysis of 19 Endogenous Androgenic Steroids by Ultra-Performance Convergence Chromatography Tandem Mass Spectrometry. *J. Chromatogr. B Anal. Technol. Biomed. Life Sci.* **2016**, *1031*, 131–138. [CrossRef]

17. Indapurkar, A.; Hartman, N.; Patel, V.; Matta, M.K. Simultaneous UHPLC-MS/MS Method of Estradiol Metabolites to Support the Evaluation of Phase-2 Metabolic Activity of Induced Pluripotent Stem Cell Derived Hepatocytes. *J. Chromatogr. B Anal. Technol. Biomed. Life Sci.* **2019**, *1126–1127*, 121765. [CrossRef] [PubMed]

18. Im, E.; Lew, B.L.; Lee, M.Y.; Lee, J.; Paeng, K.J.; Chung, B.C. Simultaneous Determination of Androgens and Prostaglandins in Human Urine Using Ultra-High-Performance Liquid Chromatography–Tandem Mass Spectrometry. *J. Chromatogr. B Anal. Technol. Biomed. Life Sci.* **2019**, *1109*, 45–53. [CrossRef]

19. Qin, F.; Zhao, Y.Y.; Sawyer, M.B.; Li, X.F. Hydrophilic Interaction Liquid Chromatography-Tandem Mass Spectrometry Determination of Estrogen Conjugates in Human Urine. *Anal. Chem.* **2008**, *80*, 3404–3411. [CrossRef]

20. Lee, Y.R.; Im, E.; Kim, H.; Lew, B.L.; Sim, W.Y.; Lee, J.; Oh, H.B.; Paeng, K.J.; Hong, J.; Chung, B.C. Untargeted Metabolomics and Steroid Signatures in Urine of Male Pattern Baldness Patients after Finasteride Treatment for a Year. *Metabolites* **2020**, *10*, 131. [CrossRef]

21. Maeda, N.; Tanaka, E.; Suzuki, T.; Okumura, K.; Nomura, S.; Miyasho, T.; Haeno, S.; Yokota, H. Accurate Determination of Tissue Steroid Hormones, Precursors and Conjugates in Adult Male Rat. *J. Biochem.* **2013**, *153*, 63–71. [CrossRef]

22. Fernandes, D.; Navarro, J.C.; Riva, C.; Bordonali, S.; Porte, C. Does Exposure to Testosterone Significantly Alter Endogenous Metabolism in the Marine Mussel Mytilus Galloprovincialis? *Aquat. Toxicol.* **2010**, *100*, 313–320. [CrossRef] [PubMed]

23. Li, Y.; Yan, Z.; Li, X.; Yin, X.; Li, K. Uplc–Tof–Ms Method for Simultaneous Quantification of Steroid Hormones in Tissue Homogenates of Zebrafish with Solid-Phase Extraction. *Molecules* **2021**, *26*, 6213. [CrossRef]

24. Ceglarek, U.; Kortz, L.; Leichtle, A.; Fiedler, G.M.; Kratzsch, J.; Thiery, J. Rapid Quantification of Steroid Patterns in Human Serum by On-Line Solid Phase Extraction Combined with Liquid Chromatography-Triple Quadrupole Linear Ion Trap Mass Spectrometry. *Clin. Chim. Acta* **2009**, *401*, 114–118. [CrossRef]

25. Koal, T.; Schmiederer, D.; Pham-Tuan, H.; Röhring, C.; Rauh, M. Standardized LC-MS/MS Based Steroid Hormone Profile-Analysis. *J. Steroid Biochem. Mol. Biol.* **2012**, *129*, 129–138. [CrossRef] [PubMed]

26. Yuan, T.F.; Le, J.; Wang, S.T.; Li, Y. An LC/MS/MS Method for Analyzing the Steroid Metabolome with High Accuracy and from Small Serum Samples. *J. Lipid Res.* **2020**, *61*, 580–586. [CrossRef]

27. Dong, Z.; Wang, C.; Zhang, J.; Wang, Z. A UHPLC-MS/MS Method for Profiling Multifunctional Steroids in Human Hair. *Anal. Bioanal. Chem.* **2017**, *409*, 4751–4769. [CrossRef] [PubMed]

28. Isobe, T.; Shiraishi, H.; Yasuda, M.; Shinoda, A.; Suzuki, H.; Morita, M. Determination of Estrogens and Their Conjugates in Water Using Solid-Phase Extraction Followed by Liquid Chromatography-Tandem Mass Spectrometry. *J. Chromatogr. A* **2003**, *984*, 195–202. [CrossRef]

29. Reddy, S.; Iden, C.R.; Brownawell, B.J. Analysis of Steroid Conjugates in Sewage Influent and Effluent by Liquid Chromatography-Tandem Mass Spectrometry. *Anal. Chem.* **2005**, *77*, 7032–7038. [CrossRef]

30. Van Liempd, S.; Cabrera, D.; Mato, J.M.; Falcon-Perez, J.M. A Fast Method for the Quantitation of Key Metabolites of the Methionine Pathway in Liver Tissue by High-Resolution Mass Spectrometry and Hydrophilic Interaction Ultra-Performance Liquid Chromatography. *Anal. Bioanal. Chem.* **2013**, *405*, 5301–5310. [CrossRef]

31. Schepers, U.; Ermer, J.; Preu, L.; Wätzig, H. Wide Concentration Range Investigation of Recovery, Precision and Error Structure in Liquid Chromatography. *J. Chromatogr. B* **2004**, *810*, 111–118. [CrossRef]

32. Bordanaba-Florit, G. Simultaneous Quantification of Steroid Hormones Using hrLC-MS in Endocrine Tissues of Male Rats and Human Samples (Dataset). 2022. Available online: https://figshare.com/articles/dataset/_/20231493 (accessed on 27 June 2022).

33. Liang, X.; Ubhayakar, S.; Liederer, B.M.; Dean, B.; Ran-Ran Qin, A.; Shahidi-Latham, S.; Deng, Y. Evaluation of Homogenization Techniques for the Preparation of Mouse Tissue Samples to Support Drug Discovery. *Bioanalysis* **2011**, *3*, 1923–1933. [CrossRef]

34. Method Validation and Quality Control Procedures for Pesticide Residues Analysis in Food and Feed. 2012. Available online: https://www.eurl-pesticides.eu/library/docs/allcrl/AqcGuidance_Sanco_2011_12495.pdf (accessed on 27 June 2022).

35. Ghosh, C.; Shinde, C.P.; Chakraborty, B.S. Influence of Ionization Source Design on Matrix Effects during LC-ESI-MS/MS Analysis. *J. Chromatogr. B Anal. Technol. Biomed. Life Sci.* **2012**, *893–894*, 193–200. [CrossRef] [PubMed]

36. Zhou, W.; Yang, S.; Wang, P.G. Matrix Effects and Application of Matrix Effect Factor. *Bioanalysis* **2017**, *9*, 1839–1844. [CrossRef] [PubMed]

37. Bobrie, A.; Colombo, M.; Krumeich, S.; Raposo, G.; Thery, C. Diverse Subpopulations of Vesicles Secreted by Different Intracellular Mechanisms Are Present in Exosome Preparations Obtained by Differential Ultracentrifugation. *J. Ayurveda Integr. Med.* **2012**, *1*, 18397. [CrossRef] [PubMed]

38. Giles, K.; Pringle, S.D.; Worthington, K.R.; Little, D.; Wildgoose, J.L.; Bateman, R.H. Applications of a Travelling Wave-Based Radio-Frequency-Only Stacked Ring Ion Guide. *Rapid Commun. Mass Spectrom.* **2004**, *18*, 2401–2414. [CrossRef]

39. Kenny, D.J.; Worthington, K.R.; Hoyes, J.B. Scanwave: A New Approach to Enhancing Spectral Data on a Tandem Quadrupole Mass Spectrometer. *J. Am. Soc. Mass Spectrom.* **2010**, *21*, 1061–1069. [CrossRef]

40. Taylor, P.J. Matrix Effects: The Achilles Heel of Quantitative High-Performance Liquid Chromatography-Electrospray-Tandem Mass Spectrometry. *Clin. Biochem.* **2005**, *38*, 328–334. [CrossRef]

41. Campbell, I. Adrenocortical Hormones. *Anaesth. Intensive Care Med.* **2008**, *9*, 420–423. [CrossRef]

42. Rosol, T.J.; Yarrington, J.T.; Latendresse, J.; Capen, C.C. Adrenal Gland: Structure, Function, and Mechanisms of Toxicity. *Toxicol. Pathol.* **2016**, *29*, 41–48. [CrossRef]

43. Rainey, W.E.; Nakamura, Y. Regulation of the Adrenal Androgen Biosynthesis. *J. Steroid Biochem. Mol. Biol.* **2008**, *108*, 281–286. [CrossRef] [PubMed]

44. Puhka, M.; Takatalo, M.; Nordberg, M.E.; Valkonen, S.; Nandania, J.; Aatonen, M.; Yliperttula, M.; Laitinen, S.; Velagapudi, V.; Mirtti, T.; et al. Metabolomic Profiling of Extracellular Vesicles and Alternative Normalization Methods Reveal Enriched Metabolites and Strategies to Study Prostate Cancer-Related Changes. *Theranostics* **2017**, *7*, 3824–3841. [CrossRef] [PubMed]

1 **Title**: Integration of proteomic and metabolomic analysis reveal distinct metabolic alterations of
2 prostate cancer-associated fibroblasts compared to normal fibroblasts from patient's stroma samples

3 **Author names**: Guillermo Bordanaba-Florit[1,†], Félix Royo[1,2], Oihane E. Albóniga[3], Aled Clayton[4],
4 Juan Manuel Falcón-Pérez[1,2,3] and Jason Webber[5,†]

5 **Affiliations:**

6 [1]Exosomes Laboratory, Center for Cooperative Research in Biosciences (CIC bioGUNE), Derio, Spain;

7 [2]Centro de Investigación Biomédica en Red de Enfermedades Hepáticas y Digestivas (Ciberehd),
8 28029 Madrid, Spain;

9 [3]Metabolomics Platform, Center for Cooperative Research in Biosciences (CIC bioGUNE), Derio,
10 Spain;

11 [4]Division of Cancer and Genetics, School of Medicine, Cardiff University, Cardiff, UK;

12 [5]Institute of Life Science, Swansea University Medical School, Swansea University, Swansea, UK.

13 [†]Corresponding authors: gbordanaba@cicbiogune.es (G. B.-F.); j.p.webber@swansea.ac.uk (J. W.)

14 **Highlights:**

15 • Lipogenic metabolic pathways are more prevalent in CAFs.
16 • Energy producing pathways alternative to glycolysis support CAFs metabolic activity.
17 • Mitochondrial metabolism is altered in the first steps of fibroblast differentiation.
18 • Extracellular vesicles provoke a higher basal respiration associated to mitochondria in normal
19   fibroblasts.

20 **Abstract:**

21 The prostate gland is a complex and heterogeneous organ composed of epithelium and stroma.
22 Prostate cancer is most commonly seen emerging from luminal epithelial cells and requires the
23 assistance of adjacent stroma. Prostatic stroma is compositionally complex, and in concert with
24 disease progression undergoes many alterations which include the emergence of cancer associated
25 fibroblasts (CAFs). This heterogeneous cell population often contains cells with a myofibroblast-like
26 phenotype that are not normally present in healthy prostate tissue. In this work, we studied the
27 metabolic rewiring of stromal fibroblasts following myofibroblast differentiation. First, the metabolic
28 abundances of normal- and cancer-associated fibroblasts derived from needle biopsies of the same
29 patient was analysed using UPLC-MS. It was determined CAFs were metabolically more active and,
30 therefore, energy producing metabolic pathways were enhanced. Also, CAFs showed a heightened
31 lipogenic metabolism as both reservoir species and building block compounds. Interestingly, lipid

metabolism affects mitochondria functioning yet the mechanisms of lipid-mediated functions are unclear. The fact oxidised fatty acids and glutathione system are elevated in CAFs strengthens the hypothesis that increased metabolic activity is related to mitochondria. In further experiments measuring the metabolic flux with a Seahorse bioanalyser, we studied whether TGF-β1 and extracellular vesicles (EVs) could stimulate myofibroblast differentiation in normal fibroblasts. An increase of basal respiration in normal fibroblasts was reported, mirroring the disease-like phenotype. This indicates an altered metabolism associated to mitochondria in CAFs and treated fibroblasts. Hence, one proposes that the change in the metabolomics profile of tumour-associated stromal fibroblasts is driven by oxygen-dependent metabolism, possibly associated to mitochondria; however, the specific mechanisms are still unclear.

Keywords:

Mass spectrometry; Prostate cancer; Metabolism; Extracellular vesicles; Human primary fibroblasts

Abbreviations:

2-deoxy-d-glucose, *2-DG*; α smooth muscle actin, *α-SMA*; Adenosine triphosphate, *ATP*; Cancer-associated fibroblast, *CAF*; Cholesteryl ester, *CE*; Ceramides, *Cer*; Extracellular acidification rate, *ECAR*; Extracellular vesicle, *EV*; Fatty acid, *FA*; Carbonyl cyanide p-trifluoro methoxyphenylhydrazone, *FCCP*; Oxydised fatty acis, *FFAox*; Glutathione, *GSH*; Hydroxyeicosapentanoic acid, *HEPE*; Liquid chromatography coupled to mass spectrometry, *LC-MS*; Lysophosphatidylcholines, *LPC*; Glycerophosphocholines, *LPE*; Mass spectrometry imaging, *MSI*; Nicotinamide adenine dinucleotide, *NAD*; N-acyl ethanolamines, *NAE*; Oxygen consumption rate, *OCR*; Prostate cancer, *PCa;* Principal component analysis, *PCA*; Phosphate buffered saline, *PBS*; Reactive oxygen species, *ROS*; Standard error of the mean, *SEM*; Tricarboxylic acid, *TCA*; Transforming growth factor beta 1, *TGF-β1*; Ultra-high performance liquid chromatography coupled to mass spectrometry, *UPLC-MS*.
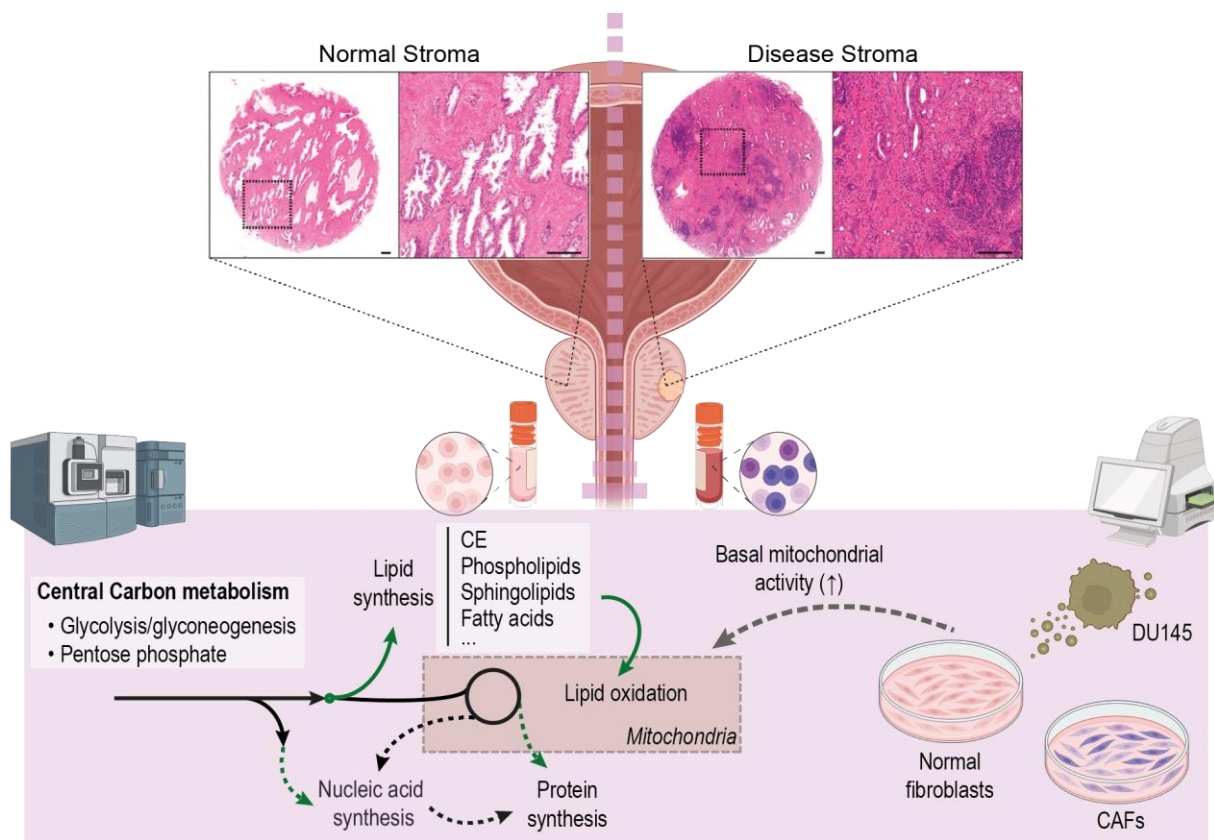
Graphical abstract:

Introduction:

The prostate gland is globally composed of epithelium and stroma, which are extremely heterogeneous tissues. The epithelium is organized as glandular acini and it contains cuboidal to columnar secretory epithelial cells with apical junction complexes, a continuous layer of basal cells[1], and sparse neuroendocrine cells, each attached to a basal lamina[2]. Beyond the basal lamina, a prominent fibromuscular stroma composed of smooth muscle, fibroblasts, blood vessels, autonomic nerve fibres, inflammatory cells, and extracellular matrix components offers physical support and contraction of the gland[3]. In prostate carcinoma (PCa), the interstitial stroma is often abnormally rich in myofibroblastic cells[4,5], capable of supporting tumour growth, vascularization, angiogenesis, and metastasis *in vivo*[6]. Transforming growth factor β1, TGF-β1, remains among the most critical factors for myofibroblastic differentiation and the generation of a tumour reactive stroma. Intriguingly, we have previously shown that cancer extracellular vesicles (EVs) can trigger fibroblast to myofibroblast differentiation in an EV-TGF-β1 dependent manner[6]. In further studies, the essential role of EVs in directing this stromal cell differentiation towards cancer-associated myofibroblast-like phenotype was described[7]. However, the mechanisms by which EV-activated stromal cells support tumour growth remain unclear.

Our previous studies with biopsy material from patients where tumoral growth was located in one half of the prostate and not the other, revealed clear differences between normal and disease regions. Histological examination showed a smooth muscle stromal architecture around glandular structures in

76 normal tissue while the glands were disorganised and showed an altered, fibrosis-like interstitial stroma

77 observed in disease-associated tissue[8]. A panel of antibody markers confirmed the higher abundance

78 of α-Smooth Muscle Actin (α-SMA)-positive myofibroblast cells in tumour-associated tissue. Strikingly,

79 EVs isolated from prostate cancer epithelial cell lines generated a myofibroblast-like phenotype in

80 normal fibroblasts[7]. In that work, we demonstrated the essential role of EVs in directing stromal

81 differentiation to a pro-tumorigenic phenotype, exhibiting pro-angiogenic properties and enhancement

82 of tumour growth in xenograft models. Further functional assays and proteomics profiling work

83 highlighted that stroma activation mediated by EV stimulation mirrors the naturally occurring fibroblast

84 differentiation during disease[8].

85 Altered metabolism is a hallmark of PCa and several metabolites and metabolic pathways are already

86 distinctive in different prostate types of tissue[9,10]. In this line, Andersen *et al.* reported higher levels of

87 energy-related pathway metabolites, such as ADP, ATP, and glucose as well as higher levels of the

88 antioxidant taurine in stromal tissue compared to cancer and non-cancer epithelium[11]. Besides,

89 increased levels of crucial metabolites for fatty acid oxidation and building blocks in lipid synthesis

90 were described in cancer tissue. Other studies also reported metabolic rewiring of reactive stroma,

91 showing different levels of certain metabolites between highly differentiated stroma compared to poorly

92 differentiated stroma[12]. The stromal-epithelial interactions have a dominant role in tumour growth,

93 invasion and metastasis. Actually, many reports over the last decades showed the interaction of

94 reactive stroma with PCa[2,12–17] and EVs influencing aspects of cancer biology such as

95 angiogenesis[7,8,18,19] and tumour progression[17,20–22]. Yet, few studies have investigated the role of

96 tumour EVs in altering metabolic processes in stromal cell compartments.

97 With the rise of *omics* era, entire sets of biomolecules – genes, proteins or metabolites - contained in a

98 biological tissue, cell, fluid, or organism can be identified. A proteomics analysis of the same matched-

99 normal and disease stroma tissues was able to distinguish both phenotypes and describe a disease-

100 like phenotype[8]. Similarly, a transcriptomic analysis of derived EVs from the same type of samples

101 discriminated normal from disease stroma samples[23]. This manuscript presents a broad semitargeted

102 metabolomics approach, which analyses the metabolome of normal and disease stroma tissues,

103 highlighting the metabolic differences of matched normal fibroblasts and cancer-associated fibroblasts

104 within individual PCa patients. Furthermore, we show an altered metabolism of normal fibroblasts

105 treated with EVs from a PCa cell line.

106 **Materials and methods:**

107 **Stromal primary cell cultures**

108 Six patient-matched normal and tumour-associated needle biopsies were isolated from radical

109 prostatectomy. These were taken from sites of palpable disease and also from apparently normal

110 tissue from the opposite side of the same prostate. Tissue collection and consenting was managed

111 through the Wales Cancer Bank. Cores were manually dissected into $1mm^3$ pieces and subjected to
112 mechanical homogenization followed by 200 U per mL collagenase-I digestion for 15 to 20 hours at 37
113 °C. Cells were cultured in Stromal Cell Basal Medium (SCBM) supplemented with human fibroblast
114 growth factor-B, insulin, fetal bovine serum (FBS) and GA-1000 (Lonza, Wokingham, UK). for around
115 two weeks until only stromal cells were retained. [8,23]Subsequent cultures were maintained in
116 DMEM/F12 media (Lonza) with 10% FBS depleted of bovine EVs. Cultures were confirmed free of
117 epithelial cells by immuno-fluorescence staining for cytokeratin prior seeding stromal cells in 96 well
118 plates [8,23]. A sample of each patient-matched prostatic stromal cell culture was collected and frozen for
119 metabolomics analysis using liquid chromatography coupled to mass spectrometry.

120 **Metabolite extraction**

121 In metabolomics, there is no single platform or method able to analyse the entire metabolome of a
122 biological sample. Therefore, metabolites were extracted by fractionating the cell samples into pools of
123 species with similar physicochemical properties. In brief, proteins were precipitated by adding methanol
124 to the cell lysate. Chloroform solvent was added to the methanol extraction mixture and this biphasic
125 mixture was incubated at -20 ºC for 30 min. Then, three different fractions were collected: (1) fatty
126 acyls, bile acids, steroids and lysoglycerophospholipids, were obtained after centrifuging the
127 supernatant at 16,000g for 15 min, drying and reconstituting in methanol, (2) for aminoacids, aliquots of
128 5 µL from the first fraction were derivatised and dried, and (3) glycerolipids, cholesteryl esters,
129 sphingolipids and glycerophospholipids were obtained by mixing the chloroform extraction mixture with
130 H_2O (pH 9) and incubating at -20 ºC for 60 min. After centrifuging at 16,000g for 15 min, the organic
131 phase from this third fraction was collected then, dried and reconstituted in 50/50% *v/v*
132 acetonitrile/isopropanol. The aqueous phase that contains polar metabolites, including central carbon
133 metabolism, was collected, dried and reconstituted in H_2O.

134 Quality control (QC) sample for calibration and validation were included in this workflow to correct for
135 response factors between and within batches; and to assess the quality of data.

136 **LC-MS analysis**
137 An appropriate UPLC-MS method was used for each platform. The instruments and the conditions for
138 the chromatographic separation and mass spectrometric detection are summarized in Table S1. A test
139 mixture of standards was analyzed before and after the entire set of randomized, duplicated sample
140 injections to check for retention time stability, mass accuracy and sensitivity. All data were processed
141 using the TargetLynx application manager for MassLynx 4.1 software (Waters Corp., Milford, USA). A
142 set of predefined features, defined as retention time - mass-to-charge ratio pairs, *Rt-m/z*,
143 corresponding to metabolites included in the analysis are fed into the program. Associated extracted
144 ion chromatograms (mass tolerance window = 0.05 Da) are then peak-detected and noise-reduced in
145 both the LC and MS domains such that only true metabolite related features are processed by the
146 software. Then, a list of chromatographic peak areas is generated for each sample injection.

147 **Data analysis**

148 *Data Normalization and quality control*

149 After data inspection in terms of reproducibility and peak integration, each metabolite was corrected
150 and normalized using the intensity of an appropriate internal standard included in the analysis and
151 following the procedure fully described by van der Kloet *et al.*[25]. Finally, any remaining zero values in
152 the corrected dataset were replaced with missing values prior averaging to obtain a dataset further
153 used for statistical analyses. A final normalization procedure was applied by dividing every sample by
154 its protein content.

155 *Multivariate and univariate analysis*
156 Once data was normalized and prepare for statistical analysis, a first approach based on multivariate
157 analysis was performed with SIMCA-P (version 13.0). Firstly, a non-supervised principal component
158 analysis (PCA) was utilised to reduce dimensionality and to study data quality, assess reproducibility of
159 the analytical procedure, visualize tendencies between groups and determine the presence of outliers.
160 Afterwards, supervised partial least squares discriminant analysis (PLS-DA) and orthogonal PLS-DA
161 (OPLS-DA) were performed followed by a suitable validation method, a cross-validation analysis of
162 variance (CV-ANOVA), integrated in SIMCA-P software. Supervised models that were validated were
163 further used for variable selection. To this end, a variable importance on projection (VIP) score and
164 absolute value of p(corr) greater than 1 and 0.8, respectively, were used as cut-off points for variable
165 selection.

166 Finally, and as a complementary statistical analysis, univariate analysis was perfomed. In order to test
167 normality, Shaphiro test was used; thence either paired student's test[26] or Wilcoxon signed-rank test
168 was applied to assess comparisons significance. After that, the dataset was expressed as a metabolite
169 fold-change and significance (p-value) and further depicted in a *volcano plot*.

170 *Pathway analysis and pathway enrichment*
171 A proper biological interpretation is crucial in any metabolomics study to deliver a comprehensive
172 assessment of experimental conditions. To evaluate the prominence of certain metabolic pathways, a
173 Pathway analysis was computed using MetaboAnalyst 5.0 and inputting a dataset of samples and
174 quantified metabolites. It performs an o-representation analysis that integrates enrichment and
175 pathway topology analysis to visualise specific altered pathways in the human metabolic network[27].
176 Then, proteomics data was included in a Joint-pathway analysis to evaluate metabolic alterations
177 considering two sets of physiologically relevant molecules in fibroblast samples. This over-
178 representation analysis module performs an integrated metabolic pathway analysis by combining
179 metabolomics and proteomics data collected from the exact same samples and methodology[27]. The
180 MetaboAnalyst 5.0 web-based tool includes the normalisation, transformation and scaling of data to
181 complete data integration.

182   Furthermore, a lipid metabolic network analysis[28] performed with LINEX 2.4.1 webapp to observe

183   functional associations of lipid classes. It computes specific lipid networks based on compounds and

184   lipid classes connections using a lipidomics dataset.

Extracellular vesicle isolation

186   EVs were purified from conditioned media of DU145 prostate cancer cell (ATCC, Teddington, UK)

187   grown in Integra bioreactor flasks (Integra Biosciences Corp, Hudson, NH, USA) [24]. EV samples were

188   collected using the sucrose cushion method and resuspended in PBS. Thence, samples were

189   quantified using the BCA-protein assay (Pierce/Thermo, Northumberland, UK), and stored at -80°C.

190   For treatments of stromal cell cultures, EV were used at 200 µg per mL (approximately equivalent to

191   1.5 ng per mL of EV-associated TGF-β1) for 72 hour.

Seahorse assay

193   Oxygen consumption rate and glycolytic activity were assessed using a XF24 Extracellular Flux

194   Analyser (Seahorse Biosciences) to probe O_2 and pH, respectively. Fibroblasts were equilibrated in

195   unbuffered media (60 min at 37 ºC in a CO_2-free incubator) prior transfer to the XF24 analyser. For

196   mitochondrial respiration, the oxygen consumption was measured over the assay. First, basal oxygen

197   consumption (OCR) was determined, and then oligomycin (1 µg per ml), FCCP (0.3 µM), FCCP (0.6

198   µM), and 2 µM rotenone were sequentially injected to assess maximal oxidative capacity, ATP

199   production, coupling efficiency (OCR percentage dedicated to produce ATP) and basal respiration. To

200   analyse glycolytic activity, the extracellular pH was measured over the assay. First, base-line (non-

201   glycolytic) extracellular acidification (ECAR) was determined, and then media alone followed by

202   glucose (10 mM), oligomycin (1 µg per ml), and 2-Deoxyglucose (0.1 M) were sequentially injected to

203   assess maximal glycolytic capacity and glycolysis rate.

204   Statistical analyses were performed by paired Student's t-test using GraphPad PRISM 9.5 software

205   (Graph Pad, San Diego, CA, USA). Each experiment was analysed individually then, the mean ± SEM

206   was represented. All p-values lower than 0.05 are considered significant as: * P>0.05, ** P>0.01, ***

207   P>0.001.

Results:

CAFs exhibit a differential proteomic, transcriptomic and metabolomics landscapes

210   In PCa, the emergence of myofibroblasts within the interstitial stroma is described as the major

211   difference between normal and tumour reactive stroma[12,29]. This reactive stroma coevolves with

212   prostate cancer in it is capable of supporting its growth. In previous studies, we have characterised

213   normal fibroblasts and CAFs derived from the same patient's needle biopsies for the typical markers of

214   reactive stroma, α-Smooth Muscle Actin (α-SMA), Cytokeratine, Desmin and Vimentin[7,8,23]. CAFs were

215   not a homogeneous population of myofibroblasts but a heterogenous mixture of fibroblasts at distinct

216 differentiation stages, including a proportion of cells which are α-SMA positive[7]. The normal fibroblasts
217 lacked α-SMA. However, they could be induced to express α-SMA when treated with either soluble or
218 vesicle-associated TGF-β1[8].

219 In 2016, Webber et al.[8] described a set of proteins that could discriminate CAFs and normal fibroblasts
220 isolated from the patient—matched needle biopsies described in this study. A more recent study
221 explored the opportunity to use EV-derived RNA from these fibroblasts as indicators of altered tumour
222 environment[23]. In this work, Shephard *et al.* identified 19 differentially expressed transcripts that
223 discriminate disease from normal stromal EVs, indicating transcriptional differences between patient
224 samples. The metabolomics study included in this work adds several findings to our published data
225 obtained by proteomics and transcriptomics. A comprehensive evaluation of data showed a clear
226 tendency of enhanced abundances in most of the metabolites in sample 1161-normal during data
227 analysis and normalization compared to other patient-matched tissues. The behaviour of this sample
228 was also different from the remaining samples as demonstrated by PCA (Fig. S1). Moreover, it is on
229 the line that describe the confidence ellipse based on Hotelling's T2 (significance level = 0.05). For
230 these reasons, sample 1161-normal was excluded from further statistical analysis. Afterwards, PLS-DA
231 and OPLS-DA models were built and the scores plots are included in Fig. 1A and 1B. A clear
232 separation tendency was observed in both models mainly through PC1. Even with this separation
233 tendency, none of the models was validated (CV-ANOVA p-value >0.05). However, those variables
234 that influence on the most in group separation were selected based on their VIP and p(corr) values. In
235 total 64 and 12 metabolites fulfil VIP greater than 1 and |p(corr)| greater than 0.8 in PLS-DA and
236 OPLS-DA, respectively. In order to select those metabolites of relevant importance, a Venn Diagram
237 including these metabolites was built to select only common metabolites in PLS-DA and OPLS-DA
238 models (Fig. 1C). Relevant metabolites include ceramides (Cer), phosphatidylcholines (PC) and
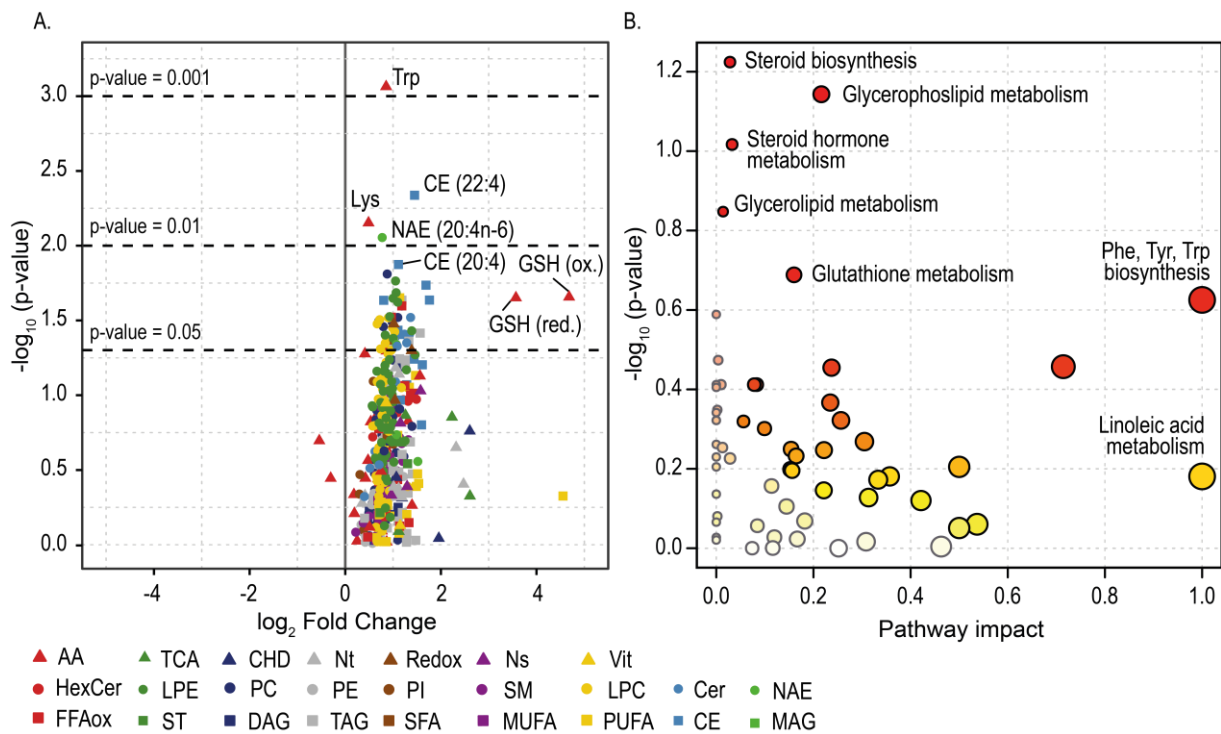239 cholesteryl esters (CE) (Table S3).

240
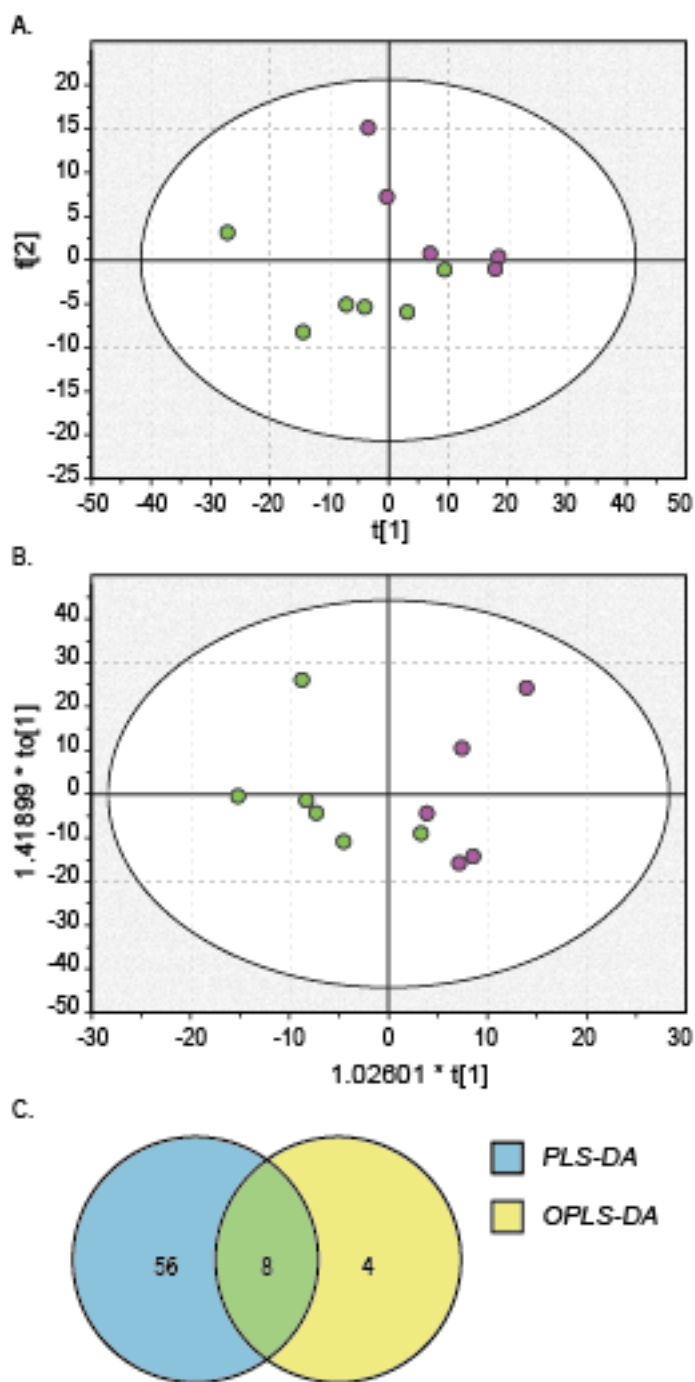
Figure 1. Summary of multivariate metabolomics analysis of normal fibroblasts and CAFs. A. Score scatter plot of the PLS-DA model of fibroblasts obtained from normal and cancer needle biopsies. Model diagnostics (A = 2; R2X = 0.682; R2Y = 0.729; Q2 = 0.337; CV-ANOVA = 0.581). In green, CAF samples and, in purple, normal fibroblasts. B. Score scatter plot of the OPLS-DA model of fibroblasts obtained from normal and cancer needle biopsies. Model diagnostics (A = 2; R2X = 0.682; R2Y = 0.721; Q2 = 0.241; CV-ANOVA = 0.799). In green, CAF samples and, in purple, normal fibroblasts. In green, CAF samples and, in purple, normal fibroblasts. C. Venn diagram of features (metabolites) that influence to the separation of CAF and normal fibroblasts groups in PLS-DA and OPLS-DA models. Results are compiled in Table S3.

Disease-associated fibroblasts show lipogenic and energy-producing metabolic alterations

Reactive stroma relevance grows upon progression and invasion of tumour cells to neighbour locations and tissues since it supports structural growth and nutrient availability. In this line, cell populations in normal stroma undergo a myofibroblast turnover constituting the so-called CAFs. In order to study the metabolic profile of this two tissue subtypes, four platforms based on UPLC-MS were utilised to analyse metabolites. They are fractionated in pools of species with similar physicochemical properties. The platforms include: (1) Fatty acyls, bile acids, steroids and lysoglycerophospholipids; (2) Glycerolipids, glycerophospholipids, sterol lipids and sphingolipids; (3) Amino acids; (4) Polar metabolites profiling, including central carbon metabolism.

Figure 2. Summary of metabolomics study (considering individual metabolites) comparing normal and cancer-associated fibroblasts isolated from needle biopsies of radical prostatectomy specimens. A. Volcano plot comparing CAFs and normal fibroblasts as -log10(p-value) against log2(fold change). The different metabolite classes are depicted in different shapes and colours; relevant metabolites are labelled. B. Pathway overrepresentation analysis depicted as –log10 (p-value) against pathway impact. Pathway impact stands for the relative importance of the specific module in the analysed metabolite set. It combines pathway overrepresentation results and centrality measures. Representative pathways were labelled, size of nodes represents pathway impact and their significance ranges from high (in red) towards orange, yellow and white indicating a lower significance. Here, all individual metabolites and their fold changes were considered to rank the enrichment and significance of each pathway. AA: aminoacids; TCA: tricarboxylic acid cycle related metabolites; CHD: Carbohydrates derivatives; Nt: Nucleotides; Redox: electron donor and acceptors; Ns: Nucleosides; Vit: Vitamins; HexCer: Hexosylceramides; LPE: Lysophosphatidylethanolamines; PC: Phosphatidylcholines; PE: Phosphatidylethanolamines; PI: Phosphatidylinositols; SM: Sphingomyelins; LPC: Lysophosphatidylcholines; Cer: Ceramides; NAE: N-

acylethanolamines; FFAox: Oxidized fatty acids; ST: Steroids; DAG: Diacylglicerides; TAG: Triacylglicerides; SFA: Saturated fatty acids; MUFA: Monounsaturated fatty acids; PUFA: Polyunsaturated fatty acids; CE: Cholesteryl esters; MAG: Monoacylglicerides.
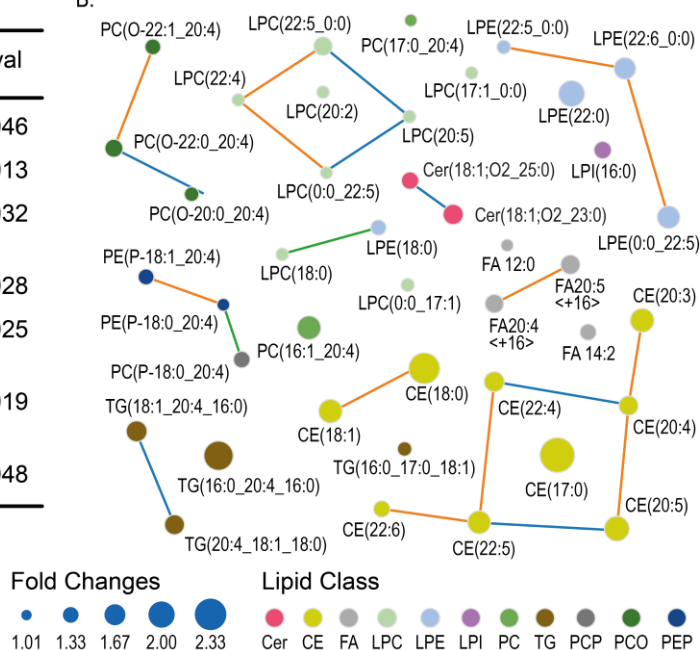
A total of 422 metabolites, of which 47 were significantly at higher levels in CAFs, were identified (Fig. 1A). The volcano plot in Fig. 1A reflects a general trend of raised metabolite levels in CAFs compared to normal fibroblasts. Metabolites showing a significantly different level in disease or normal fibroblasts (p-value <0.05) are compiled in Table S2. Among the significantly more prevalent metabolites, aminoacid tryptophan (Trp) was the only elevated metabolite for a p-value over 0.001. Glutathione (GSH) system was found elevated over 4-fold in cancer, indicating a high detoxification activity, transmembrane transport of organic solutes and/or response to reactive oxygen species[30]. Most of the altered metabolites corresponded to several classes of lipids. To describe metabolic pathways altered in CAFs compared to normal fibroblasts a pathway analysis was computed (Fig. 1B). Indeed, this over-representation analysis pinpoints that Trp/Lys/Phe metabolism and GSH system are affected in CAF population. Among lipid pathways, the analysis highlighted steroid biosynthesis, glycerol(phospho)lipid metabolism and linoleic acid (Fatty acids) metabolism. Altogether indicates that CAFs are more active metabolically and exhibit several alterations towards a lipogenic metabolism.

Considering the metabolite class, one can classify families of metabolites that participate in similar metabolic and physiological pathways. In Fig. 2A, a table summarising metabolite class fold changes significant in CAFs is presented. Both analysed polypeptides of central metabolism and, nucleosides and nucleotides were elevated in the cancer group. This could explain a more active state of CAFs compared to normal fibroblasts. Besides, one could observe elevated levels of different types of lipids in cancer samples including cholesteryl esters, n-acyl ethanolamines (NAE), ceramides and glycerophospholipids. For this reason, we analysed our quantified set of lipids derived from this metabolomics study to compute lipid associations and visualise important modules of the network (Fig. 2B). The nodes are metabolites and they are connected when they can be readily metabolised between them. In general, there are few clusters of interconnected lipids, which means there are several groups of lipids relevant in CAFs with reasonably different biological function. Considering only significant lipids in the network (Fig. 2A), one can observe that hydroxyeicosapentanoic acids (HEPE) and CE are the most relevant in terms of Fold change in the metabolic network. The accumulation of CE agrees with studies that show an abnormal cholesterol metabolism in cancer[31]. Notably, most elevated CE were those esterified to both polyunsaturated 20 and 22 carbon atom of acyl chains (Fig. 2B). Interestingly, HEPE metabolites are oxidised fatty acids (FFAox), associated to fatty acid (FA) mobilisation for energy production in mitochondria. Most of the altered lipids corresponded to glycerophospholipids specifically, lysophosphatidylcholines (LPC) and ether-linked glycerophosphocholines (LPE), which are related to mitochondria well-functioning[32,33]. Anandamine and other NAEs have important anti-inflammatory and anti-cancer properties and, have been associated to inhibition of growth in PCa.

A.

| Metabolite classification	log$_2$ FC	p-val
Ceramides	1.01	0.046
Cholesteryl esters	1.53	0.013
Hydroxyeicosapentanoic acids (HEPE)	1.18	0.032
N-acyl ethanolamines	0.91	0.028
Nucleosides and nucleotides	0.95	0.025
Polipeptides of central carbon metabolism	3.50	0.019
Lysophosphatidylcholines	0.78	0.048

309

310 **Figure 3. Summary of metabolomics study (considering metabolites class) comparing normal and cancer-**
311 **associated fibroblasts isolated from needle biopsies of radical prostatectomy specimens.** A. Comparison of
312 metabolic variations between cancer vs normal fibroblasts. In this table, the classification of metabolites is
313 considered - metabolites with similar chemical characteristics - instead of comparing each individual metabolite.
314 Fold changes of these paired samples were calculated and the significances of the paired t-test are indicated. B.
315 Representation of significant lipid metabolites found in elevated levels in matched-patient samples. Nodes
316 (metabolites) are sized according to their fold change and they are linked according to reaction connection, blue
317 line indicates chain elongation/reduction, green indicates head group modification and, orange indicates
318 saturation/desaturation. Lipid classes are also represented in different colours. Cer: Ceramides; CE: Cholesteryl
319 esters; FA: Fatty acids; LPC: Lysophosphatidylcholines; LPE: Lysophosphatidylethanolamines; LPI:
320 Lysophosphatidylinositols; PC: Phosphatidylcholines; TG: Triacylglicerides; PCP: Ether LPC; PCO: Ether PC;
321 PEP: Ether LPE.

322

323
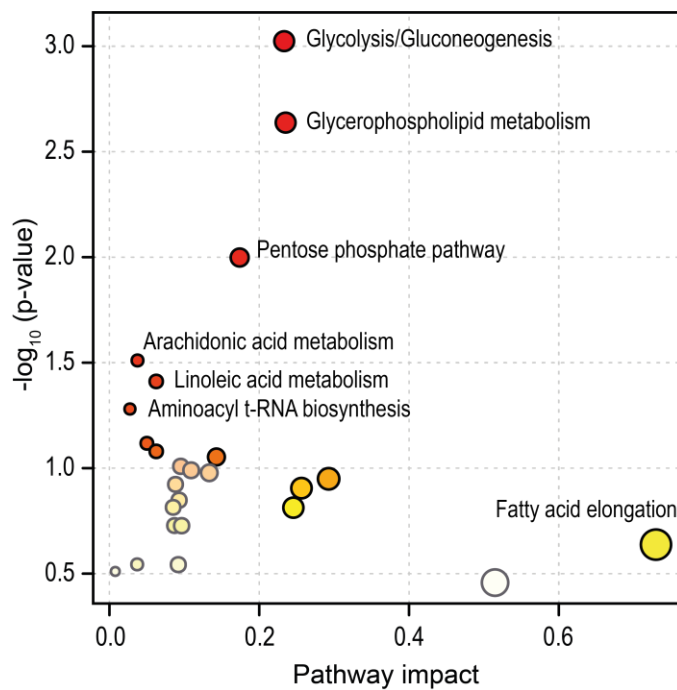
Figure 4. Joint-pathway analysis of significant proteins and metabolites differentially measured in patient-matched normal and cancer-associated stromal fibroblasts. Pathway overrepresentation analysis is depicted as –log10 (p-value) against pathway impact Pathway impact stands for the relative importance of the specific module in the analysed metabolite set. It combines pathway overrepresentation results and centrality measures. Representative pathways were labelled, size of nodes represents pathway impact and their significance ranges from high (in red) towards orange, yellow and white indicating a lower significance.

The integration of *omic* approaches often provides a better understanding of physiological outputs. A proteomic study performed by Webber et al.[8] processed the exact same set of patient-matched needle biopsies utilised in this study. As samples underwent the same experimental procedures, the integration of proteomics and metabolomics data may reveal relevant metabolic flux distributions. In Fig. 3 one can observe a joint-pathway analysis that combines significant variations of the proteome and metabolome comparing CAFs against normal fibroblasts. This analysis computed by Metaboanalyst provides the most relevant (p-value) and affected (Pathway impact) metabolic pathways. This integrated metabolic pathway analysis confirms the rewire of CAFs towards lipogenic metabolism since glycerophospholipid, arachidonic acid, linoleic acid and fatty acid metabolism were highlighted in CAFs (Fig. 3). Moreover, the fact aminoacyl t-RNA biosynthesis was over-represented proposes the elevated levels of aminoacids, nucleosides and nucleotides are related to a higher transcriptomic activity of CAFs. This phenotype is characteristic of cancer-associated tissues[34,35]. Interestingly, it is suggested that glycolysis/gluconeogenesis and pentose phosphate pathways are also over-represented. This feature is also characteristic of highly proliferative cells or tissues, however, there were no significant differences detected in metabolites of those pathways. Hence, it suggests the main central metabolism modifications are described by proteomics data.

Treatment with EVs modifies basal respiration of normal fibroblasts to a CAF-like phenotype

In previous studies with the same treatments and sample preparations, we have shown TGF-β1 associated to EVs was required to induce myofibroblast differentiation of normal fibroblasts, resulting in angiogenic and tumour-promoting characteristics[7]. Also, a proteomics study comparing EV-generated myofibroblasts and those naturally arising *in situ* confirmed their similarity[8]. The activation of myofibroblast-rich stroma is considered by some as a rate-limiting step, essential for cancer progression[7]. Thus, one could expect that the metabolism of normal fibroblast show alterations upon their treatment with EVs.
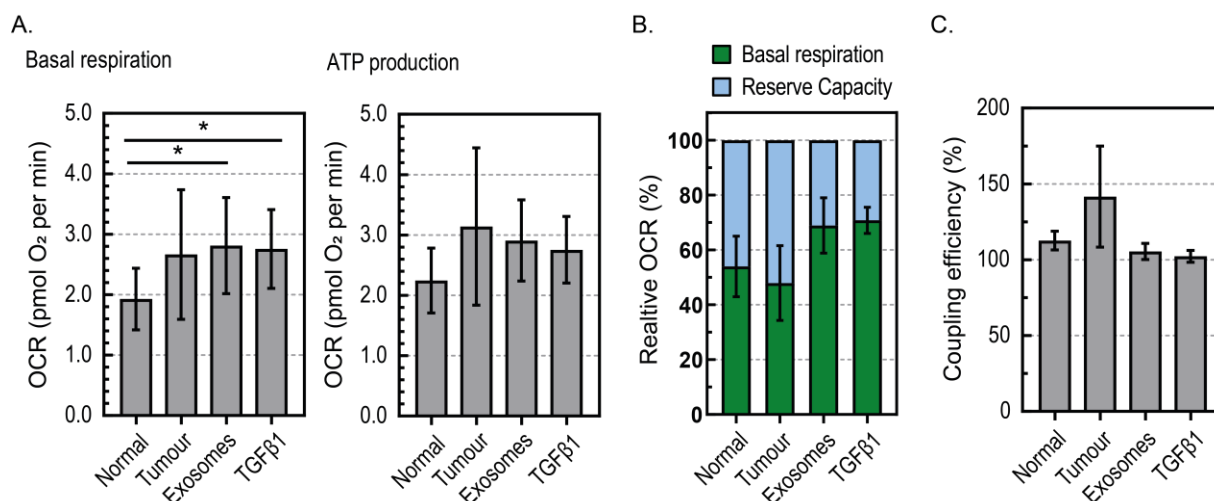
Figure 5. Analysis of mitochondrial stress assay comparing normal- and disease-associated stromal cells, untreated or pre-treated with either exosomes or TGF-β1 (data in Fig. S4). A. OCR relating to basal respiration and specifically to ATP production (mean ± SEM; n=6) was calculated. B. Maximal OCR was established as 100% and OCR apportioned between basal respiration and reserve capacity represented C. Reserve capacity expressed as percentage of basal respiration was calculated (mean ± SEM; n=6) and the efficiency of basal respiration towards ATP production was represented (mean ± SEM; n=6), as coupling efficiency.

For this reason, we have performed glycolytic and mitochondrial stress assays on normal- and disease-derived stromal fibroblasts and also, to normal fibroblasts incubated with soluble TGF-β1 (sTGF-β1) or DU145-derived EVs. Extracellular acidification rate (ECAR) in response to glucose, oligomycin (ATP synthesis inhibitor) and 2-DG (glycolysis inhibitor) was plotted over time to study the glycolytic rate of fibroblasts (Fig S3). Glucose is taken up by the cells and converted to lactate, generating ATP and protons (Fig. S4A). Glycolysis rate do not show a distinctive phenotype when comparing normal fibroblasts to CAFs. Oligomycin was used to inhibit mitochondrial ATP production, shifting energy production to glycolysis, thus revealing the maximal glycolytic capacity of fibroblasts (Fig. S4B). The difference between glycolytic capacity and basal glycolysis rate was defined as the glycolytic reserve (Fig. S4C). The fact glycolytic reserve is neither distinctive comparing normal fibroblasts to CAFs but its value is over 100% suggests that fibroblasts do not uniquely rely on glycolysis to obtain energy. In summary, no significant differences were measured between normal and disease fibroblasts nor upon

374   TGF-β1 or EV treatment regarding their use of glucose to produce energy. The fact no significant
375   differences were described in metabolomics study suggests that the typical glycolytic phenotype of PCa
376   is not readily described in stromal cells.

377   To study mitochondrial metabolism, oxygen consumption rate (OCR) in response to oligomycin (ATP
378   coupler), FCCP (an electron transport chain accelerator), and rotenone (mitochondrial inhibitor) was
379   plotted over time (Fig. S5). Oligomycin inhibits ATP synthesis, so it is utilised to describe the oxygen
380   consumption devoted to ATP synthesis (Fig. 4A) so the coupling efficiency, percentage of
381   mitochondrial respiration for ATP production, could be calculated (Fig. 4C). In Fig. 4B the contribution
382   of basal respiration and reserve capacity (%) is depicted. In general, both basal respiration and ATP
383   production associated to mitochondria tend to increase in CAFs. Moreover, treatment with soluble TGF-
384   β1 or PCa-derived EVs significantly increased basal respiration after 72 hour incubation. This result
385   suggests normal fibroblasts increased their mitochondrial activity with these treatments.

Discussion:

387   The onset of a reactive stroma and the emergence of CAF phenotypes is a feature comprehensively
388   studied in epithelial cancers including PCa [6–8,23,36]. Other PCa studies often compare metabolic
389   alterations between different types of tissues or between low and high grade of disease. In this line, a
390   report using mass spectrometry imaging (MSI) distinguished prostate compartments as well as disease
391   stages in prostate slices from patients. This MSI approach described a distinctive metabolism of
392   prostate stroma and epithelium regions as well as between non-cancerous and cancerous epithelium[11].
393   Many studies evaluated the interaction of PCa with reactive stroma[2,12–17], however, very few describe
394   metabolite levels across different types of stroma[12].

395   Previous reports using the exact same set of matched-patient stroma biopsies confirmed the existence
396   of myofibroblast-like cells within cancer regions of the tissue, by positive staining of both α-SMA, and
397   vimentin, and lack of expression of desmin or the cytokeratins[7,8,23]. Upon stimulation with soluble or
398   EV-associated TGF-β1, differentiation of normal tissue-derived fibroblasts into myofibroblasts was
399   verified by the onset of α-SMA expression[8]. Nonetheless, the cancer-associated stroma was a mixture
400   of varying proportions of fibroblasts and myofibroblasts-like cells[29,37]. One can expect that although
401   such heterogeneity is an important factor in promoting tumour growth it may well hinder our capacity to
402   fully appreciate metabolic alterations arising in CAFs. This metabolomics study has identified some
403   altered metabolites and metabolic pathways, however, it could not definitively distinguish stromal CAFs
404   from normal fibroblasts using a non-supervised PCA approach. Remarkably, adding information about
405   class, a clear tendency was observed in both PLS-DA and OPLS-DA models. Even no significant
406   model was generated; important metabolites were obtained from multivariate analysis that matches
407   with univariate analysis. This highlighted the importance of these metabolites – CE (20:5), Cer
408   (d18:1/25:0), PC (O-22:1/20:4) and PC (P-18:0/20:4) - involved in lipid biosynthesis pathways and

409 pointed them out for further studies with more samples and individuals. In fact, the lack of clear
410 significant results could be due to CAF heterogeneity. Moreover, one should be aware that prior frozen
411 samples can influence metabolomics analyses if they are not well prepared because protein content
412 could affect metabolite recoveries. Since all samples underwent the same procedures, the output in
413 this analysis will not change. In this manuscript, we present metabolomics data comparing normal and
414 cancer-associated fibroblasts from the same patient which is, to our knowledge, the first such
415 exploration. Our multiplatform analysis established elevated levels of several metabolic classes in
416 CAFs. The increment of cholesteryl esters has been already observed in other studies concerning
417 tumour cell lines and samples[31,38], which is on agreement with the upregulated tendency observed (see
418 Fig. 3). Actually, cells make reservoirs of cholesteryl ester that can be transferred to nearby or even
419 distal cells[39]. This might well be the reason myofibroblasts accumulate lipids. Seeking for energy
420 sources, epithelial cancer cells undergo a characteristic rewiring of their metabolism from an extremely
421 unproductive secretion of citric acid to a closed TCA cycle with an elevated mitochondrial respiration.
422 Besides, this rewiring is accompanied with the uptake of circulating lipids[40,41] as well as translocation of
423 lipids from adipocytes[42]. As they consume lipids and specifically, cholesteryl esters[38], supportive CAFs
424 could be fuelling either themselves with these compounds, nearby cancer cells or both. Interestingly,
425 CAFs seem to mobilise *de novo* free fatty acids as energy source; oxidised fatty acid species as HEPE
426 were elevated in cancer-associated fibroblasts. Altogether indicates a consumption of newly built lipids
427 to fuel themselves while building up cholesteryl esters reservoirs, which are easily transported and
428 readily available to transfer it between cells. The fact acyclglycerols were not accumulated in CAFs,
429 although few triacyclglycerols were increased and, acetyl-CoA shows a quite high fold change (Table
430 S2) hints that myofibroblasts preferentially store energy as cholesteryl ester compounds while the
431 oxidation of free fatty acids satisfy their energy needs.

432 The higher metabolic activity suggested by an over-representation of mostly all metabolites measured
433 in this study is further confirmed with elevated levels of nucleosides and nucleotides. When proteomics
434 data is considered the biosynthesis of tRNA aminoacyls is highlighted, which indicates a higher
435 transcriptional and translational activities. Specifically, the increment of NAD suggests a mobilisation of
436 fibroblast reducing power to generate energy in mitochondria or fuel anabolic reactions. Besides,
437 accumulation of ceramides has been comprehensively related to cell differentiation, arrest of cell cycle
438 and apoptosis[43–45]. This class, and concretely Cer(d18:1/25:0), followed the described tendency (see
439 Fig. 3, Table S2 and S3). Newly differentiated fibroblasts exhibit higher levels of ceramidesand
440 possibly, apoptotic mechanisms are counteracted by other compounds as anandamide. Anandamide is
441 an endocannabinoid - detected in higher levels in CAFs - with important anti-inflammatory and anti-
442 cancer properties[46] that demonstrated inhibition of growth in transformed cell lines from human
443 prostate[47,48].

444 A limitation of this study has been the arguably low number of samples available for metabolomics. In
445 contrast, the strength is the collection of donor matched-paired biopsy samples that reflect healthy and
446 disease tissue regions of stroma from the same patient. This type of data draws relevant conclusions

447   of processes and alterations occurring in each patient. Even so, the outcome of this study described
448   metabolic differences with sparse impact in the entire metabolome. Once combined with proteomics
449   data from the exact same set of samples, the outcome acquired a higher relevance in determining
450   important metabolic processes driving myofibroblast differentiation. The integration of significant
451   proteins and metabolites differentially measured in normal and cancer fibroblasts confirmed a major
452   alteration in lipid metabolism. A variation of glycerophospolipids - i.e. PC(O-22:1/20:4) and PC(P-
453   18:0/20:4) - indicates an enrichment of the major membrane type of lipids. Interestingly, this class of
454   lipids have been associated to mitochondria dynamics and well-functioning[32,33]. Although lipids can
455   participate in signalling processes or be used as building blocks, in this study most metabolic
456   alterations point out fuelling or energy storage processes. Major free fatty acid pathways – linoleic and
457   arachidonic - are altered together with an accumulation of cholesteryl esters and few oxidised fatty
458   acids. This indicates a mobilisation of lipids to produce energy but also the production of lipid
459   reservoirs readily available for transport. Moreover, central metabolism pathways –
460   glycolysis/gluconeogenesis and pentose phosphate - are positively altered in CAFs only including the
461   proteome to the analysis. This suggests that as protein queries were the most prominent and
462   overlapped a higher number of pathways compared to metabolites, the output of this integrative
463   analysis could be determined majorly by differences in the proteome.

464   Back in 2016, this proteomics study described many proteins altered in normal and cancer fibroblasts.
465   However, several of those were unique to specific treatments with either sTGF-β1 or EV-associated
466   TGF-β1. For instance, they described a higher presence of Annexin-I, which has a role in regulating
467   VEGF function, in CAFs as well as altered mitochondrial proteins, linking CAFs to mitochondrial
468   rearrangement. In this manuscript, we approached the assessment of metabolic alterations upon
469   sTGF-β1 or EV-associated TGF-β1 treatments by Seahorse stress assays. Even considering the
470   limitation of such assays, where O_2 consumption and pH acidification are recorded over time, the
471   glycolytic rate and oxidative mitochondrial activity of cells was assessed. ECAR informs that glycolytic
472   activity associated to CAFs was not increased. This, together with the fact that the integration of
473   proteomics and metabolomics indicates an alteration in central metabolism, suggests that these
474   pathways were not used in the catabolic but in the anabolic direction. Only basal respiration, in the
475   mitochondrial stress assay, was distinctive when comparing CAFs and normal fibroblasts. Moreover,
476   the treatment with sTGF-β1 and EVs containing TGF-β1 showed a similar outcome. This result links
477   the distinctive metabolic abundances to mitochondrial metabolism. Our metabolomics data offers a
478   plausible explanation because elevated levels of GSH are usually correlated to the presence of ROS
479   due to mitochondrial activity while altered levels of FFAox may indicate the burning of lipids in
480   mitochondria seeking for energy and counteracting ROS. Perhaps a longer stimulation or a higher
481   dose of sTGF-β1 or EVs is required to observe further metabolic alterations associated to cancer in
482   normal fibroblasts. Nonetheless, this data demonstrates that metabolic alterations are related to a
483   higher activity of mitochondria, yet the specific role of cancer-associated EVs and the metabolic
484   mechanisms in stromal differentiation and shift towards its reactive state remain unclear.

Conclusions:

The phenotype of cancer-associated stroma is characteristic and diverge from healthy stroma at both transcriptional and proteomic level. In this manuscript, we discussed metabolic differences measured in patient-matched normal and tumour fibroblasts from prostate adjacent regions. This approach has no precedents in literature. A multiplatform metabolomics analysis of these fibroblasts determined an increased metabolic activity of CAFs. Also, many lipid classes were altered, indicating an enhanced lipogenic metabolism. Lipid reservoir species as cholesteryl ester were measured in CAFs together with building block compounds as lysophosphatidylcholines. Furthermore, alterations in GSH system and oxidised fatty acids suggests the involvement of mitochondria in CAF distinct metabolism. Herewith, this integrated study points out several pathways that may be relevant during fibroblast differentiation.

Previous studies demonstrated the treatment with TGF-β1 or TGF-β1-EVs provoke a response in normal fibroblasts towards myofibroblasts. Thence, we assessed whether EVs containing TGF-β1 or soluble TGF-β1 could trigger a metabolic response in normal fibroblasts. Often, in such differentiation processes, cells desperately look for new energy sources and building blocks in order to sustain growth. According to our metabolomics and Seahorse data, the alternative pathway to obtain energy is not glycolysis. Moreover, Seahorse data shows that basal respiration associated to mitochondria was increased in CAFs so as normal fibroblasts upon TGF-β1 or EV stimulation. In conclusion, one can propose the alteration in metabolic abundances of tumour-associated fibroblasts is driven by an oxygen-dependent metabolism associated to mitochondria. The metabolic status of normal fibroblasts is altered upon EV (and TGF-β1) stimulation and it is associated to mitochondria metabolism. However, the specific mechanisms utilised to trigger different metabolic responses remains undefined.

Acknowledgements:

Funding sources:

Author contributions:

This study was conceptualised and designed by J. W., A. C., F. R. and J.M.F.-P. Experiments were performed by J. W. and F. R. with the supervision of A. C. and J.M.F.-P. Data analysis and original draft writing was done by G. B.-F. with close supervision of O. E. A. All authors critically reviewed, edited and discussed the manuscript; reading and agreeing to the published version of the article.

Conflicts of interest:

The authors declare no conflict of interest.

References:

1. El-Alfy, M., Pelletier, G., Hermo, L. S. & Labrie, F. Unique features of the basal cells of human prostate epithelium. *Microsc Res Tech* **51**, 436–446 (2000).

2. Barron, D. A. & Rowley, D. R. The reactive stroma microenvironment and prostate cancer progression. *Endocr Relat Cancer* **19**, 187–204 (2012).

3. Tessem, M. B. *et al.* A balanced tissue composition reveals new metabolic and gene expression markers in prostate cancer. *PLoS One* **11**, 1–15 (2016).

4. Yanagisawa, N. *et al.* Stromogenic prostatic carcinoma pattern (carcinomas with reactive stromal grade 3) in needle biopsies predicts biochemical recurrence-free survival in patients after radical prostatectomy. *Hum Pathol* **38**, 1611–1620 (2007).

5. Kojima, Y. *et al.* Autocrine TGF-β and stromal cell-derived factor-1 (SDF-1) signaling drives the evolution of tumor-promoting mammary stromal myofibroblasts. *Proc Natl Acad Sci U S A* **107**, 20009–20014 (2010).

6. Webber, J., Steadman, R., Mason, M. D., Tabi, Z. & Clayton, A. Cancer exosomes trigger fibroblast to myofibroblast differentiation. *Cancer Res* **70**, 9621–9630 (2010).

7. Webber, J. P. *et al.* Differentiation of tumour-promoting stromal myofibroblasts by cancer exosomes. *Oncogene* **34**, 319–333 (2014).

8. Webber, J. P. *et al.* Prostate stromal cell proteomics analysis discriminates normal from tumour reactive stromal phenotypes. *Oncotarget* **7**, 20124–20139 (2016).

9. Andersen, M. K., Giskeødegård, G. F. & Tessem, M. B. Metabolic alterations in tissues and biofluids of patients with prostate cancer. *Curr Opin Endocr Metab Res* **10**, 23–28 (2020).

10. Hanahan, D. & Weinberg, R. A. Hallmarks of cancer: The next generation. *Cell* **144**, 646–674 (2011).

11. Andersen, M. K. *et al.* Spatial differentiation of metabolism in prostate cancer tissue by MALDI-TOF MSI. *Cancer Metab* **9**, 1–13 (2021).

12. Andersen, M. K. *et al.* Integrative metabolic and transcriptomic profiling of prostate cancer tissue containing reactive stroma. *Sci Rep* **8**, 1–11 (2018).

13. Carstens, J. L. *et al.* FGFR1-WNT-TGF-β signaling in prostate cancer mouse models recapitulates human reactive stroma. *Cancer Res* **74**, 609–620 (2014).

553 14. Giatromanolaki, A., Koukourakis, M. I., Koutsopoulos, A., Mendrinos, S. & Sivridis, E. The
554   metabolic interactions between tumor cells and tumor-associated stroma (TAS) in prostatic
555   cancer. *Cancer Biol Ther* **13**, 1284–1289 (2012).

556 15. Tyekucheva, S. *et al.* Stromal and epithelial transcriptional map of initiation progression and
557   metastatic potential of human prostate cancer. *Nat Commun* **8**, 1–10 (2017).

558 16. Frankenstein, Z. *et al.* Stromal reactivity differentially drives tumour cell evolution and prostate
559   cancer progression. *Nat Ecol Evol* **4**, 870–884 (2020).

560 17. Richards, Z. *et al.* Prostate Stroma Increases the Viability and Maintains the Branching
561   Phenotype of Human Prostate Organoids. *iScience* **12**, 304–317 (2019).

562 18. Nazarenko, I. *et al.* Cell surface tetraspanin Tspan8 contributes to molecular pathways of
563   exosome-induced endothelial cell activation. *Cancer Res* **70**, 1668–1678 (2010).

564 19. Hood, J. L., Pan, H., Lanza, G. M. & Wickline, S. A. Paracrine induction of endothelium by
565   tumor exosomes. *Laboratory Investigation* **89**, 1317–1328 (2009).

566 20. Ramteke, A. *et al.* Exosomes secreted under hypoxia enhance invasiveness and stemness of
567   prostate cancer cells by targeting adherens junction molecules. *Mol Carcinog* **54**, 554–565
568   (2015).

569 21. Josson, S. *et al.* Stromal fibroblast-derived miR-409 promotes epithelial-to-mesenchymal
570   transition and prostate tumorigenesis. *Oncogene* **34**, 2690–2699 (2015).

571 22. Minciacchi, V. R. *et al.* MYC mediates large oncosome-induced fibroblast reprogramming in
572   prostate cancer. *Cancer Res* **77**, 2306–2317 (2017).

573 23. Shephard, A. P. *et al.* Stroma-derived extracellular vesicle mRNA signatures inform histological
574   nature of prostate cancer. *J Extracell Vesicles* **10**, (2021).

575 24. Mitchell, J. P., Court, J., Mason, M. D., Tabi, S. & Clayton, A. Increased exosome production
576   from tumour cell cultures using the Integra CELLine Culture System. *J Immunol Methods* **335**,
577   98–105 (2008).

578 25. van der Kloet, F. M., Bobeldijk, I., Verheij, E. R. & Jellema, R. H. Analytical error reduction
579   using single point calibration for accurate and precise metabolomic phenotyping. *J Proteome
580   Res* **8**, 5132–5141 (2009).

581 26. Moses, L. E. Matched Pairs *t* -Tests. in *Encyclopedia of Statistical Sciences* (John Wiley &
582   Sons, Inc., Hoboken, NJ, USA, 2006). doi:10.1002/0471667196.ess1551.pub2.

583 27. Pang, Z. *et al.* MetaboAnalyst 5.0: narrowing the gap between raw spectra and functional
584   insights. *Nucleic Acids Res* **49**, W388–W396 (2021).

585 28. Köhler, N., Rose, T. D., Falk, L. & Pauling, J. K. Investigating Global Lipidome Alterations with
586   the Lipid Network Explorer. *Metabolites* **11**, 488 (2021).

587 29. Tuxhorn, J. A., Ayala, G. E. & Rowley, D. R. Reactive stroma in prostate cancer progression.
588   *Journal of Urology* **166**, 2472–2483 (2001).

589 30. Jefferies, H. *et al.* Glutathione. *ANZ J Surg* **73**, 517–522 (2003).

590 31. Tosi, M. R. & Tugnoli, V. Cholesteryl esters in malignancy. *Clinica Chimica Acta* **359**, 27–45
591   (2005).

592   32.   Horvath, S. E. & Daum, G. Lipids of mitochondria. *Prog Lipid Res* **52**, 590–614 (2013).

593   33.   Funai, K., Summers, S. A. & Rutter, J. Reign in the membrane: How common lipids govern
594   mitochondrial function. *Curr Opin Cell Biol* **63**, 162–173 (2020).

595   34.   Owen, J. S., Clayton, A. & Pearson, H. B. Cancer-Associated Fibroblast Heterogeneity,
596   Activation and Function: Implications for Prostate Cancer. *Biomolecules* **13**, 67 (2022).

597   35.   Melchionna, R., Trono, P., Di Carlo, A., Di Modugno, F. & Nisticò, P. Transcription factors in
598   fibroblast plasticity and CAF heterogeneity. *Journal of Experimental & Clinical Cancer Research*
599   **42**, 347 (2023).

600   36.   Webber, J., Yeung, V. & Clayton, A. Extracellular vesicles as modulators of the cancer
601   microenvironment. *Semin Cell Dev Biol* **40**, 27–34 (2015).

602   37.   Franco, O. E. *et al.* Altered TGF-β Signaling in a Subpopulation of Human Stromal Cells
603   Promotes Prostatic Carcinogenesis. *Cancer Res* **71**, 1272–1281 (2011).

604   38.   Yue, S. *et al.* Cholesteryl Ester Accumulation Induced by PTEN Loss and PI3K/AKT Activation
605   Underlies Human Prostate Cancer Aggressiveness. *Cell Metab* **19**, 393–406 (2014).

606   39.   Galbraith, L., Leung, H. Y. & Ahmad, I. Lipid pathway deregulation in advanced prostate cancer.
607   *Pharmacol Res* **131**, 177–184 (2018).

608   40.   Wu, X., Daniels, G., Lee, P. & Monaco, M. E. Lipid metabolism in prostate cancer. *Am J Clin*
609   *Exp Urol* **2**, 111–20 (2014).

610   41.   Kuemmerle, N. B. *et al.* Lipoprotein Lipase Links Dietary Fat to Solid Tumor Cell Proliferation.
611   *Mol Cancer Ther* **10**, 427–436 (2011).

612   42.   Gazi, E. *et al.* Direct evidence of lipid translocation between adipocytes and prostate cancer
613   cells with imaging FTIR microspectroscopy. *J Lipid Res* **48**, 1846–1856 (2007).

614   43.   Condorelli, F., Canonico, P. L. & Sortino, M. A. Distinct effects of ceramide-generating
615   pathways in prostate adenocarcinoma cells. *Br J Pharmacol* **127**, 75–84 (1999).

616   44.   Fiorani, F. *et al.* Ceramide releases exosomes with a specific miRNA signature for cell
617   differentiation. *Sci Rep* **13**, 10993 (2023).

618   45.   Kimura, K., Markowski, M., Edsall, L. C., Spiegel, S. & Gelmann, E. P. Role of ceramide in
619   mediating apoptosis of irradiated LNCaP prostate cancer cells. *Cell Death Differ* **10**, 240–248
620   (2003).

621   46.   De Petrocellis, L. *et al.* The endogenous cannabinoid anandamide inhibits human breast cancer
622   cell proliferation. *Proceedings of the National Academy of Sciences* **95**, 8375–8380 (1998).

623   47.   Schmid, P. C., Wold, L. E., Krebsbach, R. J., Berdyshev, E. V. & Schmid, H. H. O. Anandamide
624   and other *N*-acylethanolamines in human tumors. *Lipids* **37**, 907–912 (2002).

625   48.   Mimeault, M., Pommery, N., Wattez, N., Bailly, C. & Hénichart, J.-P. Anti-proliferative and
626   apoptotic effects of anandamide in human prostatic cancer cell lines: Implication of epidermal
627   growth factor receptor down-regulation and ceramide production. *Prostate* **56**, 1–12 (2003).

628

629